Measurement of the double-differential $W \to \mu\nu$ cross-section at high transverse masses at $\sqrt{s} = 13\,\text{TeV}$ with the ATLAS detector
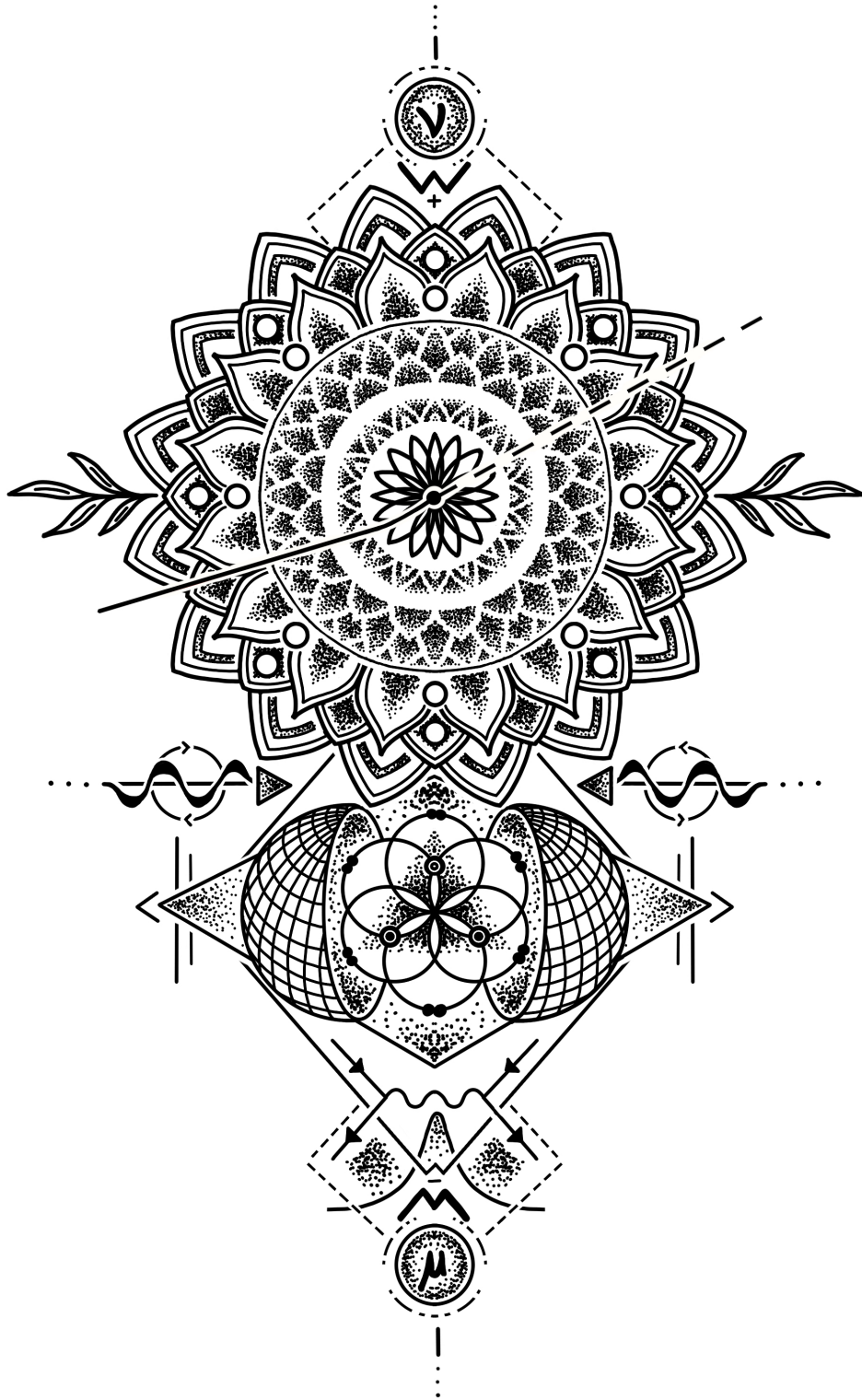
BERGISCHE UNIVERSITÄT WUPPERTAL

Fakultät für Mathematik und Naturwissenschaften

Dissertation

Johanna Wanda Kraus

October 2024

Measurement of the double-differential $W \to \mu\nu$ cross-section at high transverse masses at $\sqrt{s} = 13\,TeV$ with the ATLAS detector
Johanna Wanda Kraus, 2024

Abstract

In this thesis, a measurement of differential charged-current Drell-Yan cross-sections at high transverse masses of the W boson is presented. The decay of the W boson to a muon and a muon-neutrino is studied. Proton-proton collisions at the LHC at $\sqrt{s} = 13\,\text{TeV}$ are the basis of the data taken in 2015-2018 with the ATLAS detector, corresponding to an integrated luminosity of $140\,\text{fb}^{-1}$. Single-differential cross-sections as a function of the transverse mass, covering $m_\text{T}^\text{W} \in [200, 5000]\,\text{GeV}$, are presented. Additionally, double-differential cross-sections as a function of m_T^W and the pseudorapidity of the muon, covering $m_\text{T}^\text{W} \in [200, 2000]\,\text{GeV}$ and $|\eta(\mu)| < 2.4$, are included. Both measurements are performed separately per W-boson charge, and their asymmetry is calculated as well. The number of signal events is unfolded to the Born level. Statistical and systematic uncertainties are included in the results. Overall, the total uncertainty ranges between $\sim 3\,\%$ and $\sim 65\,\%$ in the investigated spectra. Born-level theory predictions from simulations using Powheg +Pythia 8 and Sherpa 2.2.11, respectively, are compared to the unfolded cross-sections. Finally, a combination of the muon-channel measurement performed in this thesis and a parallel electron-channel measurement is presented.

Kurzfassung

In dieser Arbeit wird eine Messung der differenziellen Wirkungsquerschnitte des geladenen Stroms des Drell-Yan-Prozesses bei hohen transversalen Massen vorgestellt. Der Zerfall des W Bosons in ein Myon und ein Myon-Neutrino wird untersucht. Proton-Proton-Kollisionen am LHC bei $\sqrt{s} = 13\,\mathrm{TeV}$ bilden die Grundlage der in den Jahren 2015-2018 mit dem ATLAS-Detektor gesammelten Daten, die einer integrierten Luminosität von $140\,\mathrm{fb}^{-1}$ entsprechen. Es werden einfach-differenzielle Wirkungsquerschnitte als Funktion der transversalen Masse präsentiert, die den Bereich $m_\mathrm{T}^\mathrm{W} \in [200, 5000]\,\mathrm{GeV}$ abdecken. Zusätzlich werden doppelt-differenzielle Wirkungsquerschnitte als Funktion von m_T^W und der Pseudorapidität des Myons, die den Bereich $m_\mathrm{T}^\mathrm{W} \in [200, 2000]\,\mathrm{GeV}$ und $|\eta(\mu)| < 2.4$ abdecken, gemessen. Die Anzahl der Signalereignisse wird auf das Born-Level entfaltet. Statistische und systematische Unsicherheiten sind in den Ergebnissen enthalten. Insgesamt reicht die Gesamtunsicherheit in den untersuchten Spektren von $\sim 3\,\%$ bis $\sim 65\,\%$. Theorievorhersagen aus Powheg +Pythia 8 und Sherpa 2.2.11 Simulationen werden mit den entfalteten Wirkungsquerschnitten verglichen. Abschließend wird eine Kombination der in dieser Arbeit durchgeführten Myon-Kanal-Messung und einer parallelen Elektron-Kanal-Messung vorgestellt.

Contents

VIII

Introduction

What is the world made of? What rules does the universe play by? Is there a fundamental mechanism to explain *everything*? These are questions that have haunted mankind throughout its existence. And still do. In order to have a complete theory representing physics at the smallest scales, the Standard Model of Elementary Particle Physics (SM) was developed. It describes all known elementary particles as well as their interactions, except for gravity, extremely well. Numerous measurements confirm SM predictions to unprecedented precision. Nevertheless, the theory is incomplete as it cannot explain phenomena like dark matter. In the quest for understanding our universe in even greater detail, huge particle accelerators are built allowing to study particles in a controlled environment. The most powerful machine to date is the Large Hadron Collider (LHC) at CERN where protons are brought to collisions at center-of-mass energies of up to $\sqrt{s} = 13.6\,\text{TeV}$. In the collisions, a large variety of particles is produced which will be measured and analyzed using multi-purpose detectors such as the ATLAS detector.

The basis of this dissertation is proton-proton-collision data at $\sqrt{s} = 13\,\text{TeV}$ taken with the ATLAS detector during the LHC Run 2, corresponding to an integrated luminosity of $140\,\text{fb}^{-1}$. The charged-current Drell-Yan (ccDY) process which is characterized by a single W boson produced from quark-antiquark annihilation ($q\bar{q}' \rightarrow W$) is studied. Here, the decay of the W boson to a muon and a muon-neutrino is analyzed ($W \rightarrow \mu\nu$). The objective is to measure the ccDY cross-section at high transverse masses covering a range of $200\,\text{GeV} < m_\text{T}^\text{W} < 5000\,\text{GeV}$. The measurement is performed single-differentially in m_T^W as well as double-differentially in the transverse mass of the W boson and the pseudorapidity of the muon, $m_\text{T}^\text{W} \otimes |\eta(\mu)|$. The unfolded Born-level cross-sections are estimated for both W-boson charges separately and their asymmetry is measured as well.

The ccDY process is a powerful tool for understanding the nature of the proton and partonic interactions. While ccDY cross-sections at the W-boson mass peak are measured precisely at various center-of-mass energies, a measurement at high transverse masses is performed for the first time. Thus, these cross-sections represent a key result themselves allowing for precise comparisons to SM predictions in this phase space. Furthermore, the cross-sections will contribute to a more complete and precise understanding of the substructure of the proton. Direct sensitivity to parton distribution functions of quarks and antiquarks in the region of high momentum fraction x is expected. Additionally, by measuring up to $m_\text{T}^\text{W} = 5\,\text{TeV}$ the energy frontier accessible at the LHC is approached and physics beyond the SM can be probed using an effective field theory [1]. Finally, the measurement is sensitive to the running electroweak coupling at high energy scales [2].

At first, the thesis is placed in the theoretical and experimental context of modern particle physics. This includes an overview of the SM and of W-boson production in proton-proton collisions in Chapter 1. Next, the experimental setup is introduced, covering the LHC and the ATLAS detector in Chapter 2. The analyzed dataset as well as simulations of all relevant processes are described in Chapter 3. The following Chapter 4 details how particles are identified and reconstructed within the detector. The event selection specific to this measurement, along with the single- and double-differential measurement binnings, is motivated in Chapter 5. A key aspect of this dissertation is the modeling of background processes, with particular attention to the data-driven multijet background estimation, as described in Chapter 6. In Chapter 7, the modeling of all processes is evaluated by comparing distributions in data with prediction in dedicated control observables. Next, Chapter 8 focuses on the unfolding of the differential cross-sections, detailing the method of Iterative Bayesian Unfolding as well as its optimization and validation. Chapter 9 provides a breakdown of the different sources of uncertainty affecting the measurement. Finally, the single- and double-differential unfolded cross-sections, along with their charge asymmetries, are presented in Chapter 10. Various theory predictions from $W \to \mu\nu$ Monte-Carlo simulations are compared to the results. Finally, a combination of the cross-sections from the muon-channel measured in this thesis and a parallel electron-channel measurement is presented in Chapter 11.

1. Theoretical and experimental context

Humanity's understanding of nature's elementary building blocks has come a long way since the postulation of *atoms*, indivisible components, by Democritus. A fundamental cornerstone was the discovery of the *electron* by Thompson in 1897 [3], a particle still considered elementary today. Additionally, Thompson was the first to shape the picture of a substructure inside atoms using his *plum-pudding model* from 1904 [4], which depicts negatively charged electrons as *plums* inside a *pudding* of positive charge. The concept of an inner structure inside atoms was reinforced and confirmed by Rutherford shortly after, by interpreting the scattering of alpha particles on gold atoms in a way that the atom must have a small dense *nucleus* [5]. His basic idea of performing a scattering experiment to inquire a substructure is an experimental technique that proved to be crucial in nuclear and particle physics, culminating in modern collider experiments. Rutherford is regarded as the discoverer of the *proton*. Together with the discovery of the *neutron* by Chadwick in 1932 [6], this simple set of three particles (electron, proton and neutron) was able to explain the structure and arrangement of atoms to great detail, summarized in the *periodic table of elements*. Smaller constituents within the proton, called *quarks*, were postulated by Gell-Man [7] in the 1960s. They were experimentally underlined by *deep-inelastic-scattering* (DIS) experiments at the *Stanford Linear Accelerator Center* (SLAC) and the *Deutsches Elektronen-Synchrotron* (DESY) in the late 1960s to early 1980s [8–10], where high-energy electrons were used to probe the inside of the proton. Eventually, this culminated in our current understanding of elementary particle physics with the *Standard Model of Elementary Particle Physics* (SM) as its central piece to describe the fundamental building blocks of our universe.

Even though the SM is well-established and was experimentally validated in an unprecedented way, it is still incomplete and not able to explain everything. Thus, this dissertation plays its part in expanding today's knowledge of particle physics. This Chapter aims to place the work presented into the theoretical and experimental context of modern particle physics. First, an overview of the SM is given in Section 1.1, including its key constituents and concepts, as well as its successes and limitations. It is followed by an introduction into proton-proton collisions in Section 1.2, including the discussion of parton distribution functions as well as the key process of this thesis, the charged-current Drell-Yan process at high transverse masses. Finally, the importance of measuring its cross-section is motivated and opportunities for future interpretations are conferred in Section 1.3.

1.1. The Standard Model of Elementary Particle Physics

The SM [11] is a relativistic, renormalizable *quantum field theory* (QFT) built around quantum fields whose excitations are identified with particles. It was developed during the 1960s to 1970s and describes all elementary particles as well as their interactions, covering three fundamental forces: *strong*, *weak* and *electromagnetic* (EM). This Chapter gives a general introduction into the key concepts of the SM relevant for particle physics experiments.

Throughout this dissertation, natural units are used, i.e. the *speed of light c* as well as the reduced *Planck constant* $\hbar$ are set to one. As a consequence, energies, masses and momenta are given in units of energy, usually *electron volts* $(eV)^{1}$. Furthermore, charges are presented as multiples of the *elementary electric charge e*.

1.1.1. Overview of fundamental particles and interactions

An overview of all particles in the SM, including their key properties, is shown in Figure 1.1. The SM is built from two kinds of particles, distinguished by their spin quantum number: *fermions* with a spin of 1/2 and *bosons* with an integer spin. The former describe matter particles and the latter are responsible for interactions.

Matter particles All matter is built from fermions. The SM contains twelve unique fermions categorized into two classes, *quarks* and *leptons*. There are three *up-type* quarks with an electric charge of +2/3 (*up*, *charm* and *top*) and three *down-type* quarks with an electric charge of −1/3 (*down*, *strange* and *bottom*). Quarks carry an additional *color charge*, which is unique to them in the group of fermions. They are arranged in three generations, based on increasing particle masses. All known matter is built from first-generation quarks, i.e. up and down quarks, which are the lightest ones. Quarks of higher generations can be produced for example in particle accelerators. However, these are not stable and decay within a very short time span.

The second kind of fermions are leptons which, again, can be separated into two categories. Firstly, the *charged leptons* with a charge of −1 include the *electron* (*e*), a long-known key component of our stable matter. It has two heavier, unstable copies called *muon* (μ) and *tau* (τ). Besides their increasing mass with a higher generation, all three particles show analogous properties and behavior, a concept known as *lepton universality*. The group of leptons is completed by electrically neutral *neutrinos* (ν), where each is partnered with one charged lepton (ν_e, ν_μ, ν_τ). A distinct feature of neutrinos is that they are massless according to the SM. However, this assumption was experimentally disproved [13], exhibiting one of the limitations of the SM in our current understanding. Lastly, each fermion has a corresponding *antiparticle*, which is a particle with the same mass and features as the original one but with an opposite charge.

---

[1] 1 eV is defined by the amount of kinetic energy gained by an electron accelerated by an electric potential difference of 1 V in vacuum.
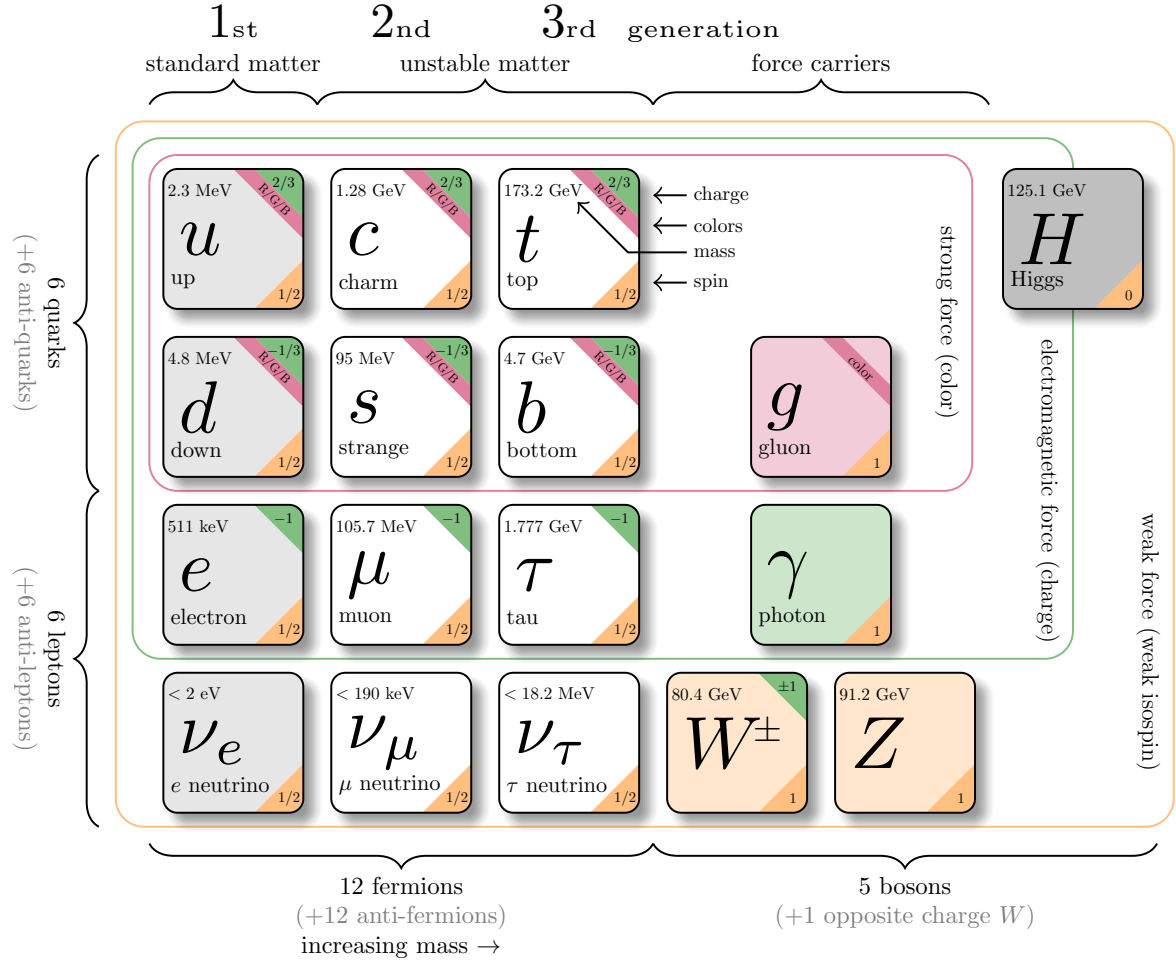
Figure 1.1.: Schematic overview of all elementary particles of the SM including their properties and interactions. Figure adapted from [12].

Fundamental interactions The SM is a QFT where interactions are mediated by *gauge bosons* which are a consequence of underlying gauge symmetries. It is a common concept in physics that symmetries allow for insights into the underlying structure of physical theories and lead to conservation laws [14]. The SM is invariant under the

$$SU(3)_C \times SU(2)_L \times U(1)_Y$$

symmetry incorporating the three fundamental interactions, strong, weak and EM. All interactions are identified with gauge bosons with distinct properties, dedicated quantum numbers and act only on specific particles. As a result, the ranges and relative strengths of the three interactions are very different. An overview is given in Table 1.1. The EM interaction is mediated by the *photon* (γ), a massless, neutral particle that couples to all particles carrying an electric charge. Thus, no self-coupling of the photon is possible, resulting in an infinite range of the EM interaction. The characteristic gauge bosons of the weak interaction are three massive particles, the neutral *Z boson* and the charged

Table 1.1.: Fundamental interactions in the SM including their range and relative strength at a distance of 1 fm [11]. Additionally the mediating boson, including information whether they are massive and electrically or color charged, and the associated quantum numbers and symmetries are given.

Interaction	Range	Relative strength	Mediator (mass, charge, color)	Quantum number	Symmetry
Electro-magnetic	∞	$\frac{1}{137}$	Photon (✗, ✗, ✗)	Electric charge Q	$U(1)_Q$
Weak	$\sim 10^{-18}$ m	10^{-6}	$W^\pm/Z$ boson (✓, ✓/✗, ✗)	Weak isospin I_3	$SU(2)_L$
Strong	$\sim 10^{-15}$ m	1	Gluon (✗, ✗, ✓)	Color charge C	$SU(3)_C$

W^+ and W^- *bosons* with a charge of ± 1 respectively. Due to the mass of the mediating boson, the strength of the weak force is small compared to the other two forces. The corresponding quantum number is the *weak isospin*, which is non-zero for all fermions, i.e. the weak interaction is the only one of the three to couple to all fermions. Lastly, the strong interaction is governed by massless and electrically neutral *gluons* which couple to the color charge. Thus, the only fermions taking part in strong interactions are quarks. Additionally, gluons are able to self-interact since they carry a color charge themselves. As a result, the strength of the strong force increases with distance, which is a unique characteristic among the interactions.

The last missing piece in the SM is the *Higgs boson*, a massive and electrically neutral particle with a spin of zero, making it the only scalar particle in the SM. It emerges from the *Higgs mechanism* by which particles in the SM obtain their masses. Features of all three fundamental forces, the unification of the EM and weak force as well as the Higgs mechanism are detailed in the following paragraphs.

1.1.2. The strong interaction

The theoretical foundation of the strong interaction is given by *Quantum Chromo Dynamics* (QCD), a gauge theory based on the non-abelian symmetry group $SU(3)_C$. In general, a special unitary group of degree n, written as $SU(n)$, consists of complex-valued, unitary $n \times n$ matrices with a determinant of one. The generators of the $SU(3)_C$ group are the eight 3×3 Gell-Mann matrices [11]. The subscript C indicates the color charge as the characteristic quantum number here. There are three color charges usually represented by *red* (r), *blue* (b) and *green* (g) plus corresponding anticharges ($\bar{r}$, $\bar{b}$, $\bar{g}$). Quarks carry a color charge and antiquarks an anticolor charge. Conversely, gluons carry a combination of a charge and anticharge based on the *color octet*

$$r\bar{g}, r\bar{b}, g\bar{r}, g\bar{b}, b\bar{r}, b\bar{g}, \frac{1}{\sqrt{2}}(r\bar{r} - g\bar{g}), \frac{1}{\sqrt{6}}(r\bar{r} + g\bar{g} + b\bar{b}).$$

Hence, in theory, eight gluons different by color state exist. However, as they cannot be distinguished experimentally, the strong interaction is associated with one gluon in common jargon.

A very distinct characteristic of the strong force arises from the fact that self-couplings of the mediating particles are possible: the strong force increases with distance. This feature is commonly represented by the *running* of the *strong coupling constant* α_s. A physical process is usually defined at a certain energy scale Q where Q can be illustrated as the momentum transfer of the interaction. Starting from a certain reference scale, called *renormalization scale* μ_R, the strong coupling constant can be extrapolated perturbatively to any given scale via [11]

$$\alpha_s(Q^2, \mu_R^2) = \frac{\alpha_s(\mu_R^2)}{1 + \alpha_s(\mu_R^2)\frac{11n_c - 2n_f}{12\pi}\ln(\frac{Q^2}{\mu_R^2})}. \tag{1.1}$$

Here, n_c corresponds to the number of distinct color charges and n_f to the number of quark flavors accessible, i.e. quarks with a mass smaller than the energy scale. However, the perturbative approach is only applicable for small values of α_s. This is not given below a certain energy scale threshold, called *infrared cut-off scale* Λ_{QCD}.

Figure 1.2 illustrates the shape of the strong coupling constant including the scales Λ_{QCD}^2, μ_R^2 and any given scale μ^2. The energy scale of a process is inversely related to the distance between particles, i.e. small distances can be identified with large energies and vice versa. Two peculiarities of the strong interaction can be deduced: *asymptotic freedom* and *quark confinement*. At short distances (high energies), e.g. below the radius
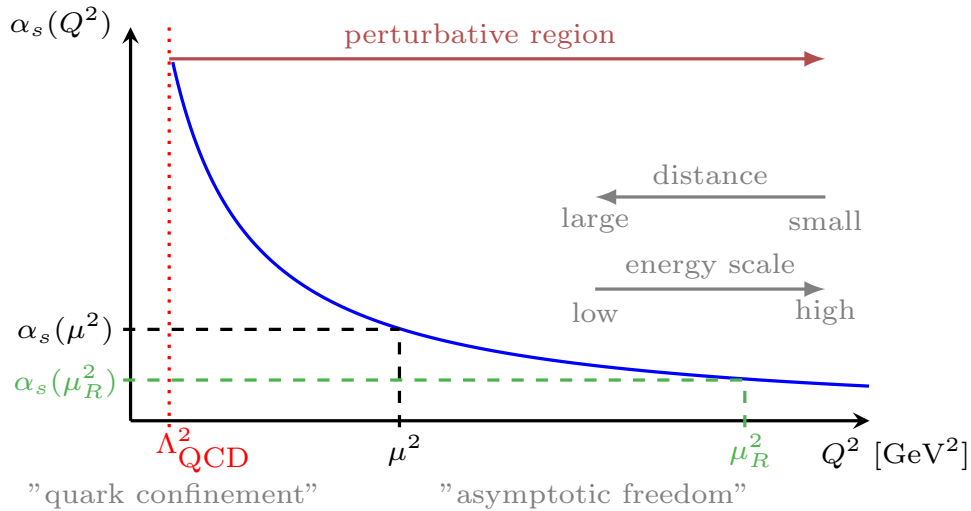
Figure 1.2.: The dependence of the strong coupling constant α_{S} on the energy scale Q^2, including the infrared cutoff scale Λ_{QCD}, the renormalization scale μ_R and an arbitrary scale $\mu^2 > \Lambda_{\mathrm{QCD}}^2$.

of the proton ($\sim 10^{-15}\,$m), the strong force is modest, as α_s approaches zero. This property, known as asymptotic freedom, allows physicists to study quarks and gluons as nearly free particles in high-energy collisions. However, at large distances (low energies), the strength of the strong force increases drastically. An effect called quark confinement states that no isolated colored particles exist. It can be illustrated as follows: When quarks move apart from each other, the force between them increases, reaching a point where it is energetically favorable to create new quark-antiquark pairs rather than having isolated quarks. In a process called *hadronization* bound, color-neutral (*white*) states are formed, known as *hadrons*. They cover two kinds of particles: *mesons* composed of a quark-antiquark pair (color+anti-color=white) and *baryons* consisting of three quarks with different colors (red+blue+green=white). The most famous representatives of baryons are the proton and the neutron.

1.1.3. The electroweak interaction

Historically, the electromagnetic and weak interactions were described by two distinct theories. However, they were unified to the *electroweak theory* in the 1960s by Glashow, Salam and Weinberg [15–18]. The following paragraphs are dedicated to the two separate interactions at first and their unification at last.

The electromagnetic interaction Electromagnetism plays a fundamental role in our everyday lives, describing phenomena like light, electricity or magnetism. Given its accessibility, the EM interaction was studied extensively long before the strong or electroweak, with classical electromagnetism culminating in Maxwell's equations in the 1860s [19]. Also in the realm of particle physics, dealing with relativistic objects, this interaction plays an essential role. The theory was extended to a quantum field theory called *Quantum Electro Dynamics* (QED) based on an abelian gauge symmetry group $\mathrm{U}(1)_\mathrm{Q}$. The mediator of the EM interaction is the massless, neutrally charged photon which couples to all particles with an electrical charge Q. Similar to the strong coupling constant α_s, the EM coupling constant α_{em} is energy-dependent ('running'). However, its strength decreases with distance, approaching the *fine-structure constant* $\alpha_{em} = \frac{e^2}{2\varepsilon_0 hc} \approx {}^1\!/_{137}$ where ε_0 is the vacuum permittivity. This energy dependency can be understood illustratively by an effect called *charge screening* where fermion-antifermion pairs are spontaneously produced and annihilated around the original particle yielding a smaller effective charge.

The weak interaction The theoretical foundation of the weak interaction is the non-abelian $\mathrm{SU}(2)_\mathrm{L}$ group with three 2×2 matrices, closely related to the Pauli matrices, as its generators. The weak isospin I is the conserved quantum number, usually its third component I_3 is given. All fermions carry a weak isospin, thus, they all are able to interact weakly. As a result, the weak interaction is the only interaction in which

neutrinos take part. It is governed by the massive Z^0 and $W^\pm$ bosons[2] which have a weak isospin themselves ($I_3 = 0, \pm 1$), allowing for triple- and quartic-gauge-couplings as well. Interactions propagated by a Z boson are called *neutral currents* (*nc*) and by W bosons *charged currents* (*cc*). In general, nc interactions do not change the flavor of fermions, meaning the Z boson couples to a fermion and its corresponding anti-fermion, or is emitted without changing the fermion flavor. On the contrary, the cc interaction is the only interaction in the SM that allows the conversion of one fermion flavor to another. The radioactive beta decay is a famous example where a down quark within the neutron is converted to an up quark, forming a proton under the emission of a W^- boson.

The weak interaction is the only one known to violate *parity*, the symmetry under mirroring all space vectors, as proven first in the Wu experiment in 1956 [20]. The concept of *chirality* ('handedness') is introduced, differentiating between *left-handed* and *right-handed* particles. In the limit of a massless particle, which must be traveling at the speed of light, the *helicity*, which can be interpreted using the particle's spin, is equal to the chirality. For left-handed particles, the spin is oriented opposite to its direction of motion and for right-handed ones they align. Massive particles combine both chiralities depending on their velocity v via $1/2(1 \pm \frac{v}{c})$. Under parity transformation, left-handedness is transformed into right-handedness. The parity violation in the weak interaction can be understood by the fact that the *cc* interaction couples only to left-handed particles. Mathematically, this is formulated using weak isospin doublets consisting of only left-handed fermions

$$\psi_L^{\text{lepton}} = \begin{pmatrix} \nu_e \\ e \end{pmatrix}_L, \begin{pmatrix} \nu_\mu \\ \mu \end{pmatrix}_L, \begin{pmatrix} \nu_\tau \\ \tau \end{pmatrix}_L, \quad \psi_L^{\text{quark}} = \begin{pmatrix} u \\ d' \end{pmatrix}_L, \begin{pmatrix} c \\ s' \end{pmatrix}_L, \begin{pmatrix} t \\ b' \end{pmatrix}_L \quad \text{with } I_3 = \begin{pmatrix} +1/2 \\ -1/2 \end{pmatrix}.$$

They consist of fermions of the same generation with the upper and lower entry being different by exactly $1e$. However, the right-handed fermions are singlets in the SM

$$\psi_R^{\text{lepton}} = e_R, \mu_R, \tau_R, \qquad \psi_R^{\text{quark}} = u_R, d_R, c_R, s_R, t_R, b_R \qquad \text{with } I_3 = 0.$$

As they have a weak isospin of zero, they do not take part in purely weak interactions. Nevertheless, they still interact via the strong and the EM force. It shall be highlighted that no right-handed neutrinos are part of the SM. This whole paragraph can be transferred to antiparticles by switching left- and right-handedness, e.g. *cc* interactions involve right-handed antifermions.

The down-type quarks denoted as d', s' and b' in the doublets above indicate them as the *weak eigenstates*. They are defined by a mixing of the *mass eigenstates* d, s and b via the *Cabibbo-Kobayashi-Maskawa* (CKM) *matrix* [21]

$$\begin{pmatrix} d' \\ s' \\ b' \end{pmatrix} = V_{\text{CKM}} \begin{pmatrix} d \\ s \\ b \end{pmatrix}, \ |V_{\text{CKM}}| = \begin{pmatrix} |V_{ud}| & |V_{us}| & |V_{ub}| \\ |V_{cd}| & |V_{cs}| & |V_{cb}| \\ |V_{td}| & |V_{ts}| & |V_{tb}| \end{pmatrix} \approx \begin{pmatrix} 0.974 & 0.225 & 0.004 \\ 0.225 & 0.973 & 0.041 \\ 0.009 & 0.040 & 0.999 \end{pmatrix}.$$

$$(1.2)$$

---

[2]For shortness, the charge superscript of the bosons will be dropped whenever not explicitly required.

The entries of the matrix cannot be predicted from theory but were determined experimentally [11]. It is worth mentioning that the entries are not independent but can be parametrized by a CP-violating phase and three Euler angles in total. The probability for a transition of quark i to quark j via the exchange of a W boson is proportional to the given element $|V_{ij}|^2$. The diagonal elements of the CKM matrix are close to unity but there are small non-zero off-diagonal elements. Thus, cross-generational transitions are generally possible (e.g. $t \to Wd$), nevertheless highly suppressed. For leptons, weak eigenstates coincide with mass eigenstates and, therefore, no transitions between generations are allowed in the SM.

Electroweak unification Experiments involving Z bosons showed inconsistencies between the neutral particle emerging from the $\mathrm{SU(2)_L}$ symmetry group and the physical Z boson. For instance, it was observed that the physical Z boson couples to both, left- and right-handed particles [11]. The solution was a unification of the weak and EM theories without compromising their distinct features. Again, the basis is a symmetry group, here $\mathrm{SU(2)_L \times U(1)_Y}$, which is closely related to the weak and EM theories described above. A new conserved charge is introduced, the *weak hypercharge* $Y = 2(Q - I_3)$, defined as a combination of the electric charge and the weak isospin. As usual, this symmetry implies the existence of four associated (massless) gauge bosons. These are the triplet W_1, W_2 and W_3 associated with the weak isospin as well as the singlet B coupling via the weak hypercharge. The physical W and Z bosons, as well as the photon, are composed via linear combinations of these four. On the one hand, the charged weak gauge bosons are given by a purely weak combination, i.e. arising solely from the $\mathrm{SU(2)_L}$ symmetry:

$$W^{\pm} = \frac{1}{\sqrt{2}}(W_1 \pm W_2). \tag{1.3}$$

On the other hand, for neutral-currents, there is a mixing between the two symmetry groups via the so-called *weak mixing angle* θ_w, a central parameter in the SM,

$$\begin{pmatrix} \gamma \\ Z^0 \end{pmatrix} = \begin{pmatrix} \cos\theta_w & \sin\theta_w \\ -\sin\theta_w & \cos\theta_w \end{pmatrix} = \begin{pmatrix} B \\ W_3 \end{pmatrix}. \tag{1.4}$$

Given this mixing, the experimental sightings of a coupling of the physical Z boson to right-handed particles can be understood.

1.1.4. The Higgs mechanism

The formalism of the SM discussed so far exhibits one major contradiction to observations of nature: all gauge bosons, as well as the fermions, would need to be massless in order to not break the underlying gauge symmetries. The missing piece of the SM puzzle was the introduction of *spontaneous symmetry breaking* and the Brout-Englert-Higgs

mechanism, commonly abbreviated to *Higgs mechanism* [22]. A complex scalar field, the Higgs field, is introduced, which consists of the following SU(2) doublet

$$\Phi = \begin{pmatrix} \phi^+ \\ \phi^0 \end{pmatrix} = \begin{pmatrix} \phi_1 + i\phi_2 \\ \phi_3 + i\phi_4 \end{pmatrix} \tag{1.5}$$

where ϕ^0 and ϕ^+ are neutral and positively charged fields, respectively. The doublet is subject to the *Higgs potential*, which includes two parameters, $\lambda > 0$ and $\mu^2 < 0$,

$$V(\Phi) = \mu^2 \Phi^\dagger \Phi + \lambda (\Phi^\dagger \Phi)^2. \tag{1.6}$$

The potential is illustrated in Figure 1.3 as a function of the real and imaginary part of a single-scalar field, exhibiting a shape that is famously compared to a *mexican hat*. It is characterized by an unstable maximum at $\Phi = 0$ and a stable but degenerate set of non-zero minima, as indicated by the red dashed circle in Figure 1.3 with radius v fulfilling $v^2 = -\mu^2/\lambda$. The minimum is identified with the physical vacuum state and v is called *vacuum expectation value* (VEV). It is a fundamental parameter of the SM and determined experimentally to about $246 \, \text{GeV}$ [23]. The concept of spontaneous symmetry breaking is closely related to the degeneration of the minimum here. It refers to a general QFT phenomenon where the Lagrangian is invariant under symmetry but the vacuum of the theory is not. By choosing one definite minimum of the infinite set of minima here, the symmetry is spontaneously broken.

A minimum is chosen in such a way that W and Z bosons acquire mass. Their masses can be expressed via the VEV v, the coupling g and the weak mixing angle θ_w as

$$m_W = \frac{gv}{2} \quad \text{and} \quad m_Z = \frac{gv}{\cos \theta_w}. \tag{1.7}$$

Furthermore, one additional new particle emerges, as the excitation of the Higgs field: the *Higgs boson* with a mass of $m_H = \sqrt{\lambda v/2}$. Lastly, fermion masses can be understood by the couplings of fermions to the Higgs field, called Yukawa couplings y_f. The relation to the fermion mass is given by $m_f = y_f v/\sqrt{2}$ implying proportionality between the fermion mass and the coupling strength.
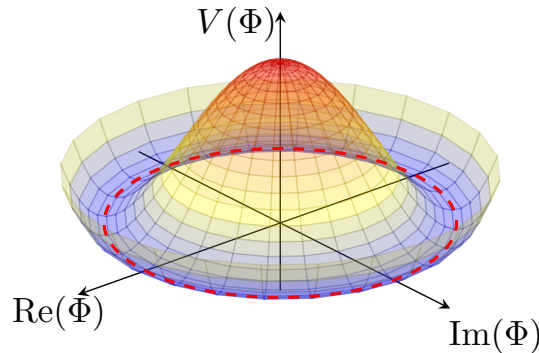
Figure 1.3.: The Higgs potential, where the red dashed line represents the minimum of the potential.

1.1.5. Predictions with the Standard Model

The SM is not limited to predicting the phenomenology of elementary particle physics *qualitatively*. Instead, the mathematical framework is also capable of making precise and accurate *quantitative* predictions of the production, interaction and decay of particles. Usually, the probability per unit area for a specific interaction to happen is described by a *cross-section* σ. It is proportional to a transition rate $\Gamma_{i \to f}$ by taking the flux of initial-state particles ϕ into consideration, $\sigma = \Gamma/\phi$. Thus, a cross-section has the dimension of an area[3]. In general in quantum mechanics, the description of transitions from initial state i to final state f is based on *matrix element calculations*. Using *Fermi's golden rule*, broken down to its most fundamental form as $\Gamma_{i \to f} = 2\pi |\mathcal{M}|^2 \times$ (phase space) [11], the calculated cross-section will be proportional to the absolute matrix element $\mathcal{M}$ squared

$$\sigma \propto |\mathcal{M}|^2. \tag{1.8}$$

Often, the transition $i \to f$ is not limited to one option and, for each one, a single matrix element needs to be calculated. Finally, the total matrix element is given by their sum. Thereby, it is important to take interferences into account, for instance in the case of two matrix elements $\mathcal{M}_1$ and $\mathcal{M}_2$,

$$|\mathcal{M}|^2 = |\mathcal{M}_1 + \mathcal{M}_2|^2 = |\mathcal{M}_1|^2 + |\mathcal{M}_2|^2 + \underbrace{\mathcal{M}_1^* \mathcal{M}_2 + \mathcal{M}_1 \mathcal{M}_2^*}_{\text{interference term}}. \tag{1.9}$$

In particle physics, a powerful technique is the usage of *Feynman diagrams* [24]. They serve as a pictorial representation of a given process and, additionally, they are the foundation for matrix element calculations based on fixed *Feynman rules*. Each diagram corresponds to one matrix element. Diagrams are constructed from a set of basic building blocks. Gauge bosons are depicted by curved lines and fermions by straight lines with an arrow indicating whether it is a particle or antiparticle[4]. Interactions between particles, where multiple lines intersect, are called *vertices*. Purely internal lines are identified as *propagators*. Each component is associated with certain rules, making the matrix element calculation straightforward once the diagram is drawn. Feynman diagrams can be constructed from any combinations of these building blocks, however, all quantum numbers (e.g. charge, weak isospin, lepton flavor number, ...) must be conserved at each vertex.

Figure 1.4(a) shows a general example of a Feynman diagram of the scattering of two fermions under the exchange of a boson. In order to calculate the full transition amplitude, all possible Feynman diagrams need to be considered. This comes with one shortcoming: in theory, there is an infinite number of diagrams, since an infinite number of internal particle *loops* can occur, next to *legs*, the radiation of a particle. Examples for a QED loop as well as a gluon loop in addition to initial state QCD radiation can be found in Figure 1.4(b) and Figure 1.4(c), respectively.

---

[3]Usually given in multiples of $1 \, \text{barn} = 1 \, \text{b} = 10^{-28} \, \text{m}^2$.

[4]In this dissertation, the convention is used that time flows from left to right.
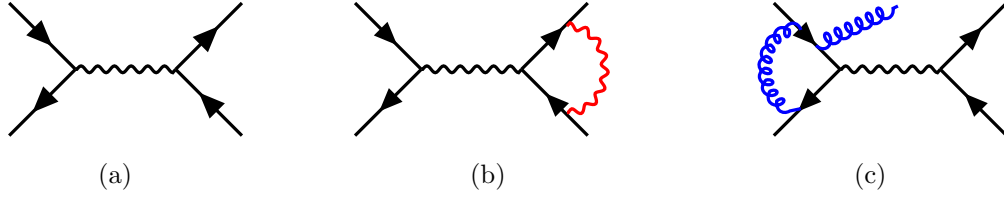
Figure 1.4.: General example of a Feynman diagram at (a) leading order, (b) including a virtual QED loop correction and (c) including a QCD loop correction and a QCD real emission.

However, Feynman rules state that each vertex introduces one factor of the coupling strength $\sqrt{\alpha}$ of the corresponding interaction to the matrix element $\mathcal{M}$. In QFT, a key approach to make reasonable approximations are *perturbative calculations* which utilize the fact that the coupling strength is small. The sum of matrix elements (taking into account interference as in Equation 1.9) and, thus, the total cross-section σ can be expanded to a certain order in α via

$$\sigma = \underbrace{\sigma_0}_{\text{LO}} + \underbrace{\sigma_1 \cdot \alpha}_{\text{NLO}} + \underbrace{\sigma_2 \cdot \alpha^2}_{\text{NNLO}} \underbrace{+ \; ...}_{\text{higher orders}} \quad . \tag{1.10}$$

The *tree level*, including no loops/legs, is referred to as *leading order* (LO), the following terms as *next-to-leading* order (NLO[5]) and *next-to-next-to-leading* order (NNLO) in the coupling strength α. Assuming a small coupling strength, higher-order contributions are eventually negligible. Since coupling strengths are generally energy-dependent, the perturbative ansatz is not always applicable, e.g. in the case of large values of α_s at small energy-scales. In the calculation of higher orders, divergences may appear which are addressed using *regularization* and *renormalization* techniques. For the former, a cut-off scale is imposed to prevent integration up to infinite momenta. For the latter, divergences can be absorbed via the redefinition of a physical parameter. An example is α_s evolved around a well-chosen renormalization scale μ_R. It should be noted that, as a result, any fixed order calculation will depend on this scale.

1.1.6. Experimental validation and limitations of the SM

The SM shows unprecedented agreement with observations of nature. Nevertheless, a few tensions were discovered. Both, validation and limitation of the SM, are discussed in the following paragraphs, giving a subjective selection of examples.

Experimental validation In a multitude of experiments targeting all kinds of particles, kinematic phase spaces or energy scales, the SM has been tested thoroughly over the

---

[5]An NLO cross-section includes the LO and NLO terms, to be precise in nomenclature.

last half a century. The result is overwhelming support in the vast majority of experiments. All particles predicted by the SM have been observed directly in experiments. A summary of various particles including the years of their theoretical prediction and experimental discovery is shown in Figure 1.5. Most particles were theorized in the 1960s and 1970s and experimentally observed in the following decades. The final piece was the experimental discovery of the Higgs boson at the Large Hadron Collider at CERN via the two independent experiments ATLAS and CMS [25, 26] in 2012. The remarkable power of the SM should be stressed here, as it is not only able to explain observed phenomena but is also capable of making accurate predictions far outside the experimental reach at that time. Furthermore, experiments conclusively underlined the number of fermion generations predicted by the SM. For example, by studying the Z boson resonance the existence of exactly three neutrino generations was confirmed [41]. A central tool are *cross-section measurements* which can be compared to theory predictions from the SM. Experimentally, cross-sections are estimated by performing a counting experiment. The number of observed events for a given process, after correcting for measurement efficiencies, is divided by the integrated luminosity, a measure incorporating properties of the initial particle flux. An extremely broad cross-section measurement program was conducted at the ATLAS experiment based on proton-proton collisions at the LHC. This is summarized in Figure 1.6, showing numerous processes involving all kinds of particles, and various underlying center-of-mass energies of the colliding protons. The measured cross-sections exhibit an outstanding agreement with the theory over a span of many orders of magnitude. As this thesis is set in the context of the ATLAS experiment, this example was chosen but it is worth noting that other experiments, particularly not limited to proton-proton collisions, also cover a wide range of cross-section measurements affirming the SM.

Additionally, measurements of the properties of SM particles achieve an ever-increasing precision, continuously yielding results in line with SM predictions. A good example is the strong coupling constant α_s, which was measured in various interactions and experiments. Its aforementioned theoretically predicted running is underscored by measurements excellently, covering a range of a few GeV up to 2 TeV, as illustrated in
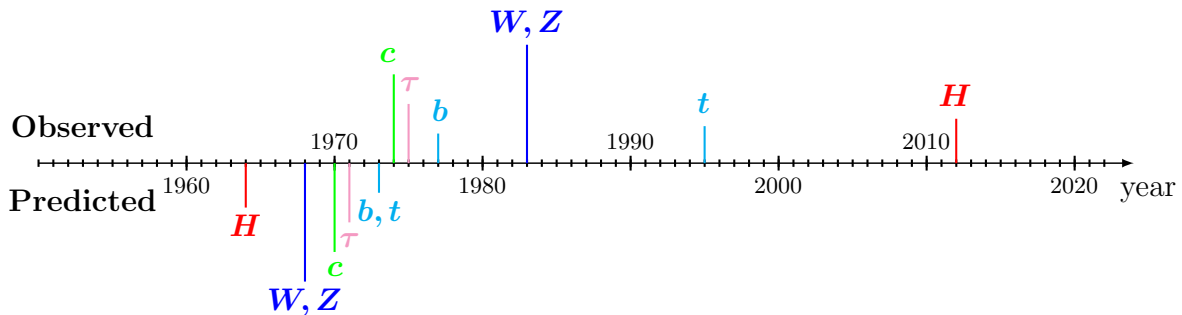
Figure 1.5.: Timeline with the years of the prediction and observation of different SM particles. References: H [27–29], W, Z [15, 16, 18], c [17], τ [30], b, t [21] (predicted), H [25, 26], W, Z [31–34], c [35, 36], τ [37], b [38], t [39, 40] (observed).
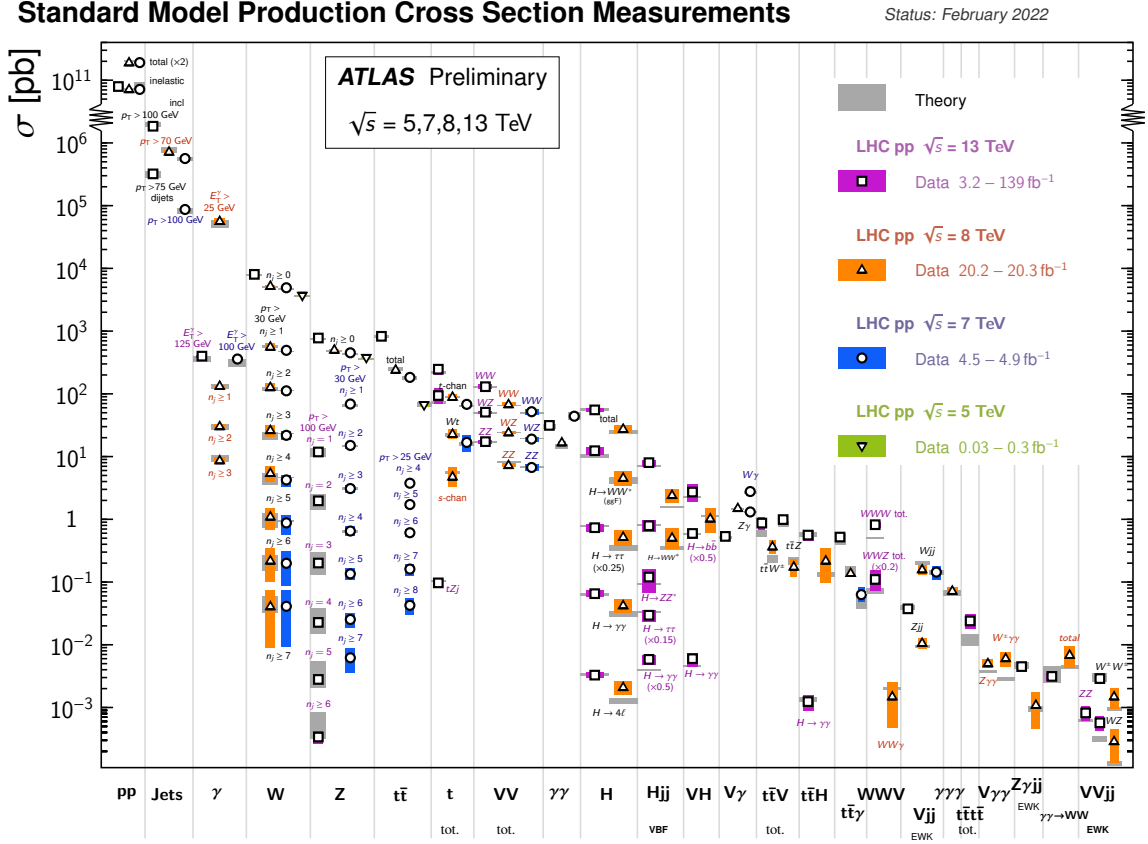
Figure 1.6.: Cross-section of different processes as measured at the ATLAS experiment together with corresponding SM predictions [42].

Figure 1.7(a). At the Z-boson resonance, α_s is determined with precision below 1% [43]. In terms of precision measurements, the weak boson sector is worth emphasizing. Masses and widths of the Z boson and W boson have been measured with unparalleled precision, with a relative uncertainty on the W-boson mass of 0.014% and Z-boson mass of 0.002% [44]. Based on the topic of this dissertation, the W-boson mass shall be discussed. A summary of different measurements is shown in Figure 1.7(b). In general, they are consistent and agree with the SM prediction[6]. However, the latest measurement conducted by the CDF collaboration contradicts the rest, exhibiting a tension of 7σ to the SM prediction [46]. This unexpected, unprecedented deviation needs to be interpreted in the context of other measurements which all support the SM prediction. For instance, ATLAS recently published an improved precision measurement of the W-boson mass which agrees with the SM prediction [48]. Lastly, it is worth noting at this point, that the high-mass W-boson cross-section measurement presented in this dissertation is not sensitive to these MeV-level mass differences.

---

[6]The W-boson mass is a free parameter in the SM and cannot be predicted from first principles. However, it is closely entangled to other fundamental parameters of the SM and by fitting these in a *global electroweak fit* [45] a consistent prediction for the SM W-boson mass can be obtained.
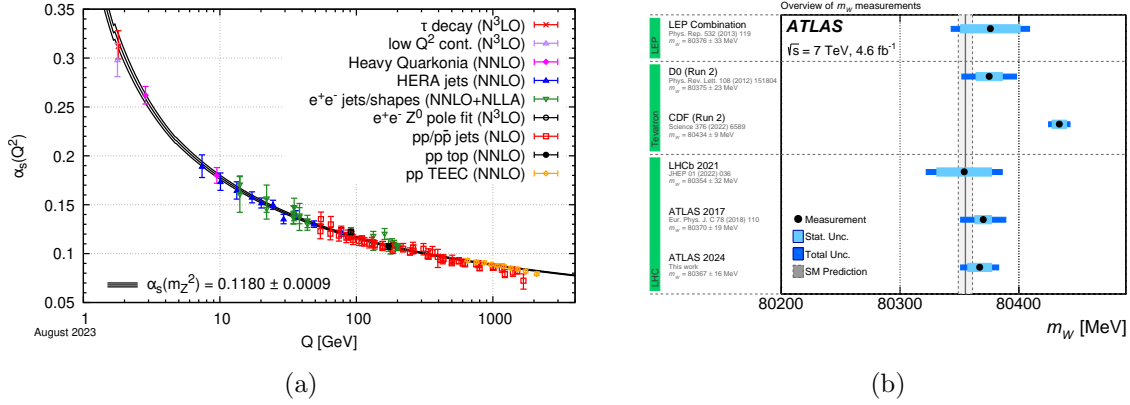
Figure 1.7.: Overview of measurements of the (a) strong coupling constant [47] and (b) W-boson mass [48].

Limitations   Although the SM has proven itself immensely successful, there are in-dications that the theory is far from complete. Hence, research in particle physics remains relevant and exciting. Frailties of the SM can be divided into two categories: unexplained observation in nature and conceptual arguments for incompleteness.

As stated in Section 1.1, the SM predicts massless neutrinos. However, by studying the rate of solar neutrinos an effect called *neutrino oscillation* was observed [49], wherein neutrinos periodically change their flavor while propagating through space. This implies that not all neutrinos can be massless, even though their mass is experimentally con-strained to be extremely small [13, 50]. Furthermore, cosmological phenomena exhibit limitations of our understanding of the universe. Gravitational lensing effects [51] and rotation curves of spiral galaxies [52] indicate the existence of a to-date unknown, non-luminous (or *dark*) matter. In addition, observations of supernovae [53] reveal an expansion of the universe at a rate that suggests the existence of an unknown form of energy, called *dark energy*. Measurements of the *Cosmic Microwave Background* indicate a composition of 68% dark energy, 27% dark matter and only 5% common matter in our universe [54]. Lastly, assuming matter and anti-matter were produced at equal amounts in the Big Bang, they would have annihilated into a universe full of pure energy. Nonetheless, here we are, living in a world made of matter. In order to explain this asymmetry, baryon-number conservation and charge-parity (CP) symmetry need to be violated in addition to a deviation from the thermal equilibrium [55]. The SM introduces CP violation in the weak sector, however not strong enough to explain the observations.

From a more conceptual point of view, the SM is limited to only three out of four fundamental forces, while Einstein's theory of *general relativity* [56] describes gravity. Eventually, a unification of all forces, describing *everything*, is desired. At contemporary energy scales, gravity is 10^{24} times weaker than the weak force, conveniently allowing it to be neglected in the calculation of SM predictions. Nevertheless, there is no funda-mental understanding of why there is such a large breach in the strength of one force with respect to the other three. Moreover, 19 free parameters in the SM cannot be

calculated from first principles but need to be measured experimentally. These are nine fermion masses, three mixing angles and one phase in the CKM matrix, three gauge couplings[7], two parameters for the Higgs sector (mass and VEV) and a CP violating phase in QCD. This leaves room for consideration if a more 'beautiful' theory with fewer degrees of freedom might be realizable. Additionally, the CP violating phase in QCD is experimentally constrained to be effectively zero (commonly known as *strong CP problem*) [57, 58] . Similarly, it is not obvious from a theoretical point of view why there are exactly three generations for both, quarks and leptons.

Many efforts are made trying to satisfy the need for a theory that complements and expands the SM, commonly epitomized as *Beyond Standard Model* (BSM) theories. Physicists rigorously search for all kinds of new particles or couplings to explain some of the shortcomings discussed. Generally, this dissertation is placed in the context of an SM precision measurement, aiming to specify and enlarge the current knowledge of the SM. However, exploring uncharted phase spaces with high precision may reveal discrepancies between prediction and measurement potentially hinting to BSM physics.

1.2. *W*-boson production in proton-proton collisions

Scattering and collider experiments have a long and significant history in nuclear and particle physics, serving as essential tools to explore the underlying structure of physical objects or to produce various non-matter particles. The current pinnacle of this field are hadron colliders like the LHC. This Section discusses the fundamentals of proton-proton (pp) collisions (Section 1.2.1), with a focus on parton distribution functions that describe the proton's substructure (Section 1.2.2). It concludes with an introduction into the charged-current Drell-Yan process (Section 1.2.3), which describes W-boson production in pp collisions and is the focus of this dissertation.

1.2.1. Physics of proton-proton collisions in a nutshell

Collisions of protons show distinct characteristics, discriminating them from lepton collisions for instance. By colliding protons, unparalleled energies can be achieved, allowing to explore uncharted phase spaces with high potential for the discovery of new phenomena. For instance, the Higgs boson was discovered in pp collisions at the LHC. An additional important motivation is that the substructure of the proton can be probed directly. Generally, pp collisions are extremely complex and challenging to describe. A simplified schematic of the collision of protons A and B is depicted in Figure 1.8.

The key characteristic is given by the fact that the proton is not an elementary, point-like particle. It is a hadron consisting of two up quarks and one down quark. These so-called

---

[7]Depending on the scheme used, the list of free parameters varies and might include for instance the weak mixing angle θ_w or weak boson masses instead.
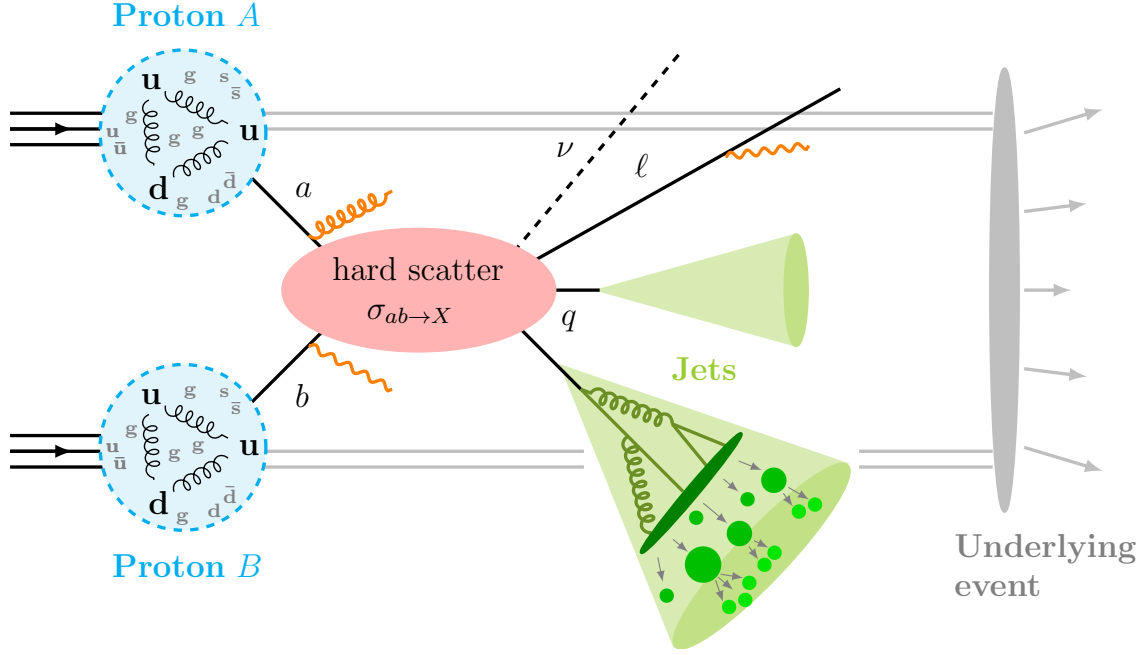
Figure 1.8.: A schematic sketch of a proton-proton collision is shown, including the substructure of the protons, the underlying event as well as the hard scattering process. One jet substructure is resolved exemplarily here, including parton shower and hadronization. Lastly, initial and final state radiation can take place, indicated exemplarily by orange lines.

valence quarks define the quantum numbers of the proton, e.g. its electric charge of $+1$. However, gluons are radiated at any time and subsequently split into quark-antiquark pairs. As a consequence, the valence quarks are accompanied by an abundance of *sea quarks*. Valence quarks, sea quarks and gluons form the *partons* inside the proton. In a high-energy pp collision, not the protons themselves interact with each other but the partons. The momentum of the initial proton is distributed among its constituents and any given parton carries a momentum fraction x. Due to the dynamic substructure of the proton, this fraction cannot be calculated from first principles. Instead, it is described by a phenomenological model via so-called *parton distribution functions*. Playing an important role in this thesis, they are discussed in detail in Section 1.2.2.

The collision interaction of parton a and parton b is described in the *hard scatter* (HS) process. Generally, it is characterized by initial state particles (here, the partons) and final state particles, including only the ones above some *hard* scale, i.e. with sufficiently high energy. It comprises the decay of unstable particles such as top quarks or weak bosons. Eventually, a set of final state particles is left, consisting of leptons, neutrinos, quarks, gluons or photons. Additionally, initial state radiation (ISR) or final state radiation (FSR) might take place. The HS process represents the part in the collision chain to be predicted by matrix element calculations as given in Section 1.1.5.

In the final state, the behavior of quarks is very distinct. No isolated quarks can

be observed but they form hadronic cascades, called *jets*. It should be noted that the formation of hadronic jets is a characteristic that is not limited to *pp* collisions but a general consequence of quark confinement in any experiment. One simplified jet substructure is highlighted in Figure 1.8. Any quark (or gluon) originating from the HS process radiates a number of *soft*, i.e. low-energy, gluons. They split further into more quark-antiquark pairs which, subsequently, radiate even more particles. Theoretically, also photons can be radiated but an EM showering is suppressed due to the smaller coupling constant. This step-by-step process is described by the *parton shower* (PS). The multitude of quarks, due to the splittings produced with ever-smaller energies each, are subject to quark confinement. In a process known as *hadronization* hadronic bound states, e.g. pions, are formed. Eventually, these hadrons decay into smaller hadrons, photons or leptons and neutrinos. Given the low parton energies, i.e. large α_s, the jet substructure cannot be described by ME calculations. In simulations, HS and PS/hadronization are usually disentangled, as described in Chapter 3.2. In an experiment, the properties, e.g. energy or orientation, of a final-state quark or gluon can only be measured by collecting the full jet activity.

In contrast, charged leptons usually produce a clean detector signature, as they are not subject to the strong force. Lastly, neutrinos, as purely weakly interacting particles, cannot be measured directly in collider experiments. However, per construction, the colliding protons carry only momentum in the longitudinal direction, hence the total transverse momentum is zero. As momentum is conserved, the sum of all transverse momenta after the collision must amount to zero as well. Therefore, the neutrino's momentum is often identified with the *missing transverse momentum*. The initial longitudinal momentum of the colliding partons is ambiguous because of the unknown fraction x, thus momentum conservation can only be exploited in the transverse direction.

All activity of the *pp* collision additional to the HS interaction is summarized in the *underlying event* (UE). It includes partons that are not interacting, i.e. colored beam remnants, radiation processes or secondary parton-parton interactions called *multi parton interactions* (MPI). Finally, it should be noted that often bunches of protons are collided to increase the number of interactions. In these dense bunches, it is likely that multiple *pp* collisions take place simultaneously, an effect called *pile-up*.

1.2.2. Parton distribution functions

As outlined above, the proton is a compound particle and its constituents, the partons, collide in high-energy *pp* collisions. Each parton carries a fraction of the total proton's momentum which is denoted as Bjorken-x, or in short x. The dynamic substructure of the proton does not fall into perturbative QCD since internal radiations and splittings happen at different energy scales, often below the cutoff scale Λ_{QCD}. Instead, *parton distribution functions* (PDFs) describe the probability for a parton to carry fraction x of the proton's momentum. The perturbative and non-perturbative parts can be separated

at a certain *factorization scale* μ_F, as described by the *factorization theorem* [59]. The convoluted cross-section $\sigma_{AB \to X}$ of protons A and B to interact is given by

$$\sigma_{AB \to X} = \sum_{a,b} \int dx_a dx_b f_{a|A}(x_a, \mu_F^2) f_{b|B}(x_b, \mu_F^2) \sigma_{ab \to X}(s, \mu_R^2). \qquad (1.11)$$

The HS cross-section of partons a and b $\sigma_{ab \to X}(s, \mu_R^2)$ can be calculated perturbatively via matrix elements, as outlined in Section 1.1.5. It depends on the renormalization scale μ_R and the center-of-mass energy s. The momentum distribution of the partons is encapsulated in the PDFs $f_{a|A}(x_a, \mu_F^2)$ and $f_{b|B}(x_b, \mu_F^2)$. An integral over all possible momenta x_a, x_b as well as a sum over all possible partons a, b is performed.

As it can be seen illustratively here, predictions of a $pp \to X$ cross-section can be made only if the PDFs are known. Hence, a sophisticated understanding and quantitative description are crucial for experiments at pp colliders. As they cannot be calculated from theory, they need to be extracted from measured data. Vice versa, by measuring the convoluted cross-section σ_{AB} and calculating the partonic cross-section σ_{ab} conclusions on the PDFs can be made.

In general, PDFs are defined as a function of the momentum fraction x of the parton as well as the energy scale Q^2. If known at a given reference scale Q_0, usually $\mathcal{O}(1\,\text{GeV})$,
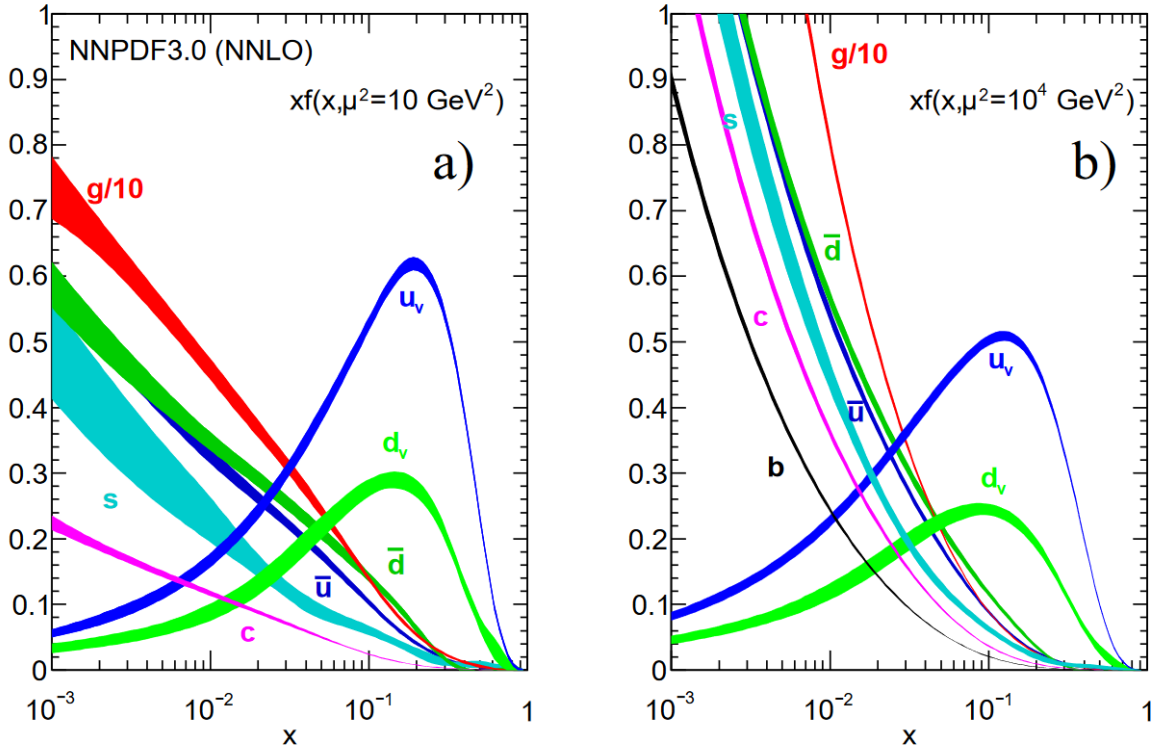
Figure 1.9.: NNLO parton distribution functions of the proton at two different energy scales, estimated by the NNPDF group [60].

the energy dependence can be evolved to any scale $Q^2 > Q_0^2$ perturbatively using the *Dokshitzer-Gribov-Lipatov-Altarelli-Parisi* (DGLAP) *equations* [61–63]. Thus, each PDF is defined at a certain order in QCD. In contrast, the shape at the reference scale can only be obtained by global fits to experimental data. Commonly, the following parametrization is employed [64],

$$f(x, Q_0^2) = a_0 x^{a_1} (1 - x)^{a_2} P(x; a_3, ...) \qquad (1.12)$$

where a_i are free parameters and P is a smooth function adding flexibility to the parametrization. It should be highlighted that each parton type is represented by a dedicated PDF. Their unique dependencies on x and Q^2 can be seen exemplarily in Figure 1.9. In general, the valence quarks, u_v and d_v, are likely to carry a large fraction of the momentum of the proton, exhibiting the maximum of their probability distribution roughly below $1/3$. In contrast, gluon as well as sea-quark PDFs are maximized for $x \to 0$, meaning these partons are most likely to carry a very small momentum fraction. Two different energy scales are shown in Figure 1.9, $Q^2 = 10 \, \mathrm{GeV}^2$ (left-hand side) and $Q^2 = 10^4 \, \mathrm{GeV}^2$ (right-hand side). Comparing the two, it can be seen that at larger energy scales, sea-quark and gluon contributions are increasingly relevant.

1.2.3. The charged-current Drell-Yan process at high transverse masses

The objective of this thesis is the measurement of the cross-section of the *charged-current Drell-Yan* (ccDY) process [65, 66] at high transverse masses. The central particle of interest is the W boson, the charged weak gauge boson introduced in Section 1.1.3. It has a measured mass of $(80.377 \pm 0.012) \, \mathrm{GeV}$ and width of $(2.085 \pm 0.042) \, \mathrm{GeV}$ [67]. It shall be noted, that there is also an analogous *neutral-current Drell-Yan* (ncDY) process, where a Z boson is produced. The fundamentals of the ccDY process, for the remainder of this thesis identified as *signal process*, are discussed in this Section.

The leading-order Feynman diagram of the ccDY process in the muonic decay channel is depicted in Figure 1.10. It is characterized by the production of a W boson via the annihilation of quarks as partons of the colliding protons. A W^+ boson is formed from an up-type quark and a down-type antiquark, and a W^- boson by a down-type quark and an up-type antiquark. As given in the CKM matrix (see Section 1.1.3), cross-generational quark couplings are possible but couplings within the same generation are dominant, e.g. in pp scattering $u\bar{d} \to W^+$ and $d\bar{u} \to W^-$. In addition, the interacting quarks can be either valence quarks or sea quarks. While the latter are always produced in pairs, the three valence quarks (uud) induce an asymmetry resulting in a higher probability to produce a W^+ boson in pp collisions. However, this asymmetry is energy-dependent as the distribution of valence to sea quarks is energy-dependent (see Section 1.2.2).

The W boson is an unstable particle with an average lifetime of $\tau_W \approx 3 \times 10^{-25} \, \mathrm{s}$.
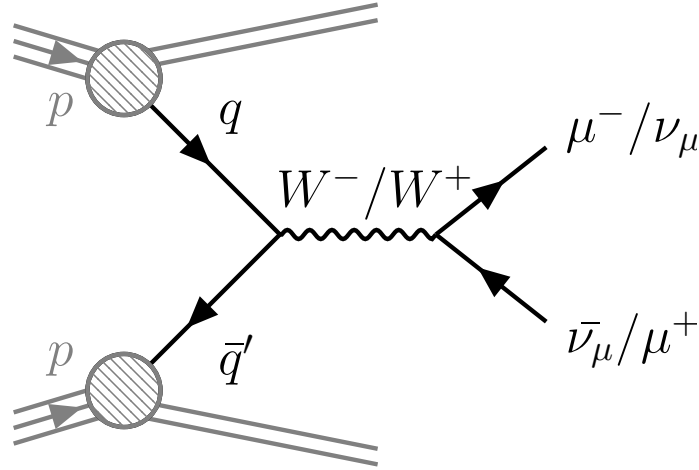
Figure 1.10.: Leading-order Feynman diagram of the charged-current Drell-Yan process in the muonic decay channel.

Only its decay products can be measured in the detector. The short-lived W boson decays with a branching ratio of $\mathcal{BR}_{\mathrm{had}} \approx 2/3$ to quarks and $\mathcal{BR}_{\mathrm{lep}} \approx 1/3$ to a charged lepton and its corresponding neutrino. Decays to different lepton flavors (e, μ, τ) have approximately[8] the same probability, as given by lepton universality. In this work, the decay into a muon and muon-neutrino is studied. A parallel electron-channel measurement is performed and both are combined ultimately. For the remainder of this thesis, for brevity reasons, the term lepton refers solely to electrons or muons. Additionally, muon-neutrino is abbreviated to neutrino.

For any unstable particle, its physical mass is described by a Breit-Wigner distribution with the maximum at the SM value of the particle's mass, as sketched in Figure 1.11. This implies a certain probability for the production of a W boson with a very large mass, far off the resonant mass peak (also called *off-shell* production). The distinctive feature of this thesis is the aim to measure the production cross-section of exactly these high-mass W bosons as a function of the so-called *transverse mass* $m_{\mathrm{T}}^{\mathrm{W}}$. Generally, the W boson is reconstructed from its decay products, here muon and neutrino, where four-vector conservation holds

$$P(W) = P(\mu) + P(\nu) \qquad \text{with} \quad P(i) = (E(i), p_x(i), p_y(i), p_z(i)), \ \ i = W, \mu, \nu. \quad (1.13)$$

The mass of the W boson is identified with the *invariant mass* m_{inv} of the μ-ν-system

$$m_W^2 = m_{\mathrm{inv}}^2 = (P(\mu) + P(\nu))^2. \quad (1.14)$$

However, in *pp* collisions, it is only possible to measure the transverse component of the neutrino via momentum conservation (as outlined in Section 1.2.1). Using the transverse information and neglecting lepton masses, the *transverse mass* $m_{\mathrm{T}}^{\mathrm{W}}$ is finally defined as

$$m_{\mathrm{T}}^{\mathrm{W}} = \sqrt{2 p_{\mathrm{T}}(\mu) p_{\mathrm{T}}(\nu)(1 - \cos \Delta \phi(\mu, \nu))} \quad (1.15)$$

---

[8]Differences due to the phase-space availability from different lepton masses are neglected here.
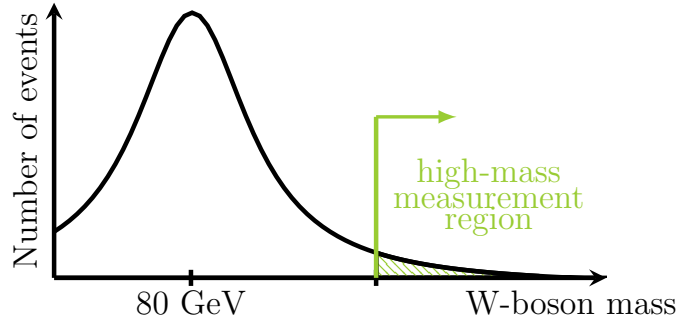
Figure 1.11.: Sketch showing the W-boson mass distribution and high-mass measurement region.

where p_T describes the transverse momentum of the given particle and $\Delta\phi(\mu,\nu)$ their distance in the transverse plane. In the measurement, $p_\mathrm{T}(\nu)$ will be identified with the absolute of the missing transverse momentum $E_\mathrm{T}^\mathrm{miss}$. It should be noted that the transverse mass is generally less than or equal to the invariant mass.

1.3. Motivation and interpretation opportunities

W and Z bosons play an extraordinary role in SM precision physics and, often, ncDY and ccDY processes are mentioned in a similar context, still yielding complementary physics information. In general, the DY process is a theoretically extremely well-understood process. Experimentally, its leptonic decay represents a clean, distinct detector signature free of hadronic final states (at LO). For the ccDY process, the final-state neutrino complicates the picture as it cannot be measured directly in the detector. Nevertheless, both processes are crucial tools for benchmark and precision tests of the SM at the LHC.

Resonant DY cross-sections were measured by the ATLAS collaboration to sub-percent-level uncertainty using the LHC Run 1 data at $\sqrt{s} = 7\,\mathrm{TeV}/8\,\mathrm{TeV}$ [68–70], as well as using early Run-2 data at $\sqrt{s} = 13\,\mathrm{TeV}$ ($81\,\mathrm{pb}^{-1}$) [71]. Straying from the resonant mass peak to the high-mass region, measurements of the ncDY process were performed at $\sqrt{s} = 7\,\mathrm{TeV}/8\,\mathrm{TeV}$ [72, 73] by the ATLAS collaboration. However, the measurement of the high-mass tail of the ccDY process is performed for the first time in this analysis, using the full Run-2 dataset at $\sqrt{s} = 13\,\mathrm{TeV}$.

By exploring the energy frontier of the LHC, sensitivity to potential new physics is expected. The phase space of interest, $m_\mathrm{T}^\mathrm{W} \in [200, 5000]\,\mathrm{GeV}$, was only analyzed by a search for a heavy charged gauge boson called W' *boson* [74, 75]. No excesses were found and exclusion limits on the W'-boson mass were set at $6\,\mathrm{TeV}$. As searches are generally not designed for high precision, the measurement presented will allow for probing potential small deviations to the SM by comparing the measured cross-sections to theory predictions. Additionally, this measurement is valuable for deepening the knowledge

in this extreme phase space. While this thesis exclusively focuses on the cross-section measurement, some motivating interpretation opportunities shall be elaborated.

Cross-section measurements are fundamental to study and constrain PDFs, as illustrated in the factorization theorem (Equation 1.11). To a large degree, DIS experiments at HERA shaped our current knowledge of PDFs and, to this day, measurements from ZEUS and H1 are widely used in PDF fits [76]. However, their coverage in the x-Q^2-plane is limited, as illustrated in Figure 1.12. High-energy LHC data provides valuable information to expand and complement it over an extremely broad energy spectrum. The sensitivity depends on the mass M and rapidity y, i.e. angular orientation (see Section 2.2), of a particle.

The high-mass $W \to \mu\nu$ measurement presented covers a transverse mass spectrum of $200\,\mathrm{GeV} < m_{\mathrm{T}}^{\mathrm{W}} < 5\,\mathrm{TeV}$ and a (pseudo)rapidity of the muon of $|\eta(\mu)| < 2.4$. Its expected coverage in the x-Q^2-plane is shown in Figure 1.12(b), obtained using a simulation of the signal process. Particular sensitivity in the high-x and high-Q^2 region of $x \in [10^{-3}, 1)$ and $Q^2 \in [10^4, 10^7]\,\mathrm{GeV}^2$ is expected. Generally, regions with high masses and high rapidities exhibit the largest PDF uncertainties [75]. Thus, this measurement will provide important constraining power in these challenging regions of phase space.

(a)   (b)
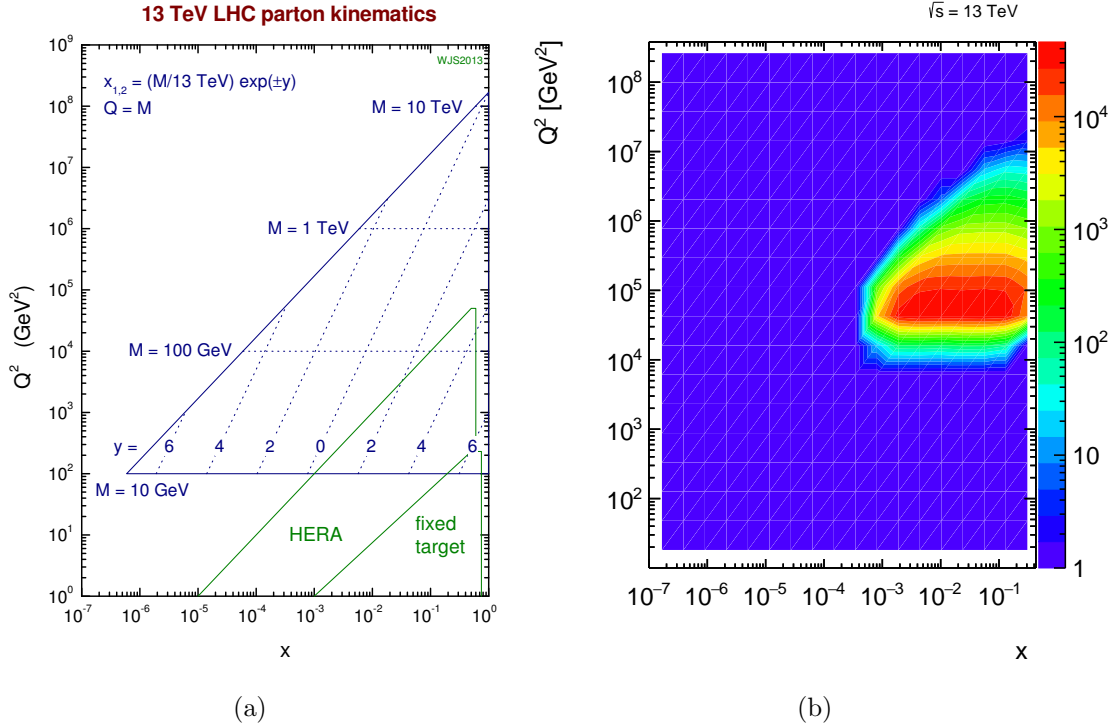
Figure 1.12.: PDF sensitivity for (a) a general particle with mass M and rapidity y in the x-Q^2-plane, compared for HERA/fixed target (green) and LHC (blue) kinematics [77], and (b) the high-mass $W^{\pm} \to \mu^{\pm}\nu$ process, as obtained with the signal POWHEG+PYTHIA8 simulation introduced in Section 3.3.

Given the production of the W boson, predominantly sensitivity to PDFs of up and down quarks, including their antiquarks, but also strange quarks and charm quarks is expected (see also Figures A.3/A.4). By measuring both charges (W^+/W^-), their asymmetry provides information on the u/d-PDF.

A second major motivation is given by the fact that small deviations in the high-energy tails, potentially too small to be visible in less precise searches, may hint at new physics. A common, model-independent tool to probe this are *Effective Field Theories* (EFTs). The general idea is sketched in Figure 1.13. Unknown new physics beyond the current energy reach is assumed, for instance, the existence of a new heavy particle. Its lower tail may affect the high-energy tail of the measurable regime in the form of a small deviation from the SM prediction. Instead of employing a dedicated theory of e.g. a specific new particle, an EFT provides a universal way to probe for new physics. The SM Lagrangian $\mathcal{L}_{\mathrm{SM}}$ is expanded by general higher-dimension operators $\mathcal{O}_i^{(d)}$ of dimension d [78],

$$\mathcal{L}_{\mathrm{SMEFT}} = \mathcal{L}_{\mathrm{SM}} + \sum_{i=1}^{N_{\mathrm{operators}}} \frac{c_i^{(d)}}{\Lambda^{d-4}} \mathcal{O}_i^{(d)}. \tag{1.16}$$

Each operator is accompanied by the energy-scale Λ of the new physics, typically $\mathcal{O}(\mathrm{TeV})$, and a dedicated Wilson coefficient $c_i^{(d)}$ which parametrizes the coupling strength of the operator and can be constrained by cross-section measurements.

For the high-mass $W \to \mu\nu$ measurement presented, sensitivity to four dimension-6[9] operators is expected, with corresponding Wilson coefficients $c_{Hl}^{(3)}$, $c_{Hq}^{(3)}$, $c_{ll}^{(1)}$ and $c_{lq}^{(3)}$ in the Warsaw basis [79, 80]. Here, the upper index indicates the corresponding gauge fields involved in the respective operator with (3) standing for the SU(2) and (1) for the U(1) generators. The lower index gives the SM fields involved. For the first two operators,

---

[9]One dimension-5 operator is present which is ignored as it violates baryon-number conservation. Terms with $d > 6$ are strongly suppressed by Λ.
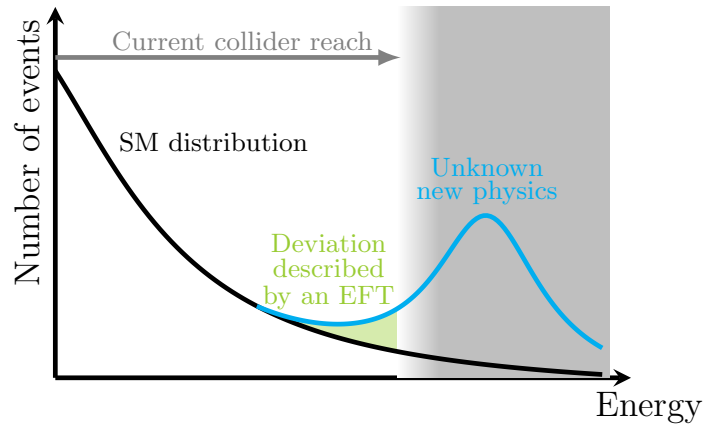
Figure 1.13.: General ideal of an effective field theory (EFT) in the context of collider physics.
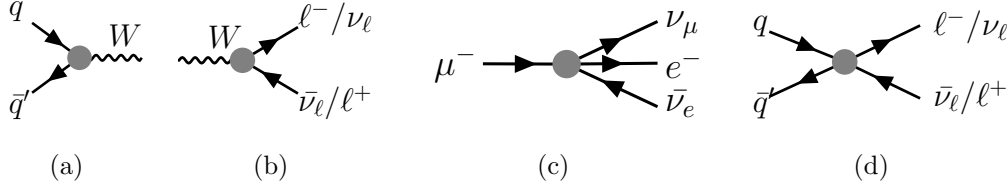
Figure 1.14.: Sensitive EFT couplings of the high-mass $W \to \mu\nu$ measurement presented in this dissertation. A gray dot indicates an EFT vertex, which incorporates unknown new physics. The corresponding Wilson coefficients are (a) $c_{Hq}^{(3)}$, (b) $c_{Hl}^{(3)}$, (c) $c_{ll}^{(1)}$ and (d) $c_{lq}^{(3)}$.

the boson-fermion-fermion couplings are modified, as illustrated in Figure 1.14(a) and Figure 1.14(b). The third operator with corresponding Wilson coefficient $c_{ll}^{(1)}$ impacts the ccDY process only indirectly, as it modifies the Fermi constant G_F determined via the muon decay, depicted in Figure 1.14(c). Lastly, $c_{lq}^{(3)}$ corresponds to a direct four-fermion interaction involving a pair of quarks and a pair of leptons, see Figure 1.14(d). For this coefficient, the by far strongest constraining power is expected. This is depicted in Figure A.2 which shows the number of events in the phase space of interest assuming additional EFT terms.

It shall be noted that also Reference [1] predicts strong EFT constraining power from the high-mass ccDY process at $\sqrt{s} = 13$ TeV. However, a different parametrization is used where the oblique parameters $W, Y, \hat{S}, \hat{T}$ in Reference [1] are essentially linear combinations of the coefficients c_i [81].

Additionally, the measurement presented exhibits constraining power to the running electroweak coupling, which is not measured precisely above the weak scale [2], and potentially sensitivity to the W-boson width [82, 83]. Both are important parameters in the electroweak theory. Finally, a direct experimental test of the SM is given by the fact that this measurement is performed in parallel in the muon channel (this thesis) and in the electron channel [77, 84, 85]. Both measurements are expected to yield the same cross-sections within uncorrelated uncertainties, as predicted by lepton flavor universality. Any significant deviations could hint to BSM physics.

2. The ATLAS experiment at the Large Hadron Collider

Collider experiments represent a powerful tool for exploring and understanding high-energy physics. Particles are accelerated to nearly the speed of light and, in high-energy collisions, a plethora of further particles is produced. They are measured in complex detectors, allowing for important conclusions about the SM and beyond. The data analyzed in this thesis is based on *pp*-collision data taken with the ATLAS detector at the Large Hadron Collider, both are presented in the following.

2.1. The Large Hadron Collider

The *Large Hadron Collider* (LHC) [86] is a circular particle accelerator and collider located at the *European Organization for Nuclear Research* (CERN). It is built in the former *Large Electron-Positron Collider* (LEP) [87] tunnel which is positioned on average 100 m underground and exhibits a circumference of 27.6 km, see Figure 2.1(a). Reaching center-of-mass (COM) energies of up to 13.6 TeV, the LHC is the largest and most powerful particle accelerator built by mankind. Protons, or in special runs heavy ions, are brought to collision at four major experiments. The two multipurpose detectors, ATLAS [88] and CMS [89], cover a broad spectrum of SM and BSM physics. Moreover, the LHCb experiment [90] focuses explicitly on B hadrons[1] and the ALICE experiment [91] studies the collisions of heavy ions.

Each proton originates as a hydrogen atom which will be stripped for its electron. Before entering the LHC, the protons are accelerated in a set of pre-accelerators. The acceleration complex is summarized in Figure 2.1(b), including the energy reached in each step. With an energy of 450 GeV, protons are injected from the *Super Proton Synchrotron* (SPS) into the LHC in opposite directions in two separate beams that only meet in the four interaction points. The LHC is designed to accelerate protons up to an energy of 7 TeV each, corresponding to a COM energy of $\sqrt{s} = 14$ TeV. During its lifetime, the maximum LHC energy was increased subsequently in its three major runs: Run 1 at $\sqrt{s} = 7/8$ TeV (in 2011/2012), Run 2 at $\sqrt{s} = 13$ TeV (2015-2018) and the ongoing Run 3 at $\sqrt{s} = 13.6$ TeV.

---

[1]A B hadron is a hadron containing a b quark.
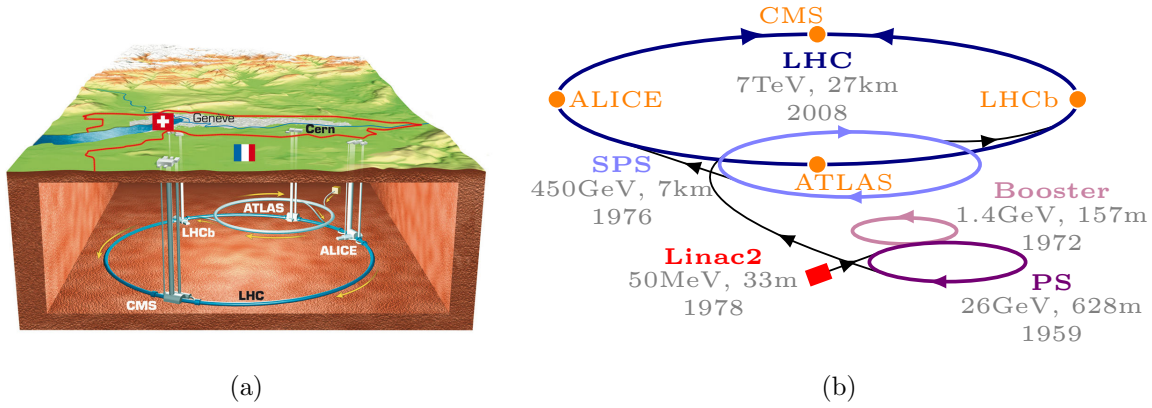
Figure 2.1.: Overview of (a) the location of the Large Hadron Collider (LHC) [92], and (b) the CERN accelerator complex, where PS stands for Proton Synchrotron and SPS for Super Proton Synchrotron. The numbers in Figure (b) are taken from Reference [93], including the circumference of the accelerator rings (for Linac2, its length is given). Both figures include the four major LHC experiments ATLAS, CMS, LHCb and ALICE.

While the first pre-accelerator, Linac2, is a linear accelerator with a length of $33\,\mathrm{m}$, all further accelerators follow the principle of a synchrotron, discussed as an example for the LHC here. The particles are held on a circular track using in total 1232 superconducting $8\,\mathrm{T}$ dipole magnets which are cooled down to a temperature of $1.9\,\mathrm{K}$. Quadrupole magnets, alternatingly vertically and horizontally focusing, and collimators are used to focus, correct and clean the beams. The acceleration itself takes place over small straight sections in superconducting cavities with a resonant radio frequency (RF) of $400\,\mathrm{MHz}$. The protons travel many rounds in the LHC and experience a small acceleration in the RF cavities per round. Lastly, the beam pipes are subject to an ultra-high vacuum with a pressure below 10^{-13} atm in order to prevent collisions with any gas atoms.

The LHC is not only outstanding in its COM energy but also the rate of collisions produced. Protons are grouped in *bunches* where, at maximum, 2556 bunches containing $\mathcal{O}(10^{11})$ protons each are collided with a bunch spacing of $25\,\mathrm{ns}$. Beam properties are summarized in the *luminosity*, a common measure for the number of interactions per time and area. Multiplied with the process-specific cross-section $\sigma_{pp\to X}$, the *integrated luminosity* $\mathcal{L}_{\mathrm{int}}$ will give the number of events produced of the given process,

$$N_{pp\to X} = \sigma_{pp\to X}\mathcal{L}_{\mathrm{int}} = \sigma_{pp\to X}\int \mathcal{L}dt. \tag{2.1}$$

Vice versa, any cross-section at a collider experiment can be measured by counting the number of events and knowing the integrated luminosity.

The *instantaneous luminosity* $\mathcal{L}$ is based on beam properties via

$$\mathcal{L} = \frac{N_b^2 n_b f_r \gamma_r}{4\pi\epsilon_n\beta^*}F \tag{2.2}$$

where N_b is the number of protons per bunch, n_b the number of bunches per beam and f_r the revolution frequency of the bunches with the relativistic gamma factor γ_r. The beam optics are described by the normalized transverse beam emittance ϵ_n, the beta function β^*, a measure for the transverse beam size at the interaction point, and the geometric luminosity reduction factor $F \leq 1$ due to a crossing angle between the beams (F equals one for head-on collisions). Table 2.1 shows a summary of the LHC characteristics during Run 2, including the parameters discussed above, separated in the data-taking years 2015-2018. Finally, it should be noted that this high-luminosity setup can only be achieved with the compromise of high pile-up, i.e. at average 34 interactions happened simultaneously in ATLAS during the LHC Run 2 [94].

Table 2.1.: LHC beam characteristics during Run 2, separated per data-taking year and compared to the design value [95].

Parameter	Design	2015	2016	2017	2018
Beam energy [TeV]	7	6.5	6.5	6.5	6.5
Bunch spacing [ns]	25	25	25	25	25
Max. number of bunches n_b	2808	2244	2200	2556	2556
Bunch population N_b [10^{11}p]	1.15	1.2	1.25	1.25	1.1
Beam focus β^* [cm]	55	80	40	40/30	30/27/25
Peak luminosity $\mathcal{L}$ [10^{34} cm^{-1}s^{-1}]	1.0	0.5	1.5	2.0	2.1

2.2. The ATLAS experiment

The ATLAS[2] detector [88] is a multipurpose particle detector at the LHC exhibiting a cylindrical, symmetrical architecture with a length of 44 m and diameter of 25 m. An overview of the ATLAS detector is shown in Figure 2.2. It is organized in the form of a *barrel*, concentrical around the beamline, and two *end-caps*, located at both sides perpendicular to the beam pipe, allowing for a solid angle coverage close to 4π. The detector comprises concentrically layered sub-detectors designed to measure and distinguish particles produced in high-energy collisions. Among others, electrons, muons, photons and hadronic jets can be detected with the help of three sub-systems: the *Inner Detector* (ID), the *Electromagnetic and Hadronic Calorimeters* (ECal/HCal) and the *Muon Spectrometer* (MS). While the calorimeters are designed to measure the energy of particles, the ID and the MS are tracking detectors embedded in a magnetic field bending the trajectories of charged particles.

---

[2]**A T**orodial **L**HC **A**pparatu**S**
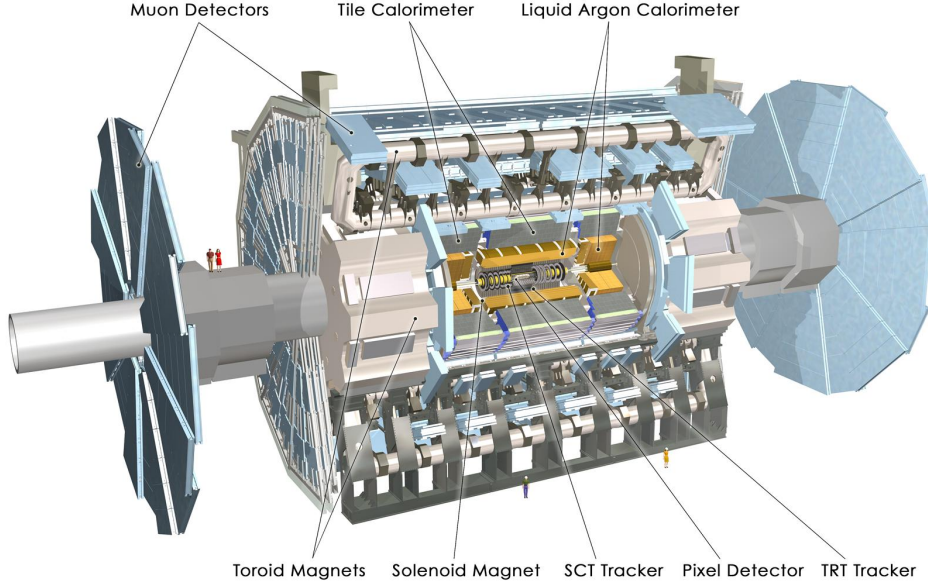
Figure 2.2.: Overview of the ATLAS detector including its sub-detectors and magnets [96]. People are shown for scale.

2.2.1. Coordinate system

ATLAS employs a right-handed cartesian coordinate system with the origin in the interaction point (IP). The z-direction corresponds to the beam direction while the positive x-direction points to the center of the LHC ring and the positive y-direction towards the surface. An overview of the coordinate system is given in Figure 2.3.

As colliding partons exhibit ambiguous momenta along the beam axis (different Bjorken-x), commonly, the *transverse momentum* of any outgoing particle is given, with an absolute value of

$$p_{\mathrm{T}} = \sqrt{p_x^2 + p_y^2}. \tag{2.3}$$

Two angles describe the spatial orientation of a particle. Exploiting the detector symmetry, cylindrical coordinates are used where $\phi \in [-\pi, \pi]$ is the azimuthal angle in the x-y plane. The polar angle $\theta \in [0, \pi]$ expresses the angle between the particle's momentum vector and the z-axis. Commonly, instead of θ, the orientation is described by the *pseudorapidity*[3] $\eta \in (-\infty, \infty)$ which is defined as

$$\eta = -\ln(\tan\frac{\theta}{2}). \tag{2.4}$$

A few examples of η values are shown in Figure 2.3(b) underlining its relation to the polar angle θ. Generally, the total particle flux in the detector is at a similar level in

---

[3]In the limit of negligible particle masses, η equals the rapidity y of a particle given by $y = \frac{1}{2}\ln(\frac{E+p_z}{E-p_z})$.

(a) Front view of ATLAS   (b) Side view of ATLAS
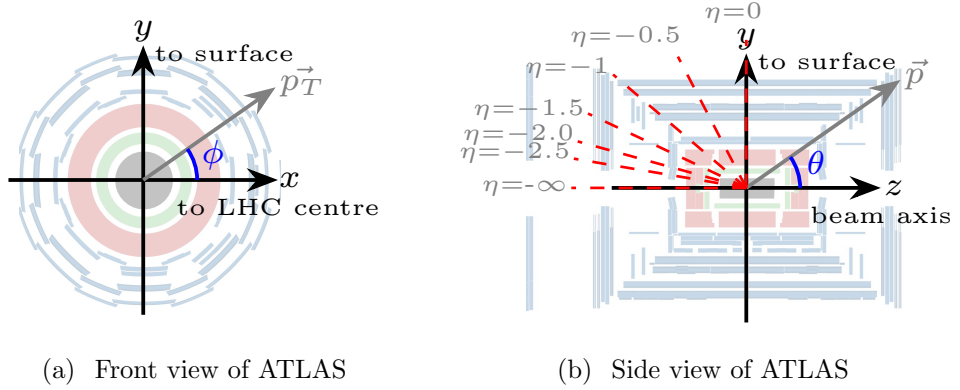
Figure 2.3.: Overview of the ATLAS coordinate system, including the angular coordinates θ, ϕ and η as well as a transverse momentum vector $\vec{p}_T$. The structure of the ATLAS detector including its sub-systems is shown in the background, inspired by the *Event-Display* style [97].

equidistant η bins. In total, the ATLAS detector has full coverage in ϕ and covers $|\eta| < 4.9$, corresponding to $1.3° < \theta < 178.7°$. Lastly, the total angular distance between two particles can be expressed as $\Delta R = \sqrt{(\Delta \eta)^2 + (\Delta \phi)^2}$. Throughout this thesis, any absolute azimuthal distance $|\Delta \phi|$ is abbreviated to $\Delta \phi$.

2.2.2. Magnet system

If subjected to a magnetic field, charged particles describe a curved trajectory due to the Lorentz force. The radius is directly dependent on the particle's momentum and charge as well as the magnetic field strength. Hence, magnetic fields are crucial additions to tracking detectors for measuring a particle's momentum. The ATLAS detector embodies two types of superconducting magnet systems [98] operated at 4.5 K. They cover the tracking detectors, with a solenoidal field for the ID and a toroidal field for the MS. The magnet system in the ATLAS detector is depicted schematically in Figure 2.4(a).

The solenoid is located in the space between the ID and the calorimeter system, extending over 5.6 m in length and 2.56 m in diameter. Its material budget is kept minimal to not disturb the calorimeters' performance. At a thickness of just 4.5 cm, the superconducting magnet provides an axial field of 2 T central strength. Field lines can be approximated parallel to the beam line, leading to a bending of charged particles in the transverse plane.

In contrast, the toroid magnet system is embedded in the MS directly, aiming to bend muons for precise momentum measurements in this sub-detector. It manifests a magnetic field strength of up to 3.5 T and covers an exceptionally large volume of more than 20 m in length and diameter, respectively. In the barrel region, eight flat air-core coils are organized radially and symmetrically around the beam axis (being an

(a)   (b)
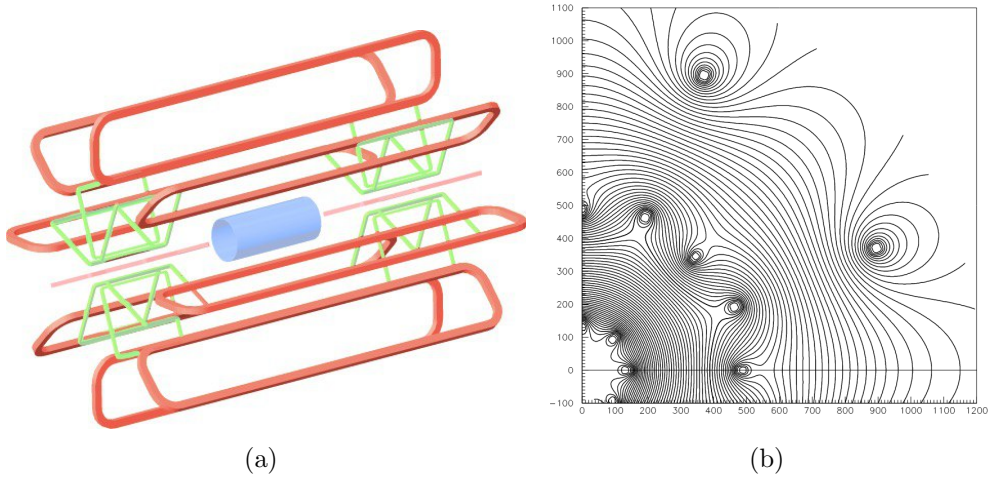
Figure 2.4.: (a) Magnet system used in ATLAS [99]. The solenoid magnet is marked blue, the barrel toroids in red and the end-cap toroids in green. (b) Magnetic field map of the toroidal magnets in the transistion region [100], where scales are given in cm.

iconic element in pictures of the ATLAS detector). With 25.3 m in length, the central toroid of ATLAS is the largest toroidal magnet ever constructed. It is completed by additional coils at both end-caps, see Figure 2.4(a). The region of $1.0 < |\eta| < 1.4$ represents a transition region between the barrel and end-cap magnet systems. This setup results in a magnetic field mostly orthogonal to the muon trajectories, in the simplest picture radially around the beam line leading to a bending in η. Clearly, this is just an approximation, as the interplay of the different magnets as well as the presence of magnetic material in the rest of the detector lead to a highly non-uniform field. The toroidal magnetic field perpendicular to the beam axis is shown for the transition region in Figure 2.4(b). Individual barrel and end-cap coils are visible. Any changes and inhomogeneities in the magnetic fields, both solenoidal and toroidal, must be understood and quantified precisely for accurate particle measurements.

Table 2.2.: Resolution and pseudorapidity coverage of the ATLAS sub-detectors [88]. The symbol $\oplus$ indicates quadratic summation.

Subdetector	Resolution	Coverage
Inner Detector	$\sigma_{p_{\mathrm{T}}}/p_{\mathrm{T}} = 0.05\% \cdot p_{\mathrm{T}}/\mathrm{GeV} \oplus 1\%$	$|\eta| < 2.5$
Electromagnetic Calorimeter	$\sigma_E/E = \frac{10\%}{\sqrt{E/\mathrm{GeV}}} \oplus 0.7\%$	$|\eta| < 3.2$
Hadronic Calorimeter	$\sigma_E/E = \frac{50\%}{\sqrt{E/\mathrm{GeV}}} \oplus 3\%$	$|\eta| < 3.2$
Forward Calorimeter	$\sigma_E/E = \frac{100\%}{\sqrt{E/\mathrm{GeV}}} \oplus 10\%$	$3.1 < |\eta| < 4.9$
Muon Spectrometer	$\sigma_{p_{\mathrm{T}}}/p_{\mathrm{T}} = 10\%$ at $p_{\mathrm{T}} = 1\,\mathrm{TeV}$	$|\eta| < 2.7$

2.2.3. Inner Detector

The *Inner Detector* (ID) [101, 102] is the closest to the beam pipe, with an inner radius of only 3.3 cm. It is a tracking detector designed to measure the trajectory of charged particles. The particle's momentum is concluded from the bending due to the solenoid magnetic field, thus less precise at very high momenta, i.e. at almost straight trajectories. The overall resolution and coverage in η of the ID are summarized in Table 2.2, set in the context of other detector components elaborated later in this Chapter. The ID is required to offer a high granularity to perform precision tracking in the busy environment close to the IP and is crucial for reconstructing the primary hard-scatter vertex. The ID is comprised of three sub-systems layered concentrically around the beam line as illustrated in Figure 2.5.

The innermost part is the *Pixel Detector* consisting of three cylindrically organized layers with in total about 80 million[4] silicon sensors. Each utilizes the principle of charge collection in a semiconductor material where ionizing particles create electron-hole-pairs that generate a measurable electrical signal. The Pixel Detector offers a high spatial resolution of 10 μm in the x-y plane and 115 μm in the z-direction. For the LHC Run 2, it was complemented by the *Insertable B-Layer* improving the tracking of particles closest to the IP [103].

Further measurements are provided by the surrounding *Semiconductor Tracker* (SCT), improving the overall precision of tracks. It is a silicon-microstrip based detector consist-

---

[4]1744 modules with 46080 pixels each
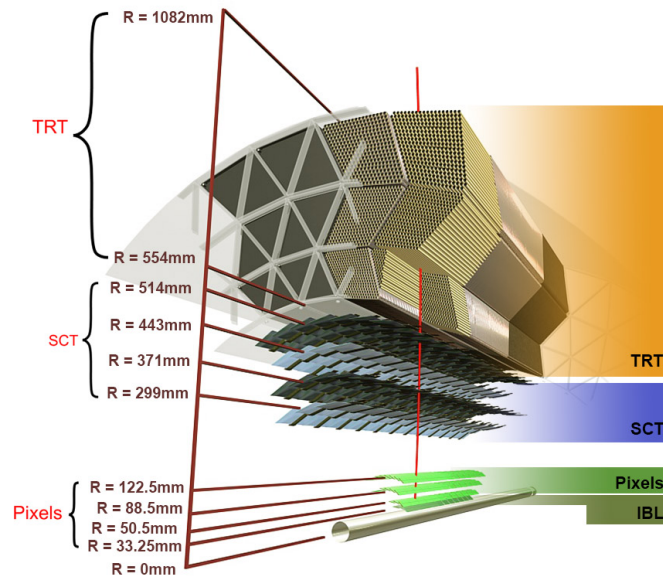
Figure 2.5.: Schematic overview of the ATLAS Inner Detector in the transverse view [101].

ing of four layers in the barrel and nine layers in the end-caps. The 6.3 million read-out channels of the SCT offer a marginally lower spatial resolution than the Pixel Detector with $17\,\mu$m in the x-y plane and $580\,\mu$m in the z-plane. However, this is justified by the lower particle flux further away from the IP.

The two silicon-based trackers are complemented by the *Transition Radiation Tracker* (TRT). It consists of 370000 4 mm-thick straw tubes organized parallel to the beam pipe in the barrel and perpendicular to it in the end-caps. Each tube is filled with a Xenon and Argon gas mixture to be ionized by traversing particles. The result are electrons that drift towards a central anode wire, producing an electrical signal.
In addition to measuring the track, the TRT provides dedicated electron identification power. It includes a radiator material emitting transition radiation that depends on the ionizing particle's Lorentz factor $\gamma = {}^{E}/m$. A typical track in the ID comprises at least three hits in the Pixel Detector, eight hits in the SCT and 30 hits in the TRT.

2.2.4. Calorimeters

The ID is surrounded by a set of calorimeters designed to identify and measure the energy of e.g. electrons, photons and jets by absorbing them. All follow the principle of sampling calorimeters built from alternating layers of a high-density absorbing material and an active material. While the former leads to the production of particle showers, the latter is used to measure the energy deposits. The calorimeter system is compound of the *Electromagnetic Calorimeter* (ECal), the *Hadronic Calorimeter* (HCal) and *Forward Calorimeters* (FCal) [104–106]. An overview in the η-plane is shown in Figure 2.6 and the resolution and coverage of all sub-systems are given in Table 2.2.

The ECal is designed to measure the energy of photons and electrons with high granularity and precision. For instance, the granularity in the middle layer of the ECal is $(\Delta\eta \times \Delta\phi) \approx (0.025 \times 0.025)$. It consists of liquid argon (LAr) as active material and lead or stainless steel as absorbers, where EM showers are produced by Bremsstrahlung or electron-positron pair-production. The total thickness of the ECal is in the order of $20 - 30\,X_0{}^5$ ensuring all EM activity is collected. Due to structural material in the barrel end-cap transition region, the acceptance is degraded for $1.37 < |\eta| < 1.52$.

Strongly interacting particles in hadronic jets deposit only a little fraction of their energy in the ECal. Instead, they are fully absorbed in the HCal. Inelastic hadronic interactions cause the showering in the steel or copper absorber material. Scintillators and LAr form the active material. In general, the absorber layers are thicker in the HCal than the ECal, due to the lower cross-section of hadronic interactions. The thickness of the HCal amounts to about $10\,\lambda^6$ at $\eta = 0$ with a mean granularity of $(\Delta\eta \times \Delta\phi) \approx (0.1 \times 0.1)$.

---

[5] The radiation length X_0 is defined as the mean distance reducing the particle's energy by $^1/_e$.
[6] The hadronic interaction length λ is defined analogously to X_0 .
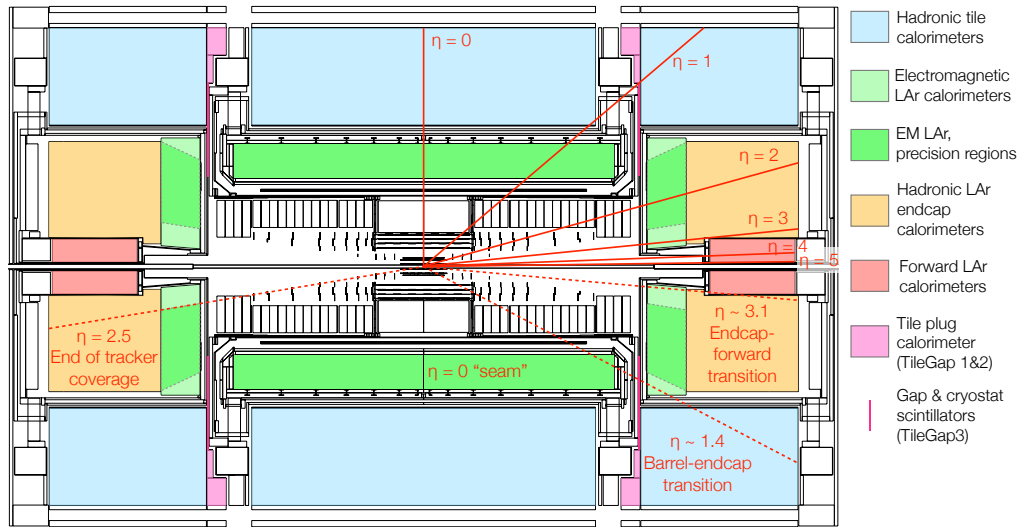
Figure 2.6.: Overview of the ATLAS calorimeter system in the longitudinal plane [107].

Finally, the solid angle coverage is completed by the LAr-based FCal, which is itself layered in an EM and hadronic component. It is the only part of the ATLAS detector covering the forward region of $3.1 < |\eta| < 4.9$ and is, among other things, important for estimating the missing transverse energy adequately.

2.2.5. Muon Spectrometer

Muons are minimal ionizing particles and produce due to their large mass, 200 times the electron mass, nearly no Bremsstrahlung, Thus, they are the only particles (besides neutrinos) that traverse the calorimeter systems with basically no interaction. However, muons represent generally promising, well-distinguishable and robust signatures in collider experiments. Thus, a dedicated stand-alone tracking system designed to measure the tracks of muons with high precision forms the outermost part of the ATLAS detector. The *Muon Spectrometer* (MS) [100] expands from 4.5 m to 11 m in the radial direction and from 7 m to 23 m in both longitudinal directions, comprising by far the largest volume of the ATLAS detector. Trajectories of traversing muons are bent by the toroidal magnet system introduced in Section 2.2.2.

Precision measurements of the track coordinates of muons are mostly provided by a multitude of *Monitored Drift Tubes* (MDTs), using in total about 350000 channels. The Ar/CO_2-gas-filled tubes follow the same detection principle as the TRT tubes (see Section 2.2.3) and are 30 mm in diameter and $70 - 630$ cm long, depending on the location in the detector. Whenever possible, the track of muons is measured in three
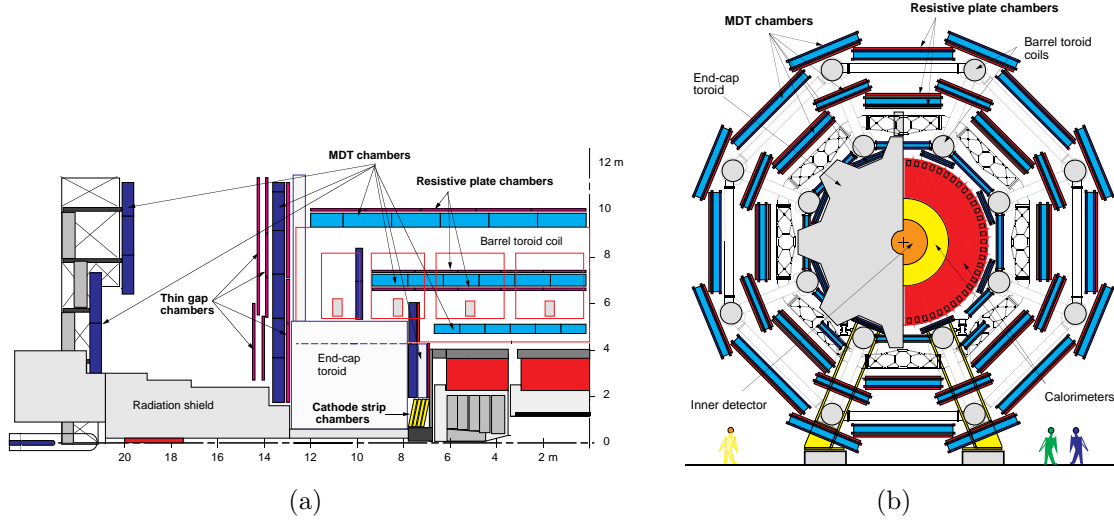
Figure 2.7.: Schematic view of the ATLAS Muon Spectrometer showing (a) one quadrant in the longitudinal view and (b) the transverse view [100].

positions, called *stations*. This is achieved by an arrangement in three layers of MDTs around the beam pipe in the barrel and three perpendicular layers in the end-caps, as illustrated schematically in Figure 2.7. Close to the beam pipe, i.e. $2 < |\eta| < 2.7$, the MDTs are complemented by high-granularity multi-wire *Cathode Strip Chambers* (CSCs) as the innermost layer (see Figure 2.7(a)). They are characterized by better handling with higher background rates in these regions. In total, the MS provides a spatial resolution of, at best, $35\,\mu$m. This can be translated to a momentum resolution of typically 2-3%, limited by multiple scattering in support-structure material, and around 10% for high-p_T muons at 1 TeV, limited by the geometric detector resolution.

The MDTs' outstanding spatial resolution is accompanied by the downside of large drift times of up to 750 ns, which is much larger than the bunch-crossing rate of the LHC (25 ns). Thus, the MS contains additional *Resistive Plate Chambers* (RPCs) in the barrel and *Thin Gap Chambers* (TGCs) in the end-caps which are optimized for time resolution, achieving $\mathcal{O}(1\,\mathrm{ns})$, compromised by a worse spatial resolution of $\mathcal{O}(1\,\mathrm{cm})$. They are placed directly around the MDTs as illustrated in Figure 2.7 and used for fast triggering decisions, as elaborated in the next Section. The muon trigger system covers a range of $|\eta| < 2.4$.

Muons cannot be measured efficiently over the full solid angle due to the sheer size and geometry of the MS as the outermost part of the ATLAS detector. The MS acceptance is compromised frequently by mechanical support structures, the toroid magnets or gaps between adjacent chambers needed for cables to the ID, calorimeters and solenoid. Remarkable regions are, for instance, at $|\eta| < 0.03$, exhibiting a $\sim 30\,\mathrm{cm}$ gap for services and cables, and the *barrel end-cap transition region* at $|\eta| \approx 1$. This transition region can be seen nicely in Figure 2.3(b), where MS components are drawn in blue. Furthermore,

the MS acceptance is interrupted by the four detector feet located at $|\eta| \approx 0.75$ and $\phi \approx -70°/-110°$ ($\approx -1.2/-2$ in radians), see Figure 2.7(b).

2.2.6. Trigger system

The LHC features a bunch-crossing rate of $40\,\mathrm{MHz}$, producing an amount of data that is neither possible nor desirable to store and process in total. It is dominated by soft processes not considered for physics analysis. In order to select relevant events with high momentum transfer, a *two-level trigger system* is implemented, providing fast event selection decisions based on different sub-systems of the ATLAS detector.

The first level consists of the hardware-based *Level-1* (L1) trigger which supplies decisions within just $2.5\,\mu\mathrm{s}$ and lowers the event rate to $100\,\mathrm{kHz}$. Utilizing a subset of the information from the calorimeters or the MS, geometric signal information in the η-ϕ-space is summarized in so-called *Regions of Interest* (RoI). In this dissertation, single-muon triggers [108] are used which are based solely on signals in the MS. A schematic overview of the MS L1 trigger procedure is depicted in Figure 2.8(a). Depending on the location, different predefined coincidence patterns between two stations (low $p_{\mathrm{T}}(\mu)$) or three stations (high $p_{\mathrm{T}}(\mu)$) are required within a spatial window in the order of $10-40\,\mathrm{cm}$.

The software-based *High-Level trigger* (HLT) is the second level of the ATLAS triggering system. It reduces the rate to $1\,\mathrm{kHz}$, a reasonable amount of data to be stored, and analyzed at a later point (*offline*). Once the L1 trigger is passed, a fast preliminary object reconstruction is performed in the RoI, referred to as *online*, as it is done in real time during data-taking. The reconstructed HLT objects need to fulfill certain momentum and isolation criteria for an event to be stored, as summarized for the muon-triggers used in this thesis in Figure 2.8(b). A logical 'or' between an isolated low-$p_{\mathrm{T}}(\mu)$ trigger and the 50-GeV trigger is used for each year of data taking.
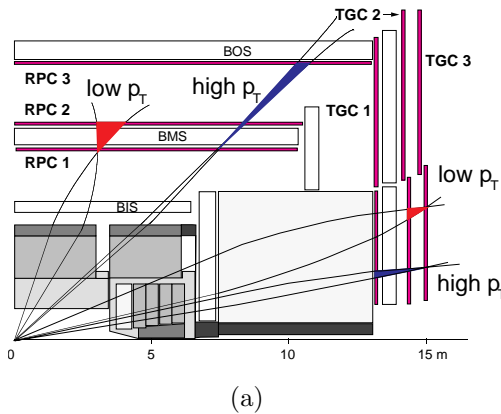
Year	Min. p_{T} [GeV]	Isolation	Min. L1 p_{T} [GeV]
2015	20	loose	15
2016-18	26	*var*-medium	-
or			
2015-2018	50	-	-

(a)   (b)

Figure 2.8.: Overview of the (a) muon L1 trigger [100] procedure and (b) single-muon HLT triggers [108] used in this dissertation.

2.2.7. Luminosity measurement

A precise knowledge of the luminosity is essential for reliable physics results. For instance, measured cross-sections are directly dependent on the integrated luminosity. Accurate measurements of the instantaneous per-bunch luminosity are provided by the *Beam Condition Monitor* [109, 110], and, in particular, the *LUCID2*[7] [111] detectors placed close to the beam pipe at $z = \pm 17\,\mathrm{m}$. They utilize the principle of Cherenkov radiation, measured by photo-multipliers, that is directly related to the visible interaction rate, meaning events containing a measurable signal. Dedicated calibrations are performed in *Van-der-Meer scans* [112] each year where the location of one beam is varied with respect to the other one.

---

[7]**LU**minosity measurements using **C**herenkov **I**ntegrated **D**etector

3. Data and simulated samples

This Chapter gives an overview of the dataset used in Section 3.1 as well as the corresponding simulated samples in Section 3.3. Additionally, the general simulation procedure via Monte-Carlo generators is described in Section 3.2.

3.1. The Run-2 dataset

This work is based on pp-collision data at $\sqrt{s} = 13\,\text{TeV}$ recorded with the ATLAS detector during the LHC Run 2. Figure 3.1(a) shows the integrated luminosity over time which was delivered by the LHC, recorded by the ATLAS detector and the fraction suitable for physics analysis. The latter is imposed on quality criteria such as fully operating sub-detectors. In total, more than 94% of the data delivered can be used for physics analysis, corresponding to an integrated luminosity of $\mathcal{L}_{\text{int}} = 140\,\text{fb}^{-1} \pm 0.83\%$ [113]. The luminosities per year of data-taking amount to $\mathcal{L}_{2015} = 3.22\,\text{fb}^{-1}$, $\mathcal{L}_{2016} = 33.0\,\text{fb}^{-1}$, $\mathcal{L}_{2017} = 44.3\,\text{fb}^{-1}$ and $\mathcal{L}_{2018} = 58.5\,\text{fb}^{-1}$ [113].

The high luminosity is achieved by colliding dense bunches of protons. However, this leads to the effect that multiple protons collide simultaneously (*pile-up*, see Section 1.2.1). The Run-2 pile-up profile is shown in Figure 3.1(b), exhibiting an average pile-up of $\langle \mu \rangle = 33.7$ with a maximum of about $\mu \approx 80$. The years 2017 and 2018 were subject to a higher pile-up than the previous years.

(a)

(b)
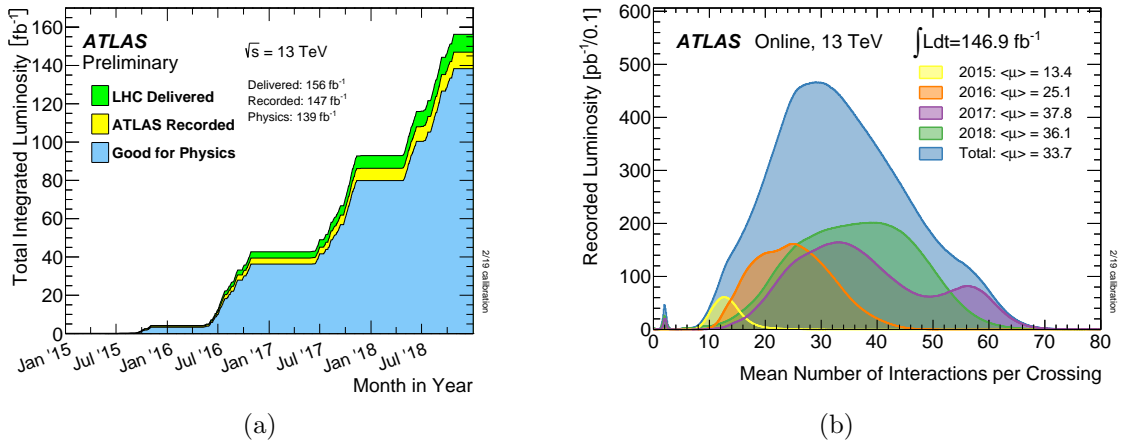
Figure 3.1.: Overview of the (a) integrated luminosity and (b) pile-up profile of the Run-2 dataset [94].

3.2. Monte-Carlo simulations of pp collisions

Simulations play a key role in high-energy physics. However, the prediction of the outcome of pp collisions in the ATLAS detector is challenging due to the complexity of both, the underlying theory and the experimental setup. A fully-analytical calculation of theoretical predictions from the SM is not possible. Instead, phenomenological models and perturbative calculations are utilized which can be combined according to the factorization theorem (see Equation 1.11). Perturbative calculations are based on complex integrals that are commonly solved using *Monte-Carlo* (MC) methods.

Event-based MC generators are able to produce accurate predictions of distributions of physical observables. They represent a powerful tool for assessing background events as well as unfolding detector effects. Usually, the full simulation chain is done in different steps implemented in distinct generators.

Parton distribution functions The momentum fraction of the interacting partons is assessed via PDFs, as described in Section 1.2.2. They are provided by dedicated groups performing global fits to measured data. Leading modern PDFs, evolved to NLO or NNLO in QCD, are determined for instance by the MSHT [114], NNPDF [115] or CT(EQ) [116] groups.

Hard scatter The main interaction between two partons is described in the HS process, including the decay of unstable massive particles. It can be estimated by perturbative ME calculations, as introduced in Section 1.1.5. Loops and real emissions might be included in the ME, with the cost of large computational efforts. Thus, HS calculations are commonly performed to NLO or NNLO in QCD. Missing higher-order contributions can be accounted for via systematic uncertainties where the scales μ_R (see Section 1.1.2) and μ_F (see Section 1.2.2) are varied. Widely used HS generators are POWHEG BOX [117–120], MADGRAPH5_AMC@NLO [121] and SHERPA[1] [122].

Parton shower + hadronization Further higher-order real emissions, culminating in the formation of hadronic jets, are approximated via non-perturbative PS algorithms [123]. This approach is justified by the enormous computational effort of higher-order MEs, but also by the fact that integrals may diverge in the limit of extremely *soft* (low energy) and *collinear* (small angle) radiation. PS and higher-order ME calculations may overlap, thus ambiguities are resolved by dedicated matching and merging algorithms [124–127]. The PS contains a cascade of particles characterized by parton splittings, dominantly[2] $q \to gq$, $g \to qq$ or $g \to gg$. Splittings are evolved from the HS scale down to ever-smaller energies, based on the probability for a parton to split at the given scale. This

---

[1]SHERPA is a multipurpose MC generator calculating both the HS and the PS.

[2]QED radiation plays a subordinate role, as $\alpha_{em} << \alpha_s$, but is taken into account nevertheless.

step-by-step procedure is repeated until energy scales of $\mathcal{O}(1 \text{ GeV})$ are reached. At that point, hadronization to color-neutral states takes place followed by decays of heavy hadrons. As the hadronization process generally falls in the non-pertubative region, phenomenological models are employed, e.g. the *Lund string model* [128] implemented in Pythia [129] or the *cluster hadronization model* [130] in Herwig [131] and Sherpa.

Underlying event   One parton per proton initiates the HS process, nevertheless, the remnants interact as well (see Section 1.2.1). Thus, a sophisticated understanding and modeling of this underlying event is essential. Due to the low energy scale of these processes, they fall in the non-perturbative QCD region. Thus, phenomenological models are used that are matched to experimental data in a process called *tuning*. The UE is usually simulated with the generator used for the parton shower.

Pile-up   The pile-up is estimated via *minimum bias events*, a very loose selection of inelastic events of strong interaction processes with low-momentum particles. It is overlaid with the HS process and modeled in Pythia 8.186 [132] with the A3 [133] set of tuned parameters and the NNPDF2.3lo PDF [134].

Detector simulation   The geometry and response of the ATLAS detector are described precisely using Geant4 [135]. As the final part of the simulation chain, it provides the interaction of final-state particles with the detector. In a digitization step, the interactions are converted to *detector hits* that are then fed through the same reconstruction algorithms as measured data. Alternatively to the *full simulation* (FS) of the detector, a *fast simulation* (called AFII) using a less-detailed, parametrized calorimeter response is employed for some systematic uncertainty samples.

The MC simulation chain allows for assessing particle information at different levels. The level after the detector simulation is called *reconstruction level*, whereas the one before is referred to as *(MC) truth level*. In measured data, only the reconstructed level is directly available and the MC simulation of the signal process can be exploited for quantifying and eliminating the impact of the measurement procedure.

3.3. Monte-Carlo samples used

Generally, MC simulation samples are produced centrally by the ATLAS collaboration and, later, exhibited to the same event selection as the data in the analysis. It shall be highlighted at this point that, generally, any new generator or software version is tested and validated thoroughly using the automated PAVER system [136, 137], which I actively contributed to.

The MC samples of the signal process as well as relevant background processes are described in the following. They were produced in three campaigns matching the data-taking periods of Run 2: `mc16a` (2015+16), `mc16d` (2017) and `mc16e` (2018). The information about all generators used is also summarized in Table 3.1.

Signal samples   The $W \to \mu\nu$ process is simulated in POWHEG BOX v1 [117–120] at NLO in QCD using the CT10NLO PDF set [138] interfaced with PYTHIA 8.186 [132] for PS, hadronization and UE, with the AZNLO [139] set of tuned parameters. Additionally, QED FSR is simulated using PHOTOS++ 3.52 [140, 141].

In order to guarantee that the MC statistical uncertainty in the high-mass tail is not a limiting factor for the analysis, the generation of the $W \to \mu\nu$ sample is performed separately in different ranges of the invariant W-boson mass. The full sample is composed of an inclusive (*peak*) sample and 19 high-mass samples (*slices*), per muon charge each. In order to avoid overlap, the peak sample is cut to cover the region of $m_{\text{inv}} < 120\,\text{GeV}$. As an addition, the slices range between $120\,\text{GeV}$ and $5000\,\text{GeV}$, plus one slice covering $m_{\text{inv}} > 5000\,\text{GeV}$, while containing at least 50000 events each. A smooth transition of all sub-samples, as illustrated in Figure 3.2(a), is ensured by scaling to the corresponding cross-section for each phase space. The detailed mass ranges, cross-sections and numbers of generated events are summarized in Table A.1 (W^+) and Table A.2 (W^-).

The POWHEG+PYTHIA8 prediction is corrected using *k-factors* [142] parametrized as a function of m_{inv}. They improve to NNLO in QCD, calculated via VRAP v0.9 [143], and the CT14NNLO PDF set [144]. Furthermore, they include NLO EW corrections (except for QED FSR), calculated via MCSANC [145] and implemented in an additive approach. The impact of the total correction on the measurement observable m_{T}^{W} can be seen in Figure 3.2(b), as an example for the positive charge. The correction increases with m_{T}^{W} to more than $10\,\%$ for $m_{\text{T}}^{\text{W}} > 2\,\text{TeV}$. The underlying correction functions in m_{inv} can be found in Figure A.1 where it can be seen that the NNLO QCD corrections increase the cross-section for $m_{\text{inv}} < 2\,\text{TeV}$ and the EW corrections generally decrease the cross-sections.

(a)   (b)
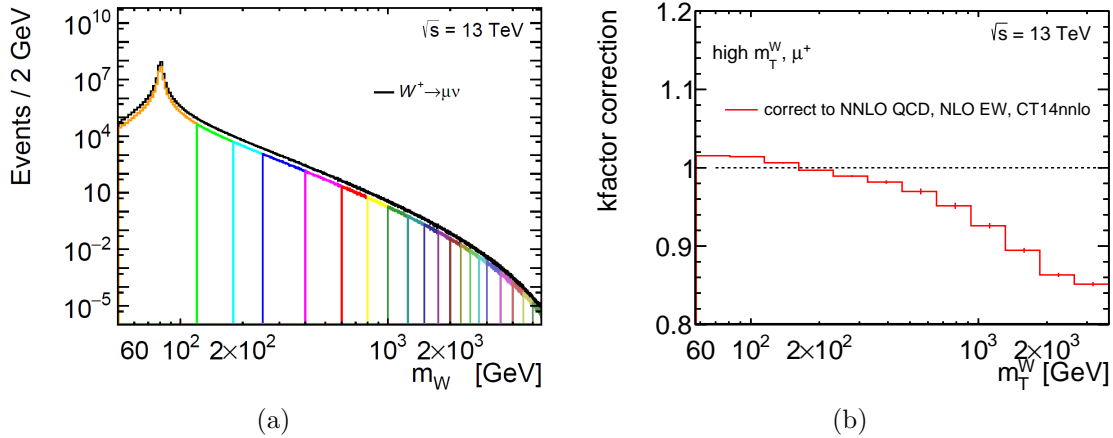
Figure 3.2.: (a) Distribution of the invariant W^+ mass, where each colored line represents one $W^+ \to \mu^+\nu$ sub-sample. The black line is the combination of all samples and is scaled by a factor of two for visibility. (b) Relative impact on the transverse-mass distribution of the mass-dependent *k-factor* applied to the $W^+ \to \mu^+\nu$ sample.

An alternative simulation of the signal process is used for the assessment of a modeling systematic uncertainty as well as comparisons of predicted to measured cross-sections. It is simulated using SHERPA 2.2.11 [122] with the NNPDF3.0nnlo PDF set [115]. Sufficient statistical power is ensured by combining an inclusive sample, with $m_{inv} < 120\,\mathrm{GeV}$, with a dedicated high-mass sample. Each consists of three sub-samples for different heavy-flavor filters. The generation was done at NLO in QCD for zero to two additional partons and at LO for up to five partons. NLO EW corrections are included via the exponentiated[3] approach. Lastly, the cross-section is corrected using a flat NNLO *k-factor* of 0.95 calculated via MATRIX v2 [146].

Background samples Precise simulations of not only the signal but also *background processes* are essential. The latter are all processes with a detector signature similar to the signal, here a single muon and E_T^{miss}. The resemblance could be caused by a comparable final state from the HS interaction but also a limited detector acceptance and efficiency.

In this dissertation, the largest background is given by the pair-production of a top quark and a top antiquark ($t\bar{t}$) via gluon-gluon fusion. Each top quark decays predominantly into a bottom quark and a W boson, which subsequently decays hadronically or leptonically. Semileptonic, i.e. one top quark decays hadronically and one leptonically, as well as dileptonic $t\bar{t}$ decays where one of the two leptons is not measured contribute here. Single top-quark production is a further background, generated in the *t-channel*, *s-channel* or a single top quark in association with a W boson (tW). The latter is the dominant contribution among the three. Interference with the $t\bar{t}$ process is removed using the diagram subtraction scheme (DS) [147]. Neutral-current DY events where the Z boson decays into a pair of muons ($Z \to \mu\mu$) or taus ($Z \to \tau\tau$), respectively, are taken into account. The former contributes to single-muon final states if one muon does not fall in the detector acceptance. For the latter, the taus decay such that one muon is measured in the final state. Analogously, the $W \to \tau\nu$ process with $\tau \to \mu\bar{\nu}_\mu\nu_\tau$ is considered. Lastly, diboson processes are simulated which consist of weak boson pairs, i.e. WW, ZZ and WZ. Hadronic or leptonic decays as well as the detector acceptance dictate the contribution of in total nine different processes[4].

All MC generators per process are summarized in Table 3.1 including the respective orders in QCD and PDF sets used. All DY backgrounds are subject to dedicated mass-dependent *k-factors*, analogously to the signal MC sample. The $t\bar{t}$ process is normalized to an inclusive NNLO+NNLL cross-section calculated using TOP++ 2.0 [148] while single-top and diboson processes are normalized to NLO cross-sections.

---

[3]Differences between additive, multiplicative and exponentiated approaches are small, see Figure F.11.

[4]$(Z \to \ell\ell + Z \to \ell\ell), (Z \to \ell\ell + Z \to vv), (Z \to \ell\ell + W \to \ell v), (W \to \ell v + Z \to vv),$
$(W^\pm \to \ell v + W^\mp \to qq), (Z \to qq + Z \to \ell\ell), (W \to qq + Z \to \ell\ell), (W \to \ell v + Z \to qq)$

Table 3.1.: List of processes simulated in MC, showing each generator used for the matrix element (ME), including the order in QCD, and showering (including PS, UE, Hadronization). The PDF and tune used are given as well. All processes marked with an * are corrected using mass-dependent *k-factors*, correcting them to NNLO in QCD, NLO EW and the CT14NNLO PDF.

Process	Matrix element	ME order	PDF set	PS, UE & Hadronization	Tune
			Signal samples ($W \to \mu\nu$)		
Default*	POWHEG v1	NLO	CT10NLO	PYTHIA 8.186	AZNLO
Alternative	SHERPA 2.2.11	NLO (0-2j)/ LO (3-5j)	NNPDF3.0NNLO	SHERPA 2.2.11	SHERPA-default
			Background samples		
$t\bar{t}$/single top	POWHEG v2	NLO	NNPDF3.0NLO	PYTHIA 8.230	A14
$Z \to \mu\nu/\tau\tau$*	POWHEG v1	NLO	CT10NLO	PYTHIA 8.186	AZNLO
$W \to \tau\nu$*	POWHEG v1	NLO	CT10NLO	PYTHIA 8.186	AZNLO
Diboson	SHERPA 2.2.1/2.2.2	NLO (0,1j)/ LO (2,3j)	NNPDF3.0NNLO	SHERPA 2.2.1/2.2.2	SHERPA-default

4. Particle identification and reconstruction

Different particles leave unique signatures in the sub-systems of the ATLAS detector, as illustrated in Figure 4.1(a), allowing for a dedicated identification and measurement per particle type. The precise and accurate reconstruction from hits, i.e. electrical signals, in the detector to particles is an essential but challenging task. Intricate algorithms are employed providing calibrated four-vectors, and additional properties of the particles, to be used in physics analyses. This Chapter highlights the objects important for the $W \to \mu\nu$ measurement presented, starting from tracks in the ID spanning to calibrated muons, electrons, jets and missing transverse momentum. The reconstruction, calibration and analysis-specific quality criteria are elaborated, with a focus on muons as they are the central particles in this thesis.

4.1. ID tracks and vertices

Charged particles leave a bent track in the ID, which is the basis for any subsequent reconstruction. Five fundamental parameters are associated with the track, see Figure 4.1(b). Angular directions are parametrized by the polar and azimuthal angles θ and ϕ. The shortest distance of the track to the IP is given by the *transverse* and *longitudinal impact parameters* d_0 and z_0. Finally, the charge-over-transverse-momentum fraction q/p_{T} is determined by measuring the curvature of the track via the *sagitta*. It is defined as the distance from the center of an arc to its chord. The sagitta method allows to conclude the radius of a circle even if only a part of the circle is given.

The start of each track reconstruction are clusters of hits in the pixel and SCT detectors, forming three-dimensional *space points*. A *track seed* is constructed from three unique space points, forming an initial particle trajectory. Subsequently, the compatibility with additional space points is examined by extrapolating through these two sub-detectors. A *track candidate* is formed by feeding various quality criteria to a neural network, quantifying whether a track is caused by a real charged particle. An ambiguity solver removes overlap between track candidates, keeping the ones with a higher track score. Finally, the track is refined using information from the TRT, which improves the resolution.

(a)   (b)
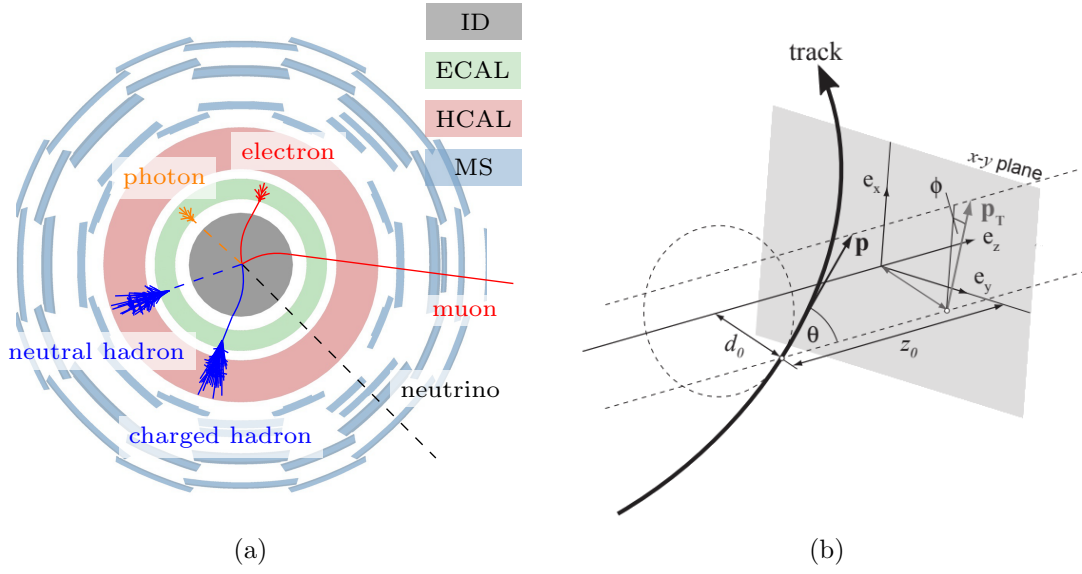
Figure 4.1.: Overview of (a) the signatures of different particles in the ATLAS detector, where a dashed line indicates invisibility, and (b) the parameters d_0, z_0, θ, ϕ and q/p which define a track in the ID [149].

Once all tracks are reconstructed, common intersection points, called *vertices*, are identified. The *primary vertex* (PV) is the collision point where the HS interaction took place. It is determined by an adaptive vertex finding algorithm [150] based on a χ^2-minimization that optimizes the compatibility of tracks with the initial vertex. The PV is characterized by the highest sum of squared momenta of associated tracks, $\sum_{i=1}^{N_{\text{track}}} p_{\text{T},i}^2$, of which a minimum of two tracks fulfill $p_{\text{T}} > 500\,\text{MeV}$. Furthermore, *secondary vertices* might occur outside of the beam-overlap region which originate from the decay of long-lived particles. Additional vertices, with at least two associated tracks passing the threshold, are part of the pile-up.

4.2. Muons

At the energy scales of the ATLAS experiment (GeV to TeV), muons are minimal ionizing particles and deposit only very little energy in the calorimeter systems. Since all other measurable particles are absorbed in the calorimeters, see Figure 4.1(a), a hit in the MS is a clear indicator for the presence of a muon, making it an object with a very clean and distinct detector signature.

4.2.1. Reconstruction

Muons are measured based on tracking in the ID and MS. The track reconstruction in the ID was explained in Section 4.1. For the MS, an independent track reconstruc-

tion is performed based on straight-line segments across multiple MS stations [151]. Three-dimensional track candidates are constructed from the segments while taking into account additional information from the trigger detectors and the influence of the toroidal magnetic field. A global χ^2 fit is performed which accounts, among other things, for the energy loss in the calorimeters, interactions with the detector material and potential misalignment between stations. Finally, outliers from the trajectories are removed, unused tracks in the vicinity are added and the fit is re-performed.

There are different strategies for combining the information from the two sub-detectors which can depend on the detector regions and impact the quality of a muon measured [152]. In this dissertation, solely *combined muons* (CB) are utilized. These are reconstructed in a final combined fit of hits in the ID and MS, yielding the most precise and accurate muon measurement available. The combination procedure is predominantly *outside-in*, i.e. MS tracks are extrapolated to the ID and matched to corresponding tracks measured there. It is complemented by an analogous *inside-out* approach, starting with ID tracks.

4.2.2. Identification

Once muon tracks are reconstructed, the identification of muon candidates is based on various criteria such as track properties, the number of hits, the fit quality or ID/MS compatibility. Different physics analyses may express distinct requirements for reconstructing muons, compromising selection efficiency and muon quality. The latter is characterized by e.g. a good suppression of muons originating from secondary hadron decays or the omission of muons in suboptimal detector regions. Various identification levels called *working points* (WP) are defined [152].
The precision measurement presented here aims for an optimal quality of the single muon in the analyzed $\mu + E_{\mathrm{T}}^{\mathrm{miss}}$ final state. Hence, the `high-`p_{T} WP is used which is specially developed for analyses examining high-mass regimes. Additionally, in order to select solely single-muon final states, events containing additional muons are vetoed. These muons are subject to the lower `Medium` quality.

For both WPs, the muon is required to possess a *charge-over-momentum significance* smaller than seven. It is defined based on the charge-over-momentum fraction q/p in each sub-detector and their respective uncertainties $\sigma^2(q/p)$ as

$$(q/p)^{\mathrm{sig}} = \frac{|(q/p)_{\mathrm{ID}} - (q/p)_{\mathrm{MS}}|}{\sqrt{\sigma^2((q/p)_{\mathrm{ID}}) + \sigma^2((q/p)_{\mathrm{MS}})}}. \tag{4.1}$$

Additionally, the `Medium` WP is characterized by at least two[1] *precisions stations*, which are stations in the MS with a least three hits each.

---

[1]For $|\eta| < 0.1$, tracks with at least one precision station but no more than one *hole* are allowed. A hole is a station where no hit is detected but one is expected given the overall trajectory.

In contrast, the `high-`p_T WP contains tighter requirements aiming to optimize the momentum resolution for muons with $p_\mathrm{T}(\mu) > 100\,\mathrm{GeV}$. For these, the challenge of almost straight trajectories emerges. In order to still allow for a precise sagitta measurement, the number of required precision stations is elevated to three. Furthermore, a veto is placed on regions in the detector that manifest a suboptimal alignment of MS stations. Examples are the transition region between barrel and end-caps ($1.01 < |\eta| < 1.1$) or the detector feet ($\phi = -1.2/-2.0$). Finally, a $p_\mathrm{T}(\mu)$-dependent cut is placed on the relative q/p uncertainty in order to reject non-optimal measurements.

The choice of the muon identification level was studied extensively in my master thesis [153]. It was seen that, at $p_\mathrm{T}(\mu) \approx 1\,\mathrm{TeV}$, the `high-`$p_\mathrm{T}$ WP improves the muon resolution by about 15% with respect to `Medium` while maintaining a good selection efficiency above 70%. Furthermore, it was shown that the usage of `Medium` instead of `high-`p_T on the veto level leads to a substantial reduction of the $Z \to \mu\mu$ background of more than 50% without compromising the signal $W \to \mu\nu$ efficiency.

4.2.3. Isolation

This aim here is selecting clean muons originating from heavy-boson decays in the HS process. These muons are normally produced well-separated from other particles. Measuring the detector activity around the particle is a powerful handle to suppress unwanted background muons originating from secondary vertices in jets.

The *isolation criterion* is quantified by the activity in a cone with size ΔR around the muon's trajectory. Different WPs are defined [152] that vary in their signal efficiency and background rejection rate. For muons selected here, a track-based isolation criterion is used, called `TightTrackOnlyFixedRad`. The sum of p_T of tracks i within a radius of 0.2 must not exceed 6% of the muon's transverse momentum[2]:

$$0.06 \cdot p_\mathrm{T}(\mu) > p_\mathrm{T}^{\mathrm{cone20}} = \sum_{i=0}^{N_{\mathrm{tracks}}} p_{\mathrm{T},i} \quad \text{with } \Delta R(i,\mu) < 0.2 \text{ and } p_{\mathrm{T},i} > 1\,\mathrm{GeV}. \qquad (4.2)$$

The isolation criterion was studied in my master thesis and compared to a p_T-dependent cone size of $\Delta R = \min(10\,\mathrm{GeV}/p_\mathrm{T}(\mu)[\mathrm{GeV}], 0.3)$ (WP: `TightTrackOnlyVarRad`). The usage of a fixed cone size shows a 5-8% smaller efficiency for undesired non-prompt muons while impacting the prompt signal muon efficiency in the sub-permill range.

4.2.4. Momentum scale and resolution corrections

Simulations include an outstanding description of the ATLAS detector. Nevertheless, the level of detail reaches its limitations at the percent to permill level. Therefore, the

---

[2]For $p_\mathrm{T}(\mu) < 50\,\mathrm{GeV}$, the cone size is p_T-dependent, see Ref. [152]. However, this analysis selects solely muons with $p_\mathrm{T}(\mu) > 65\,\mathrm{GeV}$.

scale and resolution of the momentum of muons are refinded using clean $Z \to \mu\mu$ and $J/\Psi \to \mu\mu$ events [154, 155]. A correction is applied to all MC simulations, in this analysis, separately for ID and MS. It is parametrized as follows, with Det=(ID, MS),

$$p_\mathrm{T}^{\mathrm{corr,Det}} = \frac{p_\mathrm{T}^{\mathrm{MC,Det}} + s_0^{\mathrm{Det}} + s_1^{\mathrm{Det}} \cdot p_\mathrm{T}^{\mathrm{MC,Det}}}{1 + \Delta r_1^{\mathrm{Det}} \cdot g_1 + \Delta r_2^{\mathrm{Det}} \cdot g_2 \cdot p_\mathrm{T}^{\mathrm{MC,Det}}}. \tag{4.3}$$

Here, $p_\mathrm{T}^{\mathrm{MC,Det}}$ is the uncorrected p_T in the MC simulation and g_i standard normally distributed random numbers. The factors s_i^{Det} and $\Delta r_i^{\mathrm{Det}}$ are the scale and resolution corrections, determined via a binned likelihood fit of MC to data in the invariant di-muon mass spectrum. They are estimated in bins of η and ϕ, taking into account the non-uniform detector geometry, technology and performance.

The numerator represents the scale corrections, where s_1 incorporates inaccuracies in the magnetic field description and the perpendicular dimension of the detector. Additionally, s_0 takes into account the energy loss in the calorimeters and material layers (thus, it is only applied for the MS).

Analogously, the denominator provides a parametrization of the resolution, or momentum smearing, assuming a relative uncertainty as $\sigma(p_\mathrm{T})/p_\mathrm{T} = \Delta r_1 \oplus \Delta r_2 p_\mathrm{T}$. The factor Δr_1 covers effects like multiple scattering, local magnetic field inhomogeneities and local radial hit displacements. The second factor, Δr_2, encapsulates intrinsic resolution effects due to the spatial detector resolution and residual misalignment in the MS.

4.2.5. Sagitta bias correction

Generally, dedicated procedures align the detector to extremely high precision [101, 156]. Nevertheless, residual displacements to the nominal detector geometry, or uncertainties in the alignment system, induce small biases in the measurement of the muon's momentum in both, the ID and MS. A so-called *sagitta bias* is introduced by, for instance, a rotation of detector layers with respect to each other. A schematic illustration can be found in Figure 4.2 for the ID. The muon's trajectory is bent in the transverse plane by the solenoid magnetic field. The red stars and dotted lines show the hits and trajectories for an ideal detector alignment. They are symmetrical between the two bending directions, i.e. the two muon charges. Moreover, the gray stars and solid lines show the curves if a twist between detector layers is present. In this case, a more or less pronounced curvature can be observed, depending on the charge. As a result, a charge-dependent bias on the sagitta measurement and, thus, the momentum of the muon emerges.

A dedicated sagitta-bias correction procedure is performed separately for the ID and the MS as they are subject to different biases [155]. Opposed to the scale and resolution corrections that correct the p_T in the MC samples (see Section 4.2.4), it is applied to measured data. The corrected p_T of the muon is parametrized as

$$p_\mathrm{T}^{\mathrm{corr}} = \frac{\hat{p_\mathrm{T}}}{1 - q\delta_s(\eta, \phi)\hat{p_\mathrm{T}}} \tag{4.4}$$
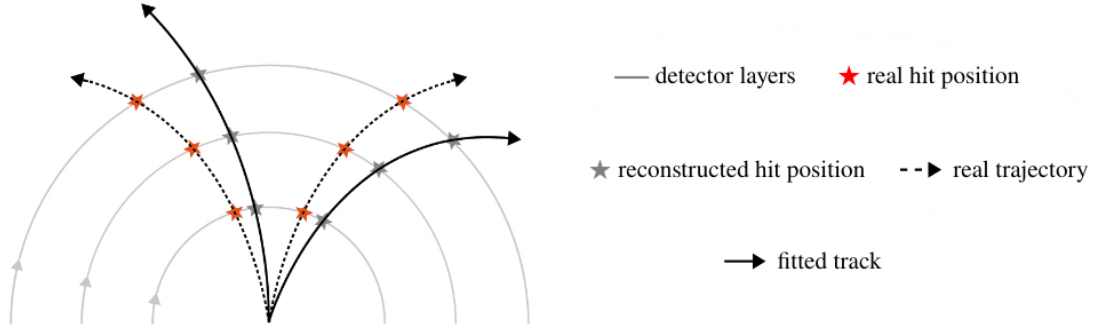
Figure 4.2.: Simplified representation of the sagitta bias in the ID caused by a deformation of the measured track in the bending plane due to a rotation of the detector layers with respect to each other [157].

where q indicates the charge of the muon, $\hat{p_\mathrm{T}}$ its uncorrected momentum and δs the correction factor. The latter is determined as a function of η and ϕ in a 48×48 grid reflecting local biases in certain detector regions. Again, the $Z \to \mu\mu$ resonance is adopted for the calibration. Two complementary methods are employed. In the first one, the variance of the resonant peak is minimized to assess δ_s. It is impacted by the sagitta bias as the p_T of both muon charges enter the variance. The second method compares the global average di-muon mass with the mean one estimated with the leading muon in a certain η-ϕ region. Finally, small asymmetries between the acceptance of the two muon charges are accounted for via MC simulations.

It is recommended to study explicitly whether the sagitta-bias correction should be applied to an analysis-specific data selection [158]. Alternatively, a systematic uncertainty accounts for the residual bias. For very high $p_\mathrm{T}(\mu)$, the sensitivity to small sagitta biases increases due to almost straight trajectories[3]. Thus, the correction was studied in detail here, see Appendix B. It was found that the distributions of measured data in the phase space analyzed are impacted up to 20% by the correction, with the largest effects at high m_T^W and forward $|\eta(\mu)|$ (see Figure B.1). Two cross-checks underline an essential improvement in performance if the correction is applied (see Figures B.3/B.4). Firstly, the consistency of agreement between data and prediction per muon charge is compared in a double ratio. Secondly, the cross-sections measured in the parallel electron channel are taken as a reference.

It shall be highlighted that the sagitta-bias correction is obtained using events at the Z-boson mass peak only and is not optimized for $p_\mathrm{T}(\mu) > 350\,\mathrm{GeV}$. However, this region plays a crucial role in the high-m_T^W measurement presented here. Thus, a systematic uncertainty accounting for the extrapolation to high $p_\mathrm{T}(\mu)$ was developed especially for this measurement. It was shown that a de-correlation of the uncertainty in barrel and end-caps is valuable as the bias is strongly η-dependent [85]. In the ideal

---

[3]The sagitta in the MS is approximately $0.5\,\mathrm{mm}$ for a muon with $p_\mathrm{T}(\mu) = 1\,\mathrm{TeV}$ [100].

case, the high-$p_{\mathrm{T}}(\mu)$ regime would be taken into account for the determination of the correction and not only in an extrapolated systematic uncertainty. However, this could not be achieved here due to time and personpower constraints.

4.2.6. Efficiency corrections

The measurement efficiency of certain criteria might vary between data and simulation. In order to account for this, dedicated correction *scale factors* (SFs) are applied to all MC simulations. They are established using the *tag-and-probe method* in $Z \to \mu\mu$ and $J/\Psi \to \mu\mu$ events [152]. The basis is the identification of a high-quality particle, the *tag*, alongside a *probe* particle constrained by the reconstructed resonance mass. By comparing how often the probe is correctly identified alongside the tag, a detection efficiency for the probe particle can be determined. Each SF is defined by the quotient of the efficiency in data over the one obtained using MC samples. The final muon SF is composed of a dedicated SF for the muon identification, isolation, trigger and *track-to-vertex-association* (TTVA), covering requirements to the impact parameters d_0 and z_0,

$$\mathrm{SF}_\mu = \mathrm{SF}_{\mathrm{Identification}} \times \mathrm{SF}_{\mathrm{Isolation}} \times \mathrm{SF}_{\mathrm{Trigger}} \times \mathrm{SF}_{\mathrm{TTVA}} \quad \text{with} \quad \mathrm{SF}_i = \frac{\epsilon_i^{\mathrm{Data}}}{\epsilon_i^{\mathrm{MC}}}. \quad (4.5)$$

All SFs are provided centrally [108, 152, 154], usually estimated per year of data taking as the running conditions changed within Run 2. They depend on the WPs used and are given as a function of well-chosen kinematic observables. The identification and trigger SFs are binned in the detector coordinates $\eta(\mu)$ and $\phi(\mu)$, while the TTVA SF is binned in $|\eta(\mu)|$ and $p_{\mathrm{T}}(\mu)$. The isolation SF depends on the p_{T} of the muon as well as its distance to the closest jet. Most SFs are very close to unity, $\mathcal{O}(1\%)$ difference. However, the difference to unity in the trigger SF extends to more than 10% in the barrel.

4.2.7. Summary of the muon selection

In this analysis, all muons need to be measured within $|\eta(\mu)| < 2.4$. In principle, the MS is able to detect muons up to $|\eta(\mu)| < 2.7$ but the muon triggering system is limiting the acceptance at high $\eta(\mu)$. Furthermore, track-to-vertex-association requirements ensure that the track of a muon points to the primary vertex of the event. The longitudinal impact parameter has to fulfill $|z_0 \sin\theta| < 0.5\,\mathrm{mm}$ and the significance of the transverse parameter has to be smaller than three, $d_0^{\mathrm{sig}} < 3$.

Three muon selection levels are defined which differ in the identification and isolation levels as well as the $p_{\mathrm{T}}(\mu)$ requirement. As a reminder, the final state of interest consists of exactly one muon in addition to $E_{\mathrm{T}}^{\mathrm{miss}}$. The selected single muon must pass the `high-`p_{T} WP (defined in Section 4.2.2) and `TightTrackOnly_FixedRad` isolation (defined in Section 4.2.3) and must have a transverse momentum larger than $65\,\mathrm{GeV}$.

Table 4.1.: Muon selection criteria at different levels.

Level	Quality	Isolation	$p_{\mathrm{T}}(\mu)$ cut
Signal tight	`HighPt`	`FCTightTrackOnly_FixedRad`	$> 65\,\mathrm{GeV}$
Veto loose	`Medium`	-	$> 20\,\mathrm{GeV}$
Matrix Method loose	`HighPt`	-	$> 65\,\mathrm{GeV}$

Additionally, two distinct loose levels are established. In order to select exclusively single-muon final states, events with additional loose-level muons are discarded. These muons have to meet the lower `Medium` quality and a transverse momentum of $20\,\mathrm{GeV}$. Finally, the *Matrix Method loose level* differs from the tight signal level by a missing isolation requirement only. This level is crucial for the estimation of the fake-muon background via the Matrix Method.

4.3. Electrons

Just like muons, electrons undergo dedicated reconstruction and calibration steps and are subject to well-chosen identification and isolation criteria. In general, they enter this dissertation only in the form that events containing additional electrons are vetoed. As they do not play a central role, electrons are described only briefly here. The parallel electron-channel measurement motivates the electron selection here, as discussed in great detail in Reference [77].

In general, electron candidates are characterized by a bent track in the ID as well as a shower in the ECal [159], as illustrated in Figure 4.1(a). Their whole energy is collected in the ECal as opposed to muons. The reconstruction takes place in several steps, beginning with *topological clusters* composed from energy deposits in the ECal. Tracks in the ID are reconstructed as elaborated in Section 4.1 and matched to the clusters. The matching algorithm aligns the barycenter of a cluster with the extrapolated track to refine the track, and a single *super-cluster* is formed that encapsulates Bremsstrahlung by the electron. The electron's momentum is determined using a multivariate technique and calibrated precisely using a binned likelihood fit at the $Z \to ee$ and $J/\Psi \to ee$ resonances.

Dedicated identification and isolation criteria are imposed on electron candidates, discriminating them from hadronic jets or converted photons. The basis of the identification is a likelihood discriminant that takes into account signals in the individual ECal layers, track conditions, the compatibility of tracks and clusters and the energy leakage into the HCal, among other things. In this analysis, electron candidates are characterized by the `LooseAndBLayer` identification, and the `FCLoose` isolation that combines track- and calorimeter-based criteria [159].

Electrons selected in this analysis are required to have a transverse momentum larger than 20 GeV and an absolute pseudorapity smaller than 2.47. If they are located in the transition region between the barrel and end-caps in the ECal ($1.37 < |\eta(e)| < 1.52$), they are excluded due to an inferior measurement in this region. The primary vertex compatibility is checked via the transverse and longitudinal impact parameters, i.e. $|z_0 \sin \theta| < 0.5$ mm and $d_0^{\mathrm{sig}} < 5$. Finally, electrons are discarded if they have bad calorimeter clusters associated with them.

4.4. Jets

Jets are initiated by quarks or gluons as a consequence of confinement, as explained in Section 1.2.1. The signal process does not contain any jets at leading order and the measurement is inclusive in jets. Nevertheless, they play an important role in the calculation of the missing transverse momentum (see Section 4.5).

In the ATLAS detector, jets are characterized by energy deposits in the calorimeter systems. In particular, they are the only objects accumulating the largest part of their energy in the HCal, see Figure 4.1(a). Jet reconstruction is based on the *PFlow algorithm* [160] that matches topological calorimeter clusters with tracks in the ID, in case of jets initialized by a charged particle. For these, the track is used to estimate the jet's momentum and the corresponding energy is subtracted from the energy cluster. Jets are constructed via the *anti-k_t algorithm* [161] in the `FastJet` software package [162]. An iterative procedure matches PFlow objects with the smallest pairwise distance d_{ij}, defined as

$$d_{ij} = \min \left(\frac{1}{k_{\mathrm{t},i}{}^2}, \frac{1}{k_{\mathrm{t},j}{}^2} \right) \cdot \frac{\Delta R_{ij}{}^2}{R^2}. \tag{4.6}$$

It is weighted with the respective transverse momenta $k_{\mathrm{t,i/j}}$, the angular distance ΔR_{ij} and a fixed radius parameter R representing the size of the jet. The matching procedure is repeated until all PFlow objects are associated with exactly one jet.

An intricate calibration of the jet energy scale (JES) [107] is applied in steps, as outlined in Figure 4.3, each dedicated to different modeling or detection effects. First, the pile-up contribution to jets is corrected for. The p_{T}-density $\rho = \langle p_{\mathrm{T}}/A \rangle$ in a jet-area A (defined in $\eta \times \phi$), the number of interactions per event μ and the number of primary vertices N_{PV} are taken into account.

Next, the jet's absolute energy and pseudorapidity are calibrated using dijet MC samples. This correction incorporates any inefficiencies in the calorimeter response, energy losses in passive material and potential jet partons outside the defined jet cone.

The objects are fed into the *Global Sequential Tool* which accounts for different JES responses depending on the jet flavor, in particular, discriminating between quark or gluon initiation. Additionally, it considers an effect called *punch-through*, where not the
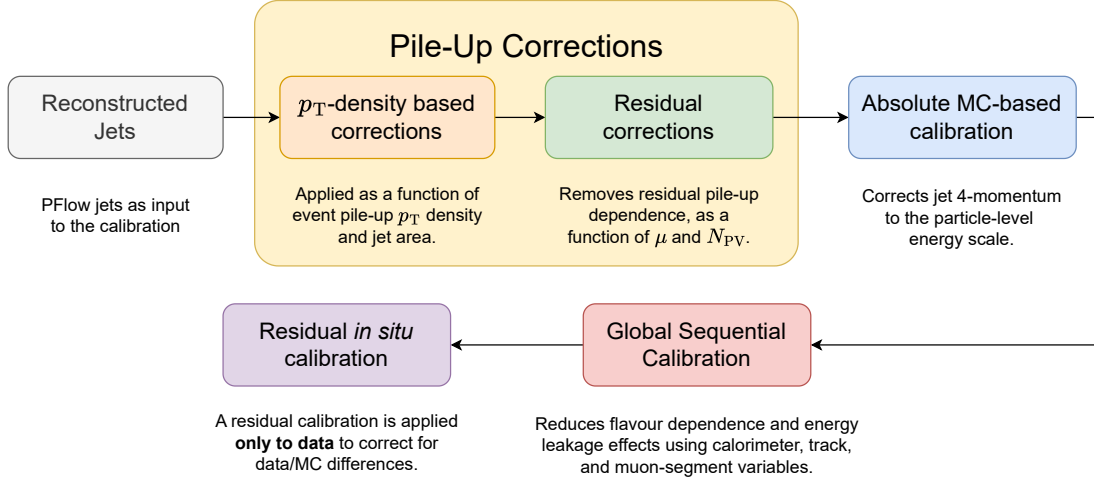
Figure 4.3.: Different steps in the JES calibration procedure depicted in a flow chart [163].

full jet activity is collected in the calorimeters.

Finally, an *in-situ* calibration addresses residual differences between data and MC simulations. A correction is applied to data based on the ratio of the jet response in data and in MC samples. It is derived in well-understood $Z \to \ell\ell$ events where the p_T of the $\ell\ell$-system is compared to the one of recoiling jets.

Furthermore, the jet energy resolution (JER) [107] is calibrated using the following parametrization

$$\frac{\sigma(p_T)}{p_T} = \frac{N}{p_T} \oplus \frac{S}{\sqrt{p_T}} \oplus C. \tag{4.7}$$

It takes into account a noise term N, accounting for pile-up and front-end electronics, a stochastic component S, for the number of calorimeter hits, and a constant term C, encapsulating energy deposits in passive material. The resolution in data and simulation is compared for dijet events. In phase spaces where the JER is worse in data than in simulation, the jet momentum is smeared to match the resolution in data. On the contrary, for finer resolution in data than in simulation, no smearing is applied to preserve the superior data quality.

In this dissertation, jets are defined with a radius parameter of $R = 0.4$. They are required to be measured with $p_T(j) > 25\,\text{GeV}$ and $|\eta(j)| < 2.5$.

4.5. Missing transverse momentum

Neutrinos cannot be measured directly in the ATLAS detector. Nevertheless, momentum conservation allows for the identification of the *missing transverse momentum* $\vec{p}_T^{\text{miss}}$

with the transverse momentum of the neutrino, as outlined in Section 1.2.1. This approach assumes that all other objects are detected correctly and no other non-interacting, potentially BSM particles are present in the event. The missing transverse momentum [164] is defined by the negative of the sum of transverse momenta of all reconstructed objects in the event, and an additional soft term, as

$$\vec{p}_\mathrm{T}^{\,\mathrm{miss}} = -(\sum_{\mathrm{electrons}} \vec{p}_\mathrm{T} + \sum_{\mathrm{photons}} \vec{p}_\mathrm{T} + \sum_{\mathrm{taus}} \vec{p}_\mathrm{T} + \sum_{\mathrm{jets}} \vec{p}_\mathrm{T} + \sum_{\mathrm{muons}} \vec{p}_\mathrm{T} + \sum_{\mathrm{soft}} \vec{p}_\mathrm{T}). \tag{4.8}$$

The absolute of $\vec{p}_\mathrm{T}^{\,\mathrm{miss}}$ is called *missing transverse energy*, denoted as $E_\mathrm{T}^{\mathrm{miss}}$. For the sake of simplicity, $E_\mathrm{T}^{\mathrm{miss}}$ is used synonymously for $\vec{p}_\mathrm{T}^{\,\mathrm{miss}}$ for the remainder of this thesis.

Objects are fed into the $E_\mathrm{T}^{\mathrm{miss}}$ calculation in the order listed here. A dedicated overlap removal procedure resolves ambiguities while favoring objects listed earlier in the sum. Photons and taus are not considered explicitly here. Finally, remaining low-energy (i.e. soft) tracks, but with a minimal p_T of $500\,\mathrm{MeV}$ and $|z_0 \sin\theta| < 2\,\mathrm{mm}$, that are not associated with any reconstructed object are summarized in a track-based soft term (TST). The TST is chosen over a calorimeter-based alternative due to its robustness against pile-up effects.

In this dissertation, events are selected if they exhibit a missing transverse momentum larger than $85\,\mathrm{GeV}$, corresponding to the energetic neutrino from the high-mass W-boson decay in the signal $W \to \mu\nu$ process.

4.6. Overlap removal

All objects are reconstructed on the basis of tracks and calorimeter clusters in the detector. As they are subject to independent reconstruction algorithms, overlap between particles may occur, e.g. a track being associated with two distinct objects. In order to avoid double counting, an *overlap removal* (OR) procedure is employed, subsequently removing the following objects from an event in the given order

- any electron with a track overlapping with another electron,

- any calorimeter muon[4] found with a shared track with an electron,

- any electron with a shared ID track with a muon,

- any jet found within a ΔR of 0.2 of an electron,

- any electron found within a ΔR of 0.4 of a jet.

Commonly, two further steps are applied to remove the overlap between muons and jets,

---

[4]A calorimeter muon leaves a track in the ID and the calorimeter but not in the MS due to a detector gap. These muons are not selected in this dissertation, so this step does not have any impact here.

- any jet with less than three associated tracks, which is found within a ΔR of 0.2 of a muon or has a track in the ID that is ghost-associated[5],

- any muon found within a ΔR of 0.4 of a jet.

However, they are explicitly not applied in this dissertation. It was found in my master thesis, that the omission of these OR steps is essential for the estimation of the multijet background via the Matrix Method. This background consists of fake muons originating in jets, thus, being likely to be very close to a jet. A significant number of loose-level (as given in Table 4.1) fake muons is achieved only by omitting these OR steps. At the same time, the number of tight-level events is affected marginally, as it is characterized by an additional isolation criterion.

---

[5]A muon is ghost-associated with a jet if its track is identified with a ghost track of the jet, which is a track in the jet direction with a momentum that is approximately zero [165].

5. Event selection and measurement binning

The reconstruction-level and truth-level event selections aiming to select events matching the signal $W \to \mu\nu$ final state are presented in Section 5.1 and Section 5.2, respectively. Additionally, the measurement binning is given and motivated in Section 5.3.

5.1. Reconstruction-level event selection

In pp collisions at the ATLAS experiment, an abundance of different physics processes is present. Thus, the first challenge is selecting a subset that predominately consists of signal $W \to \mu\nu$ events. This is achieved by subjecting the data to certain criteria designed to match the final state of the signal process. The same set of well-motivated requirements is placed on all MC samples. All criteria have been studied and optimized, where a good background rejection yet high signal efficiency is desired.

Table 5.1 shows the reconstruction-level event selection, which defines the *signal region*. Whenever regions with different requirements are used, all differences with respect to the signal region will be stated explicitly. The final state is characterized by exactly one tight-level, i.e. well-defined and isolated, muon, in addition to missing transverse momentum, corresponding to the neutrino from the W-boson decay. Each event selected is initiated by a single-muon trigger, as given in Section 2.2.6. The muon must be

Table 5.1.: Reconstruction-level event selection. Tight and loose levels are defined in Table 4.1.

Criteria	Requirement
Trigger	Single-muon triggers as defined in Figure 2.8(b)
Final state	Exactly one tight-level muon and $E_{\mathrm{T}}^{\mathrm{miss}}$
Veto	Events with additional electrons or loose-level muons
$|\eta(\mu)|$	< 2.4
$p_{\mathrm{T}}(\mu)$	$> 65\,\mathrm{GeV}$
$E_{\mathrm{T}}^{\mathrm{miss}}$	$> 85\,\mathrm{GeV}$
$m_{\mathrm{T}}^{\mathrm{W}}$	$> 200\,\mathrm{GeV}$ (+ shadow bin: $m_{\mathrm{T}}^{\mathrm{W}} \in [150, 200]\,\mathrm{GeV}$)

detected within $|\eta(\mu)| < 2.4$, driven by trigger acceptance. Furthermore, no *bad muons* are selected by imposing a cleaning cut removing muons with a suboptimal CB fit [154]. Events containing multiple leptons are discarded. The requirements to the additional lepton are loose, see Section 4.2.7 for muons and Section 4.3 for electrons. This way, in particular, the di-leptonic $t\bar{t}$ and $Z \to \ell\ell$ backgrounds are reduced substantially (see also Section 4.2.2). As the muon is the only selected final-state particle here, $p_T(\mu)$ may be abbreviated to p_T in the following, analogously for $\eta(\mu)$ and $\phi(\mu)$. If other objects are referred to it will be stated explicitly.

The key aspect of this measurement is the focus on the high-mass region determined by selecting events with $m_T^W > 200\,\text{GeV}$. This way, the largest part of ccDY events are discarded, as they are located at the resonance with $m_W \approx 80\,\text{GeV}$. In order to still exploit some knowledge of the $m_T^W < 200\,\text{GeV}$ region, a *shadow bin* has been developed which covers the range of $m_T^W \in [150, 200]\,\text{GeV}$. In principle, matching cuts on $p_T(\mu)$ and E_T^{miss} could be based on an even distribution of $m_T^W/2 = 100\,\text{GeV}$ per cut value. However, instead they are chosen to be $p_T(\mu) > 65\,\text{GeV}$ and $E_T^{\text{miss}} > 85\,\text{GeV}$ for the following reasons. Firstly, the shadow bin is only beneficial if well-populated. Thus, the cuts are chosen to match the lower bound of the shadow bin, i.e. $p_T(\mu) + E_T^{\text{miss}} > 150\,\text{GeV}$. The asymmetry between the two cuts is motivated, on the one hand, by the parallel electron-channel measurement. Here, the single-electron triggers set a lower boundary for the $p_T(e)$-cut at $65\,\text{GeV}$, and a higher E_T^{miss} cut reduces the multijet background. On the other hand, the increase of the E_T^{miss} cut to $85\,\text{GeV}$ minimizes undesired migration from the resonant mass peak to the high-mass region [84].

5.2. Truth-level event selection

The detector of any experiment is unique and subject to a distinct measurement efficiency, acceptance and resolution. In order to be able to compare different experiments and with theory predictions, the cross-sections will be presented on *truth level*, i.e. without any detector effects. This level is accessible in simulated samples due to the step-by-step generation chain explained in Section 3.2. For measured data, the truth level can only be attained via a sophisticated *unfolding procedure*, as detailed in Chapter 8.

Definition of the truth level Three distinct truth-level definitions are commonly provided in MC simulations. They differ in their treatment of QED radiation of the final-state lepton, as illustrated in Figure 5.1(a). *Born* and *Bare* level are defined before and after QED FSR, respectively. Additionally, a *Dressed* level is assigned where all photons found within a cone of size $\Delta R(\mu, \gamma) < 0.1$ originating from the same decay vertex are added to the Bare muon.

Truth-level transverse-mass distributions for the $W \to \mu\nu$ process for the three levels are shown in Figure 5.1(b). The distributions include the resonant peak as well as the

(a)   (b)
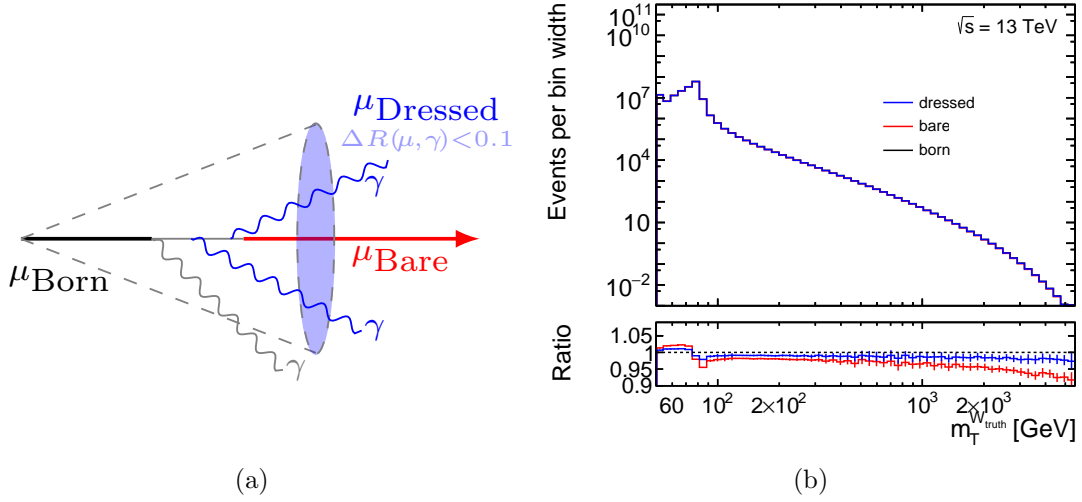
Figure 5.1.: (a) Sketch illustrating the differences between Born, Bare and Dressed muons. (b) Bare-, Born- and Dressed-level transverse-mass distributions in the $W \to \mu\nu$ sample.

high-mass tail up to several TeV. Comparing Bare and Born levels, the Bare level is shifted towards lower transverse masses. This behavior agrees with the expectation, as the underlying Bare muon possesses less energy due to the radiation of photons. The effect increases with mass (or muon momentum, respectively) reaching an approximate 5% difference at $m_{\mathrm{T}}^{\mathrm{W}} = 2\,\mathrm{TeV}$. In contrast, the Dressed level approaches the Born level again. The reason for a residual difference, about 1% at $m_{\mathrm{T}}^{\mathrm{W}} = 2\,\mathrm{TeV}$, is the limited cone size in which radiated photons are collected.

In this dissertation, the cross-sections will be presented at Born level. However, it is worth noting that any difference between Born, Bare and Dressed final states is described purely by MC simulation and a recalculation to a different level is straightforward.

Fiducial phase space   The unfolded cross-sections are measured in a well-motivated *fiducial phase space*, i.e. the truth level is subjected to a set of requirements focusing on the high-mass region. These are oriented towards the reconstruction-level requirements defined in Section 5.1, minimizing potential extrapolation and correction biases from the $W \to \mu\nu$ prediction. The fiducial cuts used are summarized in Table 5.2.

Table 5.2.: Event selection criteria on truth level.

Criteria	Requirement		
$|\eta(\mu)|$	< 2.4		
$p_{\mathrm{T}}(\mu)$	$> 65\,\mathrm{GeV}$		
$p_{\mathrm{T}}(\nu)$	$> 85\,\mathrm{GeV}$		
$m_{\mathrm{T}}^{\mathrm{W}}$	$> 200\,\mathrm{GeV}$	&	$< 5000\,\mathrm{GeV}$

5.3. Measurement binning

The following binning is chosen for the single-differential measurement in $m_{\mathrm{T}}^{\mathrm{W}}$, also referred to as *1D measurement* in the course of this thesis,

$$m_{\mathrm{T}}^{\mathrm{W}} = [(150,)200, 250, 300, 350, 425, 500, 600, 750, 900, 1100, 1400, 2000, 5000]\,\mathrm{GeV}.$$

The $150\,\mathrm{GeV}$-$200\,\mathrm{GeV}$ bin represents the shadow bin, as introduced in Section 5.1. For the double-differential binning in $m_{\mathrm{T}}^{\mathrm{W}}$ and $|\eta(\mu)|$ (*2D measurement*), bin edges in $m_{\mathrm{T}}^{\mathrm{W}}$ are chosen such that they coincide with the ones in 1D if possible. Nevertheless, the number of $m_{\mathrm{T}}^{\mathrm{W}}$ bins in 2D is lower. In particular, the 2D measurement is bound to $m_{\mathrm{T}}^{\mathrm{W}} < 2\,\mathrm{TeV}$ in contrast to $m_{\mathrm{T}}^{\mathrm{W}} < 5\,\mathrm{TeV}$ in 1D, limited by the number of data events per bin. For the same reason, the number of η bins per $m_{\mathrm{T}}^{\mathrm{W}}$ bin decreases for higher transverse masses. The 2D measurement binning is defined as

- $m_{\mathrm{T}}^{\mathrm{W}} = [(150,)200, 300, 425]\,\mathrm{GeV} \times$
  $|\eta(\mu_{\mathrm{truth}})| = [0.0,\ 0.2,\ 0.4,\ 0.6,\ 0.8,\ 1.0,\ 1.2,\ 1.4,\ 1.6,\ 1.8,\ 2.0,\ 2.2,\ 2.4]$
  $|\eta(\mu_{\mathrm{reco}})| = [0.0,\ 0.2,\ 0.4,\ 0.6,\ 0.8,\ \mathbf{1.01},\ \mathbf{1.1},\ 1.4,\ 1.6,\ 1.8,\ 2.0,\ 2.2,\ 2.4]$

- $m_{\mathrm{T}}^{\mathrm{W}} = [425, 600, 900]\,\mathrm{GeV} \times$
  $|\eta(\mu_{\mathrm{truth}})| = [0.0,\ 0.4,\ 0.8,\ 1.2,\ 1.6,\ 2.0,\ 2.4]$
  $|\eta(\mu_{\mathrm{reco}})| = [0.0,\ 0.4,\ \mathbf{1.01},\ \mathbf{1.1},\ 1.6,\ 2.0,\ 2.4]$

- $m_{\mathrm{T}}^{\mathrm{W}} = [900, 2000]\,\mathrm{GeV} \times$
  $|\eta(\mu_{\mathrm{truth}})| = [0.0,\ 0.8,\ 1.2,\ 1.8,\ 2.4]$
  $|\eta(\mu_{\mathrm{reco}})| = [0.0,\ 0.8,\ \mathbf{1.01},\ \mathbf{1.1},\ 1.8,\ 2.4]$

including a shadow bin in $m_{\mathrm{T}}^{\mathrm{W}}$ as well. A different pseudorapidity binning on truth and reconstruction level is used around the barrel end-cap transition region in the MS. At $|\eta(\mu_{\mathrm{reco}})| \in [1.01, 1.1]$, no muons are reconstructed for the `high-`p_{T} WP used (see Section 4.2.2), i.e. this bin will be empty. Opposed to that, the truth level is characterized by equidistant η bins. The transition between the two levels and binnings is handled by the unfolding procedure. It was found that the detector-motivated reconstruction-level binning leads to a more stable and flat unfolding in this challenging detector region, as compared in Figure E.7.

The single- and double-differential measurement binnings are optimized with respect to resolution, migration and data statistical uncertainty, as discussed in detail in my master thesis [153]. Even though the studies were performed on the `mc16a` period and for the single-differential measurement only, the conclusions do not change. The following paragraphs highlight the main aspects, additional considerations for the double-differential binning are stated explicitly.

Resolution A limited detector resolution leads to a smearing of the reconstructed muon momentum. This effect scales drastically with $p_\mathrm{T}(\mu)$, as the track-based muon measurement is increasingly challenging for almost straight trajectories at high $p_\mathrm{T}(\mu)$. The resolution is evaluated via the distribution of the reconstruction-level m_T^W in bins of truth-level m_T^W in the signal MC sample. The root-mean-square (RMS) of the reconstructed distribution is taken as a measure for the experimental resolution. At high m_T^W, its resolution is driven by the muon resolution, with RMS $\approx 200\,\mathrm{GeV}$ at $m_\mathrm{T}^\mathrm{W} = 1\,\mathrm{TeV}$. At the lower edge of the m_T^W spectrum investigated, the $E_\mathrm{T}^\mathrm{miss}$ resolution dominates with RMS $\approx 20\,\mathrm{GeV}$ at $m_\mathrm{T}^\mathrm{W} = 200\,\mathrm{GeV}$ (see Figure 9.2 in Reference [153]). The final binning is chosen such that the bin widths are always larger than the RMS.

Migration An event can be located in different bins on reconstruction and truth level, for instance, due to a muon reconstructed with a higher or lower momentum with respect to its generation. This is an effect known as *migration*, which is driven by two main sources here. One reason is the limited intrinsic detector resolution, in particular at very high muon momenta. On the other hand, the steeply falling m_T^W distribution causes substantial migration, also called *in-smearing*. Events may be generated at the W-boson mass peak, i.e. $m_W(\mathrm{truth}) \approx 80\,\mathrm{GeV}$, but reconstructed in the high-mass region with $m_\mathrm{T}^\mathrm{W}(\mathrm{reco}) > 200\,\mathrm{GeV}$. The effect is driven by W bosons that possess a large $p_\mathrm{T}(W)$ themselves or simply mismeasurements of $p_\mathrm{T}(\mu)$ or $E_\mathrm{T}^\mathrm{miss}$ in the detector. In principle, these are rare effects. Nevertheless, given the extreme dominance of W bosons generated at the resonant mass peak, they become sizable and represent a non-negligible challenge in this dissertation.

The bin-wise migration is determined via a so-called *migration matrix* constructed from the signal MC sample. A two-dimensional histogram connects the truth-level m_T^W with the reconstruction-level m_T^W, normalized per reconstruction-level bin. It highlights explicitly where an event is originating from given it was reconstructed in a certain m_T^W range.

The binning is optimized such that the migration is reasonably low, aiming for diagonal elements of the matrix, also called *purity*, above 50%. For instance for the $W^- \to \mu^- \bar{\nu}$ process, the purity is 61% at $m_\mathrm{T}^\mathrm{W} \in [200, 250]\,\mathrm{GeV}$, driven by the in-smearing from the mass peak, and 58% at $m_\mathrm{T}^\mathrm{W} \in [900, 2000]\,\mathrm{GeV}$, driven by the muon resolution. Migration across $\eta(\mu)$ in the double-differential measurement is negligible. All single- and double-differential migration matrices are shown in Appendix E.1.

Statical uncertainty The statistical uncertainty in data is considered for the choice of binning. The MC statistical uncertainty is not a limiting factor as the number of generated signal events is enhanced substantially (see Section 3.3). Given a counting experiment, the number of data events is described by Poisson statistics and the uncertainty is given by the square root of the number of events, $\sqrt{N}$. A compromise between as many bins as possible, retaining sensitivity to potential high-frequency effects, and a reasonable number of data events per bin needs to be made.

In the final binning, the data statistical uncertainty ranges between about 0.5% to 50% over the single-differential m_T^W range and 1% to 25% over the double-differential $m_T^W \otimes |\eta(\mu)|$ range. The relative statistical uncertainty in data before the unfolding is depicted in Appendix E.1.

6. Estimation of the multijet background

A muon leaves, in general, a clean, distinct signature in the detector, nevertheless, there is a small probability that other objects produce a similar pattern. For instance, a jet can *fake* a muon if its energy is not fully absorbed in the calorimeters, an effect known as *punch-through*. However, in particular for the chosen `high-`p_T WP, characterized by at least 3 stations in the MS, this is extremely unlikely. Instead, so-called *non-prompt* muons are the dominant source of fake muons here. A schematic illustration contrasting prompt and non-prompt muons is shown in Figure 6.1. A prompt, also called *real*, muon is a direct decay product from a heavy-boson decay in the HS interaction. This muon is likely to be isolated, as indicated by the pink cone in Figure 6.1(a). In contrast, non-prompt muons are produced in the jet shower, for instance as a product of leptonically decaying unstable mesons. As a consequence, fake muons are generally expected to be non-isolated due to the surrounding jet activity.

The fake muon background will also be referred to as *multijet background* since, in particular, pure QCD processes consisting of multiple jets are its main source. Multijet processes exhibit an extremely large production cross-section at the LHC, see Figure 1.6. Thus, even though it is very unlikely that a fake muon passes the analysis' isolation criterion, this source of background needs to be considered. Because of the extremely low selection efficiency, it is not based on MC simulations here. Instead, data-driven methods are commonly employed, in this case the Matrix Method.

(a) (b)
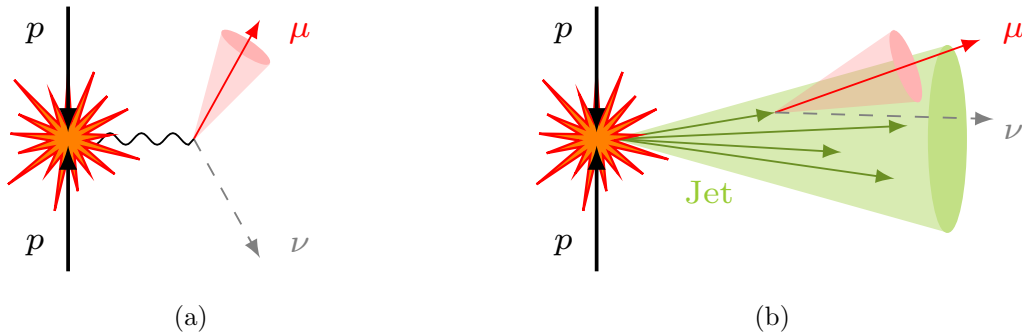
Figure 6.1.: Sketch contrasting (a) a prompt muon, from a hard-scatter heavy-boson decay, and (b) a non-prompt muon, produced in a jet. The pink cone indicates the region in which the muon isolation is evaluated.

6.1. Matrix Method

The *Matrix Method* (MM) is a data-driven method used to estimate the fake muon background. The basis is the liberation of certain identification and isolation requirements in order to obtain two muon selection levels. In this dissertation, these are the tight level and MM loose level defined in Table 4.1. They are distinguished solely by the additional isolation requirement on the tight level. A matrix provides the connection between the number of real/fake muons (N_R/N_F) and loose/tight muons (N_{LnT}/N_T):

$$\begin{pmatrix} N_T \\ N_{LnT} \end{pmatrix} = \begin{pmatrix} \epsilon_R & \epsilon_F \\ 1 - \epsilon_R & 1 - \epsilon_F \end{pmatrix} \begin{pmatrix} N_R \\ N_F \end{pmatrix} \quad \text{with} \quad \epsilon_{R/F} = \frac{N_{R/F}^T}{N_{R/F}^L}. \tag{6.1}$$

It is important to note that N_{LnT} indicates the number of loose muons explicitly failing the tight level (*loose-not-tight*). The matrix elements are characterized by so-called *real* and *fake efficiencies*, ϵ_R/ϵ_F. These are defined as the quotient of tight-level events over loose-level events and need to be derived experimentally using a set of real and fake muons, respectively. Here, $N_{R/F}^L$ includes the full loose level to correctly obtain an efficiency with $0 \leq \epsilon \leq 1$. The matrix multiplication in Eq. 6.1 states that the number of tight muons is the sum of the number of real muons, multiplied with the real efficiency, and fake muons, multiplied with the fake efficiency,

$$N_T = \epsilon_R N_R + \epsilon_F N_F. \tag{6.2}$$

The quantity of interest in this method is the number of fake muons. It can be estimated by inverting the matrix,

$$\begin{pmatrix} N_R \\ N_F \end{pmatrix} = \frac{1}{\epsilon_R(1 - \epsilon_F) - \epsilon_F(1 - \epsilon_R)} \begin{pmatrix} 1 - \epsilon_F & -\epsilon_F \\ \epsilon_R - 1 & \epsilon_R \end{pmatrix} \begin{pmatrix} N_T \\ N_{LnT} \end{pmatrix}. \tag{6.3}$$

Finally, the number of fake muons that pass the tight level, i.e. that enter the analysis' event selection, is given as

$$\epsilon_F N_F = \frac{\epsilon_F}{\epsilon_R - \epsilon_F}[\epsilon_R(N_{LnT} + N_T) - N_T] = \underbrace{\frac{\epsilon_F \epsilon_R}{\epsilon_R - \epsilon_F}}_{w_{MM}^L} \cdot N_{LnT} + \underbrace{\frac{\epsilon_F(\epsilon_R - 1)}{\epsilon_R - \epsilon_F}}_{w_{MM}^T} \cdot N_T. \tag{6.4}$$

It only depends on quantities that can be derived from data. The numbers N_{LnT} and N_T are calculated straightforward by subjecting the data to the given requirements of the loose and tight level, respectively. An adequate estimation of the real and fake efficiencies represents the major challenge of the MM. They are derived binned in well-chosen variables in dedicated regions. In practice, event weights, w_{MM}^T and w_{MM}^L in Equation 6.4, are multiplied with the numbers of tight and loose level events to obtain the total fake muon yield.

6.2. Measurement of the real efficiency

The real efficiency gives the efficiency for a real, loose muon to pass the tight level. A sample consisting of clean prompt real muons is given by the $W \to \mu\nu$ prediction. Only the high-mass slices of the sample (see Section 3.3) are used, exploiting their enhanced statistics [153]. In order to ensure the muon is in fact originating from the W-boson decay, a *truth-matching* in the form of $\Delta R(\mu_{\text{truth}}, \mu_{\text{reco}}) < 0.2$ is applied. With respect to the signal region (see Section 5.1), the m_T^W and E_T^{miss} cuts are omitted. Generally, real and fake efficiencies are calculated for $\mu^\pm$-combined samples, as no differences between the charges are expected and the higher statistical power can be taken advantage of. A binned histogram for the loose and tight selection[1] is created and the real efficiency ϵ_R is given by their bin-by-bin quotient

$$\epsilon_R = \frac{N_R^T}{N_R^L} = \frac{N_{\text{W MC}}^T}{N_{\text{W MC}}^L}. \tag{6.5}$$

Ultimately, ϵ_R is evaluated in a two-dimensional binning in the transverse momentum and pseudorapidity of the muon, as shown in Figure 6.2. One-dimensional real efficiencies are shown in Figure C.1. In general, ϵ_R is extremely high, i.e. above 99% in all bins. As the isolation requirement is the only difference between the loose and tight level, this behavior is expected for a clean $W \to \mu\nu$ sample consisting of prompt, isolated muons. The variations as a function of $p_T(\mu)$ and $|\eta(\mu)|$ are below 0.2%. The final binning of ϵ_R is chosen as a compromise between sufficient statistics per bin and a sensible representation of all dependencies. Additionally, the $|\eta(\mu)|$-binning takes into account the barrel-end-cap transition in the MS (see Section 2.2.5). The same binning is used for ϵ_R and ϵ_F, while the optimization is to a large degree driven by the fake efficiency which suffers from substantially lower statistical significance.

---

[1]For the tight selection, the tight muon SF is applied (see Section 4.2.6) and, for the loose selection, the loose-level SF.
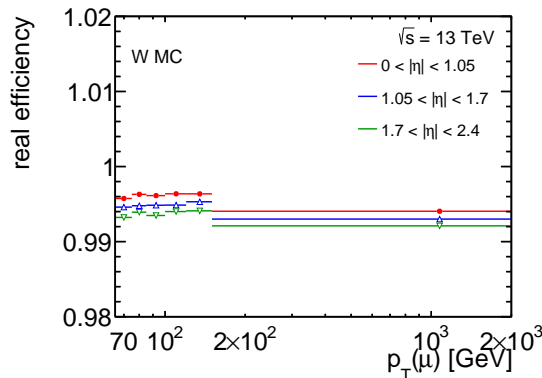
Figure 6.2.: Two-dimensional real efficiency binned in the transverse momentum and pseudorapidity of the muon.

6.3. Study of fake-muon kinematics using a dijet MC sample

In general, the occurrence of fake muons is rare. Thus, the first challenge is to define a region enriched in fake muons, providing sufficient statistical power to estimate the fake efficiency. As pure QCD processes are the main source of fake muons, this region will be referred to as *QCD-enriched region*. The first indispensable step in enriching the number of loose-level fake muons is the omission of the muon-jet overlap removal, as studied in detail in my master thesis and outlined in Section 4.6 here.

In this dissertation, the nature of fake muons is studied explicitly using simulated dijet events[2]. An `mc16a`-based dijet MC sample is generated with PYTHIA 8.230 at LO in QCD. The dijet sample is subjected to the analysis' baseline event selection (see Section 5.1), i.e. exactly one muon with $p_T > 65\,\mathrm{GeV}$. The high-mass m_T^W and E_T^{miss} cut are not applied, and no discrimination between muon charges is made. By selecting exactly one muon, the dijet sample is reduced approximately by a factor of one thousand. This low selection efficiency underlines why it is not feasible to simply use this MC sample for the multijet estimate in the signal region (see also Figure C.6 which shows the number of weighted predicted dijet events in the signal region).

The dominant source of fake muons is identified using inherent classifier tools given in the dijet sample. The `IFFTruthClassifier` [166] confirms that fake muons selected in this analysis are predominantly originating from hadron decays within jets. In particular, B hadrons and C hadrons produce non-prompt muons (see Figure C.7). They are summarized as heavy-flavor (HF) decays for the remainder of this thesis.

Ultimately, the QCD-enriched region should feature a large fraction of fake muons while keeping the real-muon fraction as low as possible. Any real-muon contamination can spoil the fake-efficiency estimate substantially. Requiring $E_T^{miss} < 65\,\mathrm{GeV}$ is the baseline for the QCD-enriched region in both, the muon and electron channel, of the measurement presented. It ensures orthogonality to the signal region and enriches, in particular, the number of fake electrons in the electron channel. Any further cuts in the muon channel are motivated in the following.

Various kinematic distributions are compared between the dijet process and the signal $W \to \mu\nu$ process. A set of variables exhibiting good separation power between the two processes is depicted in Figure 6.3 for a loose- and tight-muon selection. More variables can be found in Figure C.8. The overall integrated event yield is at a similar magnitude for both processes at the loose level (left-hand side). In contrast, on the tight level (right-hand side), the number of real muons is extremely overweight. This underlines the drastic importance of additional cuts to suppress real muons in the QCD-enriched region.

---

[2]Multijet, and in particular dijet, events are the main source of fake muons. The impact of all-hadronic DY and $t\bar{t}$ is negligible, due to their smaller production cross-sections (see Figure 1.6).
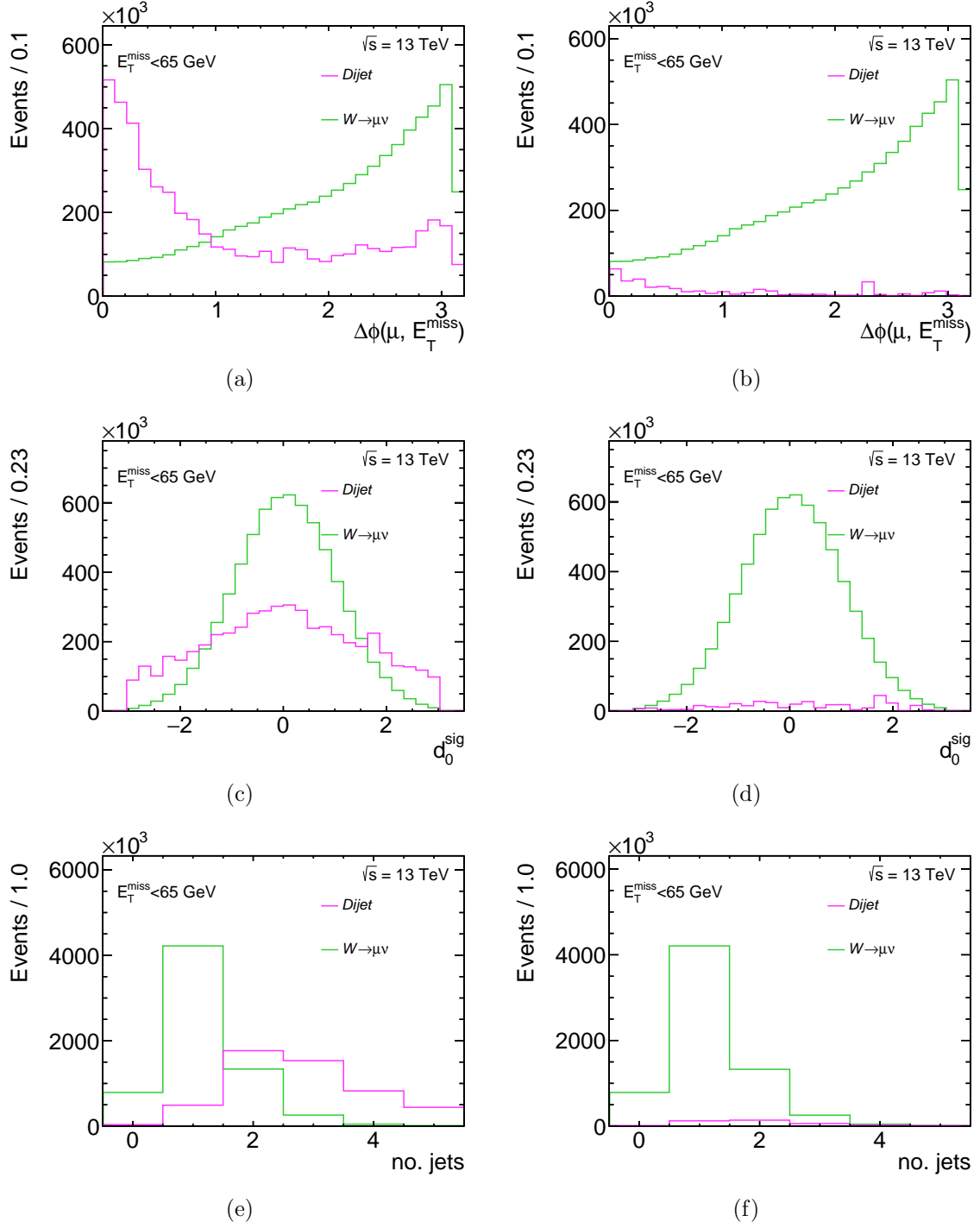
Figure 6.3.: Distributions of the azimuthal angle between muon and E_T^{miss}, the d_0 significance and the jet multiplicity predicted for the dijet process (containing fake muons) and $W \to \mu\nu$ process (containing real muons) in a region with $E_T^{miss} < 65\,\text{GeV}$. All distributions are shown for the loose level (left-hand side) and tight level (right-hand side).

The difference between dijet and $W \to \mu\nu$ distributions is most striking in $\Delta\phi(\mu, E_T^{\text{miss}})$, see Figure 6.3(a) (loose level) and Figure 6.3(b) (tight level). The signal distribution is maximal at $\Delta\phi(\mu, E_T^{\text{miss}}) \approx \pi$, corresponding to a back-to-back decay of the W boson into muon and neutrino. Opposed to that, most dijet events show a small angular separation between muon and neutrino. This can be understood by their HF origin, where the momentum of the mother particle leads to a *boost* of the two daughter particles in the same direction (see also Figure 6.1).

Additionally, the significance of the transverse impact parameter d_0^{sig} shows good separation power, see Figure 6.3(c) (loose level) and Figure 6.3(d) (tight level). The broader distribution for dijet events is caused by the non-prompt nature of fake muons.

Finally, the distributions of the jet multiplicity are compared in Figure 6.3(e) (loose level) and Figure 6.3(f) (tight level). Naively, one would expect the majority of $W \to \mu\nu$ events with zero jets. However, the strong asymmetry between the E_T^{miss} and $p_T(\mu)$ selections here can be achieved only with topologies containing additional radiation, i.e. one jet must be present. To the contrary, most dijet events contain two jets, or more. Nevertheless, on the tight level, a significant fraction of about 40% of dijet events contain only one jet. This is caused by the fact that the selection of a tight isolated muon is enhanced if the jet around it is not reconstructed (see also Figure C.9). This represents an important contribution of tight fake muons to be taken into account in the estimation of ϵ_F. Instead of requiring the presence of two jets in the QCD-enriched region, the dijet topology can be enhanced by requiring at least one jet opposite to the muon. It was found that the leading jet, i.e. the one with the highest p_T, is predominately back-to-back to the muon for tight dijet events, see Figure C.8. The final requirements defining the QCD-enriched region are shown in Table 6.1.

Table 6.1.: Event selection criteria defining a QCD-enriched region. Only the differences with respect to the general event selection defined in Table 5.1 are listed here explicitly.

Criteria	Requirement
m_T^W	no cut
E_T^{miss}	$< 65\,\text{GeV}$
jet multiplicity	≥ 1 jet with $p_T(j) > 40\,\text{GeV}$ and $\Delta\phi(j, \mu) > \frac{5}{6}\pi$
d_0 significance	> 1.5
$\Delta\phi(\mu, E_T^{\text{miss}})$	$< \frac{\pi}{6}$

6.4. Measurement of the fake efficiency

The fake efficiency cannot be calculated straightforward from MC like the real efficiency. Instead, measured data is utilized. A dataset enriched in fake muons is obtained by applying the selection cuts summarized in Table 6.1 (QCD-enriched region). Nevertheless,

given the rareness of fake muons, a notable fraction of real muons might be still present in the dataset. Real muons are generally modeled by EW MC simulations, i.e. all processes listed in Table 3.1[3]. By subtracting the number of predicted EW events from the number of data events, a dataset containing only fake muons is obtained. The fake efficiency is calculated by the bin-wise quotient of the number of tight and loose events

$$\epsilon_F = \frac{N_F^T}{N_F^L} = \frac{N_{\text{Data}}^T - N_{\text{EW MC}}^T}{N_{\text{Data}}^L - N_{\text{EW MC}}^L}. \tag{6.6}$$
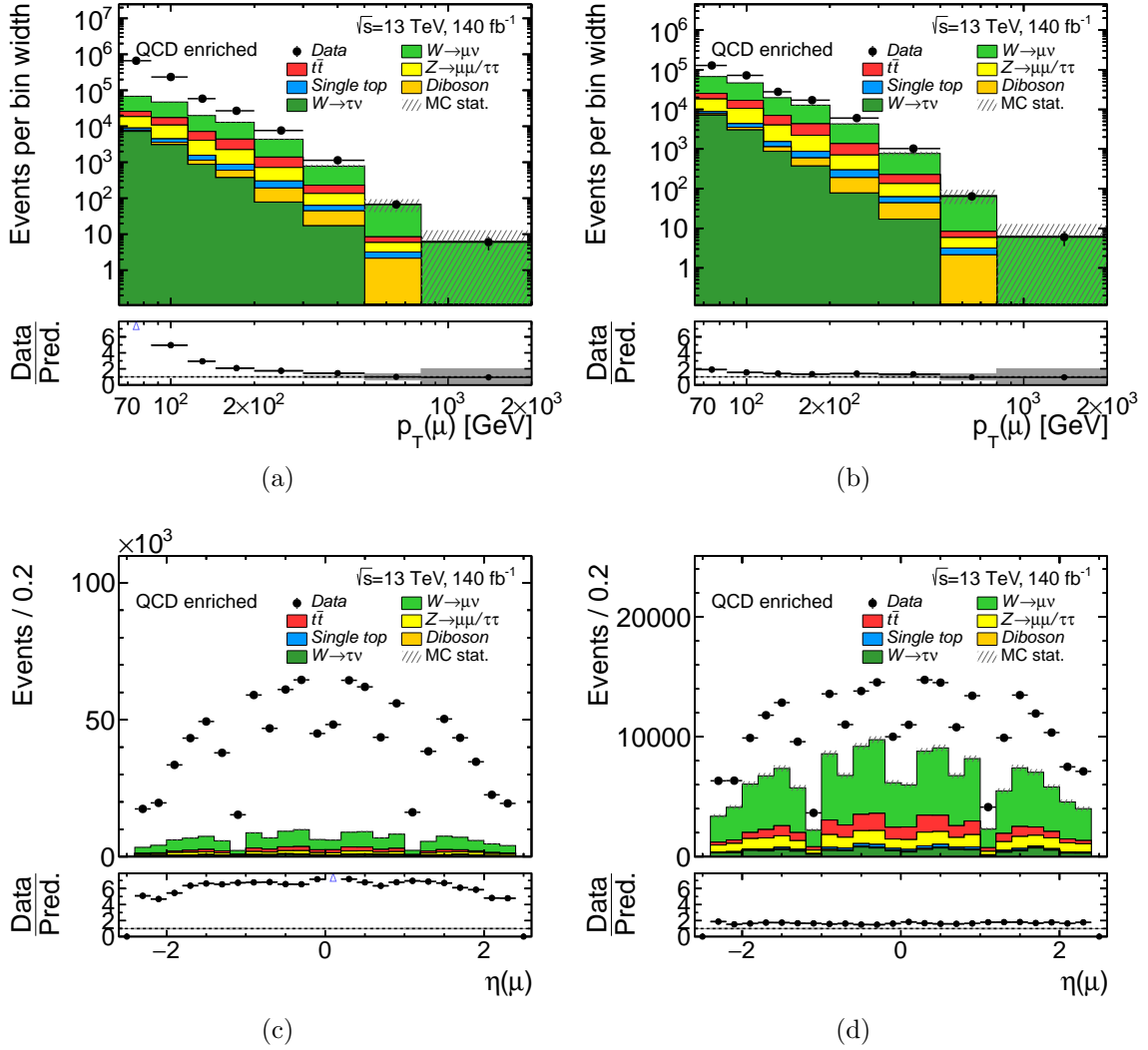
Figure 6.4.: Distributions of the transverse momentum and pseudorapidity of the muon for data and prediction in the QCD-enriched region. The loose/tight selection is shown on the left-/right-hand side. The difference between data and MC predicted events will be identified with the number of fake-muon events.

---

[3]Here, EW refers to all decay modes that are not explicitly all-hadronic. Thus, for instance, the dileptonically/semileptonically decaying $t\bar{t}$ process produced by gluon fusion is counted as EW MC.

Distributions of $p_\mathrm{T}(\mu)$ and $\eta(\mu)$ for data and EW prediction are shown in Figure 6.4 for the loose level (left-hand side) and tight level (right-hand side). The number of events containing real muons is described by the MC prediction while the difference to the number of data events is identified with events containing fake muons. The fraction of fake-muon events is substantially smaller on the tight level, see Figures 6.4(b)/6.4(d), since a fake muon is unlikely to pass the isolation criterion whereas basically all real muons pass it. Overall, the real-muon contamination in the QCD-enriched region amounts to 16% on the loose level and 60% on the tight level. However, the fraction strongly depends on the kinematic region. Strikingly, for $p_\mathrm{T}(\mu) > 500\,\mathrm{GeV}$, the numbers of data and predicted EW events are agreeing without any residual space for fake-muon events at both levels. Thus, in this statistically limited region, it will not be possible to calculate a physically meaningful fake efficiency.

The fake efficiency, calculated according to Equation 6.6, as a function of the transverse momentum of the muon is shown in Figure 6.5(a). A strong dependency is visible, as the fake efficiency amounts to $\epsilon_F \approx 0.1$ at $p_\mathrm{T}(\mu) = 65\,\mathrm{GeV}$ and consecutively approaches unity. However, given the limited statistical significance for $p_\mathrm{T}(\mu) > 500\,\mathrm{GeV}$ discussed above, the last two bins must not be taken representative. Additionally, the fake efficiency as a function of $|\eta(\mu)|$ is shown in Figure 6.5(b), separately for two $p_\mathrm{T}(\mu)$ bins. In general, ϵ_F increases with $|\eta(\mu)|$, while the effect is more pronounced at high $p_\mathrm{T}(\mu)$. In the fine $|\eta(\mu)|$ binning shown here, the fake efficiency becomes negative for $|\eta(\mu)| \in [1, 1.1]$ and $p_\mathrm{T}(\mu) > 150\,\mathrm{GeV}$. This is caused by a larger number of MC events than data events (see Figure C.4(d)) in this statistically limited region bin at the end-cap barrel transition region. Finally, it should be noted that ϵ_F does not vary with $E_\mathrm{T}^\mathrm{miss}$, see Figure C.2(a), which is an important prerequisite for the extrapolation from the QCD-enriched region ($E_\mathrm{T}^\mathrm{miss} < 65\,\mathrm{GeV}$) to the orthogonal signal region ($E_\mathrm{T}^\mathrm{miss} > 85\,\mathrm{GeV}$).

(a)   (b)
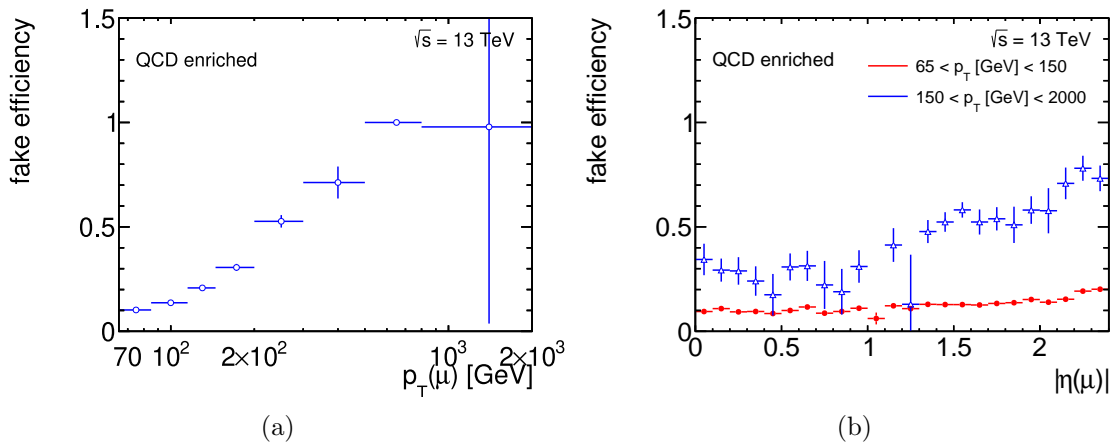
Figure 6.5.: (a) One-dimensional fake efficiency binned in the transverse momentum of the muon and (b) two-dimensional fake efficiency binned in the absolute pseudorapidity and transverse momentum of the muon.
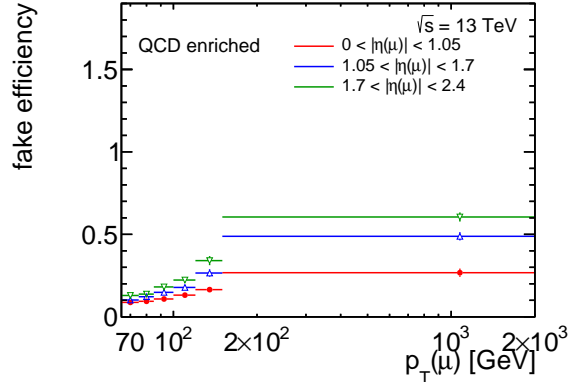
Figure 6.6.: The final fake efficiency binned two-dimensionally in the absolute pseudorapidity and transverse momentum of the muon.

Ultimately, the fake efficiency is binned two-dimensionally in three $|\eta(\mu)|$ bins and six $p_T(\mu)$ bins, see Figure 6.6. Tight- and loose-level data and predicted distributions in this exact binning can be found in Figure C.5. It is ensured that, in each bin, a reasonable number of fake-muon events is present in order to prevent unphysical efficiencies. Thus, in particular, the last $p_T(\mu)$ bin starts at $p_T(\mu) = 150\,\mathrm{GeV}$ here. Three $|\eta(\mu)|$ bins, motivated by the MS geometry, were found to represent the dependencies adequately.

6.5. Systematic uncertainties on the multijet background

The multijet estimate is directly dependent on an adequate description of the real and fake efficiencies. However, particularly, the definition of a QCD-enriched region where the fake efficiency is calculated is to a certain degree arbitrary. To cover for this, systematic uncertainties on the multijet yield are defined by varying the definition of the QCD-enriched region as listed in Table 6.2. Only one cut is varied per systematic variation while all others remain at the nominal value. For each variation, an alternative fake efficiency, with unchanged binning, is used to calculate an alternative multijet yield.

Table 6.2.: Systematic uncertainties on event selection criteria defining a QCD-enriched region. Each cut is varied independently. The * indicates at least one jet is required to fulfill $p_T(j) > 40\,\mathrm{GeV}$ and $\Delta\phi(j,\mu) > \frac{5}{6}\pi$.

Criteria	Nominal requirement	Variation 1	Variation 2
E_T^{miss}	$< 65\,\mathrm{GeV}$	$< 30\,\mathrm{GeV}$	$> 30\,\mathrm{GeV}$ and $< 65\,\mathrm{GeV}$
jet multiplicity	≥ 1 jet*	inclusive	≥ 2 jets*
d_0 significance	> 1.5	> 1.0	> 2.0
$\Delta\phi(\mu, E_T^{\mathrm{miss}})$	$< \frac{\pi}{6}$	$< \frac{\pi}{12}$	$< \frac{\pi}{3}$

Two additional uncertainties are designed to cover potential mismodeling in the EW MC processes, i.e. the real-muon contamination. As a reminder, the QCD-enriched region is characterized by asymmetric $p_{\mathrm{T}}(\mu) > 65\,\mathrm{GeV}$ and $E_{\mathrm{T}}^{\mathrm{miss}} < 65\,\mathrm{GeV}$ cuts. As a result, the EW processes here are potentially subject to a worse description than their well-understood resonant regions. The first variation consists of a scaling of the number of events predicted by all MC processes in the QCD-enriched region by a flat factor of $\pm 10\,\%$. Furthermore, the largest EW sample here, $W \to \mu\nu$, is replaced by the alternative sample using Sherpa (see Table 3.1). This variation covers shape effects only by explicitly matching the normalizations of the two $W \to \mu\nu$ samples.

6.6. Multijet closure and validation regions

The multjet estimate is validated in dedicated multijet closure and validation regions. An overview of their definitions is shown in Figure 6.7. The *closure region* (CR) matches the QCD-enriched region exactly, i.e. the multijet estimate is checked in the region where the fake efficiency was estimated. Due to the low-$E_{\mathrm{T}}^{\mathrm{miss}}$ and low-$\Delta\phi(\mu, E_{\mathrm{T}}^{\mathrm{miss}})$ requirements, the CR does not represent the high-$m_{\mathrm{T}}^{\mathrm{W}}$ region where the cross-section measurement is performed. The extrapolation towards this phase space is validated using two *validation regions* (VR) which are inclusive in $E_{\mathrm{T}}^{\mathrm{miss}}$ and $m_{\mathrm{T}}^{\mathrm{W}}$. Nevertheless, just like the CR, they are subject to QCD-enrichment cuts to obtain an adequate fraction of multijet events. The first validation region (VR1) is different from the CR only by the removed $E_{\mathrm{T}}^{\mathrm{miss}}$ requirement. For the second validation region (VR2), the $E_{\mathrm{T}}^{\mathrm{miss}}$ and $\Delta\phi(\mu, E_{\mathrm{T}}^{\mathrm{miss}})$ requirements are removed with respect to the CR. However, in order to still obtain a sensible fraction of multijet events, this region comprises events containing at least three jets.
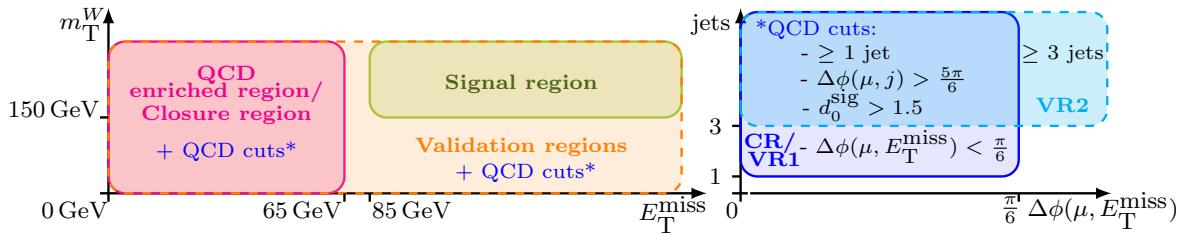
Figure 6.7.: Definitions of the multijet closure region (CR) and validation regions (VR1/VR2).

Closure region The agreement between distributions of measured data and prediction is evaluated in the CR. The latter includes the sum of all EW samples as well as the multijet estimate via the Matrix Method using the two-dimensional real and fake efficiencies depicted in Figure 6.2 and Figure 6.6. Even though the efficiencies are provided charge-combined, the multijet yield is calculated separately per charge by counting the tight/loose data events in Equation 6.4 per muon charge. In general, no

substantial differences between both charges are expected nor observed. Thus, only μ^+ distributions are shown explicitly for all regions here, see appendix C.3 for the μ^- distributions. Distributions of $p_T(\mu)$, $\eta(\mu)$, E_T^{miss} and $\Delta\phi(\mu, E_T^{miss})$ for data and prediction are shown in Figure 6.8, while more variables can be found in Appendix C.3. The gray uncertainty band represents the quadratic sum of the statistical uncertainty of the prediction and the systematic uncertainties on the multijet estimate, obtained as given in Section 6.5. The data statistical uncertainty is indicated by black error bars. The distribution of the p_T of the muon is steeply falling towards the high-momentum tail, with no statistical significance above $\sim 400\,\mathrm{GeV}$. In the η distribution, structures are visible that are caused by the MS geometry, whose acceptance is interrupted frequently as
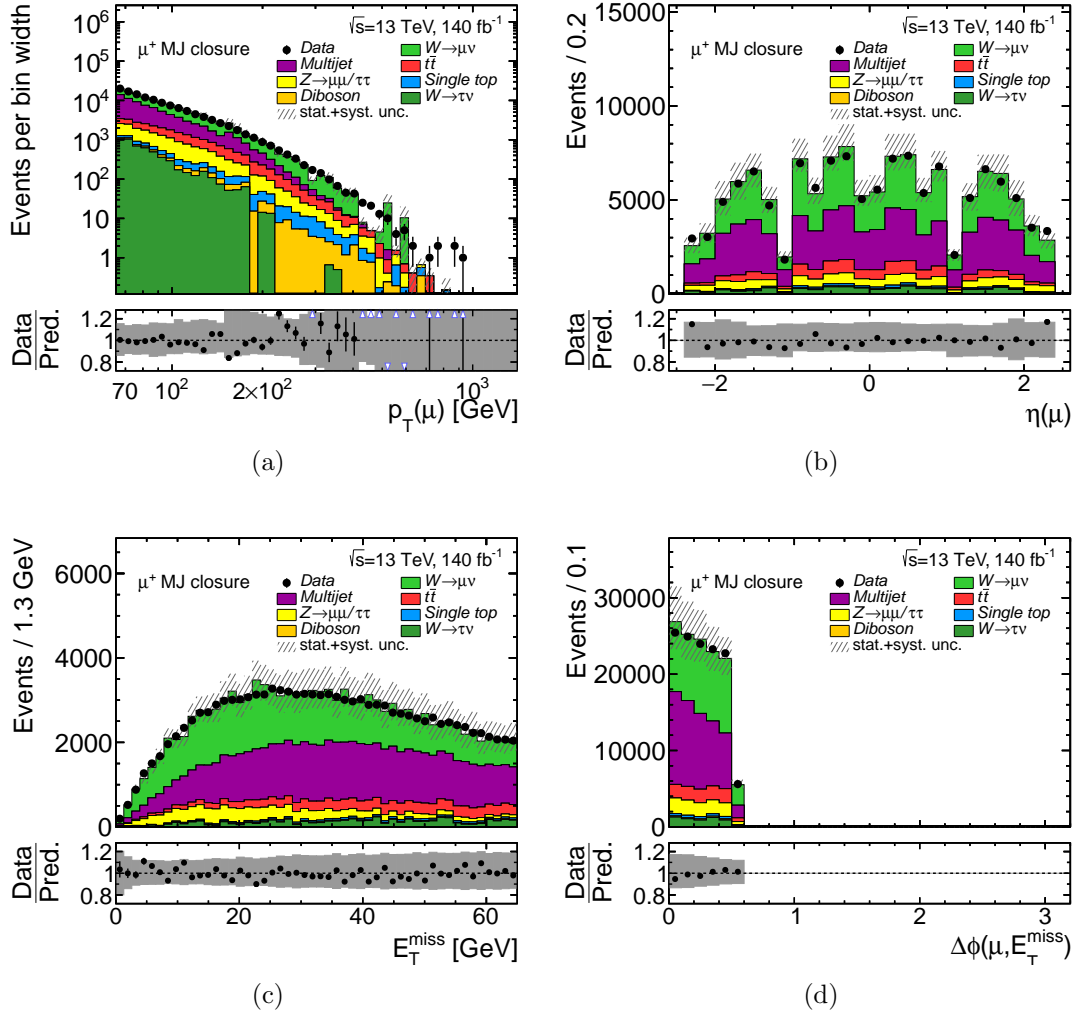
Figure 6.8.: Distributions of the (a) transverse momentum and (b) pseudorapidity of the muon, (c) missing transverse momentum, and (d) azimuthal angle between muon and E_T^{miss} for data and prediction in the closure region for a μ^+ final state. Statistical uncertainties as well as experimental uncertainties related to the multijet estimate are included.

elaborated in Section 2.2.5. In general, EW but also multijet events tend to spread over the full E_T^{miss} range of this region, with a decrease towards $E_T^{miss} \to 0$. This agrees with the expectation as fake muons from secondary HF decays are likely to be accompanied by a neutrino, i.e. E_T^{miss}. Finally, the angular distance between E_T^{miss} and the muon is depicted, which is limited to values smaller than $\pi/6$ in the CR. In general, good agreement between the numbers of data and predicted events is observed within the given uncertainties across all variables shown here and in Appendix C.3. This indicates a sensible multijet estimate. Structures are visible in the ratio of Figure 6.8(a) which are caused by the $p_T(\mu)$ binning of the fake efficiency. Nevertheless, no finer binning could be chosen due to the statistical limitation of fake-muon events. Additionally, the structures are not visible in the signal region where the cross-section measurement will be performed.

E_T^{miss} validation region (VR1)   The closure region and the signal region (SR) are orthogonal in the missing transverse momentum. The extrapolation from low E_T^{miss} (CR) to high E_T^{miss} (SR) is checked in a dedicated validation region. Loosening the E_T^{miss} requirement is the only difference between the CR and the VR1 (see also Figure 6.7). Even though the VR1 covers an extrapolation to the high-E_T^{miss} region, it shall be highlighted that its coverage differs from the SR due to additional QCD-enrichment cuts. In total, the VR1 comprises about 37 % multijet events. Again, the number of predicted events is compared to the number of data events as function of various observables, including statistical and multijet uncertainties. The E_T^{miss} distribution is shown in Figure 6.9. More variables can be found in Appendix C.3, however, they are strongly dominated by the low-E_T^{miss} region and, thus, resemble the distributions shown for the CR. Overall, the agreement between the number of predicted and data events is good. A tendency of more data events than predicted events is visible for E_T^{miss} between 150 GeV and 250 GeV.
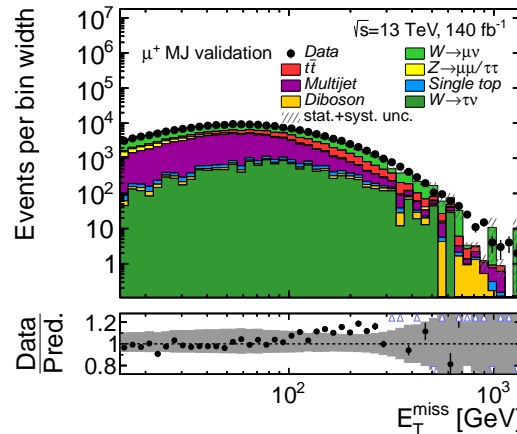
Figure 6.9.: Distribution of the missing transverse momentum for data and prediction in the first validation region (VR1) for a μ^+ final state. Statistical uncertainties as well as experimental uncertainties related to the multijet estimate are included.

$\Delta\phi(\mu, E_T^{miss})$ and m_T^W validation region (VR2)   The low-$\Delta\phi(\mu, E_T^{miss})$ restriction in the CR and VR1 suppresses events with high transverse masses (see Equation 1.15). Thus, the VR1 contains very few events with high m_T^W, particularly, no events with $m_T^W > 200\,\text{GeV}$ are present (see Figure C.14(d)). To address this, a second VR is dedicated to the validation of the extrapolation in $\Delta\phi(\mu, E_T^{miss})$ and in m_T^W. Its definition is challenging because loosening the $\Delta\phi(\mu, E_T^{miss})$ requirement increases the $W \to \mu\nu$ contribution substantially (see Section 6.3). In order to still ensure a reasonable fraction of multijet events, the VR2 is characterized by a jet multiplicity of three or larger[4]. In total, a multijet fraction of 28% is achieved in the VR2.

In this region, the alternative signal sample from SHERPA (see Section 3.3) is used as it is known to predict distributions in this challenging phase space more accurately. Nevertheless, the number of predicted $W \to \mu\nu$ events is subject to non-negligible scale uncertainties, i.e. variations of μ_R and μ_F, in this phase space. They are included in the total uncertainty in addition to the statistical and multijet uncertainties here.

Distributions of $\Delta\phi(\mu, E_T^{miss})$ and m_T^W are shown for data and prediction in Figure 6.10. More variables can be found in appendix C.3. Similar to the other regions investigated, a good agreement within the given uncertainties is notable. Overall, the multijet background can be considered well-estimated via the Matrix Method.

(a)   (b)
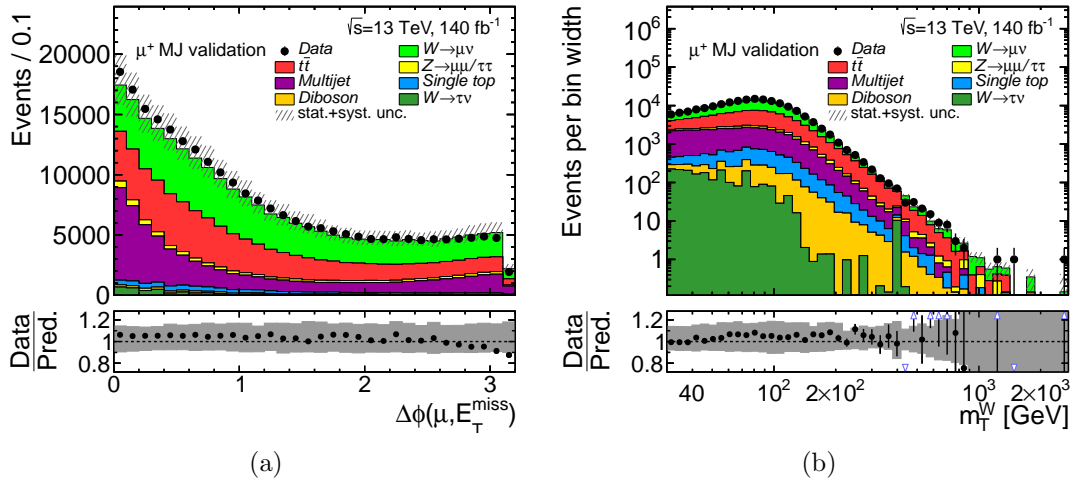
Figure 6.10.: Distributions of the (a) azimuthal angle between muon and E_T^{miss} and (b) transverse mass for data and prediction in the second validation region (VR2) for a μ^+ final state. Statistical uncertainties as well as experimental uncertainties related to the multijet estimate and scale uncertainties of the $W \to \mu\nu$ prediction are included.

---

[4]*Only* for VR2, different fake efficiencies are used. They are based on a QCD-enriched region requiring at least 3 jets. The fake efficiency is strongly dependent on the jet multiplicity (see Figure C.2(b)) and, otherwise, the multijet normalization in VR2 would be overestimated.

7. Comparison between data and prediction in the signal region

The signal region, as defined in Section 5.1, is the region where the $W \to \mu\nu$ cross-section is measured. In this Chapter, the total predicted yields and contributions from signal and background processes are presented. Additionally, distributions of data and prediction are compared in key control variables as well as the measurement observables. These comparisons are an essential tool in understanding the composition of signal and background events as well as the modeling throughout the given phase space.

7.1. Composition of signal and background

The numbers of selected events in data, signal and background samples and the data-driven multijet estimate are presented in Table 7.1. The selection is restricted to $m_{\mathrm{T}}^{\mathrm{W}} > 200\,\mathrm{GeV}$, meaning the shadow bin (see Section 5.1) is excluded here. The relative contributions from all processes are shown in Figure 7.1(a) and Figure 7.1(b), for a positive and negative muon charge, respectively. In total, 262512 (μ^+) and 185793 (μ^-) data events are selected, which will be the basis for the measurement presented.

The signal region is designed to contain a large fraction of signal events while suppressing background events as much as possible. A signal fraction of 66.4 % and 58.9 % for W^+ and W^-, respectively, is achieved. Overall, roughly 60 % more W^+ than W^- events are selected (see Table 7.1). This asymmetry is caused by the structure of the colliding protons: a proton contains two positively charged up valence quarks, whereas only one negatively charged down valence quark. Even though sea quarks will also contribute, the valence-quark asymmetry influences the W-boson production directly.

The largest background is given by $t\bar{t}$ events with a fraction of 18.4 % (μ^+) and 26.4 % (μ^-), respectively. In general, this process does not prefer any charge, see Table 7.1. Instead, the different relative numbers are driven by charge-dependent contributions of e.g. the signal process. The yield and modeling of the $t\bar{t}$ process was studied in my master thesis [153]. It is composed of about one third of dileptonic $t\bar{t}$ decays, semileptonic $t\bar{t}$ decays and decays explicitly containing intermediate tau leptons[1]. A

---

[1]A purely hadronically decaying $t\bar{t}$ is not considered in this process. It is per construction part of the multijet background.

Table 7.1.: Numbers of selected events from all signal and background processes as well as the data in the signal region. A discrimination between the muon charges is made. Only the statistical uncertainty is included.

Process	Selected events μ^+	Selected events μ^-
$W \to \tau\nu$	2817 ± 45	1512 ± 19
Multijet	3234 ± 43	3199 ± 43
Diboson	6069 ± 29	5934 ± 243
Single top	5612 ± 30	5571 ± 30
$Z \to \mu\mu/\tau\tau$	21721 ± 42	10202 ± 33
$t\bar{t}$	47625 ± 85	47724 ± 85
Total background	87011 ± 120	74142 ± 266
$W \to \mu\nu$	172114 ± 328	106438 ± 313
Total prediction	259125 ± 350	180580 ± 411
Data 2015-18	262512 ± 512	185793 ± 431
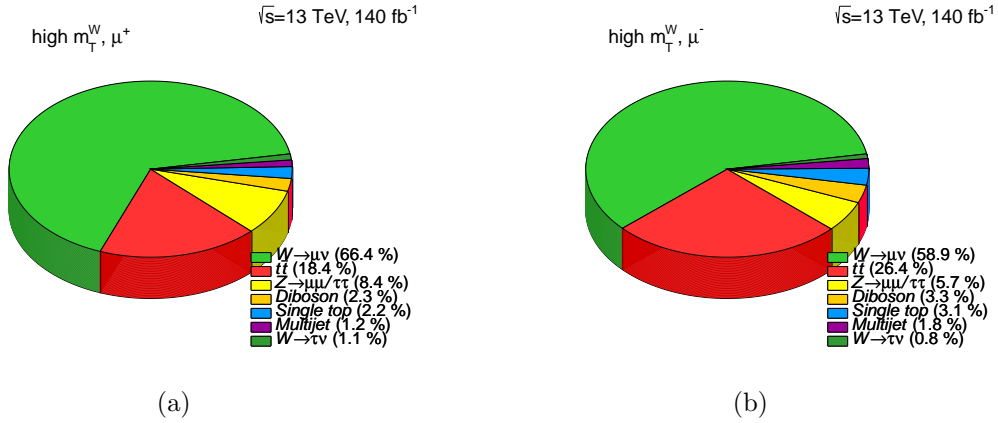
Figure 7.1.: Relative contribution of the different processes in the (a) μ^+- and (b) μ^--channel.

dileptonic $t\bar{t}$ control region containing exactly one muon and one electron was studied and an excellent modeling of this process can be assumed.

Another relevant background contribution is given by $Z \to \ell^+\ell^-$ (with $\ell = \mu, \tau$) events, with a relative fraction of 8.4 % (μ^+) and 5.7 % (μ^-). It contributes particularly if the second muon is found outside the measurement acceptance, e.g. at $|\eta(\mu)| > 2.4$. It occurs substantially more often that only the positively charged muon is measured. As investigated in my master thesis, the effect can be attributed to the forward-backward asymmetry in the ncDY process induced by the electroweak mixing. It leads to a more central production of the μ^+ than the μ^- in the $Z \to \mu^+\mu^-$ decay at high masses.

All other background processes (diboson, single top, $W \to \tau\nu$ and multijet) contribute marginally with about $1\,\%$ to $3\,\%$ depending on the process and charge.

7.2. Distributions of control variables

The number of data events is compared to the number of predicted events in the signal region with $m_{\mathrm{T}}^{\mathrm{W}} > 200\,\mathrm{GeV}$. Distributions of key variables are shown in Figure 7.2 (μ^+) and Figure 7.3 (μ^-) while both charges show predominantly analogous features. Across all plots, error bars represent the data statistical uncertainty while the gray band contains the MC statistical uncertainty and all systematic uncertainties. Experimental detector, top modeling and data-driven multijet uncertainties are taken into account.

The $p_{\mathrm{T}}(\mu)$ and $E_{\mathrm{T}}^{\mathrm{miss}}$ distributions demonstrate similar shapes. Both exhibit a maximum at about $100\,\mathrm{GeV}$ with a steeply falling tail over many orders of magnitude for higher momenta of up to 2 TeV. The regions of $p_{\mathrm{T}}(\mu) < 100\,\mathrm{GeV}$ and $E_{\mathrm{T}}^{\mathrm{miss}} < 100\,\mathrm{GeV}$ are not well-populated which is caused by the $m_{\mathrm{T}}^{\mathrm{W}} > 200\,\mathrm{GeV}$ requirement here. In general, the prediction describes the data very well over the whole spectrum within the given uncertainties. At best, the agreement is in the order of a few percent while the uncertainty increases in the high-momentum tails. An opposite trend for $p_{\mathrm{T}}(\mu^+)$ and $p_{\mathrm{T}}(\mu^-)$ is striking, with deviations of $\pm 10\,\%$ at $p_{\mathrm{T}}(\mu) \approx 400\,\mathrm{GeV}$. As investigated extensively throughout this dissertation, this trend is caused by a residual sagitta bias in the muon momentum measurement for the high-mass spectrum (see Section 4.2.5). The deviation is covered approximately by the total given uncertainty which is, in this region, dominated by the systematic uncertainty associated with the sagitta bias.

The distribution of the azimuthal separation between muon and $E_{\mathrm{T}}^{\mathrm{miss}}$ exhibits a clear trend towards $\Delta\phi(\mu, E_{\mathrm{T}}^{\mathrm{miss}}) = \pi$. Less than 100 data events with $\Delta\phi(\mu, E_{\mathrm{T}}^{\mathrm{miss}}) < 1$ and $\mathcal{O}(10^4)$ events with $\Delta\phi(\mu, E_{\mathrm{T}}^{\mathrm{miss}}) > 3$ are selected. The shape can be understood by the back-to-back topology of muon and neutrino ($E_{\mathrm{T}}^{\mathrm{miss}}$) in the signal $W \to \mu\nu$ decay. This topology is less pronounced for background processes, e.g. $t\bar{t}$ and multijet, where the muon-neutrino pair might be boosted in a similar direction. Also in this variable, the agreement between the numbers of data and predicted events is at the percent-level in the statistically significant region.

The transverse mass $m_{\mathrm{T}}^{\mathrm{W}}$ is composed of the three variables explained above, according to Equation 1.15. As only the high-mass tail is investigated, the distributions are falling, over five orders of magnitude in the range shown from $200\,\mathrm{GeV}$ to $3\,\mathrm{TeV}$. Over the whole spectrum, a good agreement between data and prediction is notable for both muon charges. It is at percent-level for $m_{\mathrm{T}}^{\mathrm{W}} \lesssim 500\,\mathrm{GeV}$ while the statistical significance decreases in the high-mass tail above $1\,\mathrm{TeV}$. For that reason, the cross-sections in $m_{\mathrm{T}}^{\mathrm{W}}$ will be measured in a coarser binning than the one shown here. The charge-opposite trends caused by the sagitta bias in the muon momentum measurement discussed for $p_{\mathrm{T}}(\mu)$ above are visible in $m_{\mathrm{T}}^{\mathrm{W}}$ as well.
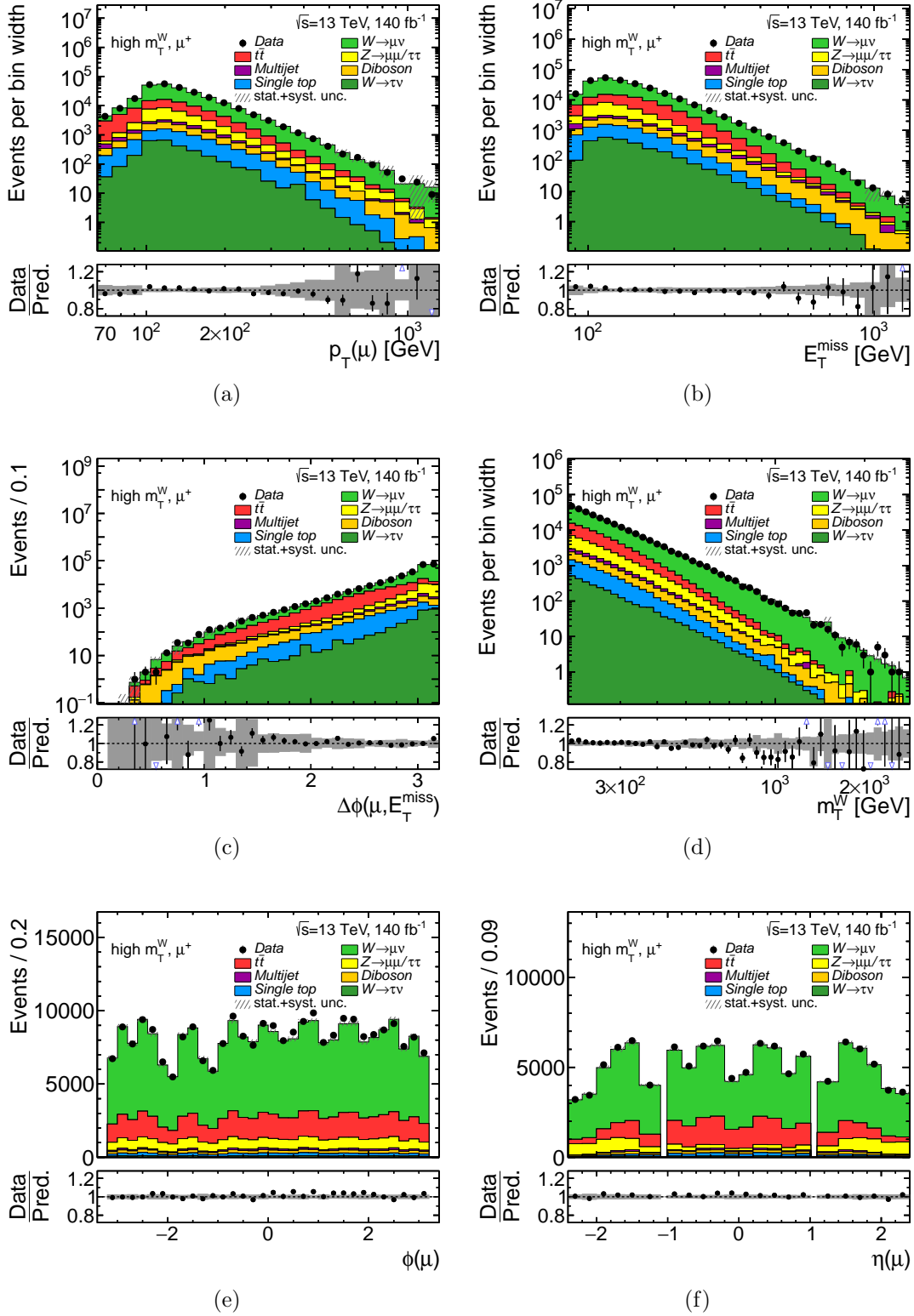
Figure 7.2.: Distributions of the (a) transverse momentum of the muon and (b) missing transverse momentum, (c) azimuthal angle between muon and E_T^{miss}, (d) transverse mass, (e) azimuthal angle of the muon and (f) pseudorapidity of the muon for data and prediction in the signal region for a μ^+ final state. Statistical and systematic uncertainties are included.
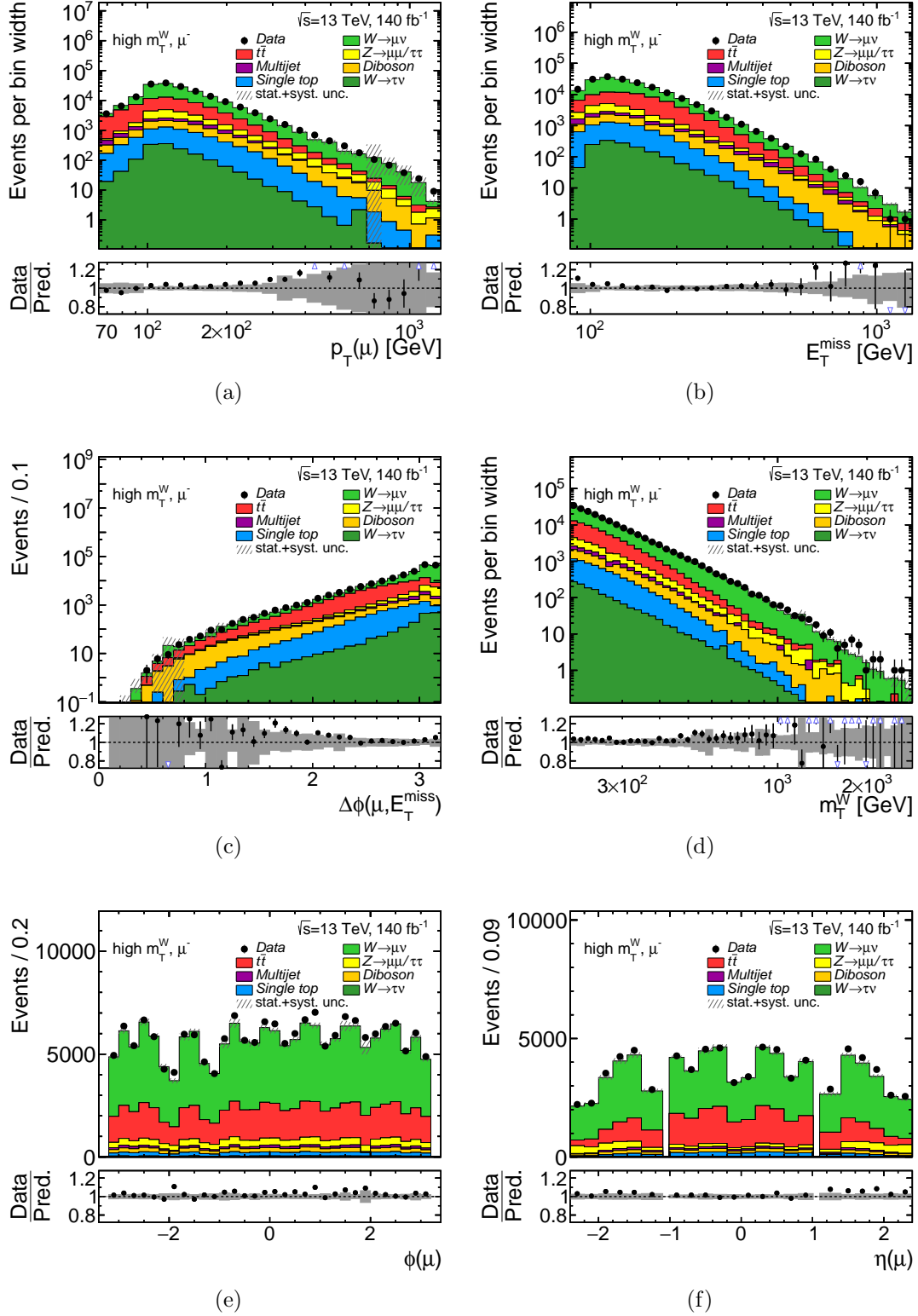
Figure 7.3.: Distributions of the (a) transverse momentum of the muon and (b) missing transverse momentum, (c) azimuthal angle between muon and $E_\mathrm{T}^\mathrm{miss}$, (d) transverse mass, (e) azimuthal angle of the muon and (f) pseudorapidity of the muon for data and prediction in the signal region for a μ^- final state. Statistical and systematic uncertainties are included.

Finally, the detector coordinates ϕ and η of the muon are shown in Figure 7.2 (μ^+) and Figure 7.3 (μ^-). Generally, the distributions of $\phi(\mu)$ are flat, as no azimuthal orientation is preferred. Nevertheless, the spectrum is characterized by structures associated with the MS geometry (see Section 2.2.5). Periodic dips can be identified with the eight toroid coils in the MS barrel. Additionally, at $\phi(\mu) \approx -1.2/-2$, the feet of the ATLAS detector are located. The limited MS acceptance is also reflected in the pseudorapidity distribution. For instance, at $\eta(\mu) \approx 0$, there is a shaft for cables to the inner sub-detectors and, at $|\eta(\mu)| \approx 1$, the transitions between barrel and end-caps. In the empty bin at $|\eta(\mu)| \in [1.01, 1.1]$, no well-defined `high-`$p_\mathrm{T}$ muons are reconstructed (see Section 4.2.1). In contrast to $\phi(\mu)$, different physics processes demonstrate distinct shapes in $\eta(\mu)$, compare e.g. $t\bar{t}$ and $Z \rightarrow \ell\ell$ in Figure 7.2(f). They originate directly from physics constraints or process-specific acceptance effects. The regions of positive and negative $\eta(\mu)$ are generally symmetrical. Thus, the final measurement will be performed as a function of $|\eta(\mu)|$, increasing the statistics by a factor of two without compromising the physics sensitivity. Overall, also in the angular variables, a good agreement between data and prediction is observed. Minor fluctuations are acceptable given the challenging MS geometry with numerous interruptions and varying measurement efficiencies.

The signal process contains no jets at LO, however, the multijet and $t\bar{t}$ processes are characterized by jet final states. Thus, the distributions of the jet multiplicity and the p_T of the leading jet are evaluated, see Figure D.5. Both variables show good agreement between data and prediction, indicating a sensible description of these background processes. Lastly, control distributions for $\mu^\pm$ combined can be found in Appendix D and distributions separated in different m_T^W bins and per data-taking period can be found in Reference [84]. All look reasonable within the given uncertainties.

7.3. Measurement observables

Observed and predicted distributions are compared for the measurement observables in the binning introduced in Section 5.3. The single-differential distributions as a function of m_T^W are shown in Figure 7.4, separated per muon charge. Over the whole spectrum from $150\,\mathrm{GeV}$ to $5\,\mathrm{TeV}$ a generally good agreement between data and prediction is observed.

Nevertheless, a few aspects are worth pointing out. A gray 'shadow' marks the shadow bin (see Section 5.3) where a slight overshoot of data of about $5-7\,\%$ is visible. This feature is expected to be related to the $E_\mathrm{T}^\mathrm{miss}$ resolution, as studied in Reference [74]. Nevertheless, for $m_\mathrm{T}^\mathrm{W} > 200\,\mathrm{GeV}$, the numbers of data and predicted events agree within a few percent. Starting at $m_\mathrm{T}^\mathrm{W} \approx 700\,\mathrm{GeV}$, the charge-opposite trends seen in the $p_\mathrm{T}(\mu)$ distributions in Section 7.2 are also visible. They are closely covered by the uncertainty band. Finally, it is worth emphasizing that the last m_T^W bin, covering $m_\mathrm{T}^\mathrm{W} \in [2, 5]\,\mathrm{TeV}$, features also an excellent description. This extreme phase space, containing only 14 (μ^+) and 7 (μ^-) data events, is expected to be highly valuable in terms of EFT interpretations.
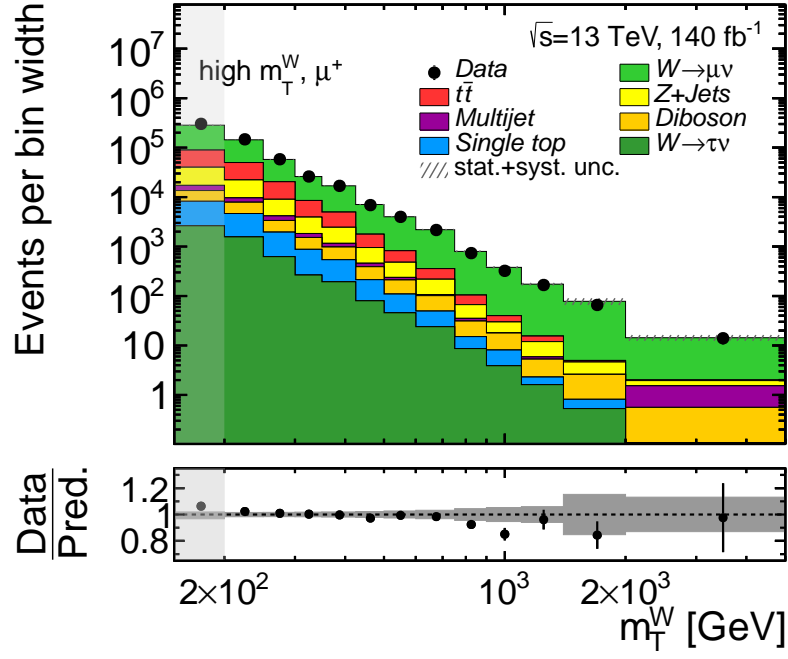
(a)
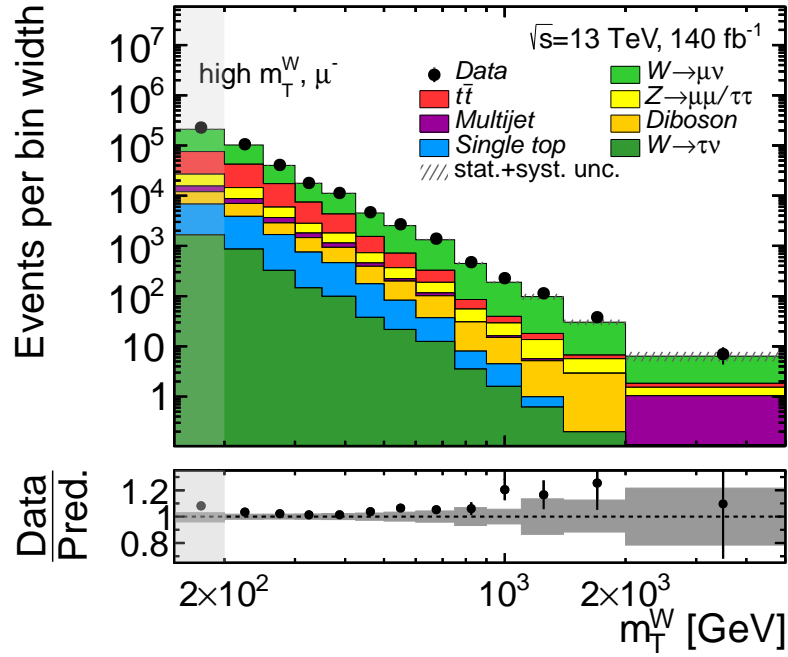
(b)

Figure 7.4.: Distributions of the transverse mass for data and prediction in the measurement binning for (a) μ^+ and (b) μ^-. Statistical and systematic uncertainties are included.

The set of distributions in the double-differential measurement binning in $m_\mathrm{T}^\mathrm{W} \otimes |\eta(\mu)|$ are shown in Figures 7.5 (μ^+) and Figure 7.6 (μ^-). Each plot shows the $|\eta(\mu)|$ distribution within one m_T^W bin, where Figure 7.5(a) and Figure 7.6(a) correspond to the respective shadow bins. As a reminder, the empty bin at $|\eta(\mu)| \approx 1$ visible in all distributions here is chosen on purpose since no `high-`p_T quality muons are reconstructed in the challenging transition region between barrel and end-caps (see Sections 4.2.1/5.3).

A generally good agreement between prediction and data is observed in the double-differential binning. All trends seen in the single-differential m_T^W distributions are reflected as well. For instance, the charge-dependent residual sagitta bias in the muon momentum measurement manifests in these 2D distributions as well. The effect is found to be particularly pronounced in the end-cap areas with $|\eta(\mu)| > 1.1$. Differences in predicted and observed events are mostly covered by the given uncertainties but not in all bins see e.g. Figure 7.6(d). This behavior is understood as the applied sagitta-bias correction is known to perform suboptimal in the extrapolation to high $p_\mathrm{T}(\mu)$ and high $\eta(\mu)$. As discussed in Section 4.2.5, no better correction could be achieved by the dedicated calibration group.

Finally, the same $m_\mathrm{T}^\mathrm{W} \otimes |\eta(\mu)|$ distributions as given in Figures 7.5 and 7.6 are shown in a very compact way in Figure 7.7. All six $|\eta(\mu)|$ distributions are shown next to each other, while different m_T^W bins are separated by vertical lines. The bins are visualized as equidistant bins, however, the labels below give the actual bin widths in $|\eta(\mu)|$. For the remainder of this dissertation, this visualization of the double-differential binning in $m_\mathrm{T}^\mathrm{W} \otimes |\eta(\mu)|$ is used for the sake of compactness. The final cross-sections will be transformed back to a separate presentation per m_T^W bin.

(a) shadow bin

(b)

(c)

(d)

(e)

(f)
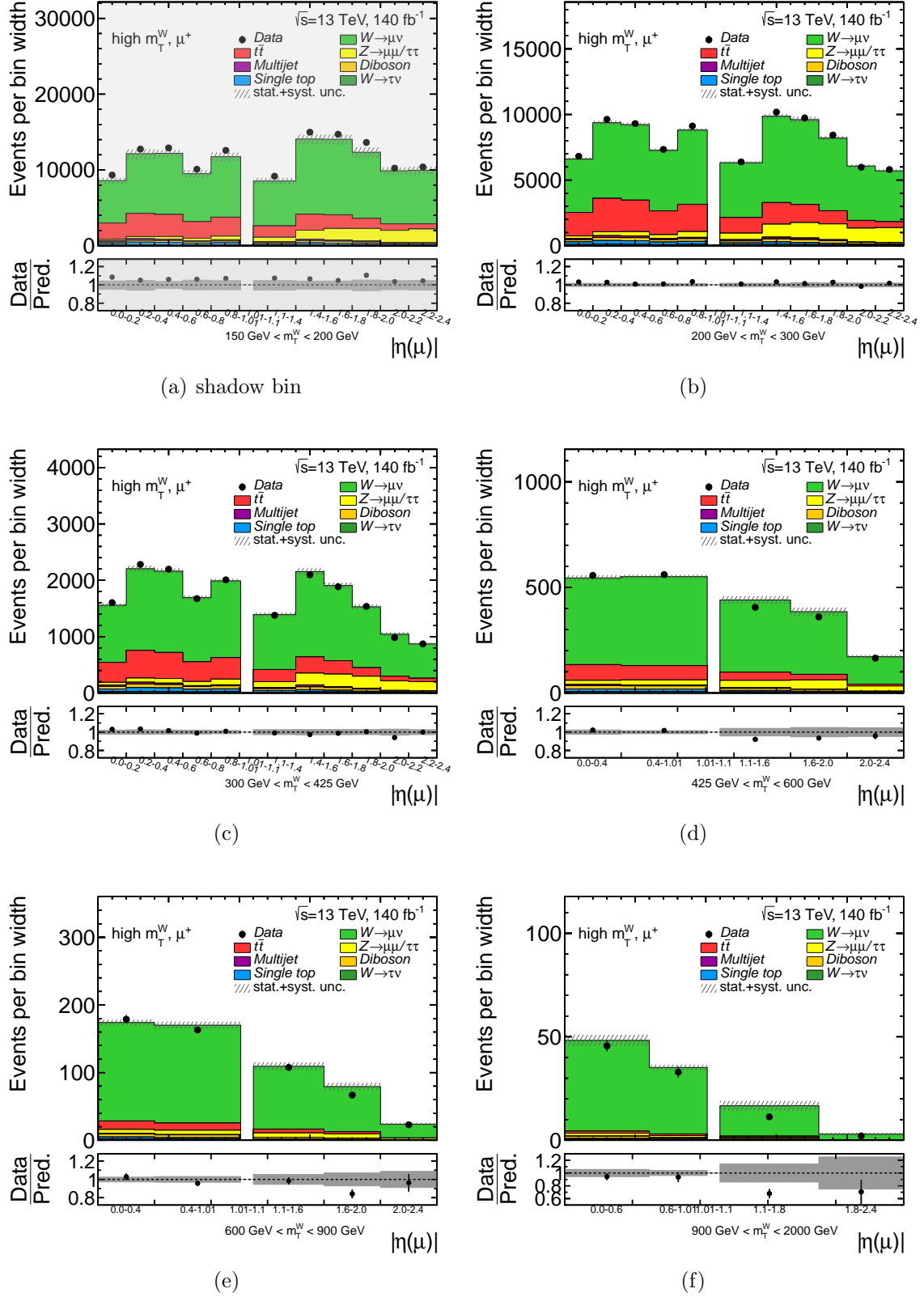
Figure 7.5.: Distributions of the pseudorapidity of the muon for data and prediction in different m_T^W bins for a μ^+ final state. Statistical and systematic uncertainties are included.

(a) shadow bin

(b)

(c)

(d)

(e)

(f)
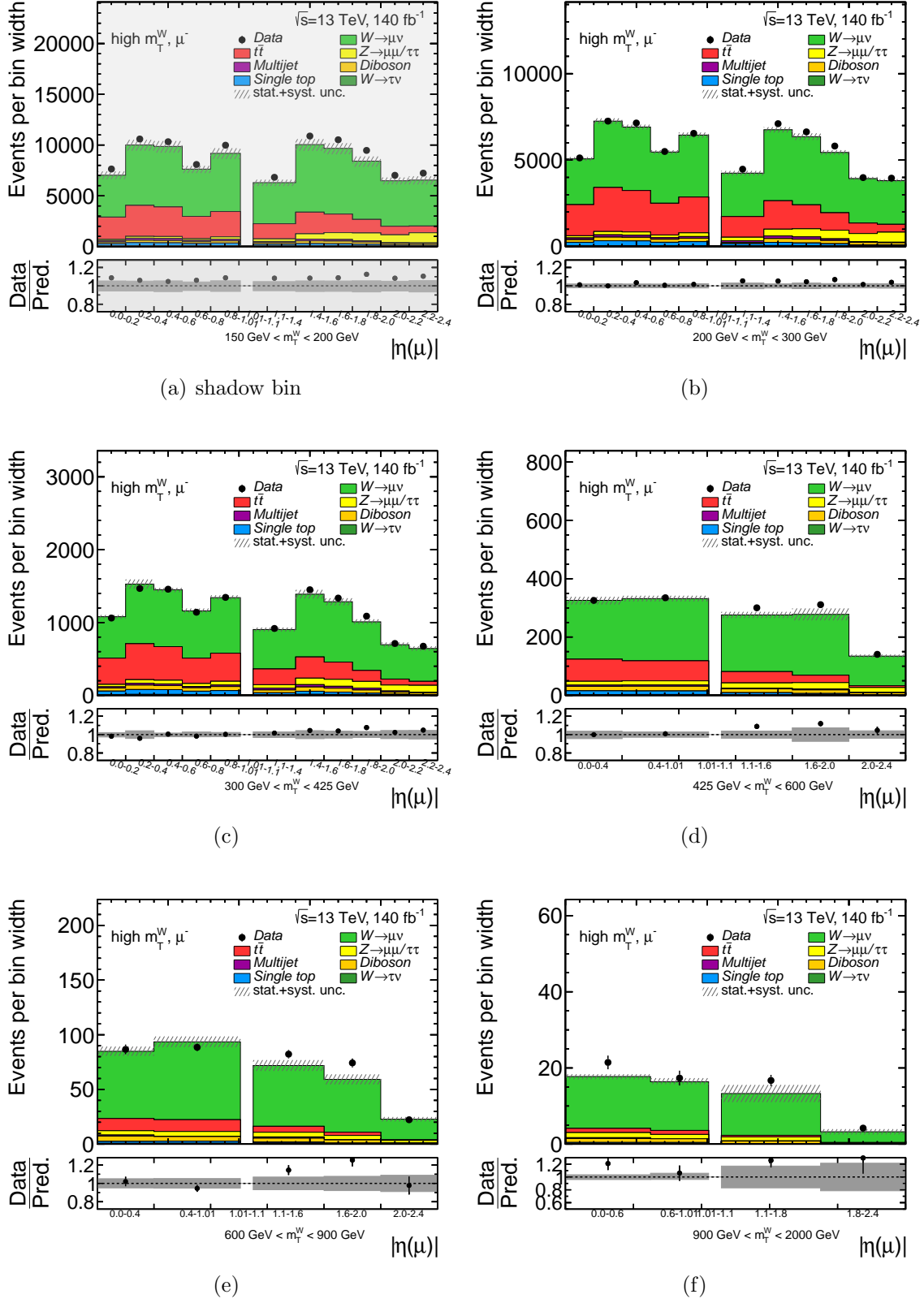
Figure 7.6.: Distributions of the pseudorapidity of the muon for data and prediction in different m_T^W bins for a μ^- final state. Statistical and systematic uncertainties are included.
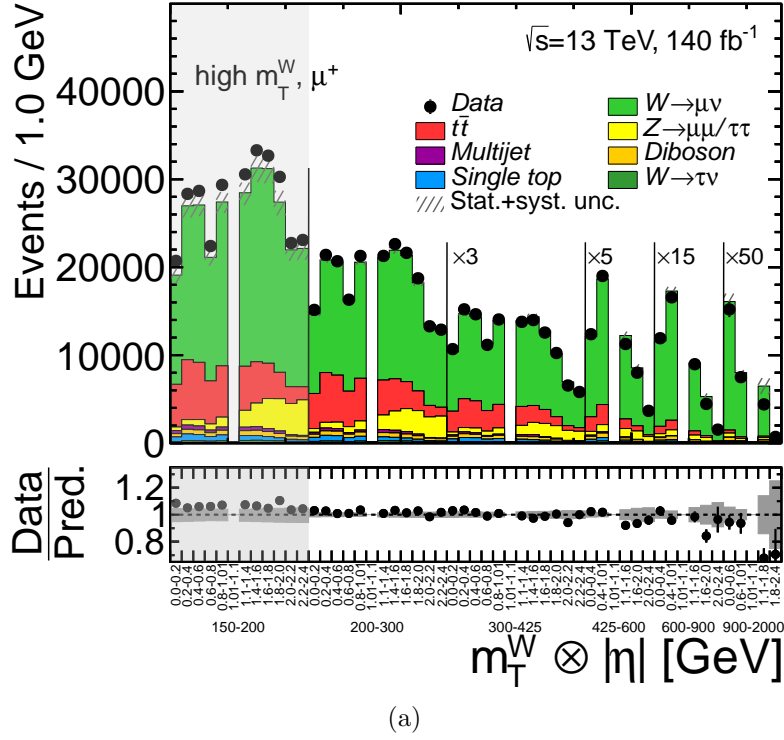
(a)
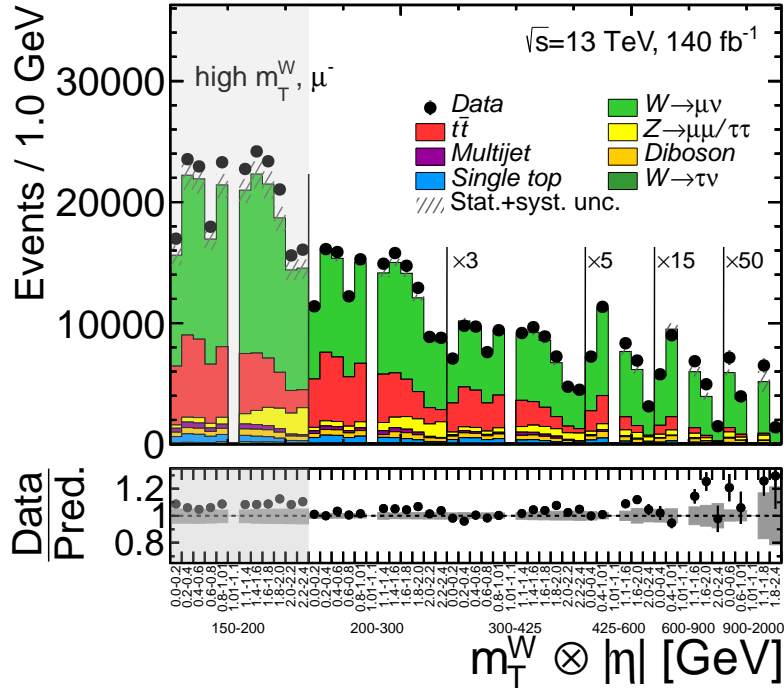
(b)

Figure 7.7.: Distributions of the pseudorapidity of the muon for data and prediction in different m_T^W bins for a (a) μ^+ and (b) μ^- final state. A compact representation is shown where different m_T^W bins are separated by vertical lines. For better readability, the numbers of events are scaled by factors of 3, 5, 15 and 50 in the higher m_T^W bins. Statistical and systematic uncertainties are included.

8. Unfolding of the differential cross-sections

In order to obtain the single- and double-differential cross-sections, the data is *unfolded* to the truth level, i.e. physics distributions without any detector distortions are obtained. The unfolding procedure is one of the major challenges in this dissertation, however, it is essential in order to compare with theory predictions or potentially other measurements. After a general introduction to the unfolding problem in Section 8.1, the method of Iterative Bayesian Unfolding is explained in Section 8.2, including a discussion of all special features in this measurement. Several tests are conducted in order to validate and quantify the unfolding performance, see Section 8.3. Finally, the treatment of statistical and systematic uncertainties in the unfolding procedure is presented in Section 8.4.

8.1. The unfolding problem

No measurement apparatus is perfect. Thus, the *truth-level* physical quantity of interest is distorted by the detector response and might appear differently on the *reconstruction level*, as illustrated schematically in Figure 8.1. Generally, the number of events measured is reduced with respect to the true number of events due to detector-specific
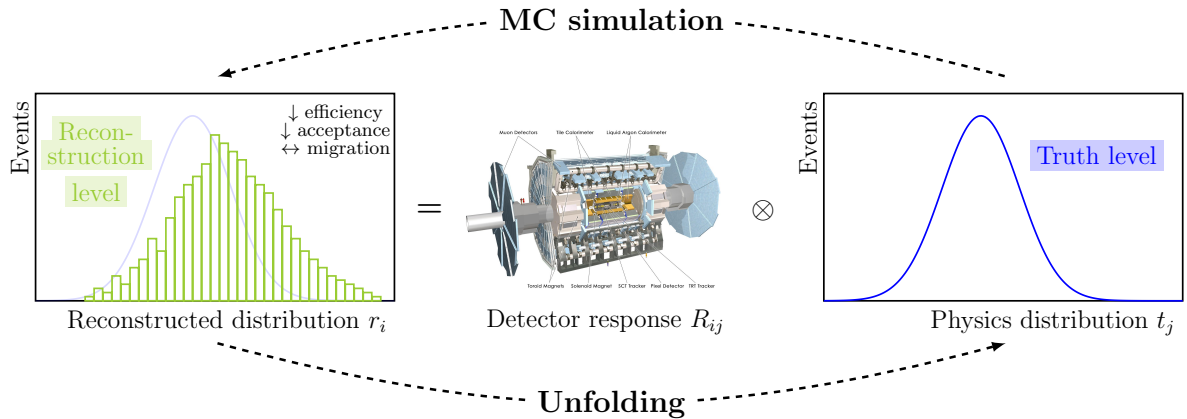
Figure 8.1.: Schematic illustration of the unfolding problem where the reconstruction level is given by a convolution of the underlying truth level and the detector response.

efficiency and *acceptance* effects. Furthermore, the limited resolution introduces a smeared distribution on the reconstruction level, an effect called *migration* where events are generated and reconstructed in different bins.

The transition from the truth level to the reconstructed level is indicated by the upper arrow pointing from right to left in Figure 8.1. It is described straightforwardly by MC simulation given the step-by-step generation chain (see Section 3.2). Mathematically, the connection between a reconstructed, measured quantify r and its underlying truth quantity t can be expressed by a convolution, or *folding*, of the truth-level distribution and the detector response [167],

$$g(r) = \int R(r|t) \cdot f(t) \, dt + b(r). \tag{8.1}$$

Here, $g(r)$ and $f(t)$ are the respective probability density functions of the reconstructed and truth level while all detector effects are encoded in the response function $R(r|t)$. A potential additional background term $b(r)$ will be omitted for the remainder of this paragraph. In practice, cross-section measurements are counting experiments in binned observables. As a result, Equation 8.1 can be simplified to a matrix multiplication

$$\vec{r} = \mathbf{R} \cdot \vec{t} \tag{8.2}$$

where $\vec{r}$ and $\vec{t}$ are the respective reconstructed and truth histograms. The matrix $\mathbf{R}$ is characterized by elements $R_{ij} = P(r_i|t_j) = P(\text{reconstructed in bin } i|\text{true value in bin } j)$, to be obtained from simulation here.

The challenge of *unfolding* is to retrieve the inverse, indicated by the lower arrow pointing from left to right in Figure 8.1. The reconstructed data is available and the truth level, free of detector effects, is desired. In theory, this is expressed by an inversion of the matrix

$$\vec{t} = \mathbf{R}^{-1} \cdot \vec{r}. \tag{8.3}$$

In practice, commonly, no direct matrix inversion is performed, as it may be accompanied by the disadvantages of large variances and strong negative correlations between bins. Two methods are widely used in high-energy physics: *Bin-by-bin Unfolding* and *Iterative Bayesian Unfolding*, however more unfolding methods exist in general.

8.2. Cross-section measurement

Generally, the cross-section in bin i can be obtained via Bin-by-bin unfolding as

$$\sigma_i = \frac{N^i_{\text{data}} - N^i_{\text{bkg}}}{C_i \cdot \mathcal{L}_{\text{int}}}. \tag{8.4}$$

The number of data events N^i_{data} is subtracted by all background events N^i_{bkg} and divided by a measurement correction factor C_i. The matrix inversion is straightforward as the

detector response is encoded in the scalar factors C_i. All bins are treated uncorrelated and the number of events is unfolded according to Equation 8.4. Finally, a cross-section is extracted by dividing by the integrated luminosity $\mathcal{L}_\text{int}$.

However, in the case of sizeable migrations between bins, as present in this dissertation, Iterative Bayesian Unfolding (IBU) is commonly employed. The differential cross-section $\frac{d\sigma}{dx_j}$ is obtained according to

$$\frac{d\sigma}{dx_j} = \frac{1}{\Delta x_j \cdot \mathcal{L}_\text{int} \cdot \epsilon_j} \sum_{i=1}^{N_\text{bins}^\text{reco}} R_{ij}^{-1} \cdot f_\text{in}^i \cdot (N_\text{data}^i - N_\text{bkg}^i) \tag{8.5}$$

where the index j/i corresponds to the respective truth/reconstruction-level bin. The differential cross-section is normalized to the bin width Δx_j here. The detector response is given by the three terms ϵ_j, f_in^i and R_{ij}^{-1}. The factors ϵ_j and f_in^i represent efficiency and in-smearing corrections while the inverted matrix R_{ij}^{-1} covers migration effects. It is approximated via conditional probabilities in the IBU method.

8.2.1. Theoretical formulation of Iterative Bayesian Unfolding

The method of Iterative Bayesian Unfolding, given by D'Agostini [168] and implemented via `RooUnfold` [169], is described in the following. The inverse matrix element R_{ij}^{-1} is identified with the conditional probability $P(t_j|r_i)$ for an event to be in truth-level bin j given it is reconstructed in bin i. It can be expressed according to Bayes' theorem as

$$P(t_j|r_i) = \frac{P(r_i|t_j) \cdot P_0(t_j)}{\sum_{k=1}^{N_\text{bins}^\text{truth}} P(r_i|t_k) \cdot P_0(t_k)} \tag{8.6}$$

where $P_0(t_j)$ is a, generally arbitrary, initial distribution of the truth level. $P(r_i|t_j)$ represents the probability for an event to be reconstructed in bin i given it was generated in bin j. This probability can be assessed via a *response matrix* R_{ij} constructed from the signal prediction. The denominator normalizes the probability by summing over all truth-level bins $N_\text{bins}^\text{truth}$. The total number of events in truth-level bin j, N_truth^j, is estimated as

$$N_\text{truth}^j = \frac{1}{\epsilon_j} \sum_{i=1}^{N_\text{bins}^\text{reco}} P(t_j|r_i) \cdot \underbrace{N_\text{reco}^i}_{f_\text{in}^i \cdot (N_\text{data}^i - N_\text{bkg}^i)} \tag{8.7}$$

where N_reco^i represents the background-subtracted, in-smearing corrected number of signal events per bin of reconstructed data. The product of $P(t_j|r_i)$ and N_reco^i indicates the number of events migrating from reconstructed bin i to truth bin j. Summing over all reconstruction-level bins $N_\text{bins}^\text{reco}$ accounts for migrations across the entire measurement

range. Finally, the unfolded number of events is corrected for unreconstructed events by multiplying with the inverse of the efficiency ϵ_j.

An appropriate initial truth-level probability distribution $P_0(t_j)$ is required in Equation 8.6. Usually, the truth distribution of the signal MC sample serves as an initial guess. In order to minimize the bias introduced by this choice, the estimation is refined in an iterative procedure. In subsequent iterations, $P_0(t_j)$ is updated to a newly computed $\hat{P}(t_j) = N^j_{\text{truth}}/(\sum_{k=1}^{N^{\text{truth}}_{\text{bins}}} N^k_{\text{truth}})$ which is the normalized probability density distribution of the unfolded level of the previous iteration. The response matrix remains unchanged throughout the whole procedure. An optimal number of iterations needs to be evaluated uniquely for any measurement using dedicated termination criteria.

8.2.2. Response matrix

The response matrix represents an essential ingredient to the IBU as it contains the probabilities $P(r_i|t_j)$ input to Equation 8.6. It is calculated via the signal MC sample using events that pass the reconstruction-level event selection (see Section 5.1) as well as the truth-level selection (see Section 5.2). Both selections include the shadow bin here. All events failing either the reconstruction-level or truth-level event selection are not included in the response matrix but considered in the correction factors ϵ_j and f^i_{in}.

The response matrix for the single-differential observable, m^{W}_{T}, is depicted in Figure 8.2(a) for μ^+ and Figure 8.2(b) for μ^-. It is constructed by filling a two-dimensional histogram with the reconstruction-level observable on the x-axis and the corresponding truth-level observable on the y-axis. A normalization per truth-level bin, i.e. per row, is performed, resulting in a matrix containing fractions in percent. The diagonal elements correspond to the fractions of events that are generated and reconstructed in the same bin. They range from 84% to 60 % here while migrations of up to 27 % to the neighboring adjacent diagonal elements are visible. Generally, the migration is asymmetric with a larger fraction of migrations to the left of the diagonal, as objects in the detector are more likely to be reconstructed with a smaller than larger energy. The majority of remaining matrix elements are close to zero. The migration, in particular at high m^{W}_{T}, is to a large degree driven by the momentum resolution of the muon measurement. As discussed in Section 5.3, the binning here is chosen such that the migration is kept at a reasonable level.

The response matrix for $m^{\text{W}}_{\text{T}} \otimes |\eta(\mu)|$ is depicted in Figure 8.2(c), as an example for the negative muon charge (see Figure E.6 for μ^+). The compact 2D visualization introduced in Section 7.3 is used. Migrations in m^{W}_{T} can be seen by comparing the diagonal elements of neighboring squares, as the vertical and horizontal lines separate the m^{W}_{T} bins. Similarly to the 1D measurement, the largest migrations are to the adjacent diagonals in m^{W}_{T}. They are with $\mathcal{O}(15\,\%)$ slightly smaller than in 1D which can be understood by the partly larger m^{W}_{T} bins chosen for the 2D measurement.

(a)

(b)

(c)
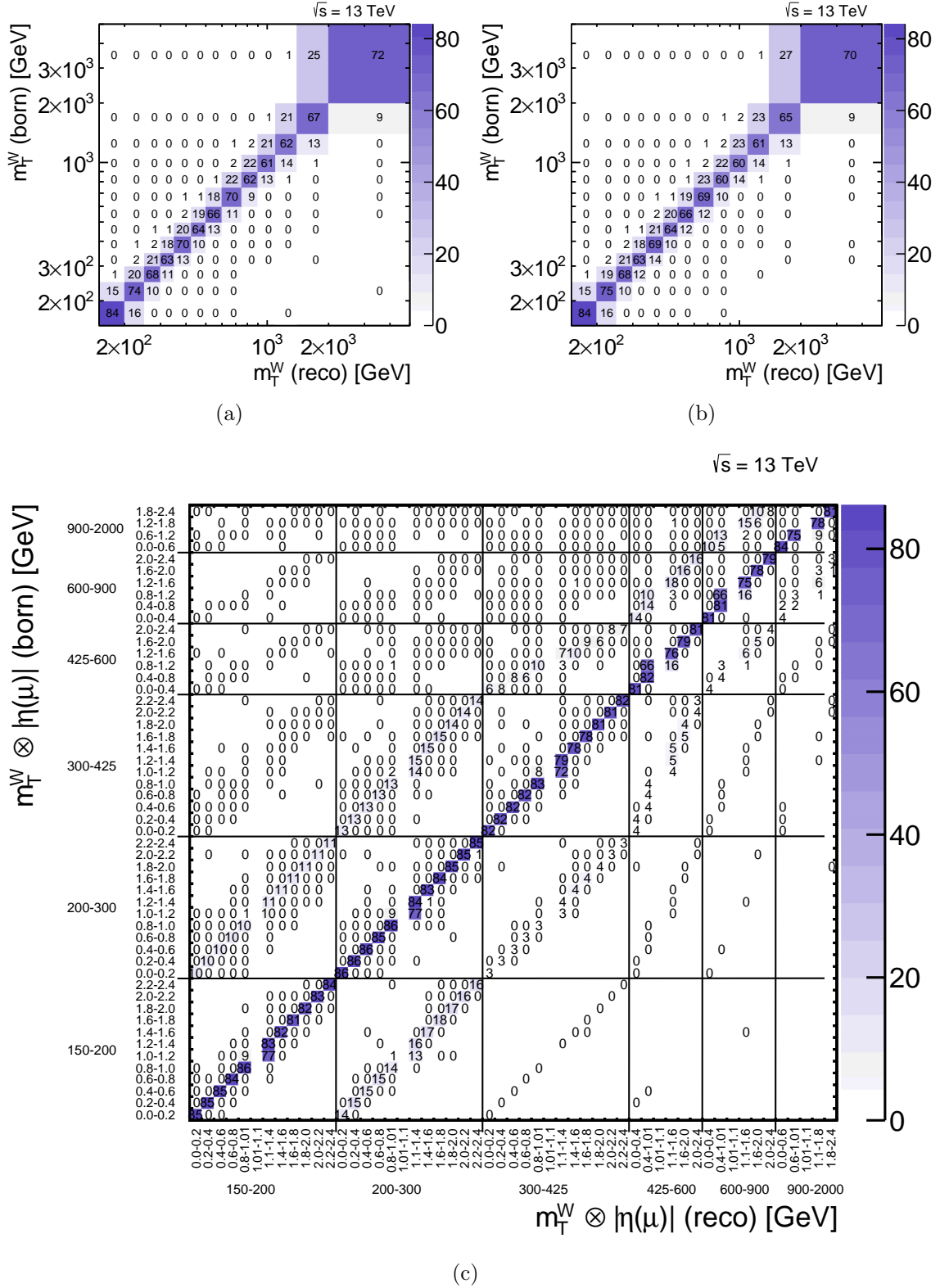
Figure 8.2.: Response matrix R_{ij} as a function of (a, b) m_T^W obtained using the $W \to \mu\nu$ simulated sample for the (a) μ^+-channel and (b) μ^--channel and (c) for $m_T^W \otimes |\eta(\mu)|$ for μ^-. All entries are given in percent. A written 0 corresponds to a fraction rounded to zero, while bins containing truly no reconstructed events do not show a number.

Migrations across $|\eta(\mu)|$ are depicted within given squares. As introduced in Section 5.3, a different η-binning is used on the reconstruction and truth level. The empty bin at $|\eta(\mu_{\text{reco}})| \in [1.01, 1.1]$ is visible across all m_{T}^{W} bins here. Only in this transition region, migrations across η are notable. If using the same equidistant η-binning on both levels, migrations in η are negligible, see Figure E.8. The migrations seen here can be identified with bin overlaps between the reconstructed and truth distributions. It shall be explained using the lower left square (shadow bin) in Figure 8.2(c) as an example. Events generated with $|\eta(\mu_{\text{truth}})| \in [1.0, 1.2]$ in this m_{T}^{W} bin are reconstructed to 9 % with $|\eta(\mu_{\text{reco}})| \in [0.8, 1.01]$ and 77 % with $|\eta(\mu_{\text{reco}})| \in [1.1, 1.4]$. So, in total, $9\% + 77\% = 86\%$ of the events are reconstructed in this m_{T}^{W} bin. The overlap between the $|\eta(\mu_{\text{truth}})| \in [1.0, 1.2]$ bin and $|\eta(\mu_{\text{reco}})| \in [0.8, 1.01]$ bin has a width of 0.01 (namely $[1.0, 1.01]$), while the corresponding overlap with $|\eta(\mu_{\text{reco}})| \in [1.1, 1.4]$ has a width of 0.1. Taking the relative fractions one ends up exactly at $^{0.01}/_{0.11} \cdot 86\% = 9\%$ and $^{0.1}/_{0.11} \cdot 86\% = 77\%$.

8.2.3. Efficiency and in-smearing corrections

The response matrix discussed above is built from events that pass the reconstruction- and truth-level selection requirements. Nevertheless, a non-negligible fraction of events fails either of the two due to efficiency and acceptance constraints. Thus, the response matrix is complemented by two binned corrections factors f_{in}^i and ϵ_j. Both are evaluated using the signal $W \to \mu\nu$ sample.

Efficiency correction ϵ_j Due to the limited detector efficiency and measurement acceptance, not every event produced in a collision is reconstructed. In the unfolding procedure, this is accounted for via a binned *efficiency correction factor* ϵ_j defined as

$$\epsilon_j = \frac{N_{\text{reco}\wedge\text{truth}}^j}{N_{\text{truth}}^j}. \tag{8.8}$$

Here, $N_{\text{reco}\wedge\text{truth}}^j$ is the number of events per truth-level bin j that pass both selections, truth and reconstruction level. The denominator N_{truth}^j contains all selected truth events, regardless if reconstructed or not.

The correction factors ϵ_j for the single- and double-differential measurement observables are shown in Figure 8.3, as an example for μ^- as the factors are very similar for both charges (see Figure E.4 for μ^+). As a function of m_{T}^{W}, the efficiency is approximately flat throughout the measurement range, with $\epsilon_j \approx 60\%$. Given the limited acceptance and efficiency for a muon measurement in the ATLAS detector, this substantial fraction of events not reconstructed is expected. Leading measurement losses are induced by the strict `high-p`$_{\text{T}}$ working point, the muon trigger efficiency and the $|\eta(\mu)|$ acceptance. The lower efficiency of $\epsilon_j \approx 40\%$ in the shadow bin is caused by the reconstruction acceptance introduced by the m_{T}^{W}, $E_{\text{T}}^{\text{miss}}$ and $p_{\text{T}}(\mu)$ requirements.
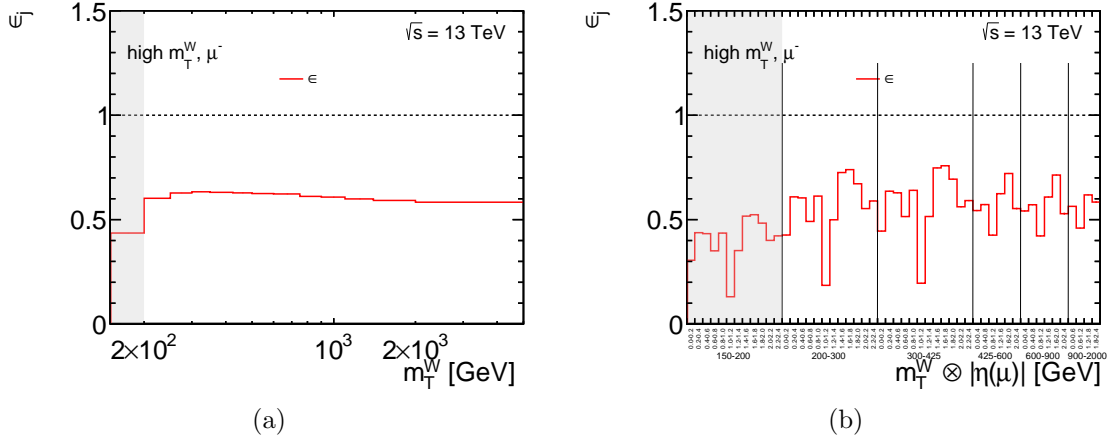
Figure 8.3.: Efficiency correction factors for (a) m_T^W and (b) $m_\mathrm{T}^\mathrm{W} \otimes |\eta(\mu)|$ as obtained using the $W \to \mu\nu$ simulated sample for the μ^--channel.

In the double-differential binning in $m_\mathrm{T}^\mathrm{W} \otimes |\eta(\mu)|$, fluctuations across η are visible, e.g. the efficiency decreases as low as $\epsilon_j \approx 20\,\%$ for $|\eta(\mu)| \in [1.0, 1.2]$. All these structures can be attributed to the measurement acceptance in the MS, which is interrupted frequently by support structures, services and the toroid magnets.

In-smearing correction f_in^i The cross-sections will be presented in a limited fiducial phase space. Hence, a fraction of events selected on the reconstruction level fails the truth-level selection. Often, these events are referred to be *in-smearing* into the measurement range. They need to be corrected for as they spoil the events generated truly in the fiducial region of interest. The *in-smearing correction factor* f_in^i is parametrized as

$$f_\mathrm{in}^i = \frac{N_{\mathrm{reco}\wedge\mathrm{truth}}^i}{N_\mathrm{reco}^i} \tag{8.9}$$

where $N_{\mathrm{reco}\wedge\mathrm{truth}}^i$ denotes the number of events per reconstruction-level bin i passing both selection levels. It is divided by the total number of reconstructed events N_reco^i. The in-smearing correction factors for the single- and double-differential unfolding procedure are presented in Figure 8.4 for μ^-. No substantial differences between charges are notable, see Figure E.5 for μ^+. Generally, f_in^i is the smallest at low m_T^W and consecutively approaches unity. It is below $50\,\%$ in the shadow bin and at $f_\mathrm{in}^i \approx 85\,\%$ in the first measurement bin. This implies that about $15\,\%$ of the events reconstructed in this bin originate from outside the fiducial phase space. They can be identified with events produced mainly at the W-boson resonance that *smear* into the high-m_T^W region. In principle, this is a rare phenomenon, however, the observed fraction is reasonable given the extreme overweight (at least five orders of magnitude) of events generated at the resonance. Careful handling of in-smearing events represents one major challenge of this analysis and cuts and binnings were chosen in a way that f_in^i is maximized.
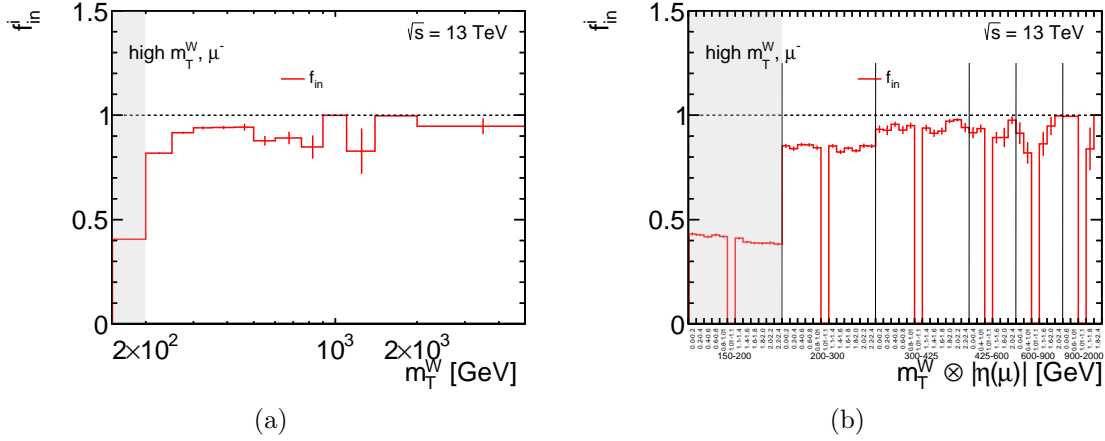
Figure 8.4.: In-smearing correction factors for (a) m_T^W and (b) $m_T^W \otimes |\eta(\mu)|$ as obtained using the $W \to \mu\nu$ simulated sample for the μ^--channel.

The in-smearing correction is mostly flat[1] across $|\eta(\mu)|$, as illustrated in Figure 8.4(b). At high m_T^W, bin-wise declines are striking in both, the single- and double-differential distributions. The correction factor f_{in}^i decreases by up to 15%, see e.g. the second to last bin in Figure 8.4(b), while it is at unity in neighboring bins. This is a statistically driven issue, indicated also by the increased statistical uncertainties in these bins. It was found that the declines are driven by $\mathcal{O}(10\text{ events})$ (see Figure F.16) which migrate from the W-boson mass peak to $m_T^W(\text{reco}) > 900\text{ GeV}$. In contrast, in neighboring bins, no in-smeared events are present. The issue occurs because the signal MC sample is constructed from sub-samples (see Section 3.3). While events contained in the peak sample possess a large MC weight, $\mathcal{O}(10^4)$, event weights in the high-mass slices are many orders of magnitude smaller. As a result, one single event with a large weight can have a substantial impact. This issue could not be eliminated as it would necessitate an increase of statistics in the peak sample unfeasible to produce.

8.2.4. Usage of a shadow bin

A *shadow bin* is an additional bin at the lower (or upper) edge of a distribution employed to stabilize the unfolding procedure. It will not be part of the cross-sections presented in the end. In particular, the handling of the in-smearing might be improved by using a shadow bin. By maximizing f_{in}^i, most of the migration is handled within the response matrix. As in-smearing from the mass peak to the high-m_T^W region represents a major challenge in this analysis, a shadow bin at the lower end of the distribution is employed, covering $m_T^W \in [150 - 200]\text{ GeV}$.

The in-smearing correction factor f_{in}^i, as defined in Section 8.2.3, is contrasted with and

---

[1]The correction factors at $|\eta(\mu)| \in [1.01, 1.1]$ are set to zero per construction, as no events are reconstructed in these bins.
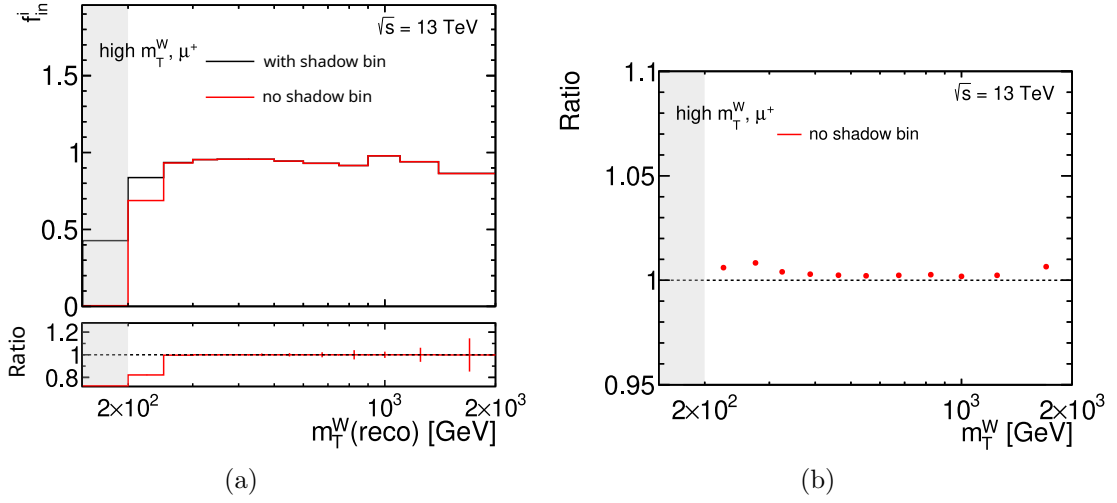
Figure 8.5.: (a) Comparison of the in-smearing correction factor f_{in}^i and (b) ratio of unfolded cross-sections with and without using a shadow bin. Both are shown for μ^+ here.

without using a shadow bin in Figure 8.5 for the single-differential W^+ measurement[2]. It can be observed that a substantial fraction of $(1 - f_{in}^i) \approx 30\%$ of events reconstructed in the first m_T^W bin (200-250 GeV) are originating from outside the fiducial phase space if no shadow bin is employed. In contrast, the in-smearing in this bin is about 15% if using a shadow bin. Since the shadow bin will not be part of the final measurement, the large in-smearing of about 50% in this bin is not relevant. In Figure 8.5(b), the unfolded cross-sections are compared for the two scenarios, showing that using a shadow bin decreases the cross-section by about 1%. It is decided to use the shadow bin here, as it provides a more refined handling of migrations across bins at the lower edge of the m_T^W spectrum.

Lastly, two aspects regarding the event selection and range of the shadow bin are worth underlining. Firstly, it is essential that the fiducial cuts on the p_T of the muon and neutrino (E_T^{miss}) are kept reasonably low to populate the shadow bin adequately. Thus, these cuts are chosen to match the lower edge of the shadow bin, i.e. $p_T^\ell + p_T^\nu = 150$ GeV. Secondly, the option of including the full mass peak as a shadow bin was investigated. This would allow for handling the full migration and in-smearing iteratively in the IBU. However, the $p_T^{\ell/\nu}$ cuts would need to be lowered substantially, which is generally not desired for a high-m_T^W measurement. The reconstruction level imposes constraints on the cuts on $p_T(\ell)$, due to the trigger threshold in the electron-channel, and E_T^{miss}, due to the construction of the Matrix Method using an inverted E_T^{miss} cut. Nevertheless, an additional shadow bin with $m_T^W \in [70 - 150]$ GeV and unchanged $p_T(\mu)$ and E_T^{miss} cuts was investigated, see Appendix E.4. Minimal in-smearing of below 1% from this bin to the high-mass region was found and, thus, the unfolding outcome remains unchanged.

---

[2]The study was performed before the single-differential measurement was extended by an additional 2-5 TeV bin.

8.2.5. Optimization of the number of iterations

The IBU is *regularized* by the number of iterations. As explained in Section 8.2.1, the truth-level distribution of the signal simulation is used as the 0th prior, inducing a potential bias towards the modeling in the simulation. On the other hand, a large number of iterations might induce undesirable large variances and correlations.

For this analysis, the number of iterations in the IBU was optimized in close cooperation with the parallel electron-channel measurement. A detailed description and discussion of all tests performed can be found in Reference [77]. Procedures and conclusions are analogous for electron and muon channels, thus, only the most important key aspects are highlighted here again. In Figure 8.6, the test results for the double-differential measurement in μ^+ are presented. The full set for both charges and single- and double-differential distributions is shown in Appendix E.5.

Evolution of the statistical uncertainty   An increase in the statistical uncertainty with the number of iterations is a known feature in IBU. Thus, a number of iterations as low as possible is desired. The evolution of the data statistical uncertainty is evaluated by comparing its distribution for 1-5 iterations here. It can be observed in Figure 8.6(a) that the statistical uncertainty grows up to a factor of two for five iterations. In contrast, for two iterations, it increases by an acceptable factor of about 30 %.

Average global correlation between bins   As the IBU corrects migrations between bins, bin-by-bin correlations are introduced naturally. They are studied in the form of an *average global correlation coefficient* (AGCC) test [170]. A statistical covariance matrix $V_{i,j}$ encoding the correlations between bins, is built by unfolding the distributions of 1000 Poisson-distributed toy experiments per observable[3]. The average ρ_{avg} is taken as a measure for the global correlation

$$\rho_{\mathrm{avg}} = \frac{1}{N_{\mathrm{bins}}} \sum_{j=1}^{N_{\mathrm{bins}}} \rho_j \quad \text{with} \quad \rho_j = \sqrt{1 - \left(V_{jj} \cdot V_{jj}^{-1} \right)^{-1}} \tag{8.10}$$

where V_{jj} and V_{jj}^{-1} are the diagonal elements of the covariance matrix and of the inverse of the covariance matrix, respectively. The ρ_{avg} is expected to evolve with the number of iterations. A small number is identified with positive correlations, while in the limit of many iterations negative correlations occur [170]. As a consequence, a minimum is expected for a certain number of iterations, providing a powerful criterion for optimal regularization. For this measurement, the minimal ρ_{avg} is obtained at two iterations in the majority of the eight investigated cases, i.e. $(1\mathrm{D}, 2\mathrm{D}) \otimes (e^+, e^-, \mu^+, \mu^-)$ [77], see Figure 8.6(b) as an example using the double-differential $W^+ \to \mu^+\nu$ measurement.

---

[3]The covariance matrix is defined as $V_{i,j} = \frac{1}{N_{\mathrm{toys}}} \sum_{\mathrm{toy}=1}^{N_{\mathrm{toys}}} (h_i^{\mathrm{nom}} - h_j^{\mathrm{toy}})^2$, see also Sec. 8.4.

(a)

(b)

(c)

(d)
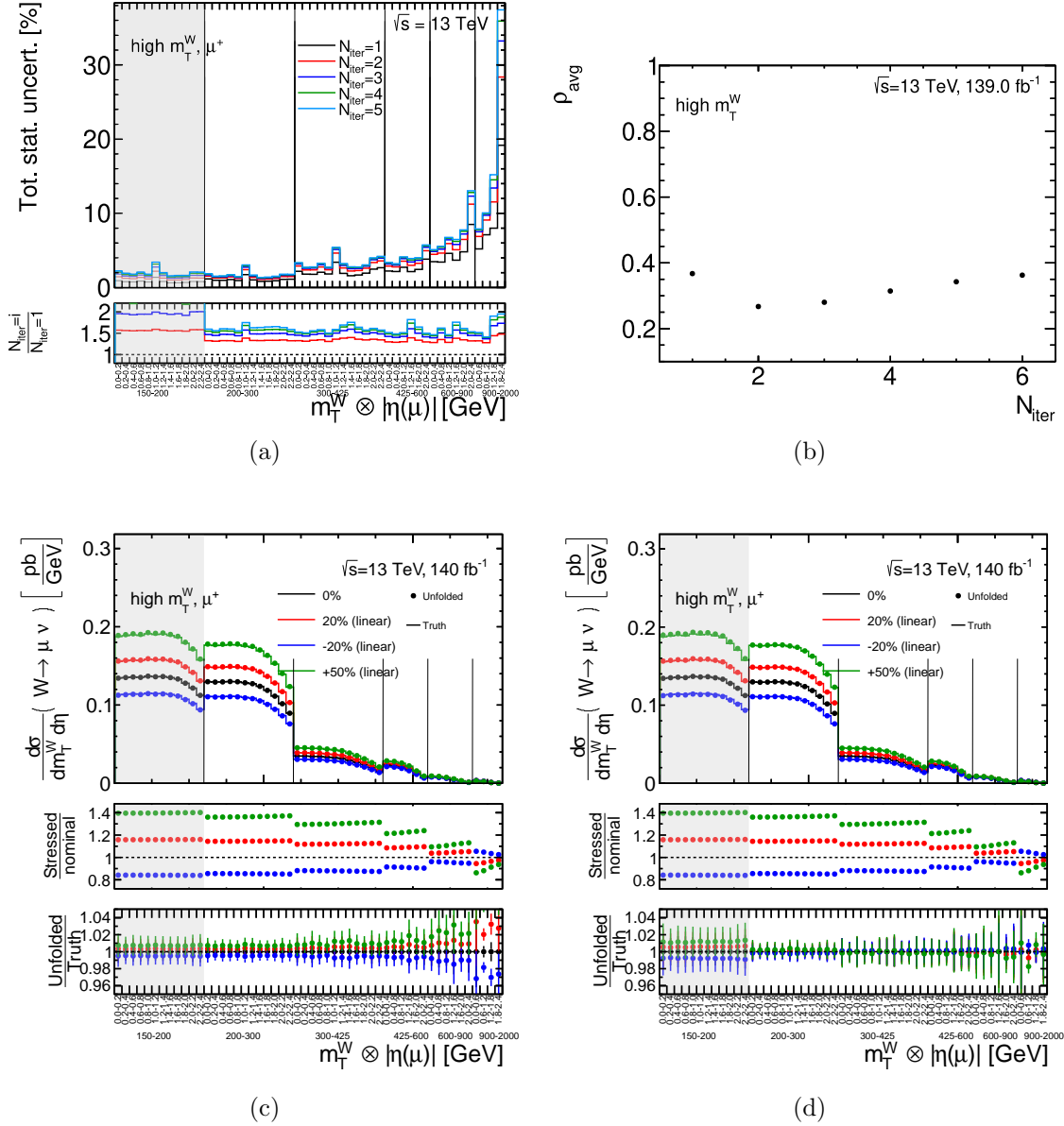
Figure 8.6.: Tests performed to obtain the optimal number of iterations. All are shown for the double-differential measurement in $m_T^W \otimes |\eta(\mu)|$ for the positive muon charge. (a) Evolution of the data statistical uncertainty with the number of iterations. (b) Average global correlation ρ_{avg} as a function of the number of iterations. (c)/(d) Stress test, where the signal MC distribution is reweighted by a linear function and then unfolded using the nominal corrections, for (c) $N_{iter} = 1$ and (d) $N_{iter} = 2$.

Stress test   The *stress test* is designed to investigate the sensitivity to different modeling between the distribution to unfold and the response matrix. It is based solely on the signal $W \to \mu\nu$ MC sample. The signal MC distribution at reconstruction level replaces measured data as unfolding input here. However, at first, the input distribution is

reweighted using different linear functions, with a maximal reweighting of 50 %, see the middle ratio in Figures 8.6(c)/8.6(d).

The stress test is performed for 1-5 iterations in the IBU, while one iteration is shown in Figure 8.6(c), two iterations in Figure 8.6(d) and more iterations in Appendix E.5. The lower ratio shows the difference between the unfolded and reweighted MC-truth distributions. While a non-closure in the order of 1 % (increasing with $m_{\mathrm{T}}^{\mathrm{W}}$) is present for one iteration, the unfolding procedure is able to recover this extreme[4] reweighting already very well at two iterations. A non-closure below 0.5 % is obtained in most of the bins for $m_{\mathrm{T}}^{\mathrm{W}} > 200\,\mathrm{GeV}$.

8.3. Tests of the unfolding procedure

The unfolding procedure is tested thoroughly in order to ensure that the setup is working correctly, provides a stable unfolding and does not bias the results. The tests described in Section 8.3.2 and Section 8.3.3 will provide an estimate for systematic uncertainties on the unfolding procedure.

8.3.1. Technical closure test

A *technical closure test* is employed in order to validate the technical implementation and consistent definitions in the unfolding machinery. The basis is the signal simulation which provides the unfolding corrections (R_{ij}^{-1}, f_{in}^{i} and ϵ_{j} in Equation 8.5) per default. Additionally, in this test, the reconstructed predicted distribution is used as the unfolding input instead of the measured, background-subtracted data. Per construction, the unfolded distribution is required to be identical to the one from the underlying MC truth level.

The reconstructed, true and unfolded distributions in the closure test are shown in Figure 8.7, for the single- and double-differential measurement, as an example for the negative muon charge. The successful closure tests for μ^{+} can be found in Figure E.17. The MC statistical uncertainty is included[5]. Indeed, the expected closure is observed, as the ratio between the unfolded and the MC truth-level distributions is exactly at unity in each bin. It shall be underlined that the closure is confirmed to higher precision than visible in Figure 8.7 by comparing the exact numbers, in addition.

---

[4]Observed differences between data and prediction are smaller than the reweighting here, see Chapter 7.

[5]The structures visible in the statistical uncertainty here are associated with the worse statistics in the peak sample, as discussed in Section 8.2.3.
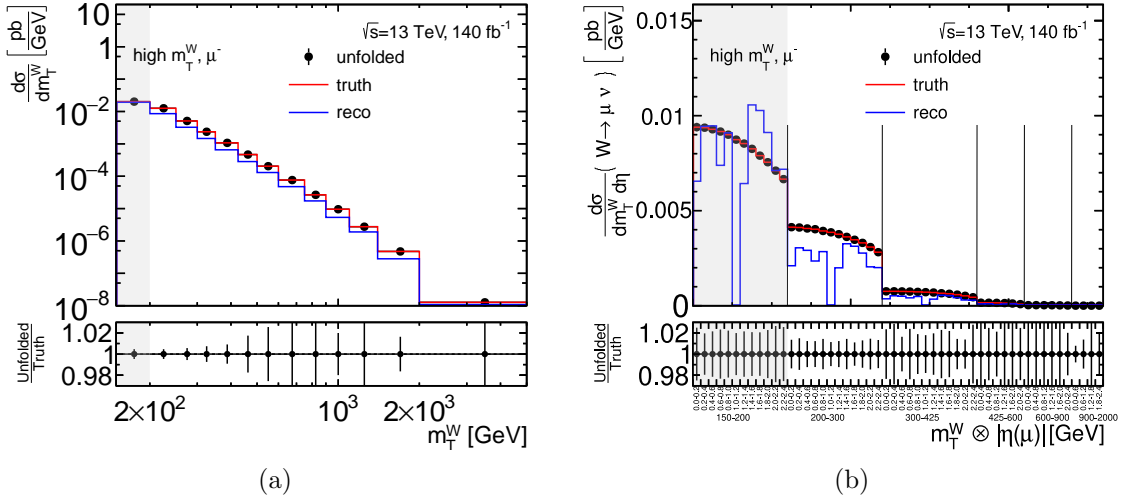
Figure 8.7.: Reconstructed, truth and unfolded distributions for (a) m_T^W and (b) $m_T^W \otimes |\eta(\mu)|$ in the technical closure test, where the predicted distribution is taken as the input of the unfolding. The μ^--channel is shown here. In (b), the truth-level $m_T^W \otimes |\eta(\mu)|$ binning labels are shown but the reconstruction-level distribution is subject to a different binning (see Section 5.3).

8.3.2. Data-driven closure test

In general, the description of physics kinematics in the signal simulation may differ from the data. Thus, it needs to be ensured that the bias induced by the given simulation is kept small. The *data-driven closure test* (DDCT) is designed to probe the sensitivity of the unfolding procedure to shape differences between data and prediction in the measurement observables. The idea is to reweight the predicted distribution to the one in data in the measurement observables, and unfold the reweighted distribution using the nominal unfolding corrections. The exact procedure is the following:

1. The predicted $W \to \mu\nu$ distribution is reweighted in m_T^W or $m_T^W \otimes |\eta(\mu)|$, respectively, at truth level with a smooth function such that the reconstruction-level distribution of this variable matches the data distribution.

2. The reweighted distribution is unfolded using the nominal response matrix.

3. The difference between the unfolded distribution and the reweighted truth-level predicted distribution is identified as the *basic unfolding uncertainty*.

Generally, the procedure is similar to the stress test described in Section 8.2.5. However, the linear reweighting function is replaced by the MC-data difference which, in principle, can take on any arbitrary shape. Additionally, the reweighting procedure described in the first bullet point above requires the usage of *truth-reco matched* events that pass

both, the reconstruction-level and the truth-level selections (see Chapter 5). Particularly, this implies that the in-smearing and efficiency corrections (see Section 8.2.3) are artificially set to unity here, which is a noteworthy difference to the nominal unfolding procedure. Any potential bias in the modeling of in-smearing will not be probed here.

At first, a smooth function encapsulating shape differences between data and predicted distributions needs to be found. The basis is the ratio $(N_{\text{data}}^i - N_{\text{bkg}}^i)/N_{\text{signal}}^i$ per bin i in the reconstructed distributions, as shown in Figure 8.8 for the single-differential observable m_{T}^{W}. These ratios differ from the ones shown in Figure 7.4, as the selection is limited to truth-reco-matched events here. Nevertheless, they exhibit similar features, for instance the opposite trends per muon charge at high m_{T}^{W}. As the DDCT is designed to probe overall shape differences and no statistical fluctuations, a smoothing is applied to the distribution. Finally, a spline fit $f(x_{\text{reco}})$ interpolates the data points. This smooth function is the basis for a truth-level event weight, $w = f(x_{\text{truth}})$, to be applied to the signal prediction. For the double-differential measurement, separate reweighting functions, i.e. separate spline fits across $|\eta(\mu)|$ distributions, are determined per m_{T}^{W} bin, see Figure E.18 (μ^+) and Figure E.19 (μ^-).

Finally, Figure 8.9 shows the unfolded and truth distributions in the DDCT for the single- and double-differential measurement and both muon charges, respectively. In the middle panel, the truth-level reweighting function is illustrated and, in the lower panel, the difference between the unfolded and reweighted MC-truth distributions. A notable difference of up to 30 % between nominal and reweighted predicted distributions can be recovered successfully to a non-closure well below 1% in the vast majority of bins. In the double-differential distributions, the non-closure extends up to 0.5 % in the shadow bin and, for $m_{\text{T}}^{\text{W}} > 600\,\text{GeV}$, some fluctuations are present. Nevertheless, also in 2D, the unfolding procure shows a very good performance and the bias induced by the signal

(a)   (b)
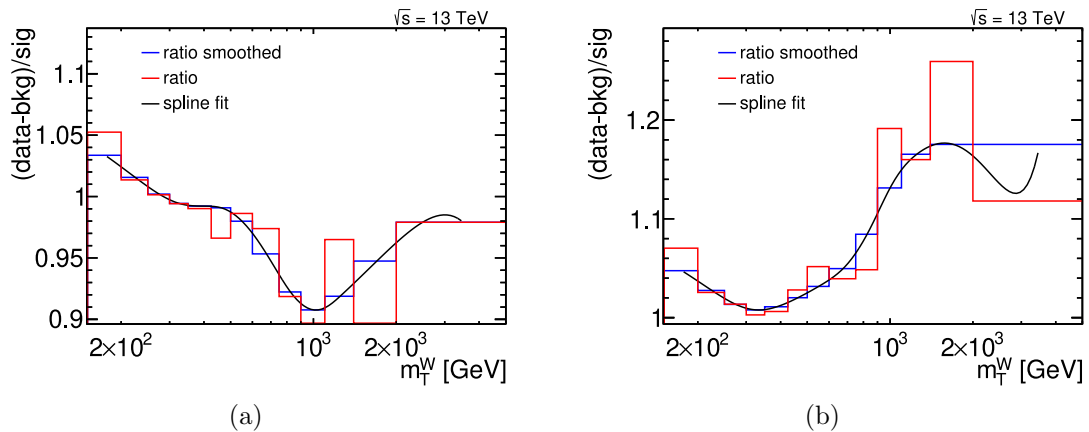
Figure 8.8.: Ratio between the background-subtracted data distribution and the predicted signal distribution on reconstruction level in the single-differential measurement binning in m_{T}^{W} in the (a) μ^+-channel and (b) μ^--channel.

prediction is small. The non-closure in the lower ratio panel will be taken as the basic unfolding uncertainty.

As a final remark, it shall be highlighted that the distributions shown in Figure 8.9 are obtained using two iterations in the IBU. Different numbers of iterations were tested, see Figures E.20-E.23, and the DDCT confirms the optimal performance at two iterations.
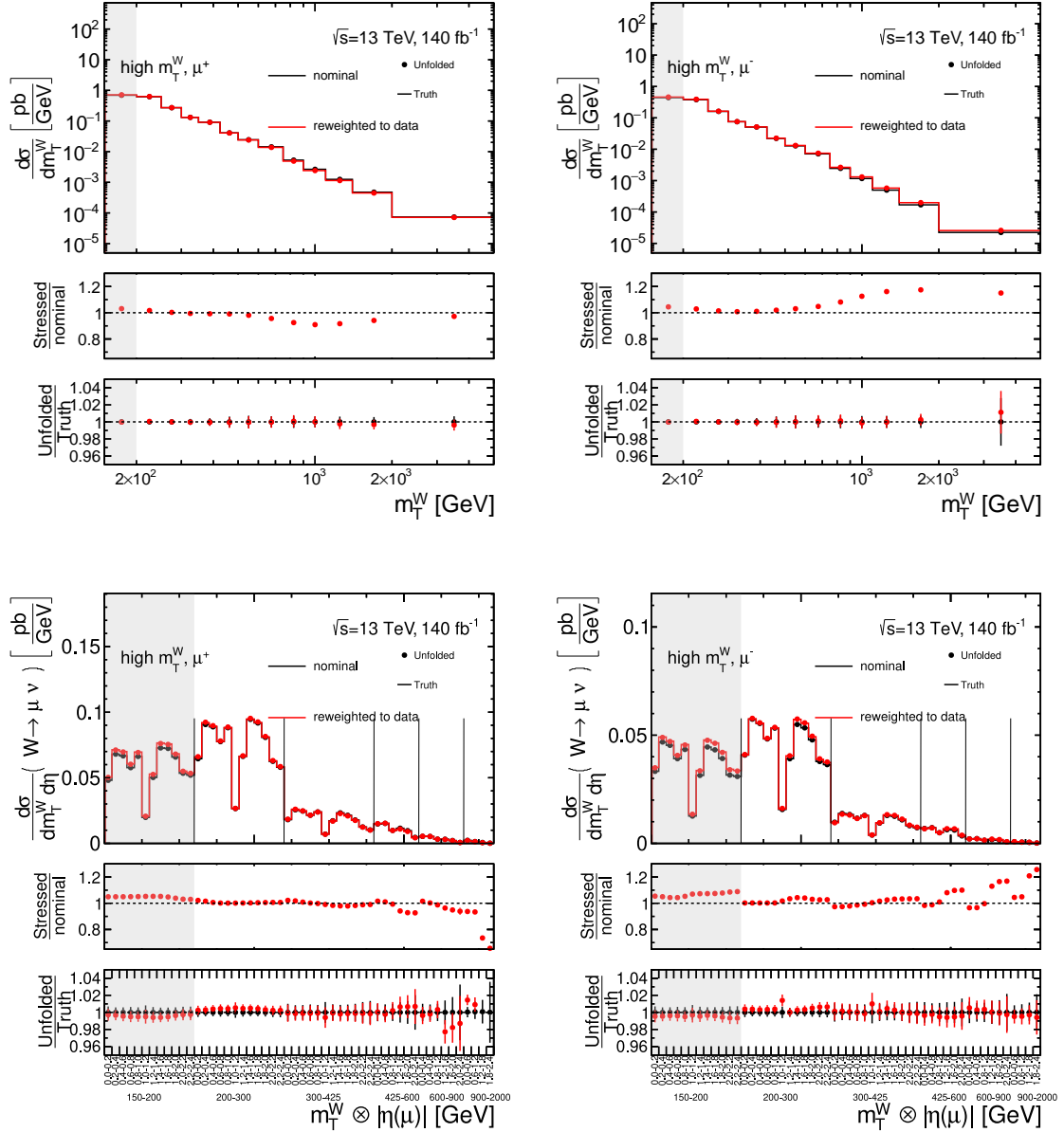
Figure 8.9.: Unfolded and MC-truth-level distributions obtained in the data-driven closure test, where the signal predicted distribution is matched to data in the measurement variables and then unfolded using the nominal response matrix. They are shown for the single- and double-differential observables in the μ^+- and μ^--channel using two iterations in the IBU.

8.3.3. Unfolding of alternative signal prediction

The data-driven closure test described in Section 8.3.2 does not cover the full sensitivity of the unfolding procedure to the modeling of the signal process. On the one hand, only events passing all reconstruction-level and truth-level requirements are considered, thus, any potential bias in the in-smearing cannot be probed explicitly. On the other hand, a residual difference can be introduced via *hidden variables*. Both aspects are closely related and tested in a second complementary test. It is based solely on MC simulations and utilizes, next to the nominal $W \to \mu\nu$ sample (Powheg+Pythia)[6], an alternative sample (Sherpa, see Section 3.3). The following procedure is employed:

1. The respective truth-level m_T^W or $m_\mathrm{T}^\mathrm{W} \otimes |\eta(\mu)|$ distribution predicted by the alternative sample is reweighted to match the nominal one.

2. The reweighted reconstruction-level distribution of the alternative sample is unfolded using the nominal response matrix and correction factors.

3. The non-closure between the unfolded distribution and the reweighted MC-truth-level distribution is taken as an additional unfolding uncertainty.

The reweighting described in the first bullet point is done to avoid double-counting with the data driven closure test. Various distributions are compared for the two $W \to \mu\nu$ predictions on truth and reconstruction level, see Appendix E.7. The reweighting mentioned in the first bullet point is based on a truth-level transverse-mass (or $m_\mathrm{T}^\mathrm{W} \otimes |\eta(\mu)|$) distribution covering $m_\mathrm{T}^\mathrm{W} \in [10, 5000]\,\mathrm{GeV}$ without any further requirements (see Figure E.24). After the reweighting, the truth-level m_T^W and $m_\mathrm{T}^\mathrm{W} \otimes |\eta(\mu)|$ distributions match exactly between the two $W \to \mu\nu$ samples (see Figures E.25/E.26). Nevertheless, residual differences between the distributions on reconstruction level can be observed, as shown for the single-differential μ^+-channel in Figure 8.10(a). The Sherpa sample predicts $\sim 5\,\%$ more events in the shadow bin and $\sim 1\,\%$ more events in the first measurement bin. The distributions for the negative charge as well as the double-differential measurements show analogous features (see Figures E.25/E.26).

This reconstruction-level difference is attributed to a difference in the distributions of the truth-level p_T of the W boson, as illustrated in Figure 8.10(b). The majority of events are generated with $p_\mathrm{T}(W) \approx 0\,\mathrm{GeV}$, where the numbers of events agree very well. However, their difference increases with the W boson's transverse momentum and reaches a maximum of $\sim 10\,\%$ at $p_\mathrm{T}(W) \approx 200\,\mathrm{GeV}$. A large momentum of the W boson can produce artificially a high reconstructed m_T^W, instead of a high generated m_T^W. In particular, events that are in-smearing from the W-boson resonance to the reconstructed high-mass region are likely to have a W boson with a large transverse momentum. As the contribution of in-smearing events is by far the largest in the shadow bin (see Figure 8.5(a)), the difference observed in Figure 8.10(a) is most prominent in this bin.

---

[6]For this test, the PDFs of the two MC samples are matched, i.e. the Powheg+Pythia MC is reweighted to NNPDF3.0 using a mass-dependent k-factor.
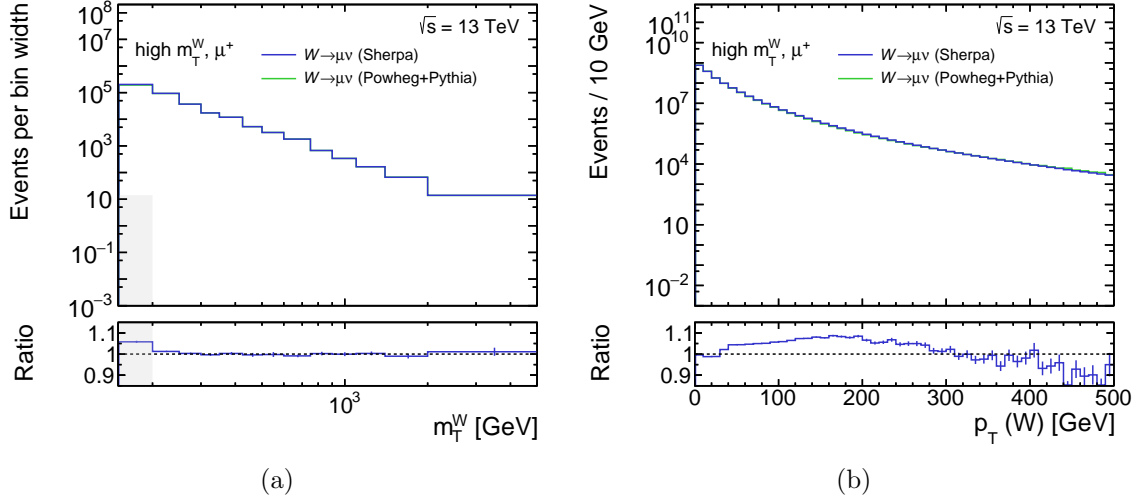
Figure 8.10.: Distributions predicted by the SHERPA and POWHEG+PYTHIA samples as a function of the (a) reconstruction-level transverse mass and (b) truth-level transverse momentum of the W boson for μ^+. The number of events predicted by SHERPA is reweighted to match the truth-level m_T^W distribution from POWHEG+PYTHIA.

The reweighted reconstruction-level SHERPA distributions are unfolded using the nominal unfolding corrections obtained with the POWHEG+PYTHIA sample. The reconstructed, true and unfolded distributions are shown in Figure 8.11 for all four measurement observables. The difference in modeling between the unfolding input (SHERPA) and the unfolding corrections (POWHEG+PYTHIA) transfers directly to a difference between the unfolded and predicted truth-level distributions here. In the shadow bin, it extends up to $10\,\%$ which underlines the importance of minimizing the in-smearing contribution in this measurement. Nevertheless, for $m_\mathrm{T}^\mathrm{W} > 200\,\mathrm{GeV}$, the non-closure is at a sensible level of $1 - 2\,\%$ at maximum. The ratios shown in Figure 8.11 exhibit partly substantial statistical fluctuations. Hence, a smoothing of the relative non-closure is applied before it is used as a systematic uncertainty on the unfolding procedure (see Figure E.28).

One last aspect shall be discussed in the context of scanning the sensitivity to hidden variables. In the test presented, the reweighting is performed such that the truth-level m_T^W and $m_\mathrm{T}^\mathrm{W} \otimes |\eta(\mu)|$ distributions match and any residual difference is incorporated in hidden variables. An alternative approach is reweighting explicitly in the hidden variable, resulting in a residual difference in the measurement observables. This approach was tested by matching the SHERPA and POWHEG+PYTHIA $p_\mathrm{T}(W)$ distributions, while the residual steps of the unfolding procedure here remain unchanged. The non-closure observed in this alternative test demonstrates an extremely similar shape and magnitude (see Figure E.27). This underlines that the hidden variable driving the non-closure here is, in fact, the p_T of the W boson.
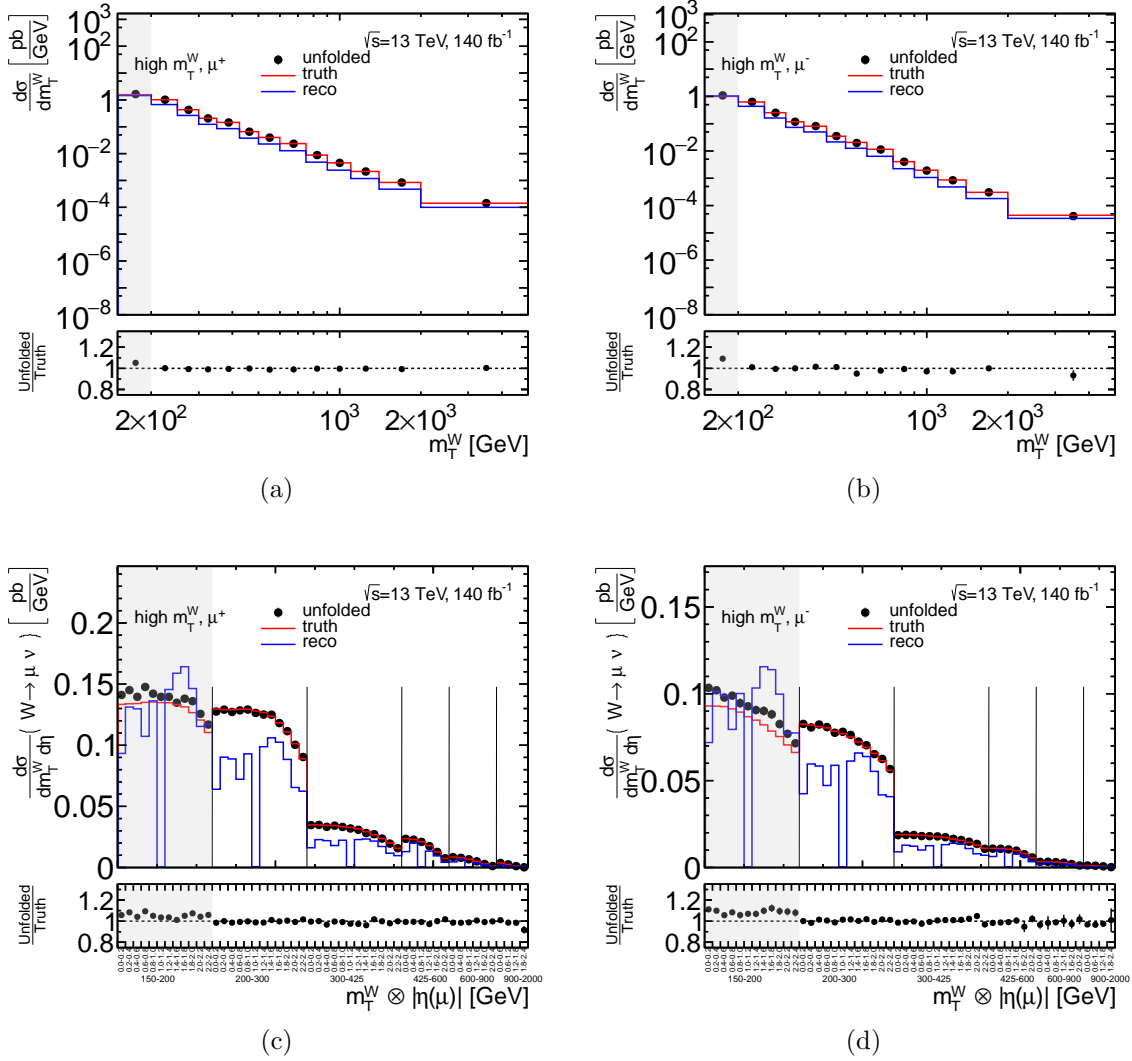
Figure 8.11.: Reconstructed, truth and unfolded distributions in the unfolding test using an alternative signal sample. The prediction of the alternative sample is reweighted to match the truth-level m_T^W and $m_T^W \otimes |\eta(\mu)|$ distributions of the nominal sample and then unfolded using the unfolding corrections of the nominal sample. The distributions are shown for the single- and double-differential observables in the μ^+- and μ^--channel using two iterations in the IBU.

8.4. Procedure of unfolding uncertainties

Any measurement is subject to statistical and systematic uncertainties. A challenge in the setup of the unfolding machinery is propagating them correctly in order to provide uncertainties on the unfolded cross-sections. The technical procedures are explained in this Section, separately for the statistical uncertainty in data, background and signal prediction as well as experimental, background-only and signal theory systematic uncertainties.

Data statistical uncertainty Being a counting experiment, data events are Poisson-distributed and the uncertainty is given by the square root of the number of events $\sqrt{N}$. In order to propagate this uncertainty to the unfolded level, a set of *toy experiments* is obtained by varying the nominal number of events reconstructed in bin i, $N_i^{\text{nom,data}}$, according to a Poisson distribution $\mathcal{P}$,

$$N_i^{\text{toy,data}} = \mathcal{P}(N_i^{\text{nom,data}}).$$
(8.11)

The alternative data yield $N_i^{\text{toy,data}}$ is unfolded via Equation 8.5 using the nominal background subtraction and unfolding corrections. The step is repeated $N_{\text{toys}} = 5000$ times, which is a reasonable compromise between minimized fluctuations and computing efforts. Finally, the unfolded data statistical uncertainty $\Delta N_j^{\text{stat,unf}}$ is given by the standard deviation of the difference between the unfolded toy result h_j^{toy} and the nominal h_j^{nom} per truth-level bin j,

$$\Delta N_j^{\text{stat,unf}} = \frac{1}{N_{\text{toys}}} \sqrt{\sum_{\text{toy}=1}^{N_{\text{toys}}} (h_j^{\text{nom}} - h_j^{\text{toy}})^2}.$$
(8.12)

Background statistical uncertainty Toy experiments are also the basis of unfolding the statistical uncertainty of the number of background events. The number of subtracted background events in Equation 8.5 is varied while the number of data events and unfolding corrections remain unchanged. However, since weighted events are used, the statistical uncertainty is given by $(\Delta N_i)^2 = \sum_{i=1}^{N_{\text{events}}} w_i^2$ where w_i are the respective weights. Toy experiments are built by varying the nominal background $N_i^{\text{nom,bkg}}$ within the given statistical uncertainty ΔN_i^{bkg} in reconstructed bin i according to

$$N_i^{\text{toy,bkg}} = N_i^{\text{nom,bkg}} \cdot (1 + \mathcal{G}(0,1)_i^{\text{toy}} \Delta N_i^{\text{bkg}})$$
(8.13)

where $\mathcal{G}(0,1)_i^{\text{toy}}$ are random numbers according to a Gaussian with zero mean and unity width. The unfolding procedure is performed using $N_{\text{toys}} = 5000$ background predictions $N_i^{\text{toy,bkg}}$. The standard deviation of the unfolded results, according to Equation 8.12, is taken as the background statistical uncertainty on the unfolded cross-section.

Signal MC statistical uncertainty As the statistical uncertainty of the signal sample enters via the unfolding corrections, it affects both, the truth and reconstructed level. The statistical uncertainty is highly correlated between the two levels since the number of generated events directly impacts the number of reconstructed events, nevertheless potentially located in different bins. The *bootstrap method* is employed, implemented via the tool described in Reference [171]. The idea is to create multiple self-consistent sets of MC simulations. They are constructed by randomly selecting events from the nominal MC sample, while each event is weighted by an additional event weight given by a Poisson with a mean of one. Thus, most events of the nominal signal sample are

selected once or not at all, however some are counted twice or more. The selection is repeated 5000 times obtaining 5000 different MC samples, so-called *bootstraps*. By varying on event level instead of histogram level, as done for data and background, correlations between levels and variables are considered.

Finally, the unfolding procedure, including nominal data and background events, is performed 5000 times using the different unfolding corrections from the bootstrap MC samples. Again, Equation 8.12 provides a measure for the signal MC statistical uncertainty on the unfolded level.

Experimental systematic uncertainties   Uncertainties introduced by the measurement apparatus, e.g. associated with the muon resolution, are summarized as experimental systematic uncertainties and are usually parametrized as alternative MC predictions. These kinds of uncertainties affect the measurement of signal and background events equally and, thus, an unfolding procedure correlated between processes is necessary. In this dissertation, the experimental uncertainties on the signal prediction and the largest background, $t\bar{t}$, are unfolded in a correlated way[7].

Two methods are commonly employed to unfold experimental systematic uncertainties, both offering a correlation between signal and background distributions. They are illustrated in the following equations, for the sake of readability in the simple picture of bin-by-bin unfolding:

$$\text{Method 1:} \quad \sigma = \frac{N_{\text{data}} - \boxed{N_{\text{bkg}}}}{\frac{\boxed{N_{\text{reco}}^{\text{signal MC}}}}{N_{\text{truth}}^{\text{signal MC}}} \cdot \mathcal{L}_{\text{int}}}, \qquad \text{Method 2:} \quad \sigma = \frac{\overbrace{\boxed{N_{\text{Asimov}}}}^{N_{\text{signal MC}} + N_{\text{bkg}}} - N_{\text{bkg}}}{\frac{N_{\text{reco}}^{\text{signal MC}}}{N_{\text{truth}}^{\text{signal MC}}} \cdot \mathcal{L}_{\text{int}}}. \quad (8.14)$$

Nevertheless, the treatment of systematic uncertainties in IBU (see Equation 8.5) is analogous. For both methods, the corresponding terms input to the unfolding procedure to be replaced by a systematically varied prediction are indicated by colored rounded boxes. In the first method, the numbers of background and the reconstruction-level signal events are varied straightforwardly in the same direction. It is worth highlighting that the number of truth-level events is not affected by experimental detector uncertainties. In the second method, an Asimov dataset is built, replacing data as unfolding input. It contains signal and background predictions, to be varied in a correlated way. Here, the number of subtracted background events and the unfolding corrections remain the nominal ones. In general, both methods are expected to yield the same results, except for approximately a change of sign to be corrected a posteriori in the second method. It is caused by the transfer from a systematic uncertainty defined on MC to an uncertainty defined on data (see also the schematic in Figure E.29). In this dissertation, the second method is used for technical reasons. The relative systematic uncertainty is given by the relative difference to the nominal unfolded cross-section.

---

[7]Experimental uncertainties on smaller backgrounds are not considered explicitly, since, for instance, a 1 % uncertainty on a 1 % background would have a negligible sub-permille-level impact.

Background-only systematic uncertainties   The unfolding of systematic uncertainties affecting only background processes, for instance, the data-driven multijet uncertainties defined in Section 6.5, is straightforward. The number of subtracted background events in Equation 8.14 in the simple bin-by-bin picture (or Equation 8.5 for IBU) is replaced by the systematic variation. This way, a larger background yield correctly provokes a smaller cross-section and vice versa.

Signal theory uncertainties   Signal theory uncertainties, e.g. PDF variations, differ from the experimental uncertainties discussed above as they affect both, the reconstruction and truth level of the signal simulation. Their impact on the unfolded cross-sections can be quantified by unfolding data using correction factors (R_{ij}, f_{in}^i and ϵ_j in Equation 8.5) obtained with the systematically varied simulation.

9. Measurement uncertainties

The measurement of any physical quantity is subject to two kinds of uncertainties: *statistical* and *systematic*. While the former can be reduced by repeating the measurement, this cannot be achieved for the latter. Each measurement would yield the same systematic bias caused by the detector calibration or presumptions in the underlying theoretical models, for instance. This Chapter provides an overview of all uncertainties considered. The statistical uncertainties are discussed in Section 9.1 and the systematic uncertainties in Section 9.3 and Section 9.4. They can be categorized into three groups:

- *Experimental* uncertainties due to the measurement of physical objects in the detector,
- *theoretical* uncertainties accounting for the MC modeling,
- uncertainties on the *methods* used, here the multijet estimation via the Matrix Method (see Section 6.5) and the unfolding via IBU (see Section 8.3).

Experimental and theoretical systematic uncertainties are evaluated by varying the number of events predicted by the $W \to \mu\nu$ and $t\bar{t}$ samples. Before the unfolding according to the prescriptions in Section 8.4, a pre-processing is applied to all systematic uncertainties as detailed in Section 9.2. A complete overview of the relative impacts on the single- and double-differential cross-sections for all relevant systematic uncertainties is presented in Figure 9.2 and Figure 9.3, for the single- and double-differential distributions, respectively. They are shown as an example for μ^- here, see Appendix F.3 for μ^+. Additionally, the direct variations of the numbers of predicted events before the unfolding can be found in Appendix F.2. In Section 9.5, a summary of all uncertainties is given for both charges explicitly.

9.1. Statistical uncertainty

Data, background and signal statistical uncertainties are unfolded separately according to the recipes described in Section 8.4. Their relative impacts on the single- and double-differential W^- cross-sections are shown in Figure 9.1. The data statistical uncertainty increases monotonously with the transverse mass and ranges between $\sim 0.5\,\%$ and $\sim 55\,\%$ here. The background statistical uncertainty is in comparison negligible in all bins, even though, in the last 1D m_T^W bin, it is increased due to a larger multijet contribution. The signal statistical uncertainty is at a similar size but mostly smaller than the one in data

(a)   (b)
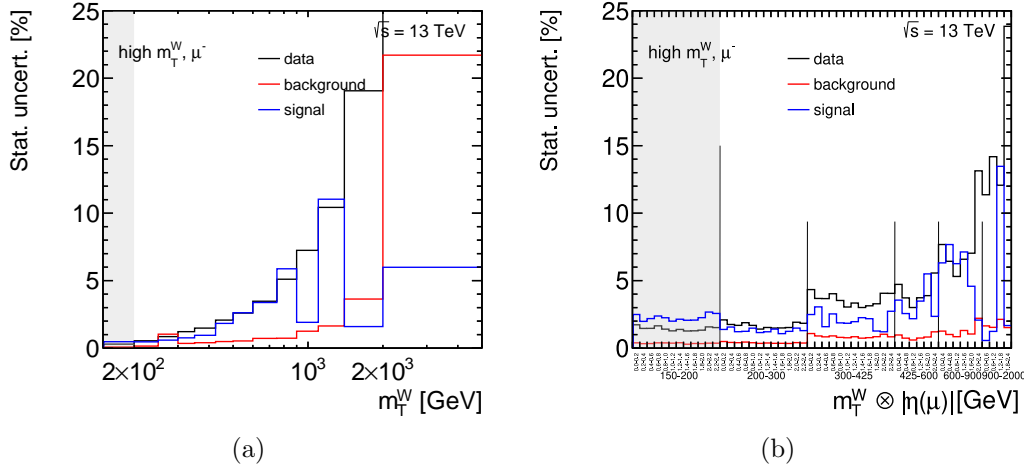
Figure 9.1.: Statistical uncertainty on the (a) single- and (b) double-differential $W^- \to \mu^- \bar{\nu}$ cross-section, separated in data, signal prediction and background prediction. The data statistical uncertainty in the last bin of the m_T^W distribution is 56 %.

because statistic-enhanced high-mass samples are used (see Section 3.3). Nevertheless, in the shadow bin, the relative statistical uncertainty in the signal is increased due to a substantial contribution of in-smearing events from the inclusive sample. In both, the single- and double-differential spectra, bin-by-bin fluctuations of the relative signal statistical uncertainty are striking. The bin-wise increased uncertainties are caused by a few events generated in the peak sample that migrate to a reconstructed m_T^W above a few hundred GeV (see also Section 8.2.3).

9.2. Pre-processing of systematic uncertainties

A set of pre-processing steps are applied to the varied $W \to \mu\nu$ and $t\bar{t}$ distributions before using them in the unfolding procedure. In general, systematic uncertainties may exhibit an unwanted statistical component. Any artificial fluctuations are minimized by applying the `ROOT` *smoothing algorithm* to all systematic uncertainties [172, 173]. Nevertheless, the worse statistical precision of the peak sample of the $W \to \mu\nu$ sample was found to induce major fluctuations (see Figure F.17). Hence, all predicted signal events with $m_\mathrm{inv}(\mathrm{truth}) < 120\,\mathrm{GeV}$ and $m_\mathrm{T}^\mathrm{W}(\mathrm{reco}) > 600\,\mathrm{GeV}$ are explicitly excluded in the estimation of all systematic uncertainties. Furthermore, the statistical significance of the $t\bar{t}$ sample is limited in the high-m_T^W tail, thus, all bins with $m_\mathrm{T}^\mathrm{W} > 600\,\mathrm{GeV}$ are merged in the evaluation of $t\bar{t}$ theory uncertainties. In general, systematic uncertainties can be defined *one-sided* or *two-sided*. For the former, only one variation with respect to the nominal is given. In contrast, the latter are characterized by an *up-variation* and a *down-variation*. If they are not explicitly known to be asymmetric, all two-sided uncertainties are *symmetrized* according to $\Delta_\mathrm{up}^\mathrm{sym} = -\Delta_\mathrm{down}^\mathrm{sym} = \frac{1}{2}(|\Delta_\mathrm{up}| + |\Delta_\mathrm{down}|)$.

Overall, systematic uncertainties are parametrized in about seventy different sources here of which many have a negligible impact on the total uncertainty. Therefore, only the relevant uncertainties are propagated by selecting the ones with a relative contribution of at least 0.5% in at least one bin of all considered observables[1]. In the following, all sources of uncertainty will be discussed but any uncertainty not shown explicitly does not pass this requirement and is assumed negligible.

9.3. Experimental systematic uncertainties

Experimental systematic uncertainties are introduced by the measurement procedure in the detector. All calibrations of the measurements of muons, jets and $E_{\mathrm{T}}^{\mathrm{miss}}$, as presented in Chapter 4, are subject to dedicated systematic uncertainties.

9.3.1. Muon uncertainties

Two kinds of uncertainties are defined in the measurement of the muon, related to efficiency and reconstruction, respectively. As discussed in Section 4.2.6, the difference in selection efficiency in data and prediction is assessed via SFs measured in di-muon events. Naturally, statistical and systematic uncertainties occur in these kinds of measurements. They are propagated to the analysis presented in the form of alternative SFs for each of the four components (identification, isolation, trigger, TTVA). One SF systematic uncertainty is associated with the veto of bad muons (see Section 5.1).
Secondly, the calibration of the muon momentum scale and resolution, as described in Section 4.2.4, is subject to systematic uncertainties. For the muon momentum scale, the transverse momentum of the muon is varied in the calibration, while, for the resolution, the track of the muon is smeared, separately for the ID and the MS.
Finally, uncertainties on the sagitta-bias corrections, as discussed in Section 4.2.5, are provided de-correlated into three components (`Global`, p_{T}-extra, `Resbias`). The first covers general global sagitta biases, not differentiating between η-regions. The second component was specially designed in cooperation with the measurement presented here, which encapsulates the extrapolation to the high-$p_{\mathrm{T}}(\mu)$ regime. It is defined solely for $|\eta(\mu)| > 1.1$, providing an effective de-correlation between barrel and end-caps. Lastly, any residual local biases as a function of η and ϕ are summarized in a third component which is, however, found negligible here.

The muon-specific systematic uncertainties on the unfolded cross-sections are shown in Figure 9.2(a) (1D) and Figure 9.3(a) (2D). Neglected muon-related uncertainties can be

---

[1]The selection is developed in cooperation with the parallel electron channel measurement, thus, in total eight observables are taken into account: $[\mathrm{1D}, \mathrm{2D}] \otimes [e^+, e^-, \mu^+, \mu^-]$.

found in Figure F.19. Overall, the muon uncertainties increase with m_T^W, ranging from $\sim 1\,\%$ to $\sim 20\,\%$ here. Given the increasing difficulty of measuring muons at very high momenta with almost straight trajectories, this shape is expected. For $m_\text{T}^\text{W} \gtrsim 600\,\text{GeV}$, the two uncertainties associated with the sagitta-bias correction are dominating. As it can be seen in Figure 9.3(a), the p_T-`extra` uncertainty acts only in the end-cap regions and is by far the largest systematic uncertainty at high m_T^W and high $|\eta(\mu)|$. For μ^+, the uncertainties are similar in shape and magnitude, see Figure F.9. However, the sagitta bias affects both charges in opposite directions, thus the up-(down-)variation has a different sign per muon charge. The given uncertainty covers the deviations between predicted and data distributions visible in Chapter 7 closely but not entirely.

9.3.2. Uncertainties on the E_T^miss soft-track term

The transverse mass is constructed from the transverse momenta and the difference in the azimuthal angle of the $W \to \mu\nu$ decay products where the neutrino is associated with the E_T^miss in an event. As explained in Section 4.5, the E_T^miss is defined at the negative vectorial sum of all reconstructed objects and an additional soft-track term. Systematic uncertainties on the hard objects are propagated directly through the calculation of the E_T^miss. Additionally, three systematic uncertainties dedicated to the soft-track term are defined. One two-sided uncertainty is associated with the scale, while two one-sided uncertainties cover the limited resolution [164]. The latter are defined by smearing the soft-term perpendicular and parallel to the mean p_T of the considered tracks.

The relative E_T^miss soft-track uncertainties on the cross-sections are shown in Figure 9.2(b) (1D) and Figure 9.3(b) (2D). They extend up to $\sim 1.5\,\%$ in the first bin of the m_T^W distribution and are the dominating uncertainties in this bin. With increasing m_T^W, their impact is negligible. For completeness, it should be noted that the E_T^miss uncertainties dominate in the shadow bin with about $4\,\%$ each (see Figure F.5).

9.3.3. Jet uncertainties

Jet uncertainties contribute to the measurement presented via the E_T^miss calculation. The detection and calibration of jets is an intricate multi-step procedure, as discussed in Section 4.4. Dedicated systematic uncertainties related to jet energy resolution (JER) and jet energy scale (JES) are provided. Simplified schemes with eight uncorrelated nuisance parameters (NPs) for JER and 29 NPs for JES are considered, parametrized as a function of the jet p_T and η [107]. JER uncertainties account for the limited resolution in the calorimeters and are derived from comparisons between observed and predicted distributions using dijet events. The JES uncertainties can be grouped into the following categories related to the different calibration steps:

- correction of the jet-p_T due to pile-up (4),

- biases in the jet η-intercalibration[2] (5),

- jet flavor response and composition (2),

- statistical precision (6), jet modeling (4), detector modeling (2) and more (4) in the in-situ calibrations,

- punch-through (1) and high-p_{T} (1) jets.

In brackets, the number of associated NPs is given. The relevant JES uncertainties on the unfolded cross-sections are shown in Figure 9.2(b) (1D) and Figure 9.3(b) (2D). Only six out of 29 NPs pass the 0.5% threshold of which three are associated with the pile-up, two with the jet flavor and one with the η-intercalibration. All neglected JES uncertainties are shown in Figures F.20/F.21 for completeness. In contrast, all eight JER uncertainties have a relative contribution above the threshold in at least one bin. They are shown in Figure 9.2(c) (1D) and Figure 9.3(c) (2D). Generally, the jet measurement induces small uncertainties on the cross-sections, with the largest extend of about 1.5% (`JER EffectiveNP 1`) in the first $m_{\mathrm{T}}^{\mathrm{W}}$ bin. The increase of the JER uncertainties in the last $m_{\mathrm{T}}^{\mathrm{W}}$ bin in Figure 9.2(c) is statistically driven, however, given the large statistical uncertainty not significant. Lastly, it should be noted jet uncertainties extend up to 4% in the shadow bin (see Figure F.5).

9.3.4. Multijet uncertainties

Uncertainties on the data-driven multijet estimate were defined in Section 6.5. They are given by alternating the definition of the QCD-enriched region or varying the real-muon estimate in this region. Their impact on the unfolded cross-sections is shown in Figure 9.2(d) (1D) and Figure 9.3(d) (2D). The total multijet uncertainty extends up to $\sim 2\%$ and is the largest at intermediate $m_{\mathrm{T}}^{\mathrm{W}}$ around 300 GeV.

Naturally, the impact of uncertainties on background processes is determined by two factors: the size of the systematic uncertainty on the background yield and the general relative contribution of the background process. The relative uncertainties on the multijet yield range between $20 - 40\%$ in the measurement distributions (see Figure F.8). For the μ^--channel, the multijet process contributes overall with about 2% while being relevant only for $m_{\mathrm{T}}^{\mathrm{W}} \lesssim 600$ GeV. Overall, the effects of $\mathcal{O}(1\%)$ observed here are sensible. It should be noted that the relative background contribution is generally smaller for μ^+ given the larger $W^+ \rightarrow \mu^+ \nu$ cross-section (see Section 7.1). Thus, all background-only uncertainties have a smaller relative impact in the μ^+-channel than in the μ^--channel.

---

[2]Well-calibrated jets in the central region, $\eta(j) < 0.8$, are used for the calibration of forward jets with $\eta(j) > 0.8$.

(a) Muon

(b) E_T^{miss} and JES

(c) JER

(d) Multijet

(e) $t\bar{t}$ theory & tW DR

(f) Rate on small backgrounds
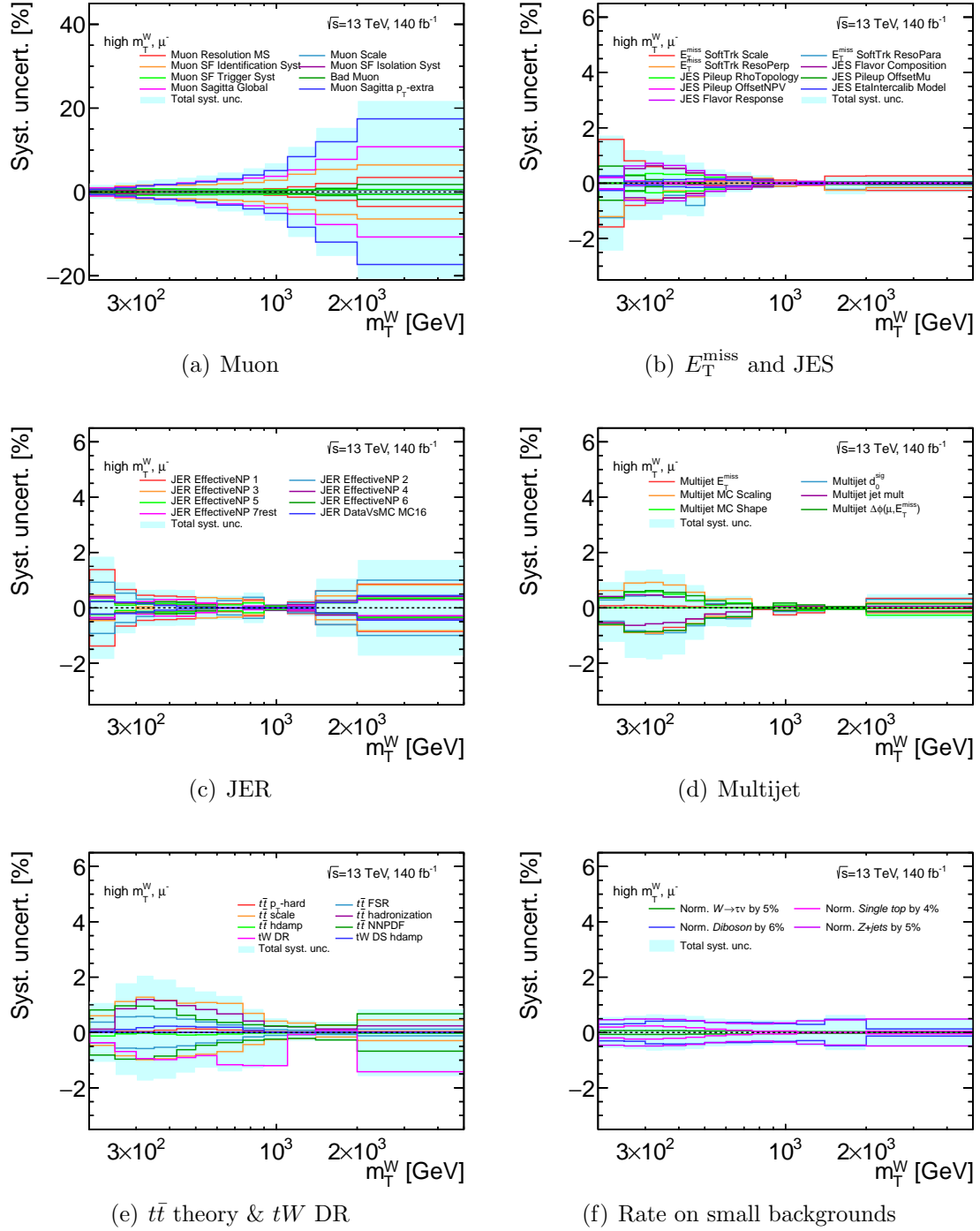
Figure 9.2.: Overview of relative systematic uncertainties on the single-differential cross-sections in m_T^W, for a negatively charged muon. The light-blue band represents the quadratic sum of all uncertainties shown in a plot.

(a) Muon

(b) E_T^{miss} and JES

(c) JER

(d) Multijet

(e) $t\bar{t}$ theory & tW DR

(f) Rate on small backgrounds
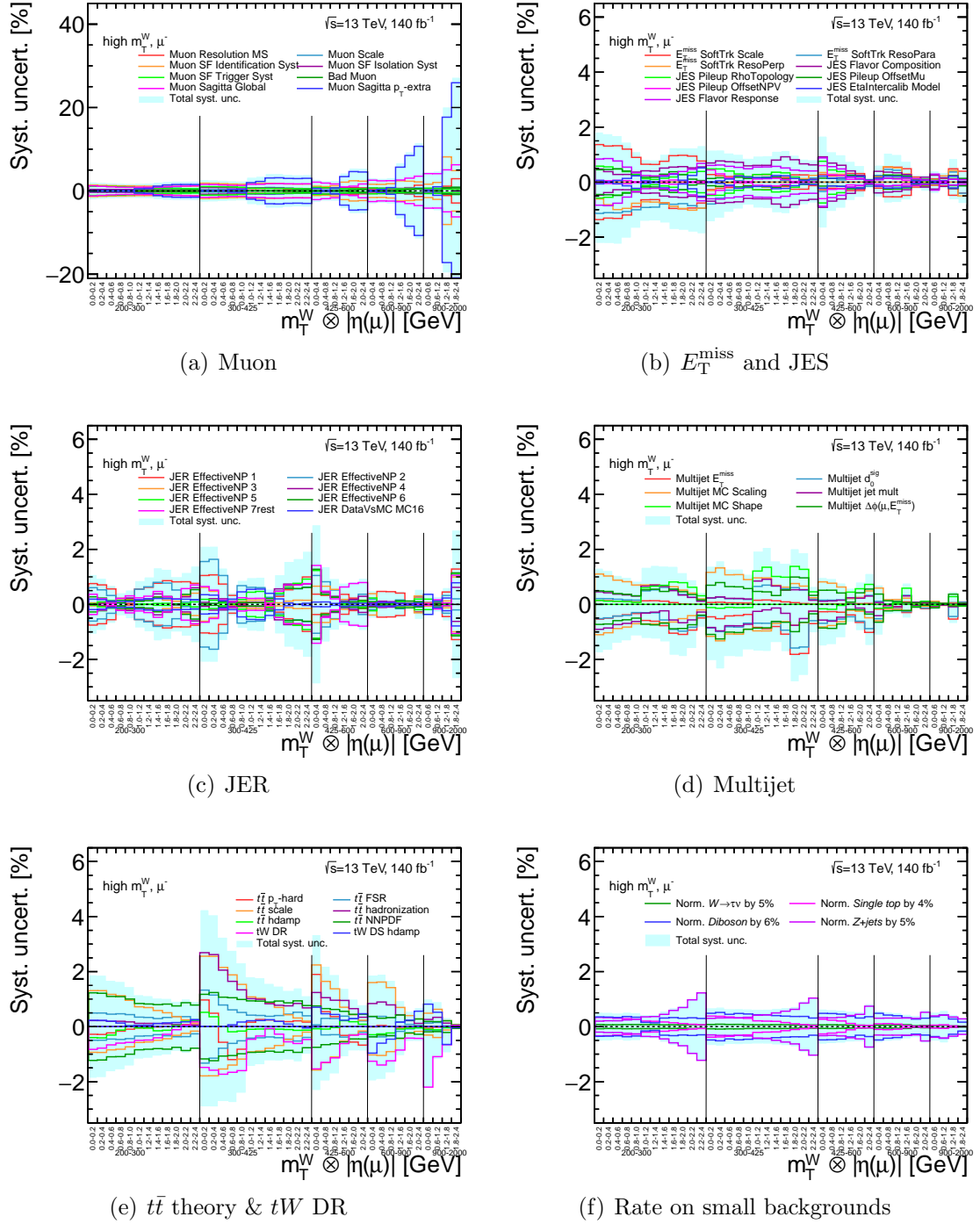
Figure 9.3.: Overview of relative systematic uncertainties on the double-differential cross-sections in $m_T^W \otimes |\eta(\mu)|$, for a negatively charged muon. The light-blue band represents the quadratic sum of all uncertainties shown in a plot.

9.3.5. Other experimental uncertainties

Two additional experimental uncertainties are not related to any of the objects specified above. The description of the pile-up in the MC samples is adjusted using an SF. A two-sided uncertainty is provided which is found mostly below 0.5% for the measured cross-sections, see Figure F.18.

Finally, the luminosity uncertainty amounts to $\pm 0.83\%$ for the analyzed Run 2 dataset [110]. As it corresponds to a flat uncertainty factor on the unfolded cross-sections it will not be stated explicitly in the following.

9.4. Theoretical systematic uncertainties

Predictions with the SM, see Section 1.1.5, and the complex MC-modeling procedure, see Section 3.2, are not free of assumptions and ambiguities. These assumptions are addressed in the form of theoretical systematic uncertainties.

9.4.1. Signal process

In principle, the distribution of predicted $W \to \mu\nu$ events is subject to theory uncertainties which might bias the unfolded cross-sections. They can depend on the choice of the strong coupling constant α_s, the renormalization and factorization scales μ_R and μ_F, the PDF or the EW correction scheme used. Nevertheless, the sensitivity to potential biases is very small as signal theory uncertainties vary both, the reconstruction and truth-level distributions, in a similar way in the unfolding procedure.

In this dissertation, any bias due to the $W \to \mu\nu$ modeling is assessed via the unfolding tests described in Section 8.3, as recommended in Reference [174]. An additional inclusion of signal theory uncertainties would culminate in a double-counting. Nevertheless, their impact was studied with the help of the SHERPA signal sample, see Appendix F.4. PDF, EW and α_s variations have a negligible impact on the unfolded cross-sections. To the contrary, variations of the scales μ_R and μ_F yield a sizable uncertainty on the cross-sections of $1 - 2\%$ (see Figure F.12). The effect is expected to be related to in-smearing events generated at the W-boson resonance with a large $p_T(W)$. It was seen that the scale uncertainties increase with the $p_T(W)$ (see Figure F.13). The bias introduced by the $p_T(W)$ modeling is addressed by the test described in Section 8.3.3.

9.4.2. $t\bar{t}$ process

The following modeling uncertainties on the largest background process, $t\bar{t}$, are considered.

ME+PS: A systematic uncertainty accounts for a potential overlap between the separate simulations of the NLO ME and the PS. It is constructed by varying the p_T-hard parameter, which dictates the initial scale of the PS, in the POWHEG BOX (ME) simulation [175]. Furthermore, the parameter in POWHEG BOX controlling the damping of radiation at high transverse momenta is varied[3] from $\mathtt{hdamp} = 1.5 \cdot m_\mathrm{top}$ to $\mathtt{hdamp} = 3 \cdot m_\mathrm{top}$. Finally, a dedicated PS and hadronization uncertainty is defined by replacing the PYTHIA 8 generator with HERWIG 7 while the ME generation remains unchanged.

The uncertainties listed above are based on alternative samples produced with the AFII detector simulation (see Section 3.2). They are evaluated with respect to a nominal $t\bar{t}$ sample obtained with the AFII simulation and the relative difference is propagated to the full-simulation nominal sample.

Renormalization and factorization scale: Scale uncertainties are taken into account by varying the scales μ_R and μ_F independently by factors of two, i.e. $(\mu_F, \mu_R) = (0.5, 1, 2) \otimes (0.5, 1, 2)$. The extreme variations $(0.5, 2)$ and $(2, 0.5)$ are not used, resulting in six variations, in total. Their envelope is taken as the final scale uncertainty[4].

Additional radiation: On the one hand, ISR is taken into consideration by fluctuating the $\mathtt{var3c}$ parameter in the A14 tune in the PS sample [176]. On the other hand, FSR uncertainties are obtained via variations of the re-normalization scale in the PS sample.

PDF: The PDF uncertainty is evaluated using one hundred replicas of the nominal NNPDF3.0nlo PDF [115]. The relative uncertainty on the $t\bar{t}$ distribution is obtained independently per replica and their RMS is taken as the final PDF uncertainty, as depicted in Figure F.6.

The theory uncertainties on the $t\bar{t}$ MC distributions are shown in Figure F.6 and vary between $\sim 2 - 10\,\%$. Overall, $t\bar{t}$ events contribute with about $20 - 30\,\%$ in the signal region, in particular, at the lower end of the m_T^W distribution and at central $|\eta(\mu)|$. The relative $t\bar{t}$ theory uncertainties on the single-differential and double-differential cross-sections are shown in Figure 9.2(e) and Figure 9.3(e), respectively. They extend up to $3\,\%$, while the largest ones are related to the PS+hadronization and scales μ_R and μ_F.

9.4.3. Interference between tW and $t\bar{t}$ processes

A one-sided systematic uncertainty accounts for the interference between the $t\bar{t}$ process and the tW process (that represents about $90\,\%$ of single-top events here). Feynman diagrams for the two processes are shown in Figure 9.4, illustrating the same final state consisting of two W bosons and two b quarks each. Two schemes are commonly used to

---

[3]The $\mathtt{hdamp}$ uncertainty is evaluated for the tW sample as well.

[4]The envelope is found to agree exactly with the variations $(\mu_F, \mu_R) = (2, 1)$ and $(\mu_F, \mu_R) = (0.5, 0.5)$.
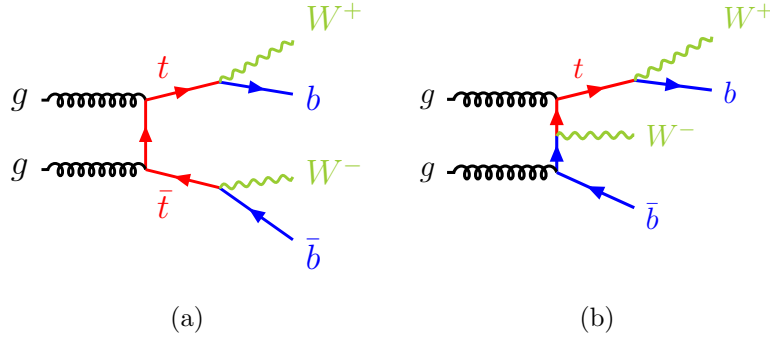
Figure 9.4.: Feynman diagrams for the (a) $t\bar{t}$ process and (b) tW process.

address this overlap: *diagram removal* (DR) [177] and *diagram subtraction* (DS) [147]. The former is given by a simple removal of the interfering diagrams, however it does not maintain gauge invariance. On the other hand, the latter includes a dedicated subtraction term that is gauge-invariant but to a certain degree arbitrary.

Both schemes are evaluated in the high-$m_{\mathrm{T}}^{\mathrm{W}}$ phase space using two different tW samples. The DS scheme was found to provide an improved agreement between data and predicted distributions in the signal region and in the top control region, as well as an improved agreement between electron- and muon-channel cross-sections [84]. Hence, the DS scheme is taken as default and the DR scheme as a systematic uncertainty here.
In the signal region, the number of predicted tW events differs substantially between the two schemes. The difference extends up to $\sim 50\,\%$ at $m_{\mathrm{T}}^{\mathrm{W}} \approx 1\,\mathrm{TeV}$ (see Figure F.7). Thus, the effect on the unfolded cross-sections is sizable even though single-top processes make up a small background (overall $2-3\,\%$, see Figure 7.1). The tW DR uncertainty on the unfolded cross-section is shown in Figure 9.2(e) (1D) and Figure 9.3(e) (2D) and extends up to $\sim 2\,\%$ at central $|\eta(\mu)|$.

9.4.4. Rate uncertainty on small background processes

Except for the $t\bar{t}$ process, all MC-based background processes have an overall contribution in the signal region of less than $10\,\%$ (see Figure 7.1). Therefore, instead of evaluating the full theoretical uncertainty model, the usage of a flat normalization uncertainty is a common and reasonable approach. The exact numbers used here are inspired by past measurements of the respective processes and amount to $5\,\%$ for $Z \to \mu\mu/\tau\tau$ and $W \to \tau\nu$ [71], $6\,\%$ for diboson [178] and $4\,\%$ for single top[5] [179].
The rate uncertainties on the differential cross-sections are shown Figure 9.2(f) (1D) and Figure 9.3(f) (2D). Only for the Z-boson process, a sizable impact of up to $1.5\,\%$ is visible. The increased uncertainty for large $|\eta(\mu)|$ values is expected as this process contributes in particular in the forward regions, see Figure 7.3(f).

---

[5]The tW cross-section uncertainty is used as the single-top process contains $90\,\%$ tW events here.

9.5. Summary

A summary of all systematic and statistical uncertainties is presented in Figure 9.5 where uncertainties related to similar sources are combined quadratically. The unfolding uncertainties discussed in Section 8.3 are included in the form of an envelope of the two smoothed non-closures (see Figure E.28). The combined uncertainties are shown explicitly for μ^+ (left-hand side) and μ^- (right-hand side) in Figure 9.5. Overall, the relative uncertainties are larger in the μ^--channel than in the μ^+-channel caused by enhanced background contributions but also larger detector uncertainties (e.g. JER). For $m_\mathrm{T}^\mathrm{W} \lesssim 400\,\mathrm{GeV}$, the uncertainties of various sources are at a similar level of $\sim 1\,\%$ each. For higher m_T^W, the statistical uncertainty as well as the muon-related uncertainties, driven by the sagitta-bias uncertainty, dominate. The light-blue band indicates the total systematic uncertainty which is in the first 1D m_T^W bin $\sim 3\,\%$ for μ^+ and $\sim 4\,\%$ for μ^- and increases with m_T^W and $|\eta(\mu)|$ to more than $20\,\%$ at the upper edge of the spectra.
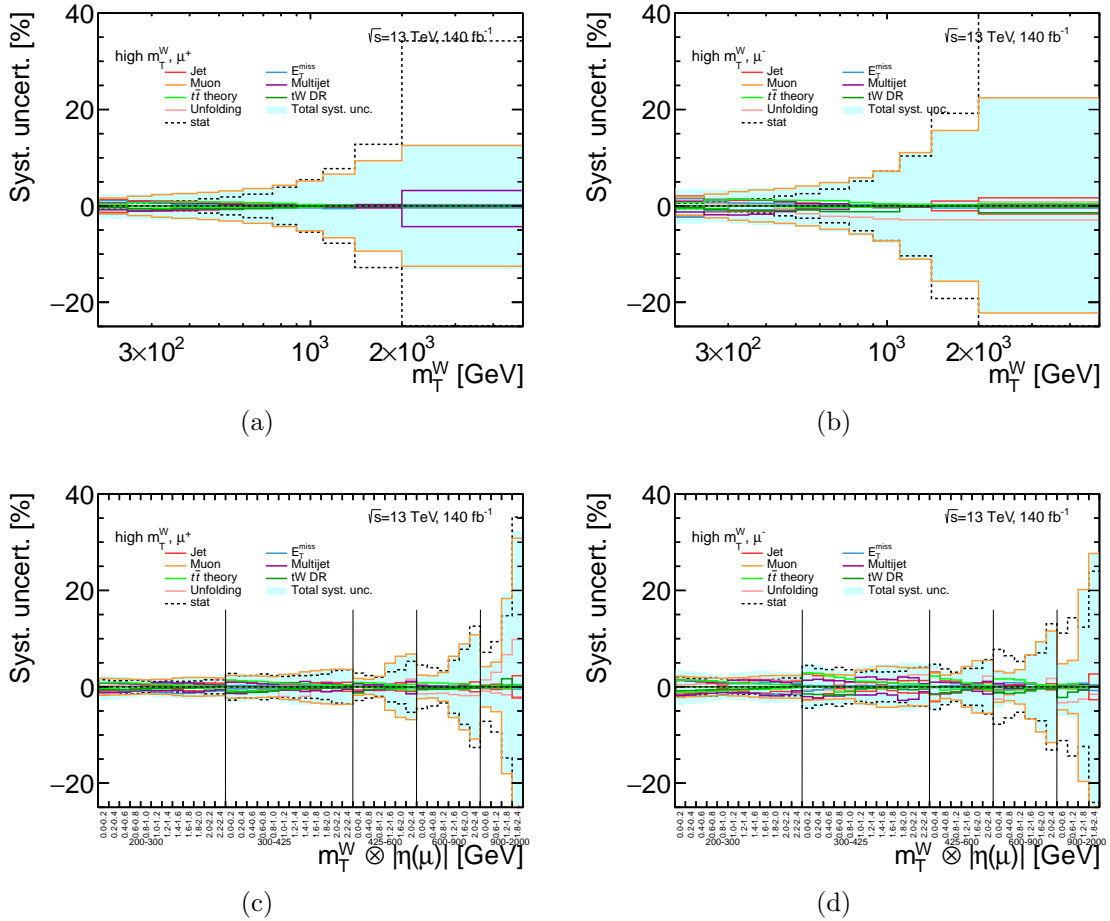
Figure 9.5.: Summary of the uncertainties on the single- and double-differential cross-sections for μ^+ (left-hand side) and μ^- (right-hand side). Uncertainties related to similar sources are combined quadratically. The light-blue band indicates the total systematic uncertainty.

10. Measurement results

In this Chapter, the final unfolded cross-sections are presented, single-differential in $m_{\mathrm{T}}^{\mathrm{W}}$ in Section 10.1 and double-differential in $m_{\mathrm{T}}^{\mathrm{W}}$ and $|\eta(\mu)|$ in Section 10.2. A discrimination per W-boson charge is made while the charge-combined cross-sections can be found in Appendix F.6. Additionally, the asymmetry between the cross-sections for both W-boson charges is measured, see Section 10.3.

10.1. Single-differential cross-sections in $m_{\mathsf{T}}^{\mathsf{W}}$

The single-differential Born-level cross-sections as a function of the transverse mass are shown in Figure 10.1 for $W^+ \to \mu^+ \nu$ and $W^- \to \mu^- \bar{\nu}$. The shadow bin (see Section 8.2.4) is no longer shown. The unfolded cross-sections are given by black dots, including the statistical uncertainty. Systematic and total uncertainties are indicated by light-blue shaded bands. All uncertainties surpassing the 0.5% threshold described in Section 9.2 are included, accounting for the detector, modeling of top-processes, data-driven multijet estimate and unfolding procedure. A tabular representation of the results, including a detailed breakdown of all considered sources of uncertainty, can be found in Table 10.1 (μ^+) and Table 10.2 (μ^-).

The cross-sections decrease over six orders of magnitude in the investigated range of $m_{\mathrm{T}}^{\mathrm{W}} \in [200, 5000]\,\mathrm{TeV}$. Overall, the cross-section is larger for W^+ than for W^- production, as expected for pp-collision data given the asymmetric valence-quark content (see Section 1.2.3). The overall measurement precision ranges between $^{+2.99}_{-2.77}\,\%$ in the first $m_{\mathrm{T}}^{\mathrm{W}}$ bin for the positive charge and $^{+65.23}_{-63.13}\,\%$ in the last bin for the negative charge. The total systematic uncertainty spans from $\sim 2.7\%$ to $\sim 25\%$, with statistical uncertainties ranging from $\sim 0.5\%$ to $\sim 65\%$, see Tables 10.1/10.2 for the exact numbers. At low $m_{\mathrm{T}}^{\mathrm{W}}$, systematic uncertainties dominate, while different experimental uncertainties related to the measurement of the muon, $E_{\mathrm{T}}^{\mathrm{miss}}$ soft track and JER are competing. Starting at $m_{\mathrm{T}}^{\mathrm{W}} \approx 400\,\mathrm{GeV}$, the statistical uncertainty dominates alongside the systematic uncertainty associated with the muon sagitta bias.

Table 10.1.: Born-level single-differential cross-section $\frac{d\sigma(W^+ \to \mu^+\nu)}{dm_{\mathrm{T}}^{\mathrm{W}}}$ including statistical and systematic uncertainties in percent. The upper (lower) row corresponds to the one standard deviation upward (downward) shift of the uncertainty source.

$m_{\mathrm{T}}^{\mathrm{W}}$ [GeV]	200 - 250	250 - 300	300 - 350	350 - 425	425 - 500	500 - 600	600 - 750	750 - 900	900 - 1100	1100 - 1400	1400 - 2000	2000 - 5000
σ [pb/GeV]	2.10e-02	8.69e-03	4.16e-03	1.92e-03	8.47e-04	3.92e-04	1.53e-04	5.22e-05	1.86e-05	6.49e-06	1.12e-06	4.03e-08
Data stat. unc.	0.41	0.62	0.85	1.05	1.49	1.86	2.42	3.83	5.45	7.76	12.65	34.36
Sig. stat. unc.	0.31	0.36	0.48	0.63	0.89	1.12	1.31	2.89	2.85	1.74	13.87	1.60
Bkg. stat. unc.	0.10	0.15	0.20	0.24	0.30	0.32	0.37	0.54	0.63	0.80	1.39	9.54
Tot. sys. unc.	2.95 / -2.72	2.90 / -2.95	3.00 / -3.15	3.11 / -3.19	3.20 / -3.26	3.37 / -3.36	3.79 / -3.68	4.46 / -4.24	5.32 / -4.97	6.83 / -6.31	9.91 / -8.85	13.93 / -12.32
Alt. MC unf. unc.	0.21	-0.62	-0.86	-1.00	-0.94	-0.68	-0.50	-0.41	-0.34	-0.28	-0.17	0.03
Basic unf. unc.	0.00	-0.01	-0.03	-0.06	-0.08	-0.06	0.01	0.03	-0.06	-0.21	-0.32	-0.39
JES Flavor Composition	-0.02 / 0.02	0.33 / -0.33	0.46 / -0.45	0.45 / -0.45	0.34 / -0.34	0.20 / -0.20	0.10 / -0.10	0.03 / -0.03	-0.03 / 0.03	-0.04 / 0.04	0.02 / -0.02	0.00 / -0.00
JES Pileup RhoTopology	-0.04 / 0.04	0.18 / -0.18	0.26 / -0.26	0.25 / -0.24	0.16 / -0.16	0.06 / -0.06	-0.02 / 0.02	-0.03 / 0.03	-0.03 / 0.03	-0.02 / 0.02	0.02 / -0.02	0.00 / -0.00
JES Pileup OffsetMu	-0.38 / 0.39	-0.21 / 0.21	-0.13 / 0.13	-0.09 / 0.09	-0.07 / 0.07	-0.06 / 0.06	-0.06 / 0.06	-0.06 / 0.06	-0.06 / 0.06	-0.06 / 0.06	-0.02 / 0.02	-0.06 / 0.06
JES Pileup OffsetNPV	-0.15 / 0.15	-0.03 / 0.03	0.02 / -0.02	0.03 / -0.03	0.02 / -0.02	0.01 / -0.01	-0.00 / 0.00	-0.01 / 0.01	-0.03 / 0.03	-0.04 / 0.04	-0.02 / 0.02	-0.03 / 0.03
JES EtaIntercalib Model	-0.13 / 0.13	-0.03 / 0.03	0.05 / -0.05	0.09 / -0.09	0.06 / -0.06	0.01 / -0.01	-0.02 / 0.02	-0.03 / 0.03	-0.03 / 0.03	-0.03 / 0.03	-0.01 / 0.01	-0.02 / 0.02
JES Flavor Response	-0.06 / 0.06	-0.37 / 0.37	-0.54 / 0.55	-0.56 / 0.57	-0.39 / 0.39	-0.15 / 0.15	-0.01 / 0.01	0.02 / -0.02	0.04 / -0.04	0.03 / -0.03	-0.01 / 0.01	-0.01 / 0.01
JER EffectiveNP 1	-0.91 / 0.93	-0.61 / 0.61	-0.38 / 0.38	-0.28 / 0.28	-0.23 / 0.23	-0.17 / 0.17	-0.13 / 0.13	-0.07 / 0.07	-0.06 / 0.06	-0.07 / 0.07	0.03 / -0.03	-0.07 / 0.07
JER EffectiveNP 2	-0.57 / 0.57	-0.34 / 0.35	-0.24 / 0.24	-0.14 / 0.14	-0.07 / 0.07	-0.07 / 0.07	-0.09 / 0.09	-0.05 / 0.05	-0.04 / 0.04	-0.05 / 0.05	0.02 / -0.02	-0.04 / 0.04
JER EffectiveNP 3	-0.29 / 0.29	-0.28 / 0.28	-0.23 / 0.23	-0.16 / 0.16	-0.11 / 0.11	-0.07 / 0.07	-0.04 / 0.04	-0.01 / 0.01	0.01 / -0.01	0.01 / -0.01	0.04 / -0.04	0.01 / -0.01
JER EffectiveNP 4	-0.29 / 0.29	-0.30 / 0.30	-0.25 / 0.25	-0.09 / 0.09	0.06 / -0.06	0.07 / -0.07	0.01 / -0.01	-0.01 / 0.01	0.01 / -0.01	0.03 / -0.03	0.06 / -0.06	0.04 / -0.04
JER EffectiveNP 5	-0.29 / 0.30	-0.29 / 0.29	-0.22 / 0.22	-0.08 / 0.08	0.07 / -0.07	0.14 / -0.14	0.10 / -0.10	0.02 / -0.02	-0.02 / 0.02	-0.02 / 0.02	0.01 / -0.01	-0.01 / 0.01
JER EffectiveNP 6	-0.26 / 0.27	-0.25 / 0.25	-0.20 / 0.20	-0.12 / 0.12	-0.05 / 0.05	-0.03 / 0.03	-0.04 / 0.04	-0.04 / 0.04	-0.02 / 0.02	-0.01 / 0.01	0.01 / -0.01	-0.00 / 0.00
JER EffectiveNP 7rest	-0.23 / 0.23	-0.23 / 0.23	-0.19 / 0.20	-0.09 / 0.09	0.03 / -0.03	0.09 / -0.09	0.05 / -0.05	-0.01 / 0.01	-0.02 / 0.02	0.01 / -0.01	0.04 / -0.04	0.02 / -0.02
JER DataVsMC MC16	-0.37 / 0.37	-0.27 / 0.27	-0.11 / 0.11	-0.01 / 0.01	0.00 / -0.00	0.00 / -0.00	-0.00 / 0.00	-0.02 / 0.02	-0.04 / 0.04	-0.05 / 0.05	-0.02 / 0.02	-0.04 / 0.04
$E_{\mathrm{T}}^{\mathrm{miss}}$ SoftTrk Scale	1.13 / -1.11	0.70 / -0.69	0.46 / -0.46	0.31 / -0.31	0.21 / -0.21	0.16 / -0.16	0.16 / -0.16	0.15 / -0.15	0.18 / -0.18	0.21 / -0.21	0.10 / -0.10	0.20 / -0.20
$E_{\mathrm{T}}^{\mathrm{miss}}$ SoftTrk ResoPara	0.78	0.53	-0.04	0.42	0.20	0.19	0.18	0.31	0.21	0.34	0.15	0.22
$E_{\mathrm{T}}^{\mathrm{miss}}$ SoftTrk ResoPerp	0.90	0.51	0.35	0.46	0.24	0.17	0.23	0.30	0.16	0.36	0.15	0.25
Muon Resolution MS	-0.15 / 0.15	-0.19 / 0.19	-0.26 / 0.26	-0.30 / 0.31	-0.30 / 0.30	-0.25 / 0.25	-0.23 / 0.23	-0.31 / 0.31	-0.48 / 0.49	-0.80 / 0.82	-1.40 / 1.44	-2.21 / 2.32
Muon Scale	0.53 / -0.52	0.55 / -0.54	0.52 / -0.52	0.47 / -0.46	0.41 / -0.41	0.37 / -0.37	0.37 / -0.36	0.37 / -0.37	0.37 / -0.37	0.37 / -0.37	0.37 / -0.36	0.38 / -0.37
Muon SF Identification Syst	-0.87 / 0.88	-1.22 / 1.25	-1.39 / 1.42	-1.37 / 1.41	-1.28 / 1.31	-1.26 / 1.29	-1.38 / 1.42	-1.58 / 1.63	-1.85 / 1.92	-2.33 / 2.44	-3.06 / 3.26	-3.61 / 3.89
Muon SF Isolation Syst	-0.23 / 0.24	-0.34 / 0.34	-0.51 / 0.51	-0.61 / 0.62	-0.60 / 0.61	-0.57 / 0.58	-0.55 / 0.56	-0.54 / 0.55	-0.52 / 0.53	-0.51 / 0.52	-0.53 / 0.53	-0.51 / 0.51
Muon SF Trigger Syst	0.70 / -0.70	0.72 / -0.71	0.70 / -0.69	0.67 / -0.66	0.64 / -0.63	0.62 / -0.61	0.61 / -0.60	0.61 / -0.60	0.61 / -0.60	0.61 / -0.60	0.60 / -0.59	0.60 / -0.60
Bad Muon	-0.20 / 0.20	-0.08 / 0.08	-0.04 / 0.04	-0.05 / 0.05	-0.08 / 0.08	-0.14 / 0.14	-0.21 / 0.21	-0.18 / 0.18	-0.12 / 0.12	-0.20 / 0.20	-0.40 / 0.41	-0.77 / 0.78
Muon Sagitta Global	0.81 / -0.79	1.00 / -0.98	1.26 / -1.23	1.43 / -1.39	1.62 / -1.57	1.87 / -1.81	2.30 / -2.20	2.82 / -2.67	3.40 / -3.18	4.43 / -4.06	7.29 / -6.36	11.00 / -9.04
Muon Sagitta p_{T}-extra	0.56 / -0.56	0.69 / -0.68	0.88 / -0.86	1.17 / -1.14	1.62 / -1.57	1.94 / -1.87	2.27 / -2.17	2.73 / -2.59	3.33 / -3.13	4.36 / -4.01	5.58 / -5.02	6.37 / -5.65
Pile-up	-0.29 / 0.30	-0.19 / 0.19	-0.14 / 0.14	-0.09 / 0.09	0.05 / -0.05	0.21 / -0.21	0.28 / -0.28	0.20 / -0.20	0.06 / -0.06	-0.03 / 0.03	-0.05 / 0.05	-0.15 / 0.15
Multijet $E_{\mathrm{T}}^{\mathrm{miss}}$	-0.34 / 0.05	-0.46 / 0.05	-0.41 / 0.04	-0.33 / 0.03	-0.26 / 0.02	-0.13 / 0.01	-0.04 / 0.01	-0.07 / 0.01	-0.02 / 0.00	-0.05 / 0.01	-0.00 / 0.00	0.02 / 0.00
Multijet d_0^{sig}	0.18 / -0.30	0.24 / -0.46	0.22 / -0.45	0.18 / -0.41	0.16 / -0.39	0.10 / -0.25	0.04 / -0.09	0.08 / -0.16	0.02 / -0.03	0.04 / -0.07	0.00 / -0.26	-0.02 / -2.90
Multijet MC Scaling	0.41 / -0.41	0.55 / -0.55	0.51 / -0.51	0.44 / -0.44	0.39 / -0.39	0.24 / -0.24	0.09 / -0.09	0.18 / -0.18	0.04 / -0.04	0.08 / -0.08	0.28 / -0.28	3.18 / -3.17
Multijet Jet Mult	-0.36 / 0.27	-0.39 / 0.28	-0.35 / 0.23	-0.29 / 0.19	-0.25 / 0.17	-0.19 / 0.10	-0.10 / 0.03	-0.09 / 0.09	-0.04 / 0.04	-0.15 / 0.03	-0.01 / 0.00	0.07 / 0.01
Multijet MC Shape	0.23	0.31	0.22	0.16	0.17	0.04	-0.03	0.06	0.01	-0.07	-0.01	0.05
Multijet $\Delta\phi(\mu, E_{\mathrm{T}}^{\mathrm{miss}})$	-0.39 / 0.23	-0.53 / 0.34	-0.49 / 0.31	-0.43 / 0.27	-0.37 / 0.27	-0.27 / 0.17	-0.13 / 0.07	-0.16 / 0.05	-0.04 / 0.01	-0.18 / 0.10	-0.01 / 0.01	0.13 / -0.08
$t\bar{t}$ p_{T}-hard	0.02 / 0.00	-0.08 / 0.00	-0.09 / 0.00	-0.07 / 0.00	-0.04 / 0.00	-0.06 / 0.00	-0.10 / 0.00	-0.09 / 0.00	-0.05 / 0.00	-0.02 / 0.00	-0.00 / 0.00	0.01 / 0.00
$t\bar{t}$ FSR	0.18 / -0.18	0.24 / -0.24	0.24 / -0.24	0.21 / -0.21	0.17 / -0.17	0.15 / -0.15	0.17 / -0.17	0.15 / -0.15	0.09 / -0.09	0.05 / -0.05	0.01 / -0.01	0.01 / -0.01
$t\bar{t}$ scales μ_R μ_F	-0.29 / 0.36	-0.50 / 0.66	-0.58 / 0.77	-0.57 / 0.75	-0.54 / 0.80	-0.46 / 0.79	-0.37 / 0.67	-0.28 / 0.50	-0.16 / 0.28	-0.08 / 0.14	-0.01 / 0.02	-0.00 / -0.00
$t\bar{t}$ hadronization	0.02 / 0.00	0.26 / 0.00	0.42 / 0.00	0.49 / 0.00	0.49 / 0.00	0.37 / 0.00	0.25 / 0.00	0.18 / 0.00	0.10 / 0.00	0.04 / 0.00	0.00 / 0.00	-0.02 / 0.00
$t\bar{t}$ hdamp	-0.06 / 0.00	-0.04 / 0.00	0.01 / 0.00	0.01 / 0.00	-0.03 / 0.00	-0.14 / 0.00	-0.27 / 0.00	-0.27 / 0.00	-0.16 / 0.00	-0.08 / 0.00	0.00 / 0.00	-0.00 / 0.00
$t\bar{t}$ PDF	-0.52 / 0.52	-0.59 / 0.59	-0.55 / 0.55	-0.49 / 0.49	-0.40 / 0.40	-0.30 / 0.30	-0.27 / 0.27	-0.24 / 0.24	-0.15 / 0.15	-0.13 / 0.13	-0.03 / 0.03	-0.07 / 0.07
tW DR	-0.33	-0.60	-0.71	-0.57	-0.62	-0.73	-0.56	-0.22	-0.00	0.05	0.03	-0.01
tW DS hdamp	-0.04	-0.03	-0.00	0.05	0.12	0.09	0.06	0.24	0.73	0.47	0.45	-0.10
Norm. $W \to \tau\nu$ by 5%	-0.08 / 0.08	-0.08 / 0.08	-0.08 / 0.08	-0.08 / 0.08	-0.08 / 0.08	-0.07 / 0.07	-0.07 / 0.07	-0.07 / 0.07	-0.07 / 0.07	-0.05 / 0.05	-0.04 / 0.04	-0.03 / 0.03
Norm. Single top by 4%	-0.13 / 0.13	-0.14 / 0.14	-0.14 / 0.14	-0.12 / 0.12	-0.10 / 0.10	-0.08 / 0.08	-0.06 / 0.06	-0.04 / 0.04	-0.06 / 0.06	-0.03 / 0.03	-0.01 / 0.01	-0.01 / 0.01
Norm. Diboson by 6%	-0.20 / 0.20	-0.23 / 0.23	-0.22 / 0.22	-0.22 / 0.22	-0.21 / 0.21	-0.19 / 0.19	-0.17 / 0.17	-0.16 / 0.16	-0.19 / 0.19	-0.13 / 0.13	-0.17 / 0.17	-0.25 / 0.25
Norm. $Z \to \ell\ell$ by 5%	-0.66 / 0.66	-0.65 / 0.65	-0.60 / 0.60	-0.54 / 0.54	-0.48 / 0.48	-0.39 / 0.39	-0.31 / 0.31	-0.25 / 0.25	-0.23 / 0.23	-0.22 / 0.22	-0.17 / 0.17	-0.20 / 0.20

Table 10.2.: Born-level single-differential cross-section $\frac{d\sigma(W^-\to\mu^-\bar{\nu})}{dm_{\mathrm{T}}^{\mathrm{W}}}$ including statistical and systematic uncertainties in percent. The upper (lower) row corresponds to the one standard deviation upward (downward) shift of the uncertainty source.

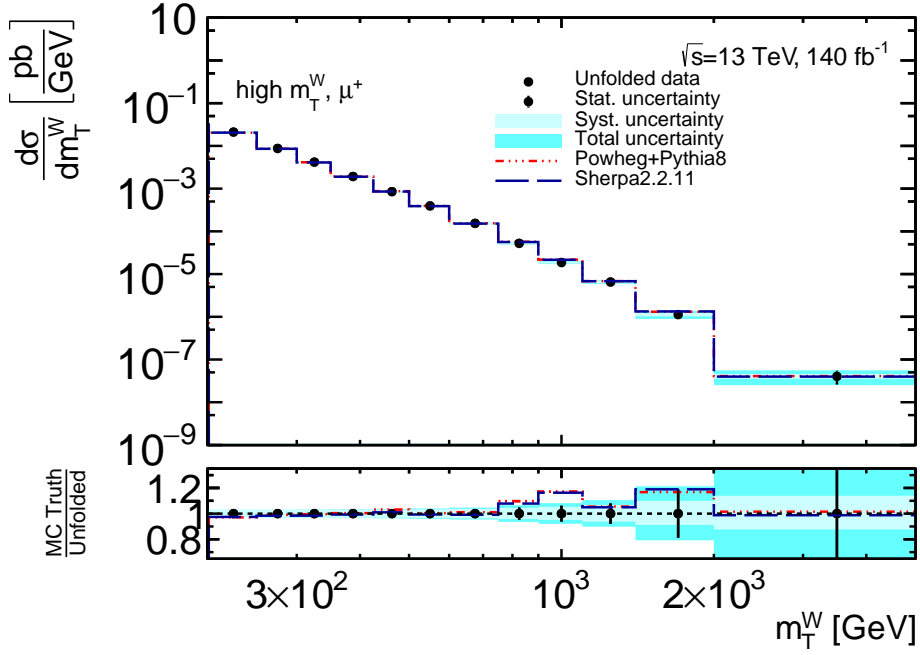| $m_{\mathrm{T}}^{\mathrm{W}}$ [GeV]	200 - 250	250 - 300	300 - 350	350 - 425	425 - 500	500 - 600	600 - 750	750 - 900	900 - 1100	1100 - 1400	1400 - 2000	2000 - 5000
σ [pb/GeV]	1.32e-02	5.25e-03	2.41e-03	1.10e-03	4.94e-04	2.22e-04	8.11e-05	2.90e-05	1.19e-05	3.44e-06	6.21e-07	1.45e-08
Data stat. unc.	0.54	0.85	1.22	1.48	2.07	2.60	3.47	5.10	7.24	10.43	19.07	55.64
Sig. stat. unc.	0.46	0.59	0.76	0.95	1.83	2.62	3.38	5.88	1.91	11.03	1.60	5.99
Bkg. stat. unc.	0.15	1.03	0.35	0.40	0.49	0.53	0.72	0.73	1.25	1.64	3.63	21.71
Tot. sys. unc.	4.25 -3.70	3.82 -3.79	4.23 -4.15	4.28 -4.23	4.36 -4.19	4.57 -4.65	5.20 -5.47	6.13 -6.28	7.37 -7.39	11.75 -10.64	17.20 -14.44	25.54 -19.56
Alt. MC unf. unc.	1.21	0.47	0.38	0.15	-0.53	-1.62	-2.16	-2.34	-2.71	-2.89	-2.90	-2.90
Basic unf. unc.	0.00	-0.01	-0.04	-0.06	-0.03	0.03	0.05	0.02	-0.01	0.01	0.27	0.83
JES Flavor Composition	-0.01 0.01	0.53 -0.52	0.64 -0.63	0.54 -0.53	0.38 -0.38	0.30 -0.29	0.22 -0.22	0.14 -0.14	0.04 -0.04	0.06 -0.06	-0.00 0.00	-0.02 0.02
JES Pileup RhoTopology	-0.01 0.01	0.30 -0.30	0.35 -0.35	0.32 -0.32	0.29 -0.28	0.22 -0.22	0.10 -0.10	0.05 -0.05	0.02 -0.02	0.04 -0.04	0.00 -0.00	-0.01 0.01
JES Pileup OffsetMu	-0.61 0.62	-0.27 0.27	-0.13 0.13	-0.04 0.04	0.03 -0.03	0.12 -0.12	0.12 -0.12	0.09 -0.09	-0.01 0.01	0.04 -0.04	-0.05 0.05	-0.06 0.06
JES Pileup OffsetNPV	-0.22 0.22	-0.08 0.08	-0.00 0.00	0.03 -0.03	0.07 -0.07	0.11 -0.11	0.10 -0.10	0.06 -0.06	0.00 -0.00	0.01 -0.01	-0.01 0.01	-0.01 0.01
JES EtaIntercalib Model	-0.26 0.26	-0.05 0.05	0.06 -0.06	0.13 -0.13	0.15 -0.15	0.15 -0.15	0.10 -0.10	0.06 -0.06	0.00 -0.00	0.02 -0.02	-0.03 0.03	-0.03 0.03
JES Flavor Response	-0.20 0.20	-0.62 0.63	-0.71 0.72	-0.64 0.64	-0.45 0.45	-0.29 0.29	-0.15 0.15	-0.07 0.07	-0.02 0.02	-0.06 0.06	-0.03 0.03	-0.01 0.01
JER EffectiveNP 1	-1.36 1.40	-0.66 0.66	-0.45 0.46	-0.42 0.43	-0.40 0.40	-0.16 0.16	0.14 -0.14	0.30 -0.30	-0.03 0.03	-0.21 0.21	-0.61 0.61	-0.85 0.86
JER EffectiveNP 2	-0.92 0.93	-0.53 0.53	-0.31 0.31	-0.21 0.21	-0.18 0.18	-0.00 0.00	0.26 -0.26	0.38 -0.38	0.09 -0.09	-0.18 0.18	-0.61 0.61	-0.99 1.01
JER EffectiveNP 3	-0.46 0.46	-0.15 0.15	0.04 -0.04	0.22 -0.22	0.31 -0.30	0.37 -0.37	0.34 -0.33	0.25 -0.25	0.05 -0.05	-0.08 0.08	-0.43 0.43	-0.82 0.83
JER EffectiveNP 4	-0.41 0.41	-0.18 0.18	-0.16 0.16	-0.14 0.14	-0.10 0.10	-0.05 0.05	-0.01 0.01	-0.00 0.00	-0.09 0.09	-0.12 0.12	-0.26 0.27	-0.40 0.41
JER EffectiveNP 5	-0.25 0.25	-0.10 0.10	-0.13 0.13	-0.15 0.15	-0.13 0.13	-0.04 0.04	0.11 -0.11	0.18 -0.18	0.06 -0.06	-0.05 0.05	-0.22 0.22	-0.35 0.35
JER EffectiveNP 6	-0.35 0.35	-0.17 0.18	-0.18 0.18	-0.22 0.22	-0.21 0.21	-0.11 0.11	-0.01 0.01	0.05 -0.05	-0.01 0.01	-0.04 0.04	-0.18 0.18	-0.30 0.30
JER EffectiveNP 7rest	-0.35 0.36	-0.20 0.20	-0.23 0.23	-0.30 0.30	-0.30 0.30	-0.17 0.17	-0.01 0.01	0.07 -0.07	-0.01 0.01	-0.07 0.07	-0.20 0.20	-0.28 0.28
JER DataVsMC MC16	-0.22 0.22	-0.21 0.21	-0.15 0.15	-0.08 0.08	-0.04 0.04	-0.01 0.01	0.00 -0.00	0.02 -0.02	0.01 -0.01	-0.03 0.03	-0.19 0.19	-0.44 0.45
$E_{\mathrm{T}}^{\mathrm{miss}}$ SoftTrk Scale	1.61 -1.56	0.81 -0.80	0.60 -0.59	0.54 -0.54	0.37 -0.37	0.06 -0.07	-0.08 0.08	-0.11 0.11	0.11 -0.11	0.04 -0.04	0.25 -0.25	0.26 -0.26
$E_{\mathrm{T}}^{\mathrm{miss}}$ SoftTrk ResoPara	1.26	0.11	0.11	0.44	0.81	0.03	-0.10	-0.12	0.11	-0.00	0.23	0.16
$E_{\mathrm{T}}^{\mathrm{miss}}$ SoftTrk ResoPerp	1.22	0.59	0.64	0.28	0.50	-0.07	-0.23	-0.18	0.11	0.09	0.25	0.16
Muon Resolution MS	-0.11 0.11	-0.24 0.24	-0.42 0.42	-0.49 0.49	-0.47 0.47	-0.49 0.50	-0.57 0.57	-0.63 0.64	-0.77 0.79	-1.22 1.25	-1.98 2.06	-3.35 3.58
Muon Scale	0.62 -0.61	0.64 -0.64	0.61 -0.60	0.56 -0.55	0.52 -0.52	0.51 -0.51	0.51 -0.51	0.47 -0.47	0.44 -0.44	0.42 -0.41	0.43 -0.42	0.43 -0.43
Muon SF Identification Syst	-0.99 1.01	-1.42 1.46	-1.61 1.67	-1.62 1.67	-1.58 1.63	-1.69 1.75	-1.92 2.00	-2.22 2.32	-2.71 2.87	-4.06 4.41	-5.11 5.68	-6.06 6.88
Muon SF Isolation Syst	-0.27 0.28	-0.41 0.41	-0.61 0.62	-0.72 0.73	-0.70 0.71	-0.66 0.67	-0.62 0.63	-0.59 0.60	-0.55 0.56	-0.56 0.56	-0.53 0.53	-0.54 0.54
Muon SF Trigger Syst	0.81 -0.79	0.83 -0.82	0.80 -0.79	0.76 -0.75	0.70 -0.69	0.65 -0.64	0.62 -0.62	0.59 -0.59	0.59 -0.59	0.58 -0.57	0.59 -0.58	0.60 -0.59
Bad Muon	-0.23 0.23	-0.09 0.09	-0.06 0.06	-0.07 0.07	-0.10 0.10	-0.10 0.10	-0.10 0.11	-0.11 0.12	-0.19 0.19	-0.38 0.38	-0.86 0.88	-1.75 1.81
Muon Sagitta Global	-0.95 0.97	-1.19 1.22	-1.40 1.45	-1.66 1.72	-2.13 2.22	-2.52 2.65	-2.76 2.92	-3.20 3.42	-3.60 3.88	-5.00 5.55	-7.22 8.43	-9.74 12.03
Muon Sagitta p_{T}-extra	-0.61 0.62	-0.96 0.98	-1.45 1.49	-1.76 1.82	-1.94 2.02	-2.35 2.47	-3.04 3.24	-3.89 4.21	-4.85 5.38	-7.77 9.19	-10.70 13.58	-14.85 20.92
Pile-up	-0.89 0.91	-0.42 0.42	-0.15 0.15	-0.00 0.00	0.09 -0.09	0.20 -0.20	0.22 -0.22	0.21 -0.21	0.13 -0.13	0.32 -0.32	0.42 -0.42	0.79 -0.78
Multijet $E_{\mathrm{T}}^{\mathrm{miss}}$	-0.54 0.07	-0.85 0.09	-0.88 0.08	-0.71 0.06	-0.40 0.04	-0.23 0.02	-0.37 0.01	-0.06 -0.00	-0.25 -0.00	-0.18 -0.00	0.04 -0.00	0.34 -0.03
Multijet d_0^{sig}	0.29 -0.48	0.42 -0.83	0.44 -0.94	0.40 -0.90	0.28 -0.65	0.15 -0.38	0.16 -0.39	0.01 -0.03	0.06 -0.14	0.05 -0.11	-0.01 0.03	-0.17 0.31
Multijet MC Scaling	0.63 -0.63	0.90 -0.90	0.92 -0.92	0.83 -0.83	0.56 -0.56	0.31 -0.31	0.32 -0.32	0.01 -0.01	0.07 -0.07	0.02 -0.02	-0.02 0.02	-0.19 0.19
Multijet Jet Mult	-0.55 0.41	-0.63 0.47	-0.58 0.46	-0.53 0.39	-0.40 0.25	-0.23 0.11	-0.15 0.15	0.00 0.00	-0.10 0.05	0.06 -0.08	0.02 -0.02	0.06 -0.14
Multijet MC Shape	0.36	0.56	0.58	0.49	0.26	0.09	0.18	0.03	0.10	-0.09	-0.05	-0.27
Multijet $\Delta\phi(\mu, E_{\mathrm{T}}^{\mathrm{miss}})$	-0.60 0.36	-0.87 0.59	-0.86 0.62	-0.81 0.56	-0.58 0.44	-0.36 0.25	-0.32 0.15	-0.02 0.03	-0.10 0.17	0.11 -0.05	0.04 -0.05	0.14 -0.12
$t\bar{t}$ p_{T}-hard	0.04 0.00	0.04 0.00	0.04 0.00	0.08 0.00	0.14 0.00	0.12 0.00	0.09 0.00	0.05 0.00	0.03 0.00	0.03 0.00	0.02 0.00	0.04 0.00
$t\bar{t}$ FSR	0.37 -0.37	0.56 -0.56	0.58 -0.58	0.53 -0.53	0.48 -0.48	0.38 -0.38	0.27 -0.27	0.16 -0.16	0.10 -0.10	0.08 -0.08	0.07 -0.07	0.12 -0.12
$t\bar{t}$ scales $\mu_R\,\mu_F$	-0.47 0.60	-0.84 1.12	-0.99 1.27	-0.95 1.16	-0.85 1.06	-0.79 1.08	-0.69 1.05	-0.44 0.69	-0.26 0.41	-0.22 0.34	-0.16 0.25	-0.29 0.46
$t\bar{t}$ hadronization	0.12 0.00	0.86 0.00	1.19 0.00	1.15 0.00	0.97 0.00	0.83 0.00	0.67 0.00	0.41 0.00	0.22 0.00	0.21 0.00	0.13 0.00	0.24 0.00
$t\bar{t}$ hdamp	-0.13 0.00	-0.05 0.00	-0.03 0.00	-0.06 0.00	-0.09 0.00	-0.08 0.00	-0.06 0.00	-0.02 0.00	-0.02 0.00	-0.01 0.00	-0.02 0.00	-0.03 0.00
$t\bar{t}$ PDF	-0.82 0.82	-0.96 0.96	-0.95 0.95	-0.85 0.85	-0.62 0.62	-0.46 0.46	-0.36 0.36	-0.28 0.28	-0.24 0.24	-0.21 0.21	-0.27 0.27	-0.67 0.68
tW DR	-0.37	-0.69	-0.94	-0.98	-0.91	-0.84	-1.17	-1.19	-1.20	-0.07	0.08	-1.42
tW DS hdamp	0.05	0.11	0.17	0.23	0.22	0.19	0.19	0.09	0.02	-0.01	-0.01	-0.01
Norm. $W\to\tau\nu$ by 5%	-0.07 0.07	-0.07 0.07	-0.07 0.07	-0.07 0.07	-0.06 0.06	-0.05 0.05	-0.06 0.06	-0.05 0.05	-0.04 0.04	-0.03 0.03	-0.03 0.03	-0.02 0.02
Norm. Single top by 4%	-0.20 0.20	-0.24 0.24	-0.24 0.24	-0.21 0.21	-0.17 0.17	-0.12 0.12	-0.08 0.08	-0.04 0.04	-0.05 0.05	-0.01 0.01	0.01 -0.01	0.05 -0.05
Norm. Diboson by 6%	-0.30 0.30	-0.32 0.32	-0.41 0.41	-0.42 0.42	-0.41 0.41	-0.36 0.36	-0.36 0.36	-0.36 0.36	-0.36 0.36	-0.29 0.32	-0.48 0.48	-0.13 0.13
Norm. $Z\to\ell\ell$ by 5%	-0.46 0.46	-0.49 0.49	-0.49 0.49	-0.47 0.47	-0.43 0.43	-0.37 0.37	-0.33 0.33	-0.31 0.31	-0.35 0.35	-0.42 0.42	-0.45 0.45	-0.49 0.49

(a)

(b)

Figure 10.1.: Born-level cross-sections differential in m_T^W for (a) $W^+ \rightarrow \mu^+\nu$ and (b) $W^- \rightarrow \mu^-\bar{\nu}$. The statistical uncertainty is represented by error bars while the systematic and total uncertainties are shown in the uncertainty band. A comparison to predictions from the POWHEG+PYTHIA and SHERPA MC samples is included.

In Figure 10.1, theory predictions of the cross-sections from the two signal MC samples are included. As introduced in Section 3.3, they differ in their order and PDF set used:

— POWHEG+PYTHIA: NNLO QCD + NLO EW, CT14NNLO

— SHERPA: 0-2j@NLO, 3-5j@LO QCD + NLO EW, NNPDF3.0NNLO

Nevertheless, both MC samples yield extremely similar predictions in the investigated phase space. Overall, the predicted cross-sections agree well with the measured cross-sections within the given statistical and systematic uncertainties. In the first $m_{\mathrm{T}}^{\mathrm{W}}$ bin, slightly smaller predicted cross-sections are visible for both charges. With increasing $m_{\mathrm{T}}^{\mathrm{W}}$, data and theory show a difference of up to 10-20 %, pointing in different directions per charge. This effect was seen before in this dissertation (e.g. Figure 7.4) and is caused by a residual charge-dependent muon sagitta bias in the data. It is closely covered by the given uncertainty band which is, next to the statistical uncertainty, dominated by the systematic uncertainty associated with the sagitta bias.

10.2. Double-differential cross-sections in $m_{\mathsf{T}}^{\mathsf{W}} \otimes |\eta(\mu)|$

The Born-level cross-sections measured double-differentially in the transverse mass of the W boson and the pseudorapidity of the muon, covering $m_{\mathrm{T}}^{\mathrm{W}} \in [200, 2000]\,\mathrm{GeV}$ and $|\eta(\mu)| \in [0, 2.4]$, are shown in Figure 10.2 and Figure 10.3, for the positively and negatively charged W-boson respectively. Each $m_{\mathrm{T}}^{\mathrm{W}}$-bin is represented by a separate plot in which the η-distribution is depicted. Additionally, the same cross-sections are presented in a compact form in Figure 10.4. As for the single-differential measurement, the statistical uncertainty is given by black bars and the systematic and the total uncertainty by respective cyan-shaded bands. Again, a comparison to theory cross-sections predicted by the POWHEG+PYTHIA and SHERPA $W \to \mu\nu$ MC samples is included. The double-differential cross-sections are presented in tabular form including all sources of uncertainty in Tables 10.3-10.7 (μ^+) and Tables 10.8-10.12 (μ^-).

Overall, consistent cross-sections are obtained between the single-differential and double-differential measurements, see also Table 10.13 where the 1D and 2D cross-sections are compared directly. The precision in the double-differential measurement ranges between ~ 3 % in the first $m_{\mathrm{T}}^{\mathrm{W}}$ bin and up to ~ 40 % in the last $m_{\mathrm{T}}^{\mathrm{W}}$ bin. In particular in higher $m_{\mathrm{T}}^{\mathrm{W}}$-bins, the total uncertainty is larger in the forward areas, i.e. $|\eta(\mu)| > 1$, which is driven by the increased sagitta bias uncertainty there. In general, also in the double-differential measurement, the two MC predictions agree reasonably well with the unfolded cross-sections within the given uncertainties. A trend of larger (smaller) predicted cross-sections is visible for μ^+ (μ^-) for $|\eta(\mu)| > 1$. It is associated with the sagitta bias in the muon momentum measurement discussed extensively throughout this dissertation, see Section 4.2.5, Section 7.2 and Section 9.3.1 for more information.

(a)

(b)

(c)

(d)

(e)
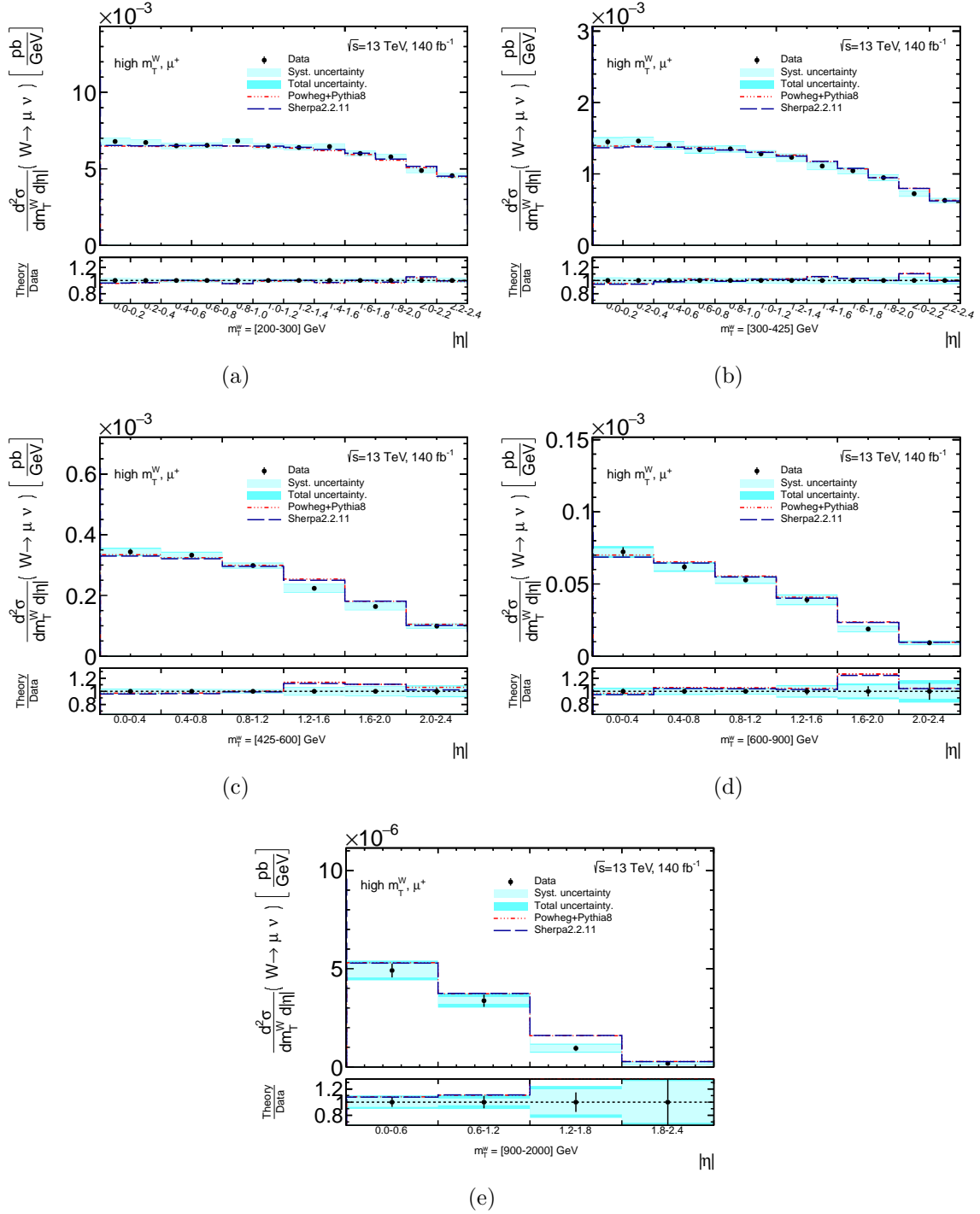
Figure 10.2.: Born-level cross-sections for $W^+ \rightarrow \mu^+ \nu$ double-differential in m_T^W and $|\eta(\mu)|$. The statistical uncertainty is represented by error bars while the systematic and total uncertainties are shown in the uncertainty band. A comparison to predictions from the POWHEG+PYTHIA and SHERPA MC samples is included.
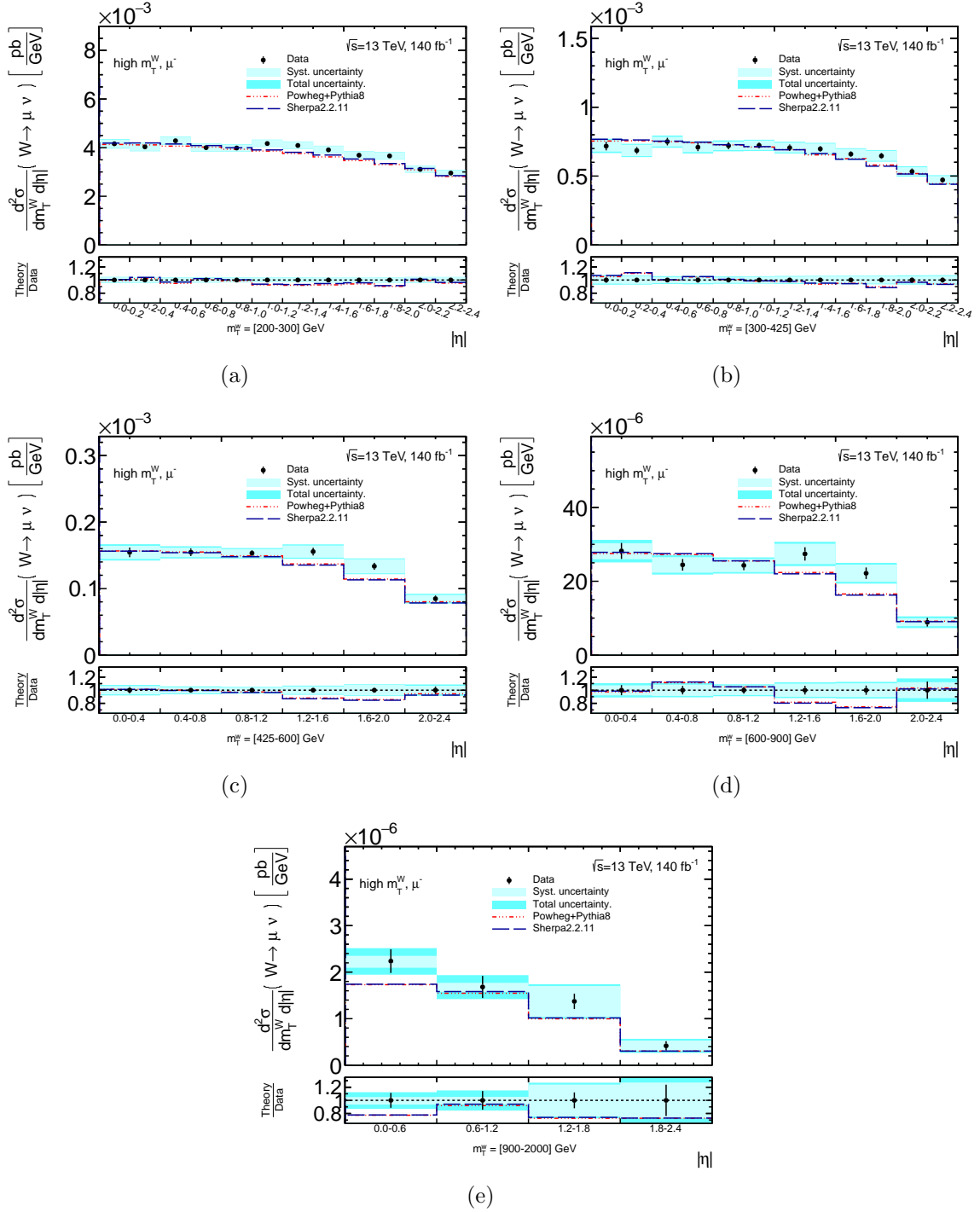
Figure 10.3.: Born-level cross-sections for $W^- \to \mu^- \bar{\nu}$ double-differential in $m_{\mathrm{T}}^{\mathrm{W}}$ and $|\eta(\mu)|$. The statistical uncertainty is represented by error bars while the systematic and total uncertainties are shown in the uncertainty band. A comparison to predictions from the POWHEG+PYTHIA and SHERPA MC samples is included.
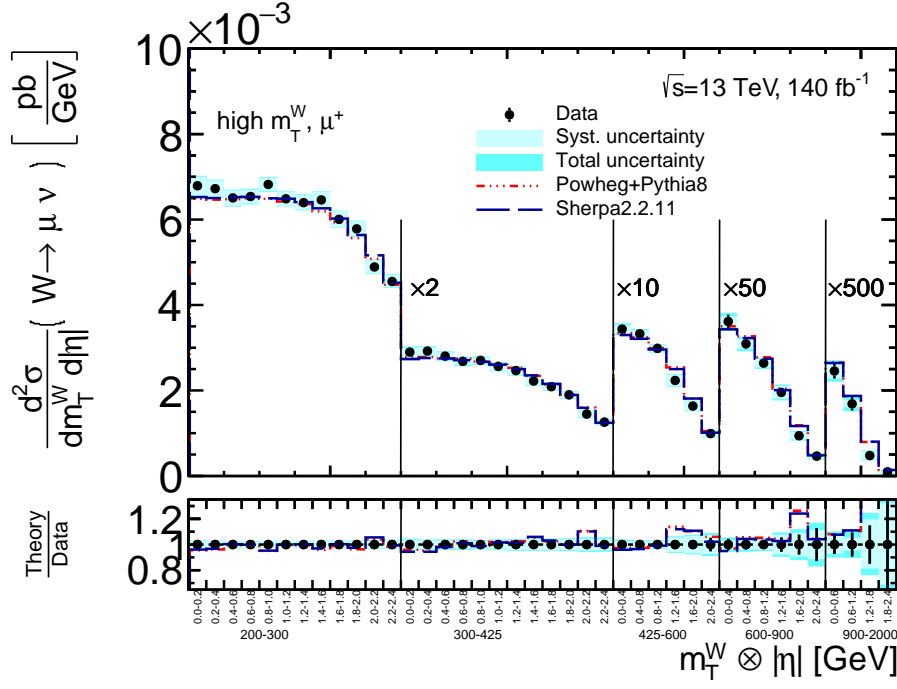
(a)
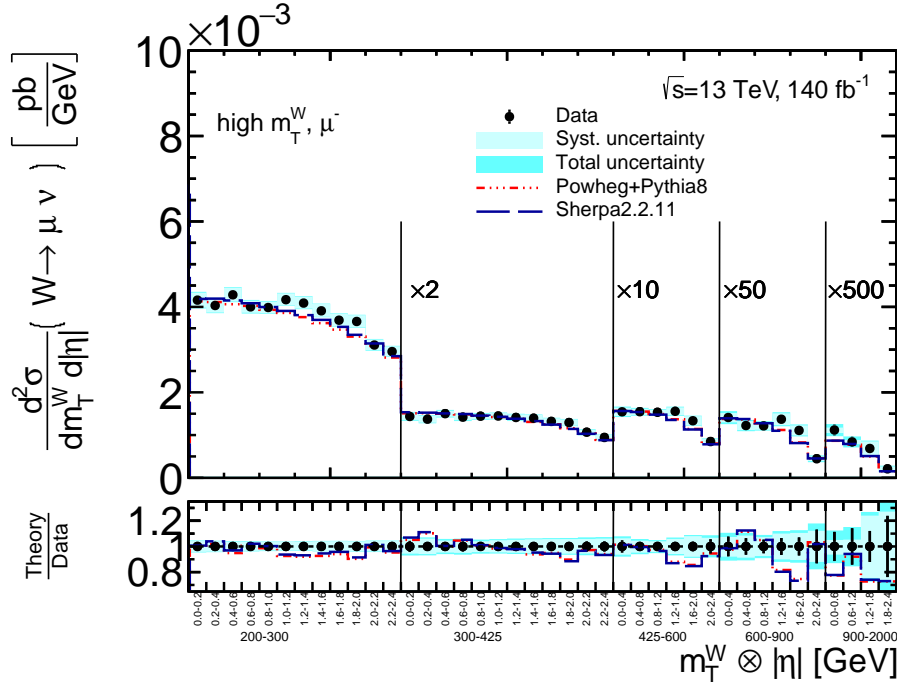
(b)

Figure 10.4.: Born-level cross-sections double-differential in m_T^W and $|\eta(\mu)|$ for (a) $W^+ \to \mu^+ \nu$ and (b) $W^- \to \mu^- \bar{\nu}$. The statistical uncertainty is represented by error bars while the systematic and total uncertainties are shown in the uncertainty band. The cross-sections for the last four m_T^W bins are scaled up for better visibility. A comparison to predictions from the POWHEG+PYTHIA and SHERPA MC samples is included.

Table 10.3.: Born-level double-differential cross-section $\frac{d^2\sigma(W^+ \to \mu^+\nu)}{dm_{\mathrm{T}}^{\mathrm{W}} d|\eta(\mu)|}$ including statistical and systematic uncertainties in percent for $m_{\mathrm{T}}^{\mathrm{W}} = [200 - 300]\,\mathrm{GeV}$. The upper (lower) row corresponds to the one standard deviation upward (downward) shift of the uncertainty source.

$|\eta(\mu)|$	0.0 - 0.2	0.2 - 0.4	0.4 - 0.6	0.6 - 0.8	0.8 - 1.0	1.0 - 1.2	1.2 - 1.4	1.4 - 1.6	1.6 - 1.8	1.8 - 2.0	2.0 - 2.2	2.2 - 2.4
σ [pb/GeV]	6.79e-03	6.72e-03	6.51e-03	6.54e-03	6.82e-03	6.49e-03	6.40e-03	6.46e-03	6.01e-03	5.78e-03	4.89e-03	4.55e-03
Data stat. unc.	1.47	1.24	1.27	1.39	1.21	1.08	1.18	1.10	1.14	1.21	1.48	1.48
Sig. stat. unc.	1.04	0.74	0.86	0.88	0.79	0.97	1.04	0.72	0.70	0.83	1.06	0.83
Bkg. stat. unc.	0.38	0.27	0.28	0.29	0.25	0.29	0.31	0.24	0.26	0.25	0.30	0.30
Tot. sys. unc.	3.05 / -3.26	2.88 / -3.05	2.66 / -2.76	2.37 / -2.40	2.17 / -2.19	2.54 / -2.37	2.61 / -2.38	2.89 / -2.61	3.08 / -2.90	3.02 / -2.93	3.05 / -2.87	3.34 / -2.80
Alt. MC unf. unc.	-1.52	-1.31	-0.91	-0.71	-0.76	-0.84	-0.76	-0.52	-0.18	0.25	0.77	1.67
Basic unf. unc.	0.24	0.31	0.40	0.44	0.46	0.48	0.49	0.49	0.43	0.33	0.24	0.22
JES Flavor Composition	0.48 / -0.48	0.45 / -0.44	0.37 / -0.37	0.31 / -0.31	0.27 / -0.27	0.34 / -0.34	0.34 / -0.35	0.37 / -0.37	0.36 / -0.36	0.26 / -0.26	0.10 / -0.10	-0.13 / 0.13
JES Pileup RhoTopology	0.64 / -0.63	0.49 / -0.49	0.35 / -0.34	0.22 / -0.22	0.14 / -0.14	0.21 / -0.21	0.22 / -0.22	0.28 / -0.28	0.30 / -0.30	0.30 / -0.30	0.31 / -0.31	0.30 / -0.30
JES Pileup OffsetMu	-0.21 / 0.21	-0.14 / 0.14	-0.08 / 0.08	-0.05 / 0.05	-0.06 / 0.06	-0.07 / 0.06	-0.06 / 0.06	-0.06 / 0.06	-0.09 / 0.09	-0.12 / 0.12	-0.08 / 0.08	-0.04 / 0.04
JES Pileup OffsetNPV	0.20 / -0.20	0.18 / -0.18	0.13 / -0.13	0.03 / -0.03	-0.04 / 0.04	0.05 / -0.05	0.06 / -0.06	0.08 / -0.08	0.07 / -0.07	0.04 / -0.04	-0.01 / 0.01	-0.09 / 0.09
JES EtaIntercalib Model	0.26 / -0.26	0.23 / -0.23	0.17 / -0.17	0.08 / -0.08	0.02 / -0.02	0.07 / -0.07	0.07 / -0.07	0.09 / -0.09	0.13 / -0.13	0.16 / -0.16	0.12 / -0.12	-0.04 / 0.04
JES Flavor Response	-0.74 / 0.75	-0.66 / 0.67	-0.52 / 0.52	-0.30 / 0.30	-0.15 / 0.15	-0.19 / 0.19	-0.20 / 0.20	-0.24 / 0.24	-0.30 / 0.30	-0.32 / 0.32	-0.27 / 0.27	-0.15 / 0.15
JER EffectiveNP 1	0.25 / -0.25	-0.24 / 0.23	-0.46 / 0.46	-0.40 / 0.40	-0.22 / 0.22	-0.08 / 0.07	-0.06 / 0.06	-0.04 / 0.03	-0.00 / -0.00	0.01 / -0.02	0.06 / -0.06	0.07 / -0.08
JER EffectiveNP 2	-0.23 / 0.23	-0.24 / 0.24	-0.18 / 0.18	-0.04 / 0.04	0.01 / -0.01	-0.32 / 0.33	-0.36 / 0.36	-0.55 / 0.55	-0.60 / 0.61	-0.59 / 0.60	-0.57 / 0.57	-0.55 / 0.56
JER EffectiveNP 3	-0.03 / 0.03	-0.04 / 0.04	-0.04 / 0.04	-0.03 / 0.03	-0.02 / 0.02	-0.07 / 0.07	-0.08 / 0.08	-0.28 / 0.28	-0.46 / 0.47	-0.53 / 0.53	-0.48 / 0.49	-0.33 / 0.33
JER EffectiveNP 4	0.23 / -0.23	0.10 / -0.10	0.02 / -0.02	-0.02 / 0.02	-0.02 / 0.02	-0.10 / 0.10	-0.11 / 0.11	-0.35 / 0.35	-0.53 / 0.54	-0.63 / 0.63	-0.66 / 0.67	-0.65 / 0.66
JER EffectiveNP 5	-0.10 / 0.10	-0.13 / 0.13	-0.14 / 0.14	-0.15 / 0.15	-0.16 / 0.16	-0.18 / 0.18	-0.18 / 0.18	-0.22 / 0.22	-0.27 / 0.27	-0.28 / 0.28	-0.27 / 0.27	-0.26 / 0.26
JER EffectiveNP 6	-0.28 / 0.29	-0.31 / 0.31	-0.25 / 0.25	-0.10 / 0.10	-0.05 / 0.05	-0.09 / 0.09	-0.09 / 0.09	-0.15 / 0.15	-0.20 / 0.20	-0.18 / 0.18	-0.07 / 0.07	0.07 / -0.07
JER EffectiveNP 7rest	0.19 / -0.19	0.17 / -0.17	0.14 / -0.14	0.10 / -0.10	0.07 / -0.07	-0.07 / 0.07	-0.08 / 0.08	-0.21 / 0.21	-0.30 / 0.30	-0.28 / 0.28	-0.19 / 0.19	-0.15 / 0.15
JER DataVsMC MC16	0.46 / -0.46	0.07 / -0.07	-0.06 / 0.06	-0.02 / 0.02	0.02 / -0.02	-0.20 / 0.20	-0.22 / 0.22	-0.32 / 0.32	-0.32 / 0.33	-0.31 / 0.31	-0.30 / 0.30	-0.29 / 0.29
$E_{\mathrm{T}}^{\mathrm{miss}}$ SoftTrk Scale	0.78 / -0.77	0.76 / -0.75	0.64 / -0.63	0.55 / -0.55	0.54 / -0.54	0.67 / -0.67	0.69 / -0.68	0.77 / -0.76	0.74 / -0.74	0.64 / -0.63	0.46 / -0.47	0.38 / -0.38
$E_{\mathrm{T}}^{\mathrm{miss}}$ SoftTrk ResoPara	0.65	0.62	0.49	0.38	0.38	0.49	0.50	0.58	0.64	0.68	0.68	0.67
$E_{\mathrm{T}}^{\mathrm{miss}}$ SoftTrk ResoPerp	0.72	0.58	0.45	0.45	0.59	0.94	0.97	1.04	0.96	0.75	0.52	0.40
Muon Resolution MS	-0.07 / 0.07	-0.08 / 0.08	-0.10 / 0.10	-0.11 / 0.11	-0.11 / 0.11	-0.12 / 0.12	-0.12 / 0.12	-0.11 / 0.11	-0.10 / 0.10	-0.09 / 0.09	-0.08 / 0.09	-0.08 / 0.08
Muon Scale	0.15 / -0.15	0.17 / -0.17	0.20 / -0.20	0.23 / -0.23	0.27 / -0.27	0.61 / -0.60	0.65 / -0.64	0.78 / -0.77	0.74 / -0.73	0.58 / -0.57	0.43 / -0.43	0.39 / -0.39
Muon SF Identification Syst	-1.17 / 1.20	-1.13 / 1.15	-1.08 / 1.11	-1.05 / 1.07	-1.02 / 1.05	-0.98 / 0.99	-0.98 / 1.00	-0.95 / 0.97	-0.94 / 0.96	-0.96 / 0.98	-0.98 / 1.00	-1.01 / 1.03
Muon SF Isolation Syst	-0.29 / 0.30	-0.29 / 0.30	-0.29 / 0.29	-0.28 / 0.28	-0.27 / 0.27	-0.25 / 0.25	-0.25 / 0.25	-0.24 / 0.24	-0.23 / 0.23	-0.21 / 0.22	-0.20 / 0.20	-0.19 / 0.19
Muon SF Trigger Syst	0.92 / -0.90	0.92 / -0.90	0.91 / -0.89	0.87 / -0.86	0.78 / -0.77	0.63 / -0.62	0.61 / -0.60	0.59 / -0.59	0.57 / -0.56	0.55 / -0.54	0.52 / -0.52	0.51 / -0.51
Bad Muon	-0.11 / 0.11	-0.11 / 0.11	-0.11 / 0.11	-0.10 / 0.10	-0.10 / 0.10	-0.12 / 0.12	-0.12 / 0.12	-0.14 / 0.14	-0.14 / 0.14	-0.16 / 0.16	-0.19 / 0.19	-0.20 / 0.20
Muon Sagitta Global	0.90 / -0.89	0.84 / -0.83	0.77 / -0.76	0.68 / -0.67	0.61 / -0.60	0.66 / -0.65	0.68 / -0.67	0.77 / -0.76	0.80 / -0.79	0.79 / -0.78	0.79 / -0.78	0.79 / -0.77
Muon Sagitta p_{T}-extra	-0.09 / 0.09	-0.08 / 0.08	-0.09 / 0.09	-0.09 / 0.09	-0.10 / 0.10	0.38 / -0.38	0.45 / -0.44	0.88 / -0.87	1.16 / -1.13	1.27 / -1.24	1.26 / -1.23	1.17 / -1.14
Pile-up	-0.20 / 0.20	-0.20 / 0.20	-0.17 / 0.17	-0.13 / 0.13	-0.08 / 0.08	-0.11 / 0.11	-0.11 / 0.11	-0.17 / 0.17	-0.13 / 0.12	-0.04 / 0.04	-0.01 / 0.01	-0.02 / 0.02
Multijet $E_{\mathrm{T}}^{\mathrm{miss}}$	-0.34 / 0.09	-0.35 / 0.09	-0.33 / 0.09	-0.24 / 0.06	-0.21 / 0.05	-0.40 / 0.09	-0.42 / 0.10	-0.44 / 0.07	-0.63 / 0.05	-0.60 / 0.01	-0.44 / 0.00	-0.37 / 0.00
Multijet d_0^{sig}	0.13 / -0.33	0.14 / -0.35	0.13 / -0.34	0.11 / -0.26	0.09 / -0.19	0.31 / -0.18	0.34 / -0.18	0.35 / -0.30	0.32 / -0.54	0.19 / -0.53	0.11 / -0.39	0.10 / -0.33
Multijet MC Scaling	0.70 / -0.70	0.71 / -0.71	0.69 / -0.69	0.53 / -0.53	0.44 / -0.44	0.48 / -0.48	0.48 / -0.48	0.38 / -0.38	0.40 / -0.40	0.30 / -0.30	0.19 / -0.19	0.16 / -0.16
Multijet Jet Mult	-0.57 / 0.29	-0.59 / 0.29	-0.56 / 0.28	-0.44 / 0.21	-0.38 / 0.19	-0.20 / 0.45	-0.18 / 0.47	-0.15 / 0.38	-0.33 / 0.32	-0.40 / 0.19	-0.28 / 0.11	-0.20 / 0.10
Multijet MC Shape	0.09	0.09	0.09	0.06	0.05	0.44	0.48	0.37	0.50	0.41	0.28	0.25
Multijet $\Delta\phi(\mu, E_{\mathrm{T}}^{\mathrm{miss}})$	-0.47 / 0.30	-0.48 / 0.33	-0.46 / 0.30	-0.37 / 0.24	-0.31 / 0.19	-0.48 / 0.36	-0.50 / 0.38	-0.41 / 0.30	-0.54 / 0.32	-0.53 / 0.22	-0.38 / 0.14	-0.27 / 0.14
$t\bar{t}$ p_{T}-hard	0.12 / 0.00	0.05 / 0.00	-0.01 / 0.00	-0.03 / 0.00	-0.03 / 0.00	0.11 / 0.00	0.13 / 0.00	0.17 / 0.00	0.14 / 0.00	0.08 / 0.00	0.05 / 0.00	0.06 / 0.00
$t\bar{t}$ FSR	0.32 / -0.32	0.35 / -0.35	0.39 / -0.39	0.35 / -0.35	0.25 / -0.25	0.21 / -0.21	0.20 / -0.20	0.18 / -0.18	0.16 / -0.16	0.15 / -0.15	0.13 / -0.13	0.11 / -0.11
$t\bar{t}$ scales $\mu_R \mu_F$	-0.58 / 0.83	-0.58 / 0.84	-0.57 / 0.80	-0.53 / 0.71	-0.46 / 0.60	-0.34 / 0.43	-0.33 / 0.41	-0.27 / 0.31	-0.22 / 0.23	-0.17 / 0.17	-0.12 / 0.12	-0.08 / 0.06
$t\bar{t}$ hadronization	0.59 / 0.00	0.52 / 0.00	0.38 / 0.00	0.23 / 0.00	0.08 / 0.00	0.05 / 0.00	0.05 / 0.00	0.10 / 0.00	0.06 / 0.00	-0.08 / 0.00	-0.18 / 0.00	-0.16 / 0.00
$t\bar{t}$ hdamp	0.08 / 0.00	0.07 / 0.00	0.03 / 0.00	-0.00 / 0.00	0.01 / 0.00	0.07 / 0.00	0.07 / 0.00	0.05 / 0.00	-0.05 / 0.00	-0.15 / 0.00	-0.17 / 0.00	-0.13 / 0.00
$t\bar{t}$ PDF	-0.76 / 0.76	-0.77 / 0.77	-0.74 / 0.74	-0.68 / 0.68	-0.61 / 0.61	-0.53 / 0.53	-0.52 / 0.52	-0.50 / 0.50	-0.52 / 0.52	-0.49 / 0.49	-0.52 / 0.52	-0.51 / 0.51
tW DR	-0.57	-0.56	-0.55	-0.48	-0.42	-0.36	-0.35	-0.30	-0.25	-0.16	-0.03	0.13
tW DS hdamp	0.00	-0.01	-0.04	-0.05	-0.05	-0.06	-0.06	-0.05	-0.03	0.01	0.08	0.13
Norm. $W \to \tau\nu$ by 5%	-0.10 / 0.10	-0.09 / 0.09	-0.09 / 0.09	-0.08 / 0.09	-0.08 / 0.08	-0.10 / 0.08	-0.10 / 0.10	-0.08 / 0.10	-0.08 / 0.08	-0.08 / 0.08	-0.07 / 0.07	-0.06 / 0.06
Norm. Single top by 4%	-0.21 / 0.21	-0.21 / 0.21	-0.20 / 0.20	-0.18 / 0.18	-0.16 / 0.16	-0.13 / 0.13	-0.13 / 0.13	-0.10 / 0.10	-0.09 / 0.09	-0.07 / 0.07	-0.06 / 0.06	-0.05 / 0.05
Norm. Diboson by 6%	-0.23 / 0.23	-0.24 / 0.24	-0.25 / 0.25	-0.23 / 0.23	-0.22 / 0.22	-0.21 / 0.21	-0.21 / 0.21	-0.20 / 0.20	-0.19 / 0.19	-0.19 / 0.19	-0.18 / 0.18	-0.18 / 0.18
Norm. $Z \to \ell\ell$ by 5%	-0.16 / 0.16	-0.19 / 0.19	-0.23 / 0.23	-0.28 / 0.28	-0.33 / 0.33	-0.56 / 0.56	-0.59 / 0.59	-0.74 / 0.74	-0.94 / 0.94	-1.12 / 1.12	-1.43 / 1.43	-1.55 / 1.55

Table 10.4.: Born-level double-differential cross-section $\frac{d^2\sigma(W^+\to\mu^+\nu)}{dm_\mathrm{T}^\mathrm{W}\,d|\eta(\mu)|}$ including statistical and systematic uncertainties in percent for $m_\mathrm{T}^\mathrm{W} = [300-425]\,\mathrm{GeV}$. The upper (lower) row corresponds to the one standard deviation upward (downward) shift of the uncertainty source.

$|\eta(\mu)|$	0.0 - 0.2	0.2 - 0.4	0.4 - 0.6	0.6 - 0.8	0.8 - 1.0	1.0 - 1.2	1.2 - 1.4	1.4 - 1.6	1.6 - 1.8	1.8 - 2.0	2.0 - 2.2	2.2 - 2.4
σ [pb/GeV]	1.45e-03	1.46e-03	1.40e-03	1.34e-03	1.35e-03	1.28e-03	1.23e-03	1.11e-03	1.04e-03	9.47e-04	7.23e-04	6.28e-04
Data stat. unc.	2.79	2.25	2.33	2.71	2.33	2.17	2.35	2.35	2.42	2.61	3.39	3.57
Sig. stat. unc.	1.50	0.94	1.58	1.20	0.90	1.51	1.57	1.72	1.10	0.99	1.87	1.25
Bkg. stat. unc.	0.71	0.47	0.47	0.52	0.44	0.46	0.50	0.50	0.51	0.59	0.74	0.70
Tot. sys. unc.	3.60 -3.69	3.35 -3.54	3.15 -3.31	2.93 -3.08	2.70 -2.89	3.09 -3.62	3.18 -4.09	3.73 -4.15	3.86 -3.89	4.07 -4.04	4.24 -4.17	4.21 -4.11
Alt. MC unf. unc.	-0.41	-0.32	-0.19	-0.21	-0.80	-2.01	-2.68	-1.98	-0.70	-0.13	-0.14	-0.14
Basic unf. unc.	-0.12	-0.12	-0.12	-0.11	-0.10	-0.11	-0.13	-0.14	-0.13	-0.12	-0.11	-0.11
JES Flavor Composition	0.98 -0.96	0.67 -0.66	0.51 -0.51	0.38 -0.37	0.33 -0.33	0.50 -0.50	0.53 -0.52	0.57 -0.57	0.48 -0.48	0.32 -0.32	0.17 -0.17	-0.01 0.01
JES Pileup RhoTopology	0.46 -0.46	0.23 -0.23	0.12 -0.12	0.07 -0.07	0.07 -0.07	0.26 -0.26	0.29 -0.29	0.42 -0.41	0.42 -0.42	0.32 -0.32	0.14 -0.14	-0.13 0.13
JES Pileup OffsetMu	0.18 -0.18	0.10 -0.10	0.10 -0.10	0.07 -0.07	0.01 -0.01	0.07 -0.07	0.08 -0.08	0.10 -0.10	0.02 -0.02	-0.02 0.02	-0.02 0.01	-0.04 0.04
JES Pileup OffsetNPV	0.33 -0.33	0.11 -0.11	0.04 -0.04	0.01 -0.01	-0.00 0.00	0.07 -0.07	0.09 -0.09	0.15 -0.15	0.16 -0.16	0.11 -0.11	0.04 -0.04	-0.04 0.04
JES EtaIntercalib Model	0.23 -0.22	0.21 -0.21	0.20 -0.20	0.17 -0.17	0.13 -0.13	0.22 -0.22	0.23 -0.23	0.31 -0.31	0.30 -0.30	0.30 -0.30	0.33 -0.33	0.32 -0.32
JES Flavor Response	-0.75 0.76	-0.82 0.84	-0.87 0.88	-0.81 0.83	-0.74 0.75	-0.72 0.73	-0.70 0.71	-0.69 0.70	-0.57 0.57	-0.36 0.36	-0.18 0.18	-0.00 0.00
JER EffectiveNP 1	-0.10 0.10	-0.05 0.04	0.13 -0.14	0.20 -0.20	0.12 -0.12	-0.10 0.09	-0.10 0.10	-0.16 0.16	-0.33 0.33	-0.43 0.43	-0.38 0.38	-0.42 0.42
JER EffectiveNP 2	-0.40 0.40	-0.41 0.41	-0.37 0.38	-0.29 0.29	-0.16 0.16	0.10 -0.11	0.12 -0.12	0.19 -0.19	0.07 -0.08	-0.07 0.07	-0.09 0.09	-0.10 0.10
JER EffectiveNP 3	-0.56 0.57	-0.53 0.54	-0.42 0.42	-0.19 0.19	-0.02 0.02	-0.01 0.01	-0.02 0.02	-0.22 0.22	-0.48 0.48	-0.56 0.57	-0.55 0.55	-0.54 0.54
JER EffectiveNP 4	-0.28 0.28	-0.21 0.21	-0.08 0.08	0.01 -0.01	0.04 -0.04	-0.08 0.08	-0.10 0.10	-0.21 0.21	-0.36 0.36	-0.52 0.52	-0.59 0.59	-0.58 0.59
JER EffectiveNP 5	-0.18 0.18	-0.12 0.12	-0.01 0.01	0.06 -0.06	0.05 -0.05	0.01 -0.01	0.00 -0.00	-0.02 0.02	-0.06 0.06	-0.09 0.09	-0.06 0.06	-0.00 0.00
JER EffectiveNP 6	-0.29 0.30	-0.21 0.21	-0.09 0.09	0.03 -0.03	0.07 -0.07	-0.11 0.11	-0.13 0.13	-0.18 0.18	-0.22 0.22	-0.23 0.23	-0.16 0.16	-0.10 0.10
JER EffectiveNP 7rest	-0.20 0.21	-0.18 0.18	-0.12 0.12	-0.01 0.01	0.08 -0.08	0.04 -0.04	0.03 -0.03	-0.09 0.09	-0.17 0.17	-0.12 0.12	-0.01 0.01	0.11 -0.11
JER DataVsMC MC16	-0.49 0.50	-0.46 0.46	-0.43 0.43	-0.39 0.40	-0.29 0.29	0.00 -0.00	0.03 -0.03	0.10 -0.10	0.11 -0.11	-0.00 0.00	-0.14 0.14	-0.20 0.20
$E_\mathrm{T}^\mathrm{miss}$ SoftTrk Scale	0.24 -0.24	0.29 -0.29	0.26 -0.26	0.24 -0.24	0.20 -0.20	0.14 -0.14	0.13 -0.13	0.14 -0.14	0.23 -0.23	0.21 -0.21	0.10 -0.11	0.12 -0.12
$E_\mathrm{T}^\mathrm{miss}$ SoftTrk ResoPara	0.16	0.15	0.09	0.07	0.05	-0.20	-0.23	-0.53	-0.58	-0.57	-0.64	-0.60
$E_\mathrm{T}^\mathrm{miss}$ SoftTrk ResoPerp	0.24	0.25	0.18	0.09	-0.00	-0.08	-0.09	-0.15	-0.10	-0.08	-0.12	-0.05
Muon Resolution MS	-0.04 0.04	-0.24 0.24	-0.33 0.33	-0.24 0.24	-0.08 0.08	-0.15 0.15	-0.16 0.17	-0.30 0.30	-0.35 0.36	-0.34 0.34	-0.32 0.32	-0.30 0.31
Muon Scale	0.19 -0.18	0.20 -0.19	0.23 -0.23	0.27 -0.27	0.32 -0.32	0.66 -0.65	0.69 -0.69	0.81 -0.80	0.80 -0.79	0.65 -0.64	0.48 -0.47	0.40 -0.40
Muon SF Identification Syst	-1.50 1.55	-1.48 1.52	-1.44 1.48	-1.37 1.41	-1.33 1.37	-1.50 1.55	-1.52 1.57	-1.56 1.61	-1.54 1.58	-1.50 1.55	-1.52 1.57	-1.53 1.58
Muon SF Isolation Syst	-0.65 0.66	-0.65 0.66	-0.64 0.65	-0.63 0.64	-0.61 0.62	-0.60 0.61	-0.59 0.60	-0.59 0.59	-0.58 0.58	-0.56 0.56	-0.55 0.55	-0.54 0.55
Muon SF Trigger Syst	0.84 -0.83	0.84 -0.83	0.83 -0.82	0.82 -0.81	0.76 -0.75	0.57 -0.56	0.55 -0.54	0.53 -0.53	0.56 -0.55	0.55 -0.55	0.53 -0.52	0.52 -0.52
Bad Muon	0.03 -0.03	0.03 -0.03	0.03 -0.03	0.03 -0.03	0.03 -0.03	-0.01 0.01	-0.02 0.02	-0.05 0.05	-0.07 0.07	-0.10 0.10	-0.15 0.15	-0.18 0.18
Muon Sagitta Global	1.43 -1.39	1.43 -1.39	1.40 -1.36	1.35 -1.31	1.29 -1.26	1.47 -1.43	1.48 -1.44	1.54 -1.50	1.53 -1.48	1.52 -1.47	1.53 -1.48	1.54 -1.49
Muon Sagitta p_T-extra	-0.02 0.02	-0.02 0.02	-0.04 0.04	-0.03 0.03	-0.07 0.07	0.96 -0.94	1.11 -1.08	1.86 -1.79	2.30 -2.19	2.66 -2.52	2.88 -2.72	2.80 -2.65
Pile-up	0.06 -0.06	0.06 -0.06	0.08 -0.08	0.10 -0.10	0.15 -0.15	-0.10 0.10	-0.12 0.12	-0.14 0.14	-0.02 0.02	0.17 -0.17	0.33 -0.33	0.43 -0.43
Multijet $E_\mathrm{T}^\mathrm{miss}$	-0.30 0.04	-0.30 0.04	-0.25 0.04	-0.21 0.03	-0.18 0.03	-0.34 0.05	-0.36 0.06	-0.57 0.07	-0.40 0.03	-0.63 0.02	-0.52 0.01	-0.29 -0.00
Multijet d_0^sig	0.15 -0.57	0.15 -0.59	0.13 -0.51	0.11 -0.42	0.09 -0.33	0.28 -0.31	0.30 -0.31	0.49 -0.45	0.22 -0.33	0.22 -0.56	0.15 -0.47	0.08 -0.26
Multijet MC Scaling	0.79 -0.79	0.79 -0.79	0.66 -0.66	0.55 -0.55	0.44 -0.44	0.40 -0.40	0.40 -0.40	0.50 -0.50	0.25 -0.25	0.29 -0.29	0.21 -0.21	0.12 -0.12
Multijet Jet Mult	-0.57 0.17	-0.59 0.17	-0.48 0.14	-0.40 0.11	-0.36 0.10	-0.11 0.34	-0.08 0.37	-0.10 0.47	-0.19 0.17	-0.31 0.19	-0.16 0.16	-0.17 0.05
Multijet MC Shape	-0.06	-0.09	-0.06	-0.06	-0.06	0.47	0.54	0.71	0.31	0.50	0.38	0.18
Multijet $\Delta\phi(\mu, E_\mathrm{T}^\mathrm{miss})$	-0.72 0.47	-0.79 0.48	-0.61 0.39	-0.52 0.32	-0.45 0.29	-0.37 0.23	-0.36 0.23	-0.43 0.21	-0.35 0.16	-0.42 0.35	-0.22 0.27	-0.24 0.10
$t\bar{t}$ p_T-hard	-0.54 0.00	-0.52 0.00	-0.38 0.00	-0.09 0.00	0.07 0.00	-0.06 0.00	-0.07 0.00	-0.26 0.00	-0.27 0.00	-0.02 0.00	0.20 0.00	0.24 0.00
$t\bar{t}$ FSR	0.57 -0.57	0.34 -0.34	0.18 -0.18	0.03 -0.03	-0.04 0.04	0.02 -0.02	0.03 -0.03	0.06 -0.06	0.08 -0.08	0.13 -0.13	0.23 -0.23	0.29 -0.29
$t\bar{t}$ scales $\mu_R\,\mu_F$	-0.93 1.31	-0.88 1.24	-0.84 1.17	-0.82 1.10	-0.73 0.92	-0.63 0.74	-0.62 0.71	-0.53 0.62	-0.43 0.52	-0.29 0.35	-0.22 0.22	-0.15 0.08
$t\bar{t}$ hadronization	0.90 0.00	0.59 0.00	0.44 0.00	0.39 0.00	0.34 0.00	0.34 0.00	0.33 0.00	0.43 0.00	0.45 0.00	0.39 0.00	0.45 0.00	0.54 0.00
$t\bar{t}$ hdamp	-0.05 0.00	-0.18 0.00	-0.22 0.00	-0.18 0.00	-0.11 0.00	-0.08 0.00	-0.07 0.00	-0.07 0.00	-0.08 0.00	-0.06 0.00	-0.05 0.00	-0.04 0.00
$t\bar{t}$ PDF	-0.59 0.59	-0.57 0.57	-0.56 0.56	-0.56 0.56	-0.53 0.53	-0.53 0.53	-0.53 0.53	-0.55 0.55	-0.59 0.59	-0.60 0.60	-0.64 0.64	-0.68 0.68
tW DR	-1.13	-1.10	-1.11	-1.12	-0.84	-0.47	-0.42	-0.36	-0.35	-0.29	-0.26	-0.25
tW DS hdamp	-0.09	-0.01	0.04	0.04	0.01	-0.05	-0.05	-0.07	-0.07	-0.04	-0.01	0.00
Norm. $W \to \tau\nu$ by 5%	-0.11 0.11	-0.09 0.09	-0.09 0.09	-0.08 0.08	-0.09 0.09	-0.08 0.08	-0.07 0.07	-0.07 0.07	-0.07 0.07	-0.07 0.07	-0.06 0.06	-0.08 0.06
Norm. Single top by 4%	-0.19 0.19	-0.18 0.18	-0.18 0.18	-0.18 0.18	-0.15 0.15	-0.13 0.13	-0.12 0.12	-0.11 0.11	-0.09 0.09	-0.07 0.07	-0.05 0.05	-0.05 0.05
Norm. Diboson by 6%	-0.27 0.27	-0.26 0.26	-0.24 0.24	-0.26 0.26	-0.24 0.24	-0.21 0.21	-0.21 0.21	-0.21 0.21	-0.22 0.22	-0.21 0.21	-0.15 0.15	-0.19 0.19
Norm. $Z \to \ell\ell$ by 5%	-0.22 0.22	-0.23 0.23	-0.26 0.26	-0.32 0.32	-0.36 0.36	-0.54 0.54	-0.56 0.56	-0.74 0.74	-0.87 0.87	-1.01 1.01	-1.29 1.29	-1.38 1.38

Table 10.5.: Born-level double-differential cross-section $\frac{d^2\sigma(W^+\to\mu^+\nu)}{dm_T^W d|\eta(\mu)|}$ including statistical and systematic uncertainties in percent for $m_T^W = [425 - 600]\,\text{GeV}$. The upper (lower) row corresponds to the one standard deviation upward (downward) shift of the uncertainty source.

$|\eta(\mu)|$	0.0 - 0.4	0.4 - 0.8	0.8 - 1.2	1.2 - 1.6	1.6 - 2.0	2.0 - 2.4
σ [pb/GeV]	3.44e-04	3.33e-04	2.98e-04	2.23e-04	1.63e-04	9.89e-05
Data stat. unc.	2.84	2.34	1.99	3.12	3.52	5.23
Sig. stat. unc.	1.38	1.28	1.19	2.39	1.73	1.28
Bkg. stat. unc.	0.47	0.37	0.32	0.58	0.71	1.21
Tot. sys. unc.	2.57 / -2.82	2.21 / -2.26	2.35 / -2.42	5.31 / -5.03	6.83 / -6.24	7.59 / -6.83
Alt. MC unf. unc.	-0.72	-0.75	-0.84	-0.75	0.01	1.45
Basic unf. unc.	-0.03	0.01	0.22	0.52	0.67	0.69
JES Flavor Composition	-0.04 / 0.04	0.03 / -0.03	0.11 / -0.11	0.51 / -0.51	0.51 / -0.51	0.49 / -0.48
JES Pileup RhoTopology	0.04 / -0.04	0.04 / -0.04	0.06 / -0.06	0.17 / -0.16	0.15 / -0.15	0.14 / -0.14
JES Pileup OffsetMu	0.04 / -0.04	0.05 / -0.05	0.05 / -0.05	0.11 / -0.11	0.06 / -0.06	0.04 / -0.04
JES Pileup OffsetNPV	-0.05 / 0.05	-0.00 / 0.00	0.00 / -0.00	0.04 / -0.04	0.00 / -0.00	-0.01 / 0.01
JES EtaIntercalib Model	0.01 / -0.01	0.02 / -0.02	0.03 / -0.03	0.08 / -0.08	0.03 / -0.03	-0.01 / 0.01
JES Flavor Response	-0.12 / 0.12	-0.13 / 0.13	-0.12 / 0.12	-0.14 / 0.14	-0.10 / 0.10	-0.10 / 0.10
JER EffectiveNP 1	0.51 / -0.51	0.27 / -0.27	0.23 / -0.23	0.06 / -0.06	-0.00 / 0.00	-0.03 / 0.03
JER EffectiveNP 2	0.45 / -0.45	0.22 / -0.22	0.11 / -0.11	-0.40 / 0.40	-0.51 / 0.52	-0.53 / 0.54
JER EffectiveNP 3	0.01 / -0.01	-0.00 / 0.00	0.05 / -0.05	0.03 / -0.03	0.02 / -0.02	0.00 / -0.00
JER EffectiveNP 4	-0.01 / 0.01	-0.01 / 0.01	0.01 / -0.01	-0.01 / 0.01	-0.08 / 0.08	-0.10 / 0.10
JER EffectiveNP 5	0.50 / -0.49	0.15 / -0.15	0.13 / -0.13	0.01 / -0.01	0.02 / -0.02	0.02 / -0.02
JER EffectiveNP 6	0.02 / -0.02	0.01 / -0.01	0.03 / -0.03	0.05 / -0.05	0.09 / -0.09	0.07 / -0.07
JER EffectiveNP 7rest	0.01 / -0.01	0.00 / -0.00	0.04 / -0.04	0.06 / -0.06	0.10 / -0.10	0.10 / -0.10
JER DataVsMC MC16	0.02 / -0.02	0.01 / -0.01	0.03 / -0.03	0.06 / -0.06	0.06 / -0.06	0.06 / -0.06
E_T^{miss} SoftTrk Scale	-0.07 / 0.07	-0.08 / 0.08	-0.12 / 0.12	-0.20 / 0.20	-0.08 / 0.08	-0.00 / -0.00
E_T^{miss} SoftTrk ResoPara	-0.23	-0.15	-0.13	-0.10	0.03	0.07
E_T^{miss} SoftTrk ResoPerp	-0.13	-0.06	-0.09	-0.11	0.05	0.18
Muon Resolution MS	0.08 / -0.08	0.04 / -0.04	-0.06 / 0.07	-0.64 / 0.65	-0.80 / 0.82	-0.82 / 0.84
Muon Scale	0.22 / -0.22	0.20 / -0.20	0.28 / -0.28	0.59 / -0.58	0.66 / -0.65	0.65 / -0.64
Muon SF Identification Syst	-0.87 / 0.89	-0.84 / 0.85	-0.97 / 0.99	-1.58 / 1.63	-1.81 / 1.88	-1.83 / 1.90
Muon SF Isolation Syst	-0.65 / 0.66	-0.64 / 0.65	-0.63 / 0.64	-0.62 / 0.63	-0.61 / 0.61	-0.59 / 0.60
Muon SF Trigger Syst	0.73 / -0.72	0.68 / -0.67	0.64 / -0.63	0.49 / -0.48	0.50 / -0.50	0.56 / -0.55
Bad Muon	0.02 / -0.02	0.03 / -0.03	0.01 / -0.01	-0.08 / 0.08	-0.17 / 0.17	-0.27 / 0.27
Muon Sagitta Global	1.11 / -1.09	1.07 / -1.05	1.23 / -1.20	1.96 / -1.89	2.26 / -2.17	2.33 / -2.23
Muon Sagitta p_T-extra	-0.02 / 0.02	-0.19 / 0.19	0.66 / -0.64	4.28 / -3.95	5.82 / -5.22	6.37 / -5.66
Pile-up	-0.02 / 0.02	0.03 / -0.03	0.05 / -0.05	0.09 / -0.09	0.03 / -0.03	0.04 / -0.04
Multijet E_T^{miss}	-0.18 / 0.00	-0.12 / 0.00	-0.15 / 0.00	-0.35 / 0.02	-0.35 / 0.02	-1.01 / 0.04
Multijet d_0^{sig}	0.11 / -0.47	0.07 / -0.33	0.09 / -0.34	0.19 / -0.44	0.14 / -0.33	0.33 / -0.89
Multijet MC Scaling	0.56 / -0.56	0.35 / -0.35	0.30 / -0.30	0.21 / -0.21	0.14 / -0.14	0.43 / -0.43
Multijet Jet Mult	-0.40 / 0.10	-0.29 / 0.05	-0.23 / 0.08	-0.01 / 0.22	-0.07 / 0.13	-0.24 / 0.32
Multijet MC Shape	-0.10	-0.09	-0.01	0.39	0.30	0.74
Multijet $\Delta\phi(\mu, E_T^{\text{miss}})$	-0.59 / 0.34	-0.42 / 0.25	-0.36 / 0.21	-0.17 / 0.06	-0.11 / 0.21	-0.29 / 0.58
$t\bar{t}$ p_T-hard	0.47 / 0.00	0.14 / 0.00	0.16 / 0.00	-0.04 / 0.00	-0.01 / 0.00	0.00 / 0.00
$t\bar{t}$ FSR	0.27 / -0.27	0.22 / -0.22	0.19 / -0.19	0.12 / -0.12	0.28 / -0.28	0.46 / -0.46
$t\bar{t}$ scales μ_R μ_F	-0.76 / 0.87	-0.65 / 0.80	-0.59 / 0.71	-0.37 / 0.45	-0.26 / 0.30	-0.19 / 0.22
$t\bar{t}$ hadronization	0.98 / 0.00	0.84 / 0.00	0.70 / 0.00	0.12 / 0.00	-0.12 / 0.00	-0.27 / 0.00
$t\bar{t}$ hdamp	0.37 / 0.00	0.23 / 0.00	0.18 / 0.00	-0.16 / 0.00	-0.29 / 0.00	-0.41 / 0.00
$t\bar{t}$ PDF	-0.34 / 0.34	-0.32 / 0.32	-0.33 / 0.33	-0.39 / 0.39	-0.47 / 0.47	-0.58 / 0.58
tW DR	-1.28	-0.62	-0.51	-0.20	-0.17	-0.13
tW DS hdamp	-0.29	-0.02	0.05	0.33	0.34	0.29
Norm. $W \to \tau\nu$ by 5%	-0.08 / 0.08	-0.08 / 0.08	-0.08 / 0.08	-0.08 / 0.08	-0.07 / 0.07	-0.05 / 0.05
Norm. Single top by 4%	-0.12 / 0.12	-0.11 / 0.11	-0.10 / 0.10	-0.08 / 0.08	-0.06 / 0.06	-0.05 / 0.05
Norm. Diboson by 6%	-0.22 / 0.22	-0.21 / 0.21	-0.21 / 0.21	-0.19 / 0.19	-0.19 / 0.19	-0.18 / 0.18
Norm. $Z \to \ell\ell$ by 5%	-0.22 / 0.22	-0.25 / 0.25	-0.32 / 0.32	-0.57 / 0.57	-0.78 / 0.78	-0.98 / 0.98

Table 10.6.: Born-level double-differential cross-section $\frac{d^2\sigma(W^+\to\mu^+\nu)}{dm_{\mathrm{T}}^{\mathrm{W}}\,d|\eta(\mu)|}$ including statistical and systematic uncertainties in percent for $m_{\mathrm{T}}^{\mathrm{W}} = [600-900]\,\mathrm{GeV}$. The upper (lower) row corresponds to the one standard deviation upward (downward) shift of the uncertainty source.

$|\eta(\mu)|$	0.0 - 0.4	0.4 - 0.8	0.8 - 1.2	1.2 - 1.6	1.6 - 2.0	2.0 - 2.4
σ [pb/GeV]	7.23e-05	6.18e-05	5.28e-05	3.91e-05	1.88e-05	9.22e-06
Data stat. unc.	4.48	3.98	3.35	5.49	7.71	12.86
Sig. stat. unc.	2.02	2.56	2.22	4.09	1.30	2.32
Bkg. stat. unc.	0.59	0.48	0.41	0.75	1.40	1.07
Tot. sys. unc.	2.74 / -3.07	2.74 / -3.01	2.93 / -3.14	6.83 / -6.43	9.68 / -8.58	11.95 / -10.16
Alt. MC unf. unc.	-1.45	-1.39	-1.19	-0.81	-0.42	-0.26
Basic unf. unc.	-0.19	-0.19	-0.59	-1.38	-1.78	-1.78
JES Flavor Composition	0.21 / -0.21	0.20 / -0.19	0.19 / -0.19	0.19 / -0.19	0.18 / -0.18	0.24 / -0.24
JES Pileup RhoTopology	0.08 / -0.08	0.08 / -0.08	0.07 / -0.07	0.06 / -0.06	0.08 / -0.08	0.08 / -0.08
JES Pileup OffsetMu	0.05 / -0.05	0.04 / -0.04	0.04 / -0.04	0.03 / -0.03	-0.03 / 0.03	-0.03 / 0.03
JES Pileup OffsetNPV	0.02 / -0.02	0.04 / -0.04	0.04 / -0.04	0.03 / -0.03	-0.00 / 0.00	0.01 / -0.01
JES EtaIntercalib Model	0.11 / -0.11	0.10 / -0.10	0.08 / -0.08	0.04 / -0.04	-0.02 / 0.02	-0.03 / 0.03
JES Flavor Response	-0.05 / 0.05	-0.02 / 0.02	-0.02 / 0.02	-0.02 / 0.02	-0.06 / 0.06	-0.12 / 0.12
JER EffectiveNP 1	0.15 / -0.15	0.15 / -0.15	0.16 / -0.16	0.13 / -0.13	0.11 / -0.11	0.18 / -0.18
JER EffectiveNP 2	0.14 / -0.14	0.14 / -0.14	0.12 / -0.12	-0.07 / 0.07	-0.04 / 0.04	0.10 / -0.10
JER EffectiveNP 3	0.12 / -0.12	0.06 / -0.06	0.07 / -0.07	0.04 / -0.04	0.16 / -0.15	0.43 / -0.43
JER EffectiveNP 4	0.20 / -0.20	0.09 / -0.09	0.08 / -0.08	0.01 / -0.01	0.14 / -0.14	0.46 / -0.45
JER EffectiveNP 5	0.18 / -0.18	0.04 / -0.04	0.04 / -0.04	0.04 / -0.04	0.11 / -0.11	0.18 / -0.18
JER EffectiveNP 6	0.06 / -0.06	0.01 / -0.01	0.02 / -0.02	0.02 / -0.02	0.06 / -0.06	0.09 / -0.09
JER EffectiveNP 7rest	0.17 / -0.17	0.05 / -0.05	0.05 / -0.05	-0.02 / 0.02	-0.02 / 0.02	-0.01 / 0.01
JER DataVsMC MC16	0.13 / -0.13	0.08 / -0.08	0.07 / -0.07	0.02 / -0.02	0.14 / -0.14	0.50 / -0.49
$E_{\mathrm{T}}^{\mathrm{miss}}$ SoftTrk Scale	-0.13 / 0.13	-0.16 / 0.16	-0.13 / 0.13	-0.06 / 0.06	0.13 / -0.13	0.20 / -0.20
$E_{\mathrm{T}}^{\mathrm{miss}}$ SoftTrk ResoPara	0.02	-0.09	-0.09	-0.11	0.02	-0.00
$E_{\mathrm{T}}^{\mathrm{miss}}$ SoftTrk ResoPerp	-0.06	-0.10	-0.09	-0.05	0.09	0.10
Muon Resolution MS	-0.04 / 0.04	-0.05 / 0.05	-0.12 / 0.12	-0.44 / 0.45	-0.58 / 0.58	-0.91 / 0.92
Muon Scale	0.11 / -0.11	0.11 / -0.11	0.20 / -0.20	0.63 / -0.62	0.68 / -0.67	0.69 / -0.68
Muon SF Identification Syst	-1.39 / 1.43	-1.36 / 1.40	-1.43 / 1.48	-1.84 / 1.91	-1.85 / 1.93	-1.83 / 1.90
Muon SF Isolation Syst	-0.59 / 0.60	-0.58 / 0.59	-0.58 / 0.59	-0.57 / 0.58	-0.55 / 0.56	-0.54 / 0.55
Muon SF Trigger Syst	0.67 / -0.66	0.63 / -0.62	0.60 / -0.59	0.46 / -0.46	0.49 / -0.48	0.54 / -0.53
Bad Muon	0.01 / -0.01	0.03 / -0.03	-0.01 / 0.01	-0.17 / 0.17	-0.30 / 0.31	-0.45 / 0.45
Muon Sagitta Global	1.80 / -1.74	1.89 / -1.82	2.02 / -1.94	2.70 / -2.57	2.96 / -2.80	3.51 / -3.28
Muon Sagitta p_{T}-extra	-0.01 / 0.01	-0.30 / 0.30	0.73 / -0.70	5.81 / -5.20	8.85 / -7.51	11.10 / -9.07
Pile-up	0.44 / -0.43	0.31 / -0.31	0.30 / -0.29	0.21 / -0.21	0.26 / -0.26	0.40 / -0.40
Multijet $E_{\mathrm{T}}^{\mathrm{miss}}$	-0.07 / -0.00	-0.04 / -0.00	-0.03 / -0.00	-0.02 / 0.00	-0.29 / 0.03	0.04 / -0.00
Multijet d_0^{sig}	0.05 / -0.21	0.02 / -0.12	0.02 / -0.09	0.00 / -0.01	0.14 / -0.24	-0.01 / 0.03
Multijet MC Scaling	0.24 / -0.24	0.13 / -0.13	0.10 / -0.10	-0.02 / 0.02	0.14 / -0.14	-0.02 / 0.02
Multijet Jet Mult	-0.17 / 0.03	-0.11 / 0.01	-0.08 / 0.00	0.04 / -0.00	-0.04 / 0.14	0.02 / -0.01
Multijet MC Shape	-0.05	-0.05	-0.03	0.03	0.27	-0.03
Multijet $\Delta\phi(\mu, E_{\mathrm{T}}^{\mathrm{miss}})$	-0.26 / 0.15	-0.16 / 0.10	-0.13 / 0.08	0.03 / -0.02	-0.10 / 0.11	0.02 / -0.02
$t\bar{t}$ p_{T}-hard	-0.15 / 0.00	-0.15 / 0.00	-0.15 / 0.00	-0.12 / 0.00	-0.11 / 0.00	-0.06 / 0.00
$t\bar{t}$ FSR	0.21 / -0.21	0.22 / -0.22	0.21 / -0.21	0.17 / -0.17	0.16 / -0.16	0.05 / -0.05
$t\bar{t}$ scales μ_R μ_F	-0.44 / 0.79	-0.43 / 0.77	-0.41 / 0.74	-0.32 / 0.58	-0.32 / 0.58	-0.13 / 0.24
$t\bar{t}$ hadronization	0.30 / 0.00	0.32 / 0.00	0.30 / 0.00	0.21 / 0.00	0.21 / 0.00	0.07 / 0.00
$t\bar{t}$ hdamp	-0.41 / 0.00	-0.38 / 0.00	-0.37 / 0.00	-0.32 / 0.00	-0.30 / 0.00	-0.12 / 0.00
$t\bar{t}$ PDF	-0.22 / 0.22	-0.24 / 0.24	-0.24 / 0.24	-0.24 / 0.24	-0.38 / 0.38	-0.18 / 0.18
tW DR	-0.57	-0.47	-0.47	-0.38	-0.30	-0.28
tW DS hdamp	0.05	0.03	0.05	0.22	0.18	0.18
Norm. $W\to\tau\nu$ by 5%	-0.07 / 0.07	-0.07 / 0.07	-0.07 / 0.07	-0.06 / 0.06	-0.05 / 0.05	-0.04 / 0.04
Norm. Single top by 4%	-0.07 / 0.07	-0.05 / 0.05	-0.04 / 0.04	-0.03 / 0.03	-0.03 / 0.03	-0.02 / 0.02
Norm. Diboson by 6%	-0.17 / 0.17	-0.18 / 0.18	-0.17 / 0.17	-0.15 / 0.15	-0.18 / 0.18	-0.09 / 0.09
Norm. $Z\to\ell\ell$ by 5%	-0.18 / 0.18	-0.20 / 0.20	-0.22 / 0.22	-0.35 / 0.35	-0.56 / 0.56	-0.57 / 0.57

Table 10.7.: Born-level double-differential cross-section $\frac{d^2\sigma(W^+ \to \mu^+\nu)}{dm_{\mathrm{T}}^{\mathrm{W}} d|\eta(\mu)|}$ including statistical and systematic uncertainties in percent for $m_{\mathrm{T}}^{\mathrm{W}} = [900 - 2000]\,\mathrm{GeV}$. The upper (lower) row corresponds to the one standard deviation upward (downward) shift of the uncertainty source.

$|\eta(\mu)|$	0.0 - 0.6	0.6 - 1.2	1.2 - 1.8	1.8 - 2.4
σ [pb/GeV]	4.91e-06	3.37e-06	9.52e-07	1.81e-07
Data stat. unc.	7.18	9.28	14.85	34.67
Sig. stat. unc.	5.72	0.60	1.32	2.99
Bkg. stat. unc.	0.60	0.76	1.61	3.74
Tot. sys. unc.	4.67 / -4.23	5.56 / -4.54	22.48 / -16.20	42.50 / -24.51
Alt. MC unf. unc.	-0.89	-1.30	-1.65	-2.06
Basic unf. unc.	1.44	3.01	6.67	9.83
JES Flavor Composition	0.19 / -0.19	-0.01 / 0.01	0.03 / -0.03	0.12 / -0.12
JES Pileup RhoTopology	0.11 / -0.11	0.04 / -0.04	-0.01 / 0.01	0.20 / -0.20
JES Pileup OffsetMu	0.10 / -0.10	0.00 / -0.00	0.04 / -0.04	-0.17 / 0.17
JES Pileup OffsetNPV	0.01 / -0.01	-0.00 / 0.00	0.03 / -0.03	-0.06 / 0.06
JES EtaIntercalib Model	0.11 / -0.11	0.01 / -0.01	0.04 / -0.04	0.02 / -0.02
JES Flavor Response	-0.06 / 0.06	-0.03 / 0.03	-0.06 / 0.06	0.15 / -0.15
JER EffectiveNP 1	-0.14 / 0.14	0.27 / -0.27	-0.15 / 0.15	0.73 / -0.72
JER EffectiveNP 2	-0.34 / 0.35	0.15 / -0.15	-0.08 / 0.08	1.40 / -1.36
JER EffectiveNP 3	-0.21 / 0.21	0.17 / -0.17	-0.16 / 0.17	0.54 / -0.54
JER EffectiveNP 4	-0.19 / 0.19	0.19 / -0.19	-0.29 / 0.29	1.14 / -1.11
JER EffectiveNP 5	-0.09 / 0.09	0.21 / -0.21	-0.23 / 0.23	0.59 / -0.59
JER EffectiveNP 6	-0.18 / 0.18	0.22 / -0.22	-0.17 / 0.17	0.69 / -0.68
JER EffectiveNP 7rest	-0.19 / 0.19	0.21 / -0.21	-0.19 / 0.19	1.18 / -1.15
JER DataVsMC MC16	-0.05 / 0.05	0.03 / -0.03	-0.00 / 0.00	-0.29 / 0.29
$E_{\mathrm{T}}^{\mathrm{miss}}$ SoftTrk Scale	-0.16 / 0.16	0.12 / -0.12	0.01 / -0.01	0.48 / -0.47
$E_{\mathrm{T}}^{\mathrm{miss}}$ SoftTrk ResoPara	-0.19	0.01	0.22	0.15
$E_{\mathrm{T}}^{\mathrm{miss}}$ SoftTrk ResoPerp	-0.11	-0.10	0.07	-0.05
Muon Resolution MS	-0.25 / 0.25	-0.76 / 0.77	-1.72 / 1.78	-1.52 / 1.57
Muon Scale	0.18 / -0.18	0.41 / -0.40	1.08 / -1.06	1.21 / -1.18
Muon SF Identification Syst	-1.66 / 1.72	-1.63 / 1.68	-4.71 / 5.18	-4.43 / 4.85
Muon SF Isolation Syst	-0.56 / 0.57	-0.54 / 0.55	-0.53 / 0.54	-0.55 / 0.55
Muon SF Trigger Syst	0.63 / -0.63	0.61 / -0.60	0.46 / -0.46	0.47 / -0.47
Bad Muon	0.03 / -0.03	-0.03 / 0.03	-0.70 / 0.71	-0.82 / 0.83
Muon Sagitta Global	3.88 / -3.61	4.03 / -3.73	5.43 / -4.91	8.34 / -7.18
Muon Sagitta p_{T}-extra	-0.05 / 0.05	0.79 / -0.71	19.80 / -14.41	40.03 / -22.62
Pile-up	0.07 / -0.07	0.11 / -0.11	-0.10 / 0.10	1.42 / -1.38
Multijet $E_{\mathrm{T}}^{\mathrm{miss}}$	-0.00 / -0.00	-0.02 / -0.00	0.04 / 0.00	0.07 / -0.00
Multijet d_0^{sig}	-0.00 / -0.03	0.02 / -0.09	-0.02 / 0.06	-0.03 / 0.06
Multijet MC Scaling	0.03 / -0.03	0.10 / -0.10	-0.04 / 0.04	-0.03 / 0.03
Multijet Jet Mult	-0.01 / -0.02	-0.07 / 0.01	0.03 / -0.03	0.02 / -0.03
Multijet MC Shape	-0.02	-0.03	-0.03	-0.05
Multijet $\Delta\phi(\mu, E_{\mathrm{T}}^{\mathrm{miss}})$	-0.04 / 0.02	-0.11 / 0.06	0.04 / -0.03	0.03 / -0.04
$t\bar{t}$ p_{T}-hard	-0.07 / 0.00	-0.06 / 0.00	-0.10 / 0.00	-0.06 / 0.00
$t\bar{t}$ FSR	0.05 / -0.05	0.06 / -0.06	0.12 / -0.12	0.05 / -0.05
$t\bar{t}$ scales μ_R μ_F	-0.11 / 0.22	-0.12 / 0.23	-0.24 / 0.44	-0.15 / 0.28
$t\bar{t}$ hadronization	0.07 / 0.00	0.08 / 0.00	0.18 / 0.00	0.14 / 0.00
$t\bar{t}$ hdamp	-0.14 / 0.00	-0.14 / 0.00	-0.23 / 0.00	-0.11 / 0.00
$t\bar{t}$ PDF	-0.03 / 0.03	-0.06 / 0.06	-0.29 / 0.29	-0.28 / 0.28
tW DR	0.17	0.02	1.67	0.01
tW DS hdamp	0.55	0.52	1.76	-0.05
Norm. $W \to \tau\nu$ by 5%	-0.06 / 0.06	-0.06 / 0.06	-0.06 / 0.06	-0.03 / 0.03
Norm. Single top by 4%	-0.02 / 0.02	-0.03 / 0.03	-0.11 / 0.11	0.01 / -0.01
Norm. Diboson by 6%	-0.16 / 0.16	-0.13 / 0.13	-0.36 / 0.36	-0.17 / 0.17
Norm. $Z \to \ell\ell$ by 5%	-0.13 / 0.13	-0.16 / 0.16	-0.37 / 0.37	-0.37 / 0.37

Table 10.8.: Born-level double-differential cross-section $\frac{d^2\sigma(W^-\to\mu^-\bar{\nu})}{dm_\mathrm{T}^\mathrm{W}\,d|\eta(\mu)|}$ including statistical and systematic uncertainties in percent for $m_\mathrm{T}^\mathrm{W}=[200-300]\,\mathrm{GeV}$. The upper (lower) row corresponds to the one standard deviation upward (downward) shift of the uncertainty source.

$|\eta(\mu)|$	0.0 - 0.2	0.2 - 0.4	0.4 - 0.6	0.6 - 0.8	0.8 - 1.0	1.0 - 1.2	1.2 - 1.4	1.4 - 1.6	1.6 - 1.8	1.8 - 2.0	2.0 - 2.2	2.2 - 2.4
σ [pb/GeV]	4.16e-03	4.03e-03	4.28e-03	4.00e-03	3.99e-03	4.17e-03	4.09e-03	3.91e-03	3.69e-03	3.66e-03	3.11e-03	2.95e-03
Data stat. unc.	2.09	1.75	1.68	1.88	1.68	1.41	1.53	1.48	1.49	1.53	1.92	1.84
Sig. stat. unc.	1.38	1.56	1.22	1.24	1.48	1.15	1.21	1.41	1.07	1.24	1.48	1.29
Bkg. stat. unc.	0.49	0.42	0.40	0.45	0.40	0.35	0.38	0.35	0.35	0.34	0.41	0.37
Tot. sys. unc.	4.12 / -4.01	3.99 / -3.83	3.78 / -3.47	3.54 / -3.21	3.23 / -2.90	3.42 / -2.84	3.59 / -2.90	3.85 / -3.28	4.01 / -3.68	3.84 / -3.63	3.90 / -3.60	3.99 / -3.50
Alt. MC unf. unc.	0.13	0.25	0.48	0.60	0.85	1.34	1.59	1.59	1.49	1.30	1.20	1.20
Basic unf. unc.	0.39	0.38	0.37	0.37	0.35	0.31	0.27	0.26	0.35	0.50	0.62	0.66
JES Flavor Composition	0.48	0.38	0.28	0.28	0.36	0.41	0.40	0.51	0.54	0.56	0.52	0.55
	-0.48	-0.38	-0.28	-0.28	-0.36	-0.41	-0.40	-0.51	-0.54	-0.56	-0.52	-0.55
JES Pileup RhoTopology	0.58	0.56	0.47	0.38	0.28	0.12	0.10	0.14	0.19	0.28	0.35	0.39
	-0.58	-0.55	-0.47	-0.38	-0.28	-0.12	-0.10	-0.14	-0.19	-0.28	-0.35	-0.39
JES Pileup OffsetMu	-0.45	-0.46	-0.48	-0.40	-0.23	-0.18	-0.18	-0.29	-0.38	-0.27	-0.11	0.06
	0.45	0.46	0.49	0.40	0.23	0.18	0.18	0.29	0.38	0.27	0.11	-0.06
JES Pileup OffsetNPV	-0.06	-0.05	-0.07	-0.06	0.02	0.01	0.01	-0.04	-0.08	-0.05	-0.02	0.03
	0.06	0.05	0.07	0.06	-0.02	-0.01	-0.01	0.04	0.08	0.05	0.02	-0.03
JES EtaIntercalib Model	-0.06	-0.01	0.06	0.13	0.23	0.04	0.01	-0.21	-0.28	-0.07	0.24	0.52
	0.06	0.01	-0.06	-0.14	-0.23	-0.05	-0.01	0.21	0.28	0.07	-0.24	-0.51
JES Flavor Response	-0.83	-0.85	-0.76	-0.54	-0.34	-0.24	-0.22	-0.25	-0.31	-0.38	-0.46	-0.68
	0.85	0.86	0.77	0.55	0.34	0.24	0.23	0.25	0.31	0.39	0.47	0.68
JER EffectiveNP 1	-0.75	-0.70	-0.56	-0.22	-0.03	-0.55	-0.62	-0.76	-0.85	-0.81	-0.82	-0.76
	0.76	0.71	0.56	0.22	0.02	0.55	0.62	0.77	0.86	0.82	0.83	0.77
JER EffectiveNP 2	-0.60	-0.53	-0.32	0.05	0.23	-0.55	-0.63	-0.79	-0.77	-0.52	-0.08	0.18
	0.61	0.53	0.33	-0.05	-0.23	0.55	0.64	0.81	0.78	0.52	0.08	-0.18
JER EffectiveNP 3	-0.05	0.06	0.12	0.16	0.17	-0.14	-0.18	-0.27	-0.15	0.11	0.32	0.41
	0.05	-0.06	-0.12	-0.16	-0.17	0.14	0.18	0.27	0.15	-0.11	-0.32	-0.40
JER EffectiveNP 4	0.01	0.04	0.08	0.15	0.22	-0.16	-0.20	-0.38	-0.29	-0.02	0.27	0.61
	-0.01	-0.04	-0.08	-0.15	-0.22	0.16	0.20	0.38	0.29	0.02	-0.27	-0.60
JER EffectiveNP 5	-0.03	0.09	0.14	0.14	0.13	0.01	0.00	-0.03	-0.04	-0.00	0.03	0.09
	0.03	-0.09	-0.14	-0.14	-0.13	-0.01	-0.00	0.03	0.04	0.00	-0.03	-0.09
JER EffectiveNP 6	-0.27	-0.23	-0.12	0.06	0.15	-0.11	-0.14	-0.27	-0.27	-0.01	0.36	0.54
	0.28	0.23	0.12	-0.06	-0.15	0.11	0.14	0.27	0.27	0.01	-0.36	-0.53
JER EffectiveNP 7rest	-0.37	-0.21	-0.03	0.22	0.31	-0.24	-0.30	-0.47	-0.27	0.20	0.58	0.71
	0.37	0.21	0.03	-0.21	-0.31	0.24	0.30	0.47	0.28	-0.20	-0.57	-0.70
JER DataVsMC MC16	0.19	0.17	0.12	0.11	0.10	-0.17	-0.20	-0.21	-0.21	-0.19	-0.19	-0.16
	-0.19	-0.17	-0.12	-0.11	-0.10	0.17	0.20	0.21	0.21	0.19	0.19	0.16
$E_\mathrm{T}^\mathrm{miss}$ SoftTrk Scale	1.38	1.33	1.34	1.21	0.90	0.65	0.64	0.76	0.97	0.98	0.95	0.77
	-1.35	-1.29	-1.31	-1.18	-0.89	-0.64	-0.64	-0.75	-0.95	-0.97	-0.94	-0.76
$E_\mathrm{T}^\mathrm{miss}$ SoftTrk ResoPara	1.15	1.12	1.13	1.08	1.01	0.93	0.92	0.80	0.81	0.79	0.86	0.96
$E_\mathrm{T}^\mathrm{miss}$ SoftTrk ResoPerp	0.62	0.83	1.01	0.96	0.77	0.72	0.73	0.76	0.89	0.97	1.03	0.95
Muon Resolution MS	0.02	0.03	0.03	0.03	0.01	-0.09	-0.11	-0.13	-0.14	-0.13	-0.12	-0.12
	-0.02	-0.03	-0.03	-0.03	-0.01	0.09	0.11	0.13	0.14	0.13	0.13	0.12
Muon Scale	0.15	0.15	0.19	0.22	0.34	0.75	0.80	0.84	0.81	0.66	0.53	0.47
	-0.15	-0.15	-0.19	-0.22	-0.34	-0.74	-0.79	-0.83	-0.79	-0.65	-0.53	-0.47
Muon SF Identification Syst	-1.37	-1.31	-1.25	-1.21	-1.17	-1.13	-1.12	-1.09	-1.06	-1.06	-1.07	-1.10
	1.41	1.34	1.28	1.24	1.20	1.15	1.15	1.11	1.09	1.08	1.10	1.13
Muon SF Isolation Syst	-0.35	-0.35	-0.35	-0.34	-0.33	-0.30	-0.30	-0.28	-0.26	-0.24	-0.23	-0.21
	0.36	0.35	0.35	0.34	0.33	0.30	0.30	0.28	0.26	0.24	0.23	0.21
Muon SF Trigger Syst	1.09	1.08	1.07	1.03	0.93	0.72	0.69	0.65	0.62	0.59	0.56	0.52
	-1.07	-1.06	-1.05	-1.01	-0.91	-0.71	-0.68	-0.64	-0.62	-0.58	-0.55	-0.52
Bad Muon	-0.15	-0.14	-0.14	-0.13	-0.12	-0.14	-0.15	-0.15	-0.16	-0.16	-0.20	-0.20
	0.15	0.14	0.14	0.13	0.12	0.15	0.15	0.15	0.16	0.16	0.20	0.20
Muon Sagitta Global	-1.19	-1.07	-0.95	-0.87	-0.85	-0.86	-0.87	-0.88	-0.96	-1.07	-1.13	-1.20
	1.22	1.10	0.97	0.89	0.86	0.88	0.88	0.90	0.98	1.10	1.16	1.23
Muon Sagitta p_T-extra	0.10	0.09	0.08	0.11	0.12	-0.51	-0.60	-1.12	-1.39	-1.51	-1.52	-1.51
	-0.10	-0.09	-0.08	-0.11	-0.12	0.51	0.61	1.15	1.43	1.55	1.57	1.56
Pile-up	-0.19	-0.06	0.14	0.26	0.19	-0.11	-0.15	-0.36	-0.50	-0.38	-0.21	-0.10
	0.19	0.06	-0.14	-0.26	-0.19	0.11	0.15	0.37	0.50	0.39	0.21	0.10
Multijet $E_\mathrm{T}^\mathrm{miss}$	-0.54	-0.50	-0.42	-0.38	-0.33	-0.58	-0.61	-0.77	-1.05	-1.09	-0.94	-0.50
	0.15	0.13	0.11	0.10	0.09	0.13	0.13	0.12	0.07	0.02	0.00	0.00
Multijet d_0^sig	0.21	0.21	0.19	0.16	0.16	0.49	0.53	0.62	0.54	0.36	0.26	0.12
	-0.52	-0.49	-0.43	-0.40	-0.30	-0.30	-0.31	-0.57	-0.91	-0.97	-0.83	-0.43
Multijet MC Scaling	1.10	1.03	0.88	0.82	0.70	0.71	0.71	0.66	0.64	0.52	0.41	0.20
	-1.10	-1.03	-0.88	-0.82	-0.70	-0.71	-0.71	-0.66	-0.64	-0.52	-0.41	-0.20
Multijet Jet Mult	-0.91	-0.86	-0.73	-0.69	-0.62	-0.32	-0.28	-0.23	-0.57	-0.67	-0.56	-0.28
	0.46	0.42	0.37	0.34	0.30	0.66	0.70	0.66	0.50	0.34	0.25	0.12
Multijet MC Shape	0.15	0.12	0.11	0.10	0.07	0.60	0.66	0.69	0.82	0.79	0.62	0.31
Multijet $\Delta\phi(\mu, E_\mathrm{T}^\mathrm{miss})$	-0.73	-0.71	-0.59	-0.56	-0.50	-0.72	-0.75	-0.68	-0.89	-0.88	-0.74	-0.39
	0.49	0.47	0.39	0.37	0.31	0.53	0.55	0.47	0.56	0.46	0.36	0.16
$t\bar{t}$ p_T-hard	-0.28	-0.28	-0.23	-0.16	-0.09	-0.05	-0.05	-0.01	0.01	0.04	0.07	0.06
	0.00	0.00	0.00	0.00	0.00	0.00	0.00	0.00	0.00	0.00	0.00	0.00
$t\bar{t}$ FSR	0.49	0.49	0.45	0.47	0.44	0.34	0.33	0.29	0.33	0.37	0.36	0.26
	-0.49	-0.49	-0.45	-0.47	-0.44	-0.34	-0.33	-0.29	-0.33	-0.37	-0.36	-0.26
$t\bar{t}$ scales μ_R μ_F	-0.93	-0.94	-0.84	-0.82	-0.74	-0.58	-0.56	-0.50	-0.44	-0.32	-0.24	-0.16
	1.31	1.31	1.17	1.12	0.96	0.72	0.69	0.59	0.50	0.36	0.25	0.13
$t\bar{t}$ hadronization	0.22	0.22	0.19	0.19	0.17	0.12	0.12	0.12	0.10	0.08	0.06	0.05
	0.00	0.00	0.00	0.00	0.00	0.00	0.00	0.00	0.00	0.00	0.00	0.00
$t\bar{t}$ hdamp	-0.40	-0.41	-0.31	-0.13	0.03	-0.05	-0.05	-0.15	-0.13	0.04	0.20	0.21
	0.00	0.00	0.00	0.00	0.00	0.00	0.00	0.00	0.00	0.00	0.00	0.00
$t\bar{t}$ PDF	-1.23	-1.21	-1.10	-1.09	-1.00	-0.84	-0.82	-0.80	-0.82	-0.75	-0.87	-0.78
	1.23	1.21	1.10	1.09	1.00	0.84	0.82	0.80	0.82	0.75	0.87	0.78
tW DR	-0.83	-0.78	-0.66	-0.60	-0.57	-0.50	-0.49	-0.41	-0.28	-0.11	0.05	0.18
tW DS hdamp	0.23	0.23	0.20	0.13	0.03	0.05	0.05	0.11	0.14	0.15	0.17	0.25
Norm. $W \to \tau\nu$ by 5%	-0.08	-0.07	-0.07	-0.08	-0.08	-0.07	-0.07	-0.07	-0.07	-0.07	-0.06	-0.07
	0.08	0.07	0.07	0.07	0.08	0.08	0.07	0.07	0.07	0.07	0.06	0.07
Norm. Single top by 4%	-0.33	-0.32	-0.30	-0.29	-0.27	-0.20	-0.19	-0.17	-0.14	-0.11	-0.09	-0.07
	0.33	0.32	0.30	0.29	0.27	0.20	0.19	0.17	0.14	0.11	0.09	0.07
Norm. Diboson by 6%	-0.35	-0.35	-0.33	-0.37	-0.34	-0.16	-0.14	-0.31	-0.33	-0.30	-0.32	-0.30
	0.35	0.35	0.33	0.37	0.34	0.16	0.14	0.31	0.33	0.30	0.32	0.30
Norm. $Z \to \ell\ell$ by 5%	-0.20	-0.21	-0.21	-0.24	-0.27	-0.36	-0.37	-0.45	-0.59	-0.69	-0.97	-1.23
	0.20	0.21	0.21	0.24	0.27	0.36	0.37	0.45	0.59	0.69	0.97	1.23

Table 10.9.: Born-level double-differential cross-section $\frac{d^2\sigma(W^- \to \mu^- \bar\nu)}{dm_T^W \, d|\eta(\mu)|}$ including statistical and systematic uncertainties in percent for $m_T^W = [300 - 425]\,\mathrm{GeV}$. The upper (lower) row corresponds to the one standard deviation upward (downward) shift of the uncertainty source.

$|\eta(\mu)|$	0.0 - 0.2	0.2 - 0.4	0.4 - 0.6	0.6 - 0.8	0.8 - 1.0	1.0 - 1.2	1.2 - 1.4	1.4 - 1.6	1.6 - 1.8	1.8 - 2.0	2.0 - 2.2	2.2 - 2.4
σ [pb/GeV]	7.18e-04	6.86e-04	7.50e-04	7.09e-04	7.20e-04	7.22e-04	7.06e-04	6.97e-04	6.59e-04	6.46e-04	5.33e-04	4.72e-04
Data stat. unc.	4.34	3.68	3.67	4.03	3.53	3.04	3.34	3.01	3.13	3.28	4.06	4.05
Sig. stat. unc.	2.49	3.05	1.59	2.53	1.87	1.84	1.96	2.25	2.18	1.27	1.21	2.73
Bkg. stat. unc.	1.08	0.90	0.83	0.90	0.79	0.77	0.84	0.74	0.77	0.85	1.03	0.84
Tot. sys. unc.	5.93 / -5.18	5.78 / -5.28	4.76 / -4.62	4.17 / -4.42	3.82 / -4.06	4.59 / -4.25	4.87 / -4.40	5.20 / -4.74	5.35 / -4.95	5.61 / -5.35	5.68 / -5.24	5.49 / -4.78
Alt. MC unf. unc.	-0.67	-0.67	-0.67	-0.67	-0.34	0.36	0.86	1.11	1.57	2.20	2.50	2.50
Basic unf. unc.	0.13	0.11	0.06	-0.01	-0.03	0.09	0.29	0.39	0.27	0.04	-0.10	-0.15
JES Flavor Composition	0.70 / -0.69	0.77 / -0.76	0.74 / -0.74	0.72 / -0.71	0.59 / -0.59	0.61 / -0.60	0.61 / -0.61	0.80 / -0.79	0.92 / -0.91	0.82 / -0.81	0.67 / -0.66	0.63 / -0.62
JES Pileup RhoTopology	0.48 / -0.48	0.48 / -0.48	0.40 / -0.40	0.30 / -0.30	0.20 / -0.20	0.28 / -0.28	0.29 / -0.28	0.36 / -0.36	0.34 / -0.34	0.19 / -0.19	0.05 / -0.05	0.01 / -0.01
JES Pileup OffsetMu	0.13 / -0.13	0.16 / -0.16	0.14 / -0.14	0.17 / -0.17	0.13 / -0.13	0.16 / -0.16	0.17 / -0.17	0.19 / -0.19	0.12 / -0.13	0.00 / -0.00	-0.09 / 0.08	-0.09 / 0.09
JES Pileup OffsetNPV	-0.44 / 0.44	-0.30 / 0.30	-0.15 / 0.15	-0.01 / 0.01	0.03 / -0.03	0.11 / -0.11	0.12 / -0.12	0.14 / -0.14	0.10 / -0.10	0.03 / -0.03	-0.01 / 0.01	-0.00 / 0.00
JES EtaIntercalib Model	0.01 / -0.01	0.05 / -0.05	0.11 / -0.11	0.23 / -0.23	0.18 / -0.18	0.16 / -0.16	0.15 / -0.15	0.24 / -0.24	0.23 / -0.23	0.13 / -0.13	0.07 / -0.07	0.09 / -0.09
JES Flavor Response	-0.60 / 0.61	-0.62 / 0.63	-0.57 / 0.58	-0.53 / 0.54	-0.48 / 0.49	-0.54 / 0.55	-0.55 / 0.55	-0.57 / 0.57	-0.51 / 0.52	-0.44 / 0.44	-0.41 / 0.41	-0.40 / 0.41
JER EffectiveNP 1	1.05 / -1.04	1.07 / -1.06	0.73 / -0.73	0.32 / -0.33	-0.01 / 0.01	-0.08 / 0.07	-0.08 / 0.07	0.00 / -0.01	0.28 / -0.29	0.53 / -0.53	0.73 / -0.73	0.99 / -0.99
JER EffectiveNP 2	1.58 / -1.53	1.66 / -1.61	1.06 / -1.04	-0.07 / 0.07	-0.68 / 0.69	-0.62 / 0.62	-0.60 / 0.61	-0.25 / 0.26	0.34 / -0.34	0.59 / -0.59	0.57 / -0.56	0.63 / -0.63
JER EffectiveNP 3	0.62 / -0.61	0.48 / -0.47	0.15 / -0.15	-0.03 / 0.03	-0.10 / 0.10	-0.15 / 0.15	-0.16 / 0.16	-0.07 / 0.07	-0.06 / 0.06	-0.12 / 0.12	-0.15 / 0.15	-0.15 / 0.15
JER EffectiveNP 4	0.07 / -0.07	0.21 / -0.21	0.21 / -0.20	0.07 / -0.07	-0.04 / 0.04	-0.07 / 0.07	-0.07 / 0.07	0.15 / -0.15	0.57 / -0.56	0.74 / -0.73	0.72 / -0.71	0.75 / -0.74
JER EffectiveNP 5	0.18 / -0.18	0.15 / -0.15	0.05 / -0.05	0.00 / -0.00	-0.17 / 0.18	-0.44 / 0.44	-0.47 / 0.47	-0.11 / 0.11	0.40 / -0.40	0.66 / -0.66	0.77 / -0.76	0.92 / -0.91
JER EffectiveNP 6	-0.03 / 0.03	0.04 / -0.04	0.10 / -0.10	0.12 / -0.12	0.07 / -0.07	0.06 / -0.06	0.06 / -0.06	0.21 / -0.21	0.48 / -0.47	0.59 / -0.58	0.58 / -0.57	0.62 / -0.61
JER EffectiveNP 7rest	0.65 / -0.65	0.52 / -0.51	0.16 / -0.16	-0.11 / 0.11	-0.24 / 0.24	-0.22 / 0.22	-0.22 / 0.22	0.04 / -0.04	0.48 / -0.48	0.70 / -0.69	0.70 / -0.69	0.76 / -0.75
JER DataVsMC MC16	0.35 / -0.35	0.34 / -0.33	0.13 / -0.13	-0.19 / 0.19	-0.45 / 0.46	-0.54 / 0.55	-0.55 / 0.56	-0.40 / 0.40	-0.20 / 0.20	-0.05 / 0.05	0.00 / -0.00	0.04 / -0.04
E_T^{miss} SoftTrk Scale	0.27 / -0.28	0.23 / -0.23	0.20 / -0.20	0.03 / -0.04	0.17 / -0.18	0.27 / -0.28	0.27 / -0.27	0.15 / -0.16	0.16 / -0.17	0.26 / -0.26	0.26 / -0.26	0.13 / -0.13
E_T^{miss} SoftTrk ResoPara	0.80	0.58	0.29	-0.05	-0.13	-0.17	-0.19	-0.19	-0.06	0.03	-0.04	-0.15
E_T^{miss} SoftTrk ResoPerp	0.31	0.16	0.03	-0.24	-0.18	0.15	0.18	0.18	0.10	-0.02	-0.13	-0.25
Muon Resolution MS	0.21 / -0.21	-0.08 / 0.08	-0.23 / 0.23	-0.30 / 0.30	-0.35 / 0.35	-0.53 / 0.54	-0.56 / 0.57	-0.64 / 0.64	-0.57 / 0.58	-0.42 / 0.42	-0.33 / 0.33	-0.30 / 0.30
Muon Scale	0.26 / -0.26	0.29 / -0.28	0.33 / -0.32	0.34 / -0.34	0.42 / -0.42	0.73 / -0.72	0.77 / -0.75	0.83 / -0.82	0.79 / -0.78	0.66 / -0.65	0.54 / -0.53	0.47 / -0.47
Muon SF Identification Syst	-1.81 / 1.88	-1.76 / 1.83	-1.69 / 1.75	-1.61 / 1.66	-1.56 / 1.61	-1.73 / 1.79	-1.76 / 1.82	-1.78 / 1.85	-1.73 / 1.79	-1.63 / 1.69	-1.60 / 1.65	-1.61 / 1.66
Muon SF Isolation Syst	-0.80 / 0.81	-0.78 / 0.79	-0.76 / 0.77	-0.74 / 0.76	-0.73 / 0.74	-0.69 / 0.70	-0.69 / 0.70	-0.67 / 0.68	-0.65 / 0.65	-0.61 / 0.62	-0.58 / 0.59	-0.55 / 0.56
Muon SF Trigger Syst	1.04 / -1.02	1.02 / -1.00	1.01 / -0.99	0.97 / -0.95	0.89 / -0.87	0.65 / -0.64	0.62 / -0.62	0.59 / -0.59	0.60 / -0.59	0.58 / -0.57	0.55 / -0.55	0.52 / -0.51
Bad Muon	0.04 / -0.04	0.05 / -0.05	0.03 / -0.03	0.05 / -0.05	0.04 / -0.04	-0.02 / 0.02	-0.02 / 0.02	-0.06 / 0.06	-0.07 / 0.07	-0.11 / 0.11	-0.17 / 0.17	-0.18 / 0.18
Muon Sagitta Global	-1.53 / 1.58	-1.49 / 1.53	-1.40 / 1.44	-1.32 / 1.36	-1.29 / 1.32	-1.53 / 1.58	-1.56 / 1.61	-1.68 / 1.74	-1.70 / 1.76	-1.67 / 1.73	-1.65 / 1.71	-1.67 / 1.73
Muon Sagitta p_T-extra	0.04 / -0.04	-0.01 / 0.01	0.03 / -0.03	0.30 / -0.29	0.28 / -0.28	-1.94 / 2.02	-2.21 / 2.31	-3.00 / 3.19	-3.05 / 3.25	-2.90 / 3.08	-2.86 / 3.04	-2.92 / 3.10
Pile-up	-0.14 / 0.14	0.08 / -0.08	0.13 / -0.13	0.16 / -0.16	0.07 / -0.07	0.04 / -0.04	0.04 / -0.04	0.17 / -0.17	0.26 / -0.26	0.28 / -0.28	0.38 / -0.37	0.59 / -0.58
Multijet E_T^{miss}	-0.45 / 0.07	-0.52 / 0.08	-0.42 / 0.06	-0.40 / 0.05	-0.37 / 0.05	-0.84 / 0.15	-0.89 / 0.16	-0.80 / 0.13	-1.08 / 0.09	-1.82 / 0.06	-1.78 / 0.03	-0.70 / 0.01
Multijet d_0^{sig}	0.23 / -0.86	0.26 / -0.99	0.21 / -0.82	0.21 / -0.82	0.18 / -0.68	0.65 / -0.68	0.70 / -0.69	0.67 / -0.65	0.57 / -0.94	0.61 / -1.59	0.52 / -1.55	0.20 / -0.59
Multijet MC Scaling	1.16 / -1.16	1.33 / -1.33	1.08 / -1.08	1.08 / -1.08	0.90 / -0.90	0.96 / -0.96	0.96 / -0.96	0.69 / -0.69	0.63 / -0.63	0.76 / -0.76	0.66 / -0.66	0.24 / -0.24
Multijet Jet Mult	-0.84 / 0.24	-0.96 / 0.27	-0.78 / 0.22	-0.78 / 0.22	-0.72 / 0.20	-0.25 / 0.85	-0.20 / 0.91	-0.13 / 0.67	-0.33 / 0.52	-0.76 / 0.53	-0.51 / 0.53	-0.25 / 0.15
Multijet MC Shape	-0.12	-0.14	-0.11	-0.12	-0.12	1.21	1.35	1.01	0.99	1.38	1.27	0.46
Multijet $\Delta\phi(\mu, E_T^{miss})$	-1.09 / 0.70	-1.26 / 0.79	-1.01 / 0.65	-1.02 / 0.64	-0.90 / 0.57	-0.86 / 0.47	-0.85 / 0.45	-0.62 / 0.32	-0.65 / 0.53	-0.99 / 0.99	-0.65 / 0.96	-0.34 / 0.33
$t\bar{t}$ p_T-hard	0.97 / 0.00	0.49 / 0.00	-0.57 / 0.00	-1.20 / 0.00	-0.82 / 0.00	0.16 / 0.00	0.26 / 0.00	0.24 / 0.00	0.19 / 0.00	0.18 / 0.00	0.21 / 0.00	0.16 / 0.00
$t\bar{t}$ FSR	1.33 / -1.33	1.15 / -1.15	0.79 / -0.79	0.61 / -0.61	0.52 / -0.52	0.42 / -0.42	0.41 / -0.41	0.37 / -0.37	0.40 / -0.40	0.45 / -0.45	0.52 / -0.52	0.39 / -0.39
$t\bar{t}$ scales $\mu_R \mu_F$	-1.79 / 2.56	-1.79 / 2.55	-1.54 / 2.15	-1.40 / 1.88	-1.18 / 1.54	-0.92 / 1.08	-0.89 / 1.03	-0.79 / 0.86	-0.69 / 0.70	-0.47 / 0.43	-0.34 / 0.31	-0.20 / 0.20
$t\bar{t}$ hadronization	2.69 / 0.00	2.62 / 0.00	2.05 / 0.00	1.65 / 0.00	1.34 / 0.00	1.02 / 0.00	0.99 / 0.00	0.83 / 0.00	0.78 / 0.00	0.76 / 0.00	0.84 / 0.00	0.68 / 0.00
$t\bar{t}$ hdamp	0.52 / 0.00	0.36 / 0.00	-0.00 / 0.00	-0.19 / 0.00	-0.16 / 0.00	-0.10 / 0.00	-0.09 / 0.00	-0.08 / 0.00	-0.09 / 0.00	-0.11 / 0.00	-0.14 / 0.00	-0.13 / 0.00
$t\bar{t}$ PDF	-1.17 / 1.17	-1.24 / 1.24	-1.07 / 1.07	-1.05 / 1.05	-0.99 / 0.99	-0.94 / 0.94	-0.93 / 0.93	-0.89 / 0.89	-0.93 / 0.93	-0.86 / 0.86	-0.94 / 0.94	-0.77 / 0.77
tW DR	-1.48	-1.59	-1.73	-1.66	-1.60	-0.46	-0.34	-0.07	-0.27	-0.55	-0.61	-0.47
tW DS hdamp	0.01	0.01	0.00	0.07	0.17	0.21	0.22	0.25	0.19	0.09	0.01	-0.05
Norm. $W \to \tau\nu$ by 5%	-0.08 / 0.08	-0.09 / 0.09	-0.08 / 0.08	-0.08 / 0.08	-0.07 / 0.07	-0.07 / 0.07	-0.07 / 0.07	-0.07 / 0.07	-0.07 / 0.07	-0.07 / 0.07	-0.06 / 0.06	-0.06 / 0.06
Norm. Single top by 4%	-0.38 / 0.38	-0.38 / 0.38	-0.35 / 0.35	-0.31 / 0.31	-0.30 / 0.30	-0.21 / 0.21	-0.20 / 0.20	-0.19 / 0.19	-0.15 / 0.15	-0.11 / 0.11	-0.08 / 0.08	-0.04 / 0.04
Norm. Diboson by 6%	-0.49 / 0.49	-0.52 / 0.52	-0.45 / 0.45	-0.48 / 0.48	-0.46 / 0.46	-0.43 / 0.43	-0.43 / 0.43	-0.40 / 0.40	-0.38 / 0.38	-0.37 / 0.37	-0.37 / 0.37	-0.31 / 0.31
Norm. $Z \to \ell\ell$ by 5%	-0.30 / 0.30	-0.32 / 0.32	-0.32 / 0.32	-0.32 / 0.32	-0.34 / 0.34	-0.42 / 0.42	-0.43 / 0.43	-0.50 / 0.50	-0.56 / 0.56	-0.63 / 0.63	-0.86 / 0.86	-1.04 / 1.04

Table 10.10.: Born-level double-differential cross-section $\frac{d^2\sigma(W^-\to\mu^-\bar\nu)}{dm_{\mathrm{T}}^{\mathrm{W}}\,d|\eta(\mu)|}$ including statistical and systematic uncertainties in percent for $m_{\mathrm{T}}^{\mathrm{W}} = [425 - 600]\,\mathrm{GeV}$. The upper (lower) row corresponds to the one standard deviation upward (downward) shift of the uncertainty source.

$|\eta(\mu)|$	0.0 - 0.4	0.4 - 0.8	0.8 - 1.2	1.2 - 1.6	1.6 - 2.0	2.0 - 2.4
σ [pb/GeV]	1.54e-04	1.55e-04	1.53e-04	1.56e-04	1.34e-04	8.48e-05
Data stat. unc.	4.72	3.72	3.01	3.73	3.89	5.56
Sig. stat. unc.	3.56	2.56	2.18	3.48	5.50	2.35
Bkg. stat. unc.	0.97	0.74	0.60	0.75	0.82	1.20
Tot. sys. unc.	5.68 / -5.45	3.95 / -4.18	3.61 / -3.77	4.84 / -4.63	6.01 / -5.61	6.40 / -5.73
Alt. MC unf. unc.	-1.65	-1.28	-0.99	-0.53	0.62	2.22
Basic unf. unc.	-0.36	-0.40	-0.48	-0.53	-0.51	-0.46
JES Flavor Composition	0.93 / -0.91	0.70 / -0.69	0.62 / -0.61	0.41 / -0.41	0.25 / -0.25	0.02 / -0.02
JES Pileup RhoTopology	0.76 / -0.75	0.44 / -0.44	0.38 / -0.38	0.23 / -0.23	0.20 / -0.20	0.09 / -0.09
JES Pileup OffsetMu	0.14 / -0.14	0.13 / -0.13	0.15 / -0.15	0.24 / -0.24	0.22 / -0.22	0.03 / -0.04
JES Pileup OffsetNPV	0.60 / -0.60	0.27 / -0.26	0.25 / -0.25	0.10 / -0.10	0.13 / -0.13	0.07 / -0.07
JES EtaIntercalib Model	0.22 / -0.22	0.14 / -0.14	0.15 / -0.15	0.20 / -0.20	0.21 / -0.21	0.07 / -0.07
JES Flavor Response	-0.87 / 0.89	-0.56 / 0.57	-0.48 / 0.48	-0.17 / 0.17	-0.11 / 0.12	-0.05 / 0.05
JER EffectiveNP 1	0.37 / -0.37	0.32 / -0.32	0.26 / -0.26	0.36 / -0.36	0.23 / -0.23	-0.09 / 0.09
JER EffectiveNP 2	1.06 / -1.04	0.83 / -0.82	0.52 / -0.52	0.14 / -0.14	-0.15 / 0.15	-0.37 / 0.37
JER EffectiveNP 3	0.66 / -0.66	0.66 / -0.65	0.55 / -0.54	0.18 / -0.18	-0.04 / 0.04	-0.15 / 0.15
JER EffectiveNP 4	1.27 / -1.24	0.43 / -0.43	0.29 / -0.29	-0.10 / 0.10	-0.18 / 0.18	-0.29 / 0.29
JER EffectiveNP 5	1.24 / -1.22	0.36 / -0.36	0.25 / -0.25	-0.02 / 0.02	-0.03 / 0.03	-0.09 / 0.09
JER EffectiveNP 6	1.29 / -1.26	0.36 / -0.36	0.26 / -0.26	-0.08 / 0.08	-0.09 / 0.09	-0.14 / 0.14
JER EffectiveNP 7rest	1.43 / -1.40	0.48 / -0.48	0.20 / -0.20	-0.63 / 0.64	-0.75 / 0.76	-0.79 / 0.80
JER DataVsMC MC16	0.08 / -0.08	0.09 / -0.09	0.03 / -0.03	0.07 / -0.07	0.04 / -0.04	-0.04 / 0.04
$E_{\mathrm{T}}^{\mathrm{miss}}$ SoftTrk Scale	-0.28 / 0.28	-0.23 / 0.22	-0.23 / 0.23	-0.31 / 0.31	-0.31 / 0.31	-0.06 / 0.06
$E_{\mathrm{T}}^{\mathrm{miss}}$ SoftTrk ResoPara	0.34	0.00	-0.08	-0.26	-0.11	0.15
$E_{\mathrm{T}}^{\mathrm{miss}}$ SoftTrk ResoPerp	-0.35	-0.29	-0.28	-0.23	-0.20	0.02
Muon Resolution MS	-0.70 / 0.71	-0.68 / 0.69	-0.71 / 0.72	-0.78 / 0.79	-0.78 / 0.79	-0.71 / 0.72
Muon Scale	0.24 / -0.24	0.23 / -0.23	0.30 / -0.30	0.54 / -0.54	0.55 / -0.55	0.52 / -0.51
Muon SF Identification Syst	-1.11 / 1.14	-1.02 / 1.04	-1.22 / 1.25	-2.05 / 2.13	-2.37 / 2.49	-2.27 / 2.37
Muon SF Isolation Syst	-0.77 / 0.78	-0.74 / 0.75	-0.72 / 0.73	-0.67 / 0.68	-0.64 / 0.65	-0.59 / 0.60
Muon SF Trigger Syst	0.85 / -0.83	0.76 / -0.75	0.70 / -0.69	0.53 / -0.53	0.51 / -0.51	0.50 / -0.50
Bad Muon	0.05 / -0.05	0.05 / -0.05	0.02 / -0.02	-0.11 / 0.11	-0.20 / 0.20	-0.28 / 0.28
Muon Sagitta Global	-2.05 / 2.14	-1.83 / 1.90	-1.63 / 1.68	-0.95 / 0.97	-1.12 / 1.15	-1.63 / 1.69
Muon Sagitta p_{T}-extra	-0.60 / 0.60	-0.06 / 0.06	-0.71 / 0.72	-3.31 / 3.54	-4.42 / 4.85	-4.33 / 4.74
Pile-up	0.24 / -0.24	0.22 / -0.22	0.22 / -0.22	0.25 / -0.25	0.19 / -0.19	0.04 / -0.04
Multijet $E_{\mathrm{T}}^{\mathrm{miss}}$	-0.27 / 0.01	-0.26 / 0.01	-0.28 / 0.01	-0.38 / 0.03	-0.66 / 0.03	-1.02 / 0.03
Multijet d_0^{sig}	0.16 / -0.69	0.15 / -0.58	0.16 / -0.53	0.22 / -0.45	0.25 / -0.61	0.33 / -0.88
Multijet MC Scaling	0.82 / -0.82	0.77 / -0.77	0.63 / -0.63	0.22 / -0.22	0.25 / -0.25	0.49 / -0.49
Multijet Jet Mult	-0.57 / 0.11	-0.61 / 0.13	-0.47 / 0.15	0.02 / 0.24	-0.14 / 0.22	-0.28 / 0.30
Multijet MC Shape	-0.16	-0.18	-0.04	0.45	0.57	0.73
Multijet $\Delta\phi(\mu, E_{\mathrm{T}}^{\mathrm{miss}})$	-0.86 / 0.51	-0.87 / 0.52	-0.71 / 0.41	-0.18 / 0.08	-0.20 / 0.42	-0.35 / 0.56
$t\bar t$ p_{T}-hard	1.90 / 0.00	0.54 / 0.00	0.36 / 0.00	-0.32 / 0.00	-0.56 / 0.00	-0.67 / 0.00
$t\bar t$ FSR	0.06 / -0.06	0.30 / -0.30	0.29 / -0.29	0.38 / -0.38	0.30 / -0.30	0.21 / -0.21
$t\bar t$ scales μ_R μ_F	-1.58 / 2.24	-1.31 / 1.64	-1.10 / 1.37	-0.53 / 0.70	-0.30 / 0.43	-0.16 / 0.23
$t\bar t$ hadronization	1.24 / 0.00	1.05 / 0.00	0.96 / 0.00	0.95 / 0.00	0.65 / 0.00	0.34 / 0.00
$t\bar t$ hdamp	-0.08 / 0.00	-0.09 / 0.00	-0.03 / 0.00	0.21 / 0.00	0.18 / 0.00	0.09 / 0.00
$t\bar t$ PDF	-0.75 / 0.75	-0.66 / 0.66	-0.62 / 0.62	-0.56 / 0.56	-0.45 / 0.45	-0.45 / 0.45
tW DR	-1.54	-1.30	-1.14	-0.62	-0.31	-0.27
tW DS hdamp	0.70	0.47	0.44	0.23	0.29	0.47
Norm. $W \to \tau\nu$ by 5%	-0.06 / 0.06	-0.07 / 0.07	-0.06 / 0.06	-0.05 / 0.05	-0.05 / 0.05	-0.05 / 0.05
Norm. Single top by 4%	-0.27 / 0.27	-0.24 / 0.24	-0.21 / 0.21	-0.11 / 0.11	-0.05 / 0.05	-0.05 / 0.05
Norm. Diboson by 6%	-0.48 / 0.48	-0.48 / 0.48	-0.45 / 0.45	-0.37 / 0.37	-0.31 / 0.31	-0.36 / 0.36
Norm. $Z \to \ell\ell$ by 5%	-0.33 / 0.33	-0.32 / 0.32	-0.34 / 0.34	-0.41 / 0.41	-0.45 / 0.45	-0.74 / 0.74

Table 10.11.: Born-level double-differential cross-section $\frac{d^2\sigma(W^- \to \mu^- \bar\nu)}{dm_\mathrm{T}^\mathrm{W} d|\eta(\mu)|}$ including statistical and systematic uncertainties in percent for $m_\mathrm{T}^\mathrm{W} = [600 - 900]\,\mathrm{GeV}$. The upper (lower) row corresponds to the one standard deviation upward (downward) shift of the uncertainty source.

$|\eta(\mu)|$	0.0 - 0.4	0.4 - 0.8	0.8 - 1.2	1.2 - 1.6	1.6 - 2.0	2.0 - 2.4
σ [pb/GeV]	2.82e-05	2.45e-05	2.43e-05	2.74e-05	2.22e-05	8.89e-06
Data stat. unc.	7.68	6.43	5.31	6.58	7.03	13.14
Sig. stat. unc.	6.31	7.67	6.26	7.12	4.58	2.07
Bkg. stat. unc.	1.26	1.01	0.85	1.30	1.04	2.21
Tot. sys. unc.	3.98 -4.74	3.84 -4.16	3.87 -3.99	7.30 -6.71	10.20 -8.80	13.03 -10.68
Alt. MC unf. unc.	-2.57	-1.65	-1.13	-0.68	0.33	1.75
Basic unf. unc.	0.53	0.41	0.26	0.07	-0.10	-0.26
JES Flavor Composition	0.39 -0.39	0.36 -0.36	0.34 -0.34	0.28 -0.28	0.10 -0.10	-0.18 0.18
JES Pileup RhoTopology	0.16 -0.15	0.15 -0.14	0.14 -0.14	0.14 -0.14	0.07 -0.07	-0.04 0.04
JES Pileup OffsetMu	0.15 -0.15	0.26 -0.26	0.25 -0.25	0.21 -0.21	0.05 -0.05	-0.11 0.11
JES Pileup OffsetNPV	0.15 -0.15	0.14 -0.14	0.12 -0.12	0.07 -0.07	-0.00 0.00	-0.06 0.06
JES EtaIntercalib Model	0.15 -0.15	0.22 -0.22	0.21 -0.21	0.17 -0.17	0.05 -0.05	-0.07 0.07
JES Flavor Response	-0.08 0.08	-0.13 0.14	-0.13 0.13	-0.15 0.15	-0.12 0.12	-0.08 0.08
JER EffectiveNP 1	-0.02 0.02	0.47 -0.47	0.46 -0.46	0.41 -0.41	0.00 -0.00	-0.27 0.27
JER EffectiveNP 2	-0.19 0.19	0.06 -0.06	0.06 -0.06	0.16 -0.16	-0.06 0.06	-0.29 0.29
JER EffectiveNP 3	-0.39 0.39	-0.04 0.04	-0.02 0.02	0.10 -0.10	-0.06 0.06	-0.30 0.31
JER EffectiveNP 4	0.07 -0.07	0.11 -0.11	0.10 -0.10	0.07 -0.07	-0.02 0.02	-0.09 0.09
JER EffectiveNP 5	-0.23 0.23	-0.03 0.03	-0.01 0.01	0.08 -0.08	-0.05 0.05	-0.19 0.19
JER EffectiveNP 6	-0.10 0.10	0.03 -0.03	0.04 -0.04	0.13 -0.13	0.12 -0.12	0.10 -0.10
JER EffectiveNP 7rest	-0.04 0.04	0.07 -0.07	0.07 -0.07	0.04 -0.04	0.03 -0.03	0.01 -0.01
JER DataVsMC MC16	-0.03 0.03	0.07 -0.07	0.07 -0.07	0.03 -0.03	-0.03 0.03	-0.05 0.05
$E_\mathrm{T}^\mathrm{miss}$ SoftTrk Scale	-0.22 0.22	-0.54 0.54	-0.54 0.54	-0.48 0.48	-0.18 0.18	0.08 -0.08
$E_\mathrm{T}^\mathrm{miss}$ SoftTrk ResoPara	-0.24	-0.46	-0.43	-0.25	0.01	0.17
$E_\mathrm{T}^\mathrm{miss}$ SoftTrk ResoPerp	-0.17	-0.56	-0.52	-0.30	-0.01	0.13
Muon Resolution MS	-0.32 0.32	-0.30 0.30	-0.32 0.32	-0.48 0.48	-0.78 0.79	-1.34 1.37
Muon Scale	0.16 -0.16	0.10 -0.10	0.18 -0.18	0.54 -0.54	0.70 -0.69	0.74 -0.73
Muon SF Identification Syst	-1.56 1.61	-1.53 1.58	-1.68 1.73	-2.36 2.48	-2.27 2.38	-2.11 2.20
Muon SF Isolation Syst	-0.64 0.65	-0.64 0.65	-0.63 0.64	-0.60 0.61	-0.58 0.58	-0.55 0.56
Muon SF Trigger Syst	0.71 -0.70	0.64 -0.63	0.61 -0.60	0.49 -0.48	0.49 -0.49	0.49 -0.49
Bad Muon	0.04 -0.04	0.09 -0.09	0.04 -0.04	-0.17 0.17	-0.31 0.31	-0.46 0.46
Muon Sagitta Global	-2.50 2.63	-2.36 2.47	-2.39 2.51	-2.54 2.67	-2.96 3.14	-3.40 3.65
Muon Sagitta p_T-extra	0.12 -0.12	0.36 -0.36	-0.78 0.81	-5.38 6.04	-7.82 9.26	-9.66 11.98
Pile-up	0.09 -0.09	0.34 -0.34	0.31 -0.31	0.18 -0.18	-0.23 0.23	-0.73 0.74
Multijet $E_\mathrm{T}^\mathrm{miss}$	-0.18 -0.00	-0.04 -0.00	-0.09 0.02	-0.30 0.09	0.06 0.00	-0.15 0.03
Multijet d_0^sig	0.11 -0.52	0.01 -0.13	0.08 -0.15	0.33 -0.26	-0.03 0.06	0.07 -0.13
Multijet MC Scaling	0.59 -0.59	0.17 -0.17	0.18 -0.18	0.23 -0.23	-0.05 0.05	0.07 -0.07
Multijet Jet Mult	-0.41 0.07	-0.12 -0.04	-0.08 0.04	0.01 0.31	0.08 -0.04	-0.03 0.05
Multijet MC Shape	-0.14	-0.12	0.05	0.59	-0.08	0.11
Multijet $\Delta\phi(\mu, E_\mathrm{T}^\mathrm{miss})$	-0.65 0.37	-0.24 0.13	-0.22 0.11	-0.22 0.06	0.06 -0.10	-0.03 0.09
$t\bar{t}$ p_T-hard	-0.01 0.00	0.04 0.00	0.01 0.00	-0.06 0.00	-0.02 0.00	-0.01 0.00
$t\bar{t}$ FSR	0.36 -0.36	0.37 -0.37	0.33 -0.33	0.17 -0.17	0.08 -0.08	0.04 -0.04
$t\bar{t}$ scales $\mu_R\,\mu_F$	-1.03 1.60	-1.05 1.62	-0.91 1.42	-0.43 0.70	-0.25 0.40	-0.17 0.28
$t\bar{t}$ hadronization	0.84 0.00	0.89 0.00	0.79 0.00	0.43 0.00	0.22 0.00	0.12 0.00
$t\bar{t}$ hdamp	-0.29 0.00	-0.26 0.00	-0.23 0.00	-0.09 0.00	-0.06 0.00	-0.04 0.00
$t\bar{t}$ PDF	-0.37 0.37	-0.30 0.30	-0.33 0.33	-0.42 0.42	-0.23 0.23	-0.28 0.28
tW DR	-1.26	-1.40	-1.24	-0.85	-0.42	-0.43
tW DS hdamp	-0.96	-0.60	-0.46	0.16	0.24	0.56
Norm. $W \to \tau\nu$ by 5%	-0.05 0.05	-0.06 0.06	-0.06 0.06	-0.07 0.07	-0.03 0.03	-0.04 0.04
Norm. Single top by 4%	-0.10 0.10	-0.11 0.11	-0.09 0.09	-0.04 0.04	-0.02 0.02	-0.03 0.03
Norm. Diboson by 6%	-0.48 0.48	-0.42 0.42	-0.40 0.40	-0.32 0.32	-0.27 0.27	-0.31 0.31
Norm. $Z \to \ell\ell$ by 5%	-0.31 0.31	-0.31 0.31	-0.31 0.31	-0.31 0.31	-0.30 0.30	-0.52 0.52

Table 10.12.: Born-level double-differential cross-section $\frac{d^2\sigma(W^-\to\mu^-\bar{\nu})}{dm_{\mathrm{T}}^{\mathrm{W}}\,d|\eta(\mu)|}$ including statistical and systematic uncertainties in percent for $m_{\mathrm{T}}^{\mathrm{W}} = [900-2000]\,\mathrm{GeV}$. The upper (lower) row corresponds to the one standard deviation upward (downward) shift of the uncertainty source.

$\lvert\eta(\mu)\rvert$	0.0 - 0.6	0.6 - 1.2	1.2 - 1.8	1.8 - 2.4
σ [pb/GeV]	2.24e-06	1.68e-06	1.37e-06	4.17e-07
Data stat. unc.	11.36	14.18	12.07	23.84
Sig. stat. unc.	0.56	1.24	13.47	1.67
Bkg. stat. unc.	1.65	1.54	2.13	1.52
Tot. sys. unc.	4.93 -6.01	5.14 -5.79	23.25 -17.83	35.50 -22.37
Alt. MC unf. unc.	-3.25	-3.10	-2.51	-1.46
Basic unf. unc.	-0.47	-0.47	-0.47	-0.47
JES Flavor Composition	0.25 -0.25	0.16 -0.16	0.24 -0.24	-0.12 0.12
JES Pileup RhoTopology	0.07 -0.07	0.00 -0.00	0.13 -0.13	0.03 -0.03
JES Pileup OffsetMu	0.01 -0.01	0.06 -0.06	0.23 -0.23	-0.14 0.14
JES Pileup OffsetNPV	0.05 -0.05	-0.02 0.02	0.10 -0.10	-0.03 0.03
JES EtaIntercalib Model	0.03 -0.03	0.06 -0.06	0.21 -0.21	-0.01 0.01
JES Flavor Response	-0.29 0.29	-0.03 0.03	-0.11 0.11	-0.09 0.09
JER EffectiveNP 1	0.06 -0.07	0.07 -0.08	0.45 -0.45	1.30 -1.27
JER EffectiveNP 2	-0.06 0.06	0.06 -0.06	0.32 -0.32	-0.20 0.20
JER EffectiveNP 3	-0.06 0.06	0.12 -0.12	-0.12 0.12	1.00 -0.99
JER EffectiveNP 4	-0.00 0.00	0.04 -0.04	0.00 -0.00	0.62 -0.62
JER EffectiveNP 5	-0.19 0.19	0.10 -0.10	-0.02 0.02	1.11 -1.09
JER EffectiveNP 6	-0.02 0.02	0.02 -0.02	-0.05 0.05	1.16 -1.13
JER EffectiveNP 7rest	0.03 -0.03	0.17 -0.17	-0.05 0.05	1.07 -1.05
JER DataVsMC MC16	-0.36 0.37	0.12 -0.12	0.23 -0.23	0.79 -0.78
$E_{\mathrm{T}}^{\mathrm{miss}}$ SoftTrk Scale	0.11 -0.12	-0.13 0.13	-0.48 0.48	0.40 -0.39
$E_{\mathrm{T}}^{\mathrm{miss}}$ SoftTrk ResoPara	-0.05	-0.16	-0.37	0.41
$E_{\mathrm{T}}^{\mathrm{miss}}$ SoftTrk ResoPerp	0.06	-0.23	-0.42	0.50
Muon Resolution MS	-0.57 0.57	-0.43 0.44	-1.11 1.13	-2.83 3.00
Muon Scale	0.46 -0.46	0.35 -0.35	0.69 -0.68	0.82 -0.81
Muon SF Identification Syst	-1.58 1.63	-1.98 2.08	-7.54 8.77	-4.64 5.10
Muon SF Isolation Syst	-0.59 0.59	-0.57 0.58	-0.57 0.58	-0.53 0.53
Muon SF Trigger Syst	0.65 -0.64	0.62 -0.61	0.42 -0.41	0.47 -0.47
Bad Muon	0.01 -0.01	-0.03 0.03	-0.78 0.79	-0.87 0.89
Muon Sagitta Global	-3.98 4.32	-3.96 4.30	-4.81 5.29	-5.89 6.66
Muon Sagitta p_{T}-extra	0.05 -0.05	-0.98 1.08	-15.02 20.77	-20.60 34.21
Pile-up	0.07 -0.07	0.23 -0.23	0.32 -0.32	0.27 -0.27
Multijet $E_{\mathrm{T}}^{\mathrm{miss}}$	-0.03 -0.00	-0.02 -0.00	-0.53 -0.02	0.09 -0.00
Multijet d_0^{sig}	0.02 -0.10	-0.02 0.00	0.06 -0.44	-0.03 0.08
Multijet MC Scaling	0.11 -0.11	-0.04 0.04	0.06 -0.06	-0.04 0.04
Multijet Jet Mult	-0.08 0.01	0.03 -0.03	-0.09 0.03	0.03 -0.03
Multijet MC Shape	-0.03	0.00	0.28	-0.07
Multijet $\Delta\phi(\mu, E_{\mathrm{T}}^{\mathrm{miss}})$	-0.13 0.07	0.04 0.01	-0.06 0.37	0.04 -0.05
$t\bar{t}$ p_{T}-hard	-0.06 0.00	-0.02 0.00	0.01 0.00	0.04 0.00
$t\bar{t}$ FSR	0.13 -0.13	0.15 -0.15	0.03 -0.03	-0.00 0.00
$t\bar{t}$ scales $\mu_R \mu_F$	-0.31 0.49	-0.40 0.63	-0.12 0.21	-0.04 0.07
$t\bar{t}$ hadronization	0.26 0.00	0.34 0.00	0.13 0.00	0.01 0.00
$t\bar{t}$ hdamp	-0.10 0.00	-0.11 0.00	-0.04 0.00	-0.02 0.00
$t\bar{t}$ PDF	-0.19 0.19	-0.18 0.18	-0.21 0.21	-0.07 0.07
tW DR	-2.20	-1.09	-0.66	0.05
tW DS hdamp	0.82	0.52	-0.65	-0.03
Norm. $W \to \tau\nu$ by 5%	-0.04 0.04	-0.05 0.05	-0.02 0.02	-0.02 0.02
Norm. Single top by 4%	-0.05 0.05	-0.06 0.06	0.03 -0.03	0.01 -0.01
Norm. Diboson by 6%	-0.36 0.36	-0.42 0.42	-0.28 0.28	-0.16 0.16
Norm. $Z \to \ell\ell$ by 5%	-0.39 0.39	-0.41 0.41	-0.35 0.35	-0.28 0.28

Table 10.13.: Comparison of the measured 1D (m_T^W) and 2D ($m_T^W \otimes |\eta(\mu)|$) cross-sections integrated per 2D m_T^W bin for each muon charge. Additionally, the relative difference ($\sigma_{2D} - \sigma_{1D})/\sigma_{1D}$ is given. Cross-sections are not normalized to bin-widths here.

m_T^W bin [GeV]	$W^+ \to \mu^+ \nu$			$W^- \to \mu^- \bar{\nu}$		
	σ_{2D} [pb]	σ_{1D} [pb]	diff.	σ_{2D} [pb]	σ_{1D} [pb]	diff.
200-300	1.48e+00	1.48e+00	-0.3%	9.21e-01	9.23e-01	-0.2%
300-425	3.49e-01	3.52e-01	-0.7%	2.00e-01	2.02e-01	-1.0%
425-600	1.02e-01	1.03e-01	-0.5%	5.85e-02	5.93e-02	-1.2%
600-900	3.05e-02	3.08e-02	-1.1%	1.63e-02	1.65e-02	-1.6%
900-2000	6.21e-03	6.34e-03	-2.0%	3.77e-03	3.78e-03	-0.4%

10.3. Charge asymmetry

The asymmetry $A_\pm$ between the $W^+ \to \mu^+ \nu$ and $W^- \to \mu^- \bar{\nu}$ cross-sections is measured in addition because uncertainties cancel partly and additional sensitivity to the u/d PDF is expected. The asymmetry is obtained per-bin as:

$$A_\pm = \frac{\sigma(W^+ \to \mu^+ \nu) - \sigma(W^- \to \mu^- \bar{\nu})}{\sigma(W^+ \to \mu^+ \nu) + \sigma(W^- \to \mu^- \bar{\nu})} \tag{10.1}$$

All systematic (detector, modeling and multijet) uncertainties are treated as correlated between charges, while the sagitta bias uncertainties are anti-correlated. Correlated uncertainties cancel to a large degree in the asymmetry but not necessarily completely as they may have different magnitudes for μ^+ and μ^-. Nevertheless, the asymmetry will be dominated by the sagitta bias systematic uncertainty and the completely uncorrelated statistical uncertainty.

The single- and double-differential asymmetries are presented in Figure 10.6 as well as in Table 10.14 (1D) and Table 10.15 (2D). Generally, the production of a W^+ boson and a W^- boson is not symmetric in pp collisions given the valence quark contribution (uud), yielding a larger cross-section for the positive charge. It can be seen in Figure 10.6(a) that the charge-asymmetry increases as a function of m_T^W. This can be understood because for the production of a W boson with a high transverse mass a large momentum of the parton, i.e. large Bjorken-x, is needed. As valence quarks are likely to carry a large fraction of the proton's momentum (see Figure 1.9), their involvement is more pronounced at high m_T^W.

The double-differential asymmetry shows an additional dependency on $|\eta(\mu)|$ in the higher m_T^W bins. It partly counteracts the energy dependence resulting in asymmetries close to zero, or even below zero, in the last three m_T^W bins of the double-differential spectrum. A positively charged muon is produced more centrally than its negatively charged

	left-handed	right-handed			right-handed	left-handed
Process	$u_v + \bar{d}_s$	$\rightarrow$	W^+	$\rightarrow$	$\mu^+ + \nu$	
	$d_v + \bar{u}_s$	$\rightarrow$	W^-	$\rightarrow$	$\bar{\nu} + \mu^-$	

Longitudinal momentum $\longrightarrow$ $\leftarrow$ $\longrightarrow$ $\leftarrow$ $\longrightarrow$
Spin $\Leftarrow$ $\Leftarrow$ $\Longleftarrow$ $\Leftarrow$ $\Leftarrow$
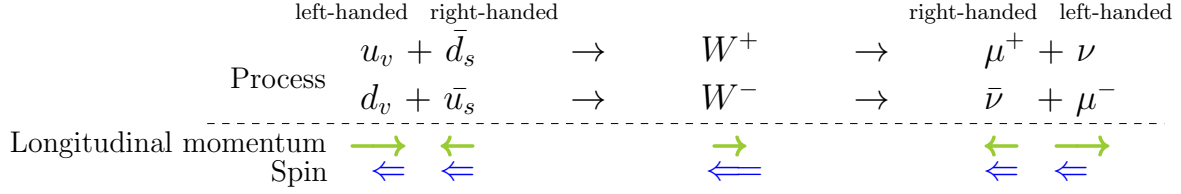
Figure 10.5.: Schematic illustration of the momentum and spin conservation in the production and decay of the ccDY process. For both charges, an annihilation between a valence quark q_v and sea quark q_s is assumed with $q = (u, d)$. The longitudinal momentum direction of a particle is indicated by a single green arrow, while the direction of spin is given by a blue double arrow.

counterpart, see also the double-differential cross-sections shown in Figure 10.2 (μ^+) and Figure 10.3 (μ^-). The effect can be understood in the context of the helicity in the W-boson decay. This is sketched schematically in Figure 10.5, assuming the annihilation of one valence quark and one sea quark. In general, the valence quark is expected to carry a larger momentum (see Figure 1.9). A key concept of the weak interaction is that it couples only to left-handed particles and right-handed anti-particles. Thus, the orientation of the fermions' spins and momentums with respect to each other are fixed by their handedness. The excess longitudinal momentum introduced by the valence quark is transferred to the left-handed particle in the final state. As a result, the μ^- is more likely than the μ^+ to possess a large longitudinal momentum, i.e. large $|\eta(\mu)|$.
It should be noted that this effect is prominent for asymmetric valence-quark sea-quark interactions which happen more often at very high m_T^W. In contrast, at lower m_T^W, the probability for symmetric sea-quark sea-quark interactions is higher for μ^- than μ^+ given the uud valence-quark content. This effect dictates a more central production for the negative charge. The two counteracting effects can explain the approximately flat charge asymmetry in the first m_T^W bin in Figure 10.6(b).

In total, the absolute uncertainty on the charge asymmetry measurement ranges between 0.0134 and 0.321 over the single- and double-differential spectra, see Tables 10.14/10.15. At lower m_T^W, the correlated systematic uncertainties (in particular, related to the charge-dependent sagitta bias in the muon momentum-measurement) dominate while, for high m_T^W, the statistical uncertainty is larger.
A comparison to predicted asymmetries given by the POWHEG+PYTHIA and SHERPA signal samples is included in Figure 10.6. Starting at $m_T^W \approx 500\,\text{GeV}$, the prediction is at the upper edge of the given uncertainty band of the measurement. For the double-differential measurement, the shapes of measured and predicted cross-sections are slightly different with the largest disagreements at high $|\eta(\mu)|$ and high m_T^W. As already discussed in the previous Sections, this behavior is to a large degree related to the charge-dependent sagitta bias in the measurement of the muon's momentum.
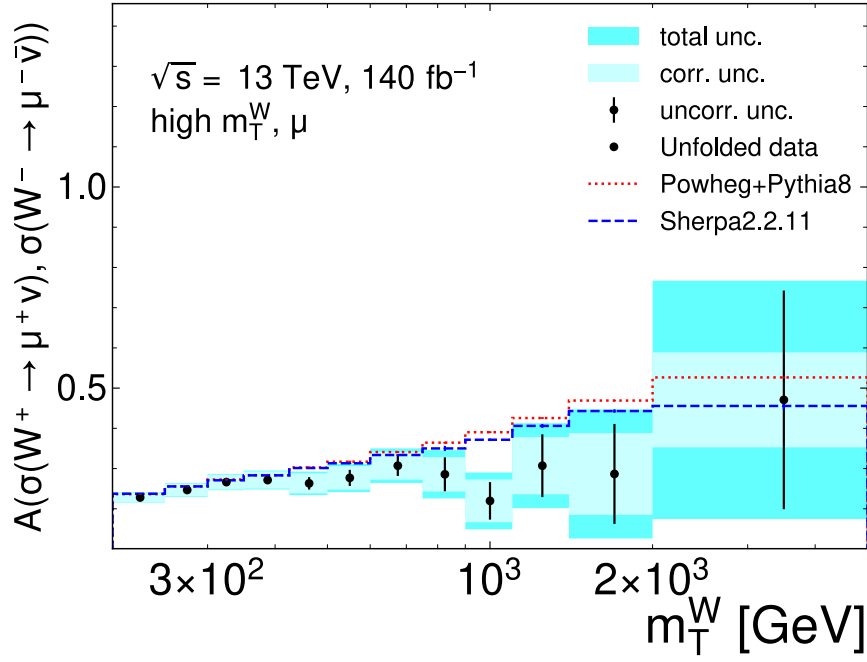
(a)
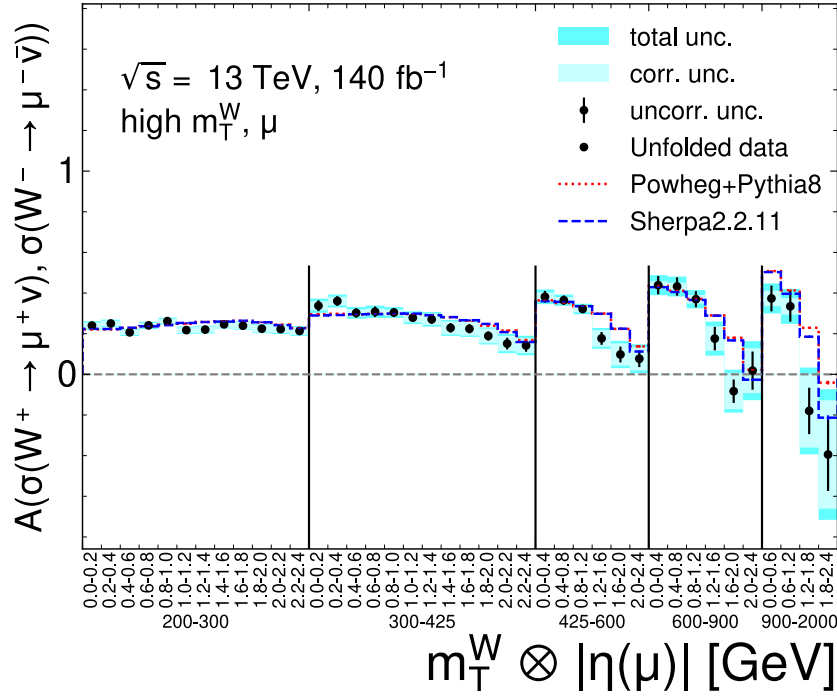
(b)

Figure 10.6.: Charge asymmetry $A_{\pm}$ of the (a) single-differential and (b) double-differential cross-section. The error bars represent the uncorrelated (systematic and statistical) uncertainties between the μ^+- and μ^-- channel, while the light-blue band corresponds to the correlated uncertainties. In addition, the predictions from POWHEG+PYTHIA and SHERPA are shown for comparison.

Table 10.14.: Charge asymmetry $A_\pm$ single-differential in m_T^W including the absolute statistical and systematic uncertainties. All systematic uncertainties are treated as correlated.

m_T^W [GeV]	200 - 250	250 - 300	300 - 350	350 - 425	425 - 500	500 - 600	600 - 750	750 - 900	900 - 1100	1100 - 1400	1400 - 2000	2000 - 5000
Asymmetry	2.28e-01	2.47e-01	2.66e-01	2.72e-01	2.63e-01	2.77e-01	3.07e-01	2.86e-01	2.20e-01	3.07e-01	2.87e-01	4.71e-01
Stat. unc.	4.24e-03	7.67e-03	8.29e-03	1.02e-02	1.54e-02	2.00e-02	2.55e-02	4.22e-02	4.66e-02	7.80e-02	1.24e-01	2.72e-01
Cor. sys. unc.	1.27e-02	1.50e-02	1.85e-02	2.13e-02	2.49e-02	2.91e-02	3.47e-02	4.27e-02	5.31e-02	7.12e-02	1.02e-01	1.18e-01
Total unc.	1.34e-02	1.68e-02	2.03e-02	2.36e-02	2.93e-02	3.53e-02	4.30e-02	6.00e-02	7.06e-02	1.06e-01	1.61e-01	2.96e-01

Table 10.15.: Charge asymmetry $A_\pm$ double-differential in $m_\mathrm{T}^\mathrm{W} \otimes |\eta(\mu)|$ including the absolute statistical and systematic uncertainties. All systematic uncertainties are treated as correlated.

$200\,\mathrm{GeV} < m_\mathrm{T}^\mathrm{W} < 300\,\mathrm{GeV}$

$|\eta(\mu)|$	0.0 - 0.2	0.2 - 0.4	0.4 - 0.6	0.6 - 0.8	0.8 - 1.0	1.0 - 1.2	1.2 - 1.4	1.4 - 1.6	1.6 - 1.8	1.8 - 2.0	2.0 - 2.2	2.2 - 2.4
Asymmetry	2.40e-01	2.50e-01	2.07e-01	2.41e-01	2.62e-01	2.18e-01	2.20e-01	2.46e-01	2.39e-01	2.25e-01	2.23e-01	2.13e-01
Stat. unc.	1.48e-02	1.31e-02	1.26e-02	1.34e-02	1.26e-02	1.13e-02	1.21e-02	1.16e-02	1.09e-02	1.18e-02	1.46e-02	1.36e-02
Cor. sys. unc.	1.55e-02	1.37e-02	1.29e-02	1.19e-02	1.17e-02	1.42e-02	1.52e-02	1.68e-02	1.79e-02	1.86e-02	1.95e-02	2.03e-02
Total unc.	2.14e-02	1.89e-02	1.80e-02	1.79e-02	1.72e-02	1.81e-02	1.95e-02	2.04e-02	2.10e-02	2.20e-02	2.44e-02	2.44e-02

$300\,\mathrm{GeV} < m_\mathrm{T}^\mathrm{W} < 425\,\mathrm{GeV}$

$|\eta(\mu)|$	0.0 - 0.2	0.2 - 0.4	0.4 - 0.6	0.6 - 0.8	0.8 - 1.0	1.0 - 1.2	1.2 - 1.4	1.4 - 1.6	1.6 - 1.8	1.8 - 2.0	2.0 - 2.2	2.2 - 2.4
Asymmetry	3.38e-01	3.61e-01	3.02e-01	3.08e-01	3.04e-01	2.79e-01	2.71e-01	2.29e-01	2.24e-01	1.89e-01	1.51e-01	1.42e-01
Stat. unc.	2.69e-02	2.38e-02	2.26e-02	2.58e-02	2.18e-02	2.08e-02	2.27e-02	2.29e-02	2.25e-02	2.22e-02	2.87e-02	3.07e-02
Cor. sys. unc.	2.25e-02	2.16e-02	1.81e-02	1.58e-02	1.51e-02	2.37e-02	2.81e-02	3.22e-02	3.33e-02	3.55e-02	3.73e-02	3.72e-02
Total unc.	3.51e-02	3.21e-02	2.90e-02	3.03e-02	2.65e-02	3.16e-02	3.61e-02	3.95e-02	4.02e-02	4.19e-02	4.71e-02	4.82e-02

$425\,\mathrm{GeV} < m_\mathrm{T}^\mathrm{W} < 600\,\mathrm{GeV}$

$|\eta(\mu)|$	0.0 - 0.4	0.4 - 0.8	0.8 - 1.2	1.2 - 1.6	1.6 - 2.0	2.0 - 2.4
Asymmetry	3.82e-01	3.65e-01	3.22e-01	1.77e-01	9.76e-02	7.68e-02
Stat. unc.	2.90e-02	2.30e-02	1.99e-02	3.15e-02	3.90e-02	4.11e-02
Cor. sys. unc.	2.16e-02	1.58e-02	1.64e-02	4.05e-02	5.45e-02	5.77e-02
Total unc.	3.61e-02	2.79e-02	2.57e-02	5.13e-02	6.70e-02	7.08e-02

$600\,\mathrm{GeV} < m_\mathrm{T}^\mathrm{W} < 900\,\mathrm{GeV}$

$|\eta(\mu)|$	0.0 - 0.4	0.4 - 0.8	0.8 - 1.2	1.2 - 1.6	1.6 - 2.0	2.0 - 2.4
Asymmetry	4.39e-01	4.32e-01	3.70e-01	1.76e-01	-8.29e-02	1.82e-02
Stat. unc.	4.51e-02	4.52e-02	3.97e-02	5.80e-02	5.76e-02	9.40e-02
Cor. sys. unc.	1.96e-02	1.89e-02	2.14e-02	6.06e-02	8.85e-02	1.11e-01
Total unc.	4.92e-02	4.90e-02	4.51e-02	8.39e-02	1.06e-01	1.45e-01

$900\,\mathrm{GeV} < m_\mathrm{T}^\mathrm{W} < 2000\,\mathrm{GeV}$

$|\eta(\mu)|$	0.0 - 0.6	0.6 - 1.2	1.2 - 1.8	1.8 - 2.4
Asymmetry	3.73e-01	3.35e-01	-1.80e-01	-3.95e-01
Stat. unc.	6.33e-02	7.59e-02	1.14e-01	1.79e-01
Cor. sys. unc.	3.79e-02	4.08e-02	1.80e-01	2.67e-01
Total unc.	7.38e-02	8.61e-02	2.14e-01	3.21e-01

11. Combination with parallel electron-channel measurement

A combination of the cross-sections measured in the muon channel, presented in this thesis, and in an electron channel [84] is performed by the analysis team [84]. Using the `HAverager` tool [180], the basis is a minimization of a χ^2-function of the form

$$\chi^2(\vec{\sigma}, \vec{b}) = \sum_{k=e,\mu} \sum_{i=1}^{N_{\text{bins}}} \frac{\left(\sigma_{\text{avg}}^i - \sigma_k^i - \sum_{j=1}^{N_{\text{sys}}} \Gamma_{j,k}^i b_j\right)^2}{\left(\delta_{k,\text{uncorr}}^i\right)^2} W_k^i + \sum_{j=1}^{N_{\text{sys}}} b_j^2. \tag{11.1}$$

A summation over the channels (here e-channel and μ-channel) and number of bins N_{bins} is done. Input parameters are the cross-sections σ_k^i and values $\Gamma_{j,k}^i$ of systematic uncertainty j in bin i of measurement $k = e, \mu$. The relative uncertainties uncorrelated between bins and channels are given in the denominator, $(\delta_{k,\text{uncorr}}^i)^2$. The factor W_k^i is one if measurement k contains a value in bin i, otherwise, it equals zero. Parameters to be optimized are the combined cross-section σ_{avg}^i per bin i and a set of shifts b_j to the correlated uncertainties. They are obtained by minimizing under the conditions $\partial\chi^2(\vec{\sigma},\vec{b})/\partial\sigma_{\text{avg}}^i = 0$ (for $i = 1, ..., N_{\text{bins}}$) and $\partial\chi^2(\vec{\sigma},\vec{b})/\partial b_j = 0$ (for $j = 1, ..., N_{\text{sys}}$). The term $\sum_{j=1}^{N_{\text{sys}}} b_j^2$ constrains the systematic shifts. The combined cross-section is given by

$$\sigma_{avg}^i = \frac{\sum_{k=1}^{N_{\text{chan}}} \left(\sigma_k^i + \sum_{j=1}^{N_{\text{sys}}} \Gamma_{j,k}^i \beta_{j,\text{avg}}\right) \frac{W_k^i}{(\delta_{k,\text{uncorr.}}^i)^2}}{\sum_{k=e,\mu} \frac{W_k^i}{(\delta_{k,\text{uncorr}}^i)^2}} \tag{11.2}$$

where $\beta_{j,\text{avg}}$ are the optimized values of the b_j above. In case of asymmetric systematic uncertainties, an iterative procedure is employed as explained in References [84, 180].

The combination procedure is performed separately for the single- and double-differential cross-sections but in one simultaneous fit for the positive and negative charge each, i.e. charge correlated. All systematic uncertainties with a contribution of more than 0.5% in at least one bin of the eight measurement distributions are considered. The uncertainties in the muon channel are discussed in Chapter 9 while additional electron-specific uncertainties are presented in Reference [84]. The full list of systematic uncertainties considered and their correlation scheme is shown in Table 11.1. Additionally, all uncertainties are classified as symmetric, asymmetric or one-sided[1].

---

[1]Here, a one-sided uncertainty is defined as an asymmetric uncertainty with a down-variation of zero.

Table 11.1.: Uncertainties considered in the combination procedure including their correlations between channels, bins and charges and whether an uncertainty is symmetric (s), asymmetric (a) or one-sided (o).

Uncorrelated between channels				Correlated between channels		
	corr. bins	corr. charges	sym		corr. bins	corr. charges	sym.
——— Muon only ———							
Muon Resolution MS	✓	✓	s	alt. MC unf. unc.	✓	✓	o
Muon Scale	✓	✓	s	basic unf. unc.	✓	✓	o
Bad Muon	✓	✓	s	Pile-up SF	✓	✓	s
Muon SF Identification Syst	✓	✓	s	JES Flavor Composition	✓	✓	s
Muon SF Isolation Syst	✓	✓	s	JES Pileup RhoTopology	✓	✓	s
Muon SF Trigger Syst	✓	✓	s	JES Pileup OffsetMu	✓	✓	s
Muon Sagitta Global	✓	✓ (anti)	s	JES Pileup OffsetNPV	✓	✓	s
Muon Sagitta p_{T}-extra	✓	✓ (anti)	s	JES EtaIntercalib Model	✓	✓	s
Multijet Muon $\Delta\phi(\mu, E_{\mathrm{T}}^{\mathrm{miss}})$	✓	✓	a	JES Flavor Response	✓	✓	s
Multijet Muon $E_{\mathrm{T}}^{\mathrm{miss}}$	✓	✓	a	JER EffectiveNP 1	✓	✓	s
Multijet Muon jet mult	✓	✓	a	JER EffectiveNP 2	✓	✓	s
Multijet Muon MC Shape	✓	✓	o	JER EffectiveNP 3	✓	✓	s
Multijet Muon d_0^{sig}	✓	✓	a	JER EffectiveNP 4	✓	✓	s
——— Electron only ———				JER EffectiveNP 5	✓	✓	s
Electron Scale L1Gain	✓	✓	s	JER EffectiveNP 6	✓	✓	s
Electron Scale L2Gain	✓	✓	s	JER EffectiveNP 7rest	✓	✓	s
Electron Scale S12	✓	✓	s	JER DataVsMC	✓	✓	s
Electron Scale LarCalib	✓	✓	s	$E_{\mathrm{T}}^{\mathrm{miss}}$ SoftTrk Scale	✓	✓	s
Electron Scale ZeeSyst	✓	✓	s	$E_{\mathrm{T}}^{\mathrm{miss}}$ SoftTrk ResoPara	✓	✓	o
Electron Scale PS B12	✓	✓	s	$E_{\mathrm{T}}^{\mathrm{miss}}$ SoftTrk ResoPerp	✓	✓	o
Electron Scale MatID	✓	✓	s	Multijet MC scaling	✓	✓	s
Electron Scale MatCryo	✓	✓	s	tW DS hdamp	✓	✓	o
Electron Scale LarEleUnconv	✓	✓	s	tW DR	✓	✓	o
Electron Scale PS	✓	✓	s	$t\bar{t}$ FSR	✓	✓	s
Electron SF ChargeMisID Syst	✓	✓	s	$t\bar{t}$ scales μ_R μ_F	✓	✓	a
Electron SF ChargeMisID Stat	✓	✓	s	$t\bar{t}$ hadronization	✓	✓	o
Electron SF simplified ID 3	✓	✓	s	$t\bar{t}$ hdamp	✓	✓	o
Electron SF simplified ID 4	✓	✓	s	$t\bar{t}$ p_{T}-hard	✓	✓	o
Electron SF simplified ID 11	✓	✓	s	$t\bar{t}$ PDF	✓	✓	o
Electron SF simplified ID 14	✓	✓	s	Norm. Single top by 4%	✓	✓	s
Electron SF simplified ID 25	✓	✓	s	Norm. Diboson by 6%	✓	✓	s
Electron SF simplified ID 32	✓	✓	s	Norm. $Z \to \ell\ell$ by 5%	✓	✓	s
Electron SF Isolation	✓	✓	s	Norm. $W \to \tau\nu$ by 5%	✓	✓	s
Multijet Electron MC Shape	✓	✓	o				
Multijet Electron $E_{\mathrm{T}}^{\mathrm{miss}}$	✓	✓	a				
Multijet Electron mix$E_{\mathrm{T}}^{\mathrm{miss}}$	✓	✓	o				
——— Statistical ———							
Data stat.	✗	✗	s				
Signal stat.	✗	✗	s				
Background stat.	✗	✗	s				

The single-differential and double-differential cross-sections in the electron, muon and combined channel are shown in Figure 11.1 and Figure 11.2, respectively. The first ratio panel shows a comparison between the cross-sections of the single channels and the combined cross-section. It is important to underline that the single channels *before* their respective systematic shifts from the combination procedure are depicted. On the contrary, the second ratio panel shows the difference of the individual cross-sections *after* their shifts with respect to the combined cross-section and normalized to the uncorrelated uncertainty. Finally, the individual shifts of all systematic uncertainties

are shown in Figure 11.3, for the single- and double-differential combination procedures.

The single-differential cross-sections show an excellent agreement between electron and muon channels, see Figure 11.1. The combination fit obtains a χ^2 per degrees of freedom of $\chi^2/ndf = 9.06/24$ with a probability of $99.75\,\%$, indicating an overestimation of uncertainties. The pulls shown in the lower ratio are below $1\,\sigma$ in nearly all bins. For $m_\mathrm{T}^\mathrm{W} > 500\,\mathrm{GeV}$, the combined cross-section shows a trend toward the electron-channel cross-sections while the muon channel yields larger/smaller cross-sections depending on the charge. This effect is related to the charge-dependent sagitta bias in the muon channel, see the discussion in Chapter 10. Similarly, it can be seen in Figure 11.3(a) that the sagitta bias uncertainties are shifted by about $1\,\sigma$ in the 1D combination procedure while all other uncertainties show negligible shifts.

The double-differential cross-sections demonstrate an overall reasonable agreement between the two channels as well, see Figure 11.2. The χ^2/ndf amounts to $91.51/80$ with a probability of $17.83\,\%$. The pulls of the shifted individual cross-sections are generally larger than for the single-differential cross-sections. Additionally, it is striking that the combined cross-section is larger than the cross-sections from both input channels over a large part of the $m_\mathrm{T}^\mathrm{W} \otimes |\eta(\mu)|$ spectrum. Given that the individual cross-sections are shown before they are shifted in the fitting procedure by systematic uncertainties, such an effect is possible.
All shifts of systematic uncertainties in the 2D combination procedure are depicted in Figure 11.3(b). Generally, the shifts are larger than for the 1D combination, nevertheless, they are below $0.5\,\sigma$ for the majority of uncertainties. The only uncertainties shifted by more than $1\,\sigma$ are `Multijet MC Scaling` and `Muon Sagitta` p_T`-extra`. The former is related to the normalization of the EW MC samples used in the QCD-enriched regions where fake efficiencies are calculated (see Section 6.4). The shift here hints towards an overestimated multijet contribution. The muon sagitta-bias uncertainty related to the $p_\mathrm{T}(\mu)$-extrapolation is shifted by more than $1.5\,\sigma$. This effect is consistent with what was seen before in this thesis. In particular, at high $p_\mathrm{T}(\mu)$ and in the end-cap regions ($|\eta(\mu)| > 1$), the muon momentum measurement is subject to a residual sagitta bias that is not entirely covered by the given correction nor associated systematic uncertainty.

Overall, the combination procedure provides a crucial cross-check of the single channels. In addition, the successful combination of the cross-sections measured in the electron and muon channel importantly underlines lepton universality, a central concept of the SM.

Particularly, the combined cross-section represents a refined result as it uses information from both channels. Not only the statistical enhancement but also the information from systematic uncertainties, in particular, addressing the sagitta bias in the muon channel, is valuable. For instance, the overall precision in the single-differential W^+ measurement can be improved to about $2\,\%$ in the first bin and $24\,\%$ in the last bin (compared to $\sim 3\,\%/38\,\%$ for μ^+-only).
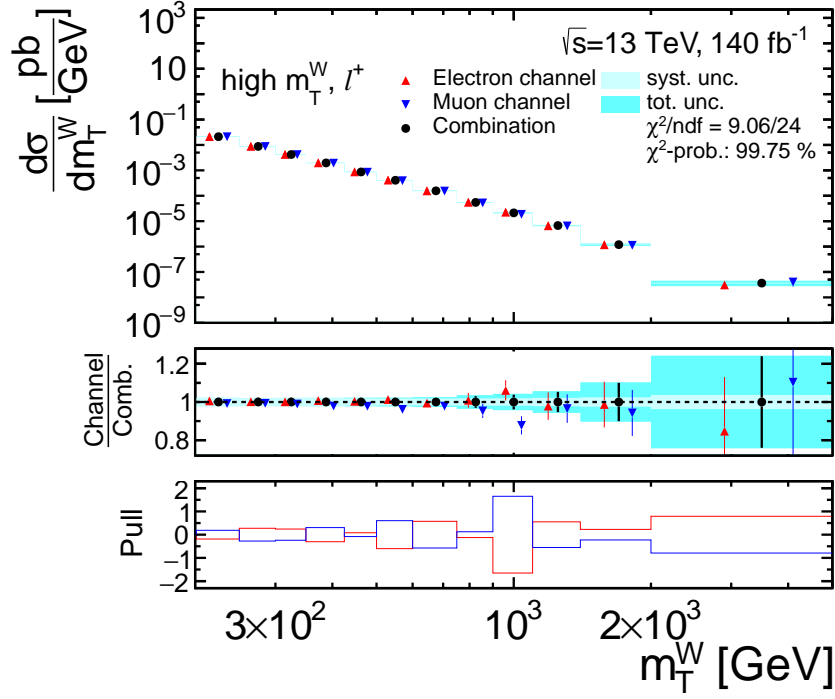
(a)
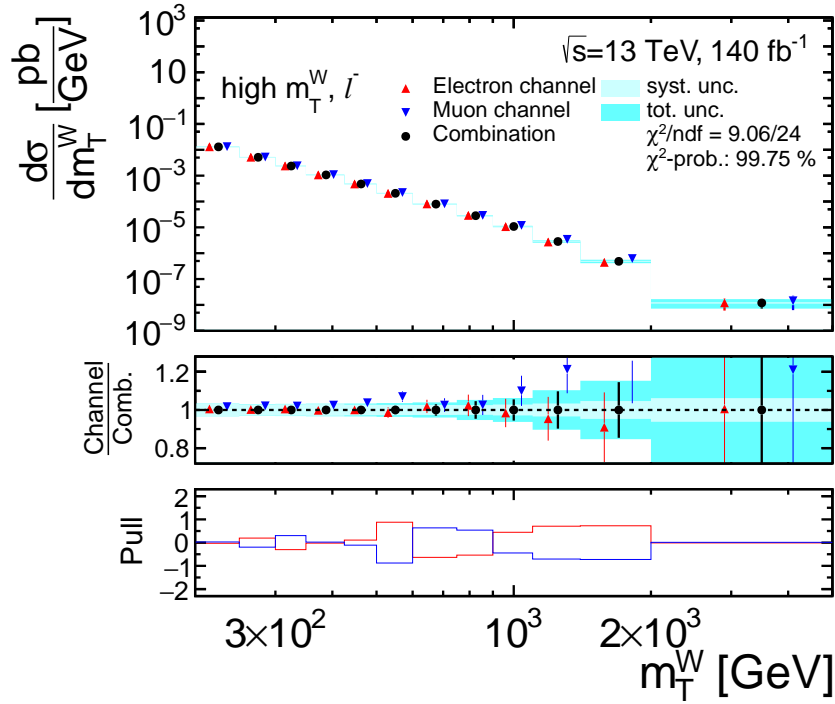
(b)

Figure 11.1.: Single-differential cross-sections for the (a) positive and (b) negative charge as a function of m_T^W measured in the muon channel, electron channel as well as their combination. In the upper ratio, the pre-fit single-channels are compared to the combined cross-section. In the bottom ratio, the residual pull normalized to the uncorrelated uncertainty between single channel and combination is shown after the shifts.
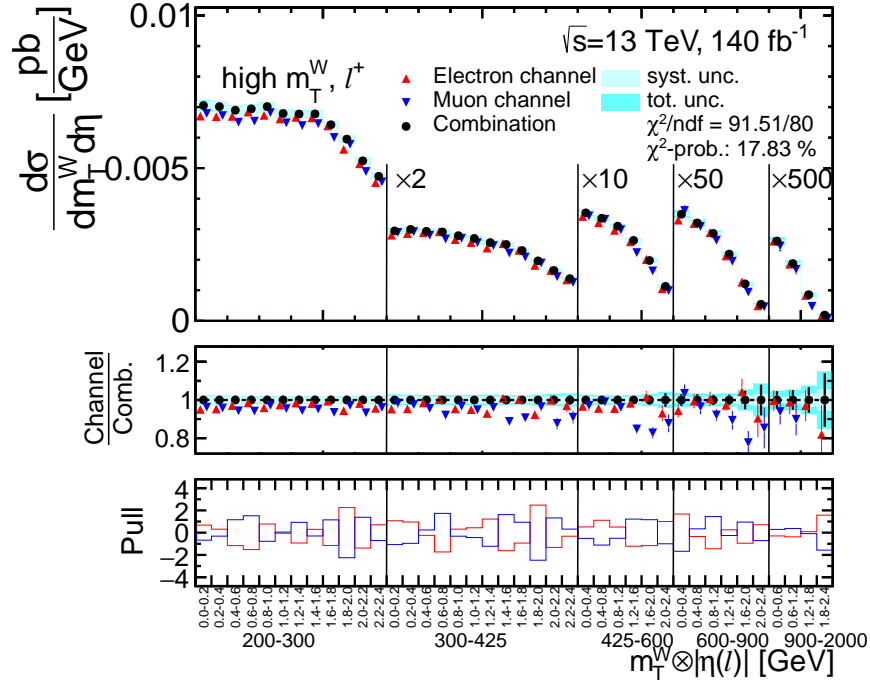
(a)
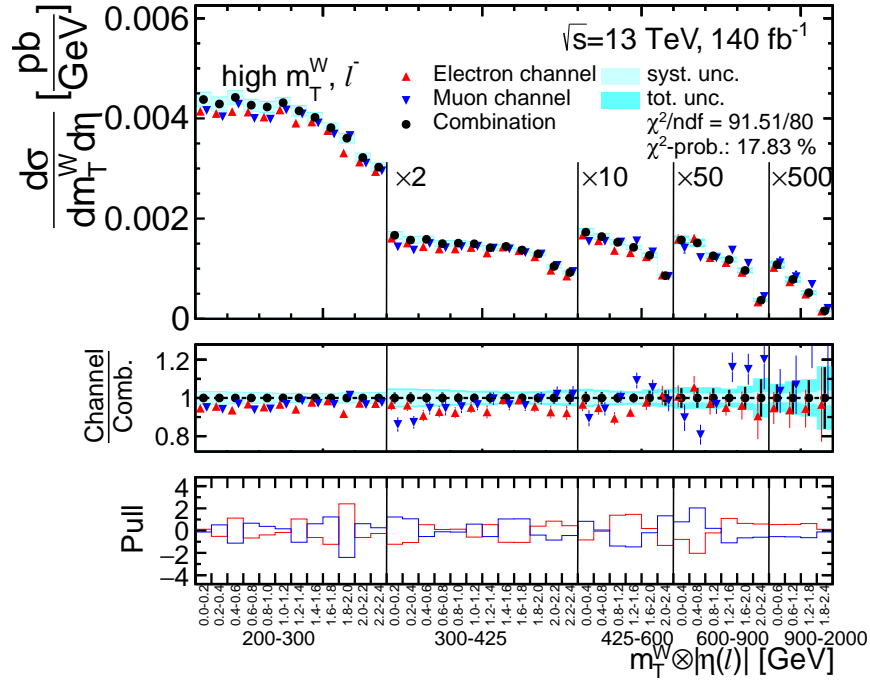
(b)

Figure 11.2.: Double-differential cross-sections for the (a) positive and (b) negative charge as a function of $m_{\mathrm{T}}^{\mathrm{W}}$ and $|\eta(\ell)|$ measured in the muon channel, electron channel as well as their combination. The cross-sections for the last four $m_{\mathrm{T}}^{\mathrm{W}}$ bins are scaled up for better visibility. In the upper ratio, the pre-fit single-channels are compared to the combined cross-section. In the bottom ratio, the residual pull normalized to the uncorrelated uncertainty between single channel and combination is shown after the shifts.

149

(a)   (b)
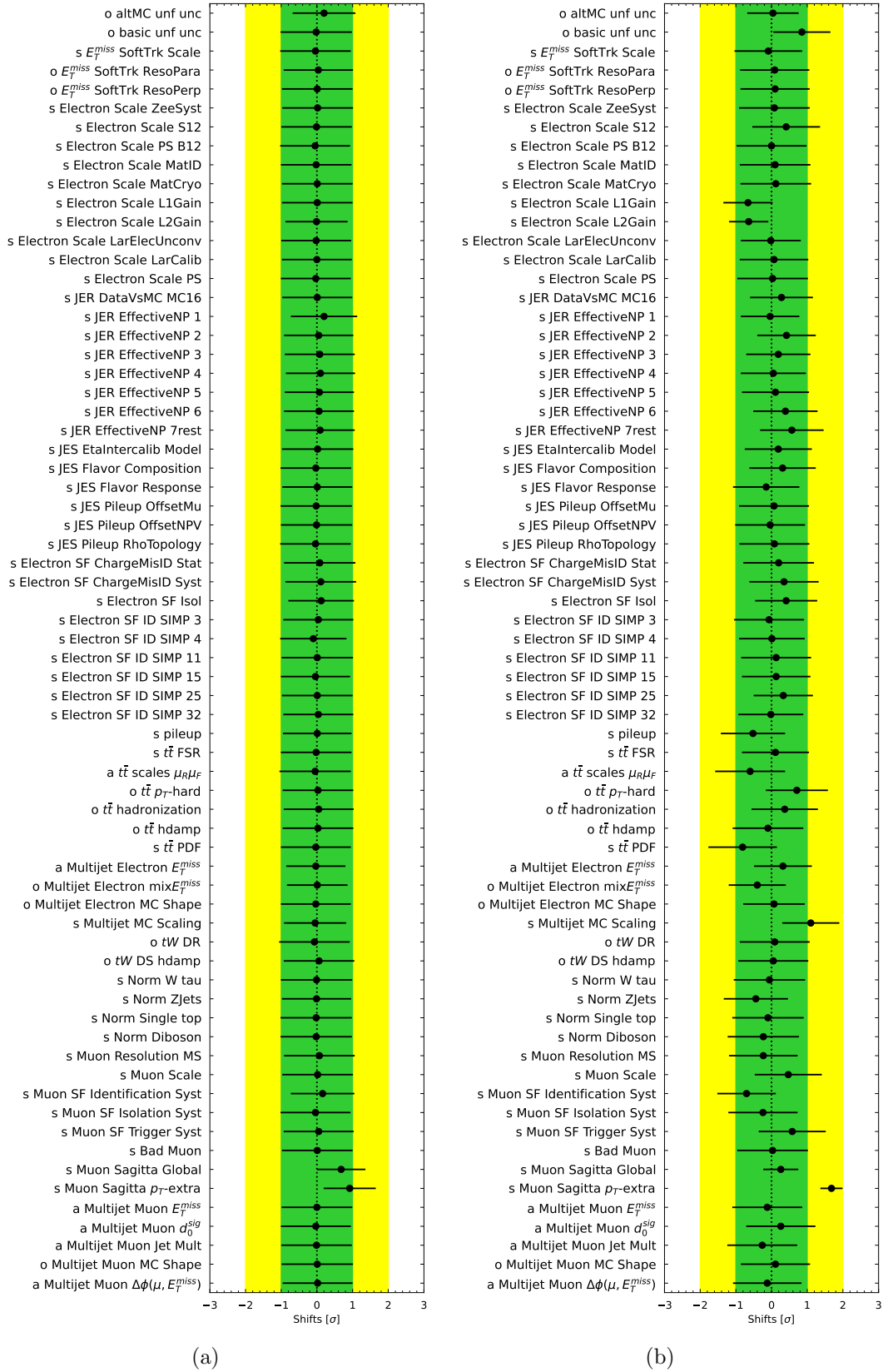
Figure 11.3.: Shifts of the systematic uncertainties induced by the combination fit of the (a) single-differential and (b) double-differential cross-sections measured in the e- and μ-channel. All uncertainties are marked whether they are symmetric (s), asymmetric (a) or one-sided (o).

Conclusion

In this thesis, a measurement of differential cross-sections of the charged-current Drell-Yan process in the muonic decay channel at high transverse masses is presented. The analysis is based on proton-proton-collision data collected at a center-of-mass energy of $\sqrt{s} = 13\,\text{TeV}$ with the ATLAS detector during the 2015-2018 data-taking period, corresponding to an integrated luminosity of $140\,\text{fb}^{-1}$. The measurement is performed separately for each W-boson charge, with the charge asymmetry also being provided. The results are presented differentially in m_T^W, in a range of $200\,\text{GeV} < m_\text{T}^\text{W} < 5000\,\text{GeV}$, and double-differentially in m_T^W and the pseudorapidity of the muon, covering $200\,\text{GeV} < m_\text{T}^\text{W} < 2000\,\text{GeV}$ and $0 < |\eta(\mu)| < 2.4$.

A measurement of the charged-current Drell-Yan cross-sections in this extreme phase space is performed for the first time. It offers crucial insights into the substructure of the proton, providing essential input for further testing the SM at the LHC. The measurement is expected to be valuable for probing parton distribution functions of quarks and antiquarks in the less-constrained high-x region. Additionally, as the measurement extends to very high energies (up to $m_\text{T}^\text{W} = 5\,\text{TeV}$), it offers sensitivity to small deviations between SM predictions and measured data at the energy frontier of the LHC. Thus, the results are expected to play an important role in confining effective field theory parameters in the future. Lastly, measuring the high-mass distribution of the ccDY process will provide constraints on the running electroweak coupling at high energy scales.

A dataset enriched in $W \to \mu\nu$ events is obtained by selecting events with exactly one muon with $p_\text{T}(\mu) > 65\,\text{GeV}$ and $|\eta(\mu)| < 2.4$, alongside $E_\text{T}^\text{miss} > 85\,\text{GeV}$. Approximately 65% of the events selected are signal events, with the $t\bar{t}$ process as the dominant background process ($\sim 25\%$). The multijet background, consisting of fake muons from B-meson decays in jets, was estimated using the Matrix Method, and amounts to less than 2%. Overall, good agreement between the distributions of data and predicted events is observed in a variety of control observables. Nevertheless, for $m_\text{T}^\text{W} \gtrsim 700\,\text{GeV}$, deviations of $10 - 20\%$ between data and predictions are present, with opposite trends for different muon charges. The cause is related to a residual charge-dependent sagitta bias in the muon momentum reconstruction. The background-subtracted data is unfolded to the Born level, correcting for detector smearing, measurement efficiency and acceptance. Due to large bin-to-bin migrations particularly from the mass peak to the high m_T^W region, the method of Iterative Bayesian Unfolding is employed. The unfolding procedure is studied rigorously with tests conducted to optimize the number of iterations, the measurement binning and the usage of a shadow bin to handle in-smearing.

The final results include both statistical and systematic uncertainties. Experimental uncertainties are associated with the measurement of the muon, E_T^{miss}, jets, and the data-driven multijet estimate. Theoretical uncertainties on top background processes are considered as well. Possible biases introduced by the signal MC sample used for the unfolding are addressed via dedicated tests where the prediction is reweighted to data or an alternative signal sample is employed. The overall precision of the single- and double-differential measurements ranges from $\sim 3\%$ at low m_T^W to $\sim 65\%$ at high m_T^W. Total systematic uncertainties span from $\sim 2.5\%$ to $\sim 40\%$, with statistical uncertainties ranging from $\sim 0.5\%$ to $\sim 65\%$. In the first m_T^W bin, the dominant uncertainties are related to the E_T^{miss} soft track and the jet energy resolution. At higher m_T^W, the leading uncertainties are due to statistical limitations and the sagitta bias in the muon momentum. The differential asymmetry between the W^+ and W^- cross-sections is measured with an absolute uncertainty spanning between 0.0134 and 0.321.

The Born-level cross-sections are compared to theoretical predictions from MC simulations using POWHEG +PYTHIA 8 and SHERPA 2.2.11, respectively. In general, the agreement between measured and predicted cross-sections is good. However, a deviation of up to 20% in opposite directions for the two muon charges is observed, attributed to the sagitta bias in the muon momentum measurement and covered approximately by the associated uncertainty.

Finally, the muon-channel cross-sections derived in this thesis are combined with electron-channel cross-sections. The combination demonstrates good agreement between the two lepton flavors, with a $\chi^2/ndf = 9.06/24$ (1D) and $\chi^2/ndf = 91.51/80$ (2D). Overall, the measurement accuracy and precision are improved by using information from both channels.

As next steps, the cross-sections presented will be compared to fixed-order theory predictions, with ongoing efforts in the analysis team focusing on comparisons using the DYTURBO tool [181]. In particular, comparisons to cross-sections predicted with different PDF sets will be performed. Additionally, the results will serve as essential inputs for global fits of ATLAS data with respect to PDF and EFT interpretations, respectively.

Future measurements will benefit from a more sophisticated treatment of the sagitta bias for high-momentum muons as it is the by-far leading systematic uncertainty here. The sagitta-bias calibration can be refined in the future by extending to high $p_T(\mu)$ regions using W-boson data alongside the Z-boson peak currently used.
Finally, the statistical uncertainty in future measurements of the $W \to \mu\nu$ high-mass tail can be mitigated by a significant increase in integrated luminosity or center-of-mass energy. This way, even higher transverse masses in the ccDY process can be probed which is a powerful handle for exploring the energy frontier of collider experiments.

Appendices

A. Various supplemental material

Table A.1.: Overview of the various samples for positive charged W boson decaying into a muon and neutrino. The process, the mass range, the cross-section, the dataset identifier (DSID) as well as the number of generated events of each sample are shown.

Process	$m_W^{\min}$ [GeV]	$m_W^{\max}$ [GeV]	σ [pb]	DSID	Events (`mc16a+mc16d+mc16e`)
$W^+ \to \mu^+\nu$	-	120	1.13×10^4	361101	39962000+49941000+66298600
$W^+ \to \mu^+\nu$	120	180	32.1	301100	4992000+5987000+8316000
$W^+ \to \mu^+\nu$	180	250	5.00	301101	1498000+1788000+2499000
$W^+ \to \mu^+\nu$	250	400	1.75	301102	600000+700000+1000000
$W^+ \to \mu^+\nu$	400	600	3.12×10^{-1}	301103	100000+100000+170000
$W^+ \to \mu^+\nu$	600	800	6.08×10^{-2}	301104	50000+50000+90000
$W^+ \to \mu^+\nu$	800	1000	1.77×10^{-2}	301105	50000+50000+90000
$W^+ \to \mu^+\nu$	1000	1250	7.29×10^{-3}	301106	50000+50000+90000
$W^+ \to \mu^+\nu$	1250	1500	2.51×10^{-3}	301107	50000+50000+90000
$W^+ \to \mu^+\nu$	1500	1750	9.86×10^{-4}	301108	50000+50000+90000
$W^+ \to \mu^+\nu$	1750	2000	4.25×10^{-4}	301109	50000+50000+88000
$W^+ \to \mu^+\nu$	2000	2250	1.95×10^{-4}	301110	50000+50000+90000
$W^+ \to \mu^+\nu$	2250	2500	9.33×10^{-5}	301111	50000+50000+90000
$W^+ \to \mu^+\nu$	2500	2750	4.63×10^{-5}	301112	50000+50000+90000
$W^+ \to \mu^+\nu$	2750	3000	2.35×10^{-5}	301113	50000+50000+90000
$W^+ \to \mu^+\nu$	3000	3500	1.84×10^{-5}	301114	50000+50000+90000
$W^+ \to \mu^+\nu$	3500	4000	5.10×10^{-6}	301115	50000+50000+90000
$W^+ \to \mu^+\nu$	4000	4500	1.43×10^{-6}	301116	50000+50000+90000
$W^+ \to \mu^+\nu$	4500	5000	4.01×10^{-7}	301117	50000+50000+90000
$W^+ \to \mu^+\nu$	5000	-	1.53×10^{-7}	301118	50000+50000+90000

Table A.2.: Overview of the various samples for negative charged W boson decaying into a muon and neutrino. The process, the mass range, the cross-section, the dataset identifier (DSID) as well as the number of generated events of each sample are shown.

Process	$m_W^{\min}$ [GeV]	$m_W^{\max}$ [GeV]	σ [pb]	DSID	Events (`mc16a+mc16d+mc16e`)
$W^- \to \mu^- \bar{\nu}$	-	120	8.28×10^4	361104	31973000+39974000+53057400
$W^- \to \mu^- \bar{\nu}$	120	180	22.2	301120	4999000+5986000+8310000
$W^- \to \mu^- \bar{\nu}$	180	250	3.28	301121	1500000+1803000+2498000
$W^- \to \mu^- \bar{\nu}$	250	400	1.08	301122	594000+698000+999000
$W^- \to \mu^- \bar{\nu}$	400	600	1.75×10^{-1}	301123	100000+100000+170000
$W^- \to \mu^- \bar{\nu}$	600	800	3.10×10^{-2}	301124	50000+50000+90000
$W^- \to \mu^- \bar{\nu}$	800	1000	8.29×10^{-3}	301125	50000+50000+90000
$W^- \to \mu^- \bar{\nu}$	1000	1250	3.16×10^{-3}	301126	50000+50000+90000
$W^- \to \mu^- \bar{\nu}$	1250	1500	1.00×10^{-3}	301127	50000+50000+90000
$W^- \to \mu^- \bar{\nu}$	1500	1750	3.68×10^{-4}	301128	50000+50000+90000
$W^- \to \mu^- \bar{\nu}$	1750	2000	1.49×10^{-4}	301129	50000+50000+90000
$W^- \to \mu^- \bar{\nu}$	2000	2250	6.53×10^{-5}	301130	50000+50000+90000
$W^- \to \mu^- \bar{\nu}$	2250	2500	3.02×10^{-5}	301131	50000+50000+90000
$W^- \to \mu^- \bar{\nu}$	2500	2750	1.45×10^{-5}	301132	50000+50000+89000
$W^- \to \mu^- \bar{\nu}$	2750	3000	7.26×10^{-6}	301133	50000+50000+90000
$W^- \to \mu^- \bar{\nu}$	3000	3500	5.67×10^{-6}	301134	50000+50000+90000
$W^- \to \mu^- \bar{\nu}$	3500	4000	1.60×10^{-6}	301135	50000+50000+90000
$W^- \to \mu^- \bar{\nu}$	4000	4500	4.72×10^{-7}	301136	50000+50000+89000
$W^- \to \mu^- \bar{\nu}$	4500	5000	1.43×10^{-7}	301137	50000+50000+90000
$W^- \to \mu^- \bar{\nu}$	5000	-	6.16×10^{-8}	301138	50000+50000+90000
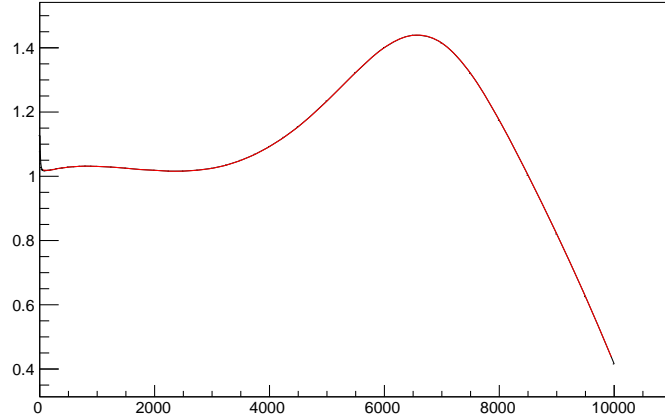
(a)
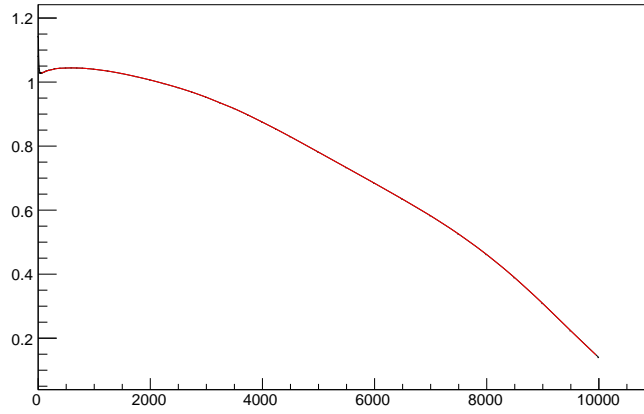
(b)
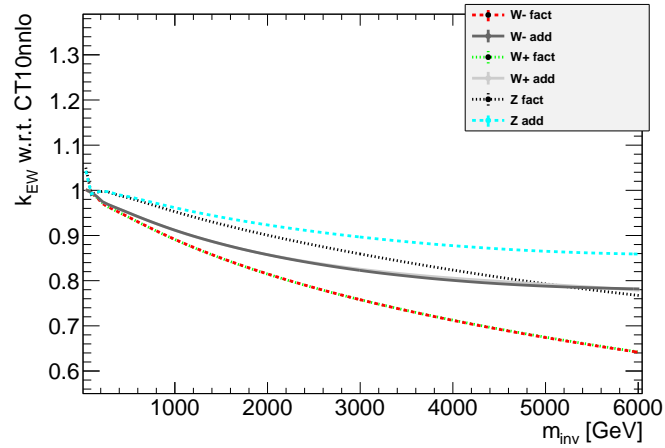
(c)

Figure A.1.: Higher-order corrections to the ccDY cross-section as a function of the invariant mass [182]. In the two upper two plots, the combined corrections correcting from NLO to NNLO in QCD as well as from the CT10NLO to CT14NNLO PDF set are shown for (a) W^+ and (b) W^- as a function of the invariant mass. In (c) different NLO EW corrections are depicted as a function of the invariant mass.
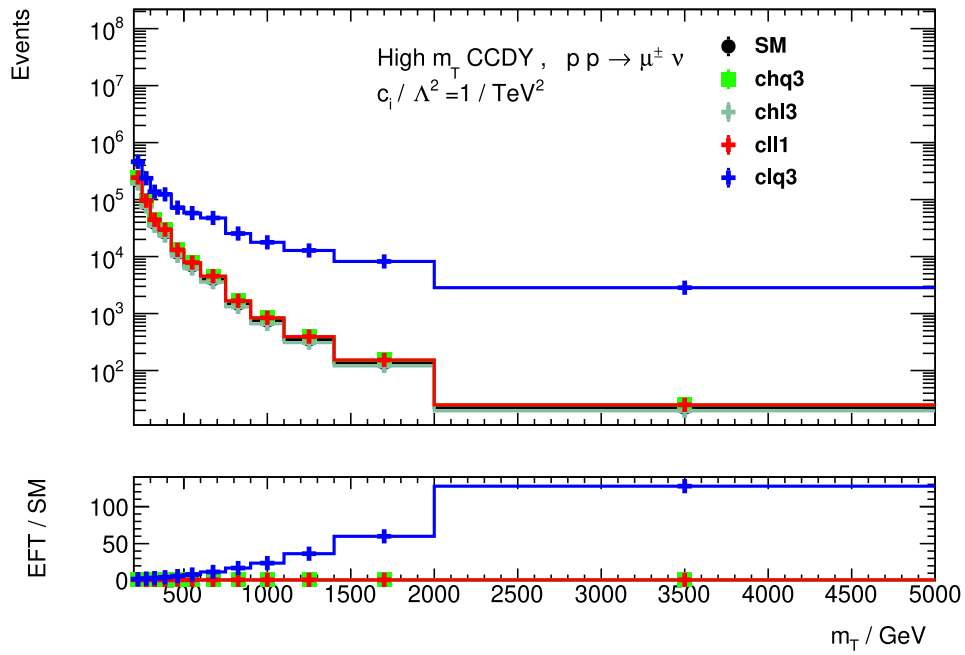
Figure A.2.: Expected number of events in the high-m_T^W phase space comparing the SM prediction as well as the addition of four different dimension-6 EFT operators using Wilson coefficients of one [183].

A.1. PDF sensitivity of the ccDY process

(a)

(b)

(c)
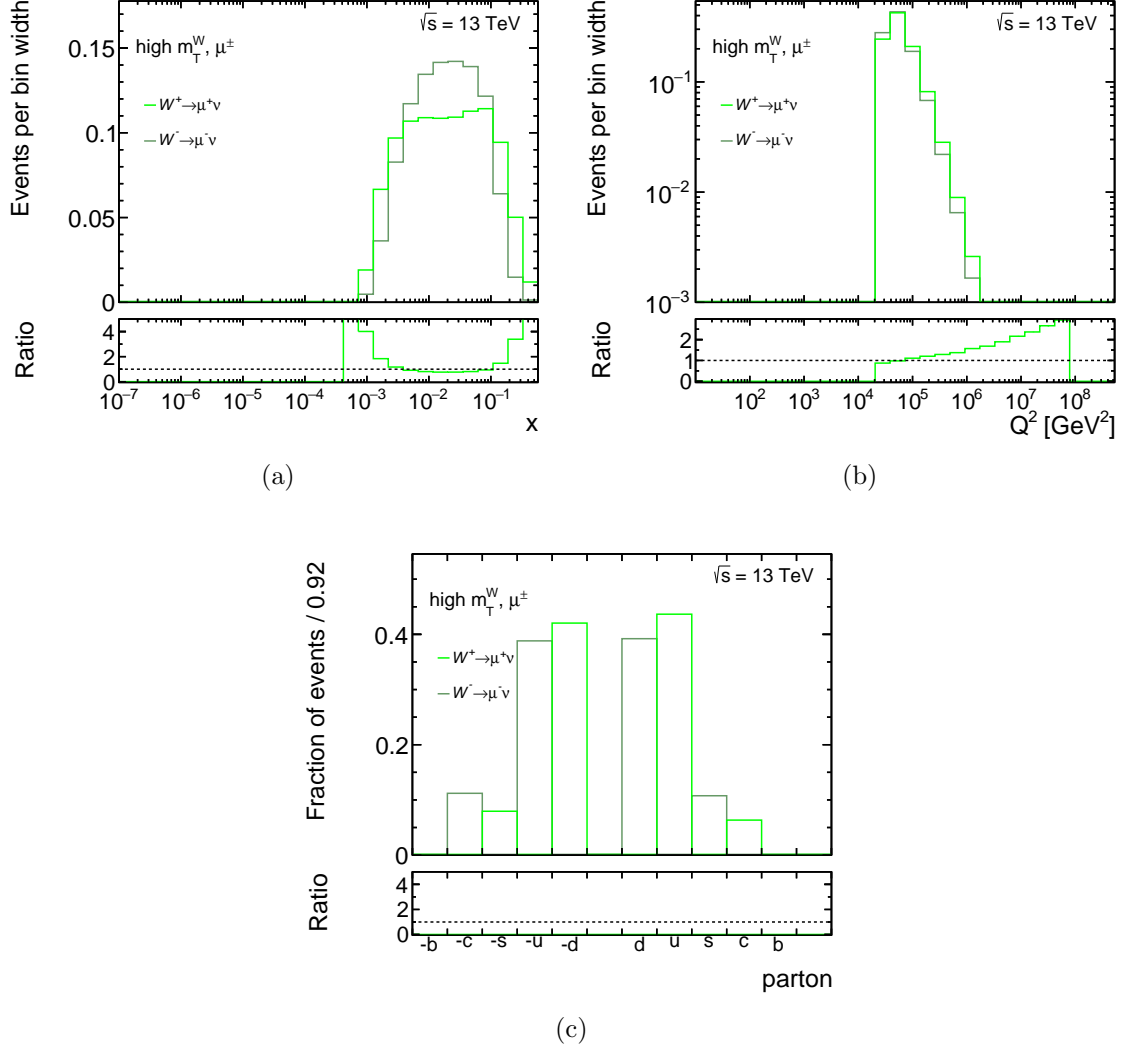
Figure A.3.: PDF information taken from the POWHEG+PYTHIA8 simulation of the signal process (as introduced in Section 3.3) including the fiducial measurement cuts given in Section 5.2.
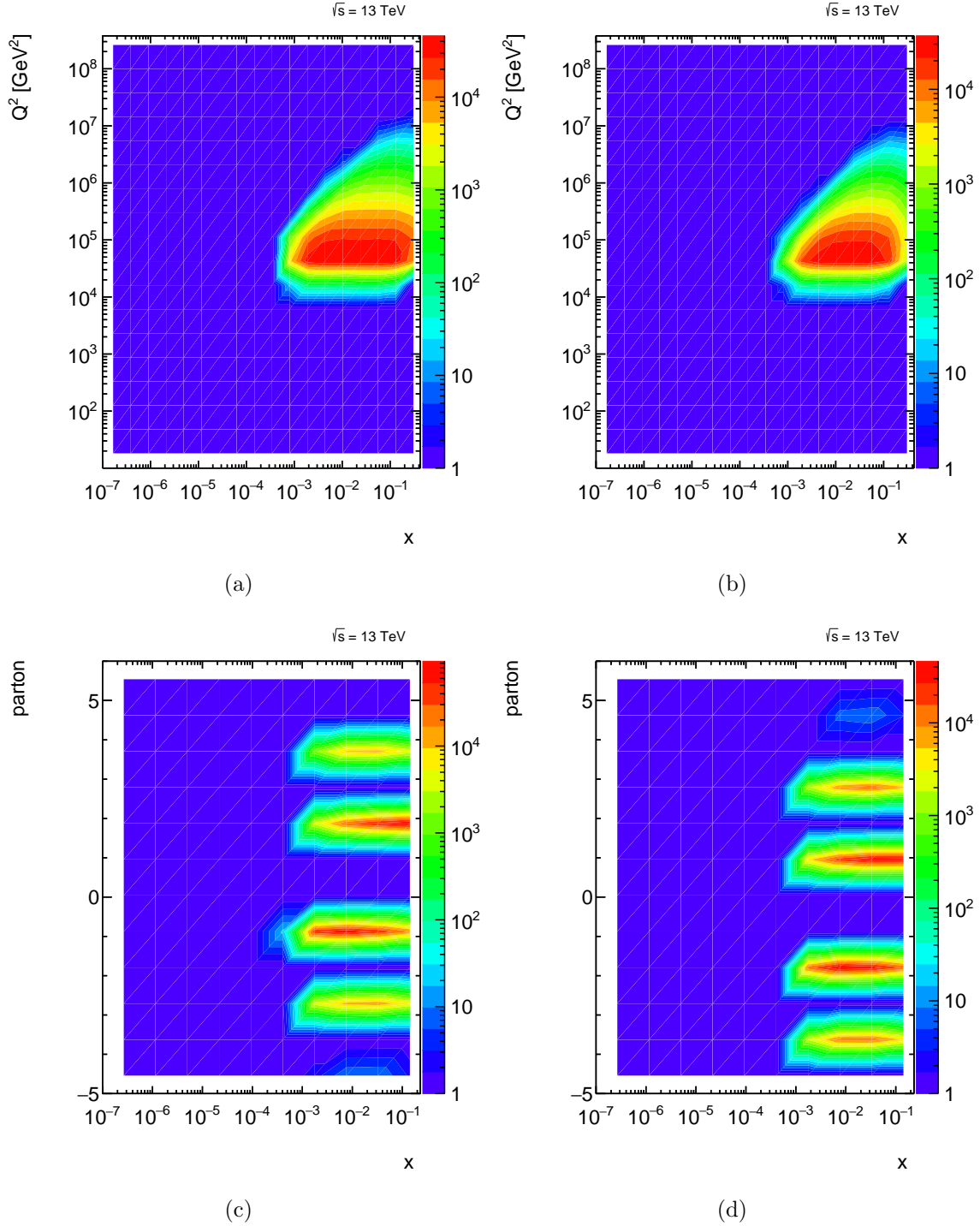
Figure A.4.: Two-dimensional PDF information taken from the POWHEG+PYTHIA8 simulation of the signal process (as introduced in Section 3.3) including the fiducial measurement cuts given in Section 5.2. The left-hand side corresponds to W^+ and the right-hand side to W^-. Partons are shown according to their PDG ID (d→1, u→2, s→3, c→4, b→5) where negative numbers correspond to antiparticles.

A.2. Feynman graphs of background processes

(a) (b) (c)
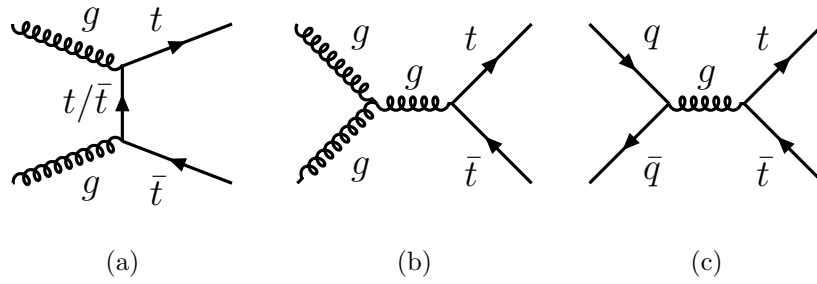
Figure A.5.: Leading-order Feynman diagrams of the $t\bar{t}$ process.

(a) (b) (c) (d)
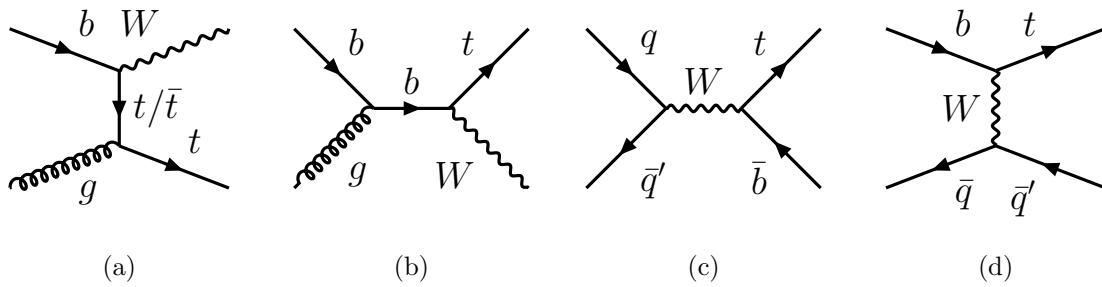
Figure A.6.: Leading-order Feynman diagrams of single-top processes (single antitop is not shown explicitly).

(a)   (b)   (c)   (d)

(e)
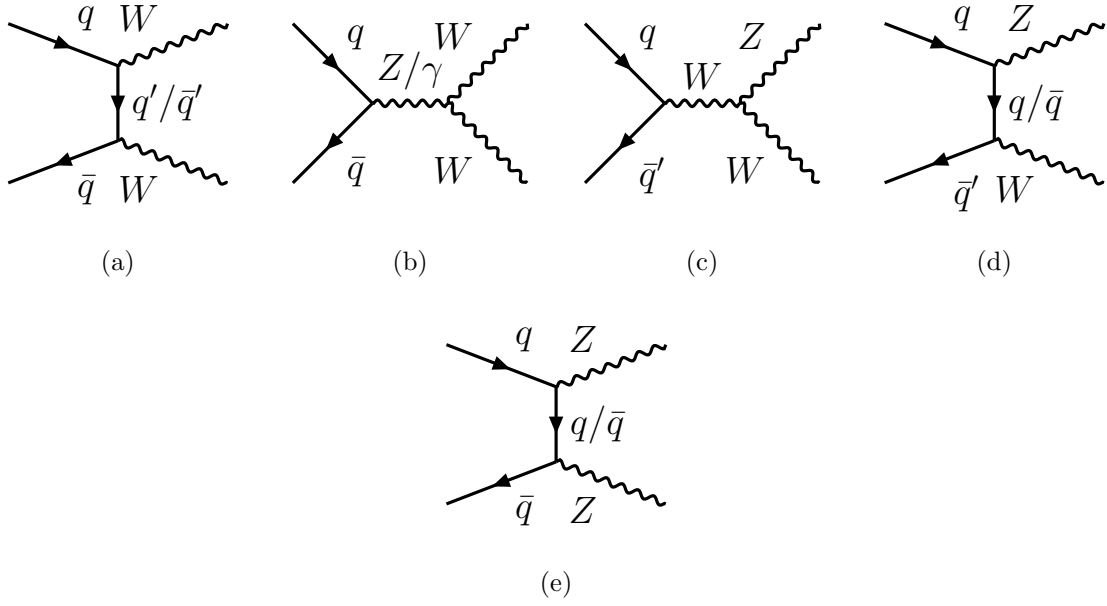
Figure A.7.: Leading-order Feynman diagrams of diboson (WW, WZ, ZZ) processes.

(a)   (b)   (c)
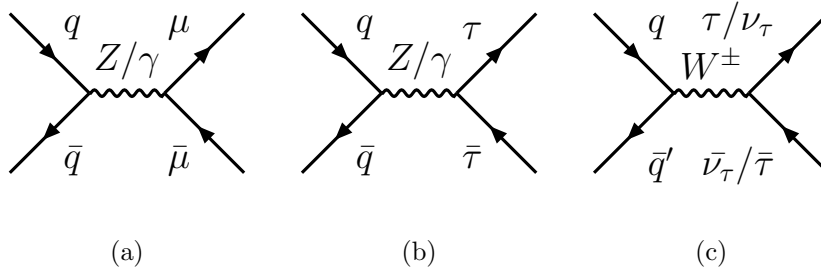
Figure A.8.: Leading-order Feynman diagrams of DY background processes considered.

(a)   (b)
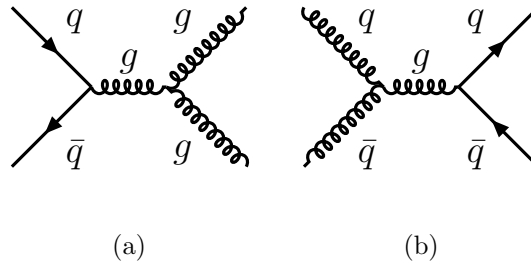
Figure A.9.: Two examples of leading-order Feynman diagrams of dijet production.

B. Sagitta bias correction

In general, it is recommended for each analysis to investigate the sagitta bias to data (see Section 4.2.5). Two options for handling this exist:

- `Setup1`: A sagitta-bias correction is applied to the data and an additional associated systematic uncertainty is provided.

- `Setup2`: Data is not corrected and the sagitta bias is addressed in a dedicated systematic uncertainty only.

In this analysis, `Setup1` is used as it was found to yield an improved performance.

A direct comparison between the data with and without correction is shown in Figure B.1, as an example for 2017 data and the variables $p_\mathrm{T}(\mu)$, m_T^W and $m_\mathrm{T}^\mathrm{W} \otimes |\eta(\mu)|$. A substantial effect of around $5-20\,\%$ is noticeable, whereas both charges show an opposite behavior.

If using `Setup2`, i.e. no data correction, some consistency issues in the MC-data comparisons between the two muon charges were visible, as depicted in Figure B.2 (without data correction) for $p_\mathrm{T}(\mu)$, m_T^W and $m_\mathrm{T}^\mathrm{W} \otimes |\eta(\mu)|$. In particular, the μ^--channel is not showing reasonable results. In contrast, the comparisons with the data correction look more sensible, as depicted in Figure 7.2(a)/7.3(a) ($p_\mathrm{T}(\mu)$), Figure 7.4 (m_T^W) and Figure 7.7 ($m_\mathrm{T}^\mathrm{W} \otimes |\eta(\mu)|$).

Finally, a good consistency between charges and lepton flavors (via a comparison with the parallel electron channel) is of great importance. This is quantified in form of electron-muon-ratios (μ/e) and double-ratios ($\mu_\mathrm{unf}^+/\mu_\mathrm{truth}^+ / \mu_\mathrm{unf}^-/\mu_\mathrm{truth}^-$) of the unfolded cross-sections, in the discriminant variables m_T^W and $m_\mathrm{T}^\mathrm{W} \otimes |\eta(\mu)|$. These are shown for both setups in Figure B.3 (without data correction) and Figure B.4 (with data correction), respectively. All in all, the ratios are more consistent if the sagitta-bias correction is applied to the data.

It should be highlighted that all studies discussed in this Section were performed at an earlier stage of the analysis. In particular, the multijet estimate in both, the electron and muon channel, was refined substantially improving the overall agreement further, see Reference [84] for details.
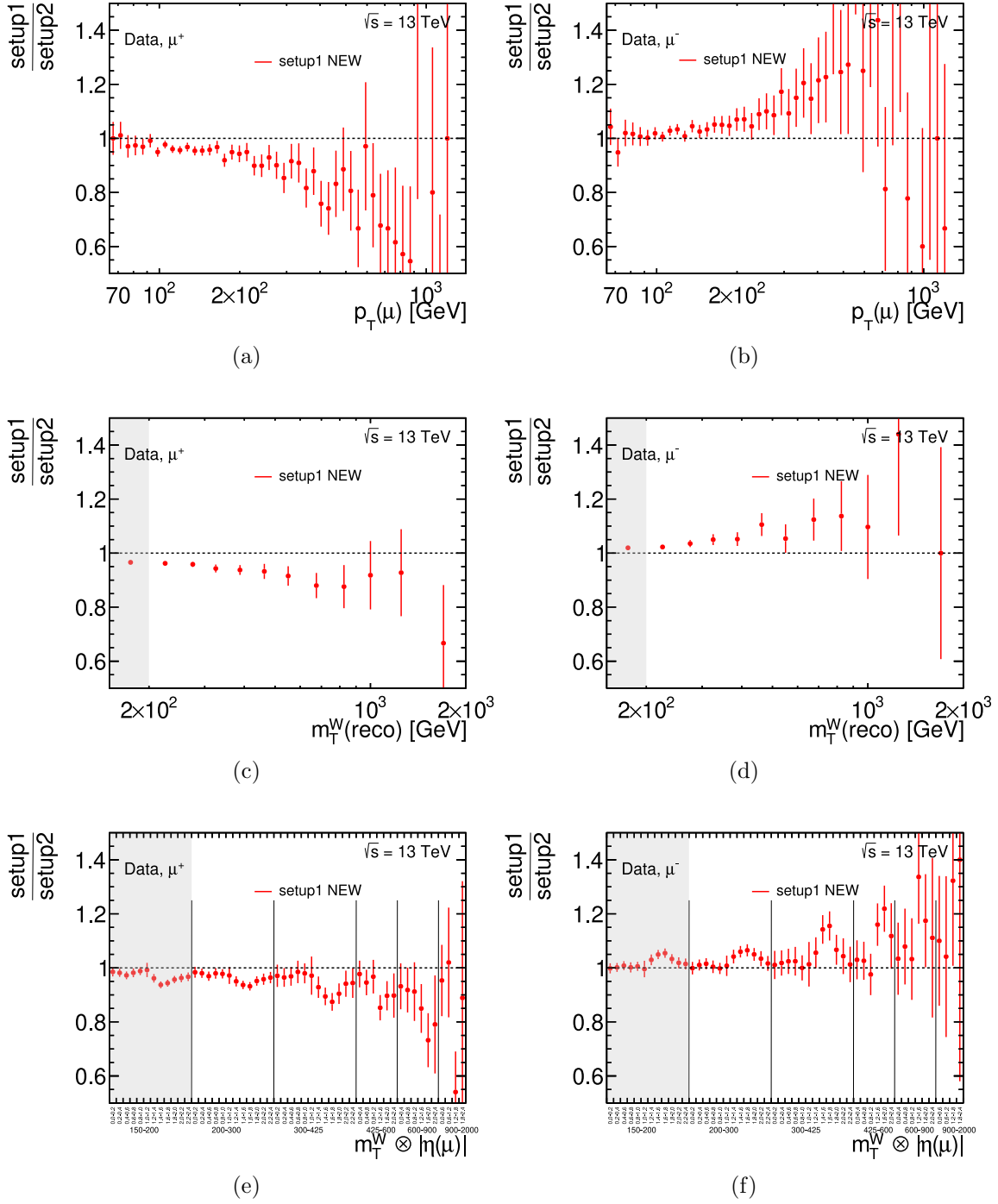
Figure B.1.: Comparison of the data yield whether the sagitta-bias correction is applied (setup1) or not applied (setup2), shown for data taken in 2017 for μ^+ (left-hand side) and μ^- (right-hand side) as a function fo the transverse momentum of the muon, the transverse mass and the transverse mass as well as the pseudorapidity of the muon.
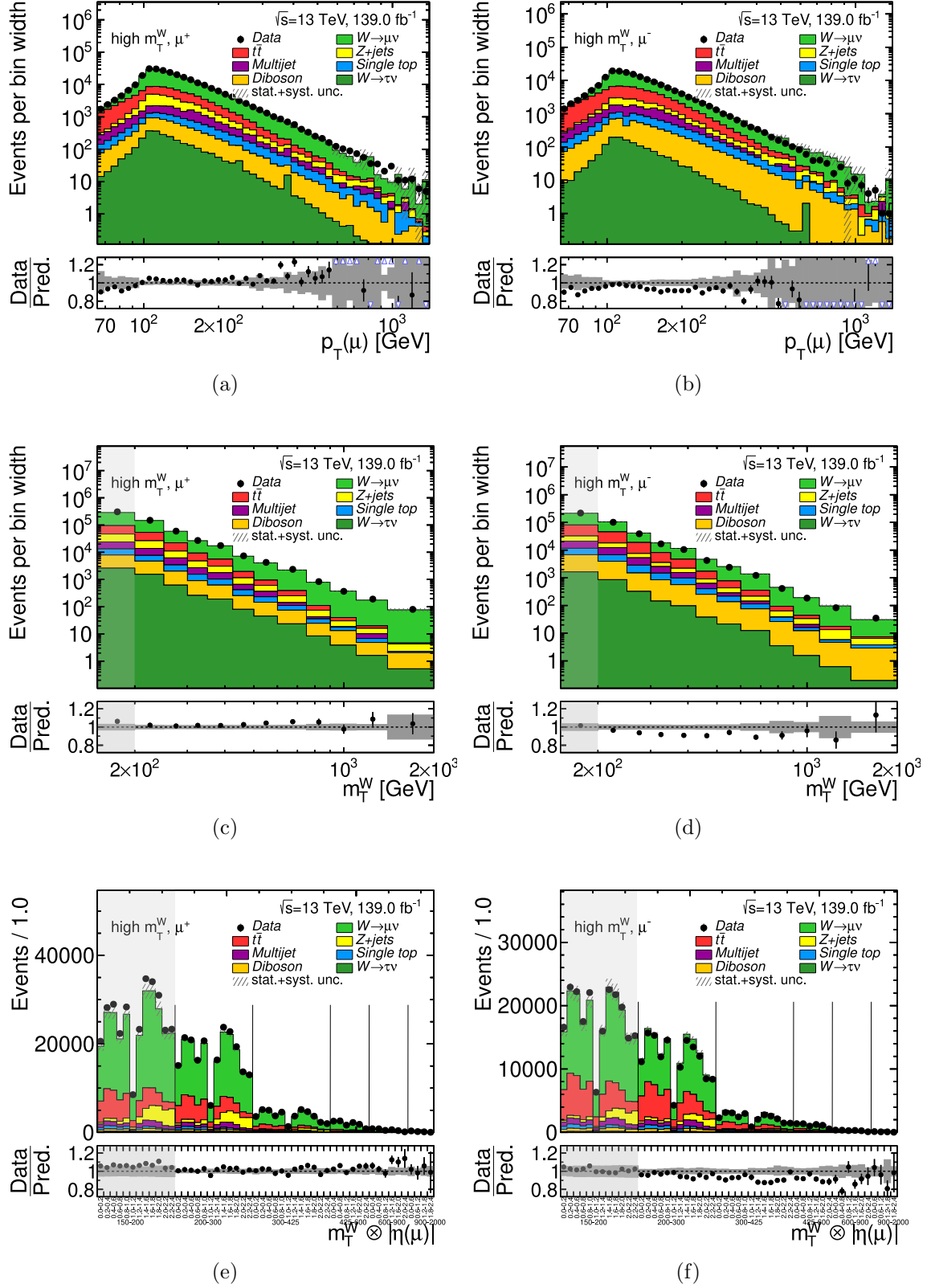
Figure B.2.: Distributions of the transverse momentum of the muon, transverse mass and transverse mass and pseudorapidity of the muon for data and prediction in the signal region for μ^+ (left) and μ^- (right). Statistical and systematic uncertainties are included. For the data distributions shown here no sagitta-bias correction is applied.

165
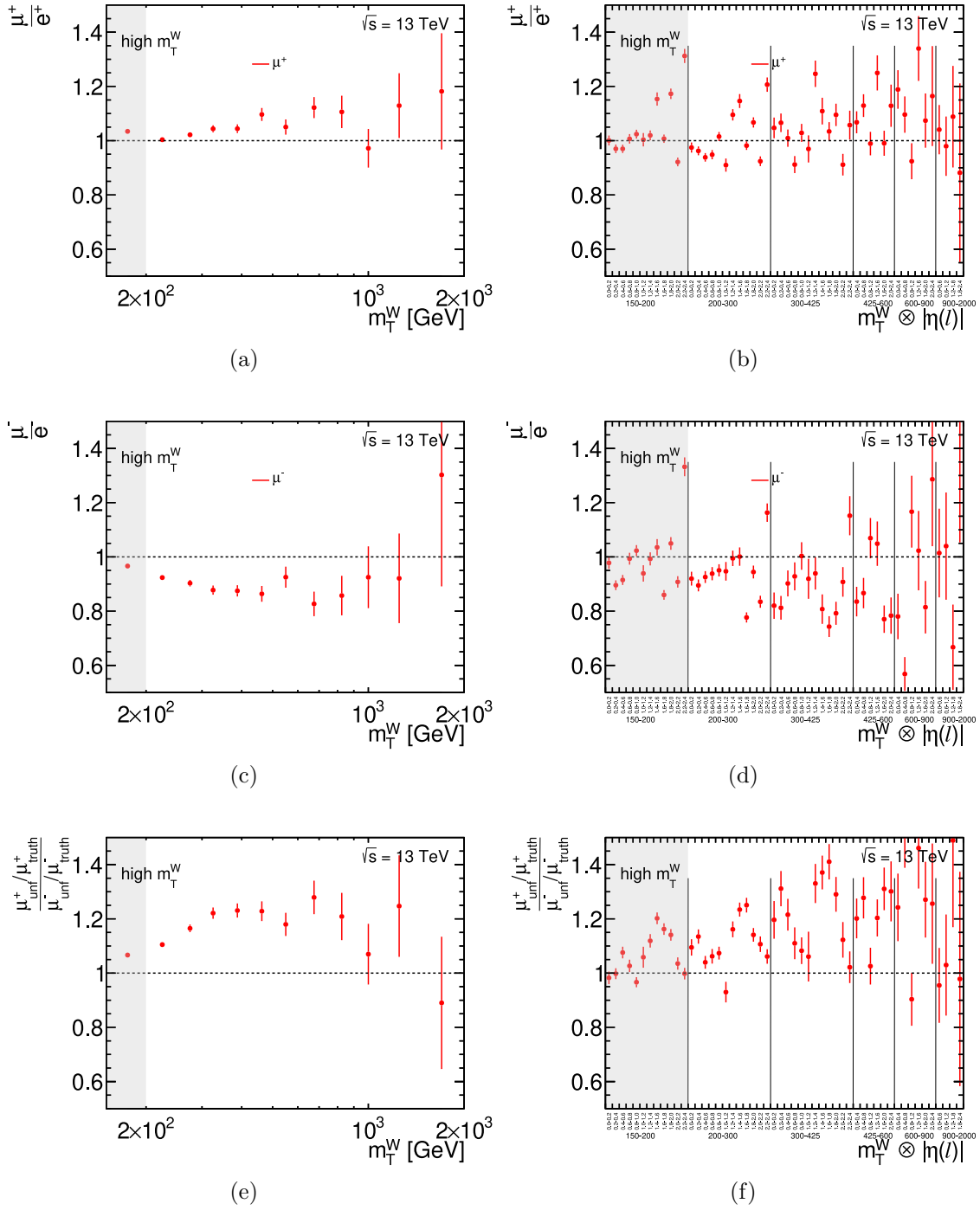
Figure B.3.: Ratios between the cross-sections obtained in the electron and muon channel for μ^+ (upper row) and μ^- (middle row) as well as double-ratios between the unfolded measured and MC predicted cross-sections in the μ^+- and μ^--channels (lower row). The single-differential (left-hand side) and double-differential (right-hand side) measurement distributions are shown. All cross-sections are based on data, that is **not corrected** for the sagitta bias.
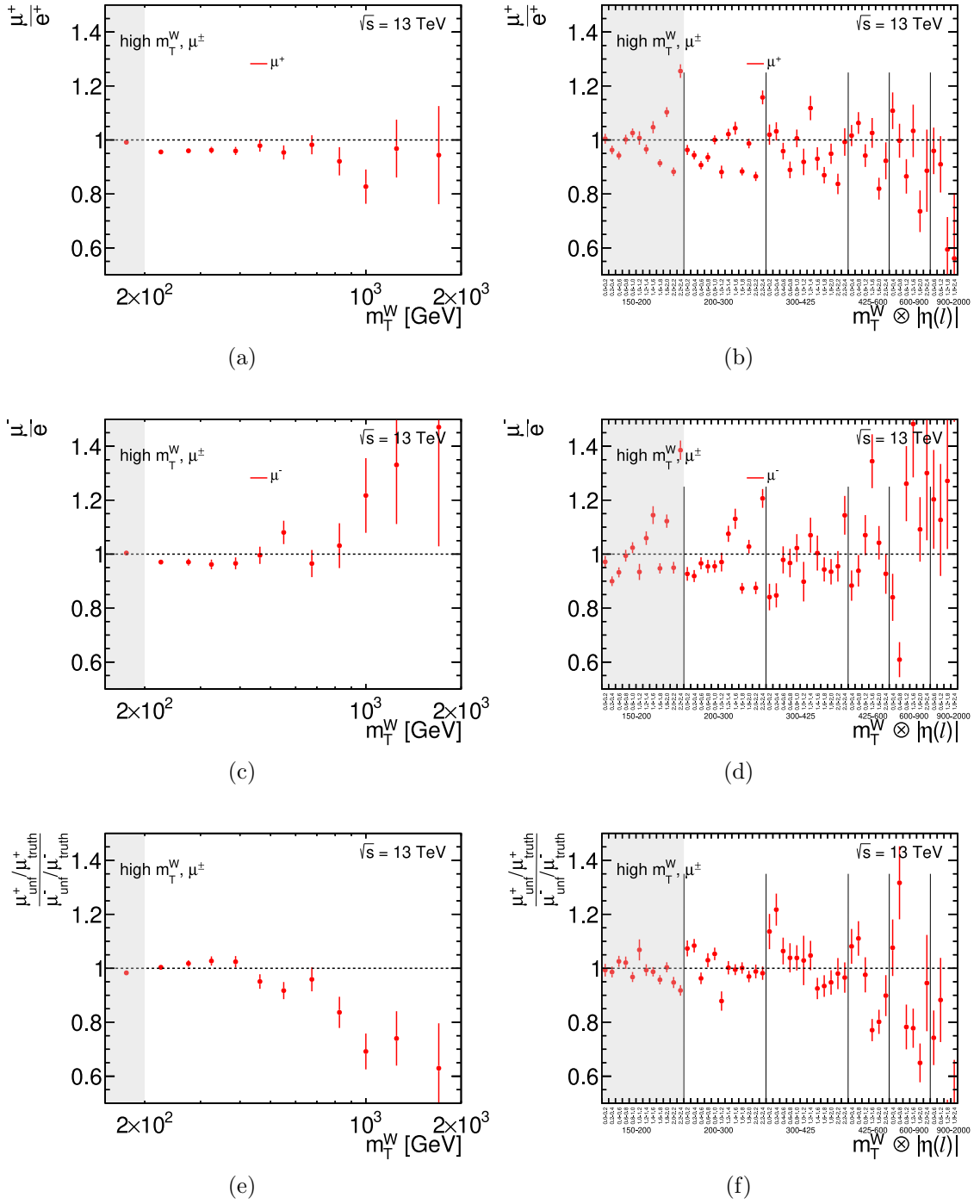
Figure B.4.: Ratios between the cross-sections obtained in the electron and muon channel for μ^+ (upper row) and μ^- (middle row) as well as double-ratios between the unfolded measured and MC predicted cross-sections in the μ^+- and μ^--channels (lower row). The single-differential (left-hand side) and double-differential (right-hand side) measurement distributions are shown. All cross-sections are based on data, that is **corrected** for the sagitta bias.

C. Multijet background: supplemental material

C.1. Real and fake efficiencies
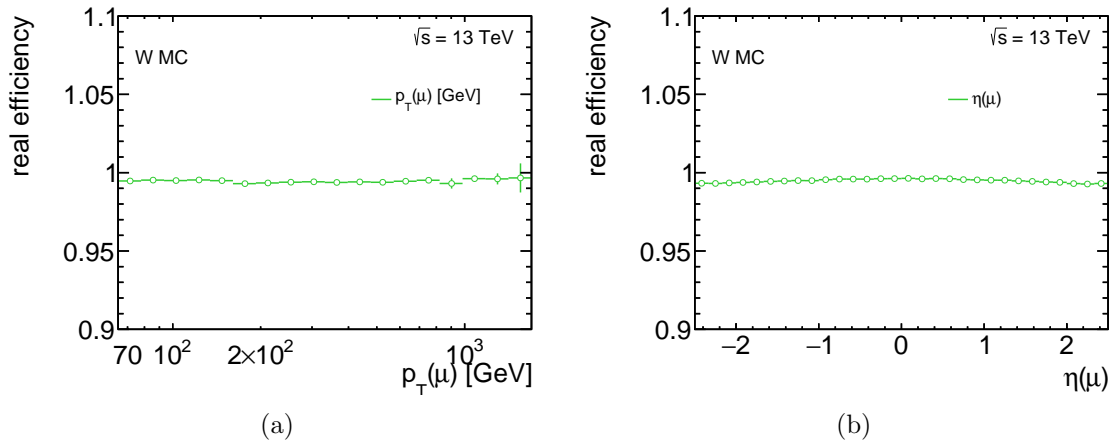
Figure C.1.: One-dimensional real-muon efficiency as a function of the muon's (a) transverse momentum and (b) pseudorapidity.

(a)   (b)
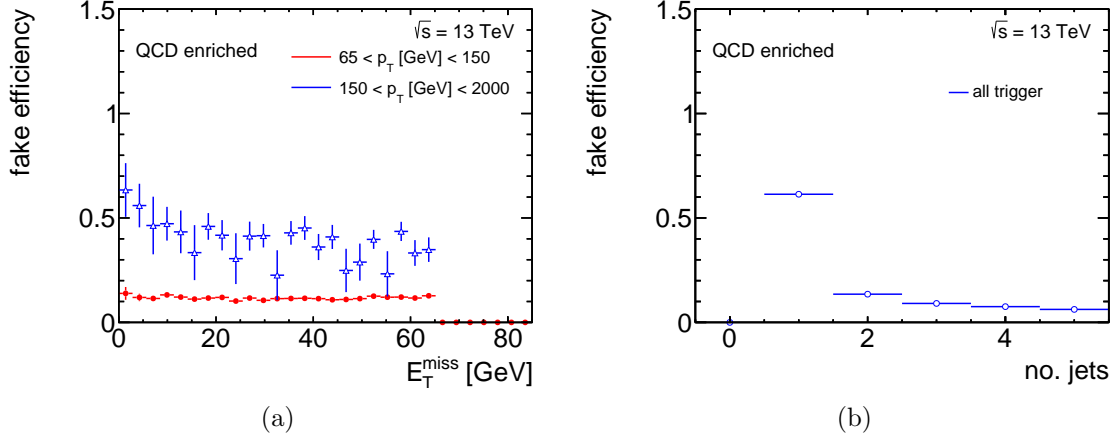
Figure C.2.: Fake muon efficiency as a function of (a) the missing transverse momentum, shown for two separate $p_{\mathrm{T}}(\mu)$ bins, and (b) the jet multiplicity.
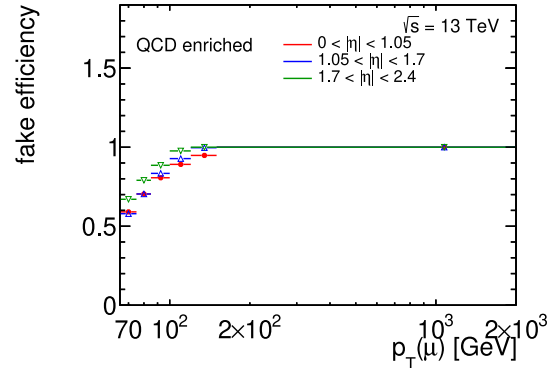
Figure C.3.: The fake muon efficiency binned in $p_{\mathrm{T}}(\mu)$ and $|\eta(\mu)|$ if the muon-jet-overlap-removal (see Section 4.6) is applied. This is the only plot in this thesis where these OR steps applied, for comparison.
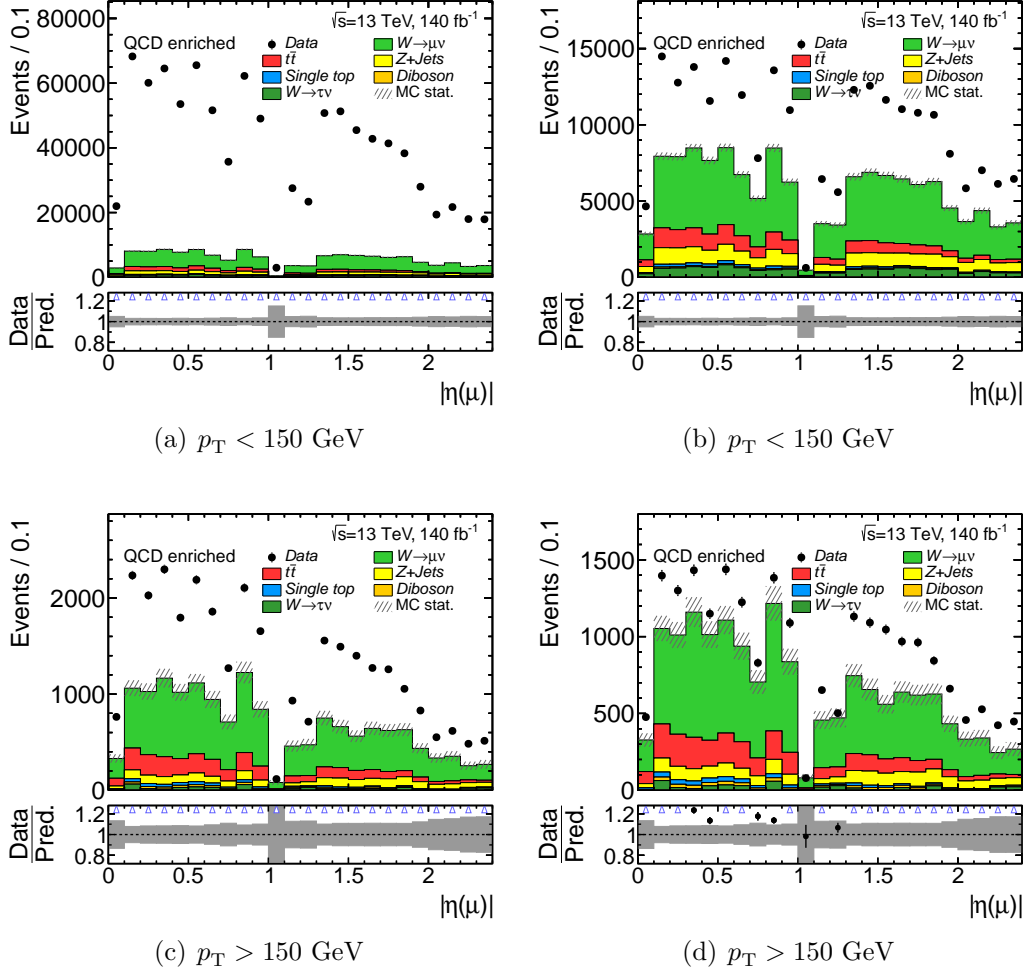
Figure C.4.: Distribution of the pseudorapidity of the muon in different bins of the p_T of the muon for data and prediction in the QCD-enriched region for $\mu^{\pm}$. Statistical uncertainties are included. The left-hand side shows the loose muon level and the right-hand side the tight muon level. The difference between data and prediction will be identified as fake-muon events.

(a) $0 < |\eta(\mu)| < 1.05$

(b) $0 < |\eta(\mu)| < 1.05$

(c) $1.05 < |\eta(\mu)| < 1.7$

(d) $1.05 < |\eta(\mu)| < 1.7$

(e) $1.7 < |\eta(\mu)| < 2.4$

(f) $1.7 < |\eta(\mu)| < 2.4$
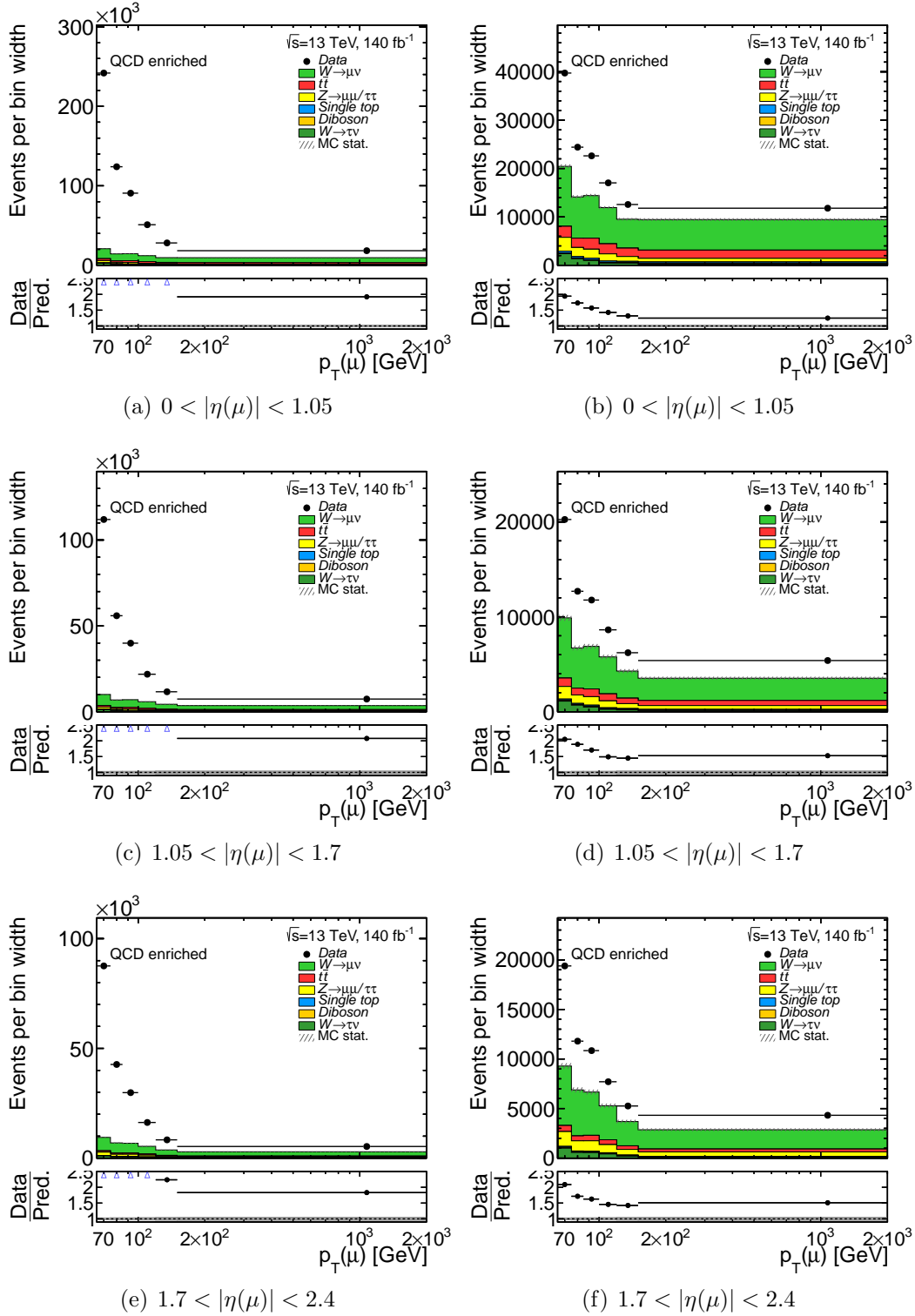
Figure C.5.: Distribution of the transverse momentum of the muon in different bins of the pseudorapidity of the muon for data and prediction in the QCD-enriched region for $\mu^{\pm}$. Statistical uncertainties are included. The binning shown is the one used for the final fake-efficiency calculation. The left-hand side shows the loose muon level and the right-hand side the tight muon level. The difference between data and prediction will be identified as fake-muon events.

C.2. Fake-muon study using a dijet MC sample
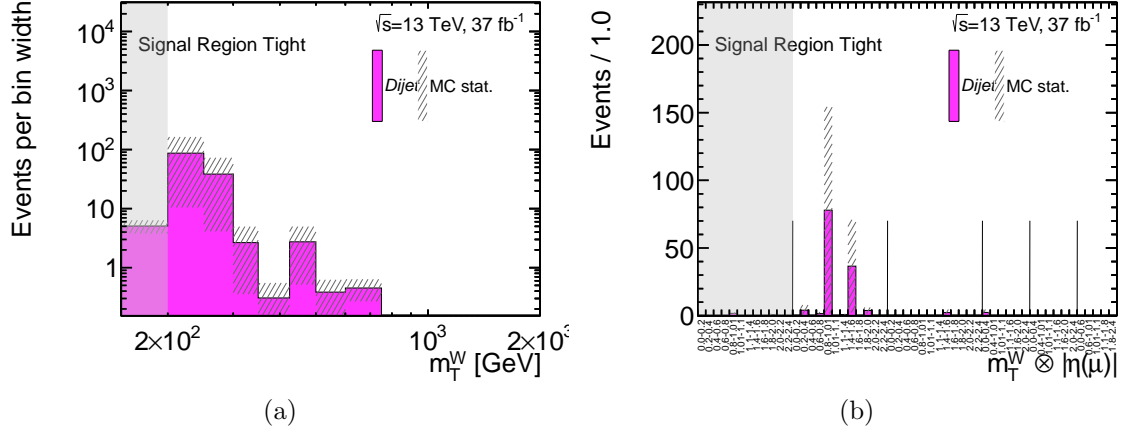
Figure C.6.: Event yield predicted by the dijet MC sample in the signal region in the measurement observables $m_{\mathrm{T}}^{\mathrm{W}}$ and $m_{\mathrm{T}}^{\mathrm{W}} \otimes |\eta(\mu)|$ for the `mc16a` period.
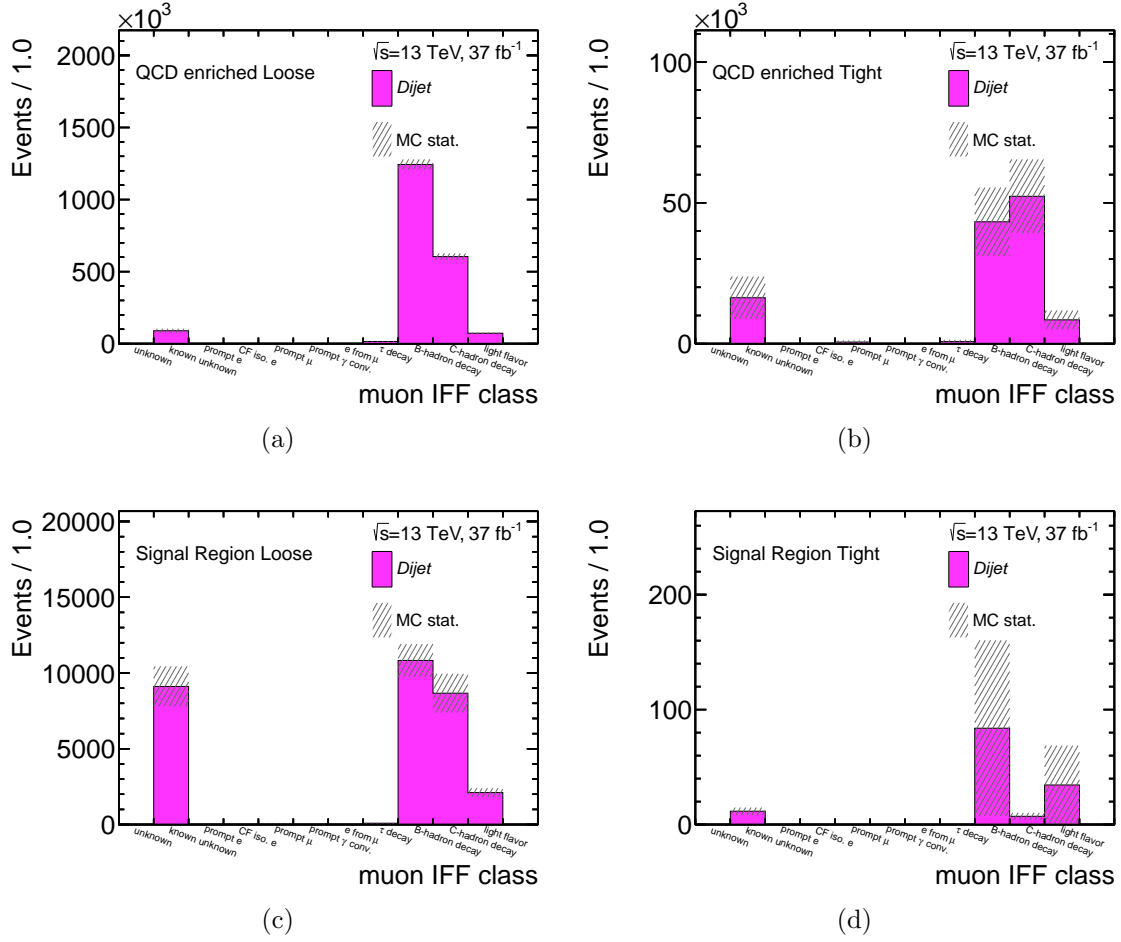
Figure C.7.: Muon classification from the `IFFclass` tool in the dijet MC sample for (a) the loose muon level in the QCD-enriched region, (b) the tight muon level in the QCD-enriched region, (c) the loose muon level in the signal region and (d) the tight muon level in the signal region.

Figure C.8.: Distributions of the missing transverse momentum, the azimuthal angle between muon and leading jet and between muon and closest jet predicted for the dijet process (containing fake muons) and $W \to \mu\nu$ process (containing real muons) in a region with $E_\mathrm{T}^\mathrm{miss} < 65\,\mathrm{GeV}$. All distributions are shown for the loose level (left-hand side) and tight level (right-hand side).
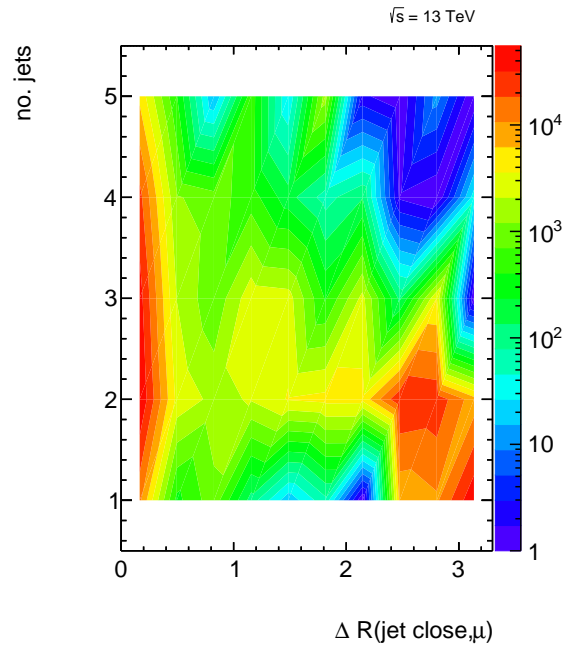
Figure C.9.: Two dimensional distribution of the jet multiplicity against the distance between muon and the closest jet shown in a region with $E_T^{\mathrm{miss}} < 65 \, \mathrm{GeV}$ for a tight muon in the dijet MC sample.

C.3. Multijet closure and validation regions
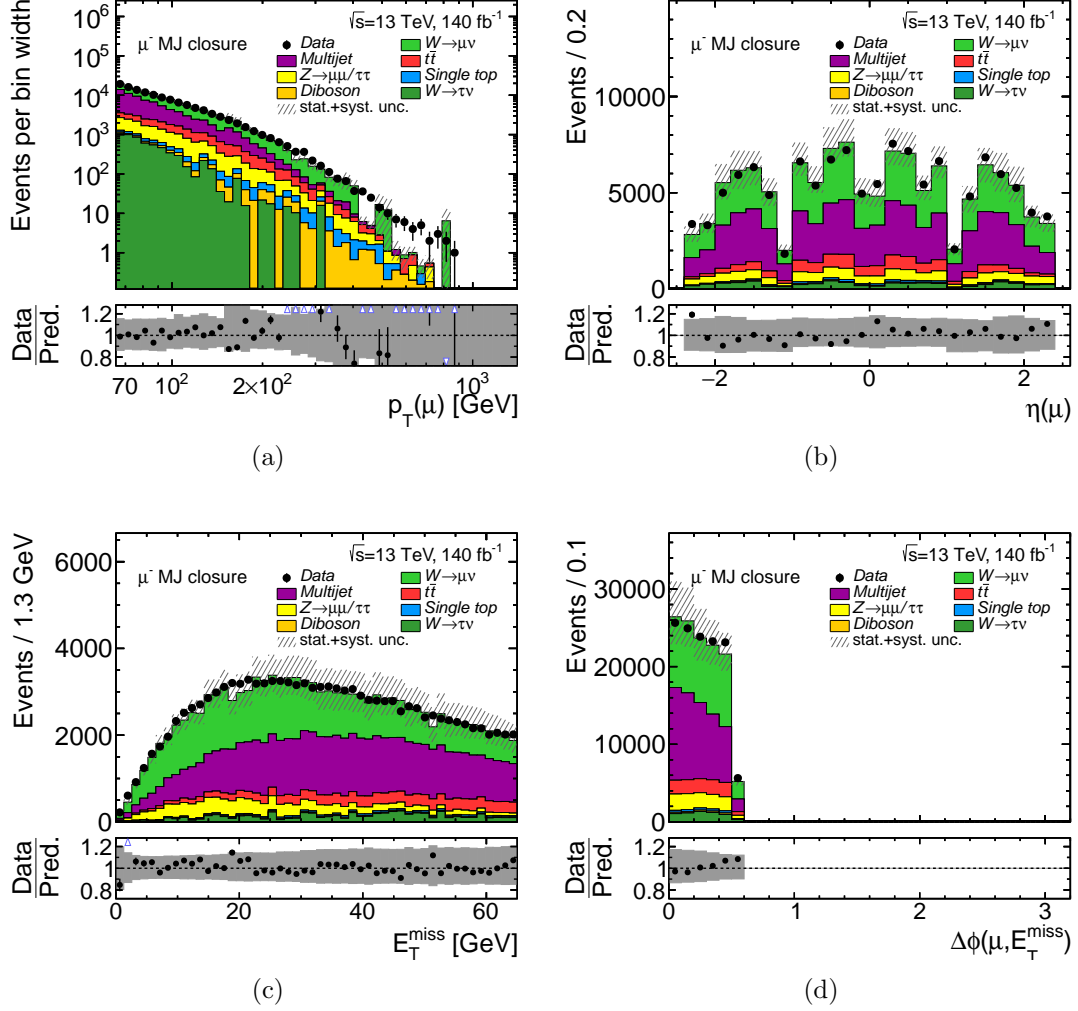
Figure C.10.: Distributions of the (a) momentum of the muon, (b) pseudorapidity of the muon, (c) missing transverse momentum and (d) azimuthal angle between muon and $E_{\mathrm{T}}^{\mathrm{miss}}$ for data and prediction in the closure region for μ^-. Statistical and multijet systematic uncertainties are included.
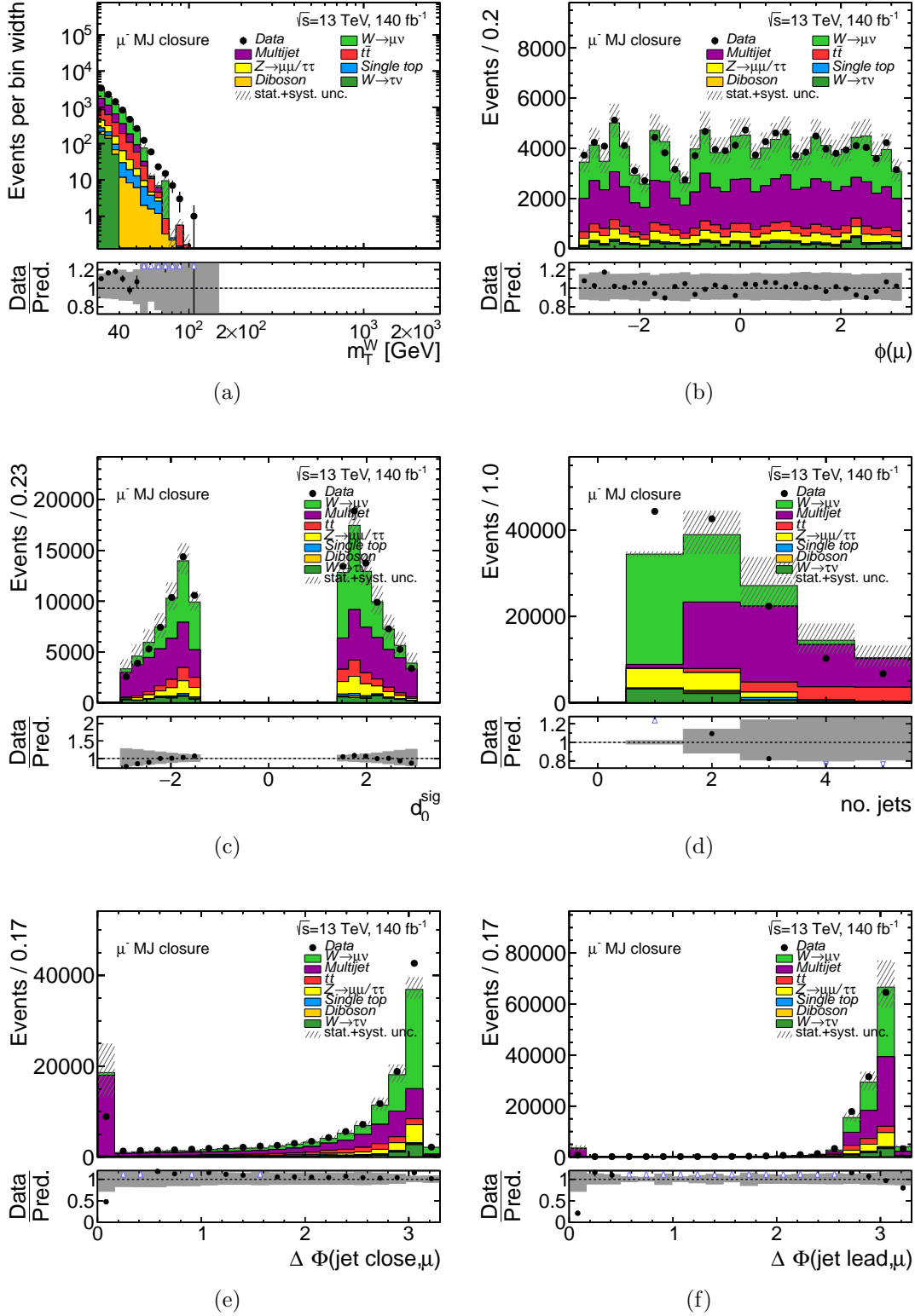
Figure C.11.: Distributions of the (a) transverse mass, (b) azimuthal angle of the muon, (c) d_0 significance, (d) jet multiplicity, (e) azimuthal angle between the muon and the closest jet, (f) azimuthal angle between the muon and the leading jet for data and prediction in the closure region for μ^-. Statistical and multijet systematic uncertainties are included.

Figure C.12.: Distributions of the (a) transverse mass, (b) azimuthal angle of the muon, (c) d_0 significance, (d) jet multiplicity, (e) azimuthal angle between the muon and the closest jet, (f) azimuthal angle between the muon and the leading jet for data and prediction in the closure region for μ^+. Statistical and multijet systematic uncertainties are included.
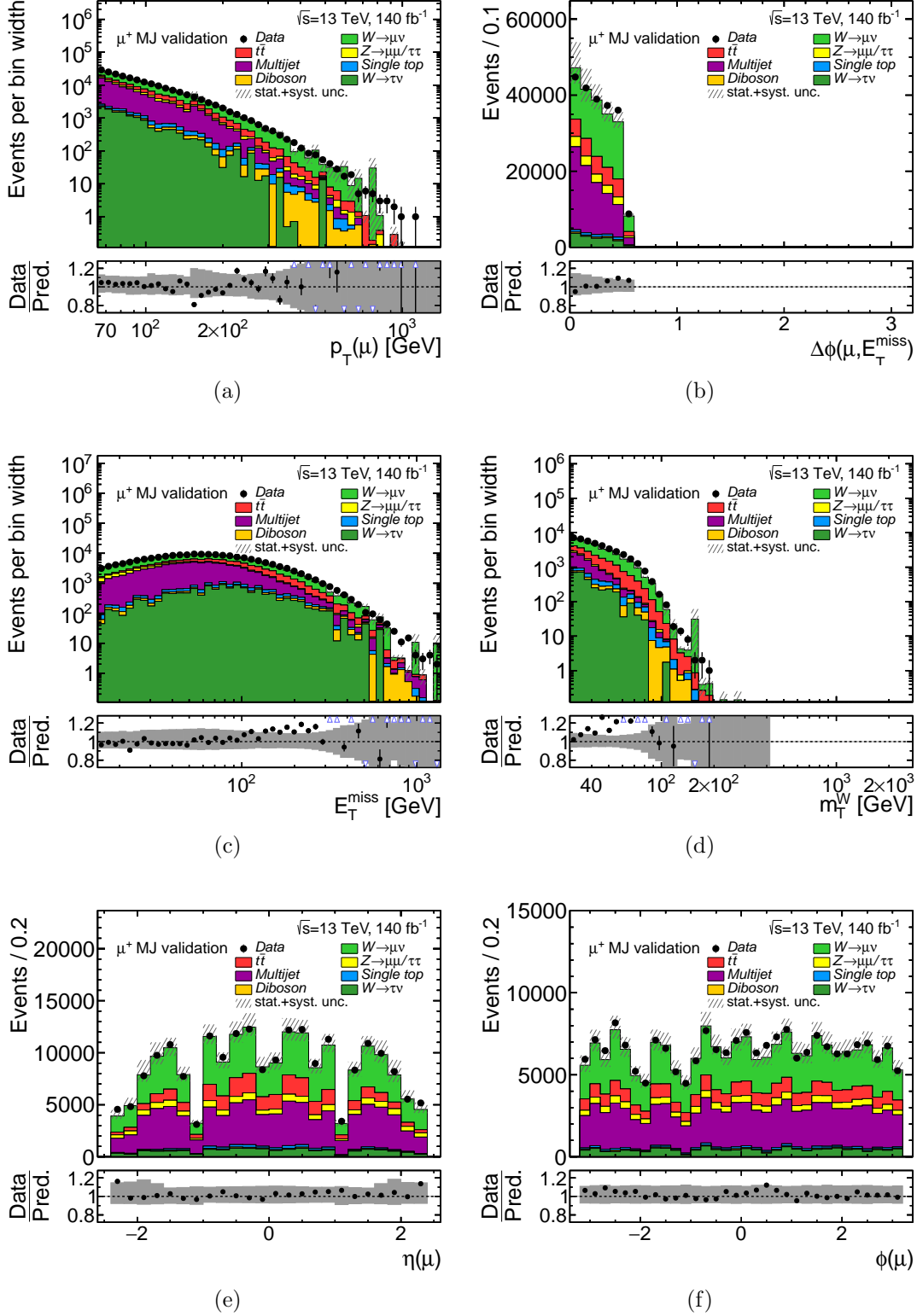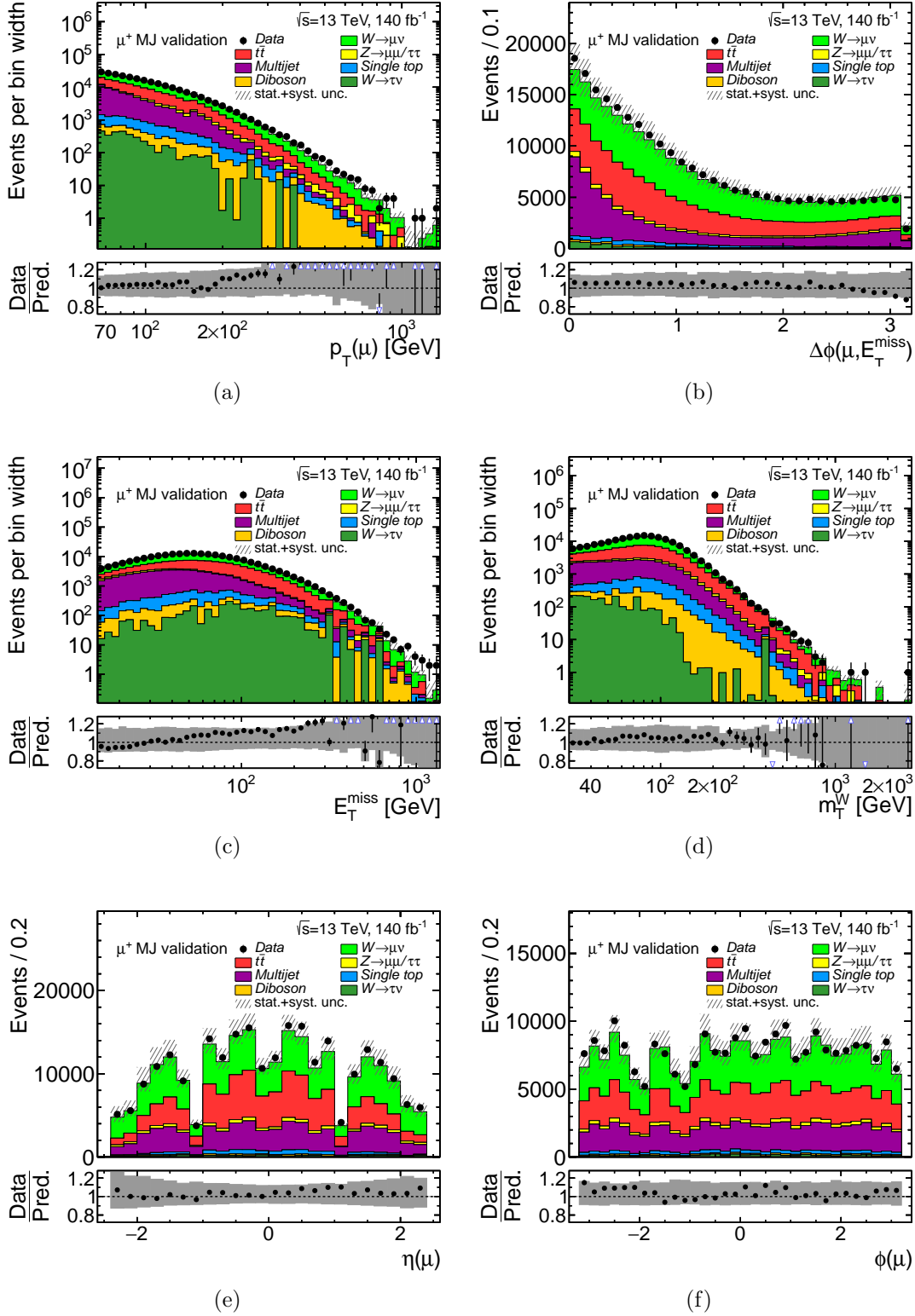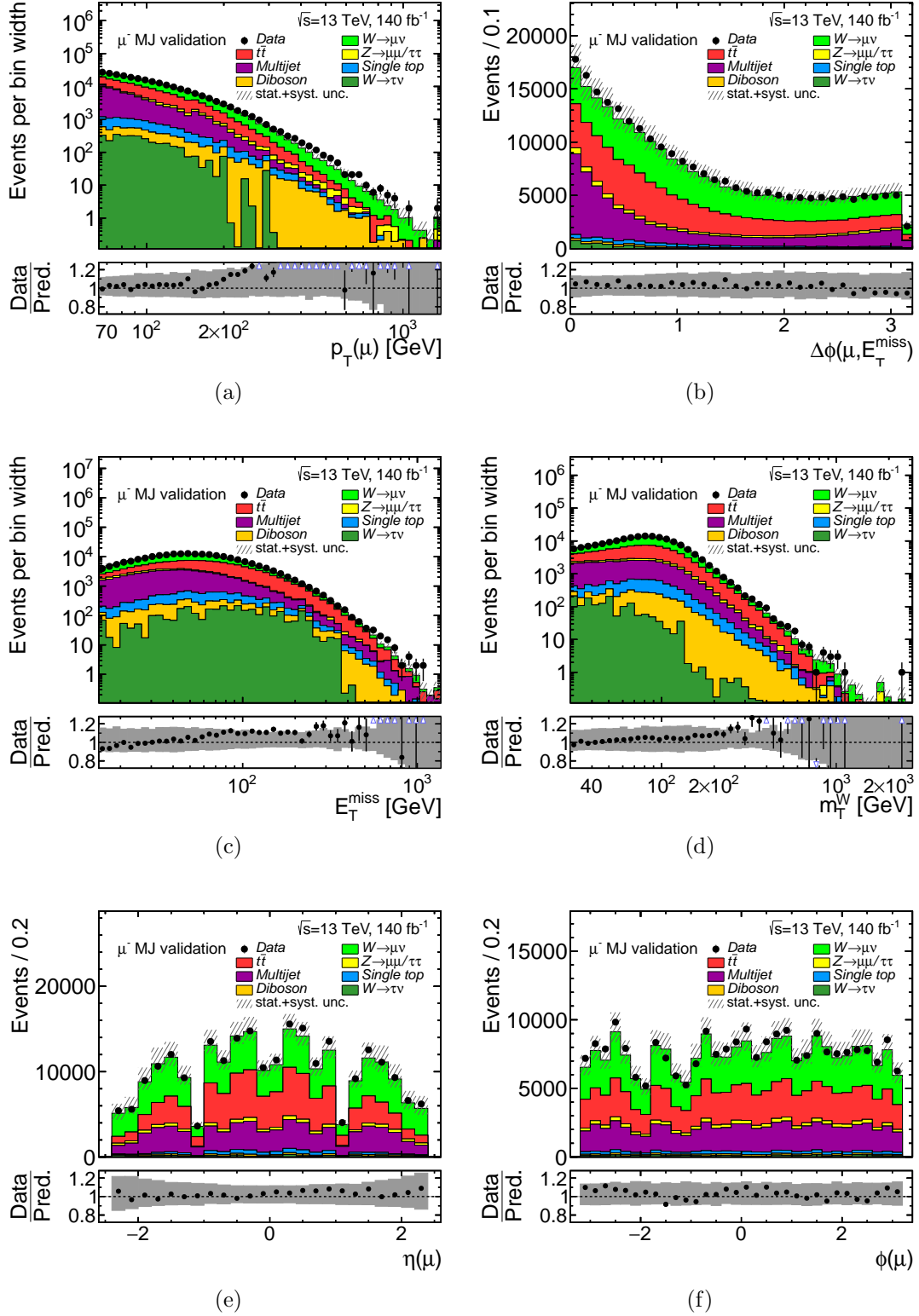
Figure C.13.: Distributions of the (a) transverse momentum of the muon, (b) azimuthal angle between muon and E_T^{miss}, (c) missing transverse momentum, (d) transverse mass of the W boson, (e) pseudorapidity and (f) azimuthal angle of the muon for data and prediction in the first validation region (VR1) for μ^+. Statistical and multijet systematic uncertainties are included.

Figure C.14.: Distributions of the (a) transverse momentum of the muon, (b) azimuthal angle between muon and $E_{\mathrm{T}}^{\mathrm{miss}}$, (c) missing transverse momentum, (d) transverse mass of the W boson, (e) pseudorapidity and (f) azimuthal angle of the muon for data and prediction in the first validation region (VR1) for μ^-. Statistical and multijet systematic uncertainties are included.

Figure C.15.: Distributions of the (a) transverse momentum of the muon, (b) azimuthal angle between muon and E_T^{miss}, (c) missing transverse momentum, (d) transverse mass of the W boson, (e) pseudorapidity and (f) azimuthal angle of the muon for data and prediction in the second validation region (VR2) for μ^+. Statistical and multijet systematic uncertainties are included as well as scale uncertainties on the $W \to \mu\nu$ SHERPA prediction.

Figure C.16.: Distributions of the (a) transverse momentum of the muon, (b) azimuthal angle between muon and E_T^{miss}, (c) missing transverse momentum, (d) transverse mass of the W boson, (e) pseudorapidity and (f) azimuthal angle of the muon for data and prediction in the second validation region (VR2) for μ^-. Statistical and multijet systematic uncertainties are included as well as scale uncertainties on the $W \to \mu\nu$ SHERPA prediction.

D. More distributions compared for data and prediction

D.1. Control plots for $\mu^{\pm}$ combined
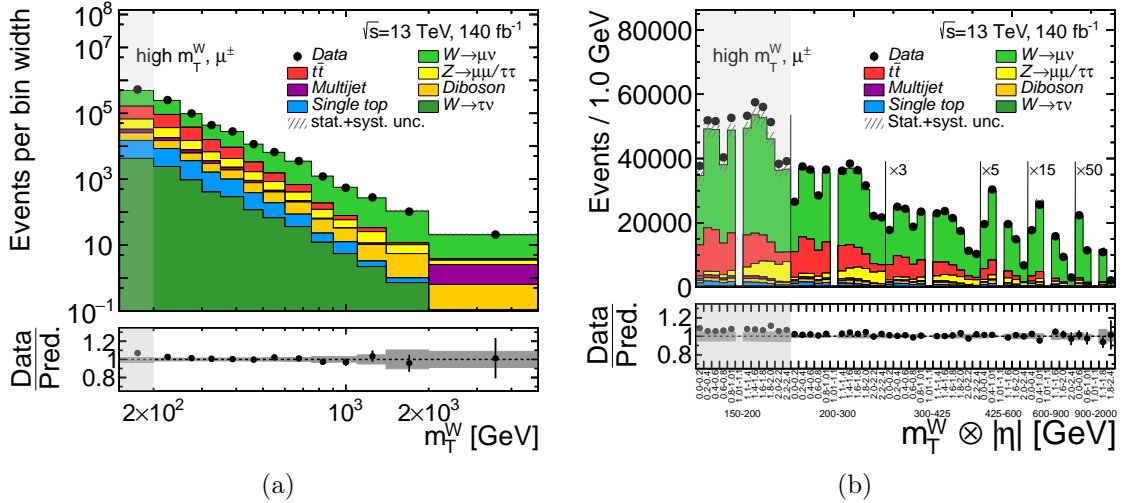
Figure D.1.: Distributions (a) single-differential in the transverse mass and (b) double-differential in the transverse mass and pseudorapidity of the muon for data and prediction in the signal region for $\mu^{\pm}$ combined. Statistical and systematic uncertainties are included.
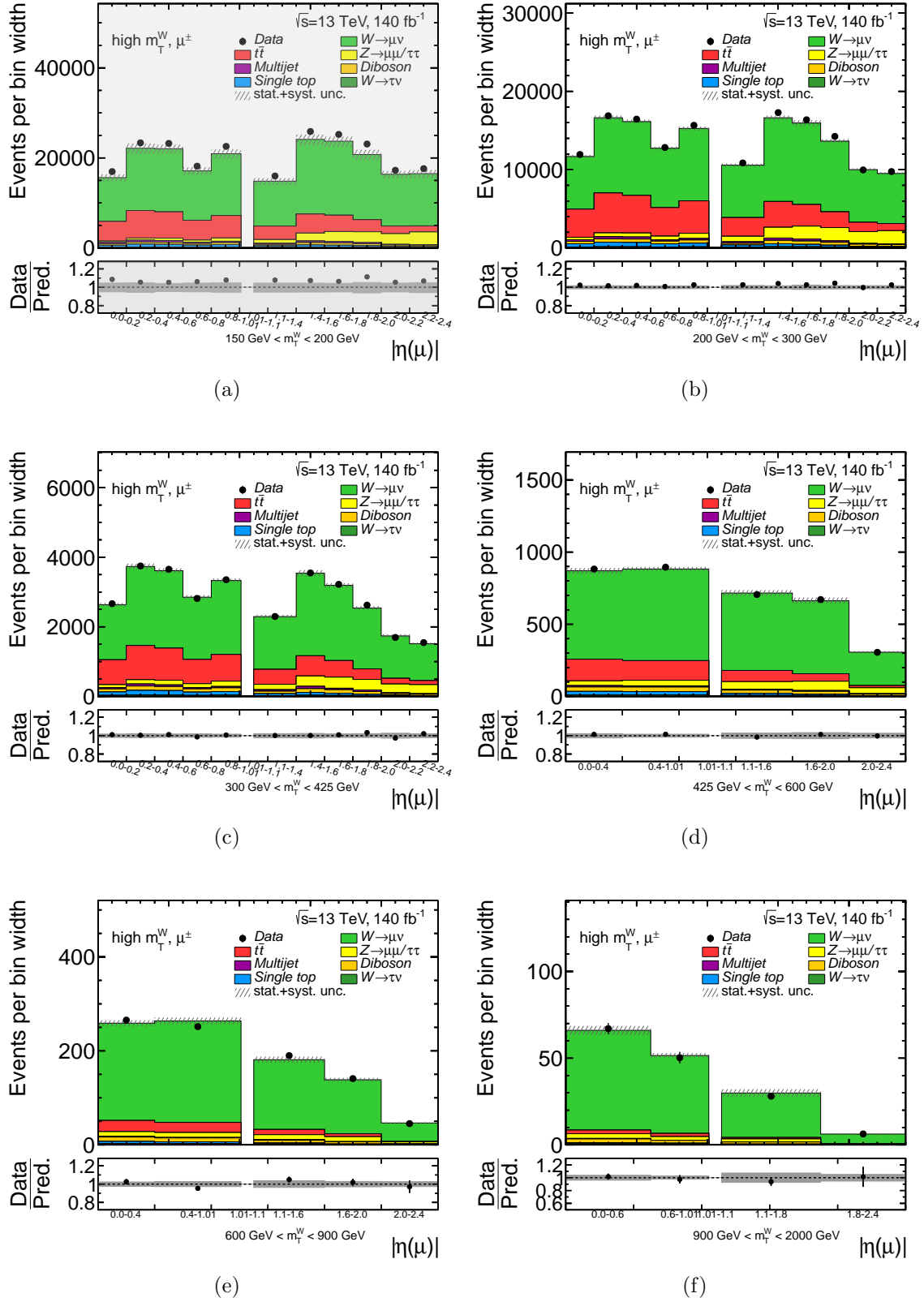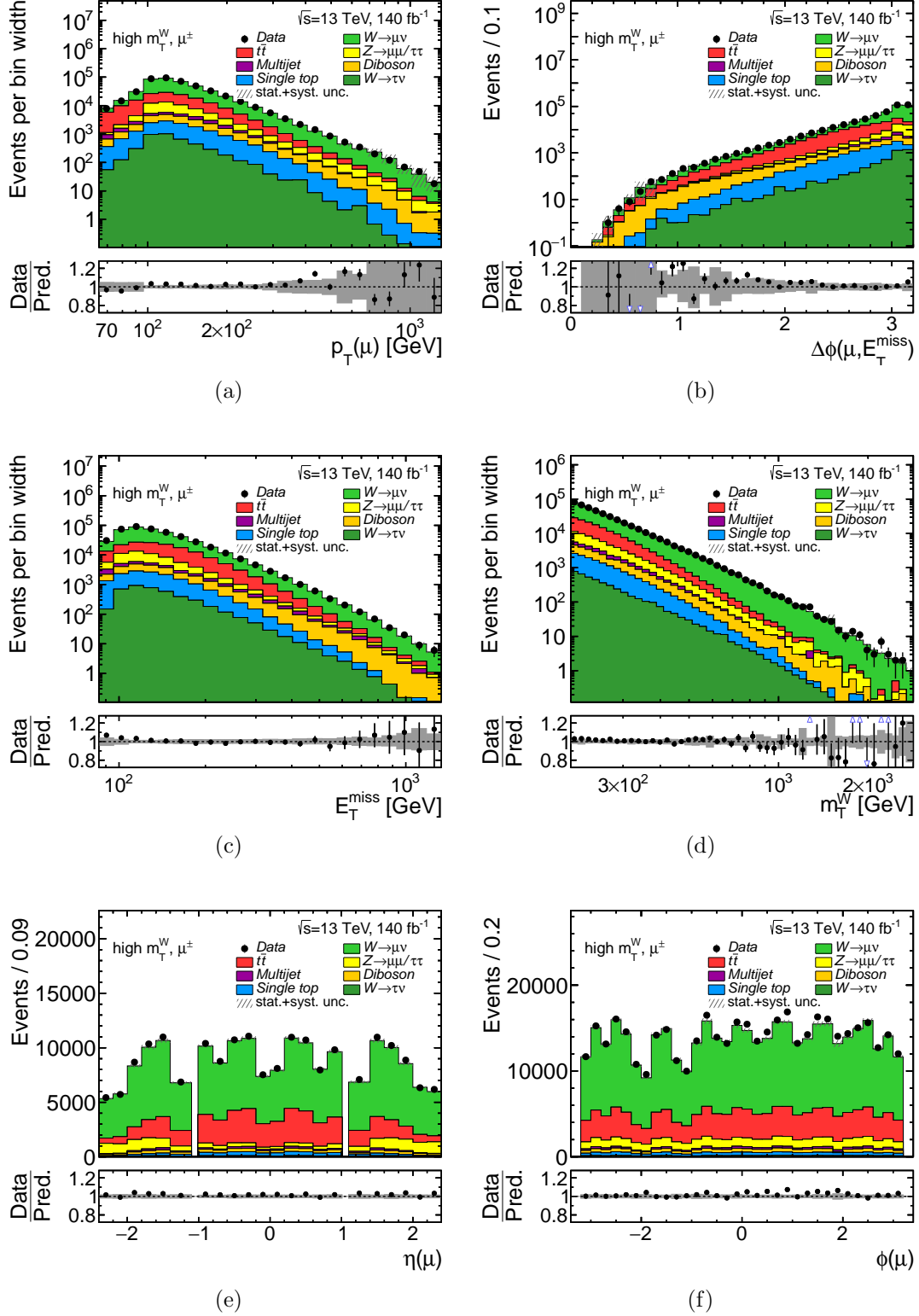
Figure D.2.: Distributions of the pseudorapidity of the muon for data and prediction in different m_T^W bins for $\mu^\pm$ combined. Statistical and systematic uncertainties are included.

Figure D.3.: Distributions of the (a) transverse momentum of the muon, (b) azimuthal angle between muon and $E_{\mathrm{T}}^{\mathrm{miss}}$, (c) missing transverse momentum, (d) transverse mass of the W boson, (d) pseudorapidity and (f) azimuthal angle of the muon in the signal region for $\mu^{\pm}$ combined. Statistical and systematic uncertainties are included.
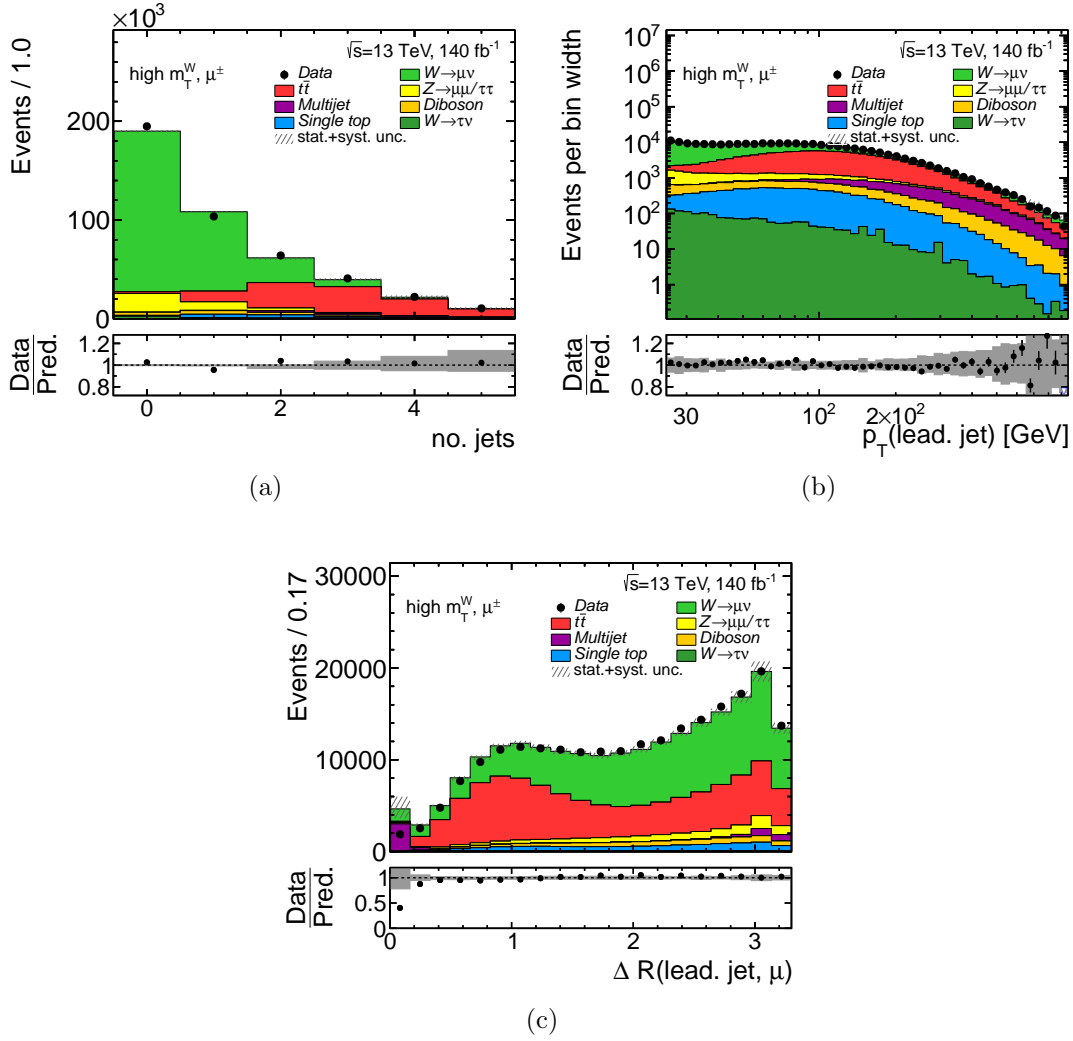
(a)

(b)

(c)

Figure D.4.: Distributions of (a) the jet multiplicity, (b) the p_T of the leading jet and (c) the angular distance between muon and the leading jet in the signal region for $\mu^{\pm}$ combined. Statistical and systematic uncertainties are included.

D.2. Additional observables for μ^{+} and μ^{-} in the signal region
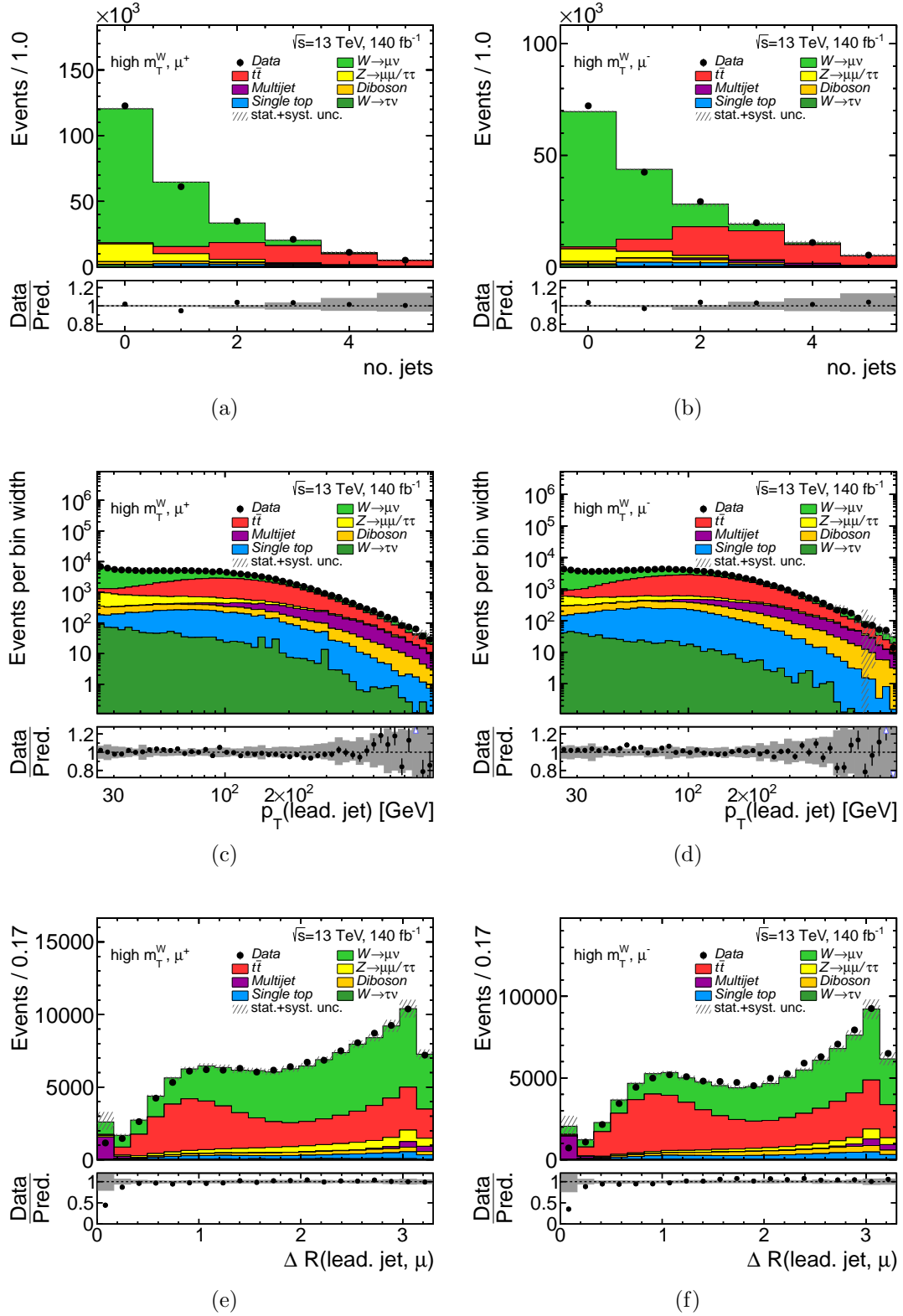
Figure D.5.: Distributions of the jet multiplicity, transverse momentum of the leading jet and angular difference between muon and leading jet for data and prediction in the signal region for μ^+ (left-hand side) and μ^- (right-hand side). Statistical and systematic uncertainties are included.

E. Unfolding: supplemental material

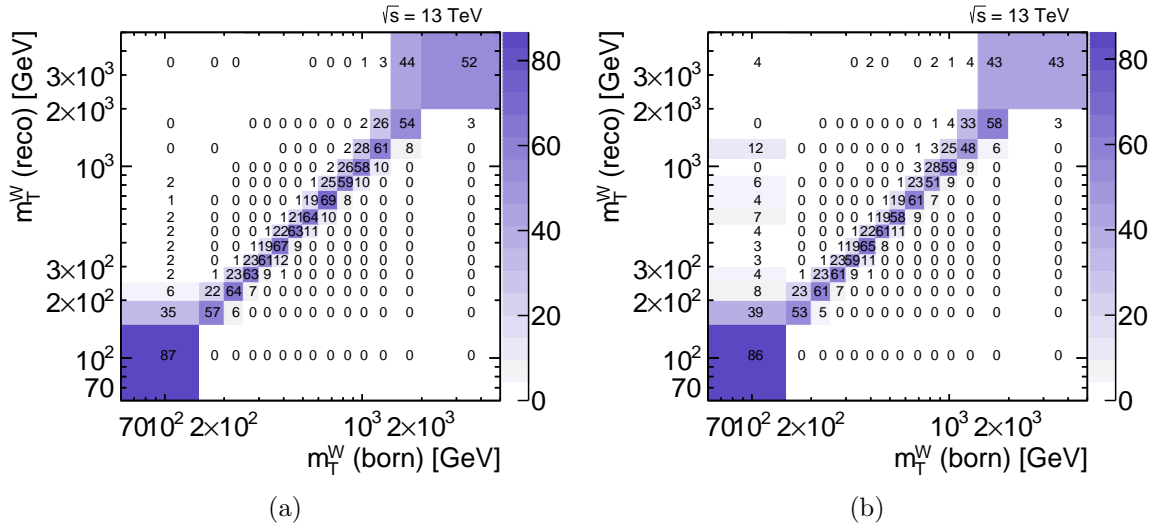## E.1. Binning optimization: migration and data statistical uncertainty

Figure E.1.: Migration matrix for the (a) $W^+ \to \mu^+ \nu$ and (b) $W^- \to \mu^- \bar{\nu}$ signal process as a function of m_T^W. The given numbers are in percent. The normalisation is done per row, i.e. reconstruction-level bin, while under- and overflow bin are considered in the normalization.
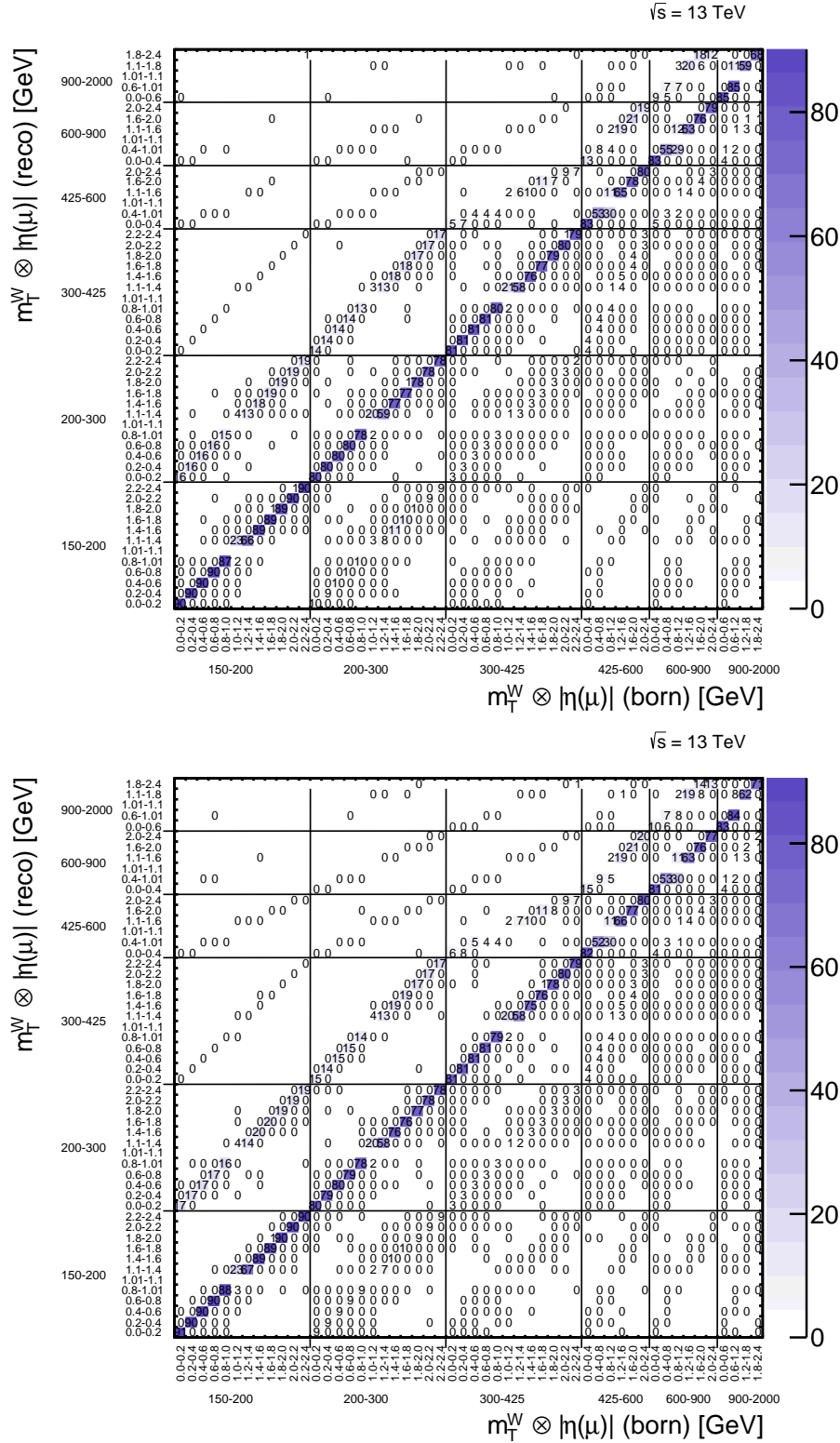
Figure E.2.: Migration matrix for the $W^+ \to \mu^+ \nu$ (upper plot) and $W^- \to \mu^- \bar{\nu}$ (lower plot) signal process as a function of m_T^W and $|\eta|$. The given numbers are in percent. The normalisation is done per row, i.e. reconstruction-level bin, while under- and overflow bin are considered in the normalization.
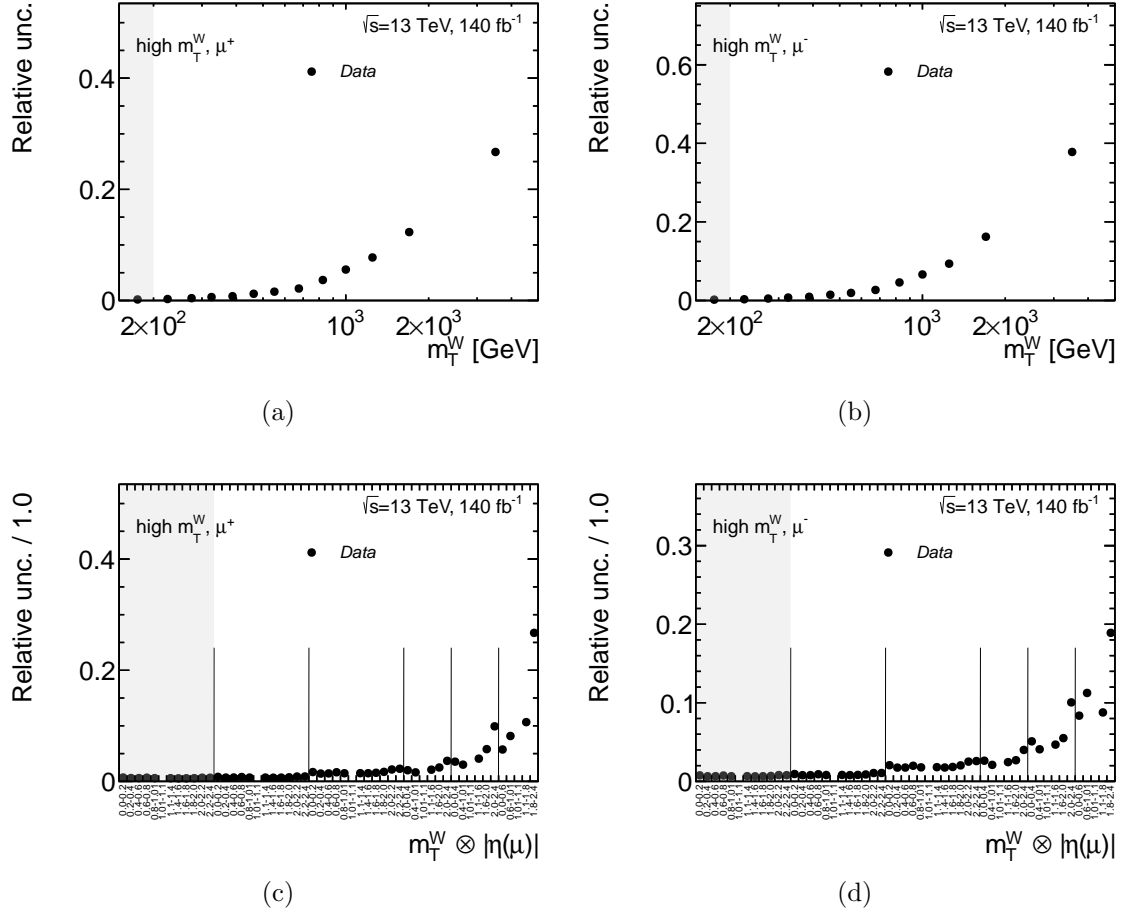
Figure E.3.: Relative statistical uncertainty in data before the unfolding procedure for a positively and negatively charged muon and the 1D and 2D measurement observables, respectively.

E.2. Unfolding corrections for positive muon charge

(a)

(b)

Figure E.4.: Efficiency correction factors for (a) m_T^W and (b) $m_T^W \otimes |\eta(\mu)|$ as obtained using the $W \to \mu\nu$ simulated sample for the μ^+-channel.

(a)

(b)

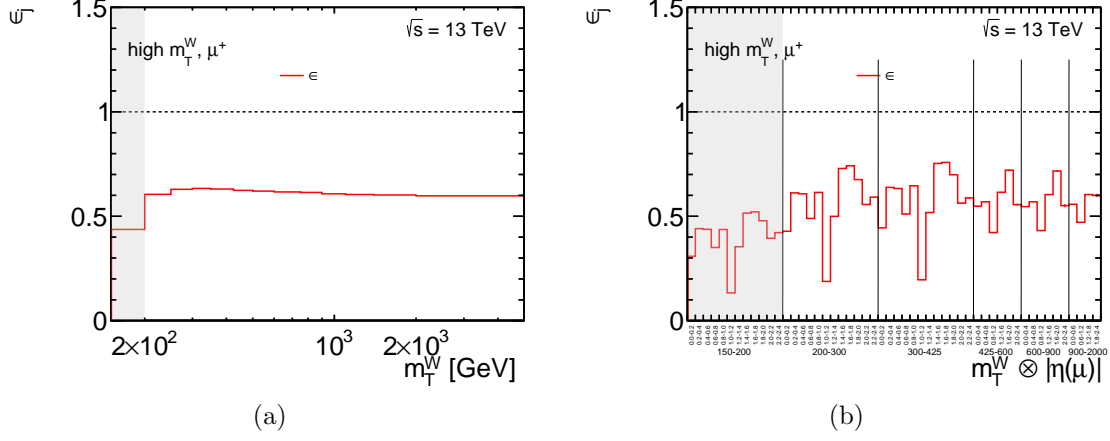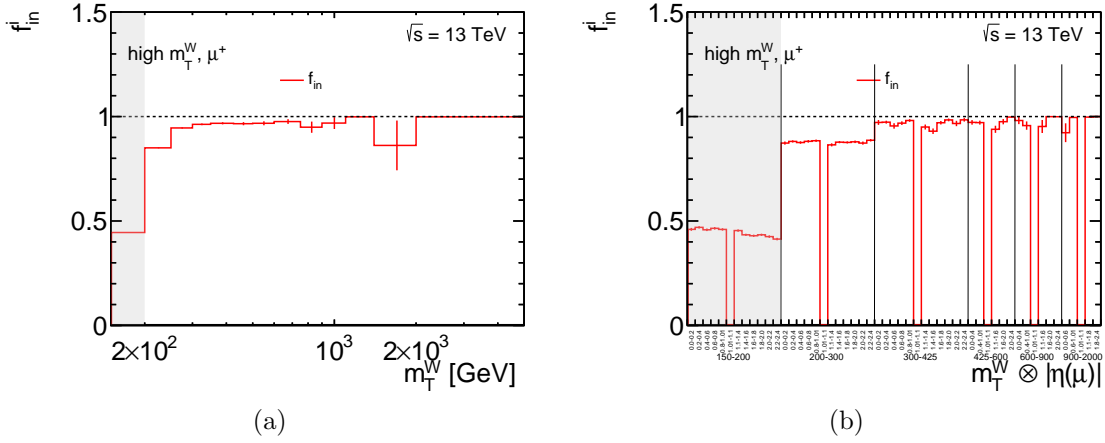**Figure E.5.:** In-smearing correction factors for (a) m_T^W and (b) $m_T^W \otimes |\eta(\mu)|$ as obtained using the $W \to \mu\nu$ simulated sample for the μ^+-channel.

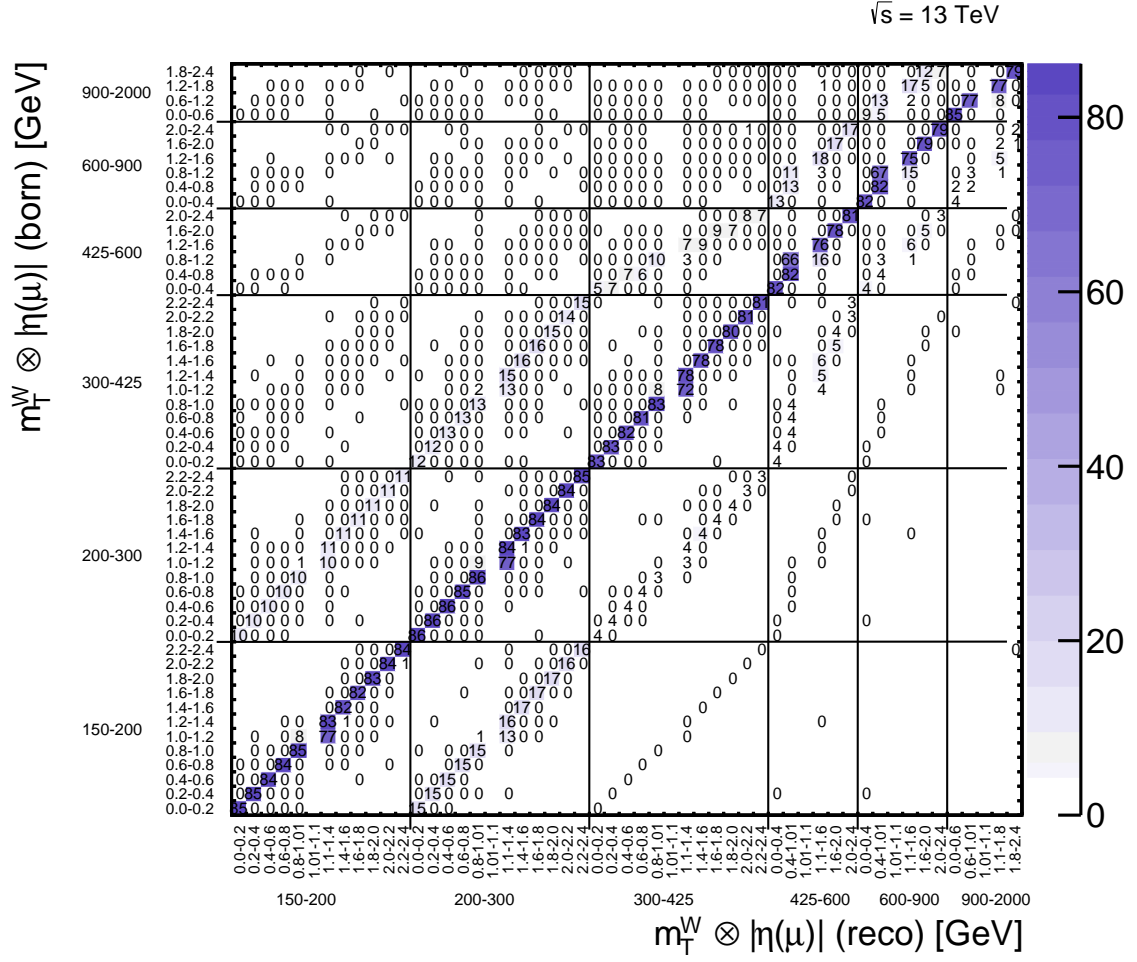**Figure E.6.:** Response matrix R_{ij} as a function of $m_{\mathrm{T}}^{\mathrm{W}} \otimes |\eta(\mu)|$ obtained using the $W \to \mu\nu$ simulated sample for the μ^+-channel. All entries are given in percent.

E.3. Unfolding in $|\eta(\mu)|$
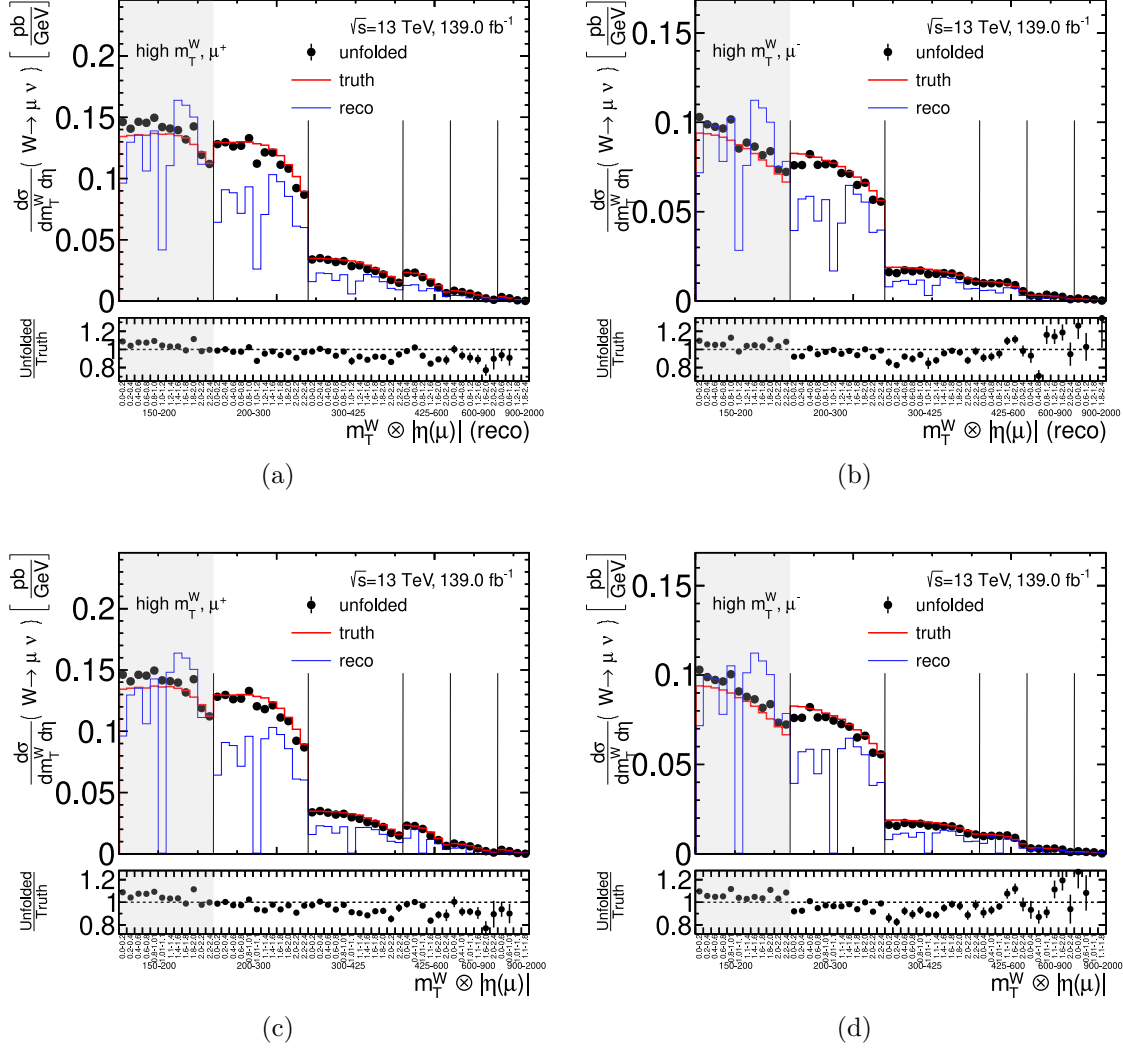
Figure E.7.: The distributions of the unfolded cross-section, as well as the reconstructed data distribution and MC truth distribution are shown, for a positive (left) and negative (right) muon final state. The upper row refers to the usage of the same binning on reconstruction and truth level in the IBU, whereas in the lower row a custom binning on reconstruction level is used, which is motivated by the detector geometry. The x-axis labeling is with respect to the binning on reconstruction level (i.e. it might differ for the truth level). It should be noted that this test was performed at an earlier stage of the analysis and does not reflect the latest cross-sections presented in the main part of this dissertation. Nevertheless, the conclusions taken here remain valid, namely that the unfolding using a custom reconstruction-level binning (lower row) tends to be more stable and flat.
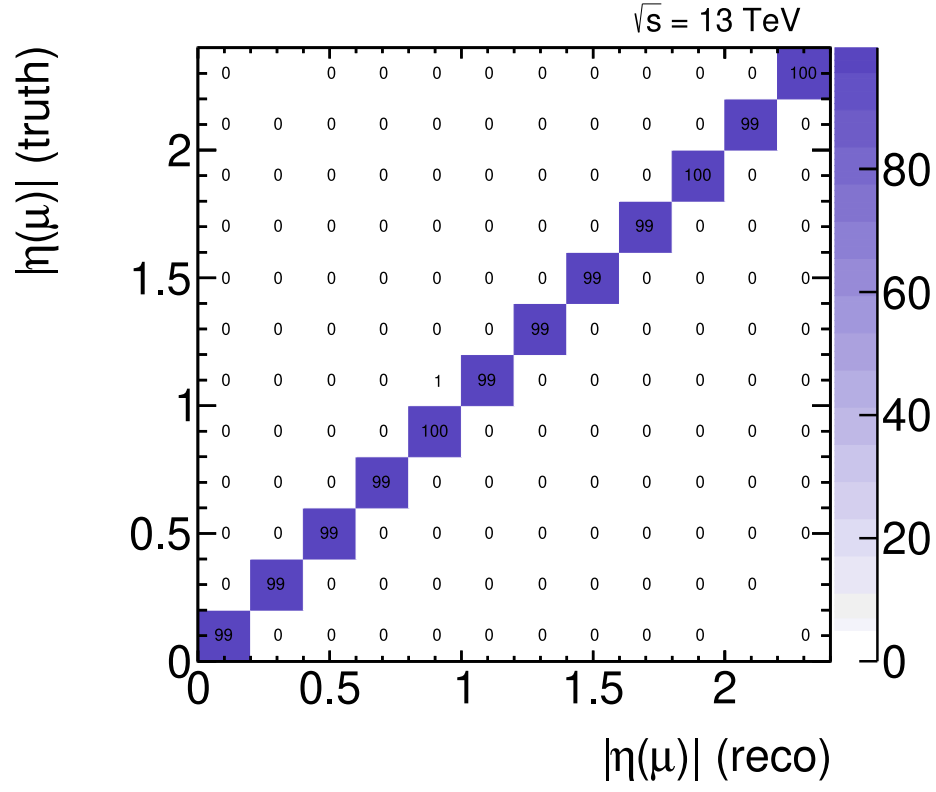
Figure E.8.: Response matrix for a single-differential unfolding in $|\eta|$ for the positive muon charge. The same binning is used on reconstruction and truth level here.

E.4. Shadow bin including the W-boson mass peak

(a)   (b)
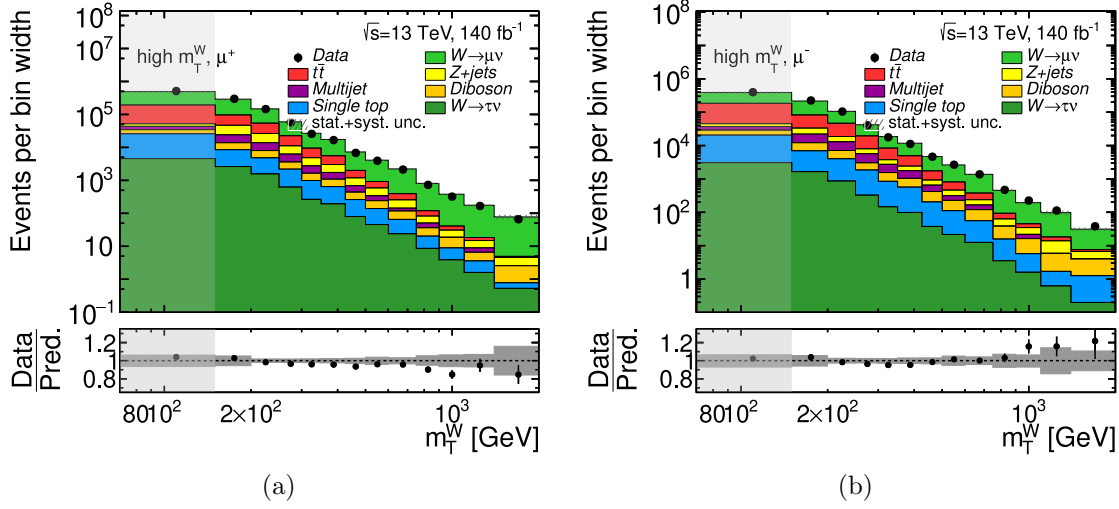
Figure E.9.: Distributions of the transverse mass for (a) μ^+ and (b) μ^- including statistical and systematic uncertainties. An additional shadow bin with $m_\text{T}^\text{W} \in [70, 150]$ GeV is included. The $p_\text{T}(\mu)$ and E_T^miss cuts remain at 65 GeV and 85 GeV, respectively. The analysis-default shadow bin from $150 - 200$ GeV is not shaded gray in the visualization here.

(a)   (b)
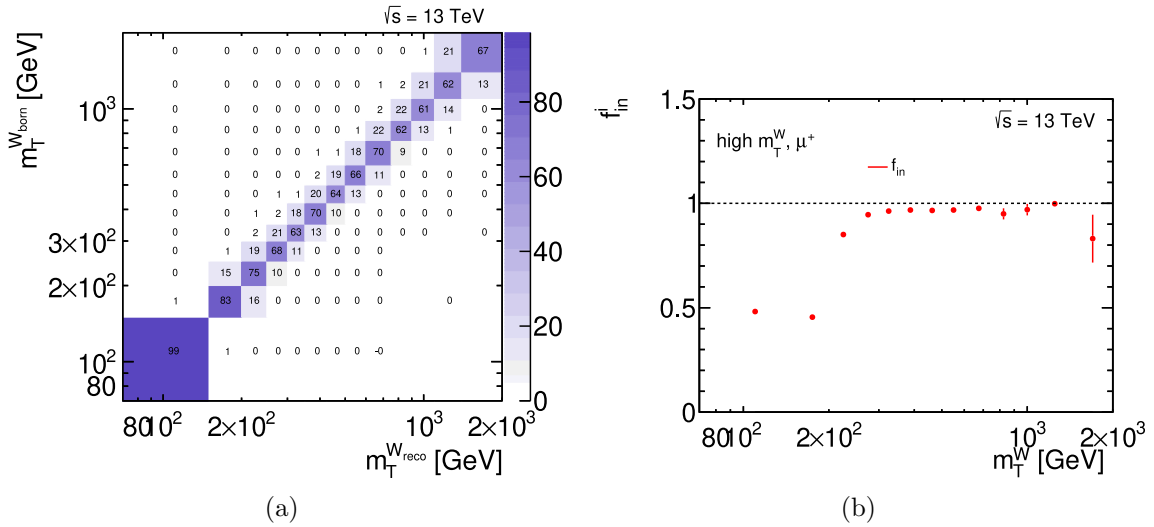
Figure E.10.: (a) Response matrix and (b) in-smearing correction factor in the single-differential measurement if a second shadow bin with $m_\text{T}^\text{W} \in [70, 150]$ GeV is used. Both are shown for the positive muon charge. It can be seen that basically no events are in-smearing from the $[70, 150]$ GeV shadow bin to the high-m_T^W measurement region.

E.5. Optimization of the number of iterations in the IBU

(a)

(b)

(c)

(d)
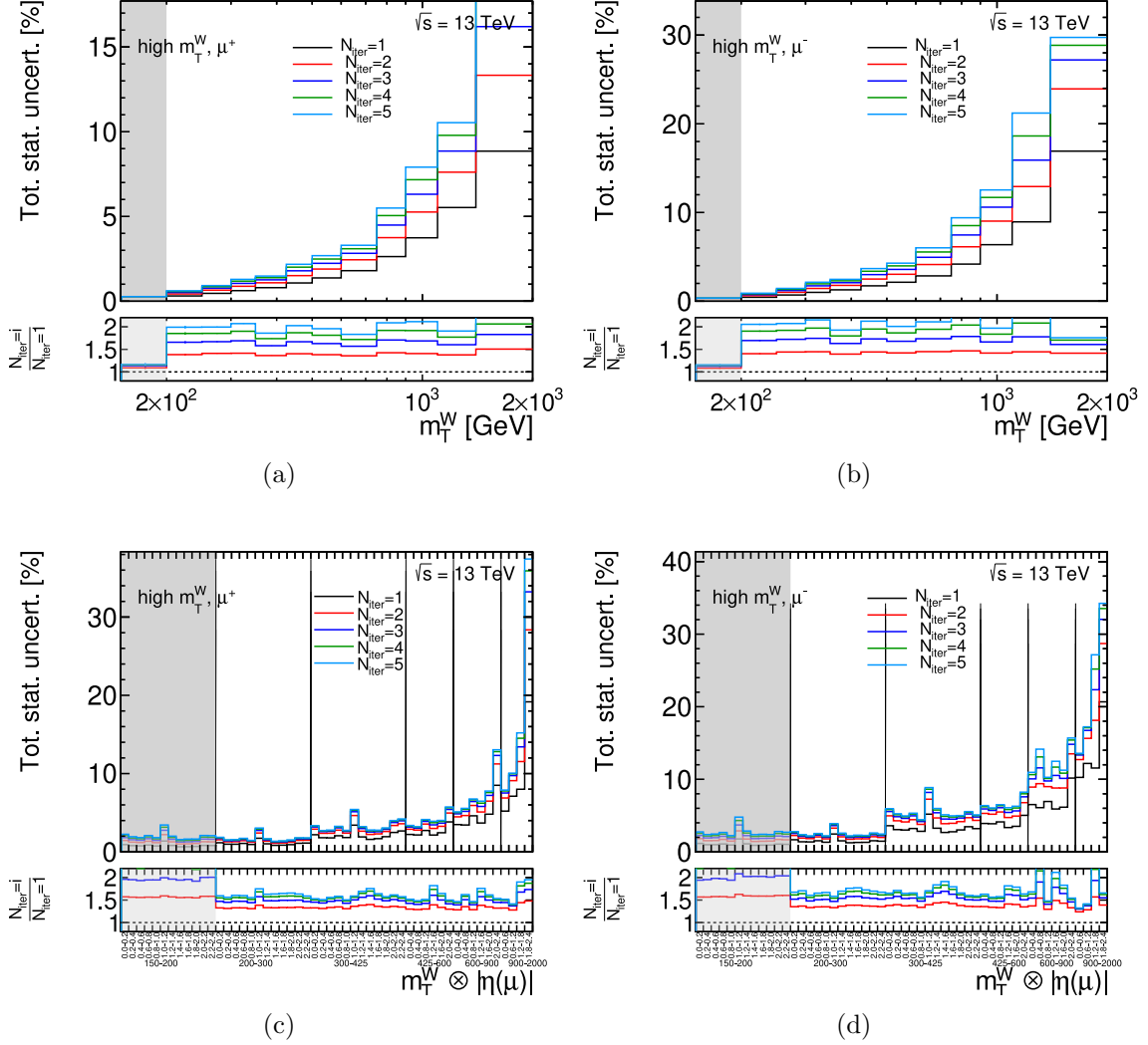
Figure E.11.: Statistical uncertainty after 1-5 iterations in the IBU. On the left, the positive muon charge is shown and on the right the negavtive muon charge, while the upper row shows the 1D measurement observable m_T^W and the lower row the 2D measurement observable $m_T^W \otimes |\eta(\mu)|$.

(a)

(b)

(c)

(d)
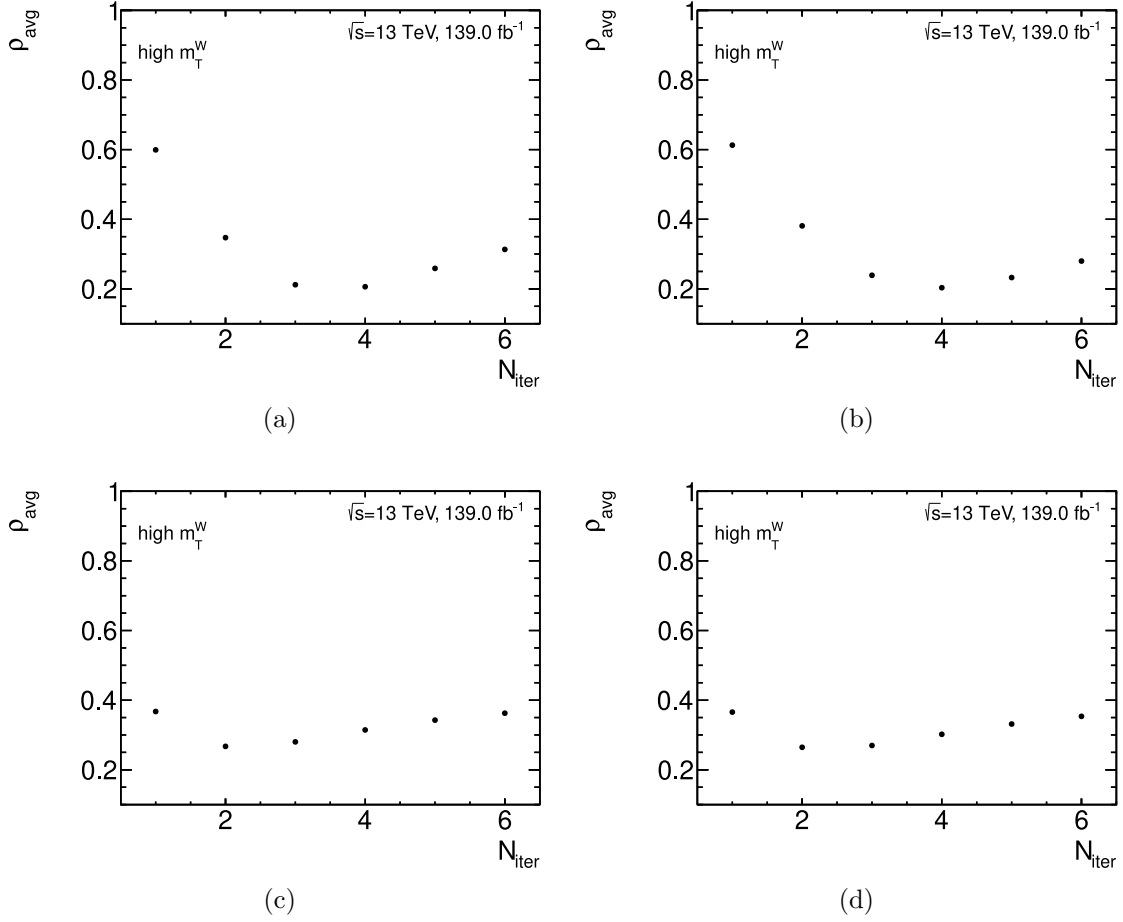
Figure E.12.: Average global correlation coefficient ρ_{avg} as a function of the number of iterations N_{iter} for a positive (left) and negative (right) muon charge. The upper row correspond to the single-differential measurement in $m_{\mathrm{T}}^{\mathrm{W}}$ and the lower row to the double-differential measurement in $m_{\mathrm{T}}^{\mathrm{W}}$ and $|\eta(\mu)|$.

(a) $N_{iter} = 1$

(b) $N_{iter} = 2$

(c) $N_{iter} = 3$

(d) $N_{iter} = 5$
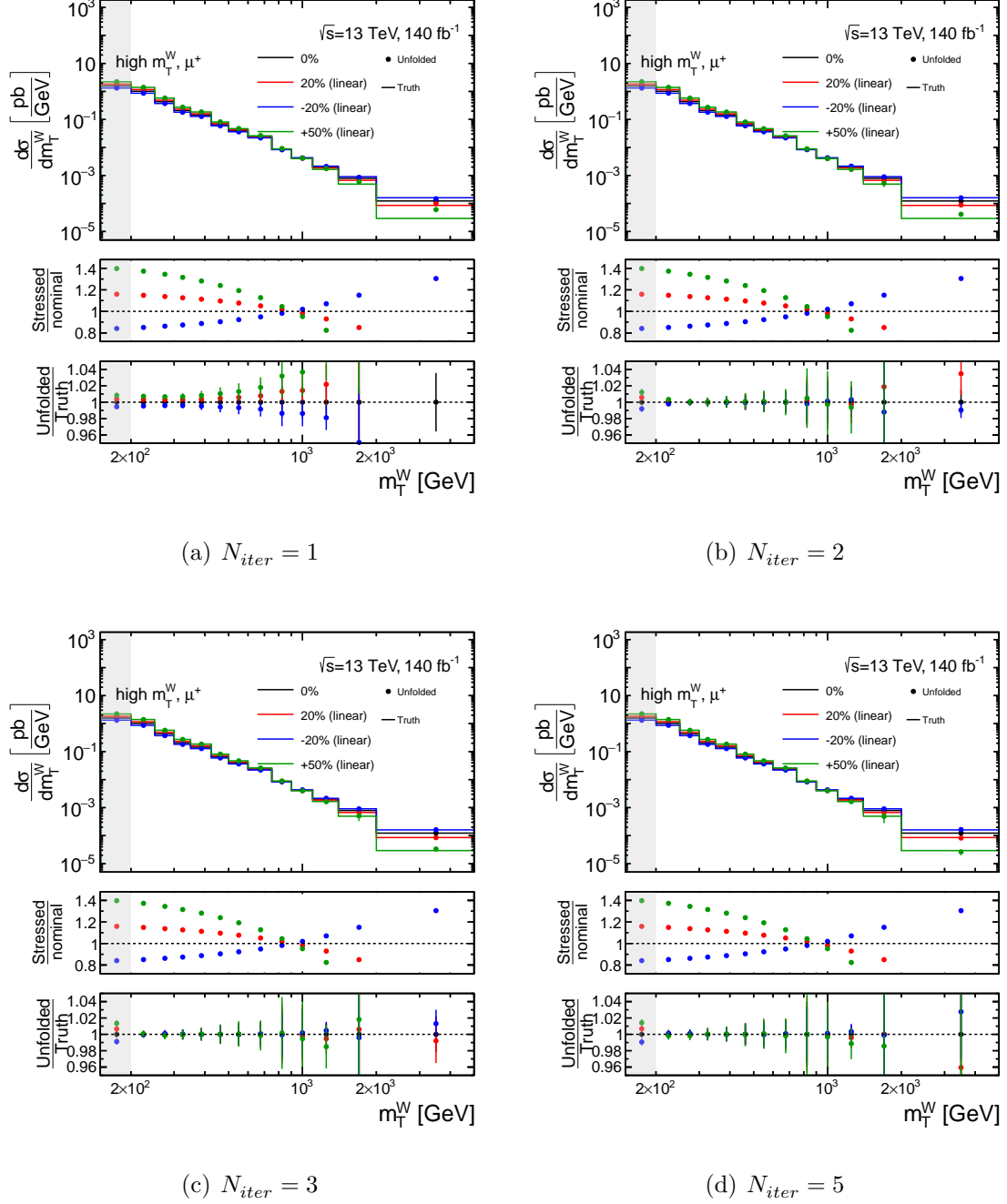
Figure E.13.: Unfolding results of the stress test, where the predicted single-differential signal m_T^W distribution is re-weighted linearly and then unfolded using the unfolding corrections of the original MC sample. All are shown for μ^+ and for 1-3 and 5 iterations in the IBU.

(a) $N_{iter} = 1$

(b) $N_{iter} = 2$

(c) $N_{iter} = 3$

(d) $N_{iter} = 5$
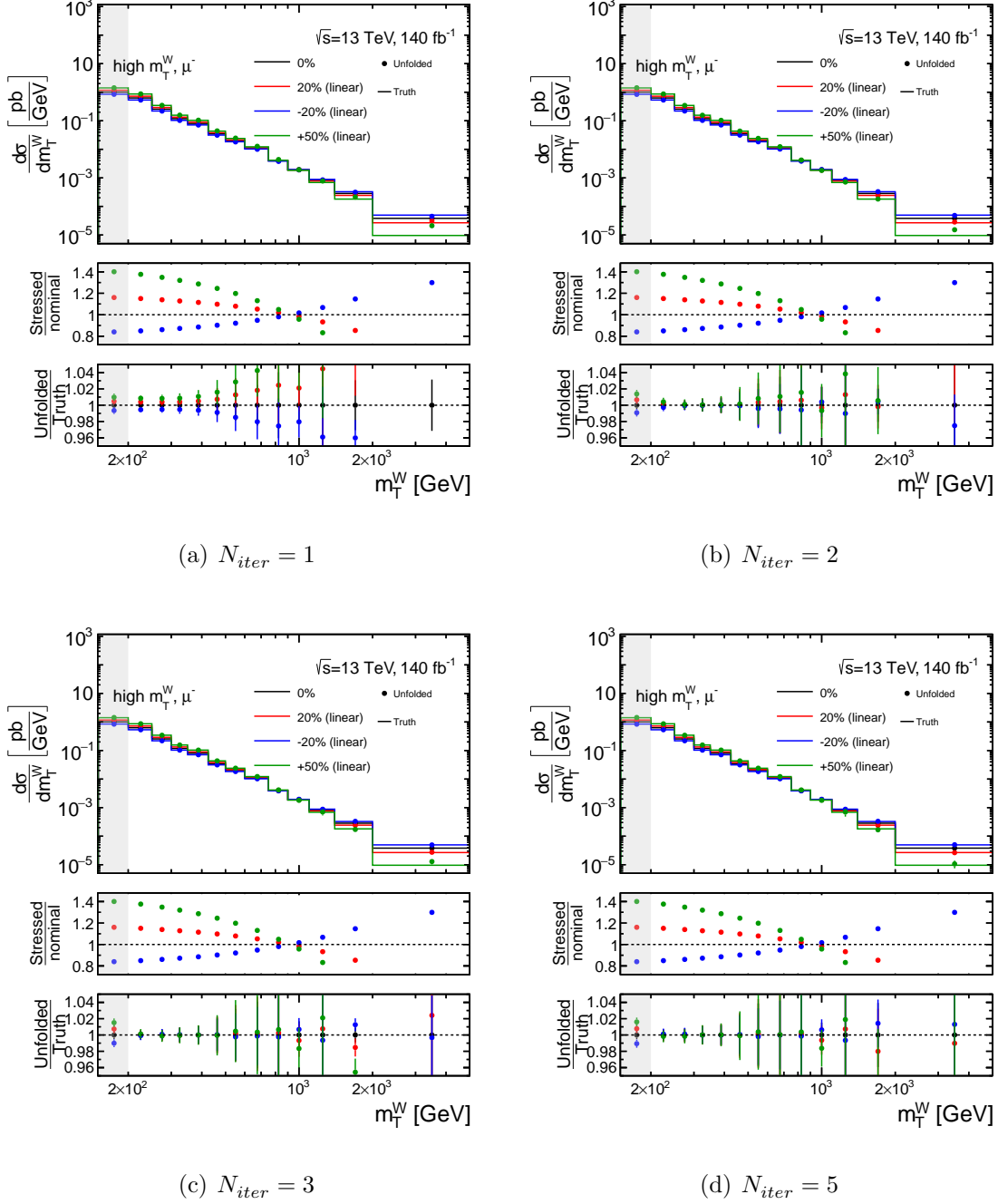
Figure E.14.: Unfolding results of the stress test, where the predicted single-differential signal m_T^W distribution is re-weighted linearly and then unfolded using the unfolding corrections of the original MC sample. All are shown for μ^- and for 1-3 and 5 iterations in the IBU.

(a) $N_{iter} = 1$

(b) $N_{iter} = 2$

(c) $N_{iter} = 3$

(d) $N_{iter} = 5$
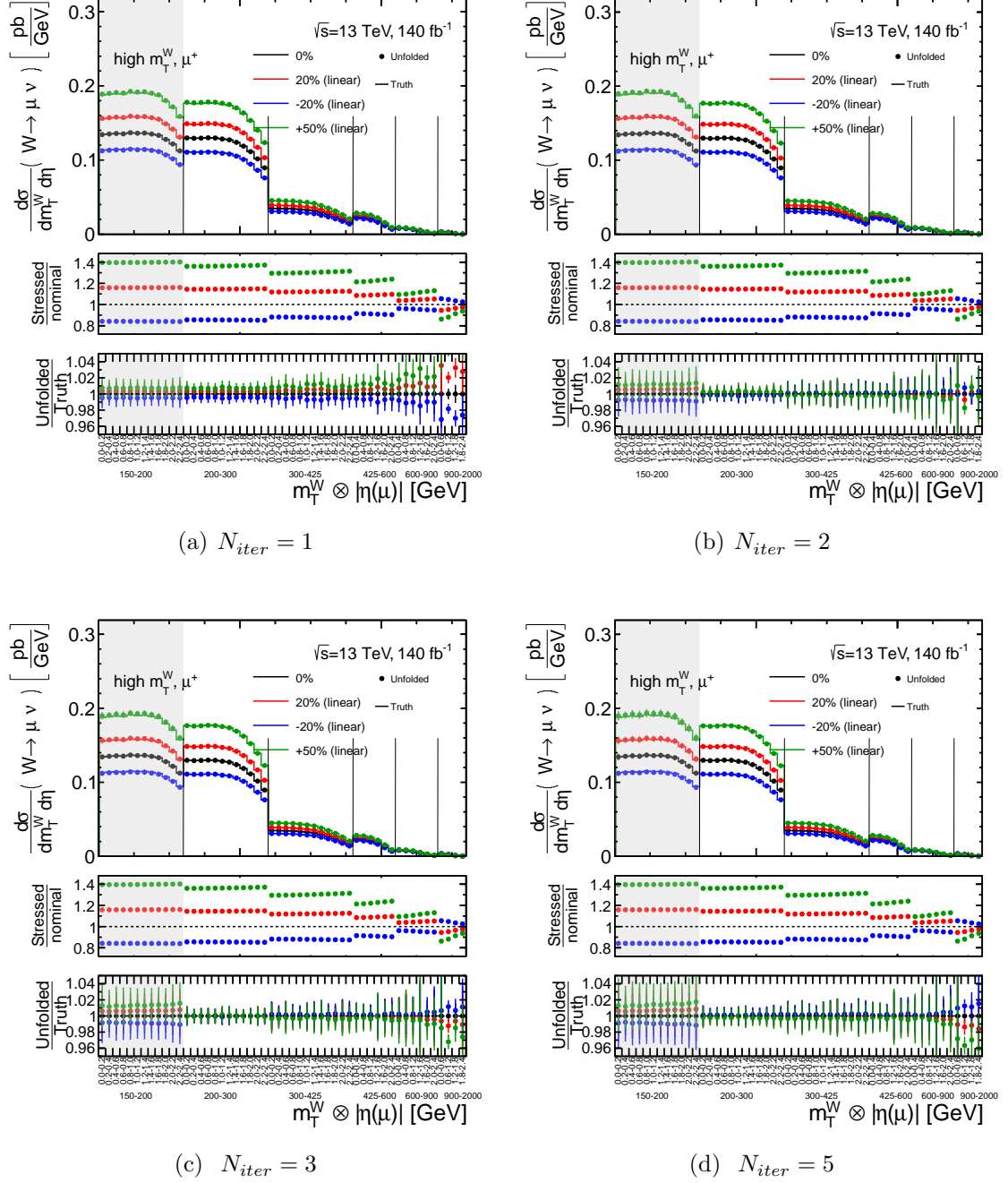
Figure E.15.: Unfolding results of the stress test, where the predicted double-differential signal $m_T^W \otimes |\eta(\mu)|$ distribution is re-weighted linearly and then unfolded using the unfolding corrections of the original MC sample. All are shown for μ^+ and for 1-3 and 5 iterations in the IBU.

(a) $N_{iter} = 1$

(b) $N_{iter} = 2$

(c) $N_{iter} = 3$

(d) $N_{iter} = 5$

Figure E.16.: Unfolding results of the stress test, where the predicted double-differential signal $m_T^W \otimes |\eta(\mu)|$ distribution is re-weighted linearly and then unfolded using the unfolding corrections of the original MC sample. All are shown for μ^- and for 1-3 and 5 iterations in the IBU.

E.6. Closure test and data-driven closure test
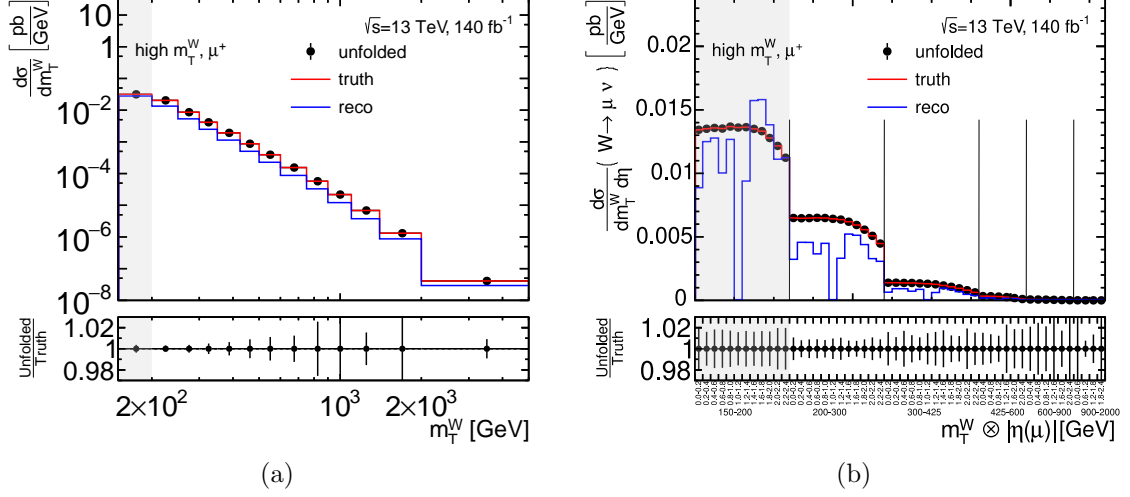
Figure E.17.: Reconstructed, truth and unfolded distributions in the technical closure test, where the predicted distribution is taken as the input of the unfolding. The μ^+-channel is shown here. In (b), the truth-level $m_T^W \otimes |\eta(\mu)|$ binning labels are shown but the reconstruction-level distribution is subject to a different binning (see Section 5.3).
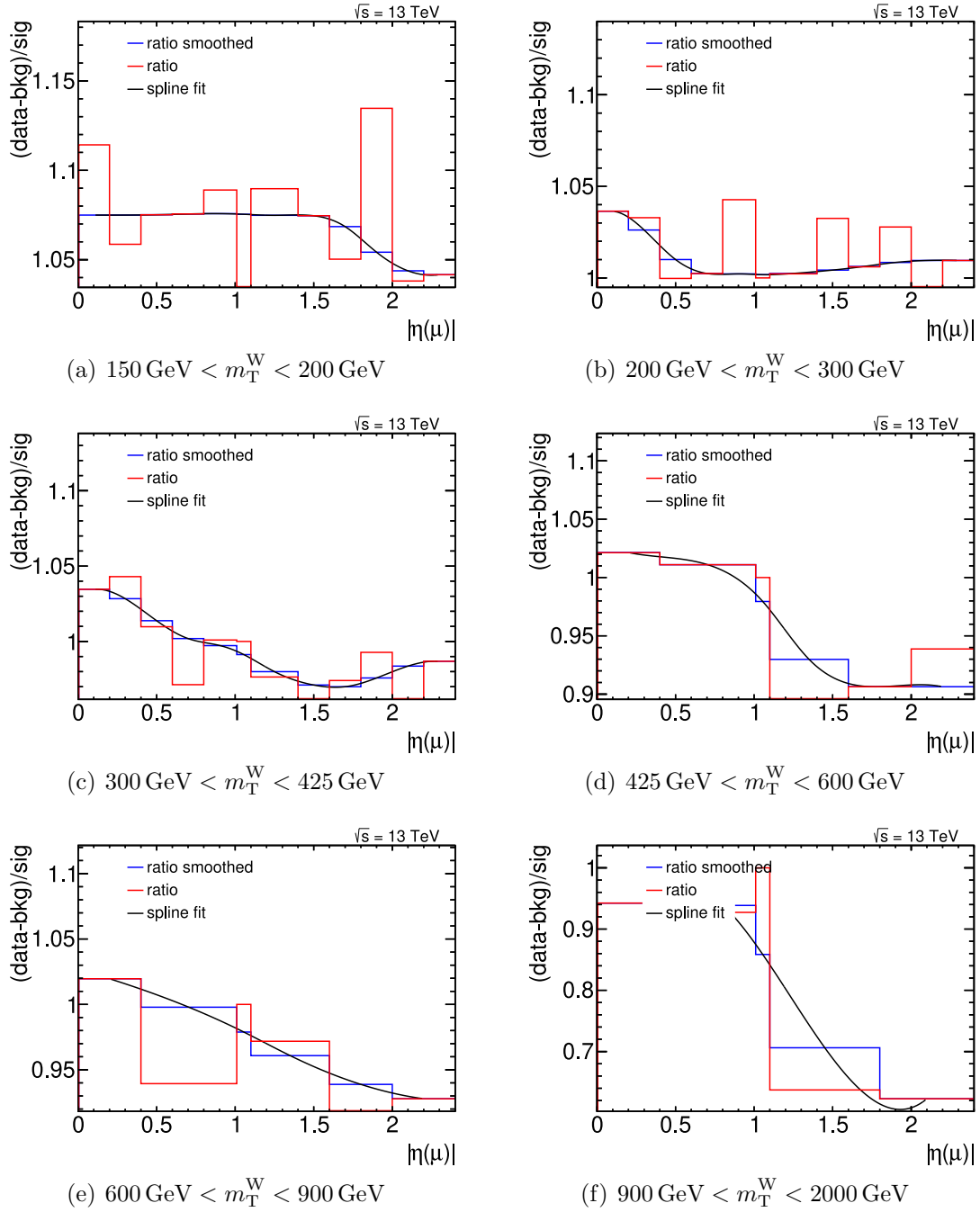
Figure E.18.: Ratio between the background-subtracted data distribution and the predicted signal distribution on reconstruction level in the double-differential measurement binning in $m_T^W \otimes |\eta(\mu)|$ in the μ^+-channel. For each m_T^W-bin, a separate spline fit is done across the given $|\eta(\mu)|$ distribution.

(a) $150\,\mathrm{GeV} < m_\mathrm{T}^\mathrm{W} < 200\,\mathrm{GeV}$

(b) $200\,\mathrm{GeV} < m_\mathrm{T}^\mathrm{W} < 300\,\mathrm{GeV}$

(c) $300\,\mathrm{GeV} < m_\mathrm{T}^\mathrm{W} < 425\,\mathrm{GeV}$

(d) $425\,\mathrm{GeV} < m_\mathrm{T}^\mathrm{W} < 600\,\mathrm{GeV}$

(e) $600\,\mathrm{GeV} < m_\mathrm{T}^\mathrm{W} < 900\,\mathrm{GeV}$

(f) $900\,\mathrm{GeV} < m_\mathrm{T}^\mathrm{W} < 2000\,\mathrm{GeV}$
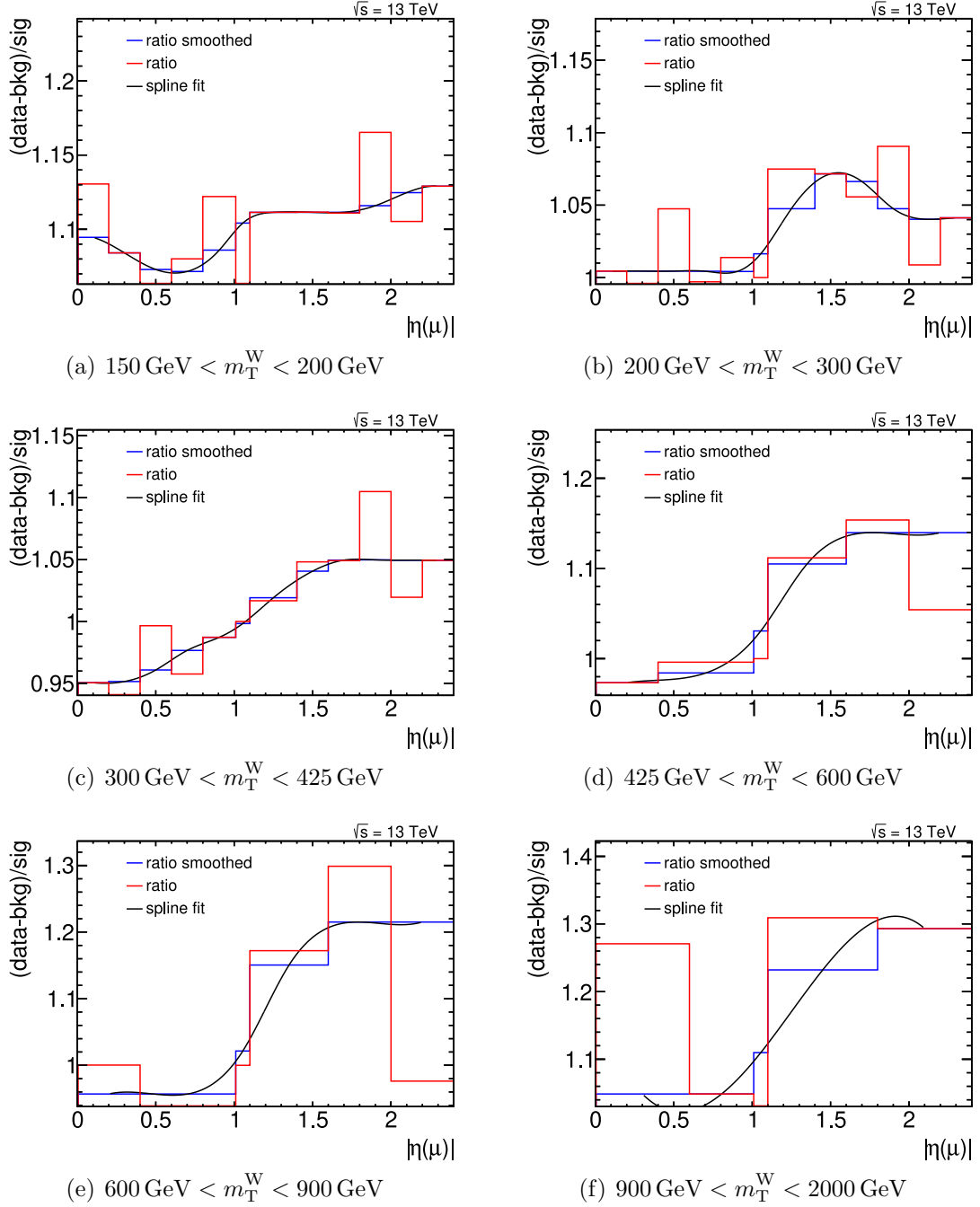
Figure E.19.: Ratio between the background-subtracted data distribution and the predicted signal distribution on reconstruction level in the double-differential measurement binning in $m_\mathrm{T}^\mathrm{W} \otimes |\eta(\mu)|$ in the μ^--channel. For each m_T^W-bin, a separate spline fit is done across the given $|\eta(\mu)|$ distribution.
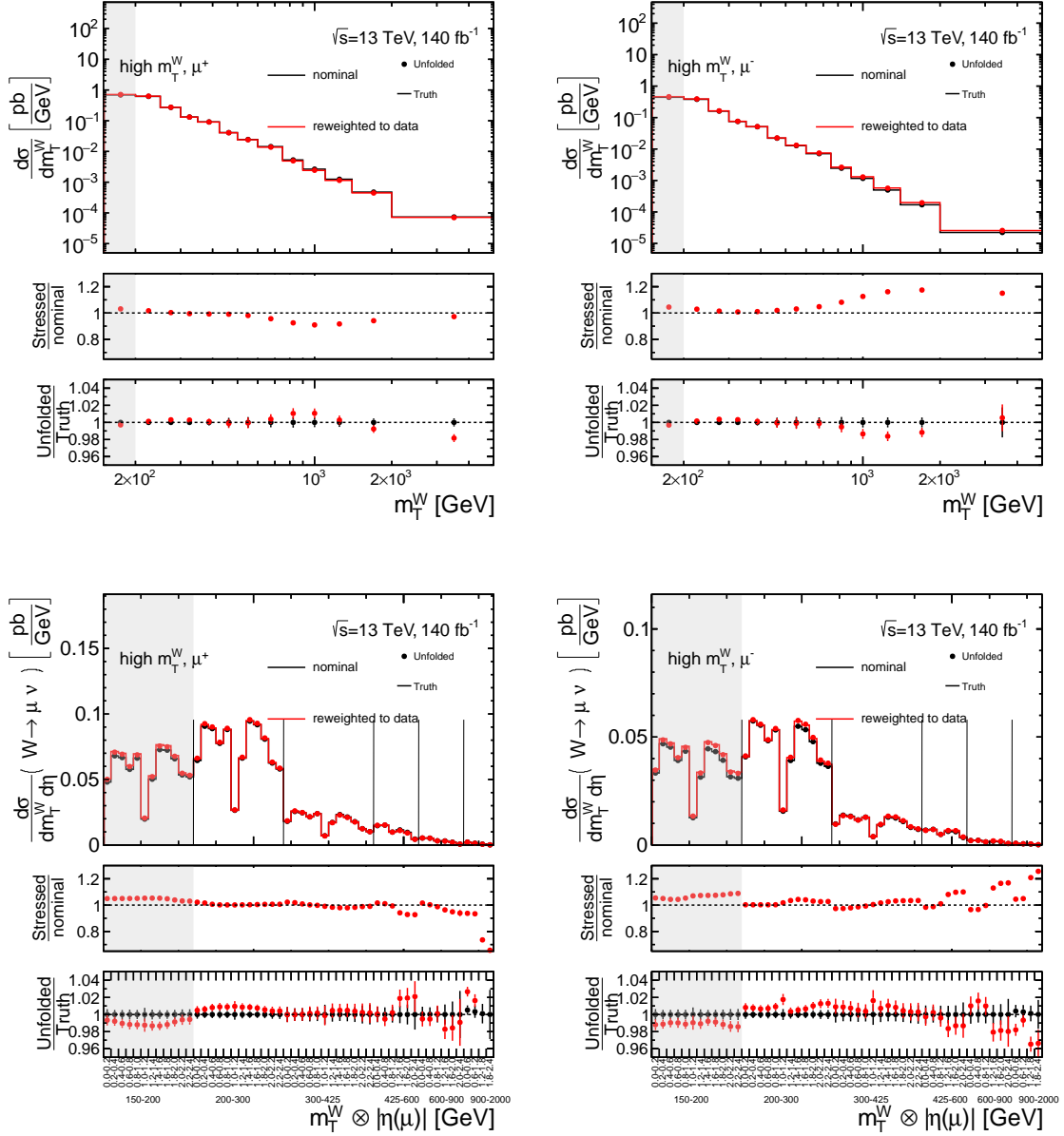
Figure E.20.: Unfolded and MC-truth-level distributions obtained in the data-driven closure test, where the signal predicted distribution is matched to data in the measurement variables and then unfolded using the nominal response matrix. They are shown for the single- and double-differential observables in the μ^+- and μ^--channel using **1** iterations in the IBU.
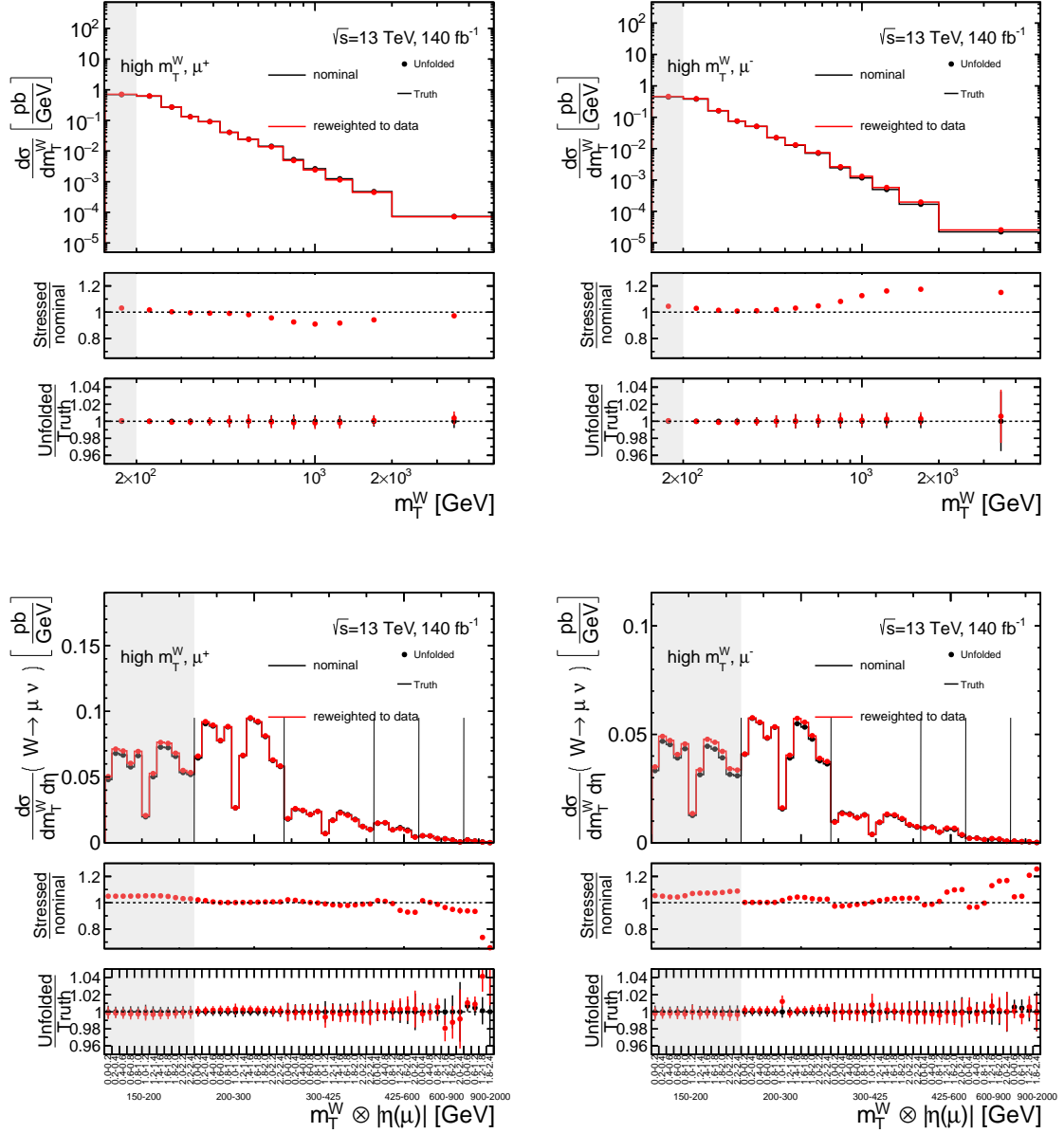
Figure E.21.: Unfolded and MC-truth-level distributions obtained in the data-driven closure test, where the signal predicted distribution is matched to data in the measurement variables and then unfolded using the nominal response matrix. They are shown for the single- and double-differential observables in the μ^+- and μ^--channel using **3** iterations in the IBU.
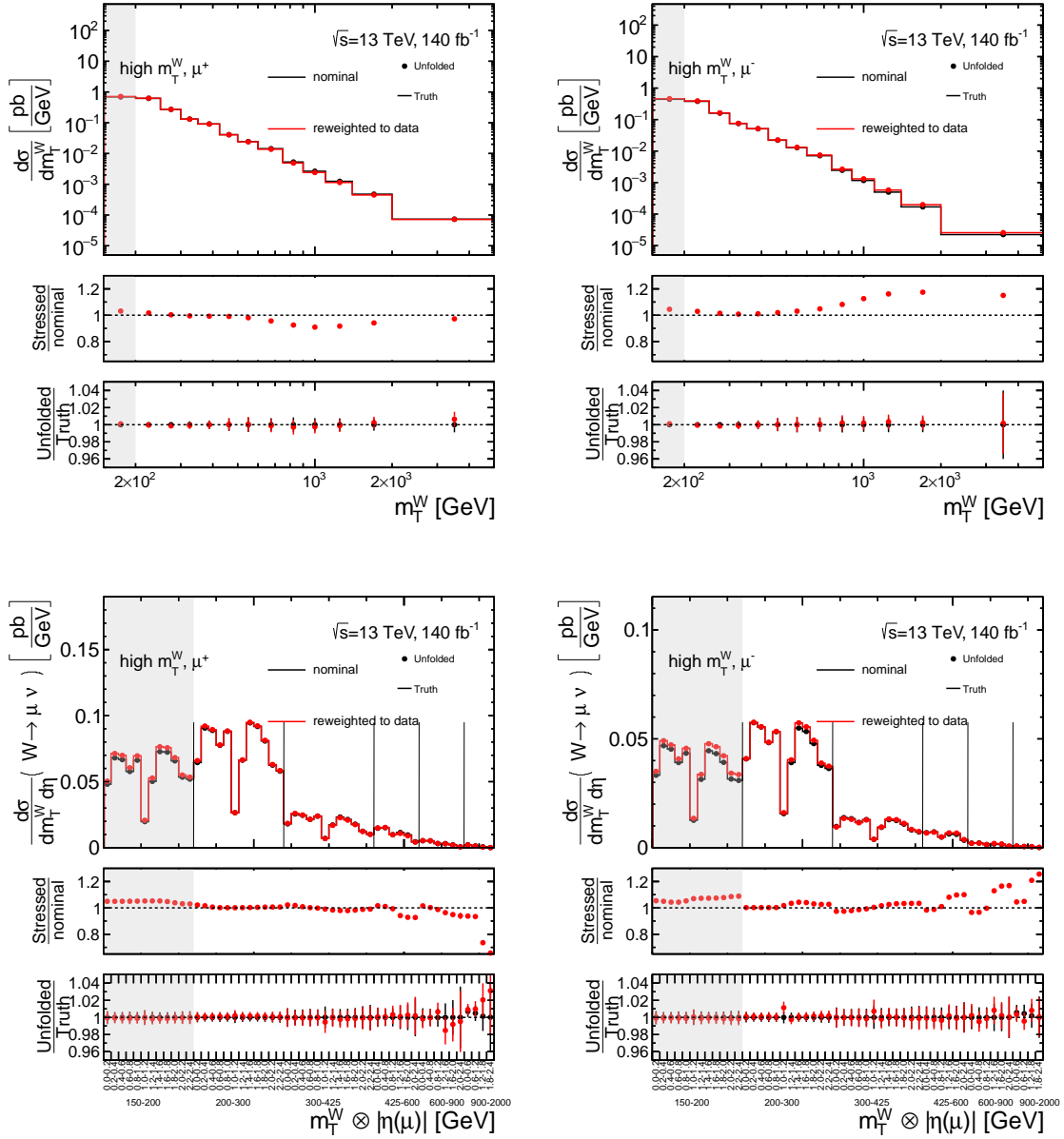
Figure E.22.: Unfolded and MC-truth-level distributions obtained in the data-driven closure test, where the signal predicted distribution is matched to data in the measurement variables and then unfolded using the nominal response matrix. They are shown for the single- and double-differential observables in the μ^+- and μ^--channel using **4** iterations in the IBU.
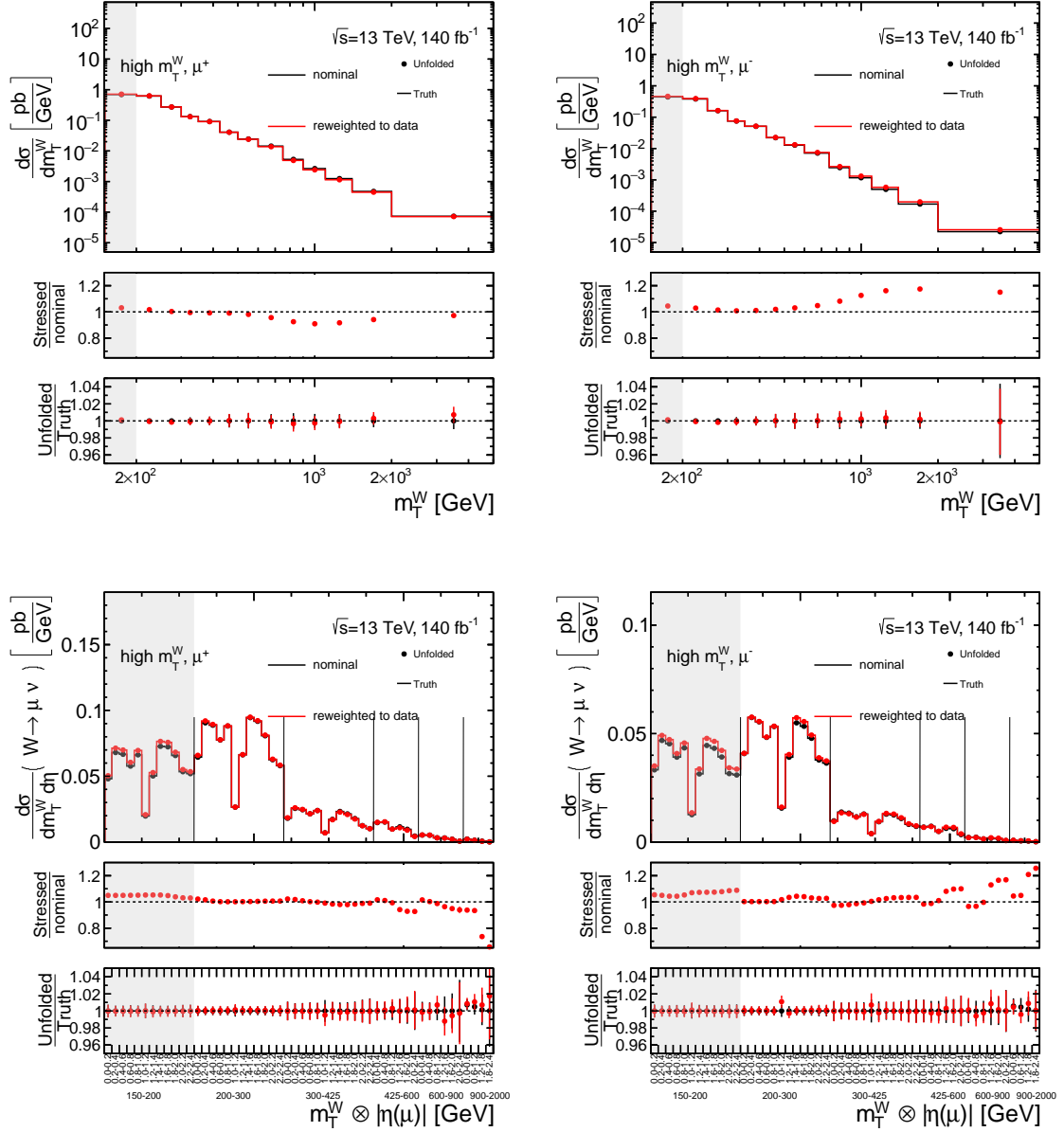
Figure E.23.: Unfolded and MC-truth-level distributions obtained in the data-driven closure test, where the signal predicted distribution is matched to data in the measurement variables and then unfolded using the nominal response matrix. They are shown for the single- and double-differential observables in the μ^+- and μ^--channel using **5** iterations in the IBU.

E.7. Comparisons between Sherpa and Powheg+Pythia signal MC samples
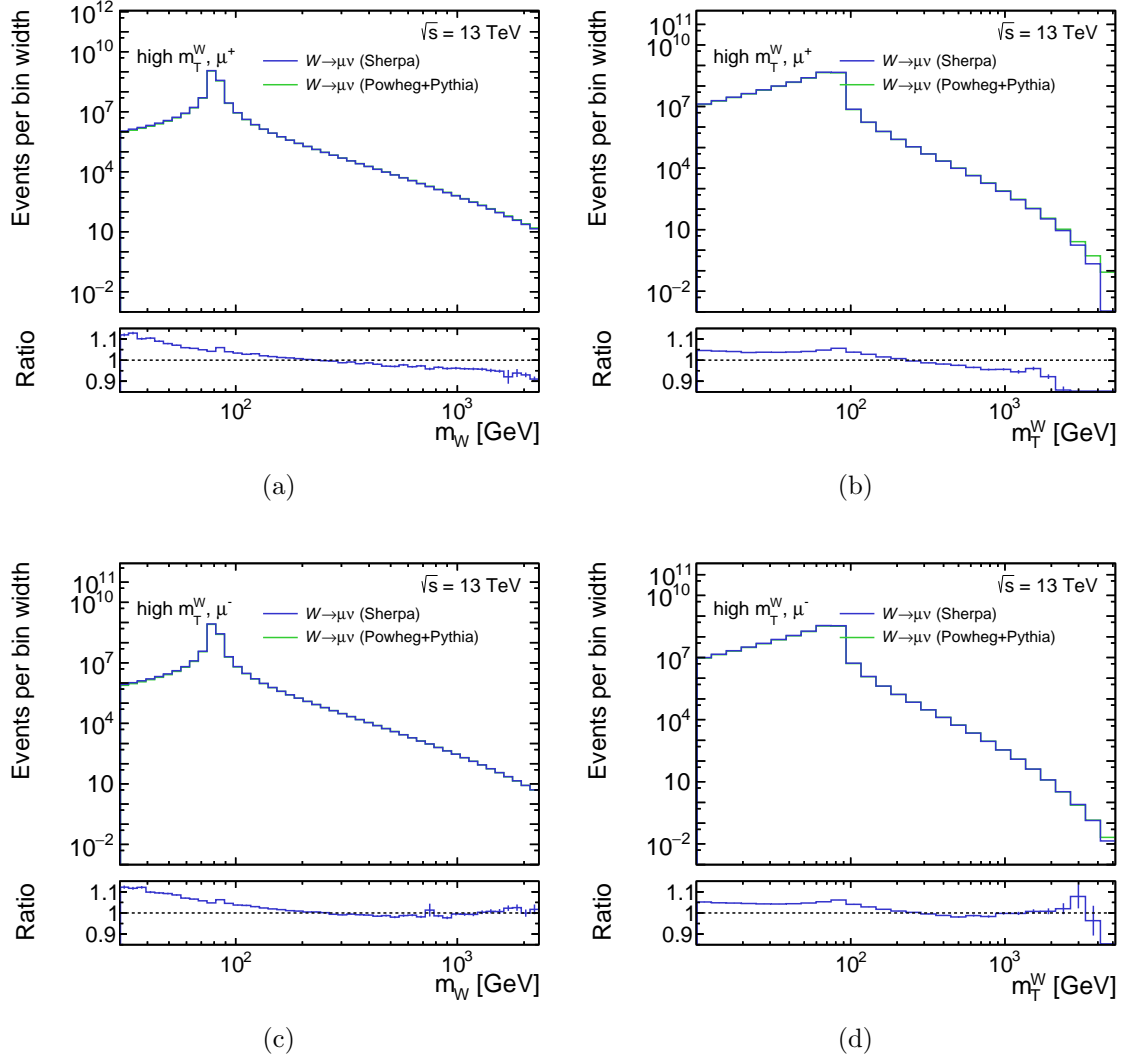
Figure E.24.: Distributions for POWHEG+PYTHIA and SHERPA signal predictions on truth level without fiducial cuts for a positively/negatively charged muon (upper/lower row) for the invariant mass (left-hand side) and transverse mass (right-hand side). Both MC samples use the NNPDF3.0NNLO PDF here.

Figure E.25.: Distributions for SHERPA and POWHEG+PYTHIA signal predictions for m_T^W and $m_T^W \otimes |\eta(\mu)|$, on truth and reconstruction level, as well as $p_T(W)$ on truth level. All distributions are including the respective high-m_T^W cuts and are shown for the μ^+-channel here. The SHERPA2.2.11 sample is reweighted to match POWHEG+PYTHIA in the truth-level measurement observables.
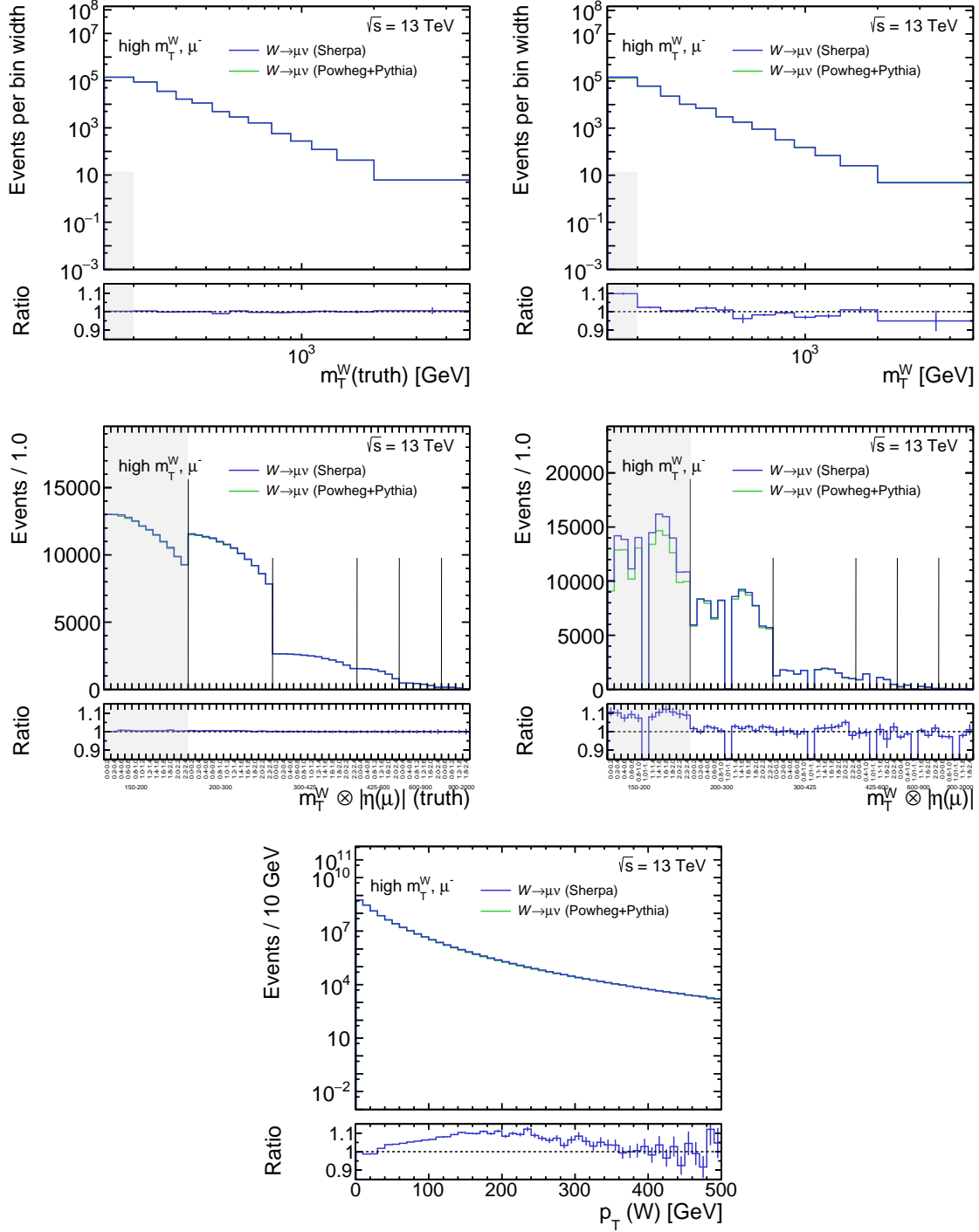
Figure E.26.: Distributions for SHERPA and POWHEG+PYTHIA signal predictions for m_T^W and $m_T^W \otimes |\eta(\mu)|$, on truth and reconstruction level, as well as $p_T(W)$ on truth level. All distributions are including the respective high-m_T^W cuts and are shown for the μ^--channel here. The SHERPA2.2.11 sample is reweighted to match POWHEG+PYTHIA in the truth-level measurement observables.

E.8. Hidden variables test: reweighting in $p_\mathrm{T}(W)$
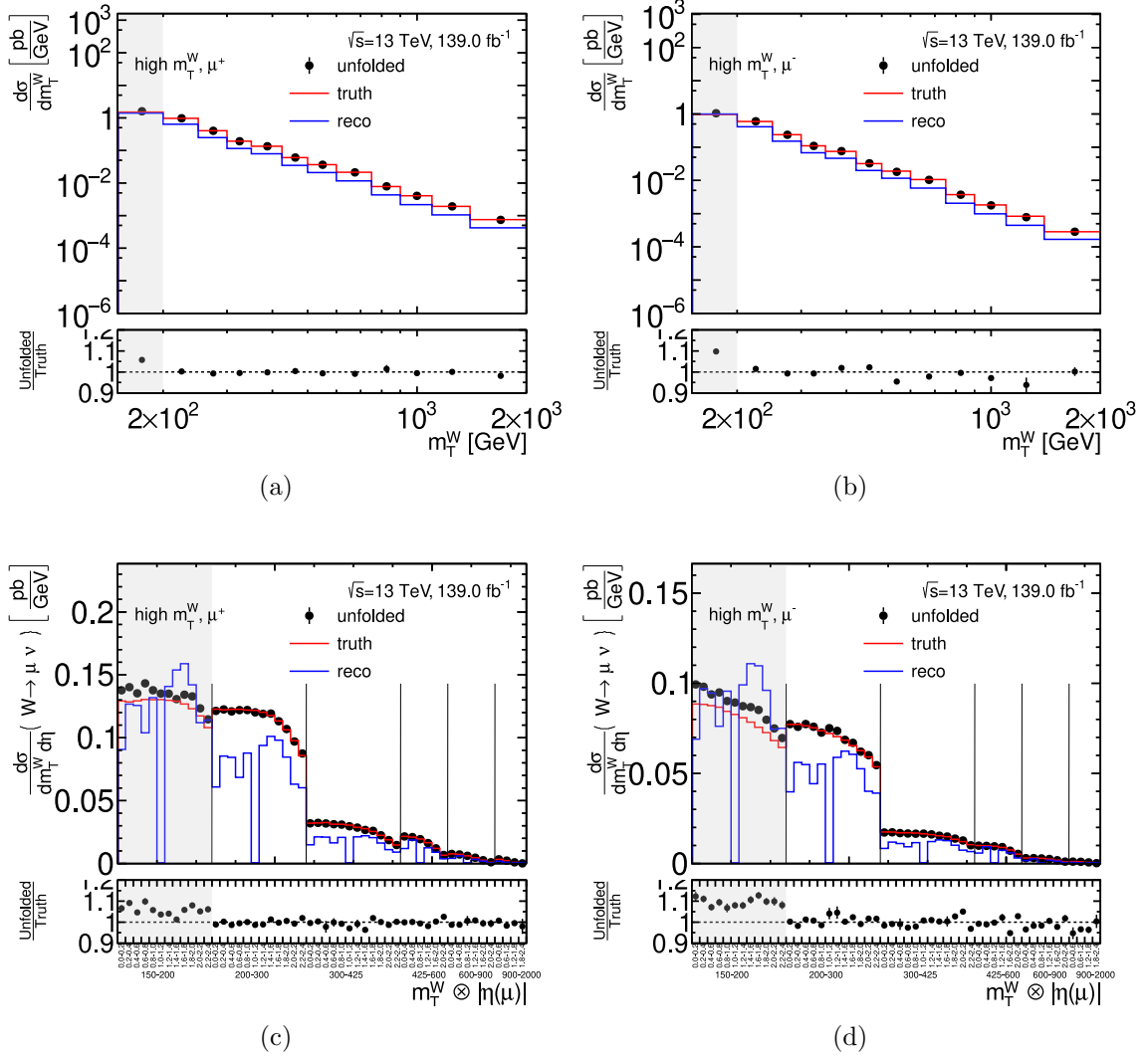
Figure E.27.: Reconstructed, truth and unfolded distributions in the unfolding test using an alternative signal sample. The prediction of the alternative sample is reweighted to match the truth-level $p_\mathrm{T}(W)$ distribution (a 'hidden variable') of the nominal sample and then unfolded using the unfolding corrections of the nominal sample. The distributions are shown for the single- and double-differential observables in the μ^+- and μ^--channel using two iterations in the IBU.

E.9. Smoothing of unfolding uncertainties

(a)

(b)

(c)

(d)
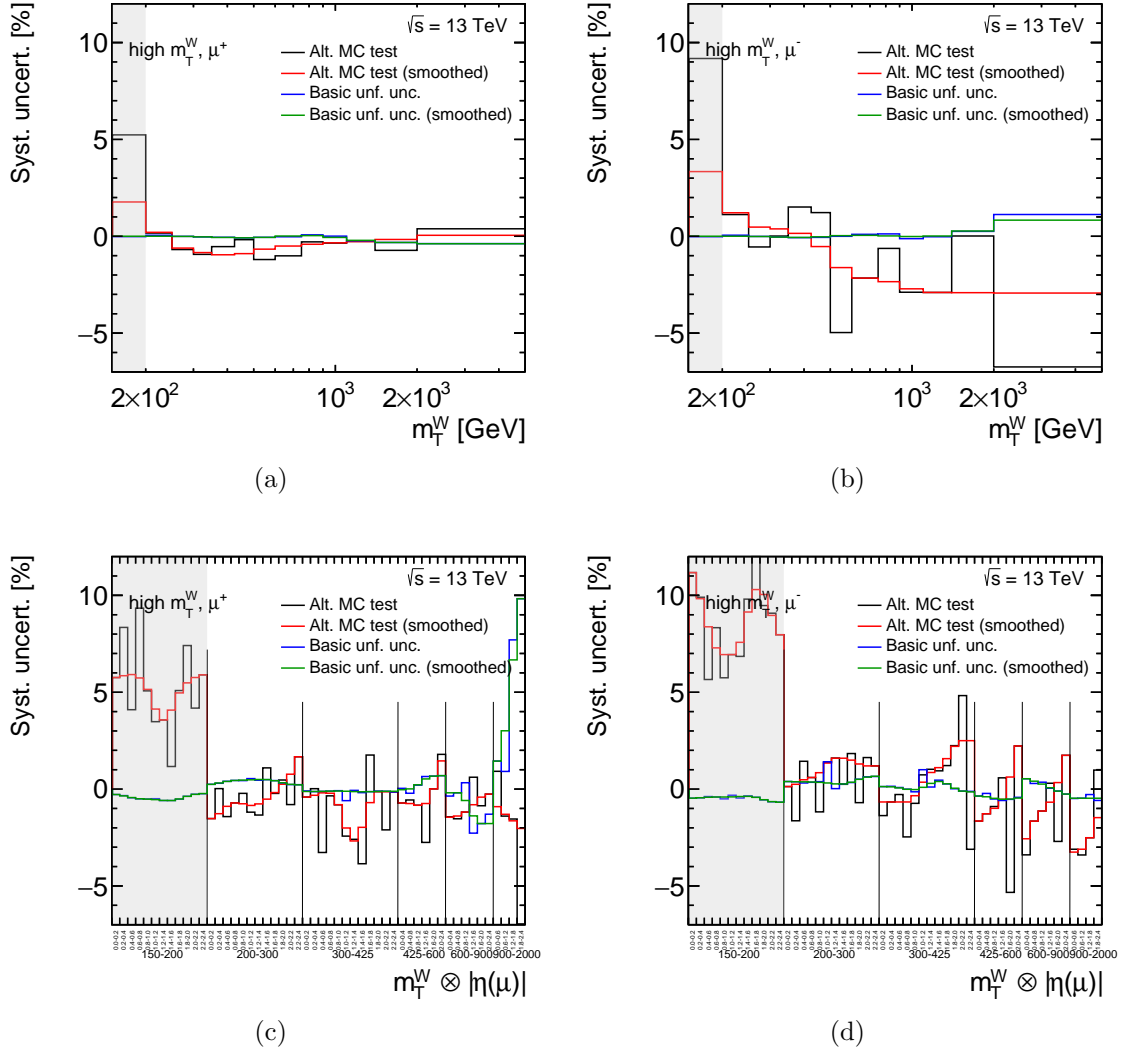
Figure E.28.: Unfolding uncertainties originating from the unfolding tests described in Chapter 8.3 for μ^+ (left-hand side) and μ^- (right-hand side) in the single- and double-differential measurement variables. The smoothed uncertainties will be added to the final results.

E.10. Unfolding of experimental systematic uncertainties
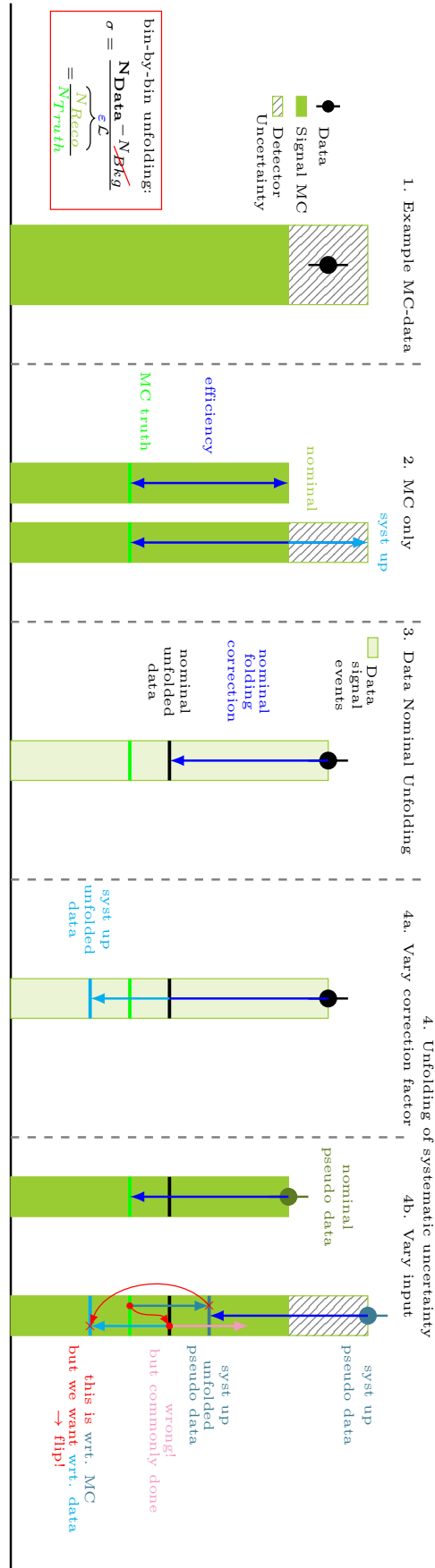
Figure E.29.: Schematic illustration of unfolding of experimental systematic uncertainties in bin-by-bin unfolding. The two methods given in Section 8.4 are compared.

F. Systematic uncertainties: supplemental material

F.1. Statistical uncertainty
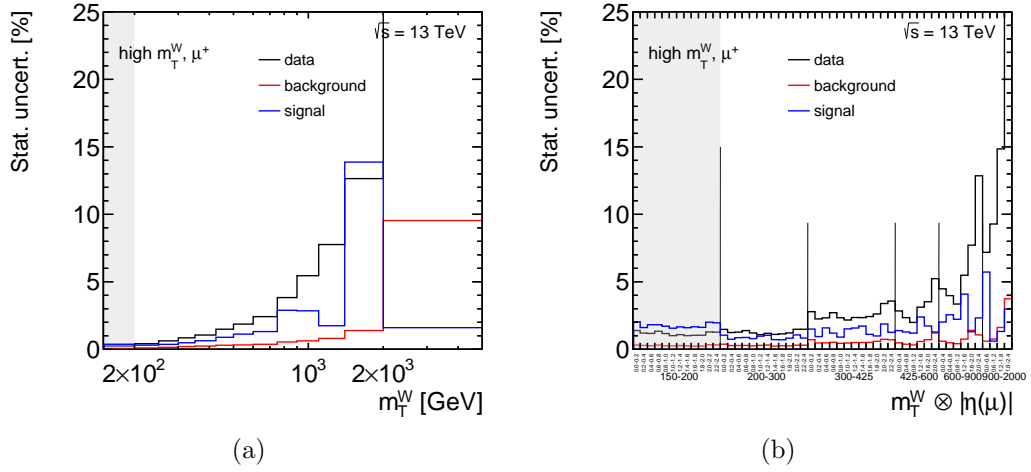
Figure F.1.: Statistical uncertainty on the (a) single- and (b) double-differential $W^+ \to \mu^+ \nu$ cross-section, separated in data, signal and background prediction.

F.2. Systematic uncertainties before the unfolding

F.2.1. Experimental systematic uncertainties with respect to the signal prediction including the shadow bin
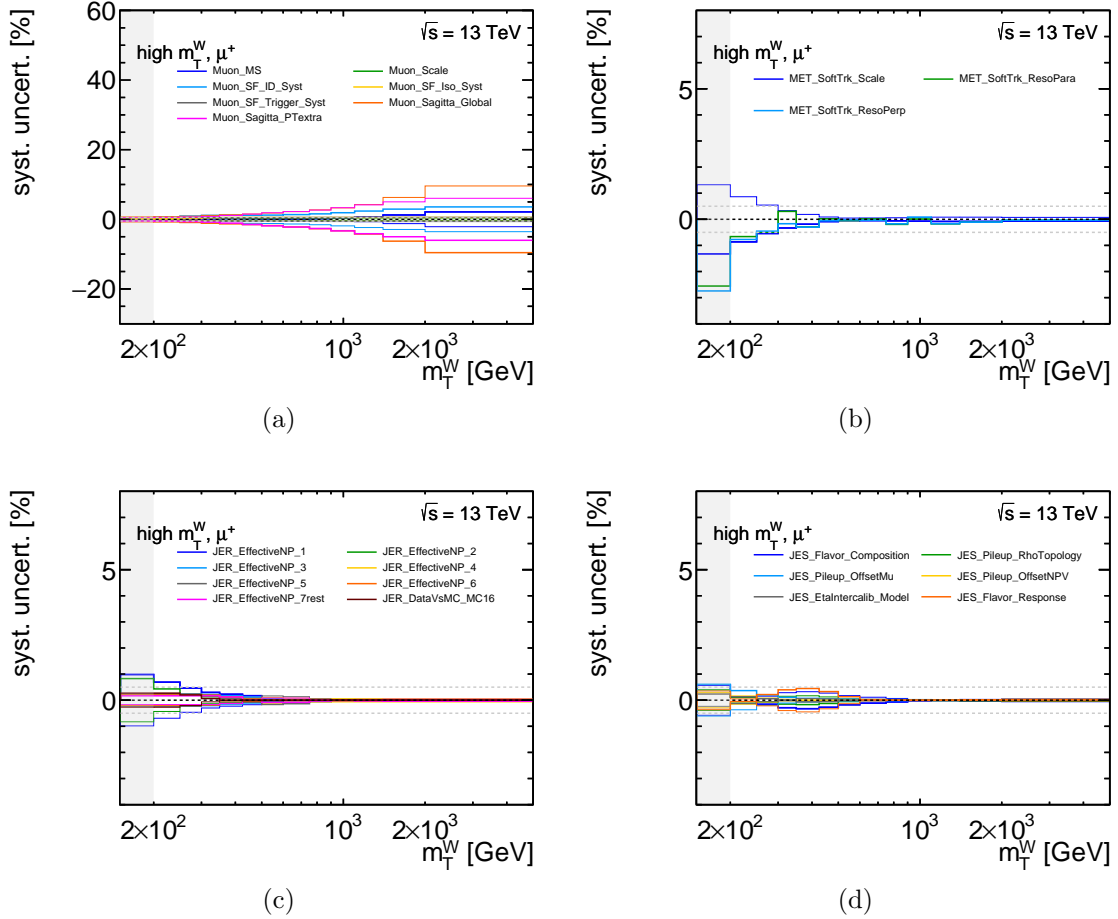
Figure F.2.: Systematic uncertainties in the μ^+-channel as a function of $m_{\mathrm{T}}^{\mathrm{W}}$ with respect to the nominal signal prediction. Only the uncertainties larger than 0.5% in at least one bin in any distribution are shown.
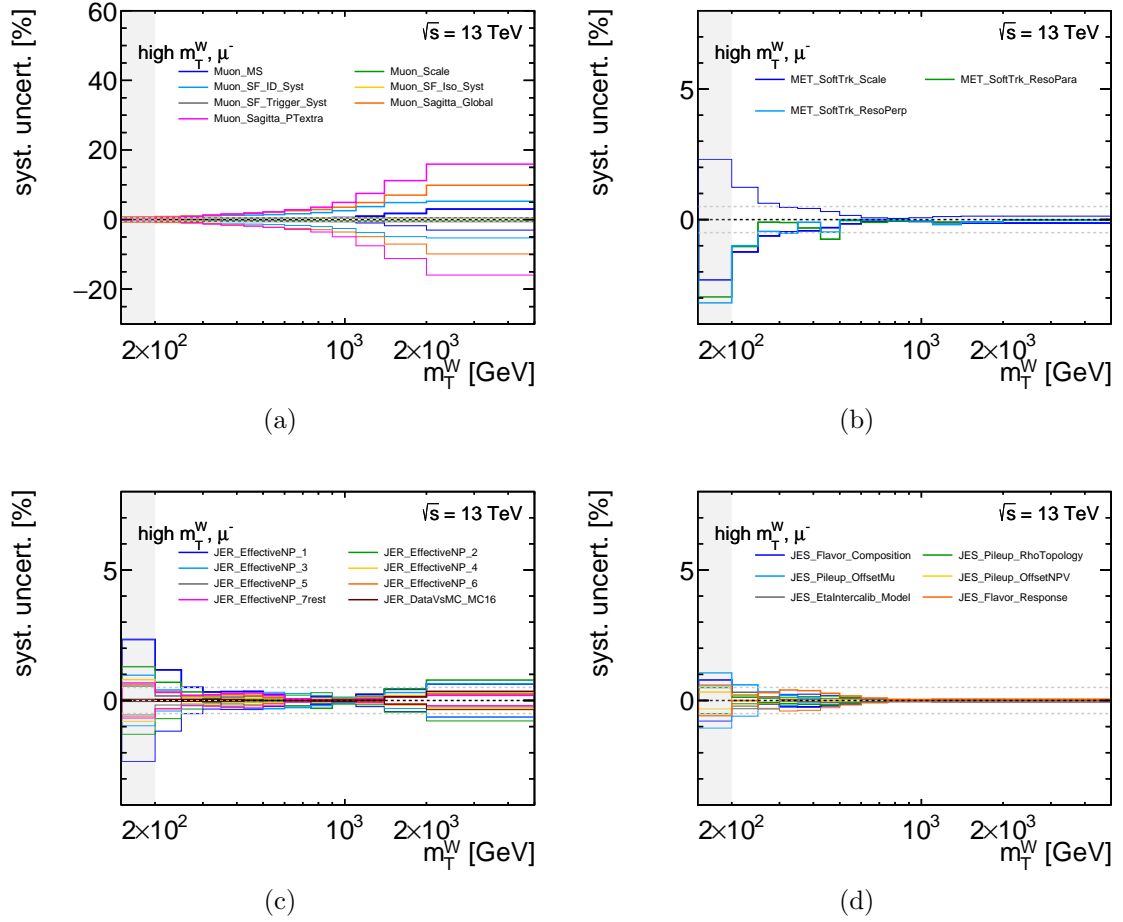
Figure F.3.: Systematic uncertainties in the μ^--channel as a function of m_T^W with respect to the nominal signal prediction. Only the uncertainties larger than 0.5% in at least one bin in any distribution are shown.
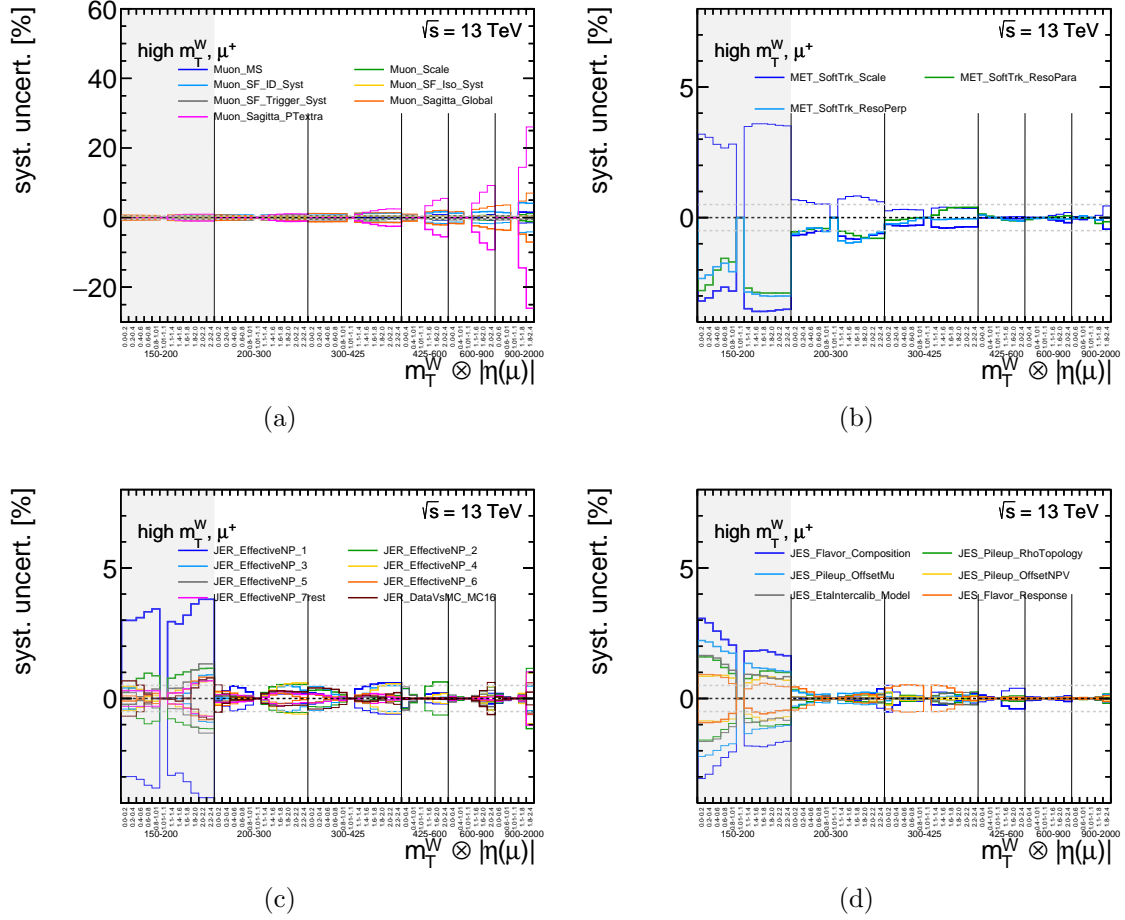
Figure F.4.: Systematic uncertainties in the μ^+-channel as a function of $m_T^W \otimes |\eta(\mu)|$ with respect to the nominal signal prediction. Only the uncertainties larger than 0.5% in at least one bin in any distribution are shown.

Figure F.5.: Systematic uncertainties in the μ^--channel as a function of $m_{\mathrm{T}}^{\mathrm{W}} \otimes |\eta(\mu)|$ with respect to the nominal signal prediction. Only the uncertainties larger than 0.5% in at least one bin in any distribution are shown.

F.2.2. Theory systematic uncertainties with respect to the top-quark background prediction

(a)

(b)

(c)

(d)
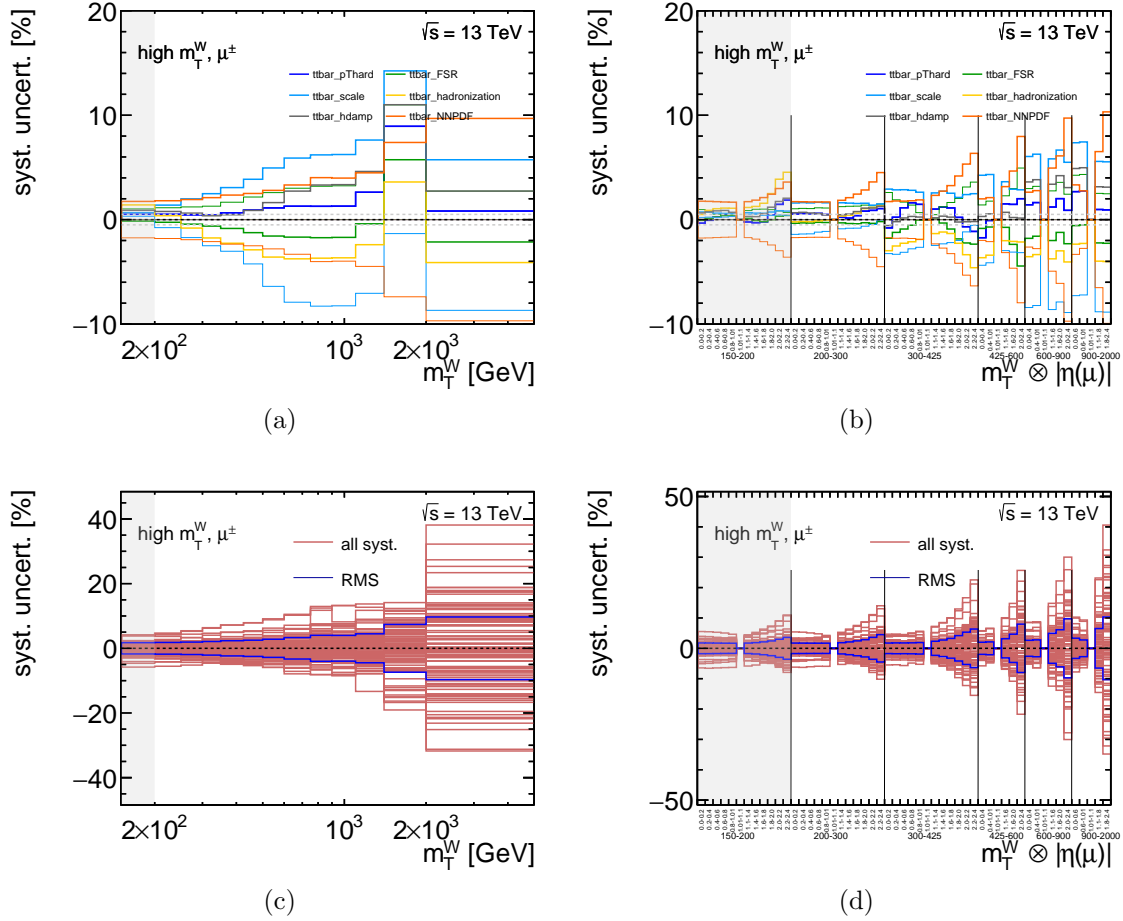
Figure F.6.: Systematic $t\bar{t}$ theory uncertainties in the $\mu^{\pm}$-channel as a function of $m_{\mathrm{T}}^{\mathrm{W}}$ (left-hand side) and $m_{\mathrm{T}}^{\mathrm{W}} \otimes |\eta(\mu)|$ (right-hand side) with respect to the nominal $t\bar{t}$ prediction. In the lower row, the 100 PDF replicas are shown explicitly as well as their RMS which is taken as the final PDF uncertainty on the $t\bar{t}$ prediction.

(a)

(b)

(c)

(d)

Figure F.7.: Distributions of $m_{\mathrm{T}}^{\mathrm{W}}$ and $m_{\mathrm{T}}^{\mathrm{W}} \otimes |\eta(\mu)|$ in the signal region for μ^+ and μ^- for the single top samples using either the DR or the DS (nominal) scheme accounting for the interference between the tW and $t\bar{t}$ processes.

F.2.3. Multijet systematic uncertainties with respect to the multijet yield

(a)

(b)
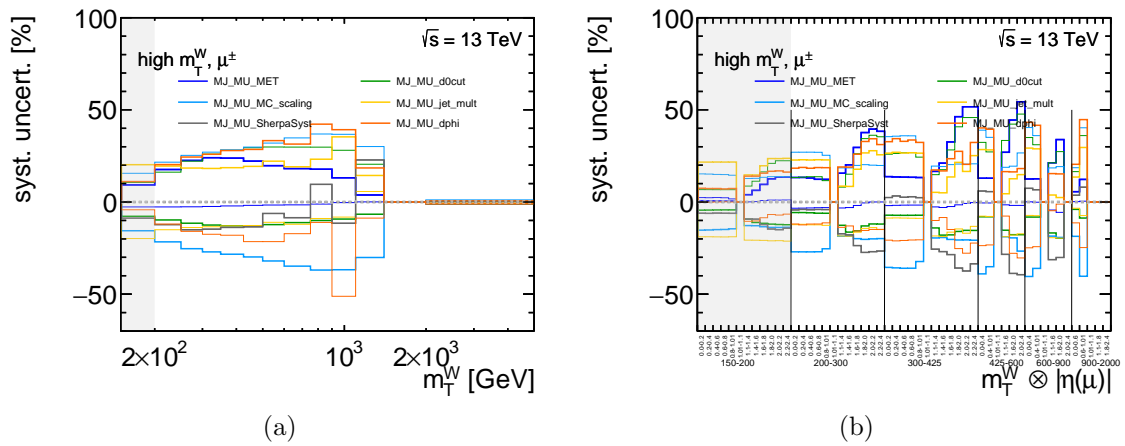
Figure F.8.: Multijet systematic uncertainties in the $\mu^{\pm}$-channel as a function of (a) $m_{\mathrm{T}}^{\mathrm{W}}$ and (b) $m_{\mathrm{T}}^{\mathrm{W}} \otimes |\eta(\mu)|$ with respect to the nominal multijet estimate.

F.3. Uncertainties on the unfolded W^+ cross-section

(a) Muon

(b) E_T^{miss} and JES

(c) JER

(d) Multijet

(e) $t\bar{t}$ theory & tW DR

(f) Rate on small backgrounds
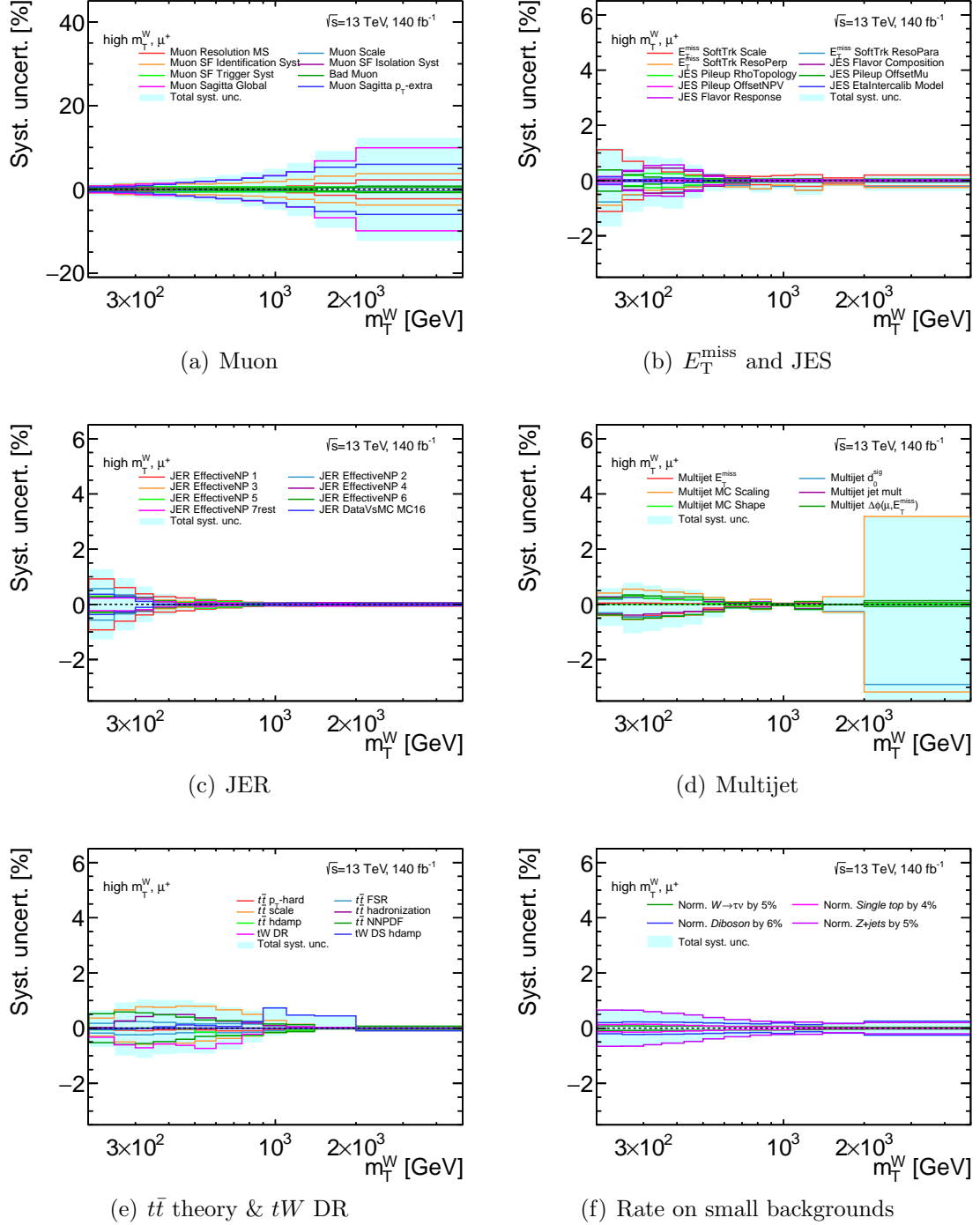
Figure F.9.: Overview of relative systematic uncertainties on the single-differential measured cross-sections, for a positively charged muon. The light-blue band represents the quadratic sum of all uncertainties shown in a plot.

(a) Muon

(b) $E_{\mathrm{T}}^{\mathrm{miss}}$ and JES

(c) JER

(d) Multijet

(e) $t\bar{t}$ theory & tW DR

(f) Rate on small backgrounds
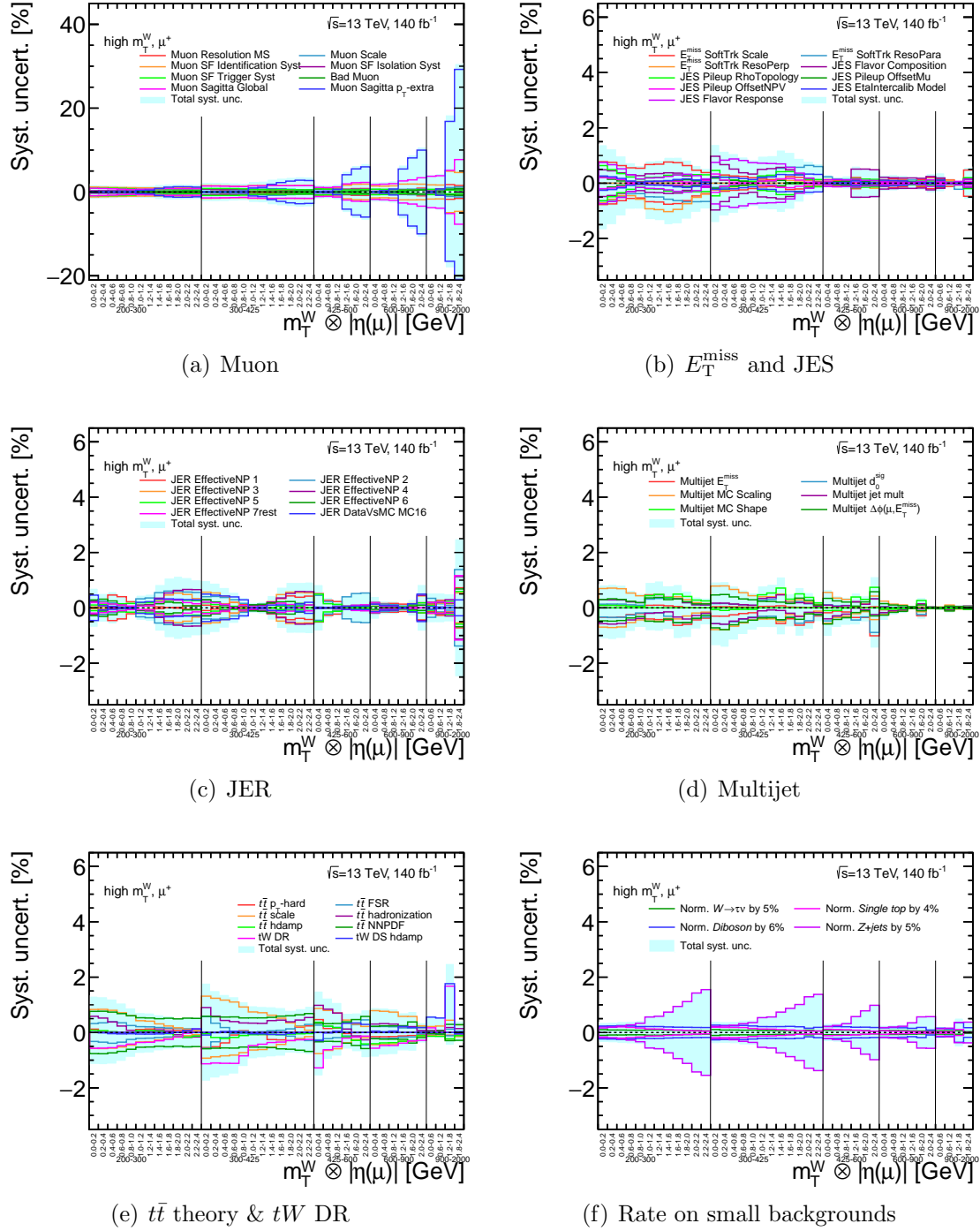
Figure F.10.: Overview of relative systematic uncertainties on the double-differential measured cross-sections, for a positively charged muon. The light-blue band represents the quadratic sum of all uncertainties shown in a plot.

F.4. Signal theory systematic uncertainties
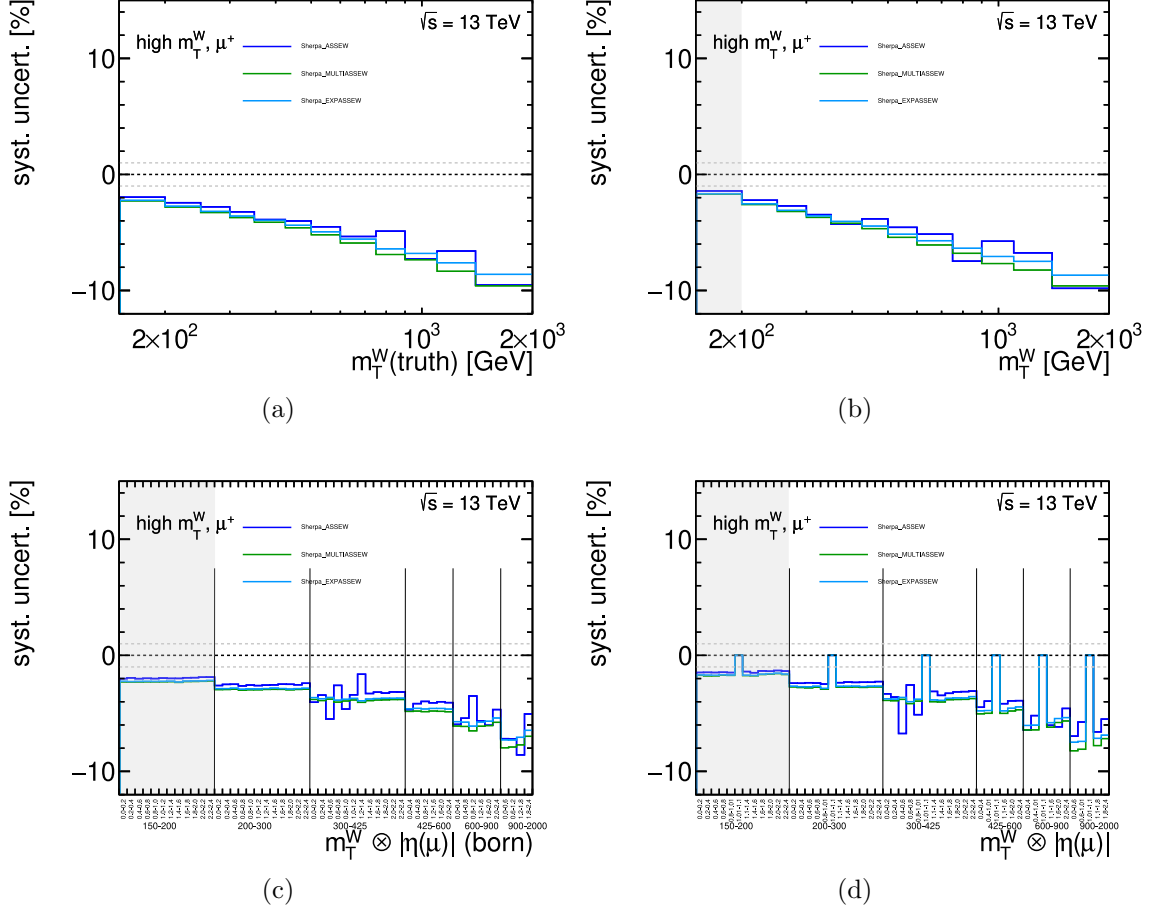
Figure F.11.: NLO electroweak corrections obtained from generator weights within the SHERPA2.2.11 signal sample, shown for m_T^W and $m_T^W \otimes |\eta(\mu)|$ on truth (left-hand side) and reconstruction (right-hand side) level. All plots are shown for the positive muon charge, since no substantial differences between the charges are expected. Artificial fluctuations are introduced by single events in the SHERPA sample with an in comparison large weight and should be ignored here.

Figure F.12.: Scale μ_R and μ_F variations obtained from generator weights within the SHERPA2.2.11 signal sample, shown for m_T^W and $m_T^W \otimes |\eta(\mu)|$ on MC truth (upper row) and reconstruction (middle row) level and unfolded level (lower row), respectively. All plots are shown for the positive muon charge, since no substantial differences between the charges are expected. Artificial fluctuations are introduced by single events in the SHERPA sample with an in comparison large weight and should be ignored here.

Figure F.13.: Scale μ_R and μ_F variations obtained from generator weights within the SHERPA2.2.11 signal sample as a function of truth p_T of the W boson. No cuts are applied to the selection shown here.

(a)

(b)

(c)

(d)

(e)

(f)

Figure F.14.: PDF variation obtained from generator weights within the SHERPA 2.2.11 signal sample, shown for m_T^W and $m_T^W \otimes |\eta(\mu)|$ on MC truth (upper row) and reconstruction (middle row) level and unfolded level (lower row), respectively. All plots are shown for the positive muon charge, since no substantial differences between the charges are expected. Artificial fluctuations are introduced by single events in the SHERPA sample with an in comparison large weight and should be ignored here.

Figure F.15.: Variations of α_s obtained from generator weights within the SHERPA2.2.11 signal sample, shown for m_T^W and $m_T^W \otimes |\eta(\mu)|$ on MC truth (upper row) and reconstruction (middle row) level and unfolded level (lower row), respectively. All plots are shown for the positive muon charge, since no substantial differences between the charges are expected. Artificial fluctuations are introduced by single events in the SHERPA sample with an in comparison large weight and should be ignored here.

F.5. Statistical fluctuations induced by the peak signal MC sample

(a)

(b)

(c)

(d)
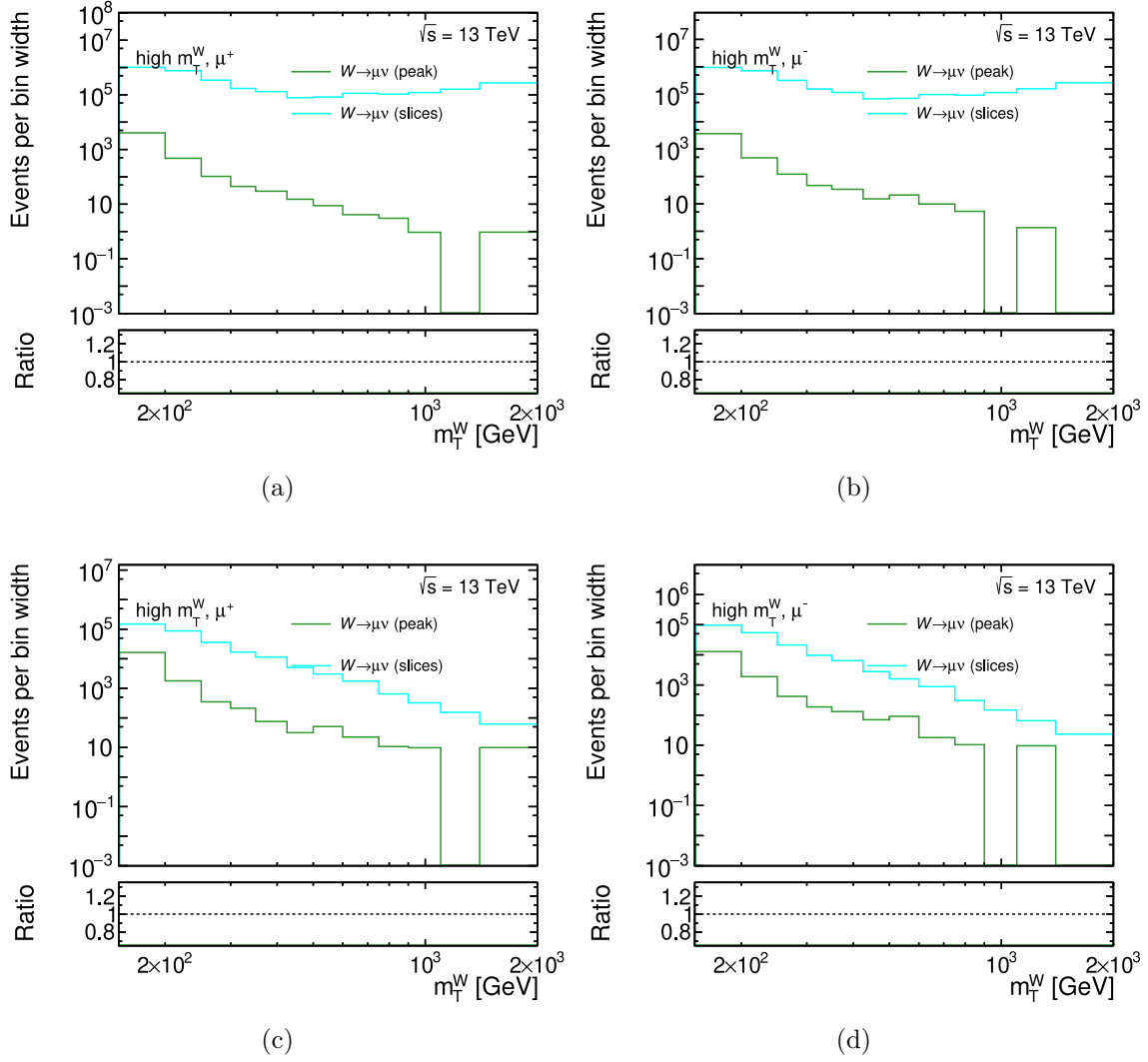
Figure F.16.: Number of events of the muon signal sample, separated into inclusive (peak) sample and high mass slices, which pass the nominal events selection described in Section 5.1. On the left, the positive muon charge is shown and, on the right, the negative one. In the upper row, the events are not weighted (in particular, no MC weight) to see the pure number of generated events, whereas, in the lower row, the number of weighted events is shown. Due to the substantially larger MC weight (which is essentially the cross-section, see Tables A.1/A.2) few events from the peak sample have a substantial impact in the high-mass tail above a few hundred GeV.
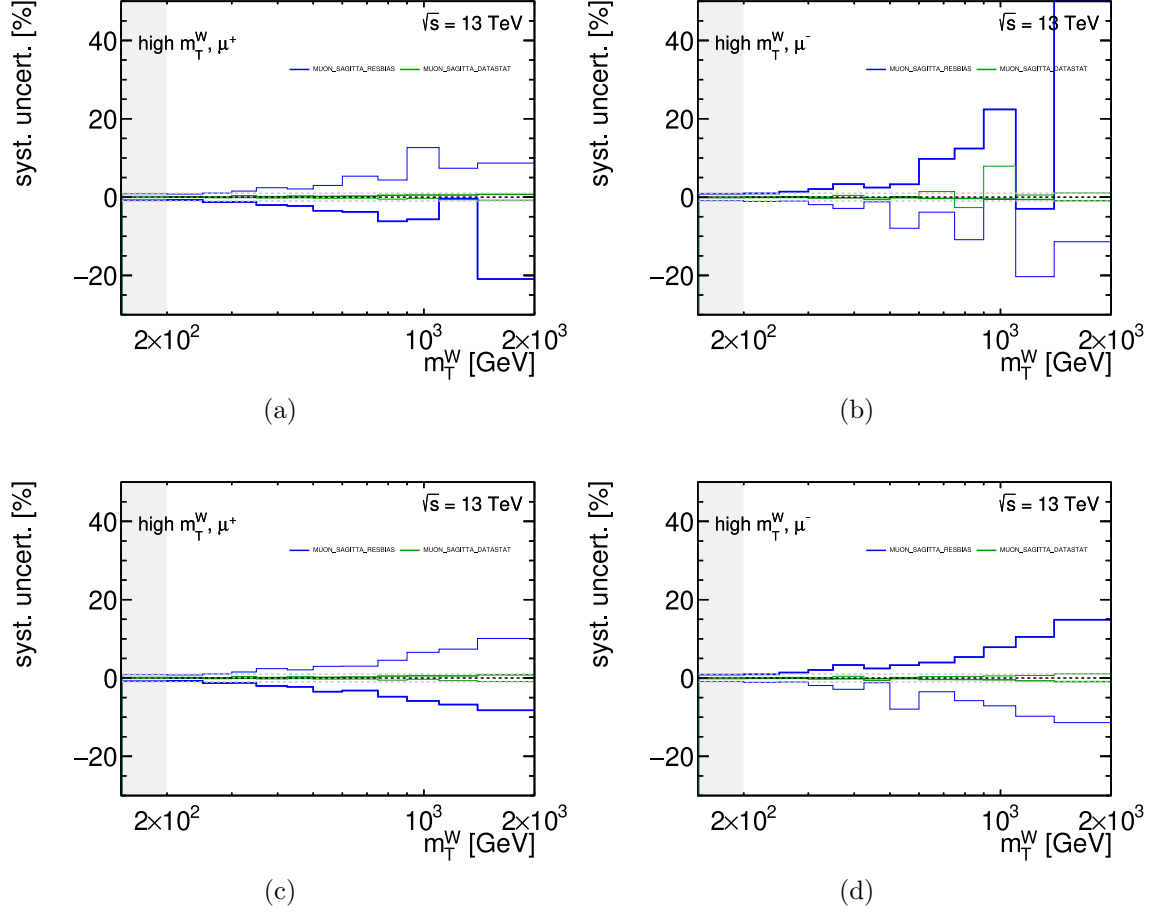
Figure F.17.: Preliminary systematic uncertainty associated with the muon sagitta-bias correction shown in percent with respect to the nominal signal prediction for μ^+ (left-hand side) and μ^- (right-hand side). No smoothing is applied here. In the upper row, the full signal sample is considered, while, in the lower row, all events with $m_{\mathrm{inv}} < 120\,\mathrm{GeV}$ (=inclusive sample) and $m_{\mathrm{T}}^{\mathrm{W}}(\mathrm{reco}) > 600\,\mathrm{GeV}$ are removed which are $\mathcal{O}(20)$ events per charge.

F.6. Small uncertainties
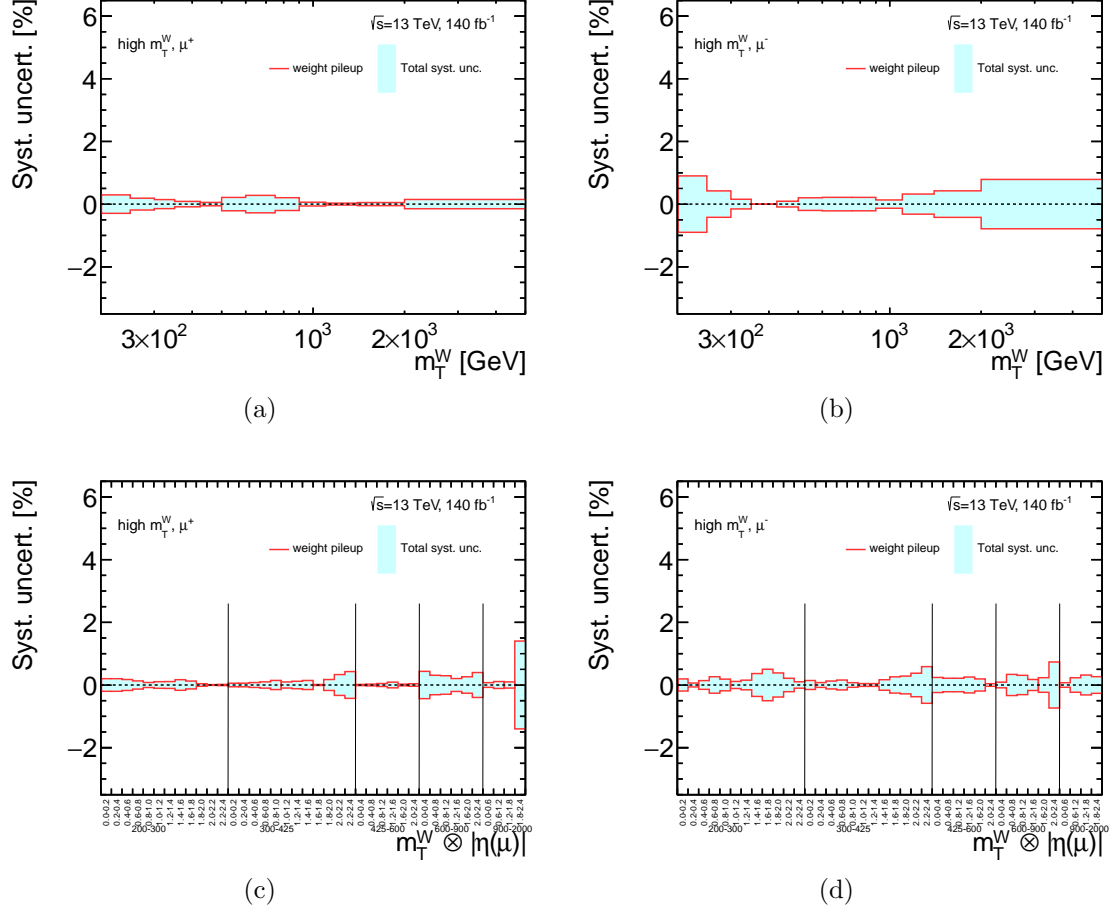
Figure F.18.: Pile-up systematic uncertainty on the unfolded cross-sections.
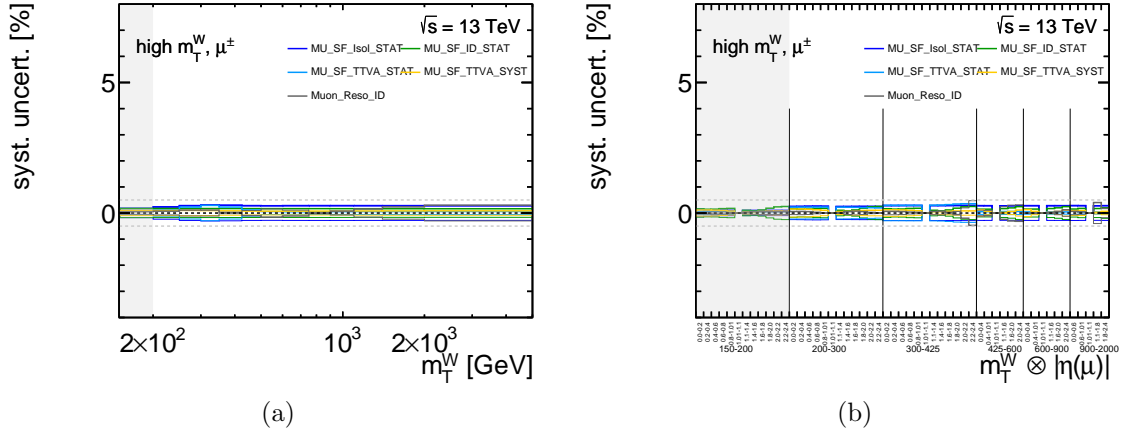
Figure F.19.: Systematic uncertainties in the $\mu^{\pm}$-channel as a function of (a) $m_{\mathrm{T}}^{\mathrm{W}}$ and (b) $m_{\mathrm{T}}^{\mathrm{W}} \otimes |\eta(\mu)|$ with respect to the nominal signal prediction. Only the muon-related uncertainties that do not pass the 0.5 % threshold are shown.

(a)

(b)

(c)

(d)
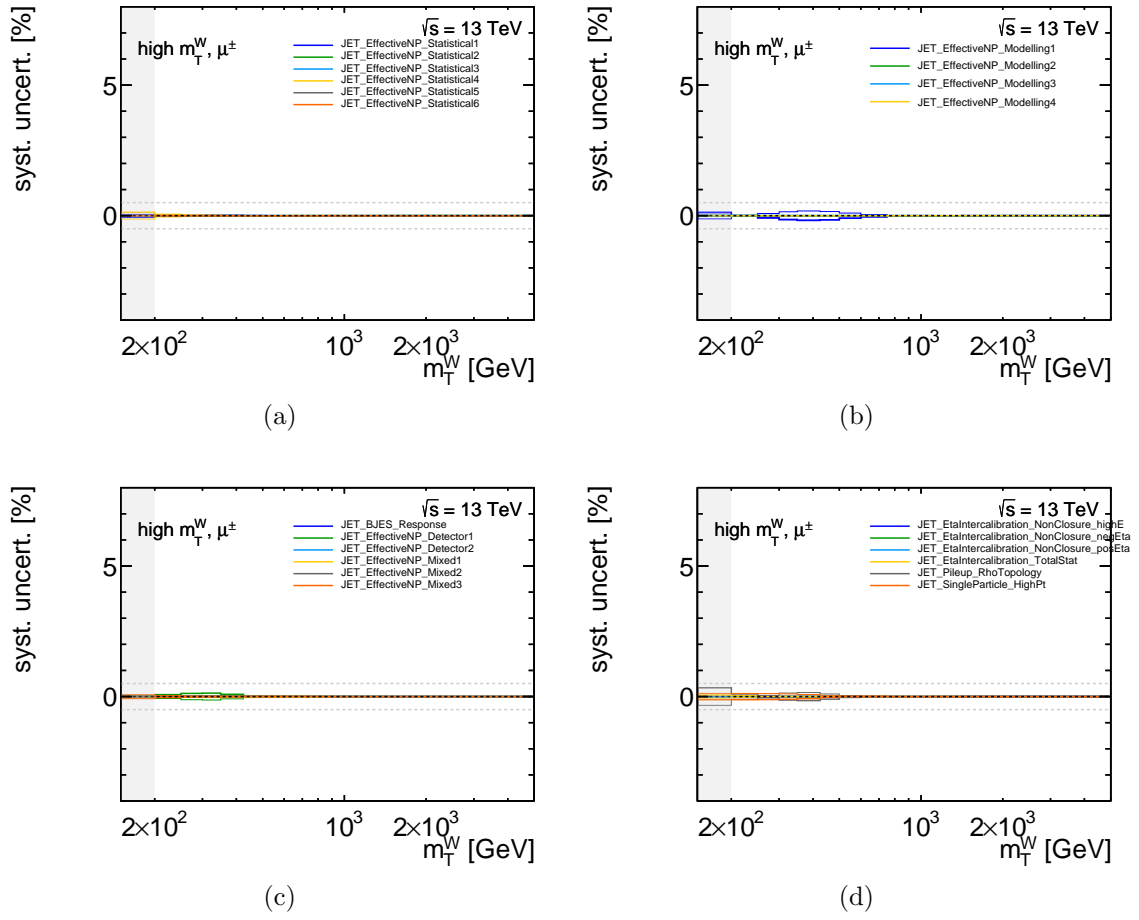
Figure F.20.: JES uncertainties in the $\mu^{\pm}$-channel as a function of $m_{\mathrm{T}}^{\mathrm{W}}$ with respect to the nominal signal prediction.
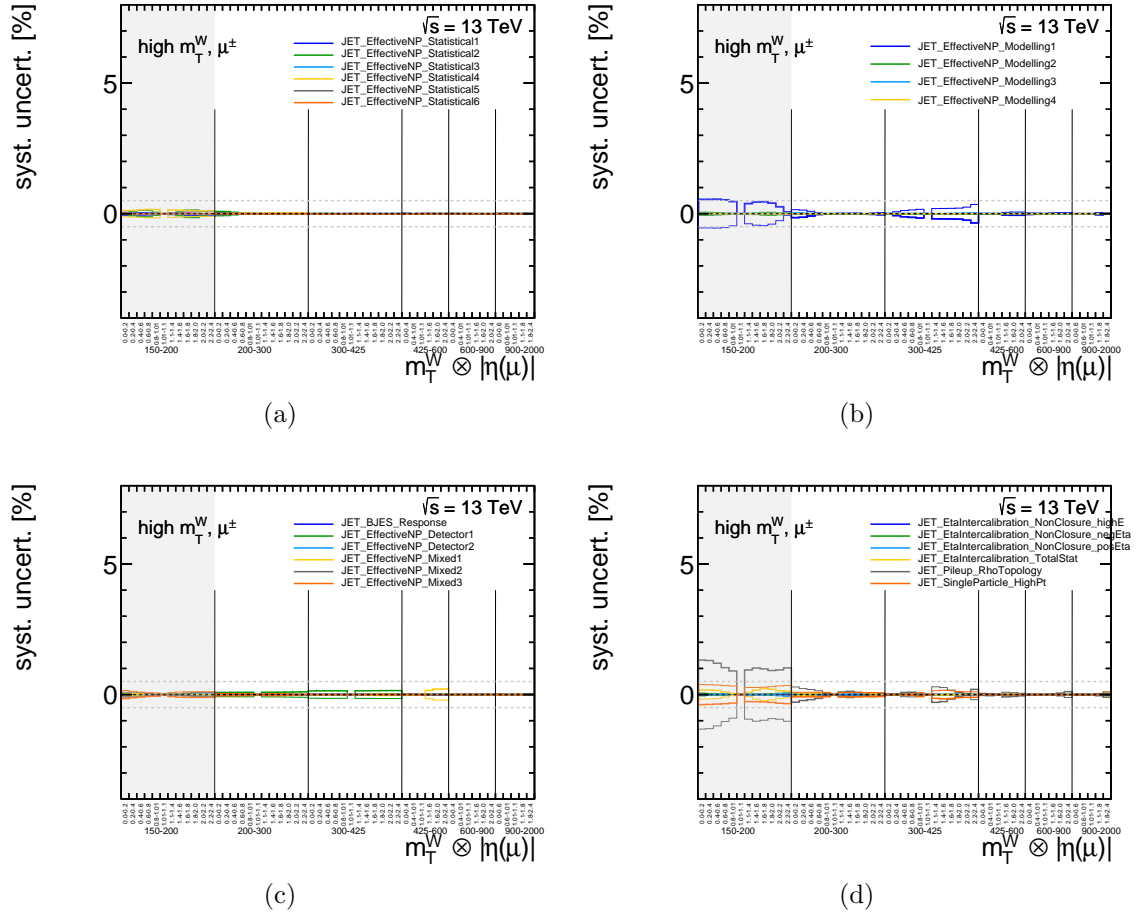
Figure F.21.: JES uncertainties in the $\mu^\pm$-channel as a function of $m_\mathrm{T}^\mathrm{W} \otimes |\eta(\mu)|$ with respect to the nominal signal prediction.

G. $W^{\pm}$ combined cross-sections
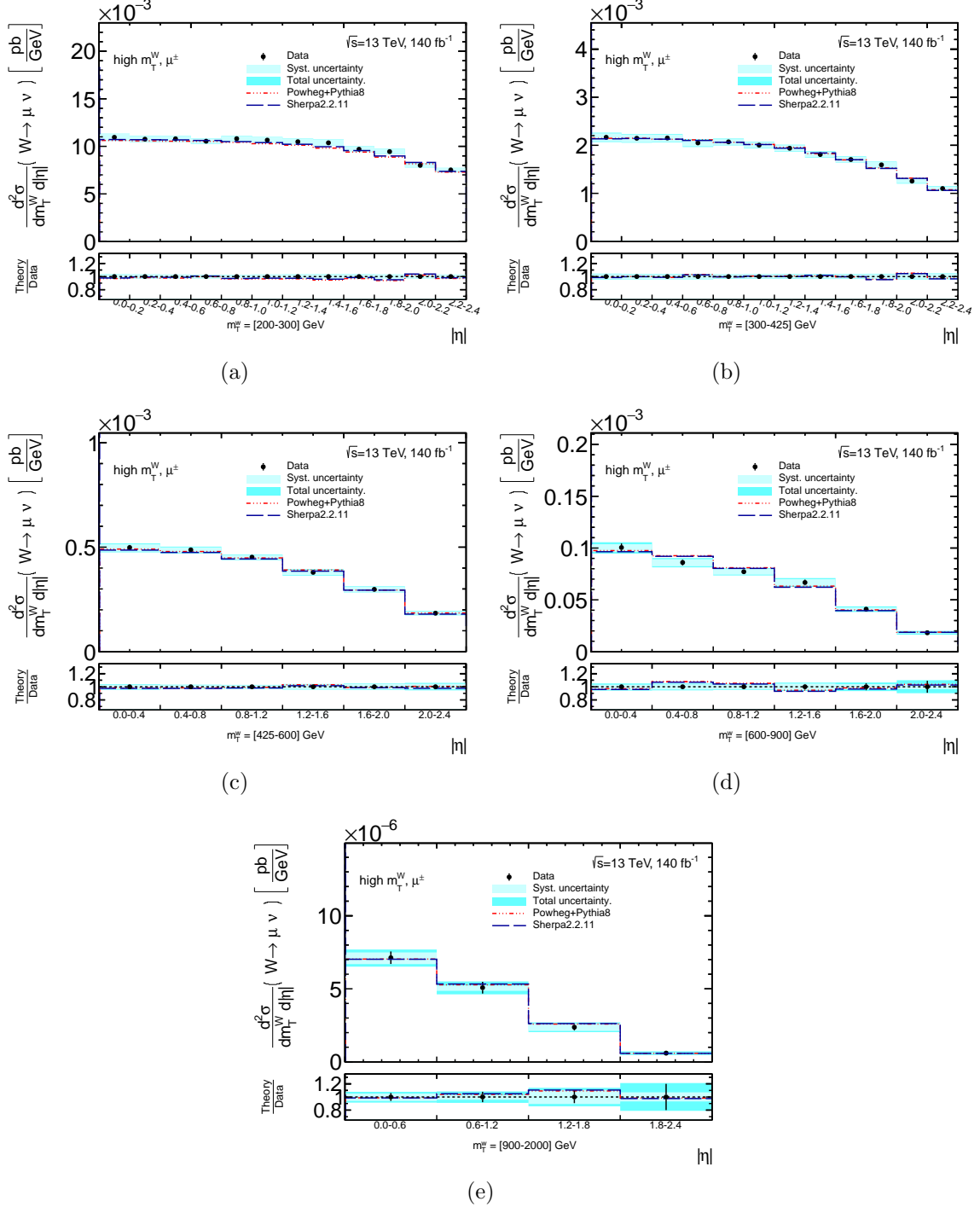
Figure G.1.: Born-level cross-sections for $W \to \mu\nu$ (charge-combined) double-differential in $m_{\mathrm{T}}^{\mathrm{W}}$ and $|\eta(\mu)|$. The statistical uncertainty is represented by error bars while the systematic and total uncertainties are shown in the uncertainty band. A comparison to predictions from the POWHEG+PYTHIA and SHERPA MC samples is included.
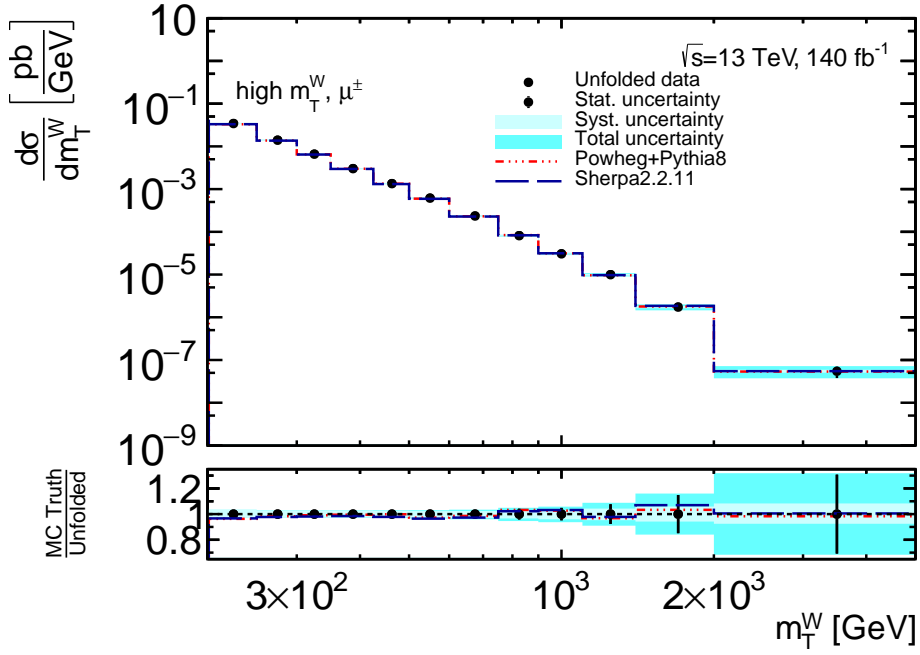
(a)
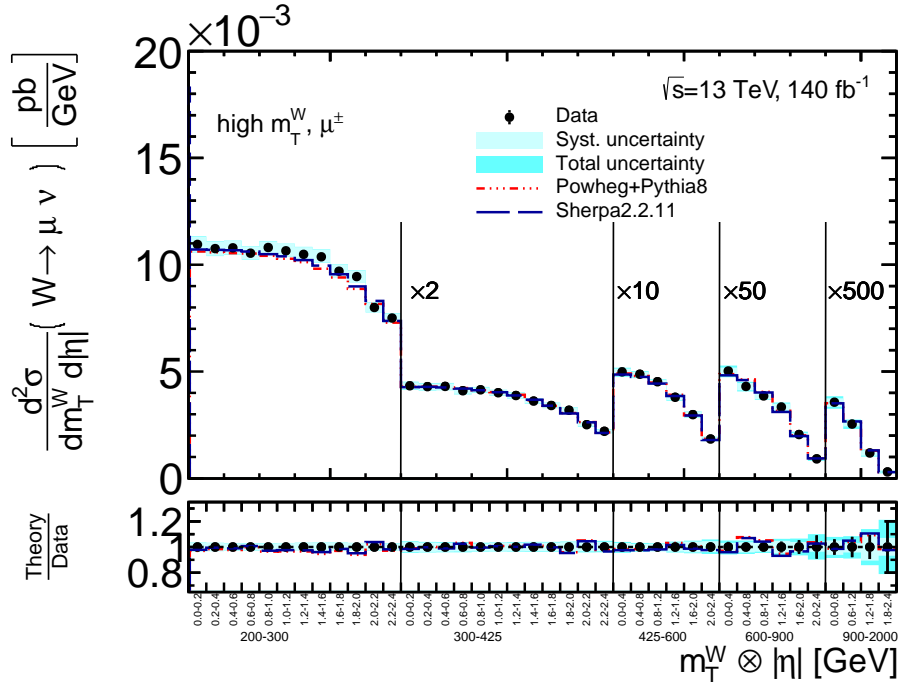
(b)

Figure G.2.: Born-level cross-sections (a) single-differential in m_T^W and (b) double-differential in m_T^W and $|\eta(\mu)|$ for $W \to \mu\nu$ (charge-combined). The statistical uncertainty is represented by error bars while the systematic and total uncertainties are shown in the uncertainty band. In (b), the cross-sections for the last four m_T^W bins are scaled up for better visibility. A comparison to predictions from the POWHEG+PYTHIA and SHERPA MC samples is included.

Table G.1.: Born-level single-differential cross-section $\frac{d\sigma(W\to\mu\nu)}{dm_{\mathrm{T}}^{\mathrm{W}}}$ including statistical and systematic uncertainties in percent. The upper (lower) row corresponds to the one standard deviation upward (downward) shift of the uncertainty source.

$m_{\mathrm{T}}^{\mathrm{W}}$ [GeV]	200 - 250	250 - 300	300 - 350	350 - 425	425 - 500	500 - 600	600 - 750	750 - 900	900 - 1100	1100 - 1400	1400 - 2000	2000 - 5000
σ [pb/GeV]	3.42e-02	1.39e-02	6.57e-03	3.01e-03	1.34e-03	6.14e-04	2.34e-04	8.12e-05	3.05e-05	9.92e-06	1.73e-06	5.45e-08
Data stat. unc.	0.33	0.51	0.69	0.86	1.21	1.49	2.00	3.10	4.35	6.16	10.77	29.20
Sig. stat. unc.	0.26	0.32	0.42	0.53	0.89	1.19	1.49	2.83	2.06	4.53	10.15	2.27
Bkg. stat. unc.	0.08	0.40	0.18	0.21	0.26	0.28	0.35	0.43	0.62	0.80	1.55	9.40
Tot. sys. unc.	3.36 -2.84	2.88 -2.85	2.91 -2.89	2.79 -2.76	2.56 -2.58	2.33 -2.83	2.35 -3.17	2.56 -3.40	3.18 -4.03	4.30 -4.73	5.90 -5.81	8.30 -7.53
Alt. MC unf. unc.	1.21	0.47	0.38	0.15	-0.53	-1.62	-2.16	-2.34	-2.71	-2.89	-2.90	-2.90
Basic unf. unc.	0.01	0.04	0.05	0.05	0.06	0.09	0.21	0.57	1.13	1.72	2.45	3.47
JES Flavor Composition	0.03 -0.03	0.41 -0.41	0.47 -0.46	0.40 -0.40	0.31 -0.31	0.21 -0.21	0.10 -0.10	0.04 -0.04	-0.02 0.02	-0.01 0.01	0.02 -0.02	-0.00 0.00
JES Pileup RhoTopology	-0.02 0.02	0.19 -0.19	0.27 -0.27	0.25 -0.25	0.15 -0.15	0.06 -0.06	0.02 -0.02	0.00 -0.00	-0.01 0.01	-0.00 0.00	0.01 -0.01	-0.01 0.01
JES Pileup OffsetMu	-0.45 0.46	-0.16 0.16	-0.10 0.10	-0.10 0.10	-0.06 0.06	-0.03 0.03	-0.03 0.03	-0.03 0.03	-0.06 0.06	-0.05 0.05	-0.02 0.02	-0.06 0.06
JES Pileup OffsetNPV	-0.17 0.17	-0.08 0.08	-0.03 0.03	-0.00 0.00	0.02 -0.02	0.04 -0.04	0.04 -0.04	0.01 -0.01	-0.02 0.02	-0.02 0.02	-0.01 0.01	-0.03 0.03
JES EtaIntercalib Model	-0.15 0.15	0.03 -0.03	0.09 -0.09	0.09 -0.09	0.07 -0.07	0.04 -0.04	0.02 -0.02	0.01 -0.01	-0.02 0.02	-0.02 0.02	-0.00 0.00	-0.03 0.03
JES Flavor Response	-0.20 0.20	-0.39 0.39	-0.47 0.48	-0.49 0.49	-0.41 0.41	-0.27 0.27	-0.09 0.09	0.03 -0.03	0.06 -0.06	0.01 -0.01	-0.03 0.03	-0.03 0.03
JER EffectiveNP 1	-1.13 1.15	-0.64 0.65	-0.39 0.39	-0.32 0.32	-0.26 0.27	-0.13 0.13	-0.07 0.07	-0.05 0.05	-0.11 0.11	-0.10 0.10	-0.05 0.05	-0.15 0.15
JER EffectiveNP 2	-0.64 0.65	-0.40 0.40	-0.22 0.23	-0.14 0.14	-0.11 0.11	-0.07 0.07	-0.05 0.05	-0.04 0.04	-0.07 0.07	-0.07 0.07	-0.05 0.05	-0.10 0.10
JER EffectiveNP 3	-0.22 0.22	-0.16 0.16	-0.12 0.12	-0.09 0.09	-0.06 0.06	-0.01 0.01	0.01 -0.01	0.01 -0.01	-0.03 0.02	-0.03 0.03	-0.01 0.01	-0.03 0.03
JER EffectiveNP 4	-0.26 0.26	-0.20 0.20	-0.13 0.13	-0.07 0.07	-0.03 0.03	-0.01 0.01	-0.03 0.03	-0.03 0.03	-0.02 0.02	-0.00 0.00	0.01 -0.01	-0.01 0.01
JER EffectiveNP 5	-0.26 0.27	-0.25 0.25	-0.18 0.18	-0.06 0.06	0.03 -0.03	0.07 -0.07	0.05 -0.05	0.00 -0.00	-0.03 0.03	-0.03 0.03	-0.01 0.01	-0.03 0.03
JER EffectiveNP 6	-0.31 0.31	-0.18 0.18	-0.10 0.10	-0.06 0.06	-0.07 0.07	-0.06 0.06	-0.06 0.06	-0.05 0.05	-0.05 0.05	-0.04 0.04	-0.02 0.02	-0.05 0.05
JER EffectiveNP 7rest	-0.26 0.27	-0.14 0.14	-0.12 0.12	-0.12 0.12	-0.11 0.11	-0.07 0.07	-0.04 0.04	-0.01 0.01	-0.02 0.02	-0.01 0.01	-0.00 0.00	-0.03 0.03
JER DataVsMC MC16	-0.30 0.30	-0.23 0.23	-0.12 0.12	-0.05 0.05	-0.03 0.03	-0.01 0.01	-0.00 0.00	-0.02 0.02	-0.04 0.04	-0.04 0.04	-0.03 0.03	-0.05 0.05
$E_{\mathrm{T}}^{\mathrm{miss}}$ SoftTrk Scale	1.31 -1.28	0.72 -0.71	0.51 -0.50	0.43 -0.42	0.31 -0.31	0.17 -0.17	0.11 -0.11	0.08 -0.08	0.18 -0.18	0.18 -0.18	0.12 -0.12	0.22 -0.22
$E_{\mathrm{T}}^{\mathrm{miss}}$ SoftTrk ResoPara	0.96	0.35	0.01	0.43	0.41	0.12	0.08	0.17	0.19	0.24	0.15	0.21
$E_{\mathrm{T}}^{\mathrm{miss}}$ SoftTrk ResoPerp	1.04	0.54	0.45	0.38	0.33	0.10	0.10	0.16	0.16	0.27	0.23	0.23
Muon Resolution MS	-0.11 0.11	-0.18 0.18	-0.30 0.30	-0.37 0.37	-0.33 0.33	-0.27 0.27	-0.29 0.29	-0.41 0.41	-0.58 0.58	-0.91 0.92	-1.57 1.62	-2.63 2.77
Muon Scale	0.54 -0.53	0.56 -0.56	0.55 -0.54	0.51 -0.50	0.45 -0.45	0.42 -0.42	0.42 -0.42	0.41 -0.41	0.40 -0.40	0.39 -0.39	0.39 -0.38	0.39 -0.38
Muon SF Identification Syst	-0.92 0.93	-1.30 1.33	-1.48 1.52	-1.46 1.51	-1.38 1.42	-1.41 1.45	-1.56 1.61	-1.79 1.86	-2.19 2.29	-2.94 3.13	-3.70 3.99	-4.30 4.70
Muon SF Isolation Syst	-0.25 0.25	-0.37 0.37	-0.55 0.55	-0.66 0.66	-0.65 0.65	-0.60 0.61	-0.57 0.58	-0.56 0.56	-0.53 0.54	-0.53 0.53	-0.52 0.53	-0.50 0.51
Muon SF Trigger Syst	0.74 -0.73	0.76 -0.75	0.74 -0.73	0.70 -0.69	0.66 -0.65	0.63 -0.62	0.62 -0.61	0.60 -0.59	0.60 -0.59	0.60 -0.59	0.59 -0.59	0.61 -0.60
Bad Muon	-0.21 0.21	-0.09 0.09	-0.05 0.05	-0.06 0.06	-0.09 0.09	-0.10 0.10	-0.10 0.10	-0.11 0.11	-0.14 0.14	-0.25 0.25	-0.54 0.54	-1.11 1.13
Muon Sagitta Global	0.10 -0.10	0.11 -0.11	0.16 -0.16	0.19 -0.19	0.27 -0.27	0.41 -0.41	0.61 -0.61	0.83 -0.82	1.18 -1.15	1.72 -1.66	2.87 -2.71	4.85 -4.43
Muon Sagitta p_{T}-extra	0.06 -0.06	-0.02 0.02	-0.00 0.00	0.14 -0.14	0.37 -0.36	0.47 -0.47	0.53 -0.52	0.55 -0.55	0.63 -0.62	0.71 -0.70	0.79 -0.77	0.92 -0.90
Pile-up	-0.35 0.35	-0.22 0.22	-0.18 0.18	-0.11 0.11	0.01 -0.01	0.13 -0.13	0.17 -0.17	0.15 -0.15	0.08 -0.08	0.08 -0.08	0.12 -0.12	0.10 -0.10
Multijet $E_{\mathrm{T}}^{\mathrm{miss}}$	-0.41 0.06	-0.61 0.07	-0.58 0.06	-0.49 0.04	-0.34 0.03	-0.17 0.01	-0.11 0.01	-0.05 0.00	-0.02 0.00	-0.02 0.00	0.01 -0.00	0.10 -0.01
Multijet d_0^{sig}	0.22 -0.37	0.31 -0.60	0.30 -0.63	0.27 -0.58	0.20 -0.46	0.11 -0.27	0.07 -0.18	0.03 -0.08	0.02 -0.04	0.03 -0.08	-0.00 0.01	-0.06 0.15
Multijet MC Scaling	0.49 -0.49	0.68 -0.68	0.65 -0.65	0.58 -0.58	0.47 -0.47	0.30 -0.30	0.22 -0.22	0.10 -0.10	0.06 -0.06	0.12 -0.12	-0.01 0.01	-0.14 0.14
Multijet Jet Mult	-0.43 0.33	-0.48 0.35	-0.43 0.32	-0.38 0.27	-0.31 0.20	-0.21 0.10	-0.12 0.08	-0.07 0.03	-0.07 0.02	-0.07 -0.01	0.00 -0.01	0.06 -0.03
Multijet MC Shape	0.28	0.40	0.36	0.28	0.20	0.06	0.04	-0.02	0.00	-0.08	-0.02	-0.04
Multijet $\Delta\phi(\mu, E_{\mathrm{T}}^{\mathrm{miss}})$	-0.47 0.28	-0.66 0.43	-0.63 0.42	-0.57 0.37	-0.45 0.33	-0.30 0.20	-0.20 0.10	-0.12 0.03	-0.06 0.07	-0.07 0.04	0.01 -0.01	0.13 -0.09
$t\bar{t}$ p_{T}-hard	-0.02 0.00	-0.02 0.00	-0.03 0.00	-0.06 0.00	-0.09 0.00	-0.08 0.00	-0.06 0.00	-0.03 0.00	-0.02 0.00	-0.01 0.00	-0.01 0.00	-0.01 0.00
$t\bar{t}$ FSR	0.25 -0.25	0.31 -0.31	0.32 -0.32	0.33 -0.33	0.33 -0.33	0.28 -0.28	0.22 -0.22	0.15 -0.15	0.10 -0.10	0.07 -0.07	0.03 -0.03	0.05 -0.05
$t\bar{t}$ scales $\mu_R\,\mu_F$	-0.36 0.46	-0.63 0.83	-0.73 0.96	-0.71 0.91	-0.66 0.91	-0.58 0.91	-0.48 0.81	-0.34 0.57	-0.20 0.33	-0.13 0.22	-0.06 0.10	-0.09 0.14
$t\bar{t}$ hadronization	0.06 0.00	0.49 0.00	0.72 0.00	0.72 0.00	0.64 0.00	0.53 0.00	0.40 0.00	0.26 0.00	0.14 0.00	0.09 0.00	0.04 0.00	0.04 0.00
$t\bar{t}$ hdamp	-0.12 0.00	-0.08 0.00	-0.01 0.00	-0.01 0.00	-0.08 0.00	-0.16 0.00	-0.21 0.00	-0.17 0.00	-0.11 0.00	-0.07 0.00	-0.03 0.00	-0.05 0.00
$t\bar{t}$ PDF	-0.64 0.64	-0.73 0.73	-0.70 0.70	-0.62 0.62	-0.48 0.48	-0.36 0.36	-0.31 0.31	-0.25 0.25	-0.18 0.18	-0.13 0.13	-0.09 0.09	-0.23 0.23
tW DR	-0.32	-0.57	-0.73	-0.76	-0.83	-0.84	-0.73	-0.64	-0.96	-0.39	-0.11	0.38
tW DS hdamp	-0.03	0.00	0.07	0.10	0.09	0.05	-0.00	0.12	0.49	0.34	0.18	-0.34
Norm. $W\to\tau\nu$ by 5%	-0.08 0.08	-0.08 0.08	-0.07 0.07	-0.08 0.08	-0.07 0.07	-0.07 0.07	-0.06 0.06	-0.06 0.06	-0.06 0.06	-0.04 0.04	-0.04 0.04	-0.03 0.03
Norm. Single top by 4%	-0.16 0.16	-0.18 0.18	-0.18 0.18	-0.15 0.15	-0.13 0.13	-0.09 0.09	-0.07 0.07	-0.04 0.04	-0.05 0.05	-0.02 0.02	-0.00 0.00	0.01 -0.01
Norm. Diboson by 6%	-0.24 0.24	-0.26 0.26	-0.29 0.29	-0.29 0.29	-0.28 0.28	-0.25 0.25	-0.24 0.24	-0.23 0.23	-0.24 0.24	-0.19 0.19	-0.28 0.28	-0.21 0.21
Norm. $Z\to\ell\ell$ by 5%	-0.58 0.58	-0.59 0.59	-0.56 0.56	-0.51 0.51	-0.46 0.46	-0.37 0.37	-0.31 0.31	-0.27 0.27	-0.27 0.27	-0.29 0.29	-0.26 0.26	-0.28 0.28

Table G.2.: Born-level double-differential cross-section $\frac{d^2\sigma(W\to\mu\nu)}{dm_{\mathrm{T}}^{\mathrm{W}}\,d|\eta(\mu)|}$ including statistical and systematic uncertainties in percent for $m_{\mathrm{T}}^{\mathrm{W}} = [200 - 300]$ GeV. The upper (lower) row corresponds to the one standard deviation upward (downward) shift of the uncertainty source.

$\|\eta(\mu)\|$	0.0 - 0.2	0.2 - 0.4	0.4 - 0.6	0.6 - 0.8	0.8 - 1.0	1.0 - 1.2	1.2 - 1.4	1.4 - 1.6	1.6 - 1.8	1.8 - 2.0	2.0 - 2.2	2.2 - 2.4
σ [pb/GeV]	1.10e-02	1.08e-02	1.08e-02	1.05e-02	1.08e-02	1.07e-02	1.05e-02	1.04e-02	9.70e-03	9.45e-03	8.00e-03	7.51e-03
Data stat. unc.	1.20	1.00	1.01	1.11	0.98	0.85	0.93	0.89	0.90	0.96	1.15	1.14
Sig. stat. unc.	0.84	0.75	0.71	0.72	0.74	0.75	0.80	0.70	0.59	0.70	0.87	0.71
Bkg. stat. unc.	0.30	0.23	0.23	0.25	0.22	0.22	0.24	0.20	0.21	0.21	0.24	0.24
Tot. sys. unc.	3.31 -3.17	3.19 -3.05	3.01 -2.82	2.80 -2.55	2.62 -2.29	2.97 -2.31	3.16 -2.35	3.29 -2.51	3.30 -2.73	3.00 -2.62	2.83 -2.47	2.79 -2.36
Alt. MC unf. unc.	0.13	0.25	0.48	0.60	0.85	1.34	1.59	1.59	1.49	1.30	1.20	1.20
Basic unf. unc.	0.51	0.51	0.51	0.51	0.51	0.57	0.68	0.75	0.77	0.79	0.77	0.70
JES Flavor Composition	0.56 -0.56	0.56 -0.55	0.53 -0.52	0.48 -0.48	0.44 -0.43	0.38 -0.38	0.37 -0.37	0.34 -0.34	0.27 -0.27	0.22 -0.22	0.14 -0.14	0.10 -0.10
JES Pileup RhoTopology	0.64 -0.63	0.54 -0.54	0.47 -0.46	0.38 -0.38	0.23 -0.23	0.07 -0.07	0.05 -0.05	0.03 -0.03	0.08 -0.08	0.19 -0.19	0.25 -0.25	0.21 -0.21
JES Pileup OffsetMu	-0.38 0.38	-0.35 0.35	-0.23 0.23	-0.13 0.13	-0.15 0.15	-0.23 0.23	-0.24 0.24	-0.22 0.22	-0.16 0.16	-0.11 0.11	-0.09 0.08	-0.07 0.07
JES Pileup OffsetNPV	-0.02 0.02	0.03 -0.03	0.09 -0.09	0.11 -0.11	0.06 -0.06	-0.03 0.03	-0.04 0.04	-0.10 0.10	-0.15 0.15	-0.12 0.12	-0.07 0.07	-0.08 0.08
JES EtaIntercalib Model	-0.07 0.07	-0.06 0.06	0.02 -0.02	0.09 -0.09	0.10 -0.10	0.04 -0.04	0.04 -0.04	0.05 -0.05	0.07 -0.07	0.11 -0.11	0.13 -0.13	0.14 -0.14
JES Flavor Response	-0.76 0.78	-0.70 0.71	-0.61 0.61	-0.45 0.46	-0.29 0.29	-0.18 0.18	-0.17 0.17	-0.18 0.18	-0.20 0.20	-0.26 0.26	-0.34 0.34	-0.45 0.45
JER EffectiveNP 1	-0.46 0.46	-0.46 0.46	-0.42 0.42	-0.31 0.31	-0.22 0.22	-0.25 0.25	-0.26 0.25	-0.31 0.31	-0.39 0.39	-0.39 0.39	-0.37 0.36	-0.34 0.33
JER EffectiveNP 2	-0.51 0.52	-0.44 0.44	-0.23 0.24	0.09 -0.09	0.21 -0.21	-0.46 0.46	-0.53 0.53	-0.67 0.68	-0.65 0.65	-0.54 0.55	-0.37 0.37	-0.28 0.28
JER EffectiveNP 3	-0.02 0.02	-0.00 0.00	0.01 -0.01	0.03 -0.03	0.05 -0.05	-0.02 0.02	-0.03 0.03	-0.24 0.25	-0.38 0.38	-0.26 0.26	-0.05 0.05	0.04 -0.04
JER EffectiveNP 4	0.32 -0.32	0.30 -0.30	0.24 -0.24	0.14 -0.14	0.11 -0.11	-0.21 0.21	-0.24 0.24	-0.40 0.41	-0.44 0.45	-0.40 0.41	-0.26 0.26	-0.03 0.03
JER EffectiveNP 5	-0.08 0.08	-0.03 0.03	0.03 -0.03	0.11 -0.11	0.14 -0.14	-0.07 0.07	-0.09 0.09	-0.22 0.23	-0.28 0.28	-0.23 0.23	-0.14 0.14	-0.10 0.10
JER EffectiveNP 6	-0.28 0.28	-0.27 0.27	-0.19 0.19	-0.03 0.03	0.06 -0.06	-0.10 0.10	-0.12 0.12	-0.13 0.13	-0.12 0.12	-0.04 0.04	0.14 -0.14	0.27 -0.27
JER EffectiveNP 7rest	0.01 -0.01	0.04 -0.04	0.05 -0.05	0.05 -0.05	0.07 -0.07	-0.10 0.10	-0.12 0.12	-0.27 0.27	-0.31 0.31	-0.17 0.17	0.06 -0.06	0.21 -0.21
JER DataVsMC MC16	0.17 -0.17	0.05 -0.05	-0.01 0.01	-0.00 -0.00	0.03 -0.03	-0.26 0.26	-0.29 0.29	-0.46 0.47	-0.44 0.44	-0.33 0.33	-0.27 0.28	-0.28 0.28
$E_{\mathrm{T}}^{\mathrm{miss}}$ SoftTrk Scale	1.00 -0.98	0.96 -0.95	0.91 -0.90	0.82 -0.82	0.68 -0.68	0.60 -0.60	0.60 -0.60	0.73 -0.72	0.84 -0.83	0.77 -0.77	0.61 -0.61	0.46 -0.46
$E_{\mathrm{T}}^{\mathrm{miss}}$ SoftTrk ResoPara	0.84	0.75	0.69	0.64	0.62	0.74	0.76	0.79	0.74	0.62	0.54	0.49
$E_{\mathrm{T}}^{\mathrm{miss}}$ SoftTrk ResoPerp	0.67	0.68	0.72	0.75	0.72	0.77	0.78	0.87	0.92	0.82	0.68	0.60
Muon Resolution MS	0.01 -0.01	0.02 -0.02	0.01 -0.01	-0.04 0.04	-0.07 0.07	-0.13 0.13	-0.14 0.14	-0.17 0.17	-0.17 0.17	-0.16 0.16	-0.14 0.14	-0.13 0.13
Muon Scale	0.15 -0.15	0.16 -0.16	0.19 -0.19	0.22 -0.22	0.31 -0.31	0.71 -0.70	0.76 -0.75	0.82 -0.81	0.76 -0.75	0.61 -0.60	0.48 -0.47	0.43 -0.43
Muon SF Identification Syst	-1.25 1.28	-1.20 1.23	-1.15 1.18	-1.11 1.13	-1.08 1.10	-1.03 1.05	-1.03 1.05	-1.01 1.03	-0.99 1.01	-1.00 1.02	-1.02 1.04	-1.04 1.07
Muon SF Isolation Syst	-0.32 0.32	-0.32 0.32	-0.31 0.31	-0.30 0.30	-0.29 0.29	-0.27 0.27	-0.27 0.27	-0.25 0.25	-0.24 0.24	-0.22 0.23	-0.21 0.21	-0.20 0.20
Muon SF Trigger Syst	0.99 -0.97	0.98 -0.96	0.97 -0.95	0.93 -0.91	0.83 -0.82	0.67 -0.66	0.65 -0.65	0.63 -0.62	0.59 -0.59	0.56 -0.56	0.54 -0.53	0.52 -0.51
Bad Muon	-0.12 0.12	-0.12 0.12	-0.12 0.12	-0.11 0.12	-0.11 0.11	-0.13 0.13	-0.13 0.13	-0.15 0.15	-0.15 0.15	-0.16 0.16	-0.19 0.19	-0.20 0.20
Muon Sagitta Global	0.09 -0.09	0.10 -0.10	0.08 -0.08	0.04 -0.04	0.03 -0.03	0.05 -0.05	0.05 -0.05	0.07 -0.07	0.08 -0.08	0.08 -0.08	0.07 -0.07	0.06 -0.06
Muon Sagitta p_{T}-extra	-0.02 0.02	-0.02 0.02	-0.02 0.02	-0.02 0.02	-0.02 0.02	0.01 -0.01	0.01 -0.01	0.06 -0.06	0.10 -0.10	0.14 -0.14	0.16 -0.16	0.16 -0.16
Pile-up	-0.34 0.34	-0.20 0.20	-0.04 0.03	0.08 -0.08	0.07 -0.07	-0.23 0.23	-0.27 0.27	-0.27 0.27	-0.14 0.14	-0.05 0.05	-0.06 0.06	-0.07 0.07
Multijet $E_{\mathrm{T}}^{\mathrm{miss}}$	-0.42 0.11	-0.41 0.11	-0.37 0.10	-0.29 0.08	-0.25 0.07	-0.47 0.11	-0.50 0.11	-0.57 0.09	-0.79 0.05	-0.79 0.01	-0.63 0.00	-0.42 0.00
Multijet d_0^{sig}	0.16 -0.40	0.16 -0.40	0.15 -0.38	0.13 -0.32	0.11 -0.23	0.37 -0.23	0.40 -0.23	0.46 -0.40	0.41 -0.68	0.25 -0.71	0.17 -0.56	0.11 -0.37
Multijet MC Scaling	0.85 -0.85	0.84 -0.84	0.77 -0.77	0.65 -0.65	0.54 -0.54	0.56 -0.56	0.57 -0.57	0.49 -0.49	0.49 -0.49	0.38 -0.38	0.27 -0.27	0.18 -0.18
Multijet Jet Mult	-0.70 0.36	-0.69 0.34	-0.63 0.32	-0.54 0.26	-0.47 0.23	-0.24 0.53	-0.22 0.56	-0.18 0.49	-0.42 0.39	-0.51 0.25	-0.39 0.17	-0.23 0.11
Multijet MC Shape	0.11	0.10	0.10	0.07	0.06	0.50	0.55	0.49	0.62	0.56	0.41	0.28
Multijet $\Delta\phi(\mu, E_{\mathrm{T}}^{\mathrm{miss}})$	-0.57 0.37	-0.57 0.38	-0.51 0.34	-0.44 0.29	-0.38 0.24	-0.58 0.43	-0.60 0.45	-0.51 0.36	-0.67 0.41	-0.66 0.31	-0.52 0.23	-0.32 0.15
$t\bar{t}$ p_{T}-hard	-0.12 0.00	-0.13 0.00	-0.13 0.00	-0.10 0.00	-0.05 0.00	0.08 0.00	0.09 0.00	0.09 0.00	0.01 0.00	-0.08 0.00	-0.10 0.00	-0.08 0.00
$t\bar{t}$ FSR	0.40 -0.40	0.40 -0.40	0.37 -0.37	0.36 -0.36	0.32 -0.32	0.29 -0.29	0.28 -0.28	0.26 -0.26	0.23 -0.23	0.19 -0.19	0.15 -0.15	0.11 -0.11
$t\bar{t}$ scales $\mu_R\,\mu_F$	-0.72 1.02	-0.72 1.03	-0.68 0.96	-0.64 0.87	-0.57 0.74	-0.44 0.53	-0.43 0.50	-0.36 0.41	-0.30 0.35	-0.23 0.26	-0.17 0.18	-0.11 0.09
$t\bar{t}$ hadronization	0.37 0.00	0.36 0.00	0.34 0.00	0.33 0.00	0.25 0.00	0.09 0.00	0.08 0.00	0.05 0.00	-0.02 0.00	-0.10 0.00	-0.12 0.00	-0.08 0.00
$t\bar{t}$ hdamp	-0.17 0.00	-0.17 0.00	-0.14 0.00	-0.07 0.00	-0.01 0.00	0.02 0.00	0.02 0.00	-0.01 0.00	-0.08 0.00	-0.12 0.00	-0.12 0.00	-0.09 0.00
$t\bar{t}$ PDF	-0.94 0.94	-0.94 0.94	-0.88 0.88	-0.84 0.84	-0.76 0.76	-0.65 0.65	-0.64 0.64	-0.61 0.61	-0.63 0.63	-0.60 0.60	-0.65 0.65	-0.62 0.62
tW DR	-0.70	-0.67	-0.61	-0.55	-0.51	-0.45	-0.44	-0.35	-0.23	-0.11	-0.02	0.04
tW DS hdamp	0.03	0.03	0.02	0.01	0.00	0.00	0.00	0.00	0.01	0.05	0.11	0.18
Norm. $W \to \tau\nu$ by 5%	-0.09 0.09	-0.08 0.08	-0.08 0.08	-0.08 0.08	-0.08 0.08	-0.09 0.08	-0.09 0.09	-0.08 0.09	-0.08 0.08	-0.08 0.08	-0.07 0.07	-0.06 0.06
Norm. Single top by 4%	-0.26 0.26	-0.25 0.25	-0.24 0.24	-0.23 0.23	-0.20 0.20	-0.16 0.16	-0.15 0.15	-0.13 0.13	-0.11 0.11	-0.09 0.09	-0.07 0.07	-0.06 0.06
Norm. Diboson by 6%	-0.28 0.28	-0.28 0.28	-0.28 0.28	-0.29 0.29	-0.26 0.26	-0.19 0.19	-0.19 0.19	-0.24 0.24	-0.24 0.24	-0.23 0.23	-0.24 0.24	-0.23 0.23
Norm. $Z \to \ell\ell$ by 5%	-0.18 0.18	-0.20 0.20	-0.22 0.22	-0.26 0.26	-0.31 0.31	-0.48 0.48	-0.50 0.50	-0.62 0.62	-0.81 0.81	-0.95 0.95	-1.25 1.25	-1.42 1.42

Table G.3.: Born-level double-differential cross-section $\frac{d^2\sigma(W\to\mu\nu)}{dm_\mathrm{T}^\mathrm{W}\,d|\eta(\mu)|}$ including statistical and systematic uncertainties in percent for $m_\mathrm{T}^\mathrm{W} = [300-425]$ GeV. The upper (lower) row corresponds to the one standard deviation upward (downward) shift of the uncertainty source.

$|\eta(\mu)|$	0.0 - 0.2	0.2 - 0.4	0.4 - 0.6	0.6 - 0.8	0.8 - 1.0	1.0 - 1.2	1.2 - 1.4	1.4 - 1.6	1.6 - 1.8	1.8 - 2.0	2.0 - 2.2	2.2 - 2.4
σ [pb/GeV]	2.17e-03	2.15e-03	2.15e-03	2.05e-03	2.07e-03	2.00e-03	1.94e-03	1.81e-03	1.70e-03	1.59e-03	1.26e-03	1.10e-03
Data stat. unc.	2.35	1.98	2.01	2.27	1.95	1.74	1.89	1.83	1.91	2.03	2.56	2.67
Sig. stat. unc.	1.30	1.21	1.16	1.20	0.87	1.17	1.23	1.38	1.09	0.78	1.24	1.37
Bkg. stat. unc.	0.60	0.43	0.43	0.46	0.40	0.41	0.45	0.42	0.43	0.49	0.61	0.54
Tot. sys. unc.	3.94 / -3.80	3.66 / -3.76	3.37 / -3.56	3.13 / -3.39	2.79 / -2.97	2.99 / -2.81	3.19 / -2.82	3.36 / -2.93	3.37 / -2.93	3.68 / -3.15	3.86 / -3.09	3.77 / -2.83
Alt. MC unf. unc.	-0.67	-0.67	-0.67	-0.67	-0.34	0.36	0.86	1.11	1.57	2.20	2.50	2.50
Basic unf. unc.	-0.79	-0.70	-0.50	-0.28	-0.03	0.37	0.71	0.81	0.64	0.38	0.27	0.27
JES Flavor Composition	0.73 / -0.72	0.68 / -0.67	0.64 / -0.63	0.59 / -0.58	0.52 / -0.52	0.57 / -0.57	0.58 / -0.58	0.63 / -0.62	0.59 / -0.58	0.50 / -0.49	0.41 / -0.41	0.27 / -0.27
JES Pileup RhoTopology	0.31 / -0.30	0.29 / -0.29	0.20 / -0.20	0.14 / -0.14	0.21 / -0.21	0.50 / -0.49	0.53 / -0.52	0.50 / -0.50	0.37 / -0.36	0.22 / -0.22	0.09 / -0.09	-0.10 / 0.10
JES Pileup OffsetMu	-0.01 / 0.01	0.01 / -0.01	0.05 / -0.06	0.09 / -0.09	0.07 / -0.07	0.05 / -0.05	0.05 / -0.05	0.06 / -0.06	0.00 / -0.00	-0.06 / 0.06	-0.07 / 0.07	-0.08 / 0.08
JES Pileup OffsetNPV	0.10 / -0.10	-0.08 / 0.08	-0.15 / 0.15	-0.09 / 0.09	0.01 / -0.01	0.03 / -0.03	0.03 / -0.03	0.00 / -0.00	0.02 / -0.02	0.03 / -0.03	0.00 / -0.00	-0.02 / 0.02
JES EtaIntercalib Model	0.09 / -0.09	0.09 / -0.09	0.09 / -0.09	0.09 / -0.09	0.10 / -0.10	0.18 / -0.18	0.19 / -0.19	0.20 / -0.20	0.12 / -0.12	0.05 / -0.05	0.03 / -0.03	-0.04 / 0.04
JES Flavor Response	-0.66 / 0.67	-0.72 / 0.73	-0.74 / 0.76	-0.72 / 0.73	-0.68 / 0.69	-0.66 / 0.67	-0.65 / 0.66	-0.66 / 0.67	-0.62 / 0.62	-0.53 / 0.54	-0.49 / 0.49	-0.47 / 0.48
JER EffectiveNP 1	0.41 / -0.41	0.42 / -0.42	0.34 / -0.35	0.18 / -0.18	0.04 / -0.04	-0.16 / 0.16	-0.17 / 0.17	-0.25 / 0.25	-0.31 / 0.31	-0.29 / 0.29	-0.18 / 0.18	-0.09 / 0.09
JER EffectiveNP 2	0.25 / -0.25	0.26 / -0.26	0.13 / -0.14	-0.16 / 0.16	-0.33 / 0.33	-0.26 / 0.26	-0.25 / 0.25	-0.09 / 0.09	0.11 / -0.11	0.18 / -0.18	0.20 / -0.20	0.23 / -0.23
JER EffectiveNP 3	-0.10 / 0.10	-0.07 / 0.07	-0.05 / 0.05	-0.06 / 0.06	-0.09 / 0.09	-0.09 / 0.09	-0.09 / 0.09	-0.17 / 0.17	-0.33 / 0.34	-0.40 / 0.41	-0.38 / 0.38	-0.36 / 0.36
JER EffectiveNP 4	-0.11 / 0.11	-0.01 / 0.01	0.02 / -0.02	0.03 / -0.03	0.02 / -0.02	0.02 / -0.02	0.01 / -0.01	0.00 / -0.00	-0.04 / 0.04	-0.05 / 0.05	-0.04 / 0.04	-0.02 / 0.02
JER EffectiveNP 5	-0.13 / 0.13	-0.09 / 0.09	-0.04 / 0.04	0.00 / -0.00	0.01 / -0.01	0.01 / -0.01	0.01 / -0.01	0.07 / -0.07	0.15 / -0.15	0.21 / -0.21	0.30 / -0.30	0.44 / -0.44
JER EffectiveNP 6	-0.15 / 0.15	-0.09 / 0.09	-0.03 / 0.03	0.01 / -0.01	0.02 / -0.02	0.04 / -0.04	0.04 / -0.04	0.09 / -0.09	0.13 / -0.13	0.13 / -0.13	0.14 / -0.14	0.16 / -0.16
JER EffectiveNP 7rest	0.06 / -0.06	0.07 / -0.07	0.05 / -0.05	0.01 / -0.01	-0.08 / 0.08	0.02 / -0.02	0.03 / -0.03	0.13 / -0.13	0.20 / -0.20	0.26 / -0.26	0.35 / -0.35	0.51 / -0.50
JER DataVsMC MC16	-0.07 / 0.07	-0.07 / 0.07	-0.07 / 0.07	-0.06 / 0.06	-0.03 / 0.03	0.03 / -0.03	0.04 / -0.04	0.05 / -0.05	0.02 / -0.02	-0.03 / 0.03	-0.03 / 0.03	-0.01 / 0.01
$E_\mathrm{T}^\mathrm{miss}$ SoftTrk Scale	0.22 / -0.22	0.24 / -0.24	0.22 / -0.22	0.15 / -0.16	0.14 / -0.15	0.18 / -0.19	0.18 / -0.18	0.15 / -0.15	0.19 / -0.20	0.22 / -0.22	0.16 / -0.16	0.13 / -0.13
$E_\mathrm{T}^\mathrm{miss}$ SoftTrk ResoPara	0.39	0.29	0.16	0.05	0.01	-0.14	-0.16	-0.22	-0.21	-0.31	-0.44	-0.48
$E_\mathrm{T}^\mathrm{miss}$ SoftTrk ResoPerp	0.29	0.18	0.06	-0.03	-0.03	-0.03	-0.04	-0.08	-0.07	-0.09	-0.15	-0.16
Muon Resolution MS	0.06 / -0.06	-0.21 / 0.21	-0.33 / 0.33	-0.27 / 0.27	-0.15 / 0.15	-0.31 / 0.31	-0.34 / 0.34	-0.44 / 0.45	-0.49 / 0.49	-0.49 / 0.50	-0.50 / 0.50	-0.54 / 0.55
Muon Scale	0.20 / -0.20	0.22 / -0.22	0.26 / -0.25	0.30 / -0.29	0.37 / -0.36	0.71 / -0.70	0.75 / -0.74	0.89 / -0.88	0.90 / -0.89	0.73 / -0.72	0.53 / -0.52	0.44 / -0.44
Muon SF Identification Syst	-1.61 / 1.67	-1.58 / 1.63	-1.53 / 1.58	-1.45 / 1.50	-1.41 / 1.45	-1.58 / 1.64	-1.60 / 1.66	-1.64 / 1.70	-1.61 / 1.66	-1.55 / 1.60	-1.55 / 1.60	-1.57 / 1.62
Muon SF Isolation Syst	-0.70 / 0.71	-0.69 / 0.70	-0.68 / 0.69	-0.67 / 0.68	-0.66 / 0.66	-0.63 / 0.64	-0.63 / 0.64	-0.62 / 0.63	-0.60 / 0.61	-0.58 / 0.58	-0.56 / 0.57	-0.55 / 0.56
Muon SF Trigger Syst	0.91 / -0.90	0.90 / -0.89	0.90 / -0.88	0.88 / -0.86	0.81 / -0.80	0.60 / -0.59	0.58 / -0.57	0.55 / -0.55	0.58 / -0.57	0.56 / -0.56	0.54 / -0.53	0.52 / -0.51
Bad Muon	0.03 / -0.03	0.03 / -0.03	0.03 / -0.03	0.04 / -0.04	0.03 / -0.03	-0.01 / 0.01	-0.02 / 0.02	-0.05 / 0.05	-0.07 / 0.07	-0.11 / 0.11	-0.16 / 0.16	-0.18 / 0.18
Muon Sagitta Global	0.33 / -0.33	0.41 / -0.41	0.43 / -0.43	0.37 / -0.37	0.26 / -0.25	0.23 / -0.23	0.24 / -0.24	0.26 / -0.26	0.27 / -0.27	0.27 / -0.27	0.27 / -0.26	0.26 / -0.25
Muon Sagitta p_T-extra	-0.01 / 0.01	-0.01 / 0.01	-0.01 / 0.01	-0.01 / 0.01	-0.01 / 0.01	-0.01 / 0.01	-0.00 / 0.00	-0.04 / 0.04	-0.06 / 0.06	-0.02 / 0.02	0.02 / -0.02	0.01 / -0.01
Pile-up	0.02 / -0.02	0.04 / -0.04	0.08 / -0.08	0.16 / -0.16	0.17 / -0.17	0.10 / -0.10	0.09 / -0.10	0.12 / -0.12	0.11 / -0.11	0.16 / -0.16	0.34 / -0.34	0.52 / -0.51
Multijet $E_\mathrm{T}^\mathrm{miss}$	-0.36 / 0.05	-0.37 / 0.05	-0.31 / 0.04	-0.28 / 0.04	-0.24 / 0.03	-0.51 / 0.08	-0.54 / 0.09	-0.66 / 0.10	-0.67 / 0.05	-1.12 / 0.04	-1.05 / 0.02	-0.47 / 0.00
Multijet d_0^sig	0.18 / -0.67	0.19 / -0.72	0.16 / -0.61	0.14 / -0.55	0.12 / -0.45	0.41 / -0.46	0.45 / -0.46	0.55 / -0.53	0.36 / -0.57	0.38 / -0.98	0.30 / -0.92	0.13 / -0.41
Multijet MC Scaling	0.91 / -0.91	0.97 / -0.97	0.81 / -0.81	0.74 / -0.74	0.60 / -0.60	0.61 / -0.61	0.60 / -0.60	0.57 / -0.57	0.40 / -0.40	0.48 / -0.48	0.40 / -0.40	0.17 / -0.17
Multijet Jet Mult	-0.66 / 0.19	-0.71 / 0.20	-0.58 / 0.17	-0.53 / 0.15	-0.49 / 0.13	-0.16 / 0.52	-0.12 / 0.57	-0.11 / 0.55	-0.25 / 0.30	-0.49 / 0.33	-0.31 / 0.32	-0.21 / 0.10
Multijet MC Shape	-0.08	-0.11	-0.08	-0.08	-0.08	0.74	0.83	0.83	0.58	0.86	0.76	0.30
Multijet $\Delta\phi(\mu, E_\mathrm{T}^\mathrm{miss})$	-0.85 / 0.54	-0.94 / 0.58	-0.75 / 0.48	-0.70 / 0.43	-0.61 / 0.39	-0.55 / 0.32	-0.54 / 0.31	-0.50 / 0.25	-0.47 / 0.30	-0.65 / 0.61	-0.40 / 0.56	-0.28 / 0.20
$t\bar{t}$ p_T-hard	0.57 / 0.00	0.04 / 0.00	-0.34 / 0.00	-0.52 / 0.00	-0.45 / 0.00	-0.26 / 0.00	-0.24 / 0.00	-0.21 / 0.00	-0.19 / 0.00	-0.02 / 0.00	0.17 / 0.00	0.21 / 0.00
$t\bar{t}$ FSR	1.05 / -1.05	0.72 / -0.72	0.57 / -0.57	0.41 / -0.41	0.13 / -0.13	0.06 / -0.06	0.06 / -0.06	0.20 / -0.20	0.29 / -0.29	0.34 / -0.34	0.40 / -0.40	0.34 / -0.34
$t\bar{t}$ scales $\mu_R\,\mu_F$	-1.21 / 1.76	-1.17 / 1.71	-1.09 / 1.56	-1.03 / 1.40	-0.89 / 1.15	-0.73 / 0.87	-0.70 / 0.84	-0.60 / 0.74	-0.51 / 0.61	-0.36 / 0.37	-0.29 / 0.24	-0.21 / 0.13
$t\bar{t}$ hadronization	1.65 / 0.00	1.36 / 0.00	1.20 / 0.00	1.13 / 0.00	0.88 / 0.00	0.55 / 0.00	0.51 / 0.00	0.47 / 0.00	0.43 / 0.00	0.45 / 0.00	0.61 / 0.00	0.63 / 0.00
$t\bar{t}$ hdamp	0.48 / 0.00	0.26 / 0.00	0.11 / 0.00	0.06 / 0.00	0.03 / 0.00	0.03 / 0.00	0.03 / 0.00	0.04 / 0.00	0.04 / 0.00	0.07 / 0.00	0.11 / 0.00	0.10 / 0.00
$t\bar{t}$ PDF	-0.78 / 0.78	-0.79 / 0.79	-0.73 / 0.73	-0.74 / 0.74	-0.69 / 0.69	-0.68 / 0.68	-0.67 / 0.67	-0.68 / 0.68	-0.73 / 0.73	-0.71 / 0.71	-0.76 / 0.76	-0.69 / 0.69
tW DR	-1.38	-1.42	-1.56	-1.52	-1.22	-0.48	-0.39	-0.27	-0.38	-0.45	-0.41	-0.32
tW DS hdamp	-0.00	-0.00	-0.00	-0.00	-0.01	0.04	0.05	0.11	0.09	0.00	-0.09	-0.16
Norm. $W\to\tau\nu$ by 5%	-0.10 / 0.10	-0.09 / 0.09	-0.09 / 0.09	-0.08 / 0.09	-0.08 / 0.08	-0.07 / 0.08	-0.07 / 0.07	-0.07 / 0.07	-0.07 / 0.07	-0.07 / 0.07	-0.06 / 0.06	-0.07 / 0.06
Norm. Single top by 4%	-0.25 / 0.25	-0.25 / 0.25	-0.24 / 0.24	-0.23 / 0.23	-0.20 / 0.20	-0.16 / 0.16	-0.15 / 0.15	-0.14 / 0.14	-0.11 / 0.11	-0.08 / 0.08	-0.06 / 0.06	-0.05 / 0.05
Norm. Diboson by 6%	-0.34 / 0.34	-0.34 / 0.34	-0.31 / 0.31	-0.33 / 0.33	-0.31 / 0.31	-0.29 / 0.29	-0.29 / 0.29	-0.29 / 0.29	-0.28 / 0.28	-0.27 / 0.27	-0.25 / 0.25	-0.24 / 0.24
Norm. $Z\to\ell\ell$ by 5%	-0.25 / 0.25	-0.26 / 0.26	-0.28 / 0.28	-0.32 / 0.32	-0.35 / 0.35	-0.49 / 0.49	-0.51 / 0.51	-0.64 / 0.64	-0.75 / 0.75	-0.86 / 0.86	-1.11 / 1.11	-1.23 / 1.23

Table G.4.: Born-level double-differential cross-section $\frac{d^2\sigma(W\to\mu\nu)}{dm_{\mathrm{T}}^{\mathrm{W}}\,d|\eta(\mu)|}$ including statistical and systematic uncertainties in percent for $m_{\mathrm{T}}^{\mathrm{W}} = [425-600]\,\mathrm{GeV}$. The upper (lower) row corresponds to the one standard deviation upward (downward) shift of the uncertainty source.

$\lvert\eta(\mu)\rvert$	0.0 - 0.4	0.4 - 0.8	0.8 - 1.2	1.2 - 1.6	1.6 - 2.0	2.0 - 2.4
σ [pb/GeV]	4.98e-04	4.87e-04	4.52e-04	3.79e-04	2.98e-04	1.84e-04
Data stat. unc.	2.42	2.03	1.69	2.42	2.57	3.79
Sig. stat. unc.	1.47	1.23	1.10	1.99	2.59	1.27
Bkg. stat. unc.	0.45	0.35	0.29	0.45	0.53	0.85
Tot. sys. unc.	2.96 / -3.77	2.34 / -2.93	2.23 / -2.71	2.89 / -2.94	3.34 / -3.19	4.33 / -3.60
Alt. MC unf. unc.	-1.65	-1.28	-0.99	-0.53	0.62	2.22
Basic unf. unc.	-1.38	-1.27	-1.21	-0.68	0.39	1.02
JES Flavor Composition	0.10 / -0.10	0.22 / -0.22	0.25 / -0.25	0.46 / -0.45	0.35 / -0.35	0.22 / -0.22
JES Pileup RhoTopology	0.04 / -0.04	0.12 / -0.12	0.16 / -0.15	0.25 / -0.24	0.18 / -0.18	0.10 / -0.10
JES Pileup OffsetMu	0.06 / -0.06	0.07 / -0.07	0.09 / -0.09	0.16 / -0.16	0.13 / -0.13	0.07 / -0.07
JES Pileup OffsetNPV	0.13 / -0.13	0.08 / -0.08	0.11 / -0.11	0.10 / -0.10	0.08 / -0.08	0.02 / -0.02
JES EtaIntercalib Model	0.10 / -0.10	0.07 / -0.07	0.08 / -0.08	0.11 / -0.11	0.08 / -0.08	0.04 / -0.04
JES Flavor Response	-0.41 / 0.41	-0.34 / 0.34	-0.30 / 0.30	-0.17 / 0.17	-0.06 / 0.06	0.01 / -0.01
JER EffectiveNP 1	0.41 / -0.40	0.27 / -0.27	0.23 / -0.23	0.20 / -0.20	0.08 / -0.08	-0.07 / 0.07
JER EffectiveNP 2	0.72 / -0.71	0.34 / -0.34	0.22 / -0.22	-0.03 / 0.03	-0.07 / 0.07	-0.15 / 0.15
JER EffectiveNP 3	0.17 / -0.17	0.18 / -0.17	0.15 / -0.15	0.07 / -0.07	-0.00 / 0.00	-0.06 / 0.06
JER EffectiveNP 4	0.76 / -0.75	0.28 / -0.28	0.12 / -0.12	-0.49 / 0.49	-0.58 / 0.58	-0.60 / 0.61
JER EffectiveNP 5	0.82 / -0.81	0.24 / -0.24	0.20 / -0.20	0.01 / -0.01	0.01 / -0.01	-0.02 / 0.02
JER EffectiveNP 6	0.56 / -0.55	0.19 / -0.19	0.16 / -0.16	0.05 / -0.05	0.03 / -0.03	-0.02 / 0.02
JER EffectiveNP 7rest	0.34 / -0.34	0.13 / -0.13	0.08 / -0.08	-0.04 / 0.04	-0.05 / 0.05	-0.09 / 0.09
JER DataVsMC MC16	0.03 / -0.03	0.03 / -0.03	0.04 / -0.04	0.07 / -0.07	0.06 / -0.06	0.03 / -0.03
$E_{\mathrm{T}}^{\mathrm{miss}}$ SoftTrk Scale	-0.10 / 0.10	-0.11 / 0.10	-0.14 / 0.13	-0.22 / 0.22	-0.15 / 0.15	0.01 / -0.01
$E_{\mathrm{T}}^{\mathrm{miss}}$ SoftTrk ResoPara	-0.03	-0.03	-0.06	-0.13	-0.07	0.04
$E_{\mathrm{T}}^{\mathrm{miss}}$ SoftTrk ResoPerp	-0.11	-0.11	-0.11	-0.13	-0.01	0.16
Muon Resolution MS	-0.29 / 0.30	-0.28 / 0.28	-0.38 / 0.38	-0.84 / 0.85	-1.01 / 1.03	-1.01 / 1.03
Muon Scale	0.25 / -0.25	0.23 / -0.23	0.31 / -0.30	0.60 / -0.59	0.64 / -0.63	0.60 / -0.59
Muon SF Identification Syst	-0.95 / 0.97	-0.90 / 0.91	-1.05 / 1.08	-1.76 / 1.82	-2.03 / 2.11	-1.99 / 2.07
Muon SF Isolation Syst	-0.69 / 0.70	-0.67 / 0.68	-0.66 / 0.67	-0.64 / 0.65	-0.62 / 0.63	-0.60 / 0.60
Muon SF Trigger Syst	0.77 / -0.76	0.70 / -0.69	0.66 / -0.65	0.51 / -0.51	0.51 / -0.51	0.50 / -0.50
Bad Muon	0.03 / -0.03	0.04 / -0.04	0.01 / -0.01	-0.09 / 0.09	-0.18 / 0.18	-0.28 / 0.28
Muon Sagitta Global	-0.31 / 0.31	-0.17 / 0.17	0.01 / -0.01	0.82 / -0.80	1.02 / -1.00	1.01 / -0.99
Muon Sagitta p_{T}-extra	-0.01 / 0.01	-0.03 / 0.03	0.09 / -0.09	0.57 / -0.56	0.99 / -0.97	1.44 / -1.40
Pile-up	0.15 / -0.15	0.12 / -0.12	0.13 / -0.13	0.12 / -0.12	0.10 / -0.10	0.05 / -0.05
Multijet $E_{\mathrm{T}}^{\mathrm{miss}}$	-0.21 / 0.01	-0.16 / 0.01	-0.20 / 0.01	-0.37 / 0.02	-0.49 / 0.02	-1.02 / 0.04
Multijet d_0^{sig}	0.13 / -0.54	0.10 / -0.38	0.11 / -0.38	0.20 / -0.44	0.19 / -0.46	0.33 / -0.89
Multijet MC Scaling	0.64 / -0.64	0.49 / -0.49	0.42 / -0.42	0.21 / -0.21	0.19 / -0.19	0.49 / -0.49
Multijet Jet Mult	-0.45 / 0.10	-0.39 / 0.08	-0.31 / 0.10	0.00 / 0.23	-0.10 / 0.17	-0.26 / 0.31
Multijet MC Shape	-0.12	-0.12	-0.02	0.41	0.43	0.74
Multijet $\Delta\phi(\mu, E_{\mathrm{T}}^{\mathrm{miss}})$	-0.67 / 0.40	-0.57 / 0.34	-0.48 / 0.28	-0.18 / 0.07	-0.15 / 0.31	-0.32 / 0.57
$t\bar{t}$ p_{T}-hard	0.53 / 0.00	0.14 / 0.00	0.09 / 0.00	-0.15 / 0.00	-0.13 / 0.00	-0.12 / 0.00
$t\bar{t}$ FSR	0.28 / -0.28	0.29 / -0.29	0.23 / -0.23	0.22 / -0.22	0.28 / -0.28	0.32 / -0.32
$t\bar{t}$ scales μ_R μ_F	-1.02 / 1.19	-0.86 / 1.07	-0.76 / 0.93	-0.43 / 0.58	-0.28 / 0.37	-0.18 / 0.23
$t\bar{t}$ hadronization	1.04 / 0.00	0.94 / 0.00	0.81 / 0.00	0.45 / 0.00	0.29 / 0.00	0.18 / 0.00
$t\bar{t}$ hdamp	0.01 / 0.00	0.01 / 0.00	0.00 / 0.00	0.02 / 0.00	0.02 / 0.00	0.01 / 0.00
$t\bar{t}$ PDF	-0.47 / 0.47	-0.43 / 0.43	-0.43 / 0.43	-0.46 / 0.46	-0.46 / 0.46	-0.52 / 0.52
tW DR	-1.38	-0.85	-0.71	-0.37	-0.25	-0.20
tW DS hdamp	0.02	0.04	0.09	0.29	0.27	0.38
Norm. $W \to \tau\nu$ by 5%	-0.07 / 0.07	-0.08 / 0.08	-0.07 / 0.07	-0.07 / 0.07	-0.06 / 0.06	-0.05 / 0.05
Norm. Single top by 4%	-0.16 / 0.16	-0.15 / 0.15	-0.13 / 0.13	-0.10 / 0.10	-0.06 / 0.06	-0.05 / 0.05
Norm. Diboson by 6%	-0.30 / 0.30	-0.30 / 0.30	-0.29 / 0.29	-0.27 / 0.27	-0.25 / 0.25	-0.27 / 0.27
Norm. $Z \to \ell\ell$ by 5%	-0.25 / 0.25	-0.27 / 0.27	-0.32 / 0.32	-0.50 / 0.50	-0.62 / 0.62	-0.87 / 0.87

Table G.5.: Born-level double-differential cross-section $\frac{d^2\sigma(W\to\mu\nu)}{dm_{\mathrm{T}}^{\mathrm{W}}\,d|\eta(\mu)|}$ including statistical and systematic uncertainties in percent for $m_{\mathrm{T}}^{\mathrm{W}} = [600-900]$ GeV. The upper (lower) row corresponds to the one standard deviation upward (downward) shift of the uncertainty source.

$|\eta(\mu)|$	0.0 - 0.4	0.4 - 0.8	0.8 - 1.2	1.2 - 1.6	1.6 - 2.0	2.0 - 2.4
σ [pb/GeV]	1.01e-04	8.60e-05	7.71e-05	6.67e-05	4.10e-05	1.82e-05
Data stat. unc.	3.96	3.44	2.87	4.14	5.27	9.09
Sig. stat. unc.	2.33	3.04	2.57	3.79	2.31	1.59
Bkg. stat. unc.	0.56	0.47	0.40	0.72	0.86	1.17
Tot. sys. unc.	2.31 -3.59	2.30 -2.94	2.32 -2.64	3.02 -3.04	3.15 -2.97	3.71 -3.05
Alt. MC unf. unc.	-2.57	-1.65	-1.13	-0.68	0.33	1.75
Basic unf. unc.	-0.65	-0.65	-0.45	0.10	0.61	0.80
JES Flavor Composition	0.26 -0.26	0.25 -0.25	0.24 -0.24	0.24 -0.24	0.22 -0.22	0.25 -0.25
JES Pileup RhoTopology	0.10 -0.10	0.09 -0.09	0.09 -0.09	0.08 -0.08	0.05 -0.05	-0.01 0.01
JES Pileup OffsetMu	0.10 -0.10	0.12 -0.12	0.11 -0.11	0.10 -0.10	0.02 -0.02	-0.01 0.01
JES Pileup OffsetNPV	0.06 -0.06	0.08 -0.08	0.08 -0.08	0.07 -0.07	0.06 -0.06	0.09 -0.09
JES EtaIntercalib Model	0.12 -0.12	0.13 -0.13	0.12 -0.12	0.10 -0.10	0.06 -0.06	0.02 -0.02
JES Flavor Response	-0.09 0.09	-0.08 0.08	-0.07 0.07	-0.05 0.05	-0.06 0.06	-0.07 0.07
JER EffectiveNP 1	0.15 -0.15	0.28 -0.28	0.28 -0.28	0.24 -0.24	0.09 -0.09	0.04 -0.04
JER EffectiveNP 2	0.09 -0.09	0.13 -0.13	0.12 -0.12	0.06 -0.06	-0.07 0.07	-0.11 0.11
JER EffectiveNP 3	0.02 -0.02	0.06 -0.06	0.07 -0.07	0.07 -0.07	0.11 -0.11	0.21 -0.20
JER EffectiveNP 4	0.12 -0.12	0.10 -0.09	0.09 -0.09	0.00 -0.00	0.09 -0.09	0.24 -0.24
JER EffectiveNP 5	0.08 -0.08	0.06 -0.06	0.07 -0.07	0.04 -0.04	0.05 -0.05	0.06 -0.06
JER EffectiveNP 6	0.03 -0.03	0.04 -0.04	0.05 -0.05	0.05 -0.05	0.08 -0.08	0.09 -0.09
JER EffectiveNP 7rest	0.11 -0.11	0.07 -0.07	0.06 -0.06	-0.00 0.00	-0.02 0.02	-0.01 0.02
JER DataVsMC MC16	0.08 -0.08	0.10 -0.09	0.08 -0.08	0.01 -0.01	0.04 -0.04	0.21 -0.21
$E_{\mathrm{T}}^{\mathrm{miss}}$ SoftTrk Scale	-0.14 0.14	-0.27 0.27	-0.26 0.26	-0.20 0.20	0.02 -0.02	0.15 -0.15
$E_{\mathrm{T}}^{\mathrm{miss}}$ SoftTrk ResoPara	-0.13	-0.24	-0.22	-0.14	0.04	0.13
$E_{\mathrm{T}}^{\mathrm{miss}}$ SoftTrk ResoPerp	-0.05	-0.26	-0.25	-0.16	0.07	0.15
Muon Resolution MS	-0.16 0.16	-0.14 0.14	-0.19 0.19	-0.47 0.48	-0.69 0.70	-1.15 1.18
Muon Scale	0.12 -0.12	0.10 -0.10	0.21 -0.21	0.71 -0.70	0.78 -0.77	0.78 -0.76
Muon SF Identification Syst	-1.45 1.49	-1.42 1.46	-1.52 1.57	-2.03 2.12	-1.99 2.08	-1.90 1.97
Muon SF Isolation Syst	-0.61 0.62	-0.60 0.61	-0.60 0.61	-0.58 0.59	-0.56 0.57	-0.55 0.55
Muon SF Trigger Syst	0.68 -0.67	0.63 -0.63	0.60 -0.59	0.46 -0.46	0.48 -0.47	0.53 -0.52
Bad Muon	0.02 -0.02	0.05 -0.05	0.01 -0.01	-0.17 0.17	-0.31 0.31	-0.45 0.45
Muon Sagitta Global	0.52 -0.51	0.58 -0.57	0.56 -0.55	0.53 -0.53	0.41 -0.41	0.39 -0.39
Muon Sagitta p_{T}-extra	-0.03 0.03	-0.08 0.08	0.19 -0.19	1.38 -1.34	1.54 -1.50	1.44 -1.40
Pile-up	0.33 -0.33	0.31 -0.31	0.27 -0.27	0.06 -0.06	0.06 -0.06	0.20 -0.19
Multijet $E_{\mathrm{T}}^{\mathrm{miss}}$	-0.10 -0.00	-0.04 -0.00	-0.06 0.01	-0.18 0.04	-0.09 0.02	0.06 -0.00
Multijet d_0^{sig}	0.06 -0.30	0.02 -0.12	0.04 -0.13	0.12 -0.17	0.05 -0.06	-0.02 0.05
Multijet MC Scaling	0.34 -0.34	0.14 -0.14	0.13 -0.13	0.10 -0.10	0.04 -0.04	-0.02 0.02
Multijet Jet Mult	-0.24 0.04	-0.11 -0.01	-0.08 0.02	0.02 0.13	0.03 0.05	0.02 -0.02
Multijet MC Shape	-0.08	-0.07	-0.00	0.26	0.07	-0.04
Multijet $\Delta\phi(\mu, E_{\mathrm{T}}^{\mathrm{miss}})$	-0.37 0.22	-0.18 0.11	-0.16 0.09	-0.08 0.01	-0.02 -0.03	0.03 -0.03
$t\bar{t}$ p_{T}-hard	-0.11 0.00	-0.08 0.00	-0.08 0.00	-0.07 0.00	-0.04 0.00	-0.03 0.00
$t\bar{t}$ FSR	0.25 -0.25	0.26 -0.26	0.24 -0.24	0.17 -0.17	0.11 -0.11	0.05 -0.05
$t\bar{t}$ scales $\mu_R\,\mu_F$	-0.61 1.01	-0.62 1.03	-0.57 0.95	-0.37 0.63	-0.28 0.48	-0.15 0.26
$t\bar{t}$ hadronization	0.46 0.00	0.49 0.00	0.45 0.00	0.31 0.00	0.22 0.00	0.09 0.00
$t\bar{t}$ hdamp	-0.37 0.00	-0.35 0.00	-0.33 0.00	-0.22 0.00	-0.17 0.00	-0.10 0.00
$t\bar{t}$ PDF	-0.26 0.26	-0.25 0.25	-0.27 0.27	-0.32 0.32	-0.29 0.29	-0.24 0.24
tW DR	-1.06	-0.96	-0.91	-0.69	-0.43	-0.42
tW DS hdamp	-0.12	-0.07	-0.04	0.15	0.30	0.63
Norm. $W \to \tau\nu$ by 5%	-0.07 0.07	-0.07 0.07	-0.07 0.07	-0.06 0.06	-0.04 0.04	-0.04 0.04
Norm. Single top by 4%	-0.08 0.08	-0.07 0.07	-0.06 0.06	-0.04 0.04	-0.02 0.02	-0.03 0.03
Norm. Diboson by 6%	-0.26 0.26	-0.25 0.25	-0.24 0.24	-0.22 0.22	-0.23 0.23	-0.20 0.20
Norm. $Z \to \ell\ell$ by 5%	-0.21 0.21	-0.23 0.23	-0.25 0.25	-0.33 0.33	-0.42 0.42	-0.54 0.54

Table G.6.: Born-level double-differential cross-section $\frac{d^2\sigma(W \to \mu\nu)}{dm_{\mathrm{T}}^{\mathrm{W}} d|\eta(\mu)|}$ including statistical and systematic uncertainties in percent for $m_{\mathrm{T}}^{\mathrm{W}} = [900 - 2000]\,\mathrm{GeV}$. The upper (lower) row corresponds to the one standard deviation upward (downward) shift of the uncertainty source.

$|\eta(\mu)|$	0.0 - 0.6	0.6 - 1.2	1.2 - 1.8	1.8 - 2.4
σ [pb/GeV]	7.13e-06	5.08e-06	2.37e-06	5.93e-07
Data stat. unc.	6.00	7.92	9.37	19.98
Sig. stat. unc.	4.22	0.63	6.55	1.61
Bkg. stat. unc.	0.67	0.71	1.41	1.59
Tot. sys. unc.	2.83 / -4.37	2.83 / -4.15	8.30 / -7.89	6.92 / -6.21
Alt. MC unf. unc.	-3.25	-3.10	-2.51	-1.46
Basic unf. unc.	-1.05	-0.41	0.90	2.50
JES Flavor Composition	0.21 / -0.21	0.04 / -0.04	0.13 / -0.13	0.00 / -0.00
JES Pileup RhoTopology	0.10 / -0.10	0.03 / -0.03	0.05 / -0.05	0.11 / -0.11
JES Pileup OffsetMu	0.09 / -0.09	0.02 / -0.02	0.11 / -0.11	-0.15 / 0.16
JES Pileup OffsetNPV	0.02 / -0.02	-0.01 / 0.01	0.06 / -0.06	-0.04 / 0.04
JES EtaIntercalib Model	0.10 / -0.10	0.02 / -0.02	0.10 / -0.10	0.01 / -0.01
JES Flavor Response	-0.11 / 0.11	-0.03 / 0.03	-0.08 / 0.08	0.02 / -0.02
JER EffectiveNP 1	-0.08 / 0.08	0.21 / -0.21	0.08 / -0.08	1.07 / -1.05
JER EffectiveNP 2	-0.28 / 0.28	0.12 / -0.12	0.05 / -0.05	0.76 / -0.75
JER EffectiveNP 3	-0.17 / 0.17	0.15 / -0.15	-0.13 / 0.13	0.84 / -0.83
JER EffectiveNP 4	-0.16 / 0.16	0.16 / -0.16	-0.15 / 0.15	1.10 / -1.08
JER EffectiveNP 5	-0.11 / 0.11	0.18 / -0.18	-0.15 / 0.15	0.91 / -0.90
JER EffectiveNP 6	-0.14 / 0.15	0.16 / -0.16	-0.12 / 0.12	0.99 / -0.97
JER EffectiveNP 7rest	-0.14 / 0.14	0.19 / -0.19	-0.13 / 0.13	1.25 / -1.22
JER DataVsMC MC16	-0.11 / 0.11	0.05 / -0.05	0.07 / -0.07	0.24 / -0.24
$E_{\mathrm{T}}^{\mathrm{miss}}$ SoftTrk Scale	-0.11 / 0.11	0.04 / -0.04	-0.19 / 0.19	0.44 / -0.43
$E_{\mathrm{T}}^{\mathrm{miss}}$ SoftTrk ResoPara	-0.17	-0.05	-0.01	0.29
$E_{\mathrm{T}}^{\mathrm{miss}}$ SoftTrk ResoPerp	-0.09	-0.15	-0.13	0.23
Muon Resolution MS	-0.32 / 0.32	-0.66 / 0.67	-1.49 / 1.53	-2.18 / 2.27
Muon Scale	0.24 / -0.24	0.39 / -0.38	0.94 / -0.92	1.01 / -0.99
Muon SF Identification Syst	-1.64 / 1.70	-1.74 / 1.81	-5.91 / 6.65	-4.54 / 4.99
Muon SF Isolation Syst	-0.57 / 0.58	-0.55 / 0.56	-0.55 / 0.56	-0.54 / 0.54
Muon SF Trigger Syst	0.64 / -0.63	0.61 / -0.61	0.44 / -0.44	0.47 / -0.47
Bad Muon	0.03 / -0.03	-0.03 / 0.03	-0.73 / 0.74	-0.85 / 0.86
Muon Sagitta Global	1.81 / -1.75	1.63 / -1.58	1.33 / -1.30	0.50 / -0.50
Muon Sagitta p_{T}-extra	-0.01 / 0.01	0.20 / -0.20	4.13 / -3.83	0.91 / -0.90
Pile-up	0.09 / -0.09	0.15 / -0.15	0.06 / -0.06	0.82 / -0.81
Multijet $E_{\mathrm{T}}^{\mathrm{miss}}$	-0.01 / -0.00	-0.01 / -0.00	-0.23 / -0.01	0.08 / -0.00
Multijet d_0^{sig}	0.00 / -0.05	-0.00 / -0.03	-0.02 / -0.17	-0.03 / 0.07
Multijet MC Scaling	0.05 / -0.05	0.02 / -0.02	-0.05 / 0.05	-0.04 / 0.04
Multijet Jet Mult	-0.03 / -0.01	-0.01 / -0.01	-0.02 / -0.04	0.03 / -0.03
Multijet MC Shape	-0.03	-0.02	-0.03	-0.06
Multijet $\Delta\phi(\mu, E_{\mathrm{T}}^{\mathrm{miss}})$	-0.06 / 0.04	-0.02 / 0.01	0.05 / -0.03	0.03 / -0.04
$t\bar{t}$ p_{T}-hard	-0.05 / 0.00	-0.04 / 0.00	-0.03 / 0.00	-0.01 / 0.00
$t\bar{t}$ FSR	0.07 / -0.07	0.09 / -0.09	0.07 / -0.07	0.01 / -0.01
$t\bar{t}$ scales μ_R μ_F	-0.17 / 0.30	-0.21 / 0.36	-0.17 / 0.31	-0.08 / 0.14
$t\bar{t}$ hadronization	0.13 / 0.00	0.15 / 0.00	0.14 / 0.00	0.05 / 0.00
$t\bar{t}$ hdamp	-0.12 / 0.00	-0.13 / 0.00	-0.12 / 0.00	-0.06 / 0.00
$t\bar{t}$ PDF	-0.07 / 0.07	-0.09 / 0.09	-0.19 / 0.19	-0.13 / 0.13
tW DR	-0.55	-0.36	0.28	0.04
tW DS hdamp	0.64	0.51	0.33	-0.04
Norm. $W \to \tau\nu$ by 5%	-0.05 / 0.05	-0.06 / 0.06	-0.04 / 0.04	-0.02 / 0.02
Norm. Single top by 4%	-0.03 / 0.03	-0.04 / 0.04	-0.03 / 0.03	0.01 / -0.01
Norm. Diboson by 6%	-0.22 / 0.22	-0.22 / 0.22	-0.31 / 0.31	-0.17 / 0.17
Norm. $Z \to \ell\ell$ by 5%	-0.21 / 0.21	-0.24 / 0.24	-0.35 / 0.35	-0.30 / 0.30

Bibliography

[1]   M. Farina et al.,
      Energy helps accuracy: electroweak precision tests at hadron colliders,
      Phys. Lett. B **772** (2017) 210, arXiv: `1609.08157` [`hep-ph`] (cit. on pp. 1, 26).

[2]   Daniele S. M. Alves et. al.,
      Running Electroweak Couplings as a Probe of New Physics, 2014,
      arXiv: `1410.6810` [`hep-ph`] (cit. on pp. 1, 26).

[3]   J. J. Thomson, *XL. Cathode Rays*, The London, Edinburgh, and Dublin
      Philosophical Magazine and Journal of Science **44** (1897) 293,
      eprint: `https://doi.org/10.1080/14786449708621070` (cit. on p. 3).

[4]   J. J. Thomson, *XXIV. On the structure of the atom: an investigation of the
      stability and periods of oscillation of a number of corpuscles arranged at equal
      intervals around the circumference of a circle; with application of the results to
      the theory of atomic structure*, The London, Edinburgh, and Dublin
      Philosophical Magazine and Journal of Science **7** (1904) 237,
      eprint: `https://doi.org/10.1080/14786440409463107` (cit. on p. 3).

[5]   E. Rutherford, *LXXIX. The scattering of α and β particles by matter and the
      structure of the atom*, The London, Edinburgh, and Dublin Philosophical
      Magazine and Journal of Science **21** (1911) 669,
      eprint: `https://doi.org/10.1080/14786440508637080` (cit. on p. 3).

[6]   J. S. Chadwick, *Possible Existence of a Neutron*, Nature **129** (1932) 312,
      URL: `https://api.semanticscholar.org/CorpusID:4076465` (cit. on p. 3).

[7]   M. Gell-Mann, *A schematic model of baryons and mesons*,
      Physics Letters **8** (1964) 214, ISSN: 0031-9163, URL: `https://www.sciencedirect.com/science/article/pii/S0031916364920013`
      (cit. on p. 3).

[8]   W. Albrecht et al.,
      Inelastic electron proton scattering at high momentum transfers,
      Physics Letters B **28** (1968) 225, ISSN: 0370-2693, URL:
      `https://www.sciencedirect.com/science/article/pii/0370269368900221`
      (cit. on p. 3).

[9]   E. D. Bloom et al., *High-Energy Inelastic $e - p$ Scattering at 6° and 10°*,
      Phys. Rev. Lett. **23** (16 1969) 930,
      URL: `https://link.aps.org/doi/10.1103/PhysRevLett.23.930`
      (cit. on p. 3).

[10] M. Breidenbach et al.,
Observed Behavior of Highly Inelastic Electron-Proton Scattering,
Phys. Rev. Lett. **23** (16 1969) 935,
URL: https://link.aps.org/doi/10.1103/PhysRevLett.23.935
(cit. on p. 3).

[11] M. Thompson, *Modern Particle Physics*,
Cambridge University Press, United Kingdom, 2013, ISBN: 9781107034266
(cit. on pp. 4, 6, 7, 10, 12).

[12] D. Galbraith and C. Burgard, *Standard Model of Physics*,
https://texample.net/tikz/examples/model-physics/, 2016 (cit. on p. 5).

[13] P. F. de Salas, S. Gariazzo, O. Mena, C. A. Ternes and M. Tórtola, *Neutrino
Mass Ordering from Oscillations and Beyond: 2018 Status and Future Prospects*,
Frontiers in Astronomy and Space Sciences **5** (2018), ISSN: 2296-987X,
URL: http://dx.doi.org/10.3389/fspas.2018.00036 (cit. on pp. 4, 16).

[14] E. Noether, *Invariante Variationsprobleme*, ger,
Nachrichten von der Gesellschaft der Wissenschaften zu Göttingen,
Mathematisch-Physikalische Klasse **1918** (1918) 235,
URL: http://eudml.org/doc/59024 (cit. on p. 5).

[15] S. Weinberg, *A Model of Leptons*, Phys. Rev. Lett. **19** (21 1967) 1264,
URL: https://link.aps.org/doi/10.1103/PhysRevLett.19.1264
(cit. on pp. 8, 14).

[16] S. L. Glashow, *Partial-symmetries of weak interactions*,
Nuclear Physics **22** (1961) 579, ISSN: 0029-5582, URL:
https://www.sciencedirect.com/science/article/pii/0029558261904692
(cit. on pp. 8, 14).

[17] S. L. Glashow, J. Iliopoulos and L. Maiani,
Weak Interactions with Lepton-Hadron Symmetry, Phys. Rev. D **2** (7 1970) 1285,
URL: https://link.aps.org/doi/10.1103/PhysRevD.2.1285
(cit. on pp. 8, 14).

[18] A. Salam, *Weak and electromagnetic interactions*, (), eprint:
https://www.worldscientific.com/doi/pdf/10.1142/9789812795915_0034
(cit. on pp. 8, 14).

[19] J. C. Maxwell, *A dynamical theory of the electromagnetic field*,
Philosophical Transactions of the Royal Society of London **155** (1865) 459
(cit. on p. 8).

[20] C. S. Wu, E. Ambler, R. W. Hayward, D. D. Hoppes and R. P. Hudson,
Experimental Test of Parity Conservation in Beta Decay,
Phys. Rev. **105** (4 1957) 1413,
URL: https://link.aps.org/doi/10.1103/PhysRev.105.1413 (cit. on p. 9).

[21] M. Kobayashi and T. Maskawa,
CP-Violation in the Renormalizable Theory of Weak Interaction,
Progress of Theoretical Physics **49** (1973) 652 (cit. on pp. 9, 14).

[22] P. W. Higgs, *Broken Symmetries and the Masses of Gauge Bosons*,
Phys. Rev. Lett. **13** (16 1964) 508 (cit. on p. 11).

[23] Tanabashi et. al., *Review of Particle Physics*, Phys. Rev. D **98** (3 2018) 030001
(cit. on p. 11).

[24] R. P. Feynman, *Space-Time Approach to Quantum Electrodynamics*,
Phys. Rev. **76** (6 1949) 769 (cit. on p. 12).

[25] ATLAS Collaboration, *Observation of a new particle in the search for the
Standard Model Higgs boson with the ATLAS detector at the LHC*,
Phys. Lett. B **716** (2012) 1, arXiv: `1207.7214` [`hep-ex`] (cit. on p. 14).

[26] CMS Collaboration, *Observation of a new boson at a mass of 125 GeV with the
CMS experiment at the LHC*, Phys. Lett. B **716** (2012) 30,
arXiv: `1207.7235` [`hep-ex`] (cit. on p. 14).

[27] P. Higgs, *Broken symmetries, massless particles and gauge fields*,
Physics Letters **12** (1964) 132, ISSN: 0031-9163, URL:
`https://www.sciencedirect.com/science/article/pii/0031916364911369`
(cit. on p. 14).

[28] F. Englert and R. Brout,
Broken Symmetry and the Mass of Gauge Vector Mesons,
Phys. Rev. Lett. **13** (9 1964) 321,
URL: `https://link.aps.org/doi/10.1103/PhysRevLett.13.321`
(cit. on p. 14).

[29] G. S. Guralnik, C. R. Hagen and T. W. B. Kibble,
Global Conservation Laws and Massless Particles,
Phys. Rev. Lett. **13** (20 1964) 585,
URL: `https://link.aps.org/doi/10.1103/PhysRevLett.13.585`
(cit. on p. 14).

[30] Y.-S. Tsai, *Erratum: Decay correlations of heavy leptons in $e^+ + e^- \rightarrow l^+ + l^-$*,
Phys. Rev. D **13** (3 1976) 771,
URL: `https://link.aps.org/doi/10.1103/PhysRevD.13.771` (cit. on p. 14).

[31] P. Bagnaia et al., *Evidence for $Z \rightarrow e^+ e^-$ at the CERN pp collider*,
Physics Letters B **129** (1983) 130, ISSN: 0370-2693, URL:
`https://www.sciencedirect.com/science/article/pii/037026938390744X`
(cit. on p. 14).

[32] G. Arnison et al., *Experimental observation of lepton pairs of invariant mass
around 95 GeV/c2 at the CERN SPS collider*, Physics Letters B **126** (1983) 398,
ISSN: 0370-2693, URL:
`https://www.sciencedirect.com/science/article/pii/0370269383901880`
(cit. on p. 14).

[33] M. Banner et al., *Observation of single isolated electrons of high transverse momentum in events with missing transverse energy at the CERN pp collider*, Physics Letters B **122** (1983) 476, ISSN: 0370-2693, URL: https://www.sciencedirect.com/science/article/pii/0370269383916052 (cit. on p. 14).

[34] G. Arnison et al., *Experimental observation of isolated large transverse energy electrons with associated missing energy at s=540 GeV*, Physics Letters B **122** (1983) 103, ISSN: 0370-2693, URL: https://www.sciencedirect.com/science/article/pii/0370269383911772 (cit. on p. 14).

[35] J. J. Aubert et al., *Experimental Observation of a Heavy Particle J*, Phys. Rev. Lett. **33** (23 1974) 1404, URL: https://link.aps.org/doi/10.1103/PhysRevLett.33.1404 (cit. on p. 14).

[36] J. E. Augustin et al., *Discovery of a Narrow Resonance in e^+e^- Annihilation*, Phys. Rev. Lett. **33** (23 1974) 1406, URL: https://link.aps.org/doi/10.1103/PhysRevLett.33.1406 (cit. on p. 14).

[37] M. L. Perl et al., *Evidence for Anomalous Lepton Production in $e^+ - e^-$ Annihilation*, Phys. Rev. Lett. **35** (22 1975) 1489, URL: https://link.aps.org/doi/10.1103/PhysRevLett.35.1489 (cit. on p. 14).

[38] S. W. Herb et al., *Observation of a Dimuon Resonance at 9.5 GeV in 400-GeV Proton-Nucleus Collisions*, Phys. Rev. Lett. **39** (5 1977) 252, URL: https://link.aps.org/doi/10.1103/PhysRevLett.39.252 (cit. on p. 14).

[39] S. Abachi et al., *Observation of the Top Quark*, Physical Review Letters **74** (1995) 2632, ISSN: 1079-7114, URL: http://dx.doi.org/10.1103/PhysRevLett.74.2632 (cit. on p. 14).

[40] F. Abe et al., *Observation of Top Quark Production in $\overline{p}p$ Collisions with the Collider Detector at Fermilab*, Phys. Rev. Lett. **74** (14 1995) 2626, URL: https://link.aps.org/doi/10.1103/PhysRevLett.74.2626 (cit. on p. 14).

[41] A. Blondel, *The Number of Neutrinos and the Z Line Shape*, (2016), URL: https://cds.cern.ch/record/2217139 (cit. on p. 14).

[42] ATLAS Collaboration, *Standard Model Summary Plots February 2022*, tech. rep., CERN, 2022, URL: http://cds.cern.ch/record/2804061 (cit. on p. 15).

[43] ATLAS Collaboration, *A precise determination of the strong-coupling constant from the recoil of Z bosons with the ATLAS experiment at $\sqrt{s} = 8\,TeV$*, (2023), arXiv: `2309.12986` `[hep-ex]` (cit. on p. 15).

[44] Particle Data Group, P. Zyla et al., *Review of Particle Physics*, Phys. Rev. D **98** (3 2018) 030001 (cit. on p. 15).

[45] J. de Blas et al., *Global analysis of electroweak data in the Standard Model*, Physical Review D **106** (2022), ISSN: 2470-0029, URL: `http://dx.doi.org/10.1103/PhysRevD.106.033003` (cit. on p. 15).

[46] T. Aaltonen et al., *High-precision measurement of the W boson mass with the CDF II detector*, Science **376** (2022) 170 (cit. on p. 15).

[47] P. D. Group et al., *Review of Particle Physics*, Progress of Theoretical and Experimental Physics **2020** (2020) 083C01, ISSN: 2050-3911, eprint: `https://academic.oup.com/ptep/article-pdf/2020/8/083C01/34673722/ptaa104.pdf` (cit. on p. 16).

[48] A. Collaboration, *Measurement of the W-boson mass and width with the ATLAS detector using proton-proton collisions at $\sqrt{s} = 7\,TeV$*, 2024, arXiv: `2403.15085` `[hep-ex]`, URL: `https://arxiv.org/abs/2403.15085` (cit. on pp. 15, 16).

[49] F. P. An et al., *Observation of Electron-Antineutrino Disappearance at Daya Bay*, Physical Review Letters **108** (2012) (cit. on p. 16).

[50] N. Aghanim et al., *Planck2018 results: VI. Cosmological parameters*, Astronomy Astrophysics **641** (2020) A6, ISSN: 1432-0746, URL: `http://dx.doi.org/10.1051/0004-6361/201833910` (cit. on p. 16).

[51] D. Clowe et al., *A Direct Empirical Proof of the Existence of Dark Matter*, The Astrophysical Journal **648** (2006) L109, ISSN: 1538-4357, URL: `http://dx.doi.org/10.1086/508162` (cit. on p. 16).

[52] V. C. Rubin, N. Thonnard and W. K. Ford Jr., *Rotational properties of 21 SC galaxies with a large range of luminosities and radii, from NGC 4605 /R = 4kpc/ to UGC 2885 /R = 122 kpc/*, Astrophys. J. **238** (1980) 471 (cit. on p. 16).

[53] A. G. Riess et al., *Observational Evidence from Supernovae for an Accelerating Universe and a Cosmological Constant*, The Astronomical Journal **116** (1998) 1009, ISSN: 0004-6256, URL: `http://dx.doi.org/10.1086/300499` (cit. on p. 16).

[54] E. Komatsu et al., *Seven-Year Wilkinson Microwave Anisotropy Probe (WMAP) Observations: Cosmological Interpretation*, The Astrophysical Journal Supplement Series **192** (2011) 18 (cit. on p. 16).

[55] A. D. Sakharov,
      Violation of CP invariance, C asymmetry, and baryon asymmetry of the universe,
      Soviet Physics Uspekhi **34** (1991) 392,
      URL: https://dx.doi.org/10.1070/PU1991v034n05ABEH002497
      (cit. on p. 16).

[56] A. Einstein, *Die Feldgleichungen der Gravitation*, Sitzungsberichte der Königlich
      Preussischen Akademie der Wissenschaften (1915) 844 (cit. on p. 16).

[57] D.-d. Wu, *A Brief Introduction to the Strong CP Problem*,
      Z. Naturforsch. A **52** (1997) 179, ed. by B. G. Englert and G. Sussmann
      (cit. on p. 17).

[58] C. Abel et al.,
      Measurement of the Permanent Electric Dipole Moment of the Neutron,
      Physical Review Letters **124** (2020), ISSN: 1079-7114,
      URL: http://dx.doi.org/10.1103/PhysRevLett.124.081803 (cit. on p. 17).

[59] J. C. Collins, D. E. Soper and G. Sterman,
      Factorization of Hard Processes in QCD, (2004),
      arXiv: hep-ph/0409313 [hep-ph] (cit. on p. 20).

[60] The NNPDF Collaboration, *Parton distributions for the LHC Run II*, 2014,
      arXiv: 1410.8849 [hep-ph] (cit. on p. 20).

[61] Y. L. Dokshitzer,
      *Calculation of the Structure Functions for Deep Inelastic Scattering and e+ e-
      Annihilation by Perturbation Theory in Quantum Chromodynamics.*,
      Sov. Phys. JETP **46** (1977) 641 (cit. on p. 21).

[62] V. N. Gribov and L. N. Lipatov,
      Deep inelastic e p scattering in perturbation theory,
      Sov. J. Nucl. Phys. **15** (1972) 438 (cit. on p. 21).

[63] G. Altarelli and G. Parisi, *Asymptotic freedom in parton language*,
      Nuclear Physics B **126** (1977) 298, ISSN: 0550-3213, URL:
      https://www.sciencedirect.com/science/article/pii/0550321377903844
      (cit. on p. 21).

[64] J. M. Campbell, J. W. Huston and W. J. Stirling,
      Hard interactions of quarks and gluons: a primer for LHC physics,
      Reports on Progress in Physics **70** (2006) 89, ISSN: 1361-6633,
      URL: http://dx.doi.org/10.1088/0034-4885/70/1/R02 (cit. on p. 21).

[65] S. D. Drell and T.-M. Yan,
      Massive Lepton-Pair Production in Hadron-Hadron Collisions at High Energies,
      Phys. Rev. Lett. **25** (5 1970) 316 (cit. on p. 21).

[66] S. D. Drell and T.-M. Yan,
      Massive Lepton-Pair Production in Hadron-Hadron Collisions at High Energies,
      Phys. Rev. Lett. **25** (13 1970) 902, Erratum (cit. on p. 21).

[67] J. B. et al. (Particle Data Group),
PR D86, 010001 (2012), `http://pdg.lbl.gov` (cit. on p. 21).

[68] ATLAS Collaboration,
Measurement of the inclusive $W^{\pm}$ and Z/γ^* cross sections in the e and μ decay channels in pp collisions at $\sqrt{s} = 7\,TeV$ with the ATLAS detector,
Phys. Rev. D **85** (2012) 072004, arXiv: `1109.5141` `[hep-ex]` (cit. on p. 23).

[69] ATLAS Collaboration, *Measurement of the Drell–Yan triple-differential cross section in pp collisions at $\sqrt{s} = 8\,TeV$*, JHEP **12** (2017) 059,
arXiv: `1710.05167` `[hep-ex]` (cit. on p. 23).

[70] ATLAS Collaboration,
Measurement of the cross-section and charge asymmetry of W bosons produced in proton–proton collisions at $\sqrt{s} = 8\,TeV$ with the ATLAS detector,
Eur. Phys. J. C **79** (2019) 760, arXiv: `1904.05631` `[hep-ex]` (cit. on p. 23).

[71] ATLAS Collaboration, *Measurement of $W^{\pm}$ and Z-boson production cross sections in pp collisions at $\sqrt{s} = 13\,TeV$ with the ATLAS detector*,
Phys. Lett. B **759** (2016) 601, arXiv: `1603.09222` `[hep-ex]`
(cit. on pp. 23, 120).

[72] ATLAS Collaboration, *Measurement of the high-mass Drell-Yan differential cross-section in pp collisions at $\sqrt{s} = 7\,TeV$ with the ATLAS detector*,
Phys. Lett. B **725** (2013) 223, arXiv: `1305.4192` `[hep-ex]` (cit. on p. 23).

[73] ATLAS Collaboration, *Measurement of the double-differential high-mass Drell-Yan cross section in pp collisions at $\sqrt{s} = 8\,TeV$ with the ATLAS detector*,
JHEP **08** (2016) 009, arXiv: `1606.01736` `[hep-ex]` (cit. on p. 23).

[74] Magnar Bugge et. al.,
Search for new particles in the charged lepton plus missing transverse energy final state using pp collisions at $\sqrt{s} = 13\,TeV$ in the ATLAS detector,
tech. rep. ATL-COM-PHYS-2016-1405, CERN, 2016,
URL: `https://cds.cern.ch/record/2217650` (cit. on pp. 23, 82).

[75] ATLAS Collaboration, *Search for a heavy charged boson in events with a charged lepton and missing transverse momentum from pp collisions at $\sqrt{s} = 13\,TeV$ with the ATLAS detector*, Phys. Rev. D **100** (2019) 052013,
arXiv: `1906.05609` `[hep-ex]` (cit. on pp. 23, 24).

[76] F. D. Aaron et al., *Combined measurement and QCD analysis of the inclusive ep scattering cross sections at HERA*, Journal of High Energy Physics **2010** (2010),
ISSN: 1029-8479, URL: `http://dx.doi.org/10.1007/JHEP01(2010)109`
(cit. on p. 24).

[77] F. Schroeder, *Measurement of the charged-current Drell-Yan single- and double-differential cross-sections at high transverse masses at $\sqrt{s} = 13\,TeV$ with the ATLAS detector*, Presented 15-07-2022, Wuppertal U., 2022,
URL: `https://cds.cern.ch/record/2825779` (cit. on pp. 24, 26, 52, 98).

[78] I. Brivio and M. Trott, *The standard model as an effective field theory*,
      Physics Reports **793** (2019) 1, ISSN: 0370-1573,
      URL: http://dx.doi.org/10.1016/j.physrep.2018.11.002 (cit. on p. 25).

[79] I. Brivio, Y. Jiang and M. Trott, *The SMEFTsim package, theory and tools*,
      Journal of High Energy Physics **2017** (2017), ISSN: 1029-8479,
      URL: http://dx.doi.org/10.1007/JHEP12(2017)070 (cit. on p. 25).

[80] B. Grzadkowski, M. Iskrzyński, M. Misiak and J. Rosiek,
      Dimension-six terms in the Standard Model Lagrangian,
      Journal of High Energy Physics **2010** (2010), ISSN: 1029-8479,
      URL: http://dx.doi.org/10.1007/JHEP10(2010)085 (cit. on p. 25).

[81] M. Madigan, *Effective Field Theories for Physics Beyond the Standard Model*,
      PhD thesis: Apollo - University of Cambridge Repository, 2021,
      URL: https://www.repository.cam.ac.uk/handle/1810/331575
      (cit. on p. 26).

[82] F. Abe et al., *A Direct measurement of the W boson width*,
      Phys. Rev. Lett. **74** (1995) 341 (cit. on p. 26).

[83] J. Smith, W. L. van Neerven and J. A. M. Vermaseren,
      The Transverse Mass and Width of the W Boson,
      Phys. Rev. Lett. **50** (1983) 1738 (cit. on p. 26).

[84] F. Ellinghaus et al., *Charged-current Drell-Yan cross sections at high transverse
      masses in pp collisions at $\sqrt{s} = 13\ TeV$*, tech. rep., CERN, 2020,
      URL: https://cds.cern.ch/record/2711872
      (cit. on pp. 26, 58, 82, 120, 145, 163).

[85] T. F. Beumker, *Analysis of a combined measurement of $W^{\pm} \to \ell^{\pm}\nu(\ell = e, \mu)$
      cross section differential in m_T^W and $m_T^W \otimes |\eta|$ at high transverse masses at
      $\sqrt{s} = 13\ TeV$ with the ATLAS detector*, Bergische Universität Wuppertal, 2023
      (cit. on pp. 26, 50).

[86] *LHC Machine*, JINST **3** (2008) S08001, ed. by L. Evans and P. Bryant
      (cit. on p. 27).

[87] *LEP design report*, Report,
      Copies shelved as reports in LEP, PS and SPS libraries, Geneva: CERN, 1984,
      URL: https://cds.cern.ch/record/102083 (cit. on p. 27).

[88] ATLAS Collaboration,
      The ATLAS Experiment at the CERN Large Hadron Collider,
      JINST **3** (2008) S08003 (cit. on pp. 27, 29, 32).

[89] CMS Collaboration, *The CMS Experiment at the CERN LHC*,
      JINST **3** (2008) S08004 (cit. on p. 27).

[90] LHCb Collaboration, *The LHCb Detector at the LHC*, JINST **3** (2008) S08005
      (cit. on p. 27).

[91] ALICE Collaboration, *The ALICE experiment at the CERN LHC*,
      JINST **3** (2008) S08002 (cit. on p. 27).

[92] P. Mouche, *Overall view of the LHC. Vue d'ensemble du LHC*,
      (2014), General Photo, URL: `https://cds.cern.ch/record/1708847`
      (cit. on p. 28).

[93] E. Mobs, *The CERN accelerator complex - August 2018. Complexe des
      accélérateurs du CERN - Août 2018*, (2018), General Photo,
      URL: `https://cds.cern.ch/record/2636343` (cit. on p. 28).

[94] ATLAS Collaboration, *ATLAS Luminosity - Public Results*, 2018,
      URL: `https://twiki.cern.ch/twiki/bin/view/AtlasPublic/`
      `LuminosityPublicResultsRun2` (cit. on pp. 29, 39).

[95] B. Salvachua, *Overview of Proton-Proton Physics during Run 2*, (2019) 7,
      URL: `https://cds.cern.ch/record/2750272` (cit. on p. 29).

[96] J. Pequenao, *Computer generated image of the whole ATLAS detector*, (2008),
      URL: `https://cds.cern.ch/record/1095924` (cit. on p. 30).

[97] ATLAS Collaboration,
      Event Displays from Run 2 physics analyses not included in publications, 2018,
      URL: `hhttps:`
      `//twiki.cern.ch/twiki/bin/view/AtlasPublic/EventDisplayRun2Physics`
      (cit. on p. 31).

[98] *ATLAS magnet system: Technical Design Report, 1*,
      Technical design report. ATLAS, Geneva: CERN, 1997,
      URL: `https://cds.cern.ch/record/338080` (cit. on p. 31).

[99] ATLAS Magnet Group, *ATLAS Magnet System*,
      URL: `http://atlas-magnet-dfs.web.cern.ch/` (cit. on p. 32).

[100] *ATLAS muon spectrometer: Technical Design Report*,
      Technical Design Report ATLAS, Geneva: CERN, 1997,
      URL: `https://cds.cern.ch/record/331068` (cit. on pp. 32, 35–37, 50).

[101] ATLAS Collaboration,
      ATLAS Inner Detector: Technical Design Report, Volume 1,
      ATLAS-TDR-4; CERN-LHCC-97-016, 1997,
      URL: `https://cds.cern.ch/record/331063` (cit. on pp. 33, 49).

[102] ATLAS Collaboration,
      ATLAS Inner Detector: Technical Design Report, Volume 2,
      ATLAS-TDR-5, CERN-LHCC-97-017, 1997,
      URL: `https://cds.cern.ch/record/331064` (cit. on p. 33).

[103] B. Abbott et al., *Production and integration of the ATLAS Insertable B-Layer*,
      JINST **13** (2018) T05008, arXiv: `1803.00844` `[physics.ins-det]`
      (cit. on p. 33).

[104]   ATLAS Collaboration,
ATLAS Calorimeter Performance: Technical Design Report,
ATLAS-TDR-1; CERN-LHCC-96-040, 1996,
URL: https://cds.cern.ch/record/331059 (cit. on p. 34).

[105]   ATLAS Collaboration,
ATLAS Liquid Argon Calorimeter: Technical Design Report,
ATLAS-TDR-2; CERN-LHCC-96-041, 1996,
URL: https://cds.cern.ch/record/331061 (cit. on p. 34).

[106]   ATLAS Collaboration, *ATLAS Tile Calorimeter: Technical Design Report,*
ATLAS-TDR-3; CERN-LHCC-96-042, 1996,
URL: https://cds.cern.ch/record/331062 (cit. on p. 34).

[107]   ATLAS Collaboration, *Jet energy scale and resolution measured in
proton–proton collisions at $\sqrt{s} = 13\,TeV$ with the ATLAS detector,*
Eur. Phys. J. C **81** (2020) 689, arXiv: 2007.02645 [hep-ex]
(cit. on pp. 35, 53, 54, 114).

[108]   ATLAS Collaboration, *Performance of the ATLAS muon triggers in Run 2,*
JINST **15** (2020) P09015, arXiv: 2004.13447 [physics.ins-det]
(cit. on pp. 37, 51).

[109]   ATLAS Collaboration, *Luminosity determination in pp collisions at $\sqrt{s} = 8\,TeV$
using the ATLAS detector at the LHC,* Eur. Phys. J. C **76** (2016) 653,
arXiv: 1608.03953 [hep-ex] (cit. on p. 38).

[110]   ATLAS Collaboration, *Luminosity determination in pp collisions at
$\sqrt{s} = 13\,TeV$ using the ATLAS detector at the LHC,*
Eur. Phys. J. C **83** (2023) 982, arXiv: 2212.09379 [hep-ex]
(cit. on pp. 38, 118).

[111]   G. Avoni et. al., *The new LUCID-2 detector for luminosity measurement and
monitoring in ATLAS,* Journal of Instrumentation **13** (2018) P07017
(cit. on p. 38).

[112]   S. van der Meer, *Calibration of the effective beam height in the ISR,* tech. rep.,
CERN, 1968 (cit. on p. 38).

[113]   xxx, *Luminosity determination in pp collisions at $\sqrt{s} = 13\,TeV$ using the
ATLAS detector at the LHC,* The European Physical Journal C **83** (2023),
ISSN: 1434-6052,
URL: http://dx.doi.org/10.1140/epjc/s10052-023-11747-w (cit. on p. 39).

[114]   L. A. Harland-Lang, A. D. Martin, P. Motylinski and R. S. Thorne,
Parton distributions in the LHC era: MMHT 2014 PDFs,
Eur. Phys. J. C **75** (2015) 204, arXiv: 1412.3989 [hep-ph] (cit. on p. 40).

[115]   The NNPDF Collaboration, R. D. Ball et al.,
Parton distributions for the LHC run II, JHEP **04** (2015) 040,
arXiv: 1410.8849 [hep-ph] (cit. on pp. 40, 43, 119).

[116] J. Pumplin et al., *New Generation of Parton Distributions with Uncertainties from Global QCD Analysis*, JHEP **07** (2002) 012, arXiv: `hep-ph/0201195` (cit. on p. 40).

[117] P. Nason,
A new method for combining NLO QCD with shower Monte Carlo algorithms,
JHEP **11** (2004) 040, arXiv: `hep-ph/0409146` (cit. on pp. 40, 42).

[118] S. Frixione, P. Nason and C. Oleari, *Matching NLO QCD computations with parton shower simulations: the POWHEG method*, JHEP **11** (2007) 070,
arXiv: `0709.2092 [hep-ph]` (cit. on pp. 40, 42).

[119] S. Alioli, P. Nason, C. Oleari and E. Re, *A general framework for implementing NLO calculations in shower Monte Carlo programs: the POWHEG BOX*,
JHEP **06** (2010) 043, arXiv: `1002.2581 [hep-ph]` (cit. on pp. 40, 42).

[120] S. Alioli, P. Nason, C. Oleari and E. Re,
NLO vector-boson production matched with shower in POWHEG,
JHEP **07** (2008) 060, arXiv: `0805.4802 [hep-ph]` (cit. on pp. 40, 42).

[121] J. Alwall et al.,
The automated computation of tree-level and next-to-leading order differential cross sections, and their matching to parton shower simulations,
JHEP **07** (2014) 079, arXiv: `1405.0301 [hep-ph]` (cit. on p. 40).

[122] T. Gleisberg et al., *Event generation with SHERPA 1.1*, JHEP **02** (2009) 007,
arXiv: `0811.4622 [hep-ph]` (cit. on pp. 40, 43).

[123] C. Bierlich et al.,
A comprehensive guide to the physics and usage of PYTHIA 8.3, 2022,
arXiv: `2203.11601 [hep-ph]` (cit. on p. 40).

[124] L. Lönnblad and S. Prestel,
Matching tree-level matrix elements with interleaved showers,
JHEP **03** (2012) 019, arXiv: `1109.4829 [hep-ph]` (cit. on p. 40).

[125] S. Frixione, P. Nason and B. R. Webber,
Matching NLO QCD and parton showers in heavy flavour production,
JHEP **08** (2003) 007, arXiv: `hep-ph/0305252` (cit. on p. 40).

[126] R. Frederix and S. Frixione, *Merging meets matching in MC@NLO*,
JHEP **12** (2012) 061, arXiv: `1209.6215 [hep-ph]` (cit. on p. 40).

[127] K. Hamilton, P. Nason, C. Oleari and G. Zanderighi, *Merging H/W/Z + 0 and 1 jet at NLO with no merging scale: a path to parton shower + NNLO matching*,
JHEP **05** (2013) 082, arXiv: `1212.4504 [hep-ph]` (cit. on p. 40).

[128] T. Sjöstrand,
Jet fragmentation of multiparton configurations in a string framework,
Nucl. Phys. B **248** (1984) 469 (cit. on p. 41).

[129] T. Sjöstrand et al., *An introduction to PYTHIA 8.2*,
Comput. Phys. Commun. **191** (2015) 159, arXiv: `1410.3012` `[hep-ph]`
(cit. on p. 41).

[130] A. Kupco, *Cluster Hadronization in HERWIG 5.9*, 1999,
arXiv: `hep-ph/9906412` `[hep-ph]` (cit. on p. 41).

[131] J. Bellm et al., *Herwig 7.0/Herwig++ 3.0 release note*,
Eur. Phys. J. C **76** (2016) 196, arXiv: `1512.01178` `[hep-ph]` (cit. on p. 41).

[132] T. Sjöstrand, S. Mrenna and P. Skands, *A brief introduction to PYTHIA 8.1*,
Comput. Phys. Commun. **178** (2008) 852, arXiv: `0710.3820` `[hep-ph]`
(cit. on pp. 41, 42).

[133] ATLAS Collaboration,
*The Pythia 8 A3 tune description of ATLAS minimum bias and inelastic
measurements incorporating the Donnachie–Landshoff diffractive model*,
ATL-PHYS-PUB-2016-017, 2016,
URL: `https://cds.cern.ch/record/2206965` (cit. on p. 41).

[134] NNPDF Collaboration, R. D. Ball et al., *Parton distributions with LHC data*,
Nucl. Phys. B **867** (2013) 244, arXiv: `1207.1303` `[hep-ph]` (cit. on p. 41).

[135] S. Agostinelli et al., *Geant4 – a simulation toolkit*,
Nucl. Instrum. Meth. A **506** (2003) 250 (cit. on p. 41).

[136] *PAVER webpage*, URL: `https://jem.cern.ch` (cit. on p. 41).

[137] *Monte Carlo Validation in ATLAS with PAVER*, tech. rep., CERN, 2024,
URL: `http://cds.cern.ch/record/2904943` (cit. on p. 41).

[138] H.-L. Lai et al., *New parton distributions for collider physics*,
Phys. Rev. D **82** (2010) 074024, arXiv: `1007.2241` `[hep-ph]` (cit. on p. 42).

[139] ATLAS Collaboration, *Measurement of the Z/γ^* boson transverse momentum
distribution in pp collisions at $\sqrt{s} = 7$ TeV with the ATLAS detector*,
JHEP **09** (2014) 145, arXiv: `1406.3660` `[hep-ex]` (cit. on p. 42).

[140] P. Golonka and Z. Was,
PHOTOS Monte Carlo: a precision tool for QED corrections in Z and W decays,
Eur. Phys. J. C **45** (2006) 97, arXiv: `hep-ph/0506026` (cit. on p. 42).

[141] N. Davidson, T. Przedzinski and Z. Was,
PHOTOS Interface in C++: Technical and physics documentation,
Comput. Phys. Commun. **199** (2016) 86, arXiv: `1011.0937` `[hep-ph]`
(cit. on p. 42).

[142] J. Butterworth et al., *Les Houches 2013: Physics at TeV Colliders: Standard
Model Working Group Report*, 2014, arXiv: `1405.1067` `[hep-ph]` (cit. on p. 42).

[143] C. Anastasiou, L. Dixon, K. Melnikov and F. Petriello,
*High-precision QCD at hadron colliders: Electroweak gauge boson rapidity
distributions at next-to-next-to leading order*, Physical Review D **69** (2004),
ISSN: 1550-2368, URL: `http://dx.doi.org/10.1103/PhysRevD.69.094008`
(cit. on p. 42).

[144] S. Dulat et al., *New parton distribution functions from a global analysis of
quantum chromodynamics*, Physical Review D **93** (2016), ISSN: 2470-0029,
URL: `http://dx.doi.org/10.1103/PhysRevD.93.033006` (cit. on p. 42).

[145] A. Arbuzov et al., *Update of the MCSANC Monte Carlo integrator, v. 1.20*,
JETP Letters **103** (2016) 131, ISSN: 1090-6487,
URL: `http://dx.doi.org/10.1134/S0021364016020041` (cit. on p. 42).

[146] *Inclusive $W^{\pm}$ and Z^0 cross sections at next-to-next-to leading order QCD for the
ATLAS experiment*, tech. rep.,
All figures including auxiliary figures are available at
https://atlas.web.cern.ch/Atlas/GROUPS/PHYSICS/PUBNOTES/ATL-
PHYS-PUB-2023-026: CERN, 2023,
URL: `https://cds.cern.ch/record/2871755` (cit. on p. 43).

[147] E. Re, *Single-top Wt-channel production matched with parton showers using the
POWHEG method*, Eur. Phys. J. C **71** (2011) 1547, arXiv: `1009.2450 [hep-ph]`
(cit. on pp. 43, 120).

[148] M. Czakon and A. Mitov, *Top++: A Program for the Calculation of the
Top-Pair Cross-Section at Hadron Colliders*,
Comput. Phys. Commun. **185** (2014) 2930, arXiv: `1112.5675 [hep-ph]`
(cit. on p. 43).

[149] *ATLAS Tracking Software Tutorial*, URL:
https://atlassoftwaredocs.web.cern.ch/trackingTutorial/idoverview/
(cit. on p. 46).

[150] ATLAS Collaboration, *Reconstruction of primary vertices at the ATLAS
experiment in Run 1 proton–proton collisions at the LHC*,
Eur. Phys. J. C **77** (2017) 332, arXiv: `1611.10235 [hep-ex]` (cit. on p. 46).

[151] J. Illingworth and J. Kittler, *A survey of the hough transform*,
Computer Vision, Graphics, and Image Processing **44** (1988) 87 (cit. on p. 47).

[152] ATLAS Collaboration, *Muon reconstruction and identification efficiency in
ATLAS using the full Run 2 pp collision data set at $\sqrt{s} = 13\,TeV$*,
Eur. Phys. J. C **81** (2021) 578, arXiv: `2012.00578 [hep-ex]`
(cit. on pp. 47, 48, 51).

[153] J. W. Kraus, *Measurement of the differential $W \rightarrow \mu + \nu$ cross section at high
transverse masses at $\sqrt{s} = 13\,TeV$ with the ATLAS detector*,
Presented 24 Nov 2020, Wuppertal U., 2020,
URL: `https://cds.cern.ch/record/2753249` (cit. on pp. 48, 60, 61, 65, 77).

[154] ATLAS Collaboration, *Muon reconstruction performance of the ATLAS detector in proton–proton collision data at $\sqrt{s} = 13\,TeV$*, Eur. Phys. J. C **76** (2016) 292, arXiv: 1603.05598 [hep-ex] (cit. on pp. 49, 51, 58).

[155] ATLAS Collaboration, *Studies of the muon momentum calibration and performance of the ATLAS detector with pp collisions at $\sqrt{s} = 13\,TeV$*, Eur. Phys. J. C **83** (2022) 686, arXiv: 2212.07338 [hep-ex] (cit. on p. 49).

[156] *Performance of the muon spectrometer alignment in 2017 and 2018 data*, tech. rep., All figures including auxiliary figures are available at https://atlas.web.cern.ch/Atlas/GROUPS/PHYSICS/PUBNOTES/ATL-MUON-PUB-2021-002: CERN, 2021, URL: https://cds.cern.ch/record/2753329 (cit. on p. 49).

[157] ATLAS Collaboration, *Alignment of the ATLAS Inner Detector in Run 2*, Eur. Phys. J. C **80** (2020) 1194, arXiv: 2007.07624 [hep-ex] (cit. on p. 50).

[158] *MCPAnalysisGuidelinesMC16.* URL: https://twiki.cern.ch/twiki/bin/viewauth/AtlasProtected/MCPAnalysisGuidelinesMC16 (cit. on p. 50).

[159] ATLAS Collaboration, *Electron reconstruction and identification in the ATLAS experiment using the 2015 and 2016 LHC proton–proton collision data at $\sqrt{s} = 13\,TeV$*, Eur. Phys. J. C **79** (2019) 639, arXiv: 1902.04655 [physics.ins-det] (cit. on p. 52).

[160] ATLAS Collaboration, *Jet reconstruction and performance using particle flow with the ATLAS Detector*, Eur. Phys. J. C **77** (2017) 466, arXiv: 1703.10485 [hep-ex] (cit. on p. 53).

[161] M. Cacciari, G. P. Salam and G. Soyez, *The anti-k_t jet clustering algorithm*, JHEP **04** (2008) 063, arXiv: 0802.1189 [hep-ph] (cit. on p. 53).

[162] M. Cacciari, G. P. Salam and G. Soyez, *FastJet user manual*, Eur. Phys. J. C **72** (2012) 1896, arXiv: 1111.6097 [hep-ph] (cit. on p. 53).

[163] M. E. Geyik, *Search for flavour-changing neutral-current couplings between the top quark and Higgs boson in multilepton final states with the ATLAS experiment*, Presented 24 Jun 2024, Wuppertal U., 2024, URL: https://cds.cern.ch/record/2902398 (cit. on p. 54).

[164] ATLAS Collaboration, *Expected performance of missing transverse momentum reconstruction for the ATLAS detector at $\sqrt{s} = 13\,TeV$*, tech. rep. ATL-PHYS-PUB-2015-023, CERN, 2015, URL: https://cds.cern.ch/record/2037700 (cit. on pp. 55, 114).

[165] M. Cacciari, G. P. Salam and G. Soyez, *The catchment area of jets*, Journal of High Energy Physics **2008** (2008) 005, ISSN: 1029-8479, URL: http://dx.doi.org/10.1088/1126-6708/2008/04/005 (cit. on p. 56).

[166]   *Truth Classification*, URL: `https://gitlab.cern.ch/atlas/athena/-`
`/tree/21.2/PhysicsAnalysis/AnalysisCommon/TruthClassification`
(cit. on p. 66).

[167]   G. Cowan, *Statistical data analysis*, 1998, ISBN: 978-0-19-850156-5
(cit. on p. 90).

[168]   G. D'Agostini, *A multidimensional unfolding method based on Bayes' theorem*,
Nuclear Instruments and Methods in Physics Research Section A: Accelerators,
Spectrometers, Detectors and Associated Equipment **362** (1995) 487,
ISSN: 0168-9002 (cit. on p. 91).

[169]   T. Adye, 'Unfolding algorithms and tests using RooUnfold', *PHYSTAT 2011*,
Geneva: CERN, 2011 313, arXiv: `1105.1160` `[physics.data-an]`
(cit. on p. 91).

[170]   Schmitt, Stefan, *Data Unfolding Methods in High Energy Physics*,
EPJ Web Conf. **137** (2017) 11008,
URL: `https://doi.org/10.1051/epjconf/201713711008` (cit. on p. 98).

[171]   *Bootstrap Generator*, URL: `https://gitlab.cern.ch/atlas-physics/sm/`
`StandardModelTools_BootstrapGenerator/BootstrapGenerator`
(cit. on p. 107).

[172]   *TH1 Class Reference - Smooth*, URL: `https://root.cern.ch/doc/master/`
`classTH1.html#a0d08651c37b622f4bcc0e1a0affefb33` (cit. on p. 112).

[173]   *Proceedings of the 1974 CERN School of Computing: Godøysund, Norway 11 -
24 Aug 1974. 3rd CERN School of Computing*, CERN, Geneva: CERN, 1974,
URL: `https://cds.cern.ch/record/186223` (cit. on p. 112).

[174]   *StandardModelUnfoldingNew*, URL: `https://twiki.cern.ch/twiki/bin/`
`viewauth/AtlasProtected/StandardModelUnfoldingNew` (cit. on p. 118).

[175]   S. Höche, S. Mrenna, S. Payne, C. T. Preuss and P. Skands,
A Study of QCD Radiation in VBF Higgs Production with Vincia and Pythia,
SciPost Phys. **12** (2022) 010, arXiv: `2106.10987` `[hep-ph]` (cit. on p. 119).

[176]   ATLAS Collaboration, *ATLAS Pythia 8 tunes to 7 TeV data*,
ATL-PHYS-PUB-2014-021, 2014,
URL: `https://cds.cern.ch/record/1966419` (cit. on p. 119).

[177]   S. Frixione, E. Laenen, P. Motylinski, C. White and B. R. Webber,
Single-top hadroproduction in association with a W boson, JHEP **07** (2008) 029,
arXiv: `0805.3067` `[hep-ph]` (cit. on p. 120).

[178]   *Multi-Boson Simulation for 13 TeV ATLAS Analyses*, tech. rep.,
All figures including auxiliary figures are available at
https://atlas.web.cern.ch/Atlas/GROUPS/PHYSICS/PUBNOTES/ATL-
PHYS-PUB-2016-002: CERN, 2016,
URL: `https://cds.cern.ch/record/2119986` (cit. on p. 120).

[179]   N. Kidonakis and N. Yamanaka,
        Higher-order corrections for tW production at high-energy hadron colliders,
        JHEP **05** (2021) 278, arXiv: 2102.11300 [hep-ph] (cit. on p. 120).

[180]   Heraverager developers, *Heraverager*, 2016 (cit. on p. 145).

[181]   S. Camarda et al., *DYTurbo: fast predictions for Drell–Yan processes*,
        The European Physical Journal C **80** (2020), ISSN: 1434-6052,
        URL: http://dx.doi.org/10.1140/epjc/s10052-020-7757-5 (cit. on p. 152).

[182]   U. Klein, *Vrap13TeV*, URL: https://hep.ph.liv.ac.uk/~uklein/Vrap13TeV/
        (cit. on p. 157).

[183]   J. Inglis, *private communication*, 2024 (cit. on p. 158).

Acknowledgements

I associate precious memories with the last few years, be it in the form of discussions about multijet or unfolding, interesting travels or exciting Kicker matches. I have grown a lot as a person and learned a lot, for which I am forever grateful.
It would not be an exaggeration to say that this dissertation would not exist without the support of my wonderful fellow human beings.

First of all, I would like to express my deepest gratitude to PD Dr. Frank Ellinghaus. You had an incredible impact on me, both personally and academically. You sparked my interest in experimental particle physics in EP3+4, and were the one to 'lure' me into the ATLAS group. After supervising my master thesis, you played a significant role in convincing me to do the PhD in the first place (which turned out to be a great decision, thank you). Throughout all this time, you supported me in the best way I could imagine. I am extremely grateful for your guidance, inspiration and commitment, our endless discussion sessions and for shaping my critical thinking (even if your attention to detail sometimes made finishing this dissertation difficult). I always enjoyed our conversations, be it in the form of late-night multijet brain storming or about metal bands and recent football results.

I would also like to thank Prof. Eram Rizvi, not only for agreeing to act as my dissertation's second referee, but also for being a constant source of inspiring and remarkably kind, constructive and goal-oriented ideas and feedback in our weekly high-m_T^W meetings. Additionally, I would like to thank Prof. Kampert and Prof. Knetchli for being part of my examination committee. I know that this is a lot of work and I appreciate your commitment to supporting me on my way to becoming a doctor.

A big thank you goes to all the members of the high-m_T^W team. Our weekly meetings have been extremely fruitful, and the work presented in this dissertation would be nowhere near as polished and nuanced without your support and feedback. Over the past five years, I have learned so much and have greatly appreciated the discussions and critical thinking in the group.

I would also like to thank the ATLAS group at the BUW, starting with Wolfgang and Dominic for their help, inspiration and feedback. My millions of data and MC events would like to express their gratitude to the cluster team: Ralf, Marisa, Torsten and Martin. Thank you to everyone I've had the pleasure of working with, past and present, which is a bunch of incredibly smart and helpful people: Marvin, Oliver, Joshua,